



HAL
open science

Analyse et modélisation de l'interaction entre thermique et turbulence dans les récepteurs solaires à haute température.

Dorian Dupuy

► **To cite this version:**

Dorian Dupuy. Analyse et modélisation de l'interaction entre thermique et turbulence dans les récepteurs solaires à haute température.. Autre. Université de Perpignan, 2018. Français. NNT : 2018PERP0038 . tel-01963569

HAL Id: tel-01963569

<https://theses.hal.science/tel-01963569>

Submitted on 21 Dec 2018

HAL is a multi-disciplinary open access archive for the deposit and dissemination of scientific research documents, whether they are published or not. The documents may come from teaching and research institutions in France or abroad, or from public or private research centers.

L'archive ouverte pluridisciplinaire **HAL**, est destinée au dépôt et à la diffusion de documents scientifiques de niveau recherche, publiés ou non, émanant des établissements d'enseignement et de recherche français ou étrangers, des laboratoires publics ou privés.

THÈSE

Pour obtenir le grade de
Docteur

Délivré par
UNIVERSITE DE PERPIGNAN VIA DOMITIA

Préparée au sein de l'école doctorale 305 :
Énergie et Environnement
Et de l'unité de recherche PROMES-CNRS (UPR 8521)

Spécialité : **Sciences de l'ingénieur**

Présentée par **Dorian Dupuy**

**ANALYSE ET MODÉLISATION DE L'INTERACTION
ENTRE THERMIQUE ET TURBULENCE DANS LES
RÉCEPTEURS SOLAIRES À HAUTE TEMPÉRATURE**

Soutenue le 27 novembre 2018 devant le jury composé de

M. Abdellah HADJADJ, PR, CORIA
M. Pierre SAGAUT, PR, M2P2
M. Gilles FLAMANT, DR, PROMES
M. Jacques MAGNAUDET, DR, IMFT
Mme Françoise BATAILLE, PR, PROMES
M. Adrien TOUTANT, MCF-HDR, PROMES

Rapporteur
Rapporteur
Examineur
Examineur
Directeur de thèse
Directeur de thèse

**Analysis and modelling of the interaction
between heat and turbulence in high-temperature
solar receivers**

**Analyse et modélisation de l'interaction entre
thermique et turbulence dans les récepteurs solaires à
haute température**

Résumé en français

1 Introduction

Confronté à ses impacts environnementaux, le secteur de l'énergie doit s'engager dans une transformation complète. Les énergies renouvelables ont un rôle décisif à jouer parce qu'elles émettent moins de gaz à effet de serre que les combustibles fossiles. Parmi les énergies renouvelables, l'utilisation de l'énergie solaire dispose d'un fort potentiel de croissance. Il existe actuellement deux technologies principales pour produire de l'électricité à partir de l'énergie solaire : le solaire photovoltaïque et le solaire thermodynamique. Si la technologie photovoltaïque est aujourd'hui prédominante, le solaire thermodynamique peut facilement être couplé à un stockage d'énergie thermique pour une production d'énergie plus flexible.

Dans les centrales solaires thermodynamiques à tour, un champ d'héliostats concentre le rayonnement solaire vers un récepteur fixe placé au sommet d'une tour. Dans le récepteur solaire circule un fluide qui, chauffé, alimente une turbine et produit de l'électricité. Les centrales solaires à tour permettent d'atteindre des températures importantes (supérieures à 1000 K) pour des cycles thermodynamiques à haut rendement. Le récepteur solaire est un composant essentiel des centrales solaires à tour puisqu'il est responsable du transfert d'énergie entre le flux solaire concentré et le fluide. L'amélioration du transfert de chaleur dans les récepteurs solaires à haute température est l'un des principaux domaines de recherche du laboratoire PROMES. Pour assurer un échange efficace, un niveau de turbulence élevé est nécessaire. L'écoulement est également soumis à un gradient de température intense car il ne reçoit le flux solaire que sur une seule face. Le gradient de température et la turbulence s'influencent l'un l'autre dans une interaction complexe. Ce couplage est caractéristique des écoulements turbulents fortement anisothermes présents dans les récepteurs solaires.

L'optimisation du récepteur solaire exige une meilleure compréhension et modélisation de l'interaction entre la température et la turbulence. Cette thèse cherche à y contribuer selon deux approches. Une première partie étudie les échanges énergétiques entre les différentes parties de l'énergie totale et en particulier ceux associés à l'énergie cinétique turbulente. Les résultats caractérisent l'effet du gradient de température sur les échanges énergétiques. Une deuxième partie étudie la modélisation de type simulation des grandes échelles (SGE) adaptée aux écoulements présents dans les récepteurs solaires. Les modèles devraient permettre de développer des simulations numériques de l'écoulement dans le récepteur solaire, ouvrant ainsi la voie à son optimisation. Dans les deux cas, l'étude est fondée sur l'analyse numérique de l'écoulement dans un canal plan turbulent fortement anisotherme. Cette géométrie simplifiée reproduit les

caractéristiques distinctives des écoulements présents dans les récepteurs solaires. En particulier, une grande partie du travail repose sur la simulation numérique directe (SND) du canal.

La section 2 introduit les paramètres physiques et numériques utilisés dans le reste de l'étude et décrit les simulations numériques directes. La section 3 présente l'étude des échanges énergétiques. La section 4 traite de la simulation des grandes échelles des écoulements turbulents fortement anisothermes.

2 Cadre physique et numérique

Pour étudier l'effet du gradient de température dans les écoulements fortement anisothermes, on modélise le récepteur solaire par un canal plan turbulent fortement anisotherme. Cette section décrit la configuration géométrique du canal et la méthode numérique utilisée pour les simulations. Avant cela, les choix faits en termes de modélisation physique sont présentés.

2.1 Cadre physique

Les écoulements présents dans les récepteurs solaires à haute température sont turbulents et fortement anisothermes, mais la vitesse du fluide est généralement faible par rapport à la vitesse du son (nombre de Mach inférieur à 10^{-2}). Cette configuration physique particulière permet de simplifier la description du mouvement des fluides. En effet, les effets purement compressibles caractéristiques des écoulements à grande vitesse, tels les ondes acoustiques, peuvent être négligés. On utilise pour cela les équations de bas nombre de Mach [219]. On considère de plus que le fluide se comporte comme un gaz parfait à la température et à la pression de fonctionnement du récepteur solaire. Dans ces conditions les équations de bas nombre de Mach peuvent être formulées de la manière suivante :

- Conservation de la masse

$$\frac{\partial \rho}{\partial t} + \frac{\partial \rho U_j}{\partial x_j} = 0, \quad (1)$$

- Conservation de la quantité de mouvement

$$\frac{\partial \rho U_i}{\partial t} = -\frac{\partial \rho U_j U_i}{\partial x_j} - \frac{\partial P}{\partial x_i} + \frac{\partial \Sigma_{ij}(\mathbf{U}, T)}{\partial x_j}, \quad (2)$$

- Conservation de l'énergie

$$\frac{\partial U_j}{\partial x_j} = -\frac{1}{\gamma P_0} \left[(\gamma - 1) \frac{\partial Q_j(T)}{\partial x_j} + \frac{\partial P_0}{\partial t} \right], \quad (3)$$

- Loi des gaz parfaits

$$T = \frac{P_0}{\rho r}, \quad (4)$$

où ρ est la masse volumique, T la température, t le temps et U_k la vitesse du fluide dans la direction de la coordonnée cartésienne d'espace x_k . La notation indicielle suit la convention de sommation d'Einstein et δ_{ij} représente le symbole de Kronecker. La pression est séparée en deux termes : la pression thermodynamique P_0 , constante dans l'espace, qui représente la pression moyenne dans le domaine et la pression mécanique P , liée aux variations de quantité de mouvement et qui varie spatialement.

Les contraintes visqueuses sont déterminées en supposant le fluide newtonien avec l'hypothèse de Stokes,

$$\Sigma_{ij}(\mathbf{U}, T) = \mu(T) \left[\left(\frac{\partial U_i}{\partial x_j} + \frac{\partial U_j}{\partial x_i} \right) - \frac{2}{3} \frac{\partial U_k}{\partial x_k} \delta_{ij} \right], \quad (5)$$

où $\mu(T)$ est la viscosité dynamique. Le flux de chaleur conductif est donnée par la loi de Fourier,

$$Q_j(T) = -\lambda(T) \frac{\partial T}{\partial x_j}, \quad (6)$$

où $\lambda(T)$ est la conductivité thermique. Pour l'air, la constante spécifique des gaz parfaits est égale à $r = 287 \text{ J kg}^{-1} \text{ K}^{-1}$. Les variations de viscosité dynamique avec la température peuvent être modélisées par la loi de Sutherland [287], valide de 220 K à 1900 K [277],

$$\mu(T) = \mu_0 \left(\frac{T}{T_0} \right)^{\frac{3}{2}} \frac{T_0 + S_1}{T + S_1}, \quad (7)$$

avec $\mu_0 = 1,716 \cdot 10^{-5} \text{ Pa s}$, $S_1 = 110,4 \text{ K}$ et $T_0 = 273,15 \text{ K}$. En revanche, on néglige les variations des capacités thermiques isochore C_v et isobare C_p et du nombre de Prandtl Pr avec la température. Les variations de conductivité thermique peuvent ainsi être déterminées par $\lambda(T) = \mu(T)C_p/Pr$, avec $Pr = 0.76$ et $C_p = 1005 \text{ J kg}^{-1} \text{ K}^{-1}$.

2.2 Configuration de l'étude

En simulant numériquement les équations de bas nombre de Mach, on étudie un écoulement turbulent statistiquement établi dans un canal plan soumis à un fort gradient de température (figure 1). À des fins de validation et de comparaison, on considère également le canal dans le cas isotherme incompressible, c'est-à-dire sans gradient de

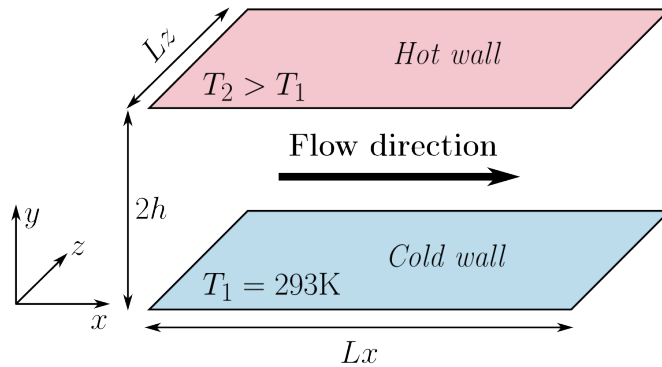


FIGURE 1 – Canal plan anisotherme bipériodique.

	Nombre de points $N_x \times N_y \times N_z$	Dimensions du domaine $L_x \times L_y \times L_z$	Tailles de mailles adimensionnées $\Delta_x^+ ; \Delta_y^+(0) - \Delta_y^+(h) ; \Delta_z^+$
DNS180-1	$384 \times 266 \times 384$	$4\pi h \times 2h \times 2\pi h$	5,8 ; 0,085 – 2,9 ; 2,9
DNS180-2	$384 \times 266 \times 384$	$4\pi h \times 2h \times 2\pi h$	8,5 ; 0,13 – 4,2 ; 4,2
DNS395-1	$768 \times 512 \times 512$	$4\pi h \times 2h \times (4/3)\pi h$	6,4 ; 0,18 – 2,9 ; 3,2
DNS395-2	$768 \times 512 \times 512$	$4\pi h \times 2h \times (4/3)\pi h$	9,1 ; 0,25 – 4,1 ; 4,6

TABLE 1 – Dimensions du domaine et tailles de mailles des simulations numériques directes.

température. Le canal est périodique dans les directions longitudinales (x) et transverses (z). Les parois du canal sont à température constante. Dans le canal isotherme, les deux parois sont à la température froide $T_1 = 293$ K. Dans le canal anisotherme, la température à la paroi froide ($y = 0$) est $T_1 = 293$ K et la température à la paroi chaude ($y = 2h$) est $T_2 = 586$ K. Cela crée un gradient de température dans la direction normale de la paroi. Comme le canal est périodique, l'action dissipatrice des contraintes de cisaillement n'est pas compensée par un gradient de pression dans la direction de l'écoulement. Une force volumique f est ajoutée pour reproduire l'effet d'un gradient de pression et maintenir un débit massique constant.

On a effectué des simulations numériques directes du canal isotherme et anisotherme aux nombres de Reynolds de frottement moyen $Re_\tau = 180$ et $Re_\tau = 395$. Ce nombre de Reynolds est défini comme la moyenne des nombres de Reynolds de frottement $Re_{\tau,\omega} = U_\tau h / \nu_\omega$ à la paroi froide et chaude, avec h la demi-hauteur du canal, ν_ω la viscosité cinématique à la paroi et $U_\tau = [\nu_\omega (\partial_y \bar{U}_x)_\omega]^{0.5}$ la vitesse de frottement. Les simulations utilisent un maillage uniforme dans les directions homogènes et suivant une loi en tangente hyperbolique dans la direction normale aux parois,

$$y_k = L_y \left(1 + \frac{1}{a} \tanh \left[\left(\frac{k-1}{N_y-1} - 1 \right) \tanh^{-1}(a) \right] \right), \quad (8)$$

avec a le paramètre de dilatation du maillage et N_y le nombre de points dans la direction normale aux parois. La taille du domaine et les tailles de mailles adimensionnées des différentes simulations sont données dans le tableau 1. Les simulations à $Re_\tau = 180$ et $Re_\tau = 395$ ont le même niveau de raffinement. Les petites différences sont dues aux contraintes de la méthode numérique (solveur multigrille) et du parallélisme.

Les simulations reposent sur la résolution numérique des équations de bas nombre de Mach par une méthode aux différences finies sur un maillage décalé [200, 212]. On utilise un schéma en temps Runge–Kutta d'ordre trois [313] et une discrétisation centrée d'ordre quatre pour la convection de la quantité de mouvement et d'ordre deux pour la diffusion. On utilise pour cela le code de calcul TrioCFD [38]. La méthode numérique est validée par une étude de convergence en maillage et la comparaison des résultats dans le cas de l'isotherme incompressible aux données de référence de Moser *et al.* [203], Vreman and Kuerten [305] et Lee and Moser [167] à $Re_\tau = 180$ et Moser *et al.* [203], Lee and Moser [167] à $Re_\tau = 395$.

3 Échanges énergétiques

Cette section présente l'étude des échanges énergétiques. La section 3.1 initie l'étude des échanges énergétiques par une discussion théorique de la décomposition sous-jacente de l'énergie totale. La section 3.2 examine l'effet du gradient de température sur les échanges énergétiques associés à l'énergie cinétique turbulente à partir des résultats des simulations numériques directes. La section 3.3 étend l'analyse à l'influence du nombre de Reynolds sur l'effet du gradient de température.

3.1 Équations des échanges énergétiques

L'étude des échanges énergétiques dans les écoulements turbulents fortement anisothermes requiert le choix d'une décomposition de l'énergie totale et des échanges énergétiques entre les différentes parties de l'énergie totale. En effet, étant donné les variations de masse volumique, la décomposition de l'énergie totale n'est pas unique et comporte une certaine part d'arbitraire [50]. Afin d'étudier les échanges énergétiques associés à l'énergie cinétique turbulente dans les domaines spatial et spectral, on établit une nouvelle représentation des échanges énergétiques entre les différentes parties de l'énergie totale fondée sur la moyenne classique ou moyenne de Reynolds (non pondérée par la masse volumique) [245]. Soit $(\overline{\quad})$ l'opérateur de moyenne statistique et (\prime) l'opérateur partie fluctuante. La décomposition de Reynolds de la vitesse $U_i = \overline{U}_i + u'_i$ conduit à une décomposition ternaire de l'énergie cinétique ρE ,

$$\rho E = \frac{1}{2} \rho U_i U_i = \rho \underline{E} + \rho e + \rho \underline{e}, \quad (9)$$

où $\rho \underline{E} = \frac{1}{2} \rho \overline{U}_i \overline{U}_i$ est l'énergie cinétique moyenne, liée au mouvement moyen, $\rho e = \frac{1}{2} \rho u'_i u'_i$ l'énergie cinétique turbulente, liée au mouvement turbulent, et $\rho \underline{e} = \rho u'_i \overline{U}_i$ l'énergie cinétique mixte, associée à la fois au mouvement moyen et au mouvement turbulent.

L'énergie totale instantanée par unité de volume est la somme des trois parties de l'énergie cinétique ρE et de l'énergie interne ρI . C'est une quantité conservative mais ces composants ne le sont pas et échangent de l'énergie entre eux. Les échanges énergétiques entre les quatre parties de l'énergie totale peuvent être formulés ainsi :

$$\frac{\partial \rho \underline{E}}{\partial t} = \underline{\Phi}^c + \underline{\Phi}^r + \overline{\mathcal{P}} + \overline{\mathcal{E}}, \quad (10)$$

$$\frac{\partial \rho e}{\partial t} = \underline{\varphi}^c + \overline{\varphi}^r + \overline{\mathcal{P}} + \overline{\mathcal{E}}, \quad (11)$$

$$\frac{\partial \rho \underline{e}}{\partial t} = \underline{\varphi}^c - \overline{\mathcal{P}} - \overline{\mathcal{E}}, \quad (12)$$

$$\frac{\partial \rho I}{\partial t} = \overline{\Phi}^{T,c} + \overline{\Phi}^\lambda - \overline{\mathcal{E}} - \overline{\mathcal{E}}, \quad (13)$$

où l'on identifie les termes suivants :

- les transferts par convection, représentant un transfert d'une partie de l'énergie cinétique par le mouvement du fluide : $\underline{\Phi}^c = -\partial_j(\rho U_j \underline{E})$ associé à l'énergie cinétique moyenne, $\underline{\varphi}^c = -\partial_j(\rho U_j e)$ associé à l'énergie cinétique turbulente,

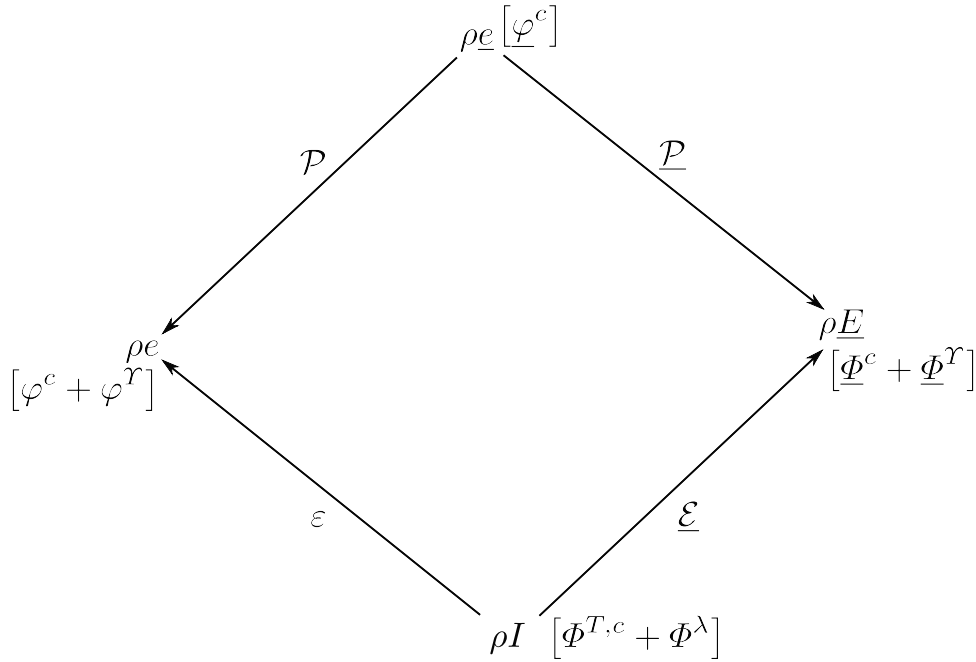


FIGURE 2 – Représentation schématique des échanges énergétiques entre les quatre parties de l'énergie totale dans la représentation ternaire. Une flèche indique une interaction entre deux quantités.

$\underline{\varphi}^c = -\partial_j(\rho U_j \underline{e})$ associé à l'énergie cinétique mixte et $\underline{\Phi}^{T,c} = -\partial_j(\rho U_j I)$ associé à l'énergie interne ;

- les transferts d'énergie liés aux contraintes totales $\mathcal{Y}_{ij} = \Sigma_{ij} - P\delta_{ij}$ (contraintes de pression et contraintes visqueuses) : $\underline{\Phi}^r = \partial_j(\mathcal{Y}_{ij} \bar{U}_i)$ associé à l'énergie cinétique moyenne et $\varphi^r = \partial_j(\mathcal{Y}_{ij} u'_i)$ associé à l'énergie cinétique turbulente ;
- le transfert d'énergie par conduction $\Phi^\lambda = \partial_j(\lambda \partial_j T)$;
- les interactions entre les différentes parties de l'énergie cinétique : l'interaction $\mathcal{P} = -\rho u'_i U_j \partial_j \bar{U}_i + \rho u'_i \bar{U}_j \partial_j \bar{U}_i - \rho u'_i (1/\rho) \partial_j \mathcal{Y}_{ij}$ entre l'énergie cinétique turbulente et l'énergie cinétique mixte et l'interaction $\underline{\mathcal{P}} = -\rho \bar{U}_i U_j \partial_j u'_i + \rho \bar{U}_i (U_j \partial_j U_i)' - \rho \bar{U}_i ((1/\rho) \partial_j \mathcal{Y}_{ij})'$ entre l'énergie cinétique moyenne et l'énergie cinétique mixte ;
- les interactions entre l'énergie cinétique et l'énergie interne : $\underline{\mathcal{E}} = -\mathcal{Y}_{ij} \partial_j \bar{U}_i$ associée à l'énergie cinétique moyenne et $\varepsilon = -\mathcal{Y}_{ij} \partial_j u'_i$ associée à l'énergie cinétique turbulente.

Ce système d'équations est représenté schématiquement sur la figure 2.

Afin d'obtenir l'équation d'évolution de la demi-trace du tenseur des corrélations de fluctuation de vitesse, on décompose la masse volumique ρ en une partie constante ρ_0 et une partie variable ρ_1 , $\rho(\mathbf{x}, t) = \rho_0 + \rho_1(\mathbf{x}, t)$, où \mathbf{x} est le vecteur position et t le temps. Cela divise chaque partie de l'énergie totale en une partie associée à ρ_0 et une partie associée à ρ_1 . L'étude des échanges énergétiques entre les huit parties résultantes de l'énergie totale décompose chaque échange énergétique identifié plus haut en une partie à masse volumique constante et une partie à masse volumique variable. De plus, les

échanges font intervenir de nouveaux termes caractérisant l'interaction entre la partie à masse volumique constante et variable de l'énergie totale. La formulation inclut au facteur scalaire ρ_0 près la demi-trace du tenseur des corrélations de fluctuation de vitesse e , permettant son étude dans les écoulements à masse volumique variable. Elle donne également un sens aux termes de son équation d'évolution en termes d'échanges énergétiques. Cette quantité ayant un équivalent spectral, il est possible d'étendre l'étude au domaine spectral pour donner l'effet des échanges énergétiques sur la tailles des structures turbulentes. Pour toute quantité physique $g(x, y, z)$, l'opérateur chapeau ($\widehat{}$) donne les coefficients du développement en série de Fourier de g [173] :

$$\widehat{g}(\mathbf{k}, y, t) = \frac{1}{L_x L_z} \int_0^{L_x} \int_0^{L_z} g(\mathbf{x}, y, t) e^{-i\mathbf{k} \cdot \mathbf{x}} d\mathbf{x}. \quad (14)$$

où $\mathbf{x} = (x, z)$ est le vecteur de position dans le plan xOz et $\mathbf{k} = (k_x, k_z)$ est le vecteur de position dans le plan $k_x Ok_z$. Dans le domaine spectral, on étudie les termes de l'équation d'évolution de $\tilde{e} = \frac{1}{2} \widehat{u}_i^* \widehat{u}_i$, L'analyse spectrale étend chaque terme de la décomposition spatiale au domaine spectral. De plus, un terme purement spectral redistribue l'énergie entre les échelles sans contribution spatiale.

Que ce soit dans les domaines spatial ou spectral, les échanges énergétiques sont décomposés pour séparer les termes présents dans des écoulements à propriétés constantes (indice I) et les termes spécifiques aux écoulements à propriétés variables (indice Γ). Ces derniers proviennent de la compressibilité de l'écoulement, des variations ou fluctuations des propriétés du fluide et de la présence d'une vitesse moyenne normale à la paroi. Dans le domaine spectral, l'équation d'évolution de la demi-trace du tenseur des corrélations de fluctuation de vitesse est ainsi donnée par

$$\frac{\partial \tilde{e}}{\partial t} = \overline{\tilde{\varphi}} + \overline{\tilde{\mathcal{P}}} + \overline{\tilde{\zeta}} + \overline{\tilde{\varepsilon}} + \overline{\tilde{\Xi}} = \overline{\tilde{\varphi}_I} + \overline{\tilde{\varphi}_\Gamma} + \overline{\tilde{\mathcal{P}}_I} + \overline{\tilde{\mathcal{P}}_{\bar{U}_y}} + \overline{\tilde{\zeta}} + \overline{\tilde{\varepsilon}_I} + \overline{\tilde{\varepsilon}_\Gamma} + \overline{\tilde{\Xi}}, \quad (15)$$

où $\overline{\tilde{\varphi}} = \overline{\tilde{\varphi}^c} + \overline{\tilde{\varphi}^p} + \overline{\tilde{\varphi}^\nu}$ représente la somme des transferts conservatifs liés à la convection, à la pression et aux contraintes visqueuses, $\overline{\tilde{\mathcal{P}}}$ la production, c'est-à-dire une interaction avec les autres parties de l'énergie cinétique, $\overline{\tilde{\zeta}} = \overline{\tilde{\zeta}^c} + \overline{\tilde{\zeta}^p} + \overline{\tilde{\zeta}^\nu}$ l'interaction avec la partie à masse volumique variable de l'énergie totale, $\overline{\tilde{\varepsilon}}$ l'interaction avec l'énergie interne et $\overline{\tilde{\Xi}}$ le terme purement spectral de transport inter-échelle. Le transfert conservatif incompressible est également décomposé en trois contributions, $\overline{\tilde{\varphi}_I} = \overline{\tilde{\varphi}_I^c} + \overline{\tilde{\varphi}_I^p} + \overline{\tilde{\varphi}_I^\nu}$. On a :

$$\begin{aligned} \overline{\tilde{\varphi}^c} &= \text{Re}(-1/2)(\widehat{\partial_y u_i^* u_i^* U_y}) & \overline{\tilde{\zeta}^c} &= \text{Re}((1/2)(\widehat{u_i^* u_i^* \partial_j U_j}) & \overline{\tilde{\varphi}_I^c} &= \text{Re}(-1/2)(\widehat{\partial_y u_i^* u_i^* u_y^*}) \\ \overline{\tilde{\varphi}^p} &= \text{Re}(-\widehat{\partial_y u_i^* P/\rho}) & \overline{\tilde{\zeta}^p} &= \text{Re}(-\widehat{u_i^* (P/\rho^2)(\partial_i \rho)}) & \overline{\tilde{\varphi}_I^p} &= \text{Re}(-1/\bar{\rho})(\widehat{\partial_y u_i^* P}) \\ \overline{\tilde{\varphi}^\nu} &= \text{Re}(\widehat{\partial_y u_i^* \Sigma_{iy}/\rho}) & \overline{\tilde{\zeta}^\nu} &= \text{Re}(\widehat{u_i^* (\Sigma_{ij}/\rho^2)(\partial_j \rho)}) & \overline{\tilde{\varphi}_I^\nu} &= \text{Re}(\bar{\nu}(\widehat{\partial_y \partial_y \tilde{e}}) + \bar{\nu}(\widehat{\partial_y \partial_y u_i^* u_y^*})) \\ \overline{\tilde{\mathcal{P}}} &= \text{Re}(-\widehat{u_i^* u_y^* (\partial_y \bar{U}_i)}) & \overline{\tilde{\varepsilon}} &= \text{Re}(-\widehat{\partial_j u_i^* \Upsilon_{ij}/\rho}) & \overline{\tilde{\mathcal{P}}_I} &= \text{Re}(-\widehat{u_x^* u_y^* (\partial_y \bar{U}_x)}) \\ \overline{\tilde{\Xi}} &= \text{Re}((1/2)(\widehat{\partial_j u_i^* u_i^* u_j^*}) - (1/2)(\widehat{u_i^* u_j^* \partial_j u_i^*})) & \overline{\tilde{\varepsilon}_I} &= \text{Re}(-2\bar{\nu}(\widehat{s'_{ij}^* s'_{ij}})) \end{aligned}$$

On utilise les mêmes notations que pour les termes complets afin d'éviter un alourdissement des notations. Les termes sont exprimés en prenant en compte les symétries de l'écoulement et son homogénéité dans les directions longitudinale et transverse

($\partial_x \bar{\cdot} = \partial_z \bar{\cdot} = 0$ et $\bar{U}_z = 0$). L'équation d'évolution de la demi-trace du tenseur des corrélations de fluctuation de vitesse dans le domaine spatial est analogue à l'équation spectrale. Les termes spatiaux peuvent être obtenus par intégration des termes spectraux sur l'ensemble des longueurs d'onde. On notera en particulier que pour tout a , un terme spectral de la forme $\text{Re}(\widehat{u}_i^* \widehat{a})$ est associé à un terme spatial $\overline{u'_i a}$.

3.2 Effet du gradient de température

On étudie l'effet du gradient de température sur les termes de l'équation d'évolution de la demi-trace du tenseur des corrélations de fluctuation de vitesse à partir des résultats des simulations numériques directes. Dans le domaine spatial, les échanges énergétiques ont été décrits dans la littérature dans le cas incompressible [203, 305] mais n'ont pas été étudiés dans le cas anisotherme. Dans le domaine spectral, l'analyse est nouvelle dans le cas isotherme et anisotherme avec la décomposition utilisée.

Dans les deux cas, on utilise la décomposition des échanges énergétiques en termes thermiques et termes incompressibles pour identifier les termes thermiques les plus importants. La production thermique est négligeable par rapport à la production incompressible. En revanche, l'interaction avec l'énergie cinétique à masse volumique variable et les termes thermiques liés au transfert conservatif et à l'interaction avec l'énergie interne ne sont pas négligeables. En particulier, les termes thermiques associés aux contraintes visqueuses ont une amplitude importante.

Le gradient de température génère une asymétrie entre les profils spatiaux des échanges énergétiques côtés chaud et froid. Les échanges énergétiques sont plus importants du côté froid que du côté chaud, sont plus localisés et se produisent plus près de la paroi. L'adimensionnement des échanges énergétiques permet d'étudier efficacement cette asymétrie. L'adimensionnement classique (+), fondé sur une combinaison linéaire de la vitesse de frottement U_τ et de la viscosité cinématique ν_ω à la paroi, n'est pas adapté aux écoulements anisothermes car il ne prend pas en compte les variations des propriétés du fluide. En revanche, il est utile d'étudier les échanges énergétiques avec l'adimensionnement semi-local (*), fondé sur une combinaison linéaire de la vitesse de frottement semi-locale $U_\tau^* = [\mu_\omega / \bar{\rho}(y) (\partial_y \bar{U}_x)_\omega]^{0.5}$ et de la viscosité cinématique moyenne $\bar{\nu}$, fonction de la distance à la paroi. Avec l'adimensionnement semi-local, l'asymétrie entre les côtés chaud et froid est considérablement réduite. Ces résultats sont en accord avec des études antérieures sur l'adimensionnement semi-local [127, 224, 225]. La superposition des deux profils n'est cependant pas atteinte pour la production, le transfert conservatif et l'interaction avec l'énergie interne (figure 3). On peut expliquer une partie des différences par un effet de bas nombre de Reynolds donné par les variations du nombre de Reynolds de friction local $U_\tau^*(y)h/\bar{\nu}(y)$ dans le canal. En particulier, l'asymétrie des profils de la production est en accord avec l'effet de variations du nombre de Reynolds dans la configuration isotherme. Les variations du nombre de Reynolds local ont également une influence sur le transfert conservatif et l'interaction avec l'énergie interne mais ne sont pas suffisantes pour expliquer l'effet du gradient de température sur ces termes.

L'étude individuelle des termes thermiques des échanges énergétiques (figure 4) montre une certaine universalité. Les trois termes thermiques les plus importants sont similaires mais de signe opposé entre le côté froid et le côté chaud. Il en résulte des

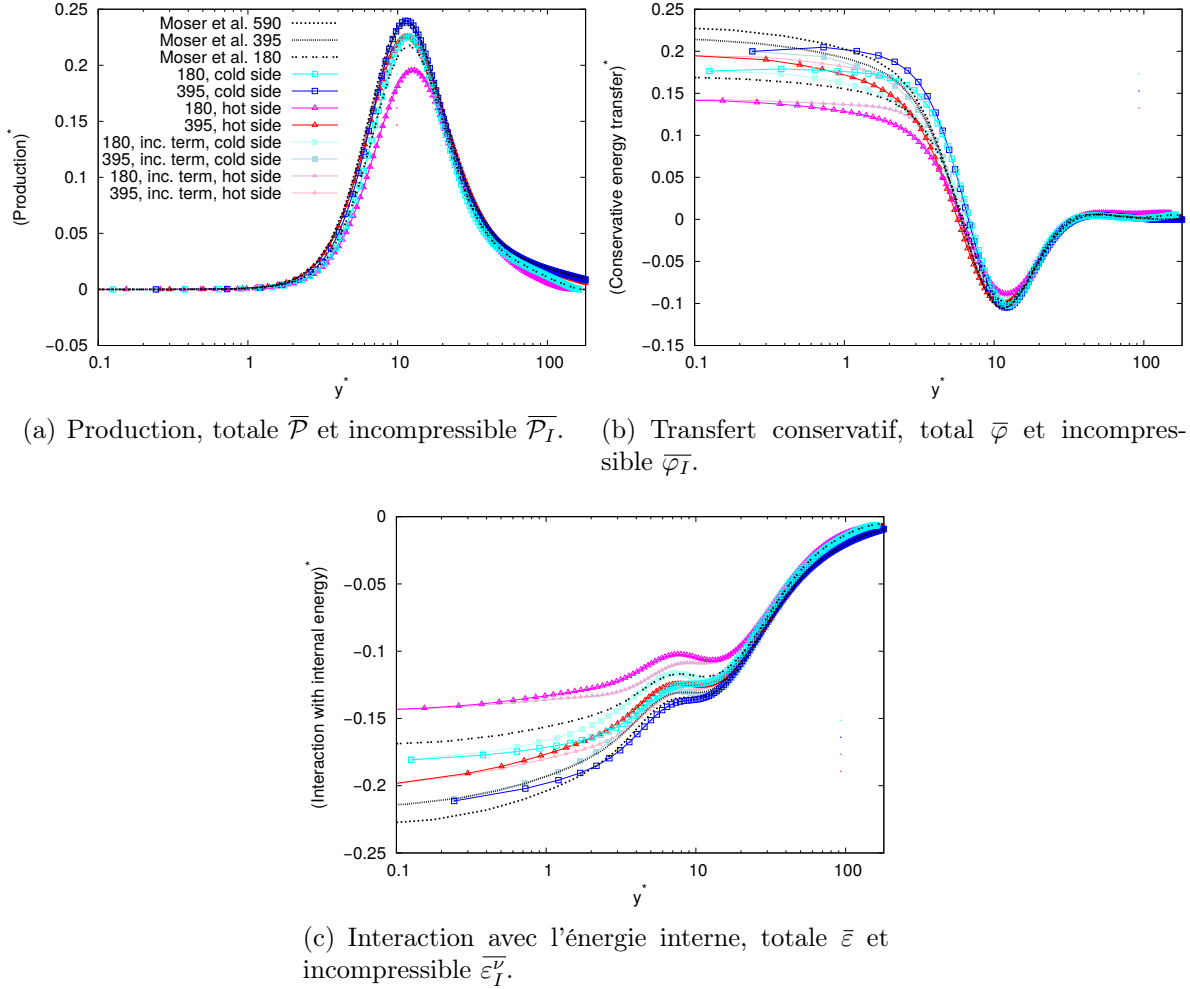


FIGURE 3 – Profils des termes de l'équation d'évolution de la demi-trace du tenseur des corrélations de fluctuation de vitesse avec l'adimensionnement semi-local à $Re_\tau = 180$ et $Re_\tau = 395$. Les résultats sont comparés aux données de référence de Moser *et al.* [203] dans un canal incompressible à $Re_\tau = 180, 395$ et 590.

deux côtés un pseudo-transfert énergétique dans la direction normale aux parois. Les termes thermiques ont une amplitude plus faible que les termes incompressibles mais ne peuvent être négligés pour une description fidèle des échanges énergétiques.

Le gradient de température modifie également les spectres de échanges énergétiques. On identifie quatre échanges énergétiques spectraux : la production, le transport inter-échelle, le transfert conservatif et l'interaction avec l'énergie interne. La production a lieu autour de $y^* = 12$ et $k^* = 0.07$ (figure 5). Le transport inter-échelle redistribue l'énergie produite entre les échelles, principalement vers les petites échelles mais aussi vers les grandes échelles (figure 6). L'énergie est de plus transférée spatialement par le transfert conservatif, principalement vers la paroi et avec peu de variations d'échelles (figure 7). Elle y est dissipée par l'interaction avec l'énergie interne (figure 8). Les échanges énergétiques spectraux ont une amplitude plus faible du côté froid que du côté chaud, mais se produisent à de plus petits nombres d'ondes, plus près de la paroi et sur une plus grande gamme d'échelles. Aussi, la plus grande amplitude spatiale des termes du côté froid semble provenir de la prise en compte d'un plus grand nombre

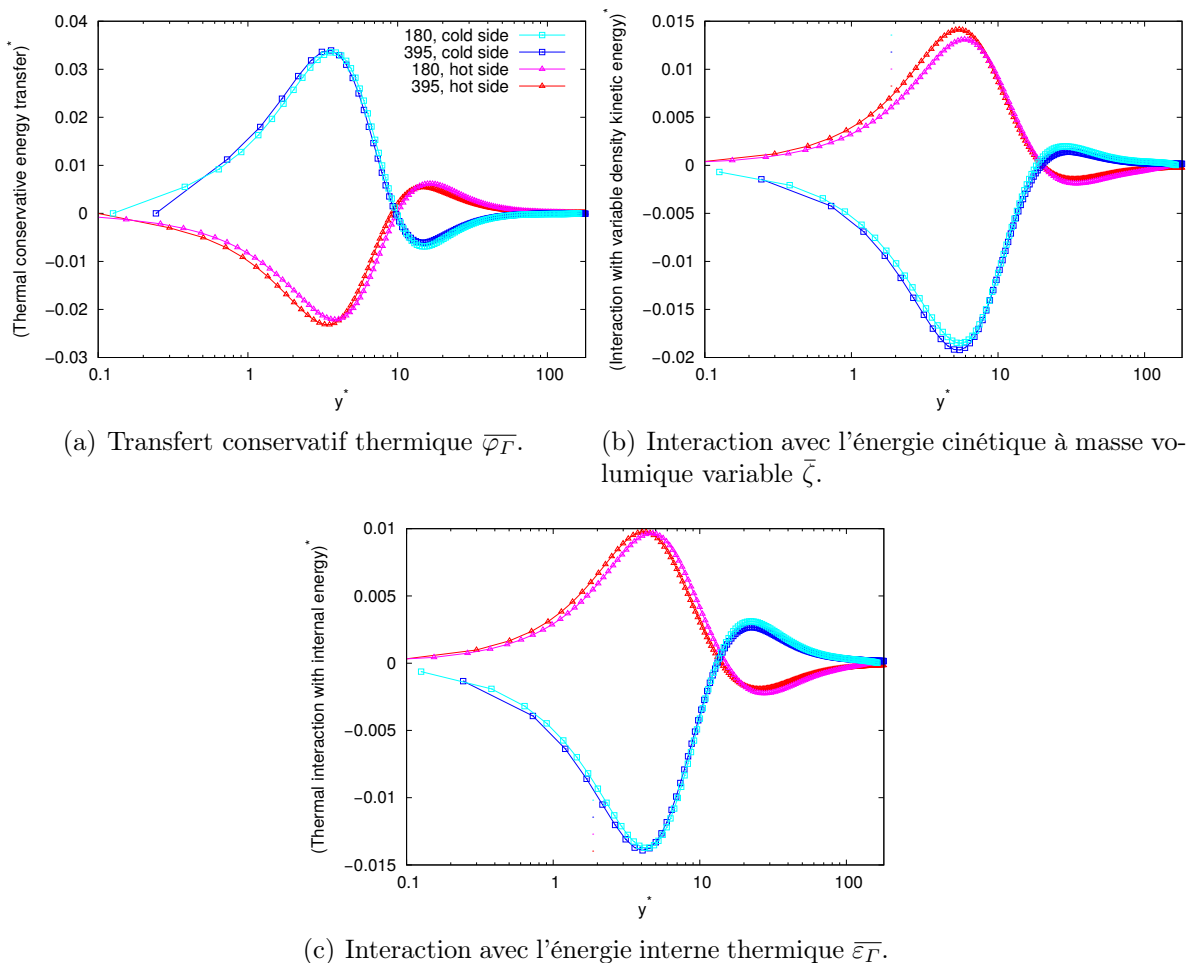


FIGURE 4 – Profils des termes thermiques de l'équation d'évolution de la demi-trace du tenseur des corrélations de fluctuation de vitesse avec l'adimensionnement semi-local à $Re_\tau = 180$ et $Re_\tau = 395$.

d'échelles dans le domaine spectral.

3.3 Effet du nombre de Reynolds

L'effet du gradient de température sur les échanges énergétiques dépend du nombre de Reynolds. À $Re_\tau = 395$, l'asymétrie entre les côtés chaud et froid est plus faible qu'à $Re_\tau = 180$. Cette réduction est facilement interprétable en considérant l'asymétrie comme l'effet combiné des variations des propriétés locales du fluide et d'un effet de bas nombre de Reynolds donné par le nombre de Reynolds de friction semi-local. Les effets de bas nombre de Reynolds sont plus faibles dans le cas incompressible aux alentours de $Re_\tau = 395$ que de $Re_\tau = 180$, ce qui impacte directement l'asymétrie obtenue dans le canal anisotherme. Avec l'adimensionnement semi-local, les échanges énergétiques se produisent plus près de la paroi à $Re_\tau = 395$ qu'à $Re_\tau = 180$, sur une plus grande gamme d'échelles et ont une plus grande amplitude spatiale. En revanche, l'effet des variations des propriétés du fluide non pris en compte par l'adimensionnement semi-local est relativement insensible au nombre de Reynolds. En particulier, le profil spatial

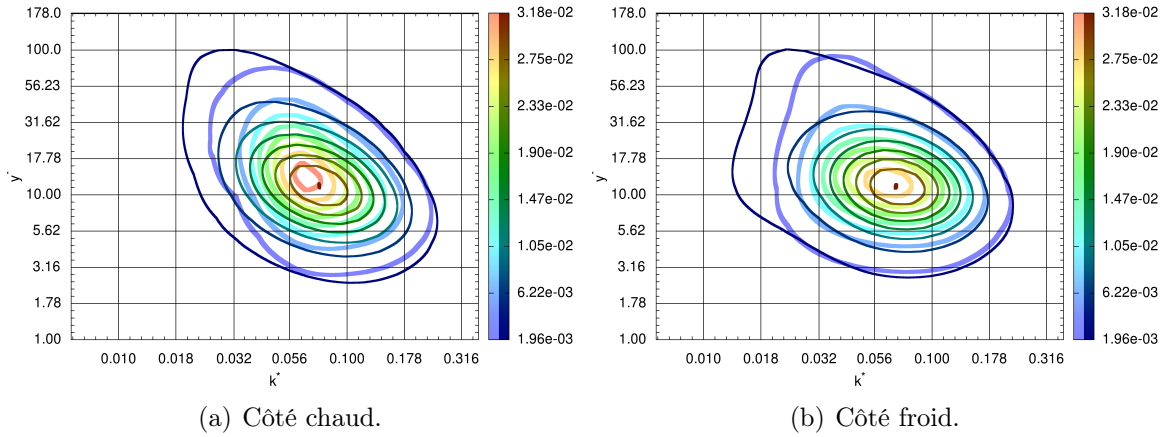


FIGURE 5 – Spectre de la production \bar{P} avec l'adimensionnement semi-local à $Re_\tau = 180$ (lignes épaisses, couleur claire) et $Re_\tau = 395$ (lignes fines, couleur foncée).

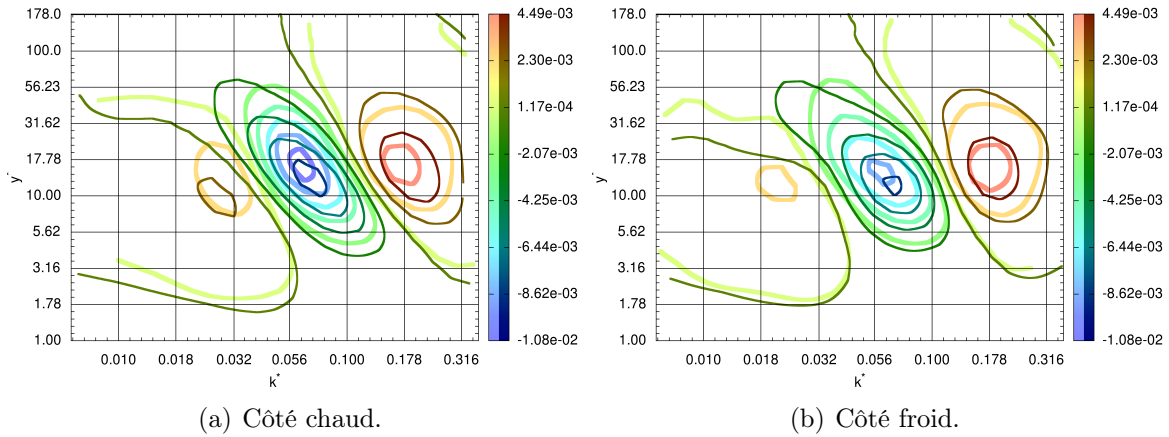


FIGURE 6 – Spectre du terme purement spectral de transport inter-échelle $\bar{\Xi}$ avec l'adimensionnement semi-local à $Re_\tau = 180$ (lignes épaisses, couleur claire) et $Re_\tau = 395$ (lignes fines, couleur foncée).

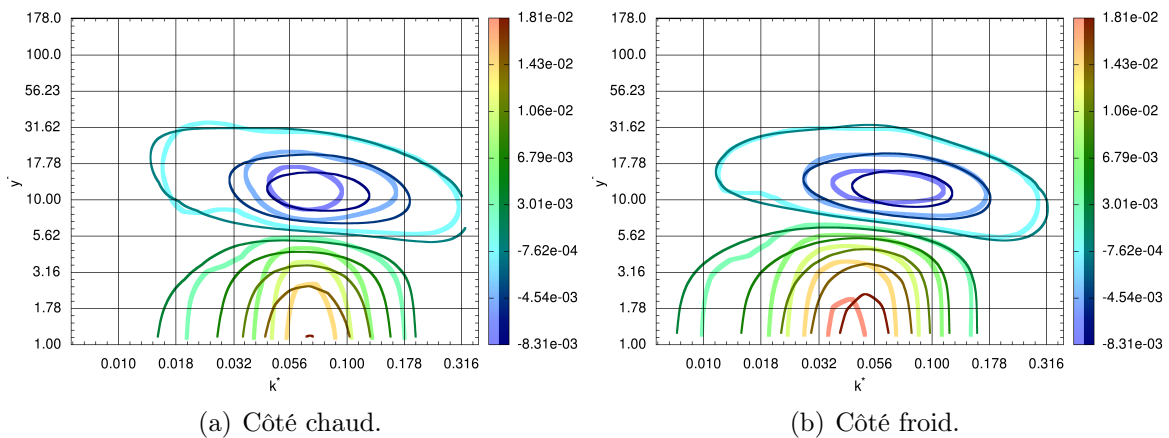


FIGURE 7 – Spectre du transfert conservatif $\bar{\varphi}$ avec l'adimensionnement semi-local à $Re_\tau = 180$ (lignes épaisses, couleur claire) et $Re_\tau = 395$ (lignes fines, couleur foncée).

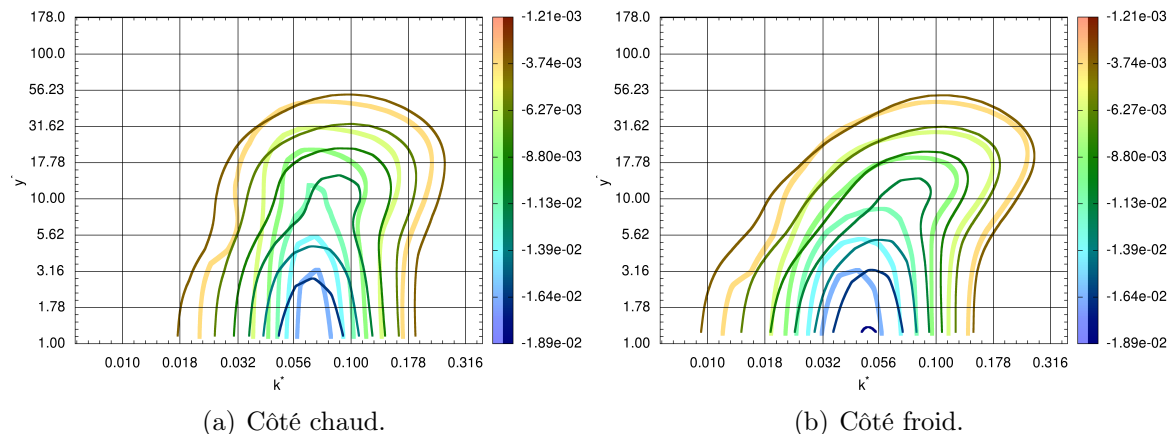


FIGURE 8 – Spectre de l'interaction avec l'énergie interne $\bar{\varepsilon}$ avec l'adimensionnement semi-local à $Re_\tau = 180$ (lignes épaisses, couleur claire) et $Re_\tau = 395$ (lignes fines, couleur foncée).

des termes thermiques n'est pas significativement affecté par le nombre de Reynolds (figure 4).

Les échanges énergétiques sont pertinents pour la modélisation de type *Reynolds-averaged Navier–Stokes* (RANS) et de type simulation des grandes échelles. La simulation des grandes échelles repose sur la modélisation des petites échelles de la turbulence. En turbulence homogène isotrope isotherme, la région à petite échelle des échanges énergétiques est purement dissipative, simplifiant la modélisation. Compte-tenu des échanges énergétiques additionnels en turbulence de paroi anisotherme, la simulation des grandes échelles de ces écoulements est rendue plus complexe.

4 Simulation des grandes échelles

Cette section traite de la simulation des grandes échelles des écoulements turbulents fortement anisothermes. La section 4.1 initie l'étude par une identification des termes à modéliser. La section 4.2 analyse la modélisation des termes les plus significatifs a priori, c'est-à-dire à partir des résultats des simulations numériques directes. La section 4.3 examine leur modélisation a posteriori, c'est-à-dire à partir de simulations des grandes échelles mettant en œuvre les modèles.

4.1 Étude des termes sous-mailles

La simulation des grandes échelles est fondée sur l'idée de séparation d'échelle. Théoriquement, cette séparation est généralement représentée par l'application d'un filtre spatial ($\bar{\cdot}$, filtre classique). Ce filtre vérifie les propriétés de conservation des constantes, $\bar{a} = a$ avec a une constante, et de linéarité, $\overline{\phi + \psi} = \bar{\phi} + \bar{\psi}$ pour n'importe quel ϕ et ψ [253]. Le filtre peut cependant être inhomogène et ne pas commuter avec la dérivation. Le filtrage des équations de bas nombre de Mach conduit à différentes formulations des équations filtrées en fonction des variables avec lesquelles on exprime les équations et de la manière dont les équations sont disposées lors du filtrage.

On considère trois formulations : la formulation Classique, la formulation Favre et la formulation Vitesse.

Dans la formulation Classique, les équations de bas nombre de Mach sont filtrées puis exprimées en termes de variables filtrées classiquement :

$$\frac{\partial \bar{\rho}}{\partial t} + \frac{\partial}{\partial x_j} (\bar{\rho} \bar{U}_j + F_{\rho U_j}) + C_{\rho U_j}^j = 0, \quad (16)$$

$$\frac{\partial}{\partial t} (\bar{\rho} \bar{U}_i + F_{\rho U_i}) = -\frac{\partial}{\partial x_j} (\bar{\rho} \bar{U}_j \bar{U}_i + F_{\rho U_j U_i}) - C_{\rho U_j U_i}^j - \frac{\partial \bar{P}}{\partial x_i} - C_P^i + \frac{\partial}{\partial x_j} (\check{\Sigma}_{ij} + F_{\Sigma_{ij}}) + C_{\Sigma_{ij}}^j, \quad (17)$$

$$\frac{\partial \bar{U}_j}{\partial x_j} + C_{U_j}^j = -\frac{\gamma-1}{\gamma P_0} \left[\frac{\partial}{\partial x_j} (\check{Q}_j + F_{Q_j}) + C_{Q_j}^j \right] - \frac{1}{\gamma P_0} \frac{\partial P_0}{\partial t}, \quad (18)$$

$$\bar{T} = \frac{P_0}{r} \left(\frac{1}{\bar{\rho}} + F_{1/\rho} \right), \quad (19)$$

La formulation Favre est fondée sur l'utilisation d'un filtre pondéré par la masse volumique ($\widetilde{\cdot}$, filtre de Favre), défini pour tout ϕ par $\widetilde{\phi} = \bar{\rho} \phi / \bar{\rho}$. Dans la formulation Favre, les équations de bas nombre de Mach sont filtrées puis exprimées en termes de variables filtrées de Favre :

$$\frac{\partial \bar{\rho}}{\partial t} + \frac{\partial \bar{\rho} \widetilde{U}_j}{\partial x_j} + C_{\rho U_j}^j = 0, \quad (20)$$

$$\frac{\partial \bar{\rho} \widetilde{U}_i}{\partial t} = -\frac{\partial}{\partial x_j} (\bar{\rho} \widetilde{U}_j \widetilde{U}_i + \bar{\rho} G_{U_j U_i}) - C_{\rho U_j U_i}^j - \frac{\partial \bar{P}}{\partial x_i} - C_P^i + \frac{\partial}{\partial x_j} (\widehat{\Sigma}_{ij} + G_{\Sigma_{ij}}) + C_{\Sigma_{ij}}^j, \quad (21)$$

$$\frac{\partial}{\partial x_j} (\widetilde{U}_j + \bar{\rho} G_{U_j/\rho}) + C_{U_j}^j = -\frac{\gamma-1}{\gamma P_0} \left[\frac{\partial}{\partial x_j} (\widehat{Q}_j + G_{Q_j}) + C_{Q_j}^j \right] - \frac{1}{\gamma P_0} \frac{\partial P_0}{\partial t}, \quad (22)$$

$$\widetilde{T} = \frac{P_0}{\bar{\rho} r}, \quad (23)$$

La formulation Vitesse est fondée sur l'approche de filtrage suggérée par Sidharth and Candler [271], Sidharth *et al.* [272]. L'équation de conservation de la quantité de mouvement est réécrite avant le filtrage comme une équation de transport de la vitesse. Les équations sont ensuite filtrées puis exprimées en termes de variables filtrées classiquement. Le système d'équations résultant est donnée par l'équation de conservation de masse (16), l'équation de conservation de l'énergie (18), la loi des gaz parfaits (19) et l'équation de transport de la vitesse :

$$\begin{aligned} \bar{\rho} \frac{\partial \bar{U}_i}{\partial t} = & -\bar{\rho} \frac{\partial}{\partial x_j} (\bar{U}_j \bar{U}_i + F_{U_j U_i}) - \bar{\rho} C_{U_j U_i}^j + \bar{\rho} \bar{U}_i \frac{\partial \bar{U}_j}{\partial x_j} + \bar{\rho} F_{U_i \partial_j U_j} + \bar{\rho} \bar{U}_i C_{U_j}^j \\ & - \frac{\partial \bar{P}}{\partial x_i} - C_P^i - \bar{\rho} F_{\partial_i P/\rho} + \frac{\partial}{\partial x_j} (\check{\Sigma}_{ij} + F_{\Sigma_{ij}}) + C_{\Sigma_{ij}}^j + \bar{\rho} F_{\partial_j \Sigma_{ij}/\rho}, \end{aligned} \quad (24)$$

Les équivalents filtrés du tenseur des contraintes de cisaillement et du flux de chaleur sont donnés par $\check{\Sigma}_{ij} = \Sigma_{ij}(\bar{\mathbf{U}}, \bar{T})$ et $\check{Q}_j = Q_j(\bar{T})$ avec le filtre classique et $\widehat{\Sigma}_{ij} = \Sigma_{ij}(\widetilde{\mathbf{U}}, \widetilde{T})$ et $\widehat{Q}_j = Q_j(\widetilde{T})$ avec le filtre de Favre. Les trois formulations font intervenir les termes sous-mailles suivants :

Équation	Formulation	Grand	Moyen	Petit ou très petit
Masse	Classique, Vitesse Favre		$\partial_j F_{\rho U_j}, C_{\rho U_j}^j$ $C_{\rho U_j}^j$	
Quantité de mouvement	Classique	$\partial_j F_{\rho U_j U_i}$	$\partial_t F_{\rho U_i}, C_{\rho U_j U_i}^j$	$C_P^i, \partial_j F_{\Sigma_{ij}}, C_{\Sigma_{ij}}^i$
	Favre	$\partial_j \bar{\rho} G_{U_j U_i}$	$C_{\rho U_j U_i}^j$	$C_P^i, \partial_j G_{\Sigma_{ij}}, C_{\Sigma_{ij}}^i$
	Vitesse	$\bar{\rho} \partial_j F_{U_j U_i}$	$\bar{\rho} C_{U_j U_i}^j, \bar{\rho} \bar{U}_i C_{U_j}^j$	$\bar{\rho} F_{U_i \partial_j U_j}, \bar{\rho} F_{\partial_i P / \rho}, C_P^i,$ $\bar{\rho} F_{\partial_j \Sigma_{ij} / \rho}, \partial_j F_{\Sigma_{ij}}, C_{\Sigma_{ij}}^i$
Énergie	Classique, Vitesse		$C_{U_j}^j$	$\partial_j F_{Q_j}, C_{Q_j}^j$
	Favre	$G_{U_j / \rho}$	$C_{U_j}^j$	$\partial_j G_{Q_j}, C_{Q_j}^j$
Loi des gaz parfaits	Classique, Vitesse Favre			$F_{1/\rho}$

TABLE 2 – Classification des termes sous-mailles dans les trois formulations.

$$C_{\rho U_j}^j = \frac{\overline{\partial \rho U_j}}{\partial x_j} - \frac{\partial \overline{\rho U_j}}{\partial x_j} \quad (25)$$

$$C_{\rho U_j U_i}^j = \frac{\overline{\partial \rho U_j U_i}}{\partial x_j} - \frac{\partial \overline{\rho U_j U_i}}{\partial x_j} \quad (26)$$

$$C_{U_j U_i}^j = \frac{\overline{\partial U_j U_i}}{\partial x_j} - \frac{\partial \overline{U_j U_i}}{\partial x_j} \quad (27)$$

$$C_P^i = \frac{\overline{\partial P}}{\partial x_i} - \frac{\partial \overline{P}}{\partial x_i} \quad (28)$$

$$C_{\Sigma_{ij}}^i = \frac{\overline{\partial \Sigma_{ij}(\mathbf{U}, T)}}{\partial x_j} - \frac{\partial \overline{\Sigma_{ij}(\mathbf{U}, T)}}{\partial x_j} \quad (29)$$

$$C_{U_j}^j = \frac{\overline{\partial U_j}}{\partial x_j} - \frac{\partial \overline{U_j}}{\partial x_j} \quad (30)$$

$$C_{Q_j}^j = \frac{\overline{\partial Q_j(T)}}{\partial x_j} - \frac{\partial \overline{Q_j(T)}}{\partial x_j} \quad (31)$$

$$F_{\rho U_j} = \overline{\rho U_j} - \bar{\rho} \bar{U}_j \quad (32)$$

$$F_{\rho U_i} = \overline{\rho U_i} - \bar{\rho} \bar{U}_i \quad (33)$$

$$G_{U_j / \rho} = \widetilde{\overline{U_j / \rho}} - \widetilde{\bar{U}_j / \bar{\rho}} \quad (34)$$

$$F_{\rho U_j U_i} = \overline{\rho U_j U_i} - \bar{\rho} \bar{U}_j \bar{U}_i \quad (35)$$

$$F_{U_j U_i} = \overline{U_j U_i} - \bar{U}_j \bar{U}_i \quad (36)$$

$$G_{U_j U_i} = \widetilde{\overline{U_j U_i}} - \widetilde{\bar{U}_j \bar{U}_i} \quad (37)$$

$$F_{\Sigma_{ij}} = \overline{\Sigma_{ij}(\mathbf{U}, T)} - \Sigma_{ij}(\bar{\mathbf{U}}, \bar{T}) \quad (38)$$

$$G_{\Sigma_{ij}} = \overline{\Sigma_{ij}(\mathbf{U}, T)} - \Sigma_{ij}(\widetilde{\mathbf{U}}, \widetilde{T}) \quad (39)$$

$$F_{Q_j} = \overline{Q_j(T)} - Q_j(\bar{T}) \quad (40)$$

$$G_{Q_j} = \overline{Q_j(T)} - Q_j(\widetilde{T}) \quad (41)$$

$$F_{1/\rho} = \frac{\bar{1}}{\rho} - \frac{1}{\bar{\rho}} \quad (42)$$

$$F_{U_i \partial_j U_j} = \overline{U_i \frac{\partial U_j}{\partial x_j}} - \bar{U}_i \frac{\partial \overline{U_j}}{\partial x_j} \quad (43)$$

$$F_{\partial_i P / \rho} = \frac{\bar{1}}{\rho} \frac{\partial \overline{P}}{\partial x_i} - \frac{1}{\bar{\rho}} \frac{\partial \overline{P}}{\partial x_i} \quad (44)$$

$$F_{\partial_j \Sigma_{ij} / \rho} = \frac{1}{\rho} \frac{\partial \overline{\Sigma_{ij}(\mathbf{U}, T)}}{\partial x_j} - \frac{1}{\bar{\rho}} \frac{\partial \overline{\Sigma_{ij}(\mathbf{U}, T)}}{\partial x_j} \quad (45)$$

Ces termes sous-mailles sont de deux types. Le premier type (dénnoté sous la forme C_α^β) provient de la non-commutation du filtre avec la dérivée et est lié aux variations de la largeur du filtre, c'est-à-dire de l'inhomogénéité du maillage SGE. Le second type (dénnoté sous la forme F_α) provient des non-linéarités, c'est-à-dire de la non-commutation entre le filtre avec la multiplication. Les termes sous-mailles $F_{\rho U_j}$ et $G_{U_j / \rho}$ sont étroitement liés par la relation $F_{\rho U_j} / \bar{\rho} = -\bar{\rho} G_{U_j / \rho}$. Ils expriment tout deux la corrélation entre la masse volumique et la vitesse.

Les différents termes sous-mailles mis en jeu dans les trois formulations sont estimés

à partir du filtrage des simulations numériques directes présentées dans la section 2. L'importance des termes sous-maïlles est étudiée à partir de leur moyenne quadratique par rapport aux termes non sous-maïlles. Étant donnée l'homogénéité de l'écoulement dans les directions longitudinales et transverses, l'analyse est réalisée en fonction de la coordonnée normale aux parois. Ceci permet de déterminer quels termes peuvent être négligés et quels termes doivent être modélisés dans les trois formulations. Un résumé de la classification des termes sous-maïlles est donné dans le tableau 2. Les grands termes sous-maïlles sont les termes sous-maïlles les plus significatifs et devraient être modélisés en premier. Les termes sous-maïlles moyens ont une amplitude plus faible. La modélisation des termes sous-maïlles de petite ou très petite amplitude n'est pas recommandée. Les termes sous-maïlles les plus importants sont des non-linéarités mais en raison de l'inhomogénéité du maillage, les erreurs de commutation filtre-dérivée peuvent aussi avoir une amplitude non-négligeable. C'est en particulier le cas si le filtre SGE utilisé est très inhomogène.

Le filtre classique est plus approprié si l'équation de conservation de la quantité de mouvement est exprimée en tant qu'équation de transport de vitesse. Le filtre de Favre élimine la nécessité de modéliser la corrélation entre la masse volumique et la vitesse dans l'équation de conservation de la masse, mais l'ajoute à l'équation de conservation de l'énergie. La corrélation entre la masse volumique et la vitesse doit donc être modélisée dans les deux cas. Aussi, les deux termes sous-maïlles les plus significatifs sont les termes sous-maïlles associés à la convection de la quantité de mouvement et à la corrélation entre la masse volumique et la vitesse quelle que soit la formulation.

4.2 Test a priori des modèles

On étudie la modélisation de ces deux termes sous-maïlles a priori, c'est-à-dire à partir des résultats des simulations numériques directes. Puisque ces deux termes sous-maïlles sont formellement similaires dans les formulations Vitesse et Favre, la même procédure de modélisation est utilisée dans les deux cas :

$$F_{U_j U_i} \approx \tau_{ij}^{\text{mod}}(\bar{\mathbf{U}}, \bar{\Delta}), \quad (46)$$

$$G_{U_j U_i} \approx \tau_{ij}^{\text{mod}}(\tilde{\mathbf{U}}, \bar{\Delta}), \quad (47)$$

$$F_{\rho U_j} \approx \pi_j^{\text{mod}}(\bar{\mathbf{U}}, \bar{\rho}, \bar{\Delta}), \quad (48)$$

$$G_{U_j/\rho} \approx \pi_j^{\text{mod}}(\tilde{\mathbf{U}}, 1/\bar{\rho}, \bar{\Delta}). \quad (49)$$

Les fonctions $\tau_{ij}^{\text{mod}}(\mathbf{U}, \bar{\Delta})$ et $\pi_j^{\text{mod}}(\mathbf{U}, \phi, \bar{\Delta})$ sont dépendantes du modèle mais ne dépendent pas de la formulation. On se concentre ici sur des modèles de type viscosité ou diffusivité sous-maïlle, dans lesquels les termes sous-maïlles sont modélisés par analogie avec la diffusion moléculaire,

$$\tau_{ij}^{\text{mod}}(\mathbf{U}, \bar{\Delta}) = -2\nu_e^{\text{mod}}(\mathbf{g}, \bar{\Delta})S_{ij}, \quad (50)$$

$$\pi_j^{\text{mod}}(\mathbf{U}, \phi, \bar{\Delta}) = -\frac{\nu_e^{\text{mod}}(\mathbf{g}, \mathbf{d}, \bar{\Delta})}{Pr_t}d_j, \quad (51)$$

avec $S_{ij} = \frac{1}{2}(g_{ij} + g_{ji})$ où \mathbf{g} est le gradient de vitesse, $g_{ij} = \partial_j U_i$ et \mathbf{d} le gradient du scalaire, $d_j = \partial_j \phi$. La viscosité sous-maïlle $\nu_e^{\text{mod}}(\mathbf{g}, \bar{\Delta})$ est donnée par le modèle utilisé.

Le nombre de Prandtl ou Schmidt sous-maille Pr_t , supposé constant, relie diffusivité sous-maille et viscosité sous-maille. Les modèles suivants, tirés de la littérature, sont étudiés : le modèle de Smagorinsky [276], le modèle WALE [213], le modèle de Vreman [304], le modèle Sigma [214], le modèle AMD [250], le modèle AMD scalaire [3], le modèle VSS [252] et le modèle de Kobayashi [147]. L'échelle de longueur du filtre est calculée suivant Deardorff [77] par $\bar{\Delta} = (\bar{\Delta}_x \bar{\Delta}_y \bar{\Delta}_z)^{1/3}$.

De plus, on propose dans ce travail deux nouveaux modèles. Premièrement, le modèle Smagorinsky anisotrope est une version modifiée du modèle Smagorinsky conçue pour impliquer les trois échelles de longueur de filtre au lieu d'une seule. L'objectif est d'améliorer l'anisotropie du modèle. Il est défini par,

$$\tau_{ij}^{\text{An.Smag.}}(\mathbf{U}, \bar{\Delta}) = -2\nu_e^{\text{Smag.}}(\mathbf{g}^a, \bar{\Delta})S_{ij}^a, \quad (52)$$

$$\pi_j^{\text{An.Smag.}}(\mathbf{U}, \phi, \bar{\Delta}) = -2\frac{\nu_e^{\text{Smag.}}(\mathbf{g}^a, \mathbf{d}^a, \bar{\Delta})}{Pr_t}d_j^a, \quad (53)$$

avec $S_{ij}^a = \frac{1}{2}(g_{ij}^a + g_{ji}^a)$ où \mathbf{g}^a est le gradient de vitesse redimensionné, $g_{ij}^a = (\bar{\Delta}_j/\bar{\Delta})\partial_j U_i$, et \mathbf{d}^a le gradient du scalaire redimensionné, $d_j^a = (\bar{\Delta}_j/\bar{\Delta})\partial_j \phi$.

Deuxièmement, le modèle mixte multiplicatif fondé sur le modèle de gradient (MMG) est construit pour avoir la même amplitude que le modèle gradient [169] et la même orientation que le tenseur des déformations ou gradient du scalaire. Il est défini par,

$$\text{Modèle MMG :} \quad \nu_e^{\text{MMG}}(\mathbf{g}, \bar{\Delta}) = -C^{\text{MMG}}\frac{G_{kk}}{|\mathbf{S}|}, \quad (54)$$

$$\text{Modèle MMG scalaire :} \quad \nu_e^{\text{SMMG}}(\mathbf{g}, \mathbf{d}, \bar{\Delta}) = -C^{\text{SMMG}}\frac{\sqrt{D_i D_i}}{\sqrt{d_m d_m}}. \quad (55)$$

Cette procédure rappelle le modèle mixte multiplicatif de Ghaisas and Frankel [113, 114] qui avait un but opposé.

Pour étudier la performance des modèles sous-maillages a priori, on compare les modèles aux termes sous-maillages calculés à partir des données SND par une analyse de régression linéaire. Notons b un modèle pour le terme sous-maille de valeur exacte a . Le coefficient de concordance [178] entre a et b (compris entre -1 et 1) mesure l'accord entre modèle et terme sous-maille, c'est-à-dire la proximité entre la relation entre les deux variables et l'identité,

$$\text{Conc}(a, b) = \frac{\langle ab \rangle - \langle a \rangle \langle b \rangle}{\langle a^2 \rangle - \langle a \rangle^2 + \langle b^2 \rangle - \langle b \rangle^2 + (\langle a \rangle - \langle b \rangle)^2}. \quad (56)$$

Un coefficient de concordance de 1 implique que le modèle et le terme sous-maille exact sont identiques. Compte tenu de l'homogénéité de l'écoulement dans les directions longitudinales et transverses, la relation linéaire est évaluée pour chaque valeur de y et la moyenne d'ensemble $\langle \cdot \rangle$ calculée comme une moyenne temporelle et sur les directions d'homogénéité.

Il n'y a pas de différences significatives entre filtre classique et filtre de Favre vis-à-vis de la performance des modèles. On présente donc seulement les résultats obtenus avec le filtre classique. Pour faciliter la comparaison, chaque modèle est mis à l'échelle pour donner lieu au même niveau de dissipation sous-maille que le terme sous-maille

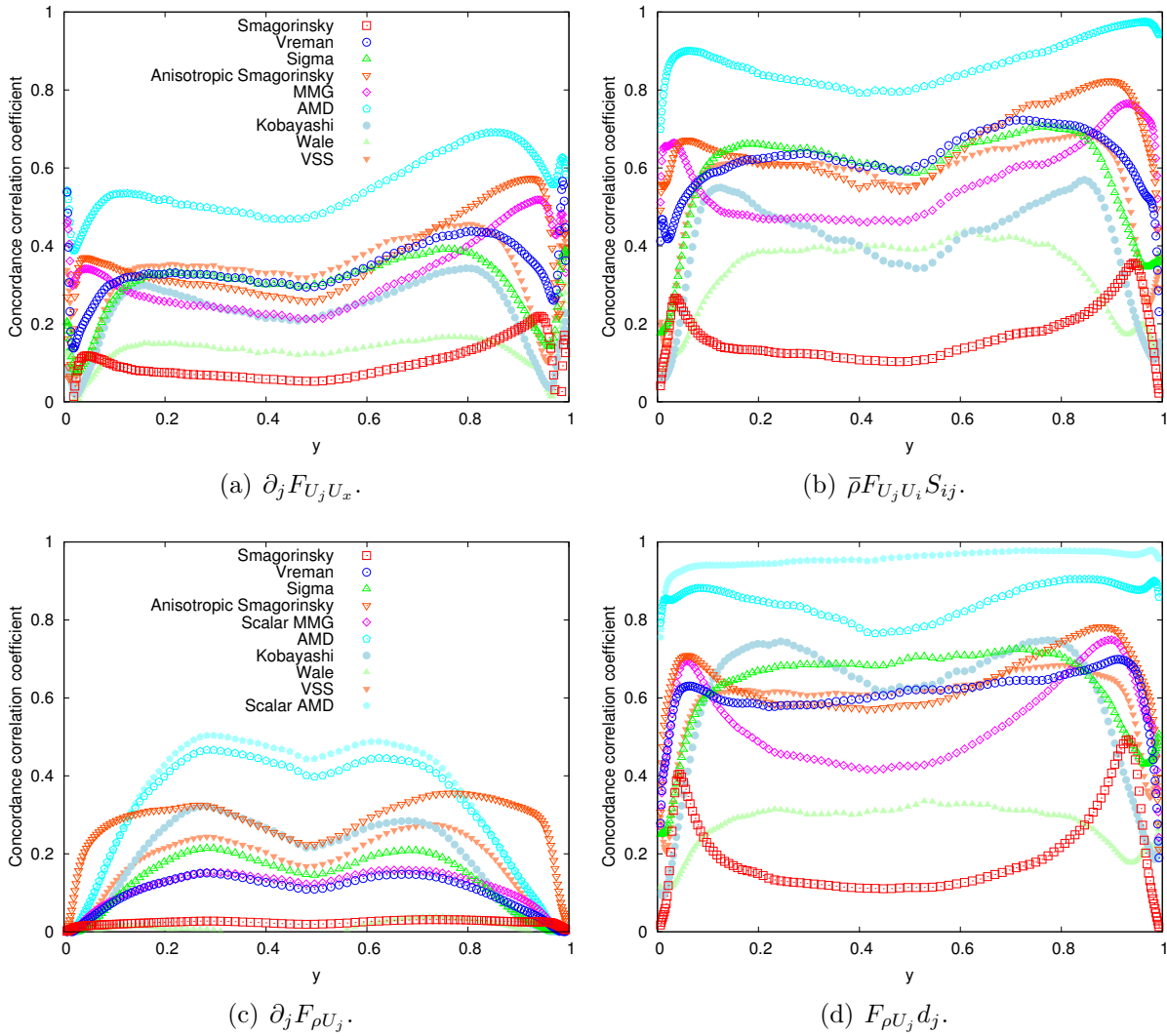


FIGURE 9 – Coefficient de concordance entre terme sous-maille et modèles pour le terme sous-maille associé à la convection de la quantité de mouvement (haut) et le terme sous-maille associé à la corrélation entre la masse volumique et la vitesse (bas). On compare à gauche la contribution des termes dans les équations de bas nombre de Mach et à droite leur contribution énergétique.

dans le volume. Les résultats sont donnés sur la figure 9. Pour les deux termes sous-mailles, les modèles étudiés sont en meilleur accord avec la contribution énergétique du terme qu'avec sa contribution dans les équations de bas nombre de Mach filtrées. Pourtant, les modèles de type viscosité ou diffusivité sous-maille sont incapable de reproduire les transferts des échelles sous-mailles aux échelles résolues, présents sur un cinquième des points du domaine. Une meilleure concordance avec le terme sous-maille est obtenue avec les modèles AMD et AMD scalaire, suivis par les modèles de Vreman, de Smagorinsky anisotrope et MMG. La mauvaise concordance du modèle de Smagorinsky s'explique par son caractère fortement surdissipatif en proche paroi. La bonne performance des modèles AMD et AMD scalaire peut être attribué au lien étroit entre ces modèles et le modèle gradient. Contrairement au modèle gradient, ces modèles sont en revanche purement dissipatifs et ne devraient pas entraîner des problèmes de stabilité numérique.

4.3 Test a posteriori des modèles

On poursuit l'étude de la modélisation des termes sous-mailles associés à la convection de la quantité de mouvement et à la corrélation entre la masse volumique et la vitesse par des tests a posteriori, c'est-à-dire à partir de simulations des grandes échelles mettant en œuvre les modèles. On considère différents modèles algébriques, sans se limiter aux modèles de type viscosité ou diffusivité sous-maille. Cela inclut, en plus des modèles fonctionnels présentés dans la section 4.2, des modèles structurels, tensoriels et mixtes tensoriels.

Avec le modèle de structurel gradient [169], les termes sous-mailles sont modélisés selon un développement en série de Taylor du filtre,

$$\tau_{ij}^{\text{Grad.}}(\mathbf{U}, \bar{\Delta}) = \frac{1}{12} C^{\text{Grad.}} G_{ij}(\mathbf{U}, \bar{\Delta}) = \frac{1}{12} C^{\text{Grad.}} \bar{\Delta}_k^2 g_{ik} g_{jk}, \quad (57)$$

$$\pi_j^{\text{Grad.}}(\mathbf{U}, \phi, \bar{\Delta}) = \frac{1}{12} C^{\text{Grad.}} D_j(\mathbf{U}, \bar{\Delta}) = \frac{1}{12} C^{\text{Grad.}} \bar{\Delta}_k^2 g_{ik} d_k, \quad (58)$$

Avec le modèle structurel de similarité d'échelle [14], les termes sous-mailles sont modélisés selon l'hypothèse de similarité d'échelle,

$$\tau_{ij}^{\text{Simil.}}(\mathbf{U}, \bar{\Delta}) = C^{\text{Simil.}} \left(\widehat{U_j U_i} - \widehat{U_j} \widehat{U_i} \right), \quad (59)$$

$$\pi_j^{\text{Simil.}}(\mathbf{U}, \phi, \bar{\Delta}) = C^{\text{Simil.}} \left(\widehat{U_j \phi} - \widehat{U_j} \widehat{\phi} \right), \quad (60)$$

où $\widehat{\cdot}$ est un filtre test explicitement calculé lors de la simulation des grandes échelles. On utilise un filtre volumique calculé comme une moyenne sur trois mailles dans les trois directions spatiales (filtre A).

Dans le but de mieux prendre en compte l'anisotropie de l'écoulement, des modèles tensoriels de la forme $\tau_{ij}^{H^{(k)\text{mod}}}(\mathbf{U}, \bar{\Delta})$ peuvent être construits à partir de n'importe quel modèle $\tau_{ij}^{\text{mod}}(\mathbf{U}, \bar{\Delta})$ et tenseur du second ordre $H_{ij}^{(k)}$,

$$\tau_{ij}^{H^{(k)\text{mod}}}(\mathbf{U}, \bar{\Delta}) = H_{ij}^{(k)} \tau_{ij}^{\text{mod}}(\mathbf{U}, \bar{\Delta}), \quad (61)$$

où aucune somme sur i et j n'est implicite. On définit à cet effet les tenseurs. $H_{ij}^{(1)} = [i \neq j]$, $H_{ij}^{(2)} = [\chi_{ij}^{xy}]$, $H_{ij}^{(3)} = [\neg \chi_{ij}^{yy}]$, $H_{ij}^{(4)} = [\chi_{ij}^{xy} \vee \chi_{ij}^{xz}]$, $H_{ij}^{(5)} = [\chi_{ij}^{xy} \vee \chi_{ij}^{yz}]$, $H_{ij}^{(6)} = [i = x \vee j = x]$ et $H_{ij}^{(7)} = [\chi_{ij}^{xx} \vee \chi_{ij}^{xy}]$, où $[\cdot]$ sont les crochets d'Iverson, valant 1 si la proposition entre crochets est satisfaite et 0 sinon, \neg la négation logique (NON), \wedge la conjonction logique (ET), \vee la disjonction logique (OR) et avec la notation $\chi_{ij}^{ab} = (i = a \wedge j = b) \vee (i = b \wedge j = a)$.

Enfin, on étudie pour chaque type de modèle des versions dynamiques correspondantes. On s'intéresse pour cela exclusivement aux modèles dynamiques fondés sur la méthode de Lilly [177] avec une moyenne sur les directions d'homogénéité et son extension à une constante globale [221], c'est-à-dire avec une moyenne sur le volume. La méthode dynamique de Lilly [177] multiplie les modèles par une fonction du temps et de la coordonnée normale aux parois, tandis que la méthode dynamique globale les multiplie par une fonction du temps uniquement. Dans les deux cas, la méthode repose sur l'utilisation d'un filtre test ($\widehat{\cdot}$).

Les simulations des grandes échelles implémentant les modèles utilisent la même méthode numérique et la même taille de domaine que les simulations numériques directes.

Re_τ	Nom	Nombre de points $N_x \times N_y \times N_z$	Dimensions du domaine $L_x \times L_y \times L_z$	Tailles de mailles adimensionnées $\Delta_x^+ ; \Delta_y^+(0) - \Delta_y^+(h) ; \Delta_z^+$
180	48B	$48 \times 50 \times 48$	$4\pi h \times 2h \times 2\pi h$	68 ; 0,50 – 25 ; 34
180	36C	$36 \times 40 \times 36$	$4\pi h \times 2h \times 2\pi h$	91 ; 2,0 – 22 ; 45
180	24C	$24 \times 28 \times 24$	$4\pi h \times 2h \times 2\pi h$	136 ; 2,0 – 35 ; 68
395	96B	$96 \times 100 \times 64$	$4\pi h \times 2h \times (4/3)\pi h$	73 ; 0,50 – 27 ; 36

TABLE 3 – Dimensions du domaine et tailles de mailles des simulations des grandes échelles. Les tailles de mailles adimensionnées sont calculées en utilisant les vitesses de friction des simulations numériques directes.

Des simulations sont réalisées avec trois maillages (“48B”, “36C” et “24C”) à $Re_\tau = 180$ et un maillage à $Re_\tau = 395$ (“96B”). Les tailles de mailles adimensionnées des différents maillages sont données dans le tableau 3. Afin de permettre la comparaison directe des résultats des simulations des grandes échelles et des simulations numériques directes, les données SND sont filtrées à la résolution des maillages SGE. La comparaison est fondée sur le formalisme SGE de Leonard [169], dans lequel les simulations des grandes échelles visent à fournir des champs résolus dont les statistiques correspondent aux statistiques d’une simulation numérique directe filtrée.

Dans la plage de nombres de Reynolds étudiée, la modélisation fonctionnelle du terme sous-maille associé à la convection de la quantité de mouvement ne semble pas pertinente, sous-estimant par exemple les frottement à la paroi et le flux de chaleur et surestimant l’écart type de la vitesse longitudinale et de la température. C’est par exemple le cas du modèle AMD (figure 10). Les prédictions sont à cet égard moins fidèles qu’avec une simulation sans modèle. De plus, les modèles fonctionnels ne parviennent pas à représenter fidèlement l’anisotropie de la turbulence, car ils n’affectent pas suffisamment l’écart type de la vitesse longitudinale par rapport aux composantes transverse et normale à la paroi. Enfin, l’asymétrie entre les côtés chaud et froid n’est pas correctement prise en compte par les modèles. D’autres approches de modélisation permettent d’améliorer ces lacunes, comme les modèles structurels, les modèles fonctionnels tensoriels et tensoriels dynamiques. Le modèle AMD tensoriel fondé sur le tenseur $H^{(4)}$ (modèle $H^{(4)}$ AMD) est l’un des modèles tensoriels non dynamiques identifiés comme pertinents pour le terme sous-maille associé à la convection de la quantité de mouvement (figure 10). Bien que l’effet du terme sous-maille sur l’écoulement ne soit pas correctement représenté, le modèle améliore les prédictions de la simulation comparé au cas sans modèle.

La modélisation du terme sous-maille associé à la corrélation entre la masse volumique et la vitesse est utile et bénéfique pour la prédiction des statistiques relatives à la température, mais ne modifie pas de façon significativement la vitesse. Les modèles étudiés augmentent le flux de chaleur à la paroi et réduisent l’écart type de la température. Cependant, la prédiction précise de l’écoulement nécessite l’accord de la force du modèle avec l’effet du modèle pour le terme sous-maille associé à la convection de la quantité de mouvement. Avec le modèle $H^{(4)}$ AMD, un impact important est nécessaire car ce modèle diminue la prédiction du flux de chaleur à la paroi par rapport à une simulation sans modèle. Ceci peut être atteint avec des modèles fonctionnels ou struc-

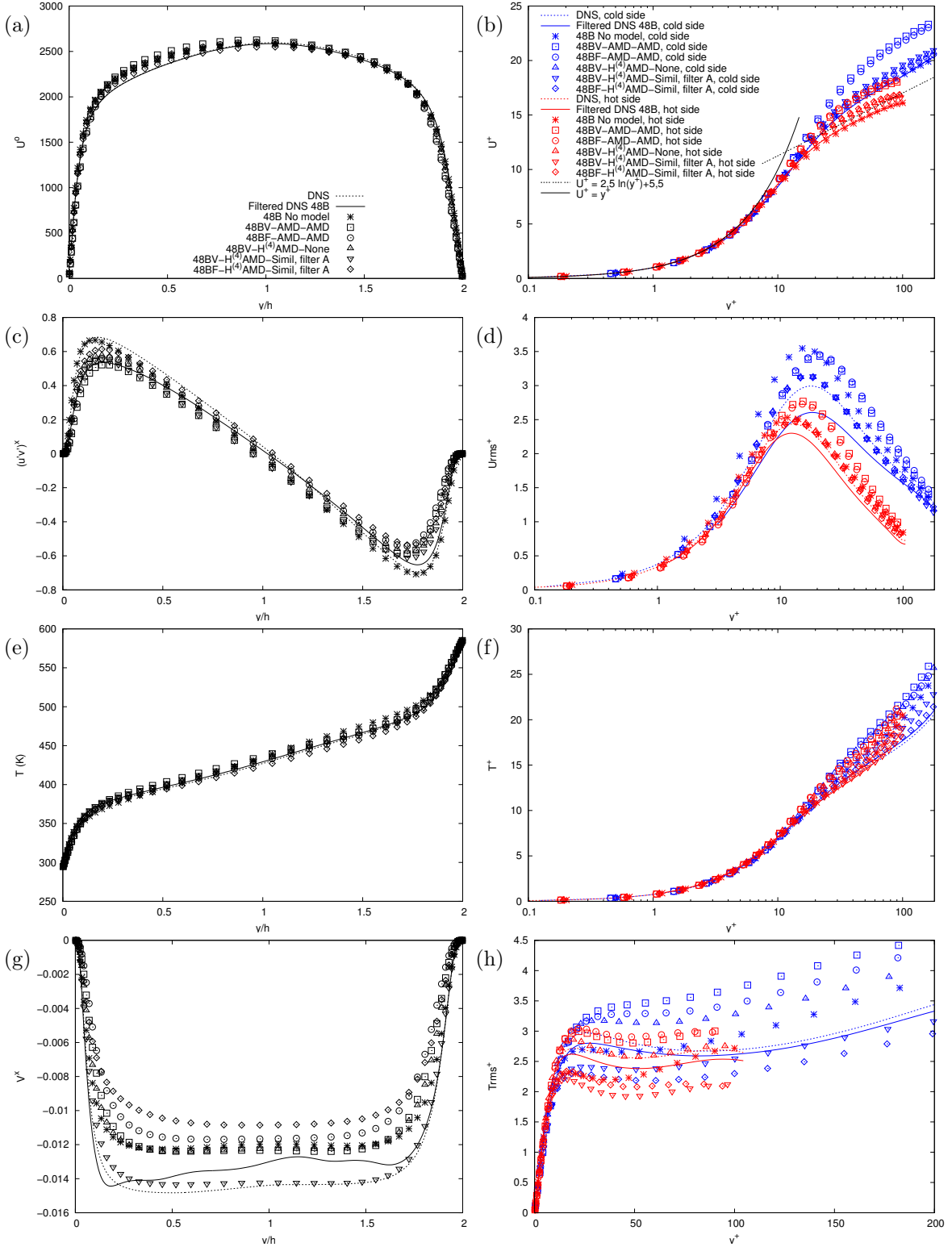


FIGURE 10 – Comparaison de simulation des grandes échelles avec le modèle AMD et le modèle AMD tensoriel fondé sur le tenseur $H^{(4)}$ pour le terme sous-maille associé à la convection de la quantité de mouvement et le modèle de similarité d'échelle fondée sur le filtre A pour le terme sous-maille associé à la corrélation entre la masse volumique et la vitesse dans les formulations Vitesse et Favre pour les profils de la vitesse longitudinale $\langle U_x \rangle$ (a, b), la covariance de la vitesse longitudinale et normale aux parois $\langle u'_x u'_y \rangle$ (c), l'écart type de la vitesse longitudinale $\sqrt{\langle u'^2_x \rangle}$ (d), la température $\langle T \rangle$ (e, f), la vitesse normale aux parois $\langle U_y \rangle$ (g) et l'écart type de la température $\sqrt{\langle T'^2 \rangle}$ (h) dans le canal anisotherme à $Re_\tau = 180$ avec le maillage 48B.

turel. La figure 10 présente les résultats obtenus avec le modèle de similarité d'échelle fondé sur le filtre A. Les résultats suggèrent que la formulation Favre est préférable à la formulation Vitesse pour une prédiction précise de la température moyenne avec la méthode numérique et les schémas utilisés. Les profils de la vitesse moyenne et de la covariance de la vitesse longitudinale et normale aux parois sont également légèrement plus satisfaisants dans la formulation Favre.

5 Conclusion

Cette thèse est consacrée aux écoulements turbulents soumis à un fort gradient de température, présents dans les récepteurs solaires à haute température. L'analyse peut être divisée en deux parties. La première partie caractérise l'influence du gradient de température sur les échanges énergétiques entre les différentes parties de l'énergie totale. La deuxième partie analyse la modélisation sous-maille de ces écoulements pour la simulation des grandes échelles.

L'énergie cinétique turbulente est produite à partir d'énergie cinétique moyenne, redistribuée vers les grandes et petites échelles, transférée vers la paroi et convertie en énergie interne. Le gradient de température crée une asymétrie entre les échanges énergétiques du côté chaud et du côté froid du canal. L'asymétrie est due aux variations des propriétés locales du fluide et à un effet de bas nombre de Reynolds. Les variations des propriétés locales du fluide sont prises en compte dans une certaine mesure par l'adimensionnement semi-local et modifient les échelles de vitesse et de longueur de la turbulence. L'effet de bas nombre de Reynolds est donné par les variations du nombre de Reynolds de friction semi-local. Cet effet est accentué à bas nombre de Reynolds et dépend donc du nombre de Reynolds de friction moyen. La décomposition des échanges énergétiques en termes thermiques et termes incompressibles montre un impact négligeable de l'effet de bas nombre de Reynolds sur les termes thermiques.

La simulation des grandes échelles des écoulements fortement anisothermes peut avec les équations de bas nombre de Mach être effectuée dans deux formulations appelées formulation Vitesse et formulation Favre. Les deux formulations sont a priori similaires mais les résultats a posteriori suggèrent que la formulation de Favre est plus appropriée avec les schémas numériques et la discrétisation utilisés. Les modèles étudiés ne prédisent pas correctement l'anisotropie de la turbulence ou l'asymétrie entre le côté chaud et le côté froid mais améliorent les résultats par rapport à une simulation sans modèle. Les modèles tensoriels ou tensoriels dynamiques semblent avantageux par rapport aux modèles de type viscosité sous-maille. La modélisation du terme sous-maille associé à la corrélation entre la masse volumique et la vitesse est cruciale pour la prédiction précise du flux de chaleur. Les modèles de type diffusivité sous-maille et les modèles structurels semblent pertinents pour ce terme sous-maille. La principale limite de l'étude est la dépendance de l'analyse aux erreurs numériques. Une caractérisation de l'influence des erreurs numériques est nécessaire à une meilleure compréhension des résultats des simulations des grandes échelles. L'adoption d'un paradigme de filtrage explicite peut par exemple être utilisé pour séparer erreurs numériques et erreurs de modélisation.

Bibliographie

- [3] M. Abkar, H. J. Bae, and P. Moin. Minimum-dissipation scalar transport model for large-eddy simulation of turbulent flows. *Physical Review Fluids*, 1(4) :041701, 2016.
- [14] J. Bardina, J. Ferziger, and W. C. Reynolds. Improved subgrid-scale models for large-eddy simulation. In *13th Fluid and Plasma Dynamics Conference*, page 1357, 1980.
- [38] C. Calvin, O. Cueto, and P. Emonot. An object-oriented approach to the design of fluid mechanics software. *ESAIM : Mathematical Modelling and Numerical Analysis*, 36(05) : 907–921, 2002.
- [50] P. Chassaing, R. A. Antonia, F. Anselmet, L. Joly, and S. Sarkar. *Variable density fluid turbulence*. Springer Science & Business Media, 2013.
- [77] J. W. Deardorff. A numerical study of three-dimensional turbulent channel flow at large reynolds numbers. *Journal of Fluid Mechanics*, 41(2) :453–480, 1970.
- [113] N. S. Ghaisas and S. H. Frankel. A priori evaluation of large eddy simulation subgrid-scale scalar flux models in isotropic passive-scalar and anisotropic buoyancy-driven homogeneous turbulence. *J. Turbulence*, 15(2) :88–121, 2014.
- [114] N. S. Ghaisas and S. H. Frankel. Dynamic gradient models for the sub-grid scale stress tensor and scalar flux vector in large eddy simulation. *Journal of Turbulence*, 17(1) : 30–50, 2016.
- [127] P. G. Huang, G. N. Coleman, and P. Bradshaw. Compressible turbulent channel flows : DNS results and modelling. *J. Fluid Mech.*, 305 :185–218, 1995.
- [147] H. Kobayashi. The subgrid-scale models based on coherent structures for rotating homogeneous turbulence and turbulent channel flow. *Physics of Fluids*, 17(4) :045104, 2005.
- [167] M. Lee and R. D. Moser. Direct numerical simulation of turbulent channel flow up to $Re_\tau \approx 5200$. *Journal of Fluid Mechanics*, 774 :395–415, 2015.
- [169] A. Leonard. Energy cascade in large eddy simulations of turbulent fluid flows. *Advances in Geophysics*, 18A :237–248, 1974.
- [173] M. Lesieur. *Turbulence in Fluids*. Fluid Mechanics and Its Applications. Springer, 2008. ISBN 9781402064357.
- [177] D. K. Lilly. A proposed modification of the germano subgrid-scale closure method. *Physics of Fluids A : Fluid Dynamics*, 4(3) :633–635, 1992.
- [178] L. I.-K. Lin. A concordance correlation coefficient to evaluate reproducibility. *Biometrics*, pages 255–268, 1989.
- [200] Y. Morinishi, T. S. Lundhomas, O. V. Vasilyev, and P. Moin. Fully conservative higher order finite difference schemes for incompressible flow. *J. Comput. Phys.*, 143(1) :90–124, 1998.
- [203] R. D. Moser, J. Kim, and N. N. Mansour. Direct numerical simulation of turbulent channel flow up to $Re_\tau = 590$. *Phys. Fluids*, 11(4) :943–945, 1999.
- [212] F. Nicoud. Conservative high-order finite-difference schemes for low-Mach number flows. *J. Comput. Phys.*, 158(1) :71–97, 2000.
- [213] F. Nicoud and F. Ducros. Subgrid-scale stress modelling based on the square of the velocity gradient tensor. *Flow, Turbulence and Combustion*, 62(3) :183–200, 1999. ISSN 1386-6184.
- [214] F. Nicoud, H. Baya Toda, O. Cabrit, S. Bose, and J. Lee. Using singular values to build a subgrid-scale model for large eddy simulations. *Physics of Fluids*, 23(8) :085106, 2011.
- [219] S. Paolucci. On the filtering of sound from the Navier–Stokes equations. Technical Report SAND82-8257, Sandia National Labs., Livermore, CA (USA), 1982.
- [221] N. Park, S. Lee, J. Lee, and H. Choi. A dynamic subgrid-scale eddy viscosity model with a global model coefficient. *Physics of Fluids*, 18(12) :125109, 2006.

- [224] A. Patel, B. J. Boersma, and R. Pecnik. Scalar statistics in variable property turbulent channel flows. *Physical Review Fluids*, 2(8) :084604, 2017.
- [225] R. Pecnik and A. Patel. Scaling and modelling of turbulence in variable property channel flows. *Journal of Fluid Mechanics*, 823, 2017.
- [245] O. Reynolds. On the dynamical theory of incompressible viscous fluids and the determination of the criterion. *Proceedings of the Royal Society of London*, 56(336-339) :40–45, 1894.
- [250] W. Rozema, H.J. Bae, P. Moin, and R. Verstappen. Minimum-dissipation models for large-eddy simulation. *Physics of Fluids*, 27(8) :085107, 2015.
- [252] S. Ryu and G. Iaccarino. A subgrid-scale eddy-viscosity model based on the volumetric strain-stretching. *Physics of Fluids*, 26(6) :065107, 2014.
- [253] P. Sagaut. *Large eddy simulation for incompressible flows : an introduction*. Springer Science & Business Media, 2006.
- [271] G. S. Sidharth and G. V. Candler. Stretched-vortex based subgrid-scale modeling for variable-density flows. In *45th AIAA Fluid Dynamics Conference*, page 2782, 2015.
- [272] G. S. Sidharth, A. Kartha, and G. V. Candler. Filtered velocity based LES of mixing in high speed recirculating shear flow. In *46th AIAA Fluid Dynamics Conference*, page 3184, 2016.
- [276] J. Smagorinsky. General circulation experiments with the primitive equations : I. the basic experiment. *Monthly weather review*, 91(3) :99–164, 1963.
- [277] A. J. Smits and J.-P. Dussauge. *Turbulent shear layers in supersonic flow*. Springer Science & Business Media, 2006.
- [287] W. Sutherland. The viscosity of gases and molecular force. *The London, Edinburgh, and Dublin Philosophical Magazine and Journal of Science*, 36(223) :507–531, 1893.
- [304] A. W. Vreman. An eddy-viscosity subgrid-scale model for turbulent shear flow : Algebraic theory and applications. *Physics of fluids*, 16(10) :3670–3681, 2004.
- [305] A. W. Vreman and J. G. M. Kuerten. Comparison of direct numerical simulation databases of turbulent channel flow at $Re_\tau = 180$. *Phys. Fluids*, 26(1) :015102, 2014.
- [313] J. H. Williamson. Low-storage Runge-Kutta schemes. *J. Comput. Phys.*, 35(1) :48–56, 1980.

Table of contents

Résumé en français	ii
1 Introduction	iii
2 Cadre physique et numérique	iv
2.1 Cadre physique	iv
2.2 Configuration de l'étude	v
3 Échanges énergétiques	vii
3.1 Équations des échanges énergétiques	vii
3.2 Effet du gradient de température	x
3.3 Effet du nombre de Reynolds	xii
4 Simulation des grandes échelles	xiv
4.1 Étude des termes sous-mailles	xiv
4.2 Test a priori des modèles	xvii
4.3 Test a posteriori des modèles	xx
5 Conclusion	xxiii
General introduction	1
1 Physical and numerical settings	5
1.1 Physical setting	6
1.1.1 Navier–Stokes Equations	6
1.1.2 Low Mach number equations	10
1.1.3 Variations of the fluid properties	14
1.1.4 Turbulence	15
1.2 Numerical schemes and resolution algorithm	15
1.2.1 Resolution algorithm	16
1.2.2 Stability timestep	18
1.2.3 Numerical schemes	18
1.3 Study configuration	22

1.3.1	Channel flow configuration	22
1.3.2	Numerical settings	23
1.3.3	Data acquisition	25
1.3.4	Validation	26
Part I Energy exchanges		31
2	Introduction of part I	33
3	Equations of energy exchanges in variable density turbulent flows	37
3.1	Introduction of chapter 3	37
3.2	Paper 1	38
3.2.1	Introduction	38
3.2.2	Energy exchanges between the different parts of total energy in the ternary decomposition	40
3.2.3	Spectral equation of the mean density turbulence kinetic energy	48
3.2.4	Conclusion	51
3.3	Conclusion of chapter 3	54
4	Turbulence kinetic energy exchanges in flows with highly variable fluid properties	55
4.1	Introduction of chapter 4	55
4.2	Paper 2	56
4.2.1	Introduction	57
4.2.2	Energy exchanges associated with the half-trace of the velocity fluctuation correlation tensor in the ternary decomposition	59
4.2.3	Study configuration	64
4.2.4	Results	72
4.2.5	Conclusion	103
4.3	Conclusion of chapter 4	107
5	Effect of the Reynolds number on turbulence kinetic energy exchanges	109
5.1	Introduction of chapter 5	109
5.2	Results	109
5.2.1	Effect of the Reynolds number in the spatial domain	110
5.2.2	Effect of the Reynolds number in the spectral domain	114
5.3	Conclusion of chapter 5	123

6	Conclusion of part I	125
Part II Large-eddy simulation		127
7	Introduction of part II	129
7.1	Filtering	130
7.2	Modelling	132
7.2.1	Structural models	133
7.2.2	Functional models	134
7.2.3	Mixed models	134
7.2.4	Dynamic models	135
7.3	Objectives of this work	137
8	Study of the large-eddy simulation subgrid terms of a low Mach number anisothermal channel flow	139
8.1	Introduction of chapter 8	139
8.2	Paper 3	140
8.2.1	Introduction	140
8.2.2	Low Mach number equations	142
8.2.3	Filtering of the low Mach number equations	143
8.2.4	Numerical study configuration	148
8.2.5	Results and discussion	151
8.2.6	Conclusion	161
8.3	Conclusion of chapter 8	165
9	A priori tests of subgrid-scale models in an anisothermal turbulent channel flow at low Mach number	167
9.1	Introduction of chapter 9	167
9.2	Paper 4	168
9.2.1	Introduction	169
9.2.2	Filtering of the low Mach number equations	170
9.2.3	Subgrid-scale models	172
9.2.4	Numerical study configuration	175
9.2.5	Asymptotic near-wall behaviour of the models	177
9.2.6	Results and discussion	178
9.2.7	Conclusion	191
9.3	Tensorial models	195

9.3.1	Definition	195
9.3.2	A priori tests	195
9.4	Conclusion of chapter 9	200
10	A posteriori tests of subgrid-scale models in an anisothermal turbulent channel flow at low Mach number	201
10.1	Introduction of chapter 10	201
10.2	Filtered low Mach number equations	202
10.3	Subgrid-scale models	204
10.3.1	Constant-parameter models	204
10.3.2	Dynamic models	206
10.4	Numerical study configuration	209
10.4.1	Channel flow configuration	209
10.4.2	Numerical settings	210
10.4.3	Filtering process	210
10.5	Results and discussion	211
10.5.1	Simulation without subgrid-scale models	212
10.5.2	Large-eddy simulation in the incompressible isothermal case	218
10.5.3	Large-eddy simulation in the anisothermal case	234
10.6	Conclusion of chapter 10	248
11	Conclusion of part II	257
	General conclusion and perspectives	259
	Appendices	263
A	Link between spatial and spectral correlations	265
B	Formulation and decomposition of the energy exchanges	267
B.1	Energy exchanges with the decomposition of density in a constant and variable part	267
B.1.1	General considerations	267
B.1.2	One-stage formulation	268
B.1.3	Two-stage formulation	270
B.2	Decomposition of the terms associated with constant density turbulence kinetic energy	276
B.2.1	Hypothesis and geometry	277

B.2.2	Decomposition in the spatial domain	277
B.2.3	Decomposition in the spectral domain	284
C	A priori tests of tensorial eddy-viscosity models	293
D	A posteriori tests	303
D.1	Tables of friction Reynolds number	303
D.1.1	Isothermal simulation at $Re_\tau = 180$	303
D.1.2	Anisothermal simulation at $Re_\tau = 180$	305
D.1.3	Anisothermal simulation at $Re_\tau = 395$	310
D.2	Tables of wall heat flux	312
D.2.1	Anisothermal simulation at $Re_\tau = 180$	312
D.2.2	Anisothermal simulation at $Re_\tau = 395$	318
D.3	Tables of thermodynamical pressure	320
D.3.1	Anisothermal simulation at $Re_\tau = 180$	320
D.3.2	Anisothermal simulation at $Re_\tau = 395$	325
D.4	Table of dynamic parameters	327
E	Spectral analysis of turbulence in anisothermal channel flows	331
E.1	Introduction	331
E.2	Momentum and spectral transport equations	333
E.2.1	Basic equations for direct numerical simulations	333
E.2.2	Equations and models for large-eddy simulations	334
E.2.3	Turbulent kinetic energy equation	336
E.2.4	Decomposition of TKE evolution terms	336
E.3	Simulated datasets and validation	338
E.3.1	Channel flow configuration	338
E.3.2	Numerical set up	339
E.3.3	Data collection and filtering for spectral analysis	340
E.3.4	Validation of the mean field profiles	340
E.3.5	Validation of the spectra measurements	341
E.4	Isothermal energy transport of distinctive Reynolds numbers	343
E.4.1	Isothermal turbulent spectra at low Reynolds number	344
E.4.2	Reynolds number effects on isothermal turbulent spectra	345
E.5	Anisothermal turbulent spectra of distinctive Reynolds numbers	345
E.5.1	Anisothermal turbulent spectra at low Reynolds number	345

E.5.2 Reynolds number effects on anisothermal turbulent spectra . . .	357
E.6 Conclusion	358
Nomenclature	367
List of figures	377
List of tables	380
Bibliography	380

General introduction

Energy is required by all economic activities, such as transportation, heating, cooling, lighting, producing goods or running electronic computing devices. Following the Industrial Revolution, energy consumption has increased massively, sustained by the extraction of fossil fuels. The use of fossil fuels has increased the concentration of greenhouse gas in the atmosphere, resulting in an ongoing climate change. In order to address this climate change, countries around the world have pledged to reduce their greenhouse gas emissions. Governments and energy market players need to undertake a complete transformation of the energy sector to achieve a more sustainable economic model.

Renewable energies have a decisive role to play in sustainable development policies, because they emit less greenhouse gases than fossil fuels. There is already a clear annual increase in global renewable electricity capacity. This emergence is explained by state subsidies, technological innovations and economies of scale. Within renewable energy, the use of solar energy has one of the largest future growth potential. There are currently two main technologies to produce electricity from solar energy: photovoltaic (PV) and concentrated solar power (CSP). Although photovoltaic systems currently dominates, concentrated solar power plants can easily be coupled with a thermal energy storage for a more flexible power generation. This ability will be crucial for the future development of the CSP sector.

In concentrated solar power plants, solar radiation is concentrated by mirrors or lenses to a solar receiver, in which a fluid flows. Heated, the fluid powers directly or indirectly a turbine, producing electricity. Solar power tower is the second most common CSP technology, after parabolic trough. In solar power towers, the solar field is composed of a large number of heliostats, tracking the sun on two axes, and the solar receiver is placed at the top of a tower (figure 1(a)). This configuration can reach high concentration factors, hence high temperatures. Different types of heat transfer fluid can be used, as water, molten salt or air. We focus on pressurised air, which can operate on an open cycle, avoids the need for an heat exchanger with the thermodynamic cycle, does not require cooling water and allows high temperatures (larger than 1000 K). This enables the use of high-efficiency thermodynamic cycles. However, this requires the development of efficient solar receivers operating at high temperature.

The solar receiver is a critical component of solar power towers, since it is responsible for the energy transfer between the concentrated solar flux and the fluid (figure 1(b)). This transfer is very important for the efficiency of the conversion of solar energy into electricity. The enhancement of the heat transfer in high-temperature solar receivers is one of the main research topics of PROMES laboratory. To ensure an effective energy

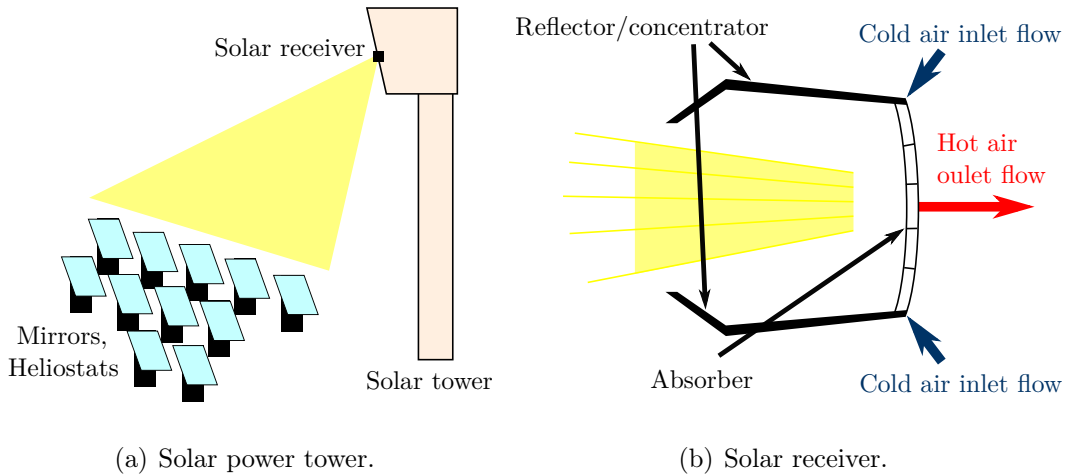


Figure 1 – Solar power tower and high-temperature solar cavity receiver.

exchange, it is useful to have turbulence in the solar receiver. Since the solar flux is received only on one side of the solar receiver, the flow is also subjected to a large temperature gradient. The temperature gradient and turbulence influences one another in a complex interaction. This coupling is characteristic of the strongly anisothermal turbulent flows found in solar receivers.

The internal geometry of the solar receiver, and the flow within, should be optimised to improve the solar power tower. In particular, the heat transfer towards the fluid should be maximised and the pressure loss minimised. This objective requires a better understanding and modelling of the interaction between temperature and turbulence. First, a better characterisation of the influence of temperature on turbulence would enable the development of mental heuristics and intuition regarding the effect of the temperature gradient and the approximations that can be made for optimisation of the solar receiver. Second, the accurate modelling of strongly anisothermal turbulent flows would allow the development of numerical simulations of the flow in the solar receiver taking into account the strong coupling between temperature and turbulence, paving the way for its optimization.

In this thesis carried out in PROMES laboratory, strongly anisothermal turbulent flows are investigated following two approaches. A first part studies the energy exchanges between the different parts of total energy and in particular the energy exchanges associated with turbulence kinetic energy. The results characterise the effect of the temperature gradient on the energy exchanges. A second part studies the large-eddy simulation (LES) modelling suited to the flows found in solar receiver. The results also characterise the effect of the temperature gradient with regard to the small-scale variations of the turbulent fields. In both cases, the investigation is based on numerical analyses of a strongly anisothermal turbulent channel flow, a simplified geometry that reproduces the distinctive features of the flows found in solar receiver. In particular, a large part of the work relies on the direct numerical simulation (DNS) of the channel.

Chapter 1 presents the physical and numerical settings used throughout the rest of the manuscript and describes the direct numerical simulations. Chapter 2 introduces the study of the energy exchanges with a brief comparison with homogeneous isotropic

incompressible turbulence. Chapter 3 provides a theoretical discussion of the decomposition of total energy underlying the energy exchanges. Chapter 4 investigates the effect of the temperature gradient on the energy exchanges associated with turbulence kinetic energy from the results of the direct numerical simulations. Chapter 5 extends the analysis to the influence of the Reynolds number on the effect of the temperature gradient. Chapter 6 concludes with regard to the physical phenomena governing the energy exchanges. Chapter 7 introduces the study of the large-eddy simulation with a brief overview of the LES paradigm. Chapter 8 investigates which terms should be modelled. Chapter 9 analyses the modelling of the most significant terms a priori, that is from the results of the direct numerical simulations. Chapter 10 examines their modelling a posteriori, that is from large-eddy simulations implementing the models. Chapter 11 concludes with regard to the LES modelling.

Chapters 3, 4 and 8 reproduce articles published in international peer-reviewed journals, respectively:

- D. Dupuy, A. Toutant, and F. Bataille. Equations of energy exchanges in variable density turbulent flows. *Physics Letters A*, 382(5):327–333, 2018 [89];
- D. Dupuy, A. Toutant, and F. Bataille. Turbulence kinetic energy exchanges in flows with highly variable fluid properties. *Journal of Fluid Mechanics*, 834:5–54, 2018 [91];
- D. Dupuy, A. Toutant, and F. Bataille. Study of the large-eddy simulation subgrid terms of a low mach number anisothermal channel flow. *International Journal of Thermal Sciences*, 135:221–234, 2018 [90].

Chapter 9 reproduces an article submitted for publication in an international peer-reviewed journal:

- D. Dupuy, A. Toutant, and F. Bataille. A priori tests of subgrid-scale models in an anisothermal turbulent channel flow at low mach number. (Submitted for publication) [86].

Chapters 5 and 10 present original materials.

A complementary study to this work has been published in

- F. Aulery, D. Dupuy, A. Toutant, F. Bataille, and Y. Zhou. Spectral analysis of turbulence in anisothermal channel flows. *Computers & Fluids*, 151:115–131, 2017 [11].

The paper is given in appendix E.

Chapter 1

Physical and numerical settings

The flows found in solar receivers are turbulent and subjected to a strong asymmetric heating, since the solar flux is collected to only on one side of the solar receiver. The typical Reynolds number is 10^5 and the typical solar flux is 600 kW m^{-2} , generating a temperature gradient of around 300 K over 1 cm. The temperature gradient creates large variations of the fluid properties (density, viscosity and thermal conductivity) in the solar receiver. The variations of the fluid properties have a significant impact on the velocity field and, conversely, the velocity influences the temperature field. This strong coupling between turbulence and the temperature gradient characterises the rich and complex behaviour of the flows found in solar receivers.

In order to study the effect of the interaction between temperature and turbulence, we investigate strongly anisothermal turbulent flows from the direct numerical simulation of the set of partial differential equations that govern their evolution. This is currently the only available theoretical method for the reliable and precise prediction of turbulent flows since, due to their strongly nonlinear nature, the equations governing the flow have no exact analytical solutions. The large computational complexity of direct numerical simulation limits its domain of applicability to simple geometries and moderate Reynolds numbers. To study the effect of the temperature gradient on strongly anisothermal turbulent flows in the context of wall turbulence, we model the solar receiver by a strongly anisothermal turbulent channel flow. The direct numerical simulation of fully developed turbulent channel flows with and without temperature gradient will provide high-resolution three-dimensional data which will be used throughout the rest of the manuscript.

In this chapter, we specify the physical and numerical settings of the investigations. We first discuss the choices made in terms of physical modelling, namely the use of the low Mach number equations. Then, we describe the method used for the direct numerical simulation of these equations, the resolution algorithm and the numerical schemes used. Finally, we give more specifically the physical and numerical configuration of the direct numerical simulations.

1.1 Physical setting

The motion of fluids is described by the Navier–Stokes equations which express the laws of classical mechanics and of thermodynamics. In high-temperature solar receivers, the flows are turbulent and subjected to large variations of the fluid properties. However, the velocity of the fluid in solar receivers is small compared to the speed of sound, as the typical Mach number is below 10^{-2} . Hence, the purely compressible effects found in high-speed flows, such as acoustic waves, are negligible. This particular physical configuration found in solar receivers let us simplify the Navier–Stokes equations under the low Mach number hypothesis, leading to the low Mach number equations. Two main assumptions are made in addition to the Navier–Stokes equations:

- The speed of the flow in the solar receiver is small compared to the speed of sound neglect and acoustic effects are negligible.
- The fluid in the solar receiver behaves like an ideal gas at the operating temperature and pressure of the solar receiver.

The model used are relevant to the flows found in high-temperature solar receivers and allows the coupling between temperature and velocity.

This section presents the more general Navier–Stokes equations and the derivation of the low Mach number equations for an ideal gas. In both cases, we give the underlying hypotheses and the domain of application. At last, the turbulent character of the flow described by these equations is briefly recalled.

1.1.1 Navier–Stokes Equations

1.1.1.1 General case

We consider a non-relativistic flow under the continuum hypothesis. Without loss of generality, no body forces are taken into account. In particular, gravity is neglected. The fluid is monophasic, non-reactive and without dissociation or molecular ionisation effects. No heat sources are considered and radiative heat transfers are neglected.

Under these conditions, a complete description of the flow is given by the knowledge of the spatiotemporal fields of velocity and of the state variables (in the thermodynamic sense) of the system. Knowing the state equation of the fluid, relating the state variables, the behaviour of the fluid may be determined using the evolution equations of velocity and any two independent state variables, generally among density ρ , temperature T , pressure P , internal energy I , entropy S or enthalpy H . The behavior of the unselected state variables may be inferred from the two independent state variables using the equation of state.

The Navier–Stokes equations is a system of equations of this type that can model the behaviour of a fluid in accordance with the hypotheses established above. They express in a differential and local form three laws of conservation which govern the flow [208, 282]:

- Mass conservation

$$\frac{\partial \rho}{\partial t} + \frac{\partial \rho U_j}{\partial x_j} = 0, \quad (1.1)$$

- Momentum conservation

$$\frac{\partial \rho U_i}{\partial t} + \frac{\partial \rho U_j U_i}{\partial x_j} = \frac{\partial \mathcal{Y}_{ij}}{\partial x_j}, \quad (1.2)$$

- Total energy conservation

$$\frac{\partial \rho(E + I)}{\partial t} + \frac{\partial \rho U_j(E + I)}{\partial x_j} = -\frac{\partial Q_j}{\partial x_j} + \frac{\partial \mathcal{Y}_{ij} U_i}{\partial x_j}, \quad (1.3)$$

with x_i the Cartesian coordinate in the i -th direction, U_i the velocity in the i -th direction, \mathcal{Y}_{ij} the component of the total stress tensor with the i and j indices, Q_j the conductive heat flux in the j -th direction, t the time and $(E + I)$ the total energy per unit mass, sum of internal energy per unit mass I and of kinetic energy per unit mass $E = \frac{1}{2}U_i U_i$. The index notation follows Einstein's summation convention and δ_{ij} is the Kronecker delta.

The fact that the Navier–Stokes equations are conservation laws is reflected mathematically by the conservative form of equations (1.1)–(1.3), where all terms except the time derivative are in the form of a divergence. Mass, momentum and energy cannot be created or destroyed and are constants in an isolated system. The mass conservation equation is an assumption of classical mechanics [119]. The momentum conservation equation expresses Newton's second law [211], that is the equality between the variations of momentum and the sum of external forces. The energy conservation equation expresses the first law of thermodynamics [65], that is the equality between the variations of total energy and the sum of the external work and the heat flux received.

The total stress tensor \mathcal{Y}_{ij} is given by the contributions of viscous stress Σ_{ij} and pressure stress,

$$\mathcal{Y}_{ij} = \Sigma_{ij} - P\delta_{ij}. \quad (1.4)$$

For a Newtonian fluid, the relationship between viscous stress and the rate of deformation tensor is linear,

$$\Sigma_{ij} = 2\mu S_{ij} + \eta S_{kk}\delta_{ij}, \quad (1.5)$$

where μ , called dynamic viscosity, and η , the second viscosity, are in general functions of the state variables and S_{ij} is the rate of deformation tensor,

$$S_{ij} = \frac{1}{2} \left(\frac{\partial U_i}{\partial x_j} + \frac{\partial U_j}{\partial x_i} \right). \quad (1.6)$$

Under Stokes' hypothesis [282], $\eta = -\frac{2}{3}\mu$ and the viscous stress tensor is given by

$$\Sigma_{ij} = 2\mu S_{ij} - \frac{2}{3}\mu S_{kk}\delta_{ij}. \quad (1.7)$$

The conductive heat flux is given by Fourier's law [99],

$$Q_j = -\lambda \frac{\partial T}{\partial x_j}. \quad (1.8)$$

with T the temperature and λ is the thermal conductivity, in general functions of the state variables. Knowledge of the fluid properties μ , η and λ in functions of the state variables is required to close the system.

In addition to equations (1.1)–(1.3), the second law of thermodynamics [66] imposes a lower bound on the variations of entropy S ,

$$\frac{\partial \rho S}{\partial t} + \frac{\partial \rho U_j S}{\partial x_j} \geq -\frac{\partial}{\partial x_j} \left(\frac{Q_j}{T} \right). \quad (1.9)$$

This is, assuming a Newtonian fluid and Fourier's law, always satisfied if $\lambda \geq 0$, $\mu \geq 0$ and $\eta \geq -\frac{2}{3}\mu$. This may be shown by the comparison of equation (1.9) with equation (1.15) below.

1.1.1.2 Alternative Formulations

The transport equation of internal energy I , enthalpy H , entropy S , temperature T and pressure P may be used in place of the mass conservation equation (1.1) or the total energy conservation equation (1.3) to close the system (1.1)–(1.3). This makes it possible to establish alternative formulations of the Navier–Stokes equations.

First, we multiply the momentum conservation equation (1.2) by U_i to obtain the transport equation of kinetic energy,

$$\frac{\partial \rho E}{\partial t} + \frac{\partial \rho U_j E}{\partial x_j} = -U_j \frac{\partial P}{\partial x_j} + U_i \frac{\partial \Sigma_{ij}}{\partial x_j}. \quad (1.10)$$

Subtracting this equation from the total energy conservation equation (1.3), we obtain the transport equation of internal energy,

$$\frac{\partial \rho I}{\partial t} + \frac{\partial \rho U_j I}{\partial x_j} = -\frac{\partial Q_j}{\partial x_j} - P \frac{\partial U_j}{\partial x_j} + \Sigma_{ij} \frac{\partial U_i}{\partial x_j}. \quad (1.11)$$

Let us denote $v = 1/\rho$ the specific volume. The transport equation of enthalpy $H = I + Pv = I + P/\rho$ follows directly,

$$\frac{\partial \rho H}{\partial t} + \frac{\partial \rho U_j H}{\partial x_j} = -\frac{\partial Q_j}{\partial x_j} + \frac{\partial P}{\partial t} + U_j \frac{\partial P}{\partial x_j} + \Sigma_{ij} \frac{\partial U_i}{\partial x_j}. \quad (1.12)$$

To obtain the entropy transport equation, we express internal energy as a function of entropy and specific volume,

$$\frac{DI}{Dt} = T \frac{DS}{Dt} - P \frac{Dv}{Dt}, \quad (1.13)$$

where the total derivative $D \cdot /Dt$ corresponds to a material derivative,

$$\frac{D \cdot}{Dt} = \frac{\partial \cdot}{\partial t} + U_j \frac{\partial \cdot}{\partial x_j}. \quad (1.14)$$

Injecting (1.13) into (1.11), we obtain the transport equation of entropy,

$$\frac{\partial \rho S}{\partial t} + \frac{\partial \rho U_j S}{\partial x_j} = -\frac{1}{T} \frac{\partial Q_j}{\partial x_j} + \frac{\Sigma_{ij}}{T} \frac{\partial U_i}{\partial x_j}. \quad (1.15)$$

The temperature transport equation may be obtained from the internal energy transport equation (1.11) or the enthalpy transport equation (1.12). In the first case, internal energy is first expressed as a function of temperature and specific volume,

$$\frac{DI}{Dt} = C_v \frac{DT}{Dt} + P(\beta T - 1) \frac{Dv}{Dt}, \quad (1.16)$$

with $C_v = (\partial I / \partial T)_v$ the isochoric heat capacity and $\beta = (1/P)(\partial P / \partial T)_v$ the isochoric thermal pressure coefficient. Injecting (1.16) into (1.11), we obtain

$$C_v \frac{\partial \rho T}{\partial t} + C_v \frac{\partial \rho U_j T}{\partial x_j} = -\frac{\partial Q_j}{\partial x_j} - \beta T P \frac{\partial U_j}{\partial x_j} + \Sigma_{ij} \frac{\partial U_i}{\partial x_j}. \quad (1.17)$$

In the second case, enthalpy is expressed as a function of temperature and pressure,

$$\frac{DH}{Dt} = C_p \frac{DT}{Dt} + v(1 - \alpha T) \frac{DP}{Dt}, \quad (1.18)$$

with $C_p = (\partial H / \partial T)_p$ the isobaric heat capacity and $\alpha = (1/v)(\partial v / \partial T)_p$ the isobaric thermal expansion coefficient. Injecting (1.18) into (1.12), we obtain

$$C_p \frac{\partial \rho T}{\partial t} + C_p \frac{\partial \rho U_j T}{\partial x_j} = -\frac{\partial Q_j}{\partial x_j} + \alpha T \frac{\partial P}{\partial t} + \alpha T U_j \frac{\partial P}{\partial x_j} + \Sigma_{ij} \frac{\partial U_i}{\partial x_j}, \quad (1.19)$$

The pressure transport equation is derived from (1.17) and (1.19),

$$\frac{\partial P}{\partial t} + \frac{\partial U_j P}{\partial x_j} = -\frac{\gamma - 1}{\alpha T} \frac{\partial Q_j}{\partial x_j} + P \left(1 - \frac{\gamma \beta}{\alpha} \right) \frac{\partial U_j}{\partial x_j} + \frac{\gamma - 1}{\alpha T} \Sigma_{ij} \frac{\partial U_i}{\partial x_j}, \quad (1.20)$$

with $\gamma = C_p / C_v$ the adiabatic index. If we introduce the isothermal compressibility $\chi_T = -(1/v)(\partial v / \partial P)_T$ and the isentropic compressibility $\chi_S = -(1/v)(\partial v / \partial P)_S$, the factor $\gamma \beta P / \alpha$ can be expressed as a function of the speed of sound $c = \sqrt{1/(\rho \chi_S)}$ using the triple product rule $(\partial P / \partial T)_v (\partial T / \partial v)_P (\partial v / \partial P)_T = -1$, which implies $\alpha = \beta P \chi_T$, and Reech's relation $\gamma = C_p / C_v = \chi_T / \chi_S$ [243],

$$\frac{\gamma \beta P}{\alpha} = \frac{\gamma}{\chi_T} = \rho c^2. \quad (1.21)$$

In general, the heat capacities and the adiabatic index are functions of the state variables.

1.1.1.3 Case of an ideal gas

An ideal gas is a fluid satisfying the equation of state

$$P = r \rho T, \quad (1.22)$$

where r is the ideal gas specific constant. In an ideal gas, the heat capacities depend only on the temperature and obey Mayer's relation, $C_p - C_v = r$. In addition, $\alpha = \beta = 1/T$. Therefore, internal energy and enthalpy depend only on temperature. The expression of the transport equations of temperature and pressure are simplified:

$$C_v \frac{\partial \rho T}{\partial t} + C_v \frac{\partial \rho U_j T}{\partial x_j} = -\frac{\partial Q_j}{\partial x_j} - P \frac{\partial U_j}{\partial x_j} + \Sigma_{ij} \frac{\partial U_i}{\partial x_j}, \quad (1.23)$$

$$C_p \frac{\partial \rho T}{\partial t} + C_p \frac{\partial \rho U_j T}{\partial x_j} = -\frac{\partial Q_j}{\partial x_j} + \frac{\partial P}{\partial t} + U_j \frac{\partial P}{\partial x_j} + \Sigma_{ij} \frac{\partial U_i}{\partial x_j}, \quad (1.24)$$

$$\frac{\partial P}{\partial t} + \frac{\partial U_j P}{\partial x_j} = -(\gamma - 1) \frac{\partial Q_j}{\partial x_j} + P(1 - \gamma) \frac{\partial U_j}{\partial x_j} + (\gamma - 1) \Sigma_{ij} \frac{\partial U_i}{\partial x_j}. \quad (1.25)$$

These expressions are valid even if the heat capacities and adiabatic index are temperature dependent.

1.1.2 Low Mach number equations

The low Mach number equations are an approximation of the Navier–Stokes equations suited to flows where the compressibility effects due to velocity are negligible but with large variations of fluid properties (density, viscosity and thermal conductivity). The approximation neglects the effect of acoustic waves and allows the use of numerical method intended for incompressible flows [206, 205]. The low Mach number hypothesis is generally considered relevant if the characteristic flow velocity U^b is small compared to the speed of sound c^b , and more specifically when the Mach number $Ma = U^b/c^b$ is below 0.3.

We use the method developed by Paolucci [219] to derive the low Mach number equations for an ideal gas. Derivations of the low Mach number equations may also be found in [186, 179, 193, 205, 128, 20, 22, 267, 12, 323, 157]. The approach is based on two steps. First, the Navier–Stokes equations are nondimensionalised, introducing dimensionless numbers that characterise the relative importance of the competing physical processes. Then, each dimensionless variable is expressed as a power series of the squared Mach number, giving rise to the low Mach number equations if only the smaller orders are kept.

1.1.2.1 Nondimensionalisation of the Navier–Stokes equations

The Navier–Stokes equations are nondimensionalised in the case of an ideal, Newtonian gas under Stokes’ hypothesis by introducing for each variable a value characteristic of the flow considered. We define a length scale representative of the flow x^b , a velocity scale U^b , a time scale $t^b = x^b/U^b$, a temperature scale T^b , a density scale ρ^b , a pressure scale $P^b = r\rho^b T^b$, a dynamic viscosity scale $\mu^b = \mu(T^b)$, a thermal conductivity scale $\lambda^b = \lambda(T^b)$, an isochoric heat capacity scale $C_v^b = C_v(T^b)$ and an isobar heat capacity scale $C_p^b = C_p(T^b)$:

$$x^\circ = \frac{x}{x^b}, \quad (1.26) \qquad P^\circ = \frac{P}{P^b}, \quad (1.31)$$

$$t^\circ = \frac{t}{t^b}, \quad (1.27) \qquad \mu^\circ = \frac{\mu}{\mu^b}, \quad (1.32)$$

$$U^\circ = \frac{U}{U^b}, \quad (1.28) \qquad \lambda^\circ = \frac{\lambda}{\lambda^b}, \quad (1.33)$$

$$T^\circ = \frac{T}{T^b}, \quad (1.29) \qquad C_v^\circ = \frac{C_v}{C_v^b}, \quad (1.34)$$

$$\rho^\circ = \frac{\rho}{\rho^b}, \quad (1.30) \qquad C_p^\circ = \frac{C_p}{C_p^b}. \quad (1.35)$$

The introduction of nondimensionalised variables in the Navier–Stokes equations leads to the definition of three dimensionless numbers that characterise the flow. The Reynolds number,

$$Re = \frac{\rho^b U^b x^b}{\mu^b}, \quad (1.36)$$

represents the ratio between the convective and viscous transfers of momentum. The Prandtl number,

$$Pr = \frac{\mu^b C_p^b}{\lambda^b}, \quad (1.37)$$

represents the ratio between the momentum diffusivity and the thermal diffusivity. Finally, The Mach number,

$$Ma = \frac{U^b}{c^b}, \quad (1.38)$$

already defined, where, for an ideal gas, the speed of sound representative of the flow is given by $c^b = \sqrt{\gamma r T^b}$.

With the energy conservation equation expressed as the temperature transport equation (1.17), the Navier–Stokes equations and the ideal gas law are in their nondimensionalised form given by:

- Mass conservation

$$\frac{\partial \rho^\circ}{\partial t^\circ} + \frac{\partial \rho^\circ U_j^\circ}{\partial x_j^\circ} = 0, \quad (1.39)$$

- Momentum conservation

$$\frac{\partial \rho^\circ U_i^\circ}{\partial t^\circ} + \frac{\partial \rho^\circ U_j^\circ U_i^\circ}{\partial x_j^\circ} = -\frac{1}{\gamma Ma^2} \frac{\partial P^\circ}{\partial x_i^\circ} + \frac{1}{Re} \frac{\partial \Sigma_{ij}^\circ}{\partial x_j^\circ}, \quad (1.40)$$

- Energy conservation (transport of temperature)

$$C_v^\circ \frac{\partial \rho^\circ T^\circ}{\partial t^\circ} + C_v^\circ \frac{\partial \rho^\circ U_j^\circ T^\circ}{\partial x_j^\circ} = -\frac{\gamma}{Re Pr} \frac{\partial Q_j^\circ}{\partial x_j^\circ} - (\gamma - 1) P^\circ \frac{\partial U_j^\circ}{\partial x_j^\circ} + \gamma (\gamma - 1) \frac{Ma^2}{Re} \Sigma_{ij}^\circ \frac{\partial U_i^\circ}{\partial x_j^\circ}, \quad (1.41)$$

- Ideal gas law

$$P^\circ = \rho^\circ T^\circ, \quad (1.42)$$

with Σ_{ij}° the nondimensionalised viscous stress tensor,

$$\Sigma_{ij}^\circ = 2\mu^\circ S_{ij}^\circ - \frac{2}{3}\mu^\circ S_{kk}^\circ \delta_{ij}, \quad (1.43)$$

and Q_j° the nondimensionalised conductive heat flux,

$$Q_j^\circ = -\lambda^\circ \frac{\partial T^\circ}{\partial x_j^\circ}. \quad (1.44)$$

For reference, we also give the nondimensionalised transport equations of temperature, as deduced from (1.19),

$$C_p^\circ \frac{\partial \rho^\circ T^\circ}{\partial t^\circ} + C_p^\circ \frac{\partial \rho^\circ U_j^\circ T^\circ}{\partial x_j^\circ} = -\frac{1}{Re Pr} \frac{\partial Q_j^\circ}{\partial x_j^\circ} + \frac{\gamma - 1}{\gamma} \frac{\partial P^\circ}{\partial t} + \frac{\gamma}{\gamma - 1} U_j^\circ \frac{\partial P^\circ}{\partial x_j^\circ} + (\gamma - 1) \frac{Ma^2}{Re} \Sigma_{ij}^\circ \frac{\partial U_i^\circ}{\partial x_j^\circ}, \quad (1.45)$$

and of pressure (1.20),

$$\frac{\partial P^\circ}{\partial t^\circ} + \frac{\partial U_j^\circ P^\circ}{\partial x_j^\circ} = -\frac{\gamma}{RePr} \frac{\partial Q_j^\circ}{\partial x_j^\circ} + P^\circ (1 - \gamma) \frac{\partial U_j^\circ}{\partial x_j^\circ} + \gamma(\gamma - 1) \frac{Ma^2}{Re} \Sigma_{ij}^\circ \frac{\partial U_i^\circ}{\partial x_j^\circ}. \quad (1.46)$$

In the nondimensionalised form (1.39)–(1.42), the pressure gradient in the momentum conservation equation leads to a singularity when the Mach number tends to zero. This implies that the pressure tends to a constant [6] and leads to the establishment of a system of equations where the pressure is split in two terms, the low Mach number equations. To show this, one possible approach is to perform an asymptotic development of the variables of equations (1.39)–(1.42) as a function of the squared Mach number [179, 205, 193].

1.1.2.2 Asymptotic development of Navier–Stokes equations

An asymptotic development of each nondimensionalised variable as a function of the squared Mach number Ma^2 is carried out:

$$U^\circ = U^{(0)} + Ma^2 U^{(1)} + \mathcal{O}(Ma^4), \quad (1.47)$$

$$T^\circ = T^{(0)} + Ma^2 T^{(1)} + \mathcal{O}(Ma^4), \quad (1.48)$$

$$\rho^\circ = \rho^{(0)} + Ma^2 \rho^{(1)} + \mathcal{O}(Ma^4), \quad (1.49)$$

$$P^\circ = P^{(0)} + Ma^2 P^{(1)} + \mathcal{O}(Ma^4), \quad (1.50)$$

$$\lambda^\circ = \lambda^{(0)} + Ma^2 \lambda^{(1)} + \mathcal{O}(Ma^4), \quad (1.51)$$

$$\mu^\circ = \mu^{(0)} + Ma^2 \mu^{(1)} + \mathcal{O}(Ma^4), \quad (1.52)$$

$$C_v^\circ = C_v^{(0)} + Ma^2 C_v^{(1)} + \mathcal{O}(Ma^4), \quad (1.53)$$

$$C_p^\circ = C_p^{(0)} + Ma^2 C_p^{(1)} + \mathcal{O}(Ma^4), \quad (1.54)$$

$$\gamma^\circ = \gamma^{(0)} + Ma^2 \gamma^{(1)} + \mathcal{O}(Ma^4), \quad (1.55)$$

$$Q_j^\circ = Q_j^{(0)} + Ma^2 Q_j^{(1)} + \mathcal{O}(Ma^4), \quad (1.56)$$

$$\Sigma_{ij}^\circ = \Sigma_{ij}^{(0)} + Ma^2 \Sigma_{ij}^{(1)} + \mathcal{O}(Ma^4). \quad (1.57)$$

Injecting these asymptotic developments into the nondimensionalised Navier–Stokes equations (1.39)–(1.42), we obtain,

$$\frac{\partial \rho^{(0)}}{\partial t^\circ} + \frac{\partial \rho^{(0)} U_j^{(0)}}{\partial x_j^\circ} = \mathcal{O}(Ma^2), \quad (1.58)$$

$$\frac{\partial \rho^{(0)} U_i^{(0)}}{\partial t^\circ} + \frac{\partial \rho^{(0)} U_j^{(0)} U_i^{(0)}}{\partial x_j^\circ} = -\frac{1}{\gamma^{(0)} Ma^2} \frac{\partial P^{(0)}}{\partial x_i^\circ} - \frac{1}{\gamma^{(0)}} \frac{\partial P^{(1)}}{\partial x_i^\circ} + \frac{1}{Re} \frac{\partial \Sigma_{ij}^{(0)}}{\partial x_j^\circ} + \mathcal{O}(Ma^2), \quad (1.59)$$

$$C_v^{(0)} \frac{\partial \rho^{(0)} T^{(0)}}{\partial t^\circ} + C_v^{(0)} \frac{\partial \rho^{(0)} U_j^{(0)} T^{(0)}}{\partial x_j^\circ} = -\frac{\gamma^{(0)}}{RePr} \frac{\partial Q_j^{(0)}}{\partial x_j^{(0)}} - (\gamma^{(0)} - 1) P^{(0)} \frac{\partial U_j^{(0)}}{\partial x_j^\circ} + \mathcal{O}(Ma^2), \quad (1.60)$$

$$P^{(0)} = \rho^{(0)} T^{(0)} + \mathcal{O}(Ma^2). \quad (1.61)$$

In the energy conservation equation, the term related to the viscous stress (the dissipation) does not give any contributions of order below $\mathcal{O}(Ma^2)$.

By grouping in each equation the terms of the same order and imposing that each grouping must separately be equal to zero, the system of equations (1.58)–(1.61) is reduced at the order $\mathcal{O}(Ma^{-2})$ to

$$\frac{\partial P^{(0)}}{\partial x_i^\circ} = 0, \quad (1.62)$$

expressing the homogeneity of the zeroth-order pressure. In other words, the spatial variations in pressure are at least of order $\mathcal{O}(Ma^2)$ and $P^{(0)}$ is a function of time only.

At the order $\mathcal{O}(Ma^0)$, the system of equations (1.58)–(1.61) is reduced to

$$\frac{\partial \rho^{(0)}}{\partial t^\circ} + \frac{\partial \rho^{(0)} U_j^{(0)}}{\partial x_j^\circ} = 0, \quad (1.63)$$

$$\frac{\partial \rho^{(0)} U_i^{(0)}}{\partial t^\circ} + \frac{\partial \rho^{(0)} U_j^{(0)} U_i^{(0)}}{\partial x_j^\circ} = -\frac{1}{\gamma^{(0)}} \frac{\partial P^{(1)}}{\partial x_i^\circ} + \frac{1}{Re} \frac{\partial \Sigma_{ij}^{(0)}}{\partial x_j^\circ}, \quad (1.64)$$

$$C_v^{(0)} \frac{\partial \rho^{(0)} T^{(0)}}{\partial t^\circ} + C_v^{(0)} \frac{\partial \rho^{(0)} U_j^{(0)} T^{(0)}}{\partial x_j^\circ} = -\frac{\gamma^{(0)}}{RePr} \frac{\partial Q_j^{(0)}}{\partial x_j^\circ} - (\gamma^{(0)} - 1) P^{(0)} \frac{\partial U_j^{(0)}}{\partial x_j^\circ}, \quad (1.65)$$

$$P^{(0)} = \rho^{(0)} T^{(0)}. \quad (1.66)$$

These equations are very close to the Navier–Stokes equations (1.39)–(1.42) and form with (1.62) the nondimensionalised low Mach number equations. The gradient of the second-order pressure appears in the conservation equation of the momentum. Since the zeroth-order pressure is constant in space, it may be seen that the mass conservation equation and the conservation equation of the momentum are not affected by the asymptotic development. In the energy conservation equation, dissipation is neglected. Finally, the contribution of the second-order pressure is neglected in the energy conservation equation and the ideal gas law.

1.1.2.3 Low Mach number equations

The redimensionalisation of equations (1.39)–(1.42) leads to the low Mach number equations. Removing the exponent ⁽⁰⁾ and denoting $P_0 = P^b P^{(0)}$ and $P = Ma^2 P^b P^{(1)}$ or, equivalently, using $\rho^b (U^b)^2 / \gamma$ as the pressure scale to redimensionalise $P^{(1)}$, the low Mach number equations are given by:

- Mass conservation

$$\frac{\partial \rho}{\partial t} + \frac{\partial \rho U_j}{\partial x_j} = 0, \quad (1.67)$$

- Momentum conservation

$$\frac{\partial \rho U_i}{\partial t} = -\frac{\partial \rho U_j U_i}{\partial x_j} - \frac{\partial P}{\partial x_i} + \frac{\partial \Sigma_{ij}}{\partial x_j}, \quad (1.68)$$

- Energy conservation

$$\frac{\partial U_j}{\partial x_j} = -\frac{1}{\gamma P_0} \left[(\gamma - 1) \frac{\partial Q_j}{\partial x_j} + \frac{\partial P_0}{\partial t} \right], \quad (1.69)$$

- Ideal gas law

$$T = \frac{P_0}{\rho r}, \quad (1.70)$$

where the pressure is separated in two terms: the thermodynamical pressure P_0 , constant in space, which represents the mean pressure in the domain, and the mechanical pressure P , spatially varying, related to variations in the momentum. The homogeneity of the thermodynamical pressure may be interpreted as the consequence of the infinite speed of the acoustic waves, in the approximation of low Mach number, leading to an instantaneous uniformisation of pressure.

The particular form of the energy conservation equation (1.69) is obtained by injecting (1.66) into the energy conservation equation (1.65) and using the fact that the thermodynamical pressure is constant in space. The local energy conservation is imposed by a constraint on the divergence of the velocity [212].

When the Mach number tends towards zero, the solutions of the Navier–Stokes equations (1.1)–(1.3) converge to the solution of the low Mach number equations (1.67)–(1.70) [5, 6]. If conductive heat transfers are neglected, the low Mach number equations give rise to the incompressible Navier–Stokes equations [206, 205].

1.1.3 Variations of the fluid properties

The system of equations (1.67)–(1.70) describes the physics of low Mach number flows but its resolution requires closing the system by giving the expressions of the ideal gas specific constant, the heat capacities and the properties of the fluid as a function of the state variables. These expressions depend on the gas under consideration. For air, the ideal gas specific constant is $r = 287 \text{ J kg}^{-1} \text{ K}^{-1}$. The variations of dynamic viscosity with temperature may be modelled by Sutherland’s law [287], valid from 220 K to 1900 K [277],

$$\mu = \mu_0 \left(\frac{T}{T_0} \right)^{\frac{3}{2}} \frac{T_0 + S_1}{T + S_1}, \quad (1.71)$$

with $\mu_0 = 1.716 \cdot 10^{-5} \text{ Pa s}$, $S_1 = 110.4 \text{ K}$ and $T_0 = 273.15 \text{ K}$. Within this temperature range, the variations of the adiabatic index of air are very small. Neglecting these variations, it follows for an ideal gas that the isochoric and isobaric heat capacities, C_v and C_p , are constant. Finally, the variations of thermal conductivity may be expressed using the Prandtl number,

$$\lambda = \frac{\mu C_p}{Pr}. \quad (1.72)$$

The Prandtl number is assumed constant over the temperature range considered, with $Pr = 0.76$ and $C_p = 1005 \text{ J kg}^{-1} \text{ K}^{-1}$.

1.1.4 Turbulence

The Navier–Stokes equations and the low Mach number equations form a highly nonlinear system of equations whose solution can, depending on the Reynolds number, be turbulent. Turbulent flows are chaotic and exhibit, at every point, numerous eddies of various scales. They are also three-dimensional and characterised by a spatiotemporal irregularity, an unpredictability of trajectories, a rotational kinematics and an enhanced diffusion and dissipation. The majority of flows encountered in nature and engineering applications are turbulent. Turbulence is useful in heat exchangers because it tends to accelerate homogenisation and mixing, thus improving the efficiency of heat and momentum transfers.

The flow regime is characterised by the Reynolds number (1.36). For a given problem, the flow becomes turbulent if the Reynolds number exceeds a critical value, usually between 2000 and 3000 [244, 48], with a fairly rapid transition. Below this value, the flow is laminar as the friction forces outweigh inertial forces and quickly absorb any perturbation.

Because of the chaotic nature of turbulent flows, independent experiments or simulations with arbitrarily close (but different) initial conditions give rise to a different result. This leads to the definition of the Reynolds average or statistical average, defined as the average over a large number of independent experiments,

$$\langle G(x, y, z, t) \rangle = \lim_{N \rightarrow \infty} \frac{1}{N} \sum_{i=1}^N G_i(x, y, z, t), \quad (1.73)$$

where G_i is the value of G during the experiment i and N the number of experiments. The Reynolds decomposition corresponds to the decomposition of G into an average part and a fluctuating part ($'$),

$$G = \langle G \rangle + G'. \quad (1.74)$$

where the fluctuating part, with no statistical mean, is the deviation from the statistical mean. This is represented in figure 1.1.

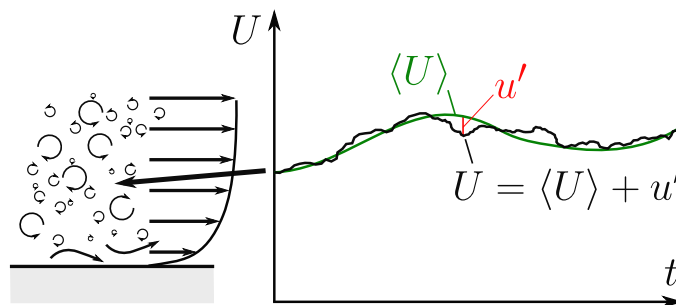


Figure 1.1 – Reynolds decomposition of the velocity field.

1.2 Numerical schemes and resolution algorithm

The resolution of Navier–Stokes equations is an extremely difficult problem because these equations are highly nonlinear and coupled. Exact analytical solutions have only

been found for the most simple problems and in the absence of turbulence, and the existence and regularity of the solutions of the Navier–Stokes equations remains an open problem [132]. Nevertheless, numerical simulation offers a way to analyse and predict the behaviour of complex flows.

The numerical simulation of turbulent flows, however, remains a difficult task due to the inherent chaotic and multi-scale nature of turbulence. The resolution without models of the Navier–Stokes equations, called direct numerical simulation, requires a sufficient spatiotemporal resolution to describe the smallest turbulent structures while ensuring that the computational domain is large enough to capture the largest flow structures. As a result, the direct numerical simulation of turbulent flows requires considerable computer resources, and is therefore only practicable for simple geometries and for a moderate Reynolds number.

In spite of this, the direct numerical simulation of turbulence has since its advent [100, 218] proved to be a powerful tool for the fundamental study of turbulence. The usefulness of direct numerical simulation is due to two unique characteristics. First, they give access to all the three-dimensional fields that characterise the fluid as a function of time, making it possible to determine any quantity of interest from the simulation, including those that would be difficult or impossible to determine experimentally. Second, direct numerical simulation allows complete control over turbulence, through initial and boundary conditions, and the manipulation of resolved equations. Reliable scientific inferences may be drawn from the results of direct numerical simulations because the mathematical models expressed by the Navier–Stokes equations (Newtonian fluid, Fourier’s law, ideal gas) provide a relevant and valid description of the dynamics of many flows, at all turbulence scales [202].

The direct numerical simulation of the low Mach number equations (1.67)–(1.70) allows the use of different numerical methods than the Navier–Stokes equations (1.1)–(1.3) because of the removal of acoustic waves and the decomposition of pressure in two terms [206, 205]. In order to resolve the low Mach number equations from direct numerical simulation, we use a finite difference method in a staggered grid system [200, 212] and a third-order Runge–Kutta time scheme [313] using the TrioCFD software [38]. The resolution algorithm and the numerical schemes are presented in this section.

1.2.1 Resolution algorithm

The resolution algorithm used to resolve the low Mach number equations (1.67)–(1.70) is presented in this section. The algorithm aims to ensure that as many conservation properties as possible are exactly verified numerically. The algorithm ensures the local and global conservation of energy, using the energy conservation equation to determine both the thermodynamical and mechanical pressures. The mass conservation is only guaranteed locally. The overall conservation of the mass is ensured by the quality of the computation of the divergence of the mass flux.

A projection method is used to compute pressure and velocity. Projection methods were introduced in the context of numerical simulations by Chorin [54], Temam [289] following the basic ideas of prior works [171, 172, 152, 105]. Projection models are based on a two-step procedure. First, an intermediate velocity field is computed by ignoring the pressure term in the momentum conservation equation. Then, the in-

intermediate velocity is corrected using a pressure equation to impose the constraint of the energy conservation equation on the divergence of the velocity. This results in the decoupling of the computations of the velocity and the pressure fields. The low Mach number equations can be resolved, at each timestep, from the resolution of a sequence of decoupled equations.

We solve at each timestep the variables in the following order:

1. the density from the mass conservation equation,

$$\frac{\rho^{n+1} - \rho^n}{\Delta t} = -\nabla \cdot (\rho^n \mathbf{U}^n) = 0; \quad (1.75)$$

2. the thermodynamical pressure and temperature using a fixed-point iteration, namely $P_0^{n+1} = P_0^{n+1,3}$ and $T^{n+1} = T^{n+1,3}$ where $P_0^{n+1} = P_0^{n+1,k}$ and $T^{n+1} = T^{n+1,k}$ are computed from $P_0^{n+1} = P_0^{n+1,0}$ and $T^{n+1} = T^{n+1,0}$ and the iteration for k from 0 to 3 (value empirically determined to obtain convergence) of:

- (a) the thermodynamical pressure from the integration on the whole domain of the energy conservation equation,

$$P_0^{n+1,k+1} = \frac{P_0^n}{1 - \frac{\gamma - 1}{V} \frac{\Delta t}{P_0^{n+1,k}} \int_{\omega} \lambda_{\omega} \nabla T^{n+1,k} dS}, \quad (1.76)$$

- (b) the temperature from the ideal gas law,

$$T^{n+1,k+1} = \frac{P_0^{n+1,k+1}}{r \rho^{n+1}}; \quad (1.77)$$

3. the kinematic viscosity from Sutherland's law ($\mu_0 = 1.716 \cdot 10^{-5}$ Pa s, $S_1 = 110.4$ K, $T_0 = 273.15$ K),

$$\mu^{n+1} = \mu_0 \left(\frac{T^{n+1}}{T_0} \right)^{\frac{3}{2}} \frac{T_0 + S_1}{T^{n+1} + S_1}; \quad (1.78)$$

4. the thermal conductivity from the Prandtl number ($C_p = 1005$ J kg⁻¹ K⁻¹, $Pr = 0.76$),

$$\lambda^{n+1} = \frac{\mu^{n+1} C_p}{Pr}; \quad (1.79)$$

5. the divergence of velocity from the energy conservation equation,

$$(\nabla \cdot \mathbf{U})^{n+1} = \frac{1}{\gamma P_0^{n+1}} \left[(\gamma - 1) \nabla \cdot (\lambda^{n+1} \nabla T^{n+1}) - \frac{P_0^{n+1} - P_0^n}{\Delta t} \right]; \quad (1.80)$$

6. an intermediate velocity from the momentum conservation equation without the pressure term,

$$\begin{aligned} \rho^n \frac{\mathbf{U}^* - \mathbf{U}^n}{\Delta t} &= -\rho^n (\mathbf{U}^n \cdot \nabla) \mathbf{U}^n \\ &+ \nabla \cdot (\mu^n (\nabla \mathbf{U}^n + \nabla^T \mathbf{U}^n)) - \frac{2}{3} \nabla (\mu^n (\nabla \cdot \mathbf{U})^n). \end{aligned} \quad (1.81)$$

7. the mechanical pressure from the divergence of the intermediate velocity,

$$\nabla \cdot \left(\frac{1}{\rho^n} \nabla P^n \right) = \frac{(\nabla \cdot \mathbf{U})^* - (\nabla \cdot \mathbf{U})^{n+1}}{\Delta t} \quad (1.82)$$

8. the velocity from the momentum conservation equation,

$$\rho^n \frac{\mathbf{U}^{n+1} - \mathbf{U}^*}{\Delta t} = -\nabla P^n. \quad (1.83)$$

To simplify the expressions, the derivatives are given with an explicit Euler discretisation. In the actual algorithm, the time derivatives are discretised using a third-order Runge–Kutta method [251, 153].

1.2.2 Stability timestep

The timestep Δt of the simulation is determined at each timestep in order to respect stability criteria. The energy conservation equation acting as a constraint on the pressure in the resolution algorithm, it has no associated stability constraints. The timestep of the simulation is therefore only determined by the stability requirements of the momentum conservation equation.

Two stability criteria are used. In accordance with the Courant–Friedrichs–Lewy condition [69], the timestep of the simulation must be small enough for the fluid to be at no point of the domain able to travel more than one mesh in one timestep. In other words, the convection stability timestep defined by

$$\frac{1}{\Delta t_{\text{conv}}} = \max_{x,y,z} \left[\frac{U_x}{\Delta x} + \frac{U_y}{\Delta y} + \frac{U_z}{\Delta z} \right]. \quad (1.84)$$

In addition, we associate to the momentum diffusion a stability timestep defined by

$$\frac{1}{\Delta t_{\text{diff}}} = \max_{x,y,z} \left[2\nu \left(\frac{1}{\Delta x^2} + \frac{1}{\Delta y^2} + \frac{1}{\Delta z^2} \right) \right]. \quad (1.85)$$

The timestep of the simulation is the half of the harmonic mean of these two values,

$$\frac{1}{\Delta t} = \frac{1}{\Delta t_{\text{conv}}} + \frac{1}{\Delta t_{\text{diff}}}. \quad (1.86)$$

In practice, the timestep is only updated if it is less than the previous timestep, or if the difference is more than 5 %.

1.2.3 Numerical schemes

The equations are discretised in a rectangular three-dimensional grid with a nonuniform grid spacing. A finite difference scheme is used in a staggered grid system. The scalar variables (pressure, density, temperature, viscosity, thermal conductivity etc.) are stored at the same points while the velocity components are distributed around these locations (see figure 1.2). The scalar variables are located at the centre of the

rectangular cells of the grid while and the velocity components at the centre of the faces of the cell they are perpendicular to. All the terms of the mass and energy conservation equations are discretised at the same location as the scalar variables. The terms of the momentum conservation equation in the i -th direction are discretised at the centre of the faces perpendicular to the i -th direction.

In the remaining part of this section, we give the discretisations and numerical schemes used in more details. In order to describe the nonuniform staggered grid system, we introduce a formalism to describe the discretisation of staggered fields. The reader in a hurry might prefer to skip this part up to section 1.3.

In each direction k , we define an uniform grid coordinate $\xi_k^n = n\Delta_k$, where Δ_k is a constant. A monotonic differentiable function f_k maps the points of the uniform computational grid to the nonuniform grid. That is, the nonuniform grid coordinate is given by $x_k^n = f_k(\xi_k^n)$. The points of the uniform grid are triplets of the form $(\xi_x^n, \xi_y^n, \xi_z^n)$, associated with the point of the nonuniform grid $(x^{n_x}, y^{n_y}, z^{n_z})$. These points may be given by a position vector $\mathbf{x}^{n_x, n_y, n_z} = x_k^{n_k} \mathbf{e}_k$, where \mathbf{e}_k is the unit vector in direction k .

Consider that the points of the form $(x_x^{n_x}, x_y^{n_y}, x_z^{n_z})$ corresponds to the centre of the cells. Then, we denote $\phi^{n_x, n_y, n_z} = \phi(x_k^{n_k} \mathbf{e}_k) = \phi(x^{n_x}, y^{n_y}, z^{n_z})$ the value of the three-dimensional field ϕ discretised at the centre of the cells. In order to account for the staggered discretisation of velocity, we denote $\phi_{[i:\alpha]}^{n_x, n_y, n_z}$ the field ϕ staggered α cells in the i -th direction,

$$\phi_{[i:\alpha]}^{n_x, n_y, n_z} = \phi(x_k^{n_k} \mathbf{e}_k + (x_i^{n_i+\alpha} - x_i^{n_i}) \mathbf{e}_i), \quad (1.87)$$

where summation is carried over k but not over i . For instance, the value of ϕ at the centre of a face perpendicular to the x direction is represented by $\phi_{[x:-1/2]}^{n_x, n_y, n_z} = \phi(x^{n_x-1/2}, y^{n_y}, z^{n_z})$. We have the property $\phi_{[x:1]}^{n_x, n_y, n_z} = \phi^{n_x+1, n_y, n_z}$. The stacking of the staggering operator is allowed,

$$\phi_{[i:\alpha][j:\beta]}^{n_x, n_y, n_z} = \phi(x_k^{n_k} \mathbf{e}_k + (x_i^{n_i+\alpha} - x_i^{n_i}) \mathbf{e}_i) + (x_j^{n_j+\beta} - x_j^{n_j}) \mathbf{e}_j. \quad (1.88)$$

where summation is carried over k but not over i or j . For instance, $\phi_{[x:-1/2][y:-1/2]}^{n_x, n_y, n_z} = \phi(x^{n_x-1/2}, y^{n_y-1/2}, z^{n_z})$ represents the value of ϕ at the centre of an edge of the cell. Notice also that $\phi_{[x:1/2][x:1/2]}^{n_x, n_y, n_z} = \phi^{n_x+1, n_y, n_z}$.

With this formalism, we have knowledge in the staggered grid system of pressure P^{n_x, n_y, n_z} , temperature T^{n_x, n_y, n_z} , density ρ^{n_x, n_y, n_z} , viscosity μ^{n_x, n_y, n_z} and thermal conductivity λ^{n_x, n_y, n_z} at the centre of the cells and of the three components of velocity $U_{k[k:-1/2]}^{n_x, n_y, n_z}$ at the centre of the faces they are perpendicular to, namely $U_{x[x:-1/2]}^{n_x, n_y, n_z}$, $U_{y[y:-1/2]}^{n_x, n_y, n_z}$ and $U_{z[z:-1/2]}^{n_x, n_y, n_z}$. More generally, if ϕ^{n_x, n_y, n_z} is a three-dimensional field discretised at the centre of the cells and $U_i^{n_x, n_y, n_z}$ the i -th component of velocity, the values of $\phi_{[i:\alpha]}^{n_x, n_y, n_z}$ and $U_{i[i:\alpha-1/2]}^{n_x, n_y, n_z}$ are available if α is an integer. Otherwise, their value may be estimated using an interpolation.

The following unweighted interpolation operator is defined,

$$\bar{\phi}^{[i:\alpha]} = \frac{\phi_{[i:\alpha+1/2]} + \phi_{[i:\alpha-1/2]}}{2}. \quad (1.89)$$

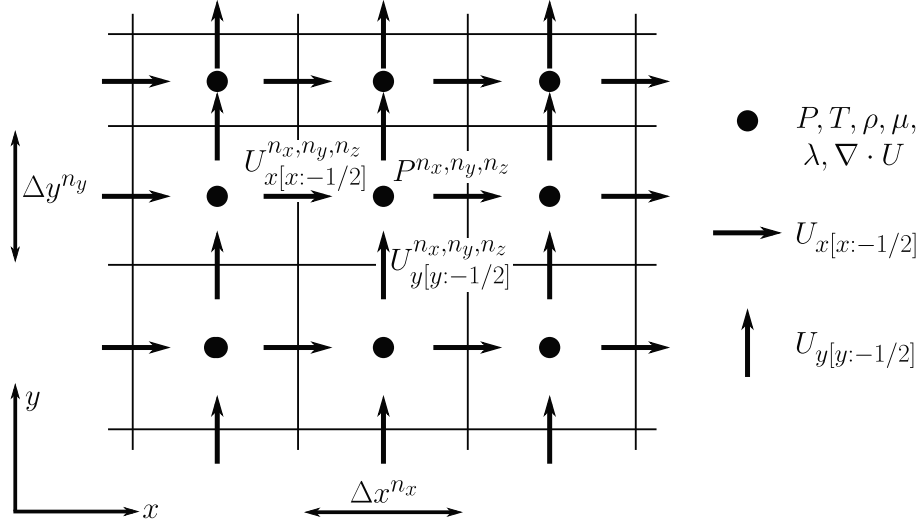


Figure 1.2 – Staggered grid system.

We extend this definition to a two-dimensional interpolation using

$$\bar{\phi}^{[i:\alpha,j:\beta]} = \begin{cases} \bar{\phi}^{[i:\alpha][j:\beta]} & \text{if } i \neq j \\ \phi_{[i:\alpha+\beta]} & \text{if } i = j, \end{cases} \quad (1.90)$$

where no interpolation is carried out if $i = j$ because the value of $\phi_{[i:\alpha+\beta]}$ is supposed available.

In addition, we introduce the notation

$$\Delta^{[i:\alpha]} \phi^{n_x, n_y, n_z} = \phi_{[i:\alpha+1/2]}^{n_x, n_y, n_z} - \phi_{[i:\alpha-1/2]}^{n_x, n_y, n_z}. \quad (1.91)$$

It follows that $\Delta x_j^{n_j} = \Delta^{[j:0]} x_j^{n_j} = x_j^{n_j+1/2} - x_j^{n_j-1/2}$ is the cell size the j -th direction.

1.2.3.1 Mass conservation equation

The mass convection is discretised using the third-order QUICK scheme [170] with a FRAM filtering [46],

$$\left(\frac{\partial \rho U_j}{\partial x_j} \right) = \frac{\Delta^{[j:1/2]} (\rho_{j[j:-1/2]}^* U_{j[j:-1/2]})}{\Delta x_j}, \quad (1.92)$$

with,

$$\rho_{j[j:-1/2]}^* = \begin{cases} (1 - \delta_{j[j:-1/2]}^*) \left(\frac{\rho^{+\rho_{j[-1]}}}{2} - \frac{(\Delta x_j^{[j:-1/2]})^2}{8} \text{Curv}_j \right) + \delta_{j[j:-1/2]}^* \rho & \text{if } U_{j[j:-1/2]} \geq 0 \\ (1 - \delta_{j[j:-1/2]}^*) \left(\frac{\rho^{+\rho_{j[-1]}}}{2} - \frac{(\Delta x_j^{[j:-1/2]})^2}{8} \text{Curv}_{j[j:-1]} \right) + \delta_{j[j:-1/2]}^* \rho_{j[-1]} & \text{if } U_{j[j:-1/2]} < 0, \end{cases} \quad (1.93)$$

where

$$\text{Curv}_j = \frac{\rho_{[j:1]} - \rho}{\Delta x_j \overline{\Delta x_j}^{[j:1/2]}} - \frac{\rho - \rho_{[j:-1]}}{\Delta x_j \overline{\Delta x_j}^{[j:-1/2]}}, \quad (1.94)$$

and $\delta_{j[j:-1/2]}^* = \max(\delta_{j[j:-1]}, \delta_j)$, where

$$\delta_j = \left[2 \left(\frac{\rho - \rho_{\min,j}}{\rho_{\max,j} - \rho_{\min,j}} \right) - 1 \right]^4. \quad (1.95)$$

with $\rho_{\min,j} = \min(\rho_{[j:-1]}, \rho_{[j:1]})$ and $\rho_{\max,j} = \max(\rho_{[j:-1]}, \rho_{[j:1]})$.

1.2.3.2 Momentum conservation equation

The momentum convection is discretised using a fourth-order centred scheme [12],

$$\left(\frac{\partial U_j U_i}{\partial x_j} \right)_{[i:-1/2]} = \frac{\overline{\Delta x_j}^{[j:1/2]} \left(\overline{U_{j[j:-1/2]}}^{[i:-1/2]} \overline{U_{i[i:-1/2]}}^{[j:-1/2]} \right)}{\overline{\Delta x_j}^{[i:-1/2]}}, \quad (1.96)$$

with

$$\overline{U_{j[j:-1/2]}}^{[i:-1/2]} = \frac{U_{j[j:-1/2]} \overline{\Delta x_i}^{n_i-1[j:-1/2]} + U_{j[i:-1][j:-1/2]} \overline{\Delta x_i}^{n_i[j:-1/2]}}{\overline{\Delta x_i}^{n_i-1[j:-1/2]} + \overline{\Delta x_i}^{n_i[j:-1/2]}}, \quad (1.97)$$

and

$$\begin{aligned} \overline{U_{i[i:-1/2]}}^{[j:-1/2]} = & \\ & g_1 \left(\overline{\Delta x_i}^{n_i-1[i:-1/2,j:-1/2]}, \overline{\Delta x_i}^{n_i[i:-1/2,j:-1/2]}, \overline{\Delta x_i}^{n_i+1[i:-1/2,j:-1/2]} \right) U_{i[i:-1/2][j:-2]} \\ & + g_2 \left(\overline{\Delta x_i}^{n_i-1[i:-1/2,j:-1/2]}, \overline{\Delta x_i}^{n_i[i:-1/2,j:-1/2]}, \overline{\Delta x_i}^{n_i+1[i:-1/2,j:-1/2]} \right) U_{i[i:-1/2][j:-1]} \\ & + g_3 \left(\overline{\Delta x_i}^{n_i-1[i:-1/2,j:-1/2]}, \overline{\Delta x_i}^{n_i[i:-1/2,j:-1/2]}, \overline{\Delta x_i}^{n_i+1[i:-1/2,j:-1/2]} \right) U_{i[i:-1/2]} \\ & + g_4 \left(\overline{\Delta x_i}^{n_i-1[i:-1/2,j:-1/2]}, \overline{\Delta x_i}^{n_i[i:-1/2,j:-1/2]}, \overline{\Delta x_i}^{n_i+1[i:-1/2,j:-1/2]} \right) U_{i[i:-1/2][j:1]}, \end{aligned}$$

with,

$$g_1(d_1, d_2, d_3) = -\frac{(d_2)^2 (d_2 + 2d_3)}{8d_1 (d_2 + d_1) (d_1 + d_2 + d_3)}, \quad (1.98)$$

$$g_2(d_1, d_2, d_3) = \frac{(d_2 + 2d_1) (d_2 + 2d_3)}{8d_1 (d_2 + d_3)}, \quad (1.99)$$

$$g_3(d_1, d_2, d_3) = \frac{(d_2 + 2d_1) (d_2 + 2d_3)}{8d_3 (d_1 + d_2)}, \quad (1.100)$$

$$g_4(d_1, d_2, d_3) = -\frac{(d_2)^2 (d_2 + 2d_1)}{8d_3 (d_2 + d_3) (d_1 + d_2 + d_3)}. \quad (1.101)$$

The terms of the momentum diffusion are given by a second-order discretisation,

$$\frac{\partial}{\partial x_j} \left(\mu \frac{\partial U_i}{\partial x_j} \right)_{[i:-1/2]} = \frac{\overline{\Delta x_j}^{[j:1/2]} \left(\overline{\mu}^{[i:-1/2,j:-1/2]} \frac{\overline{\Delta x_j}^{[j:-1/2]} U_{i[i:-1/2]}}{\overline{\Delta x_j}^{[i:-1/2,j:-1/2]}} \right)}{\overline{\Delta x_j}^{[i:-1/2]}} \quad (1.102)$$

$$\frac{\partial}{\partial x_j} \left(\mu \frac{\partial U_j}{\partial x_i} \right)_{[i:-1/2]} = \frac{\Delta^{[j:1/2]} \left(\bar{\mu}^{[i:-1/2, j:-1/2]} \frac{\Delta^{[i:-1/2]} U_{j[j:-1/2]}}{\Delta x_i^{[i:-1/2, j:-1/2]}} \right)}{\Delta x_j^{[i:-1/2]}} \quad (1.103)$$

$$\frac{\partial}{\partial x_i} \left(\mu \frac{\partial U_i}{\partial x_i} \right)_{[i:-1/2]} = \frac{\Delta^{[i:1/2]} \left(\mu^{[i:-1]} \frac{\Delta^{[i:-1/2]} U_{i[i:-1/2]}}{\Delta x_i^{[i:-1]}} \right)}{\Delta x_i^{[i:-1/2]}} \quad (1.104)$$

1.2.3.3 Energy conservation equation

The divergence of velocity is computed using a second-order centred discretisation,

$$\left(\frac{\partial U_i}{\partial x_i} \right) = \frac{\Delta^{[i+1/2]} U_{i[i:-1/2]}}{\Delta x_i} \quad (1.105)$$

The temperature diffusion is discretised according to the following second-order scheme,

$$\frac{\partial}{\partial x_j} \left(\lambda \frac{\partial T}{\partial x_j} \right) = \frac{\Delta^{[j:1/2]} \bar{\lambda}^{[j:-1/2]} \frac{\Delta^{[j:-1/2]} T}{\Delta x_j^{[j:-1/2]}}}{\Delta x_j} \quad (1.106)$$

1.3 Study configuration

Using the above-described numerical method, direct numerical simulations of fully developed turbulent channel flows with and without temperature gradient are carried out. This geometry provides a very simplified model of the flow in a high-temperature solar receiver and is one of the simpler configuration that reproduces the distinctive features of low Mach number strongly anisothermal turbulent flows. The channel has been simulated in the incompressible isothermal case and in the anisothermal case at a mean friction Reynolds number of 180 and 395. The results of the direct numerical simulation are representative of the wall turbulence of strongly anisothermal turbulent flows and are therefore meaningful for the flows found in solar receivers.

In this section, the geometrical configuration of the channel and the numerical setting used for the simulations are described. The validation of the numerical method is discussed and the mean flow variables are given. The results of the direct numerical simulations will be investigated throughout the rest of the manuscript.

1.3.1 Channel flow configuration

We consider a fully developed three-dimensional turbulent channel flow under a strong temperature gradient, as represented in figure 9.1. For validation and comparison purposes, we also consider the channel in the incompressible isothermal case, that is without temperature gradient. The channel is periodic in the streamwise (x) and spanwise (z) directions. The wall-normal direction is denoted (y). The channel walls are at constant temperature. In the isothermal channel, the two walls are at the cold temperature $T_1 = 293$ K. In the anisothermal channel, the temperature of the cold wall ($y = 0$) is $T_1 = 293$ K and the temperature of the hot wall ($y = 2h$) is $T_2 = 586$ K.

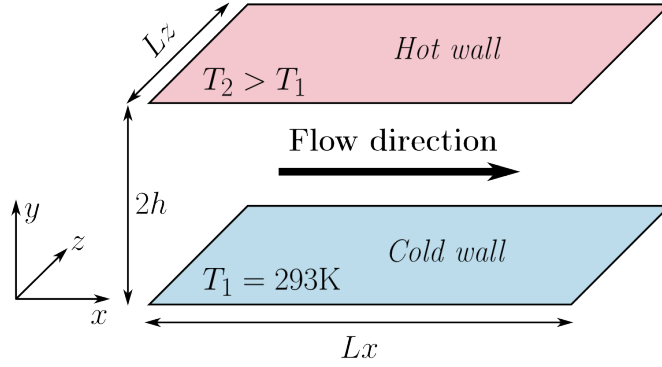


Figure 1.3 – Biperiodic anisothermal channel flow.

This creates a temperature gradient in the wall-normal direction. Since the channel is periodic, the dissipative action of the viscous shear stress is not balanced out by a streamwise pressure gradient. A streamwise volume force f is added to the channel to replicate the effect of a streamwise pressure gradient and maintain a constant mass flow rate.

For all simulations, a constant Prandtl number $Pr = 0.76$ is assumed. The flow is therefore characterised by the Reynolds number. It is customary in wall turbulence to define for this purpose the friction Reynolds number, defined by

$$Re_{\tau,\omega} = \frac{U_\tau h}{\nu_\omega}, \quad (1.107)$$

with h the half-height of the channel, ν_ω the wall kinematic viscosity and U_τ the friction velocity,

$$U_\tau = \sqrt{\nu_\omega \left(\frac{\partial \bar{U}_x}{\partial y} \right)_\omega}. \quad (1.108)$$

In the anisothermal channel, the two walls have a different friction Reynolds number. We define the mean friction Reynolds number as the average of the friction Reynolds number at the cold and hot sides,

$$Re_\tau = \frac{1}{2} (Re_{\tau,1} + Re_{\tau,2}). \quad (1.109)$$

We carried out direct numerical simulations of the isothermal and anisothermal channel at $Re_\tau = 180$ and $Re_\tau = 395$. These friction Reynolds number have been selected to enable an easier comparison with reference data from the literature (in particular [203]). The mean flow variables of the direct numerical simulations are given in table 1.1. The bulk Mach number of all simulations is below 2×10^{-2} , justifying the low Mach number hypothesis.

1.3.2 Numerical settings

The simulations use a regular mesh in the homogeneous directions (x and z) and a nonuniform mesh in the wall-normal coordinate direction (y). The wall-normal grid

	DNS180-1	DNS180-2	DNS395-1	DNS395-2
Mass flow rate, kg/s	9.40×10^{-3}	1.11×10^{-2}	1.57×10^{-2}	1.76×10^{-2}
Bulk velocity $U^b = \frac{1}{2h} \int_0^{2h} \bar{U}_x dy$, m/s	1.88×10^0	3.24×10^0	4.72×10^0	7.68×10^0
Bulk temperature $T^b = \frac{1}{2h} \int_0^{2h} \bar{T} dy$, K	2.93×10^2	4.32×10^2	2.93×10^2	4.33×10^2
Bulk density $\rho^b = \frac{1}{2h} \int_0^{2h} \bar{\rho} dy$, kg/m ³	1.78×10^0	1.23×10^0	1.78×10^0	1.23×10^0
Bulk dynamic viscosity $\mu^b = \frac{1}{2h} \int_0^{2h} \bar{\mu} dy$, Pa s	1.81×10^{-5}	2.40×10^{-5}	1.81×10^{-5}	2.41×10^{-5}
Bulk kinematic viscosity $\nu^b = \frac{1}{2h} \int_0^{2h} \bar{\nu} dy$, m ² /s	1.02×10^{-5}	2.02×10^{-5}	1.02×10^{-5}	2.01×10^{-5}
Bulk thermal conductivity $\lambda^b = \frac{1}{2h} \int_0^{2h} \bar{\lambda} dy$, W/(m K)	2.39×10^{-2}	3.18×10^{-2}	2.39×10^{-2}	3.19×10^{-2}
Bulk Reynolds number $Re = \rho^b U^b h / \mu^b$	2.77×10^3	2.47×10^3	6.93×10^3	5.85×10^3
Bulk Mach number $Ma = U^b / \sqrt{\gamma r T^b}$	5.48×10^{-3}	7.77×10^{-3}	1.38×10^{-2}	1.84×10^{-2}
Centerline streamwise velocity $U_{x,\text{centre}}$, m/s	2.20×10^0	3.80×10^0	5.41×10^0	8.84×10^0
Centerline wall-normal velocity $ U_{y,\text{centre}} $, m/s	—	2.98×10^{-3}	—	6.24×10^{-3}
Centerline Temperature T_{centre} , K	—	4.27×10^2	—	4.30×10^2
Cold friction velocity $U_{\tau,1}$, m/s	1.20×10^{-1}	1.78×10^{-1}	2.67×10^{-1}	3.79×10^{-1}
Cold friction temperature $T_{\tau,1}$, K	—	5.45×10^0	—	5.14×10^0
Cold friction Reynolds number $Re_{\tau,1} = \rho_1 U_{\tau,1} h / \mu_1$	1.76×10^2	2.60×10^2	3.93×10^2	5.56×10^2
Cold wall heat flux $Q_1 = \lambda_1 (\partial_y \bar{T})_1 $, W/m ²	—	1.73×10^3	—	3.49×10^3
Cold wall shear stress $\tau_1 = \mu_1 (\partial_y \bar{U}_x)_1$, Pa	2.56×10^{-2}	5.64×10^{-2}	1.27×10^{-1}	2.56×10^{-1}
Hot friction velocity $U_{\tau,2}$, m/s	1.20×10^{-1}	2.36×10^{-1}	2.67×10^{-1}	5.05×10^{-1}
Hot friction temperature $T_{\tau,2}$, K	—	8.13×10^0	—	7.59×10^0
Hot friction Reynolds number $Re_{\tau,2} = \rho_2 U_{\tau,2} h / \mu_2$	1.76×10^2	1.05×10^2	3.93×10^2	2.27×10^2
Hot wall heat flux $Q_2 = \lambda_2 (\partial_y \bar{T})_2 $, W/m ²	—	1.71×10^3	—	3.45×10^3
Hot wall shear stress $\tau_2 = \mu_2 (\partial_y \bar{U}_x)_2$, Pa	2.56×10^{-2}	4.95×10^{-2}	1.27×10^{-1}	2.29×10^{-1}
Mean friction Reynolds number $Re_\tau = \frac{1}{2}(Re_{\tau,1} + Re_{\tau,2})$	1.76×10^2	1.83×10^2	3.93×10^2	3.92×10^2
Mean wall heat flux $Q = \frac{1}{2}(Q_1 + Q_2)$, W/m ²	—	1.72×10^3	—	3.47×10^3
Mean wall shear stress $\tau = \frac{1}{2}(\tau_1 + \tau_2)$, Pa	2.56×10^{-2}	5.30×10^{-2}	1.27×10^{-1}	2.43×10^{-2}

Table 1.1 – Mean flow variables of the direct numerical simulations.

points are given by a hyperbolic tangent law,

$$y_k = L_y \left(1 + \frac{1}{a} \tanh \left[\left(\frac{k-1}{N_y-1} - 1 \right) \tanh^{-1}(a) \right] \right), \quad (1.110)$$

with a the mesh dilatation parameter and N_y the number of grid points in the wall-normal direction. The numerical settings of the direct numerical simulations are given as follows:

Isothermal simulation at $Re_\tau = 180$ (DNS180-1)

The domain size is $4\pi h \times 2h \times 2\pi h$, with $h = 15$ mm, and the mesh used contains $384 \times 266 \times 384$ grid points. The cell sizes in wall units are $\Delta_x^+ = 5.8$, $\Delta_y^+ = 0.085$ at the wall and 2.9 at the centre of the channel and $\Delta_z^+ = 2.9$. The mesh dilatation parameter is $a = 0.0970$.

Anisothermal simulation at $Re_\tau = 180$ (DNS180-2)

The same mesh and domain as the incompressible isothermal simulation at $Re_\tau = 180$ is used. Given the higher friction Reynolds number at the cold side, the cell sizes in wall units are $\Delta_x^+ = 8.5$, $\Delta_y^+ = 0.13$ at the wall and 4.2 at the centre of the channel and $\Delta_z^+ = 4.2$.

Isothermal simulation at $Re_\tau = 395$ (DNS395-1)

The domain size is $4\pi h \times 2h \times 4/3\pi h$ and the mesh used contains $768 \times 512 \times 512$ grid points. The cell sizes in wall units are $\Delta_x^+ = 6.4$, $\Delta_y^+ = 0.18$ at the wall and 2.9 at the centre of the channel and $\Delta_z^+ = 3.2$. The mesh dilatation parameter is $a = 0.0937$.

Anisothermal simulation at $Re_\tau = 395$ (DNS395-2)

The same mesh and domain as the incompressible isothermal simulation at $Re_\tau = 395$ is used. Given the higher friction Reynolds number at the cold side, the cell sizes in wall units are $\Delta_x^+ = 9.1$, $\Delta_y^+ = 0.25$ at the wall and 4.1 at the centre of the channel and $\Delta_z^+ = 4.6$.

The simulations at $Re_\tau = 180$ and $Re_\tau = 395$ have the same level of refinement. The small differences are due to the constraints of the numerical method (multigrid solver) and parallelism.

The mass flow rate is imposed by the streamwise volume force f . The volume force is determined using a control loop,

$$f_{t+1} = f_t + C_0 \frac{D_{\text{target}} - 2D_t + D_{t-1}}{\Delta t}, \quad (1.111)$$

with $C_0 = 3/(10L_y L_z)$ a damping constant, D the mass flow rate, D_{target} the targeted mass flow rate and $t - 1$, t and $t + 1$ indices related to the previous, current and next time step respectively. This is equivalent to a non-constant streamwise pressure gradient whose small fluctuations maintain the mass flow rate around a targeted value.

1.3.3 Data acquisition

The turbulence statistics are computed using two data collection procedures. In the first method, the statistics are computed on the fly during the simulation. In the second method, the statistics are computed from instantaneous DNS data saved during the simulation. The on-the-fly computation of the statistics makes use of the information of every timestep of the simulation. The post-simulation computation of the statistics use the saved DNS data, available once every 200 timestep due to storage size constraints. Identical results are obtained using the two methods.

The knowledge of the mean and fluctuating flow variables is required for some posttreatments, for instance the computation of the terms of the turbulence kinetic energy budget. In that case, the statistics are computed in two steps. First, the mean flow variables are computed following the ergodic hypothesis as an average over time and the homogeneous directions. Then, the more complex statistics are computed using the mean flow variables computed in the first step. If the statistics are computed from saved DNS data, the same DNS data may be used for the two steps. The data collection duration is 61 characteristic time (h/U_τ) for the isothermal simulation at $Re_\tau = 180$, 42 characteristic time for the anisothermal simulation at $Re_\tau = 180$, 29 characteristic time for the isothermal simulation at $Re_\tau = 395$ and 40 characteristic time for the anisothermal simulation at $Re_\tau = 395$.

	Number of grid points $N_x \times N_y \times N_z$	Dimension of the domain $L_x \times L_y \times L_z$	Cell sizes in wall units $\Delta_x^+; \Delta_y^+(0) - \Delta_y^+(h); \Delta_z^+$
DNS180-1	$384 \times 266 \times 384$	$4\pi h \times 2h \times 2\pi h$	5.8 ; 0.085 – 2.9 ; 2.9
MED180-1	$192 \times 190 \times 192$	$2\pi h \times 2h \times (4/3)\pi h$	5.8 ; 0.16 – 3.7 ; 3.9
COA180-1	$96 \times 118 \times 64$	$2\pi h \times 2h \times (4/3)\pi h$	12 ; 0.17 – 6.7 ; 12
120A180-1	$120 \times 102 \times 120$	$4\pi h \times 2h \times 2\pi h$	19 ; 0.085 – 9.7 ; 9.4
96A180-1	$96 \times 88 \times 96$	$4\pi h \times 2h \times 2\pi h$	24 ; 0.085 – 12 ; 12
72A180-1	$72 \times 68 \times 72$	$4\pi h \times 2h \times 2\pi h$	31 ; 0.085 – 16 ; 16
48A180-1	$48 \times 50 \times 48$	$4\pi h \times 2h \times 2\pi h$	47 ; 0.085 – 23 ; 24
36A180-1	$36 \times 40 \times 36$	$4\pi h \times 2h \times 2\pi h$	63 ; 0.085 – 30 ; 31
24A180-1	$24 \times 28 \times 24$	$4\pi h \times 2h \times 2\pi h$	94 ; 0.085 – 46 ; 47
DNS180-2	$384 \times 266 \times 384$	$4\pi h \times 2h \times 2\pi h$	8.5 ; 0.13 – 4.2 ; 4.2
MED180-2	$192 \times 190 \times 192$	$2\pi h \times 2h \times (4/3)\pi h$	8.6 ; 0.25 – 6.1 ; 7.0
120A180-2	$120 \times 102 \times 120$	$4\pi h \times 2h \times 2\pi h$	27 ; 0.13 – 14 ; 14
96A180-2	$96 \times 88 \times 96$	$4\pi h \times 2h \times 2\pi h$	34 ; 0.13 – 17 ; 17
72A180-2	$72 \times 68 \times 72$	$4\pi h \times 2h \times 2\pi h$	45 ; 0.13 – 23 ; 23
48A180-2	$48 \times 50 \times 48$	$4\pi h \times 2h \times 2\pi h$	68 ; 0.13 – 33 ; 34
36A180-2	$36 \times 40 \times 36$	$4\pi h \times 2h \times 2\pi h$	91 ; 0.13 – 43 ; 45
24A180-2	$24 \times 28 \times 24$	$4\pi h \times 2h \times 2\pi h$	136 ; 0.13 – 66 ; 68
DNS395-1	$768 \times 512 \times 512$	$4\pi h \times 2h \times (4/3)\pi h$	6.4 ; 0.18 – 2.9 ; 3.2
DNS395-2	$768 \times 512 \times 512$	$4\pi h \times 2h \times (4/3)\pi h$	9.1 ; 0.25 – 4.1 ; 4.6
96B395-2	$96 \times 100 \times 64$	$4\pi h \times 2h \times (4/3)\pi h$	73 ; 0.50 – 27 ; 36

Table 1.2 – Computational domain and grid spacing of the simulations.

1.3.4 Validation

The numerical method is validated by a mesh convergence study and the comparison of the results in the incompressible isothermal case to the reference data from the literature. The mesh convergence is verified from the simulation of the channel with meshes of increasing refinement. A list of the meshes used is given in table 1.2. The mesh convergence is given in the isothermal channel at $Re_\tau = 180$ in figure 1.4, in the anisothermal channel at $Re_\tau = 180$ in figure 1.5, in the isothermal channel at $Re_\tau = 395$ in figure 1.6, in the anisothermal channel at $Re_\tau = 395$ in figure 1.7. The mesh convergence of all statistics is attained for the isothermal simulation at $Re_\tau = 180$. In the anisothermal channel at $Re_\tau = 180$, the mean streamwise velocity, the covariance of streamwise and wall-normal velocity and the mean temperature are converged but there is a small difference between the medium and fine meshes for the standard deviation of temperature. The convergence of the simulations at $Re_\tau = 395$ follows since they use a similar mesh refinement.

Besides, the results are compared in the incompressible case to the reference data of Moser *et al.* [203], Vreman and Kuerten [305] and Lee and Moser [167] at $Re_\tau = 180$ and Moser *et al.* [203], Lee and Moser [167] at $Re_\tau = 395$. These numerical results have been validated against experimental data [63, 92, 151, 9]. The results of the

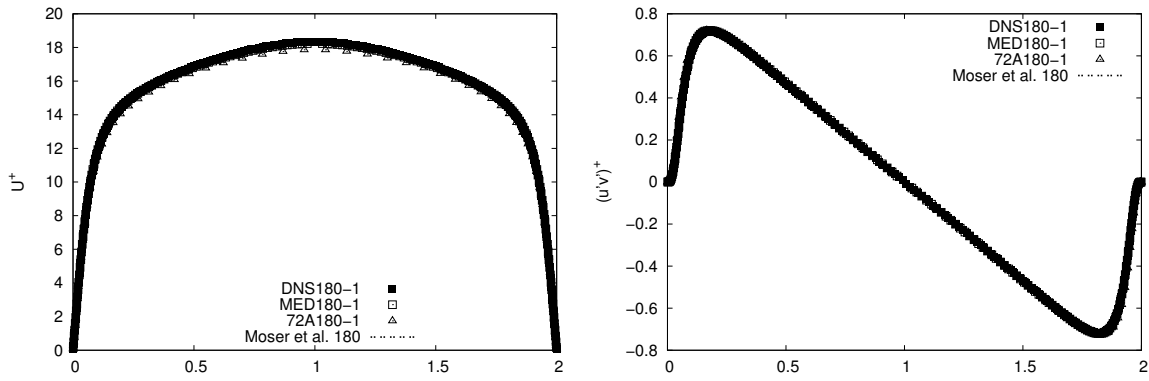


Figure 1.4 – Mesh convergence of the profiles of the mean streamwise velocity $\langle U_x \rangle$ (left) and the covariance of streamwise and wall-normal velocity $\langle u'_x u'_y \rangle$ (right) in the isothermal channel at $Re_\tau = 180$. The values are scaled by the friction velocity. The reference data is from Moser *et al.* [203].

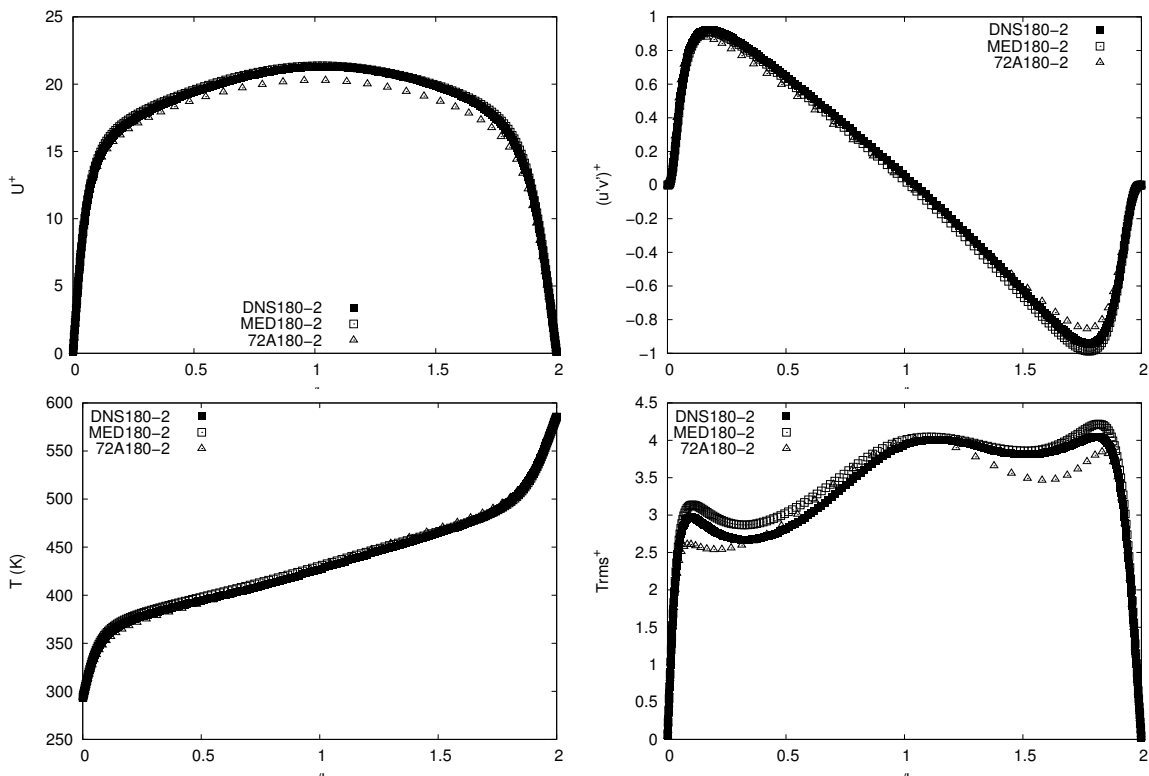


Figure 1.5 – Mesh convergence of the profiles of the mean streamwise velocity $\langle U_x \rangle$ (top left), the covariance of streamwise and wall-normal velocity $\langle u'_x u'_y \rangle$ (top right), the mean temperature $\langle T \rangle$ (bottom left) and the standard deviation of temperature $\sqrt{\langle T'^2 \rangle}$ (bottom right) in the anisothermal channel at $Re_\tau = 180$. The values are scaled by the friction velocity and the friction temperature.

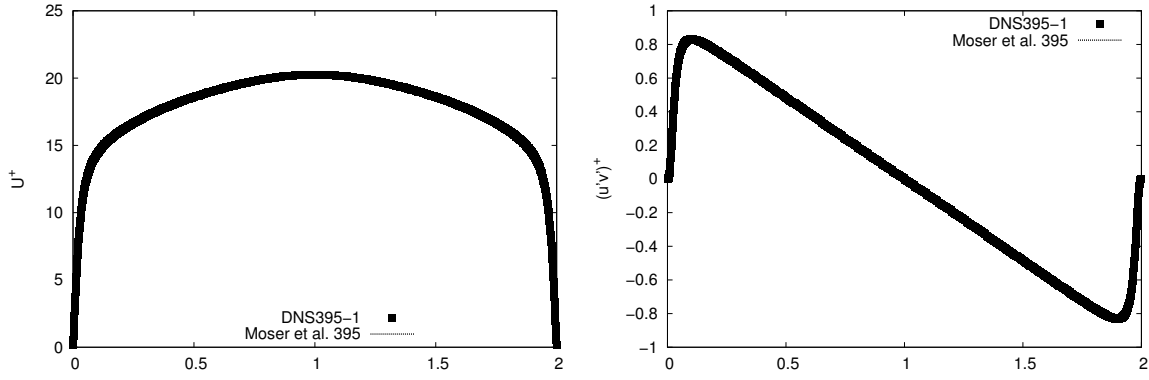


Figure 1.6 – Mesh convergence of the profiles of the mean streamwise velocity $\langle U_x \rangle$ (left) and the covariance of streamwise and wall-normal velocity $\langle u'_x u'_y \rangle$ (right) in the isothermal channel at $Re_\tau = 395$. The values are scaled by the friction velocity. The reference data is from Moser *et al.* [203].

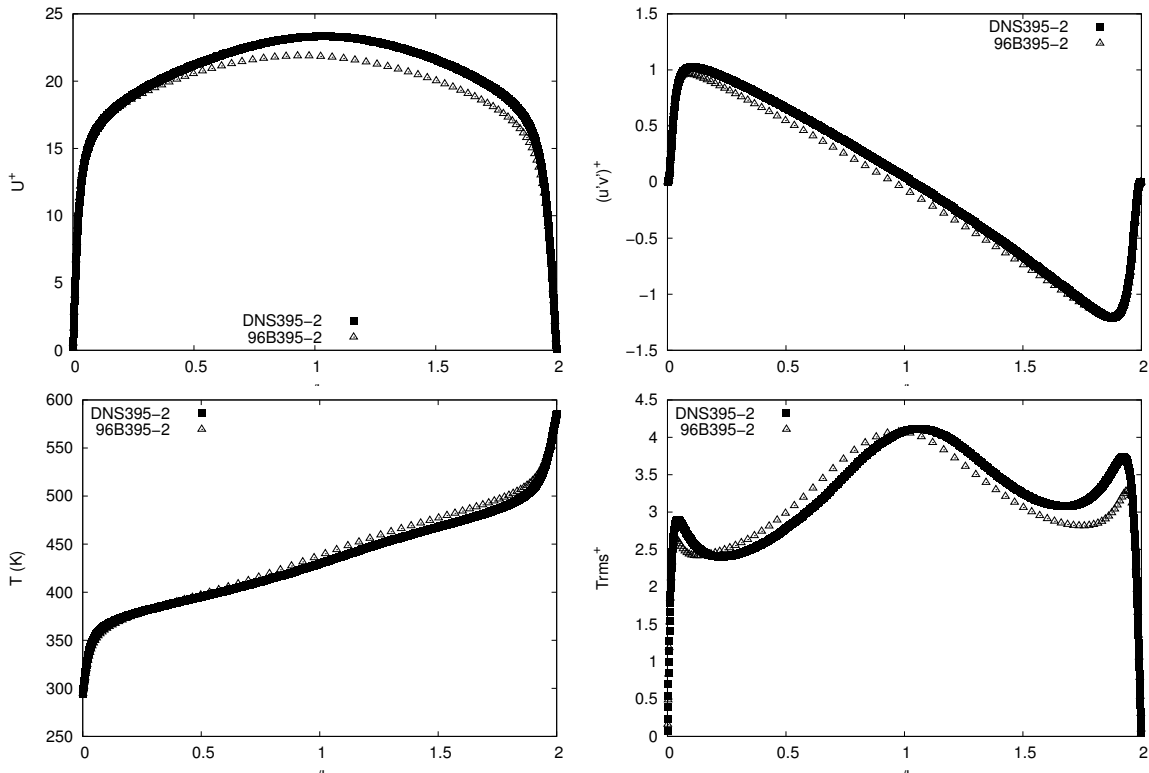


Figure 1.7 – Mesh convergence of the profiles of the mean streamwise velocity $\langle U_x \rangle$ (top left), the covariance of streamwise and wall-normal velocity $\langle u'_x u'_y \rangle$ (top right), the mean temperature $\langle T \rangle$ (bottom left) and the standard deviation of temperature $\sqrt{\langle T'^2 \rangle}$ (bottom right) in the anisothermal channel at $Re_\tau = 395$. The values are scaled by the friction velocity and the friction temperature.

isothermal direct numerical simulations are nearly identical to the reference profiles, validating the numerical method at the incompressible limit. This is shown in figure 1.4 at $Re_\tau = 180$ and in figure 1.6 at $Re_\tau = 395$. In the anisothermal configuration, no direct simulation data is available from the literature. The results have been compared to experimental data for a similar friction Reynolds number and temperature gradient by Bellec *et al.* [21]. The results are also compared to the reference data of Aulery *et al.* [10] at $Re_\tau = 180$ and Toutant and Bataille [290] at $Re_\tau = 395$, but these simulations use the same numerical code.

Conclusion

The strongly anisothermal low Mach number turbulent flows found in solar receivers are subjected to large variations of the fluid properties without the purely compressible effects of high-speed flows such as acoustic waves. The simplification of the Navier–Stokes equations in the limit of low Mach number but taking into account the variations of the fluid properties with temperature leads to the low Mach number equations. This removes acoustic effects from the Navier–Stokes equations and lets us focus on the study of the interaction between turbulence and the temperature gradient. The low Mach number equations and the ideal gas law leads to a distinctive form of the energy conservation equation, which imposes the local energy conservation by a constraint on the divergence of the velocity. The numerical simulation of the low Mach number equations has less timestep constraints because of the removal of acoustical waves and allows the use of a resolution algorithm based on a projection method to compute pressure and velocity.

The direct numerical simulation with this numerical method of strongly anisothermal turbulent channel flows is to some extent representative of the strongly anisothermal turbulent flows found in solar receivers. The direct numerical simulations provide an accurate description of the effects of the interaction between turbulence and the temperature gradient on the motion of the fluid. The direct numerical simulations are used to carry out an investigation of the energy exchanges between the different parts of total energy in the spatial and spectral domains. In particular, the study of the energy exchanges associated with the half-trace of the velocity fluctuation correlation tensor, computed from the direct numerical simulations, lets us infer the effect of the wall, the temperature gradient and the friction Reynolds number on the energy exchanges. The filtering of the instantaneous direct numerical simulation data is used to estimate the subgrid terms involved in the large-eddy simulation of the low Mach number equations. It also allows the a priori investigation of the subgrid-scale modelling, by comparing subgrid-scale models to the exact subgrid terms computed from the direct numerical simulations. Finally, the direct numerical simulations and filtered direct numerical simulations provide useful reference data for the interpretation of the results of large-eddy simulations.

Part I

Energy exchanges

Chapter 2

Introduction of part I

Energy exchanges in fluids are the transformation of energy between different forms and its transfer between locations. The study of the energy exchanges rely on the physical decomposition of total energy into internal energy, associated with temperature, and kinetic energy and the further decomposition of kinetic energy to associate a kinetic energy to the turbulent motion and a kinetic energy to the mean motion. Given the differences of physical implications, the knowledge of the different parts of total energy and not only total energy is often necessary for a satisfactory description of the flow behaviour. The energy exchanges are fundamental processes in turbulence which drives the evolution of the different parts of total energy. In particular, the energy exchanges associated with turbulence kinetic energy redistribute the energy from the scales and locations it is produced to other scales and locations [197]. These spatial transfer and interscale transport of turbulence kinetic energy determine the continuous spectrum of turbulence kinetic energy and its spatial profile. The knowledge of the energy exchanges associated with turbulence kinetic energy are important because this quantity gives a measure of the intensity of turbulence. It is critical for the modelling of the Reynolds-averaged Navier–Stokes (RANS) equations, since most models are based on the estimation of turbulence kinetic energy, either directly or from the modelling of the energy exchanges. The energy exchanges are also relevant to the large-eddy simulation of turbulent flows, which models the filtering out of small scales of the turbulence kinetic energy spectrum.

Homogeneous isotropic incompressible turbulence is a well-documented canonical case for the study of the energy exchanges [16, 104, 297]. Theories and models of homogeneous isotropic incompressible turbulence have been validated with experiments and direct numerical simulations [254]. Since the flow is homogeneous, there are no spatial transfer of energy on statistical average. The only relevant part of total energy is turbulence kinetic energy, produced through a forcing and irreversibly converted to internal energy, that is dissipated. The production of turbulence kinetic energy occurs at large scales and the dissipation at small scales, given by Kolmogorov length scale [311]. In the intermediate range of scales, called inertial subrange, an energy cascade transports the energy towards small scales [288]. The Reynolds number has a large effect on the energy exchanges. At higher Reynolds number, the dissipation occurs at smaller scales, separating distinctly the peaks of production and dissipation (figure 2.1). Accordingly, a large inertial subrange is created where the interscale transport is zero, or equivalently where a constant spectral flux transports turbulence

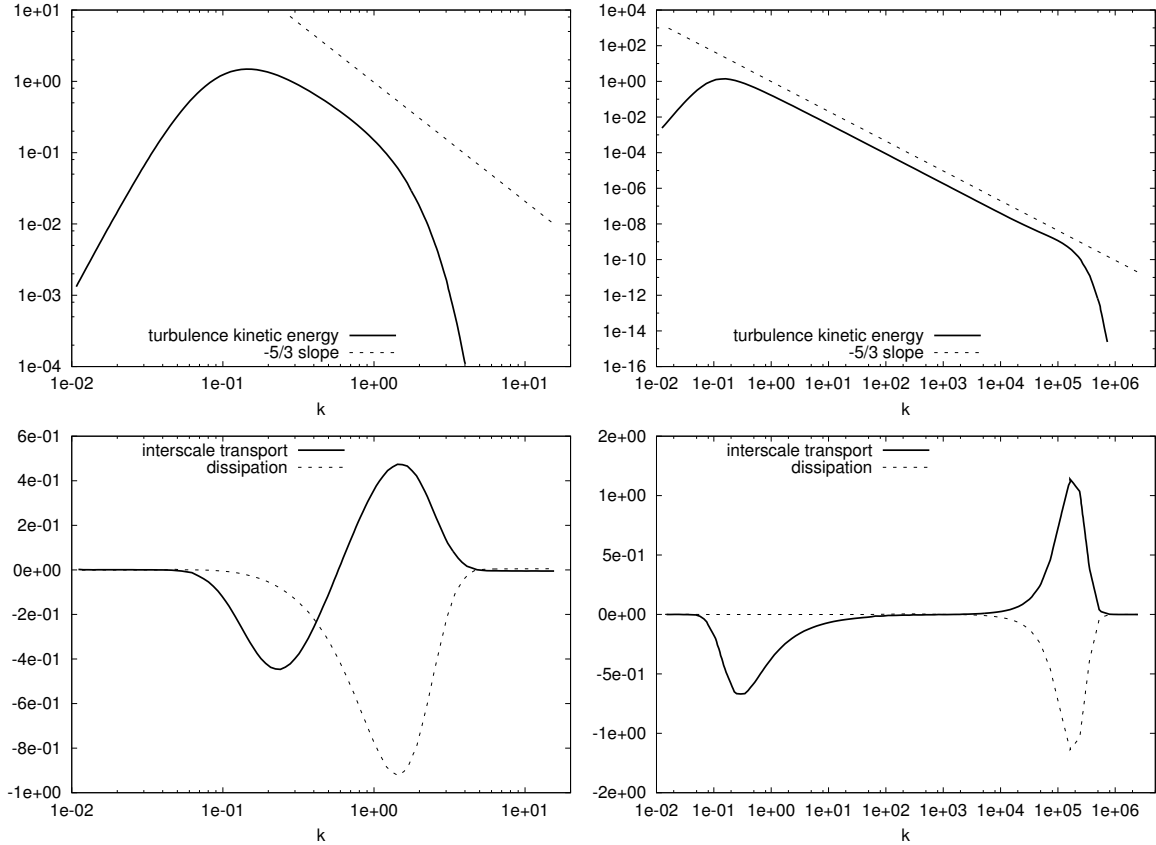


Figure 2.1 – Typical spectra of turbulence kinetic energy (top) and of interscale transport and the interaction with internal energy, premultiplied by the wavenumber k (bottom) in homogeneous isotropic incompressible turbulence at Taylor Reynolds number of $Re_\lambda = 30$ (left) and $Re_\lambda = 10^5$ (right). The scales are arbitrary. The straight lines are Kolmogorov’s $-5/3$ slope. The spectra are from eddy-damped quasi-normal Markovian simulations of W. Bros given in Sagaut and Cambon [254].

kinetic energy towards small scales without production or dissipation. The energy exchanges determine the spectrum of turbulence kinetic energy, which follows, in the limit of infinite Reynolds number, the universal Kolmogorov’s $-5/3$ slope in the inertial subrange [108].

In the strongly anisothermal turbulent flows found in solar receivers, this canonical description of the energy exchanges is modified by the influence of the walls and the temperature gradient. Wall-bounded turbulent flows are intrinsically anisotropic and inhomogeneous in the wall-normal direction. They provide a very different physics from homogeneous isotropic turbulence [134] because of a two-way interaction between the structures of the inner and outer layers [34, 80, 192]. Under the low Mach number hypothesis, the effect of dissipation on internal energy is neglected, whereas its effect on kinetic energy is taken into account. The energy exchanges are reduced to the interaction between mean kinetic energy and turbulence kinetic energy. In the inner layer, the mean velocity gradient provides without forcing a production of turbulence kinetic energy, converting mean kinetic energy to turbulence kinetic energy, while the dissipation mainly occurs in the viscous layer [136]. Unlike in homogeneous isotropic turbulence, the energy is hence both transferred spatially and transported in between scales, adding additional effects to the classical energy cascade [183, 134, 83, 188, 85,

28, 59]. This has been demonstrated by studies of the statistically averaged energy exchanges in the spectral domain [28, 165, 197, 166, 262]

The temperature gradient adds another layer of complexity to this heavy modification of the homogeneous isotropic energy exchanges. In strongly anisothermal turbulent flows, the temperature gradient leads to significant variations of the fluid properties (density, viscosity and thermal conductivity), altering the behaviour of flow and the energy exchanges [35, 168, 127, 164]. The effect of the variations of the fluid properties on the energy exchanges is not only found in high-temperature solar receivers and benefit to and from the study of the high-speed flows [67, 161, 101, 84, 198], heat exchangers and cooling systems [329, 39, 163, 330] or fluids at supercritical pressure within a small temperature range [319, 226, 210]. In each case, the variations of the fluid properties modifies the mean flow variables and the incompressible near-wall scaling fails. In strongly anisothermal turbulent channel flows, the temperature dependence of the fluid properties creates an asymmetry between the hot and cold sides of the channel related to the alteration of the energy exchanges. The direct numerical simulation of strongly anisothermal turbulent flows can provide high-resolution data useful for the study of the energy exchanges, for instance through the statistically averaged production, spatial transfer, interscale transport and dissipation of turbulence kinetic energy.

We investigate the energy exchanges in strongly anisothermal turbulent channel flows from the direct numerical simulations. In particular, we focus on the energy exchanges associated with the half-trace of the velocity fluctuation correlation tensor, a part of turbulence kinetic energy. A spectral analysis of each energy exchange is carried out to give both the spatial and spectral dependence of the energy exchanges. Chapter 3 develops a new representation of the energy exchanges based on the Reynolds averaging, providing a theoretical basis for the investigation and the interpretation of the energy exchanges. Chapter 4 studies on this basis the effect of the temperature gradient on the energy exchanges associated with the half-trace of the velocity fluctuation correlation tensor at $Re_\tau = 180$. Chapter 5 carries on the study to $Re_\tau = 395$ to investigate the combined effect of the Reynolds number and the variations of the fluid properties on the energy exchanges.

Chapter 3

Equations of energy exchanges in variable density turbulent flows

3.1 Introduction of chapter 3

The study of the energy exchanges in strongly anisothermal turbulent flows requires the choice of a decomposition of total energy and of the energy exchanges between the different parts of total energy. Indeed, in variable density flows, the decomposition of total energy is not unique and involves some arbitrariness in the identification of a kinetic energy of the mean motion and a kinetic energy of the turbulent motion [50]. Accordingly, it is difficult to determine the turbulence kinetic energy spectrum in variable density flows. In this chapter, we provide a new representation of the energy exchanges between the different parts of total energy based on the Reynolds averaging. The Reynolds decomposition of velocity leads to the ternary decomposition of kinetic energy into turbulence kinetic energy, mean kinetic energy and a mixed kinetic energy, related to the interaction between the turbulent motion and the mean motion. The Reynolds decomposition of density then extends the decomposition of total energy, splitting each term in a mean density part and a fluctuating density part.

To devise the formulation of the energy exchanges, we temporarily work with the Navier–Stokes equations directly instead of the low Mach number equations. This is necessary for a consistent description of the energy exchanges since the low Mach number equations neglect the effect of dissipation on internal energy. Care is taken to provide a formulation that generalises to the local instantaneous energy exchanges. This lets us consider the statistically averaged energy exchanges as the statistical average of instantaneous energy exchanges, which is not possible with the classical representation of the energy exchanges in the incompressible case. While the instantaneous energy exchanges are not explored further in this thesis, they can be investigated theoretically or from direct numerical simulations. Kida and Ohkitani [143, 142] provide an example of such investigation in forced isotropic turbulence.

The study of the scale dependence of the energy exchanges from direct numerical simulations is eased by the formulation and the use of the Reynolds average. Indeed, the formulation includes the mean density turbulence kinetic energy, product of the mean density and the half-trace of the velocity fluctuation correlation tensor. This quantity is

a good approximation of turbulence kinetic energy under Morkovin's hypothesis [201], valid in the strongly anisothermal turbulent channel flows investigated. However, the mean density turbulence kinetic energy is simpler to handle and has unlike turbulence kinetic energy an univocal spectral equivalent. Using this fact, we extend the analysis to the spectral domain considering to carry out the Fourier transform a flow with two homogeneous and periodic directions. The spectral energy exchanges are given with a one-to-one correspondence with the spatial energy exchanges, except for the addition of a purely spectral term corresponding to the interscale transport of kinetic energy. This is used with slight changes in chapters 4 and 5 to study the energy exchanges from the direct numerical simulations of strongly anisothermal turbulent channel flows presented in section 1.3.

3.2 Paper 1

This section reproduces the paper D. Dupuy, A. Toutant, and F. Bataille. Equations of energy exchanges in variable density turbulent flows. *Physics Letters A*, 382(5):327–333, 2018 [89].

Abstract

This paper establishes a new formulation of the energy exchanges between the different parts of total energy. The decomposition uses the Reynolds averaging. This leads to a ternary decomposition of kinetic energy into the turbulence kinetic energy, the mean kinetic energy and the mixed kinetic energy, acting as an exchange term between the mean and turbulent motion. The formulation is then extended to distinguish a mean and fluctuating density part of each part of total energy. The formulation thus includes the mean density turbulence kinetic energy, product of the mean density and the half-trace of the velocity fluctuation correlation tensor. Its evolution equation is given in the spectral domain.

3.2.1 Introduction

This paper addresses the energy exchanges in turbulent flows with highly variable fluid properties. This covers flows with a high Mach number (high speed flows), such as the flows around a high-speed aircraft, or through a high speed jet or a nozzle [110], and low Mach number flows submitted to a strong temperature gradient, found for instance in heat exchangers, propulsion systems or nuclear or concentrated solar power plants [15, 191, 73, 264, 265, 266, 290]. The study of the energy exchanges between the different parts of total energy is a useful tool for both turbulence modelling and the fundamental understanding of turbulence. More detailed information is obtained through the study of the energy exchanges in the spectral domain [183, 81, 83, 324, 325, 83, 188, 85, 28, 59, 60, 61, 62, 165, 197]. However, while kinetic energy is fundamental property of any flow, it is not the case of its decomposition into turbulence kinetic energy and mean kinetic energy.

In incompressible flows with constant fluid properties, such decomposition is unique. The averaged kinetic energy is decomposed clearly, unambiguously and straightforwardly into the sum of two contributions: the kinetic energy of the mean motion associated with the mean velocity and the kinetic energy of the turbulent motion associated with the velocity fluctuation [see e.g. 312, 235]. In compressible flows with highly variable density, this analysis is hindered by additional density-velocity correlations. The decomposition of kinetic energy becomes more complex and arbitrary. It is even more difficult in the spectral domain. The choice ultimately depends on the physical role given to the additional density-velocity correlations with respect to what constitutes the mean motion and the turbulent motion [50]. The most popular and successful decomposition extends the incompressible decomposition to the compressible case through the introduction of a density weighted averaging. This decomposition was widely developed by Favre [94, 95, 96]. Since, it has been used extensively by various authors [168, 127, 120, 185, 233]. Another approach, the mixed weighted decomposition, mixes density weighted averaging and Reynolds averaging. It was first introduced by Bauer *et al.* [17] and further studied by Ha Minh *et al.* [122, 123]. In this formulation, kinetic energy is seen as the product of the velocity and the density weighted velocity. In a third method, kinetic energy is decomposed using a change of variable based on the density square root weighted velocity. This decomposition was first proposed by Yih [318] then adopted by various authors [144, 247, 68, 10, 11]. This change of variable allows the study of kinetic energy to be extended easily to the spectral domain. Finally, Chassaing [47] [see also 70, 13, 49, 50] suggested the decomposition of kinetic energy using the Reynolds averaging. From a modelling perspective, the use of the unweighted averaging may be advantageous in low Mach number flows, in which the energy conservation acts as a constraint on the divergence of the velocity [212]. The square of the fluctuating velocity (without the density) is also encountered for instance in the modelling of two-phase flows [291] or in variable density flows, provided the momentum equation is divided by the density before averaging [272]. In a variable density setting, the use of the Reynolds averaging necessarily leads to the decomposition of kinetic energy into three parts, called ternary decomposition. The kinetic energy is thus split into turbulence kinetic energy, mean kinetic energy and a mixed kinetic energy, related to both the mean and turbulent motions. However, we believe the underlying idea behind the ternary decomposition has not been taken to its logical conclusion as no interaction between the mixed kinetic energy and another part of total energy was identified.

This paper aims to establish a new formulation of the energy exchanges between the different parts of total energy in a ternary decomposition that gives to the mixed kinetic energy a full role. The formulation is compared to the formulation of Chassaing [47] and the differences between the two formulations with regard to the physical interpretation of the terms are discussed. We then take the decomposition further and split the density into a mean and fluctuating part. This leads to the definition of the mean density part of total energy and the fluctuating density part of total energy. The mean density turbulence kinetic energy, product of the mean density and the half-trace of the velocity fluctuation correlation tensor, appears in the mean density part of the decomposition as exchanging energy with the other parts of total energy. This quantity is approximately equal to the turbulence kinetic energy in flows satisfying Morkovin's hypothesis [201].

Once the new formulation of the energy exchanges established, we focus more specifically on the mean density turbulence kinetic energy. We establish its evolution equation in spectral domain, recognizing that the mean density turbulence kinetic energy has with the Reynolds averaging a clear spectral equivalent. The spectral equation extends the spatial equation to the spectral domain, associating to each spatial term a spectral equivalent. To the knowledge of the authors, this has not been achieved in the literature for variable density flows. A purely spectral term that redistributes the energy between scales is identified, as in the work of Lee and Moser [165] and Mizuno [197]. In order to carry out the Fourier transform, we consider a flow with two homogeneous and periodic directions. This does not lead to a loss of generality as the equations given may easily be adapted to a flow with one or three homogeneous directions.

The complete representation of the energy exchanges between the different parts of total energy is presented in section 4.2.3 and the equation of the mean density turbulence kinetic energy in the spectral domain in section 4.2.4.

3.2.2 Energy exchanges between the different parts of total energy in the ternary decomposition

3.2.2.1 General considerations

In this section, we describe a new formulation of the energy exchanges between the different parts of total energy in a ternary decomposition. We will establish the formulation obtained from the decomposition of velocity, but not density, with the Reynolds averaging, referred to as the one-stage formulation in this paper, and from the decomposition of both the velocity and density, referred to as the two-stage formulation in this paper. The two-stage formulation is required to write the spectral equation of the mean density turbulence kinetic energy. We first define here a few useful quantities and give some general remarks on the derivation of the formulation.

The total energy per unit volume $\rho(E + I)$ is a conservative quantity. Its components however are not as they exchange energy among themselves. In the following, the evolution equation of each part of total energy in the ternary representation will be given and we will identify the energy exchanges between these quantities. Many consistent formulations of the energy exchanges can be proposed. The formulation was devised according to the following criteria:

- Each term of the formulation must be either interpreted as a conservative energy transfer or an interaction with exactly one of the other parts of total energy.
- If a term is to be interpreted as a conservative energy transfer, it must be written in a conservative form, that is as a divergence; otherwise, it must be written in a non-conservative form.
- The formulation must be symmetrical, in particular with respect to the manner in which it deals with fluctuations and statistically averaged quantities.
- The formulation must correctly behave when considering a limit case such as laminar, homogeneous or incompressible flows. In particular, a quantity that

becomes instantaneously equal to zero must not be associated with any energy exchange.

We consider a non-relativistic compressible flow with highly variable fluid properties under the continuity hypothesis. Without loss of generality, no body forces are taken into account which means gravity is neglected and there is no heat source. The flow is governed by the Navier–Stokes equations under the following form [109]:

- mass conservation

$$\frac{\partial \rho}{\partial t} + \frac{\partial \rho U_j}{\partial x_j} = 0, \quad (3.1)$$

- momentum conservation

$$\frac{\partial \rho U_i}{\partial t} + \frac{\partial \rho U_j U_i}{\partial x_j} = \frac{\partial \mathcal{Y}_{ij}}{\partial x_j}, \quad (3.2)$$

- energy conservation

$$\frac{\partial \rho I}{\partial t} + \frac{\partial \rho U_j I}{\partial x_j} = \frac{\partial}{\partial x_j} \left(\lambda \frac{\partial T}{\partial x_j} \right) + \mathcal{Y}_{ij} \frac{\partial U_i}{\partial x_j}, \quad (3.3)$$

with ρ the density, T the temperature, I the internal energy per unit mass, t the time, U_i the i -th component of the velocity, \mathcal{Y}_{ij} the component of the total stress tensor with the i and j indices and x_i the Cartesian coordinate in the i -th direction. Einstein summation convention is used. The total stress tensor \mathcal{Y}_{ij} is given by the contributions of the viscous shear stress tensor and of the pressure stress. We will keep the total stress tensor undissociated throughout this paper because the pressure and viscous contributions are formally similar.

3.2.2.2 One-stage formulation

The instantaneous total energy per unit volume $\rho(E + I)$ is the sum of the instantaneous kinetic energy per unit volume ρE and the internal energy per unit volume ρI . In the ternary decomposition, the kinetic energy is decomposed into three parts by splitting the velocity into a mean and fluctuating part [following 245], namely $U_i = \overline{U}_i + u'_i$, where the overline ($\overline{\quad}$) denotes the statistical average and the prime symbol ($'$) the fluctuating part. We use a lowercase u' for the velocity fluctuation for a better visual differentiation but there is no further underlying differences. We obtain [47]

$$\rho E = \frac{1}{2} \rho U_i U_i = \rho \underline{E} + \rho e + \rho \underline{e}, \quad (3.4)$$

with $\rho \underline{E} = \frac{1}{2} \rho \overline{U}_i \overline{U}_i$ the mean kinetic energy, associated with the mean motion, $\rho e = \frac{1}{2} \rho u'_i u'_i$ the turbulence kinetic energy, associated with the turbulent motion, and $\rho \underline{e} = \rho u'_i \overline{U}_i$ the mixed kinetic energy, associated with both the mean and turbulent motion. This results in a fourfold decomposition of total energy.

The evolution equation of total energy $\overline{\rho(E + I)}$ is given by

$$\frac{\partial \overline{\rho(E + I)}}{\partial t} = \overline{\Phi^c} + \overline{\Phi^r} + \overline{\Phi^\lambda}, \quad (3.5)$$

with: Φ^c the convection, Φ^r the transfer by the total stress and Φ^λ the transfer by conduction, given by:

$$\Phi^c = - \frac{\partial \rho U_j (E + I)}{\partial x_j}, \quad (3.6)$$

$$\Phi^r = \frac{\partial \Upsilon_{ij} U_i}{\partial x_j}, \quad (3.7)$$

$$\Phi^\lambda = \frac{\partial}{\partial x_j} \left(\lambda \frac{\partial T}{\partial x_j} \right). \quad (3.8)$$

These three terms are conservative terms that represent the transfer of total energy by three different physical phenomena. With the fourfold decomposition of total energy, this equation becomes four equations associated with each part of total energy. This has two effects. First, the various conservative energy transfer terms are distributed among the four parts of kinetic energy. Secondly, additional non-conservative terms emerge. From the decomposition of total energy into kinetic energy and internal energy appears a new term \mathcal{E} that represents the interaction between these two quantities. From the decomposition of kinetic energy into three terms appears two new terms $\underline{\mathcal{P}}$ and $\overline{\mathcal{P}}$ that represent an interaction between the different parts of kinetic energy.

The energy exchanges between the four parts of total kinetic energy may be written as:

$$\frac{\partial \overline{\rho E}}{\partial t} = \overline{\Phi^c} + \overline{\Phi^r} + \overline{\mathcal{P}} + \overline{\mathcal{E}}, \quad (3.9)$$

$$\frac{\partial \overline{\rho e}}{\partial t} = \overline{\varphi^c} + \overline{\varphi^r} + \overline{\mathcal{P}} + \overline{\mathcal{E}}, \quad (3.10)$$

$$\frac{\partial \overline{\rho \underline{e}}}{\partial t} = \overline{\varphi^c} - \overline{\mathcal{P}} - \overline{\underline{\mathcal{P}}}, \quad (3.11)$$

$$\frac{\partial \overline{\rho I}}{\partial t} = \overline{\Phi^{T,c}} + \overline{\Phi^\lambda} - \overline{\mathcal{E}} - \overline{\mathcal{E}}, \quad (3.12)$$

where we identify the following terms:

- the convection Φ^c , decomposed into: $\underline{\Phi^c}$ associated with the mean kinetic energy, φ^c associated with the turbulence kinetic energy, $\overline{\varphi^c}$ associated with the mixed kinetic energy and $\Phi^{T,c}$ associated with internal energy,

$$\underline{\Phi^c} = - \frac{\partial \rho U_j \underline{E}}{\partial x_j}, \quad (3.13)$$

$$\varphi^c = - \frac{\partial \rho U_j e}{\partial x_j}, \quad (3.14)$$

$$\overline{\varphi^c} = - \frac{\partial \rho U_j \overline{e}}{\partial x_j}, \quad (3.15)$$

$$\Phi^{T,c} = - \frac{\partial \rho U_j I}{\partial x_j}, \quad (3.16)$$

- the transfer by the total stress Φ^r , decomposed into: $\underline{\Phi}^r$ associated with the mean kinetic energy and φ^r associated with the turbulence kinetic energy,

$$\underline{\Phi}^r = \frac{\partial \Upsilon_{ij} \bar{U}_i}{\partial x_j}, \quad (3.17)$$

$$\varphi^r = \frac{\partial \Upsilon_{ij} u'_i}{\partial x_j}, \quad (3.18)$$

- the interaction between the turbulence kinetic energy and the mixed kinetic energy \mathcal{P} ,

$$\mathcal{P} = -\rho u'_i U_j \frac{\partial \bar{U}_i}{\partial x_j} + \rho u'_i U_j \frac{\partial \bar{U}_i}{\partial x_j} - \rho u'_i \frac{1}{\rho} \frac{\partial \Upsilon_{ij}}{\partial x_j}, \quad (3.19)$$

- the interaction between the mean kinetic energy and the mixed kinetic energy $\underline{\mathcal{P}}$,

$$\underline{\mathcal{P}} = -\rho \bar{U}_i U_j \frac{\partial u'_i}{\partial x_j} + \rho \bar{U}_i \left(U_j \frac{\partial U_i}{\partial x_j} \right)' - \rho \bar{U}_i \left(\frac{1}{\rho} \frac{\partial \Upsilon_{ij}}{\partial x_j} \right)', \quad (3.20)$$

- the interaction between kinetic energy and internal energy \mathcal{E} , decomposed into: $\underline{\mathcal{E}}$ associated with the mean kinetic energy and ε associated with the turbulence kinetic energy,

$$\underline{\mathcal{E}} = -\Upsilon_{ij} \frac{\partial \bar{U}_i}{\partial x_j}, \quad (3.21)$$

$$\varepsilon = -\Upsilon_{ij} \frac{\partial u'_i}{\partial x_j}. \quad (3.22)$$

This set of equations is represented in a schematic form in figure 4.1.

In the limit case $\bar{\mathbf{U}} = \mathbf{0}$, the mean kinetic energy \underline{E} and the mixed kinetic energy \underline{e} vanish as do all energy exchange terms associated with these two quantities. The formulation reduces to the sole exchanges between turbulence kinetic energy and internal energy and describes the well-known rate of decay of turbulence kinetic energy and the paired gain of internal energy [16]. Similarly, the formulation reduces to the exchanges between mean kinetic energy and internal energy in the limit case $\mathbf{u}' = \mathbf{0}$.

We compare the energy exchanges in the present formulation to the ternary decomposition of Chassaing [47]. While Chassaing [47] did not explicitly give the energy exchanges between the different parts of total energy, he gave enough information to identify the energy exchanges without ambiguity. The formulation of Chassaing [47] may be written using the notations of this paper as:

$$\frac{\partial \rho \bar{E}}{\partial t} = \bar{\Phi}^c + \bar{\Phi}^r + \bar{Y} + (\bar{\mathcal{P}} + \bar{X} - \bar{Y}) - \bar{X} + \bar{\mathcal{E}}, \quad (3.23)$$

$$\frac{\partial \rho \bar{e}}{\partial t} = \bar{\varphi}^c + \bar{\varphi}^r + (\bar{\mathcal{P}} - \bar{X}) + \bar{X} + \bar{\varepsilon}, \quad (3.24)$$

$$\frac{\partial \rho \bar{e}}{\partial t} = \bar{\varphi}^c - \bar{Y} - (\bar{\mathcal{P}} - \bar{X}) - (\bar{\mathcal{P}} + \bar{X} - \bar{Y}), \quad (3.25)$$

$$\frac{\partial \rho \bar{I}}{\partial t} = \bar{\Phi}^{T,c} + \bar{\Phi}^\lambda - \bar{\mathcal{E}} - \bar{\varepsilon}, \quad (3.26)$$

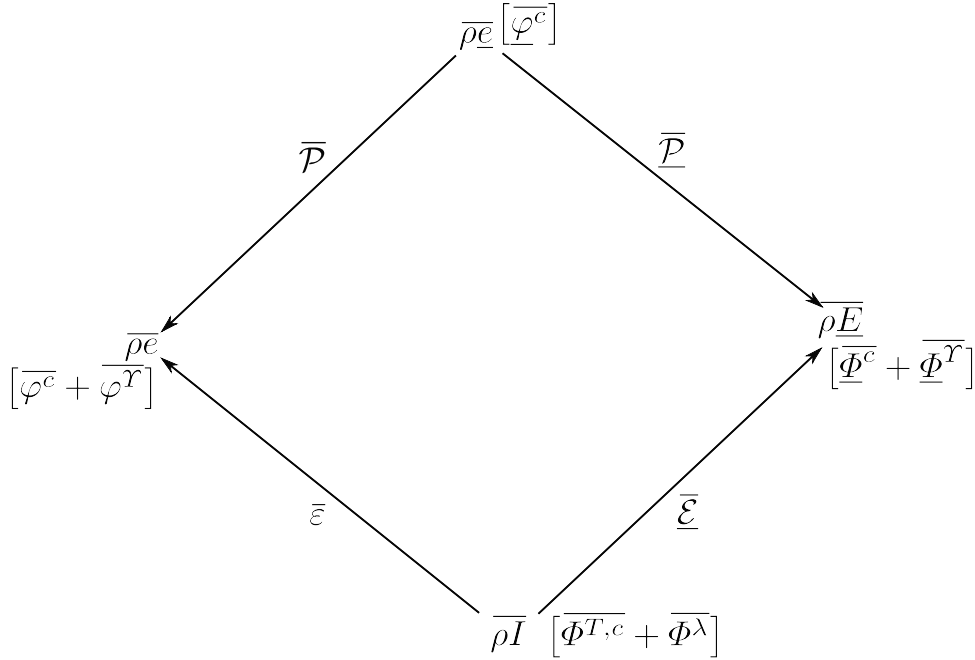


Figure 3.1 – Schematic representation of the energy exchanges between the four parts of total kinetic energy (in the one-stage formulation). An arrow represents an interaction between two quantities. The orientation of the arrow gives the sign of the term according to classical thermodynamic convention. (The term is positive in the right-hand side of the evolution equation of the quantity towards which the arrow points and negative in the other). The conservative energy transfers are represented within square brackets.

with:

$$\overline{X} = -\overline{\rho u'_i u'_j} \frac{\partial \overline{U}_i}{\partial x_j}, \quad (3.27)$$

$$\overline{Y} = -\frac{\partial \overline{\rho u'_j e}}{\partial x_j}. \quad (3.28)$$

It is represented in a schematic form in figure 3.2.

The formulation presented in this paper and the formulation of Chassaing [47] are mathematically equivalent. However, the energy exchanges identified and the interpretation given to the terms are different. The differences can be attributed to two main changes. First, the present formulation associates to the four parts of total energy a convective term related to both the mean and turbulent motion, that is of the transport by advection and diffusion. However, the formulation of Chassaing [47] only associates an advective term to the mixed kinetic energy $\overline{\rho e}$, but no diffusive term. Due to this, the term \overline{Y} , diffusion of mixed kinetic energy in the present formulation, instead appears in the evolution equation of the mean kinetic energy $\overline{\rho E}$ and is interpreted as the power of the Reynolds stress through the mean motion. In addition, there is in the formulation of Chassaing [47] a direct energy exchange \overline{X} between turbulence kinetic energy and mean kinetic energy whereas any interaction between turbulence kinetic energy and mean kinetic energy occurs through the mixed kinetic energy in the present formulation. Both of these changes modify the energy exchange associated with mixed

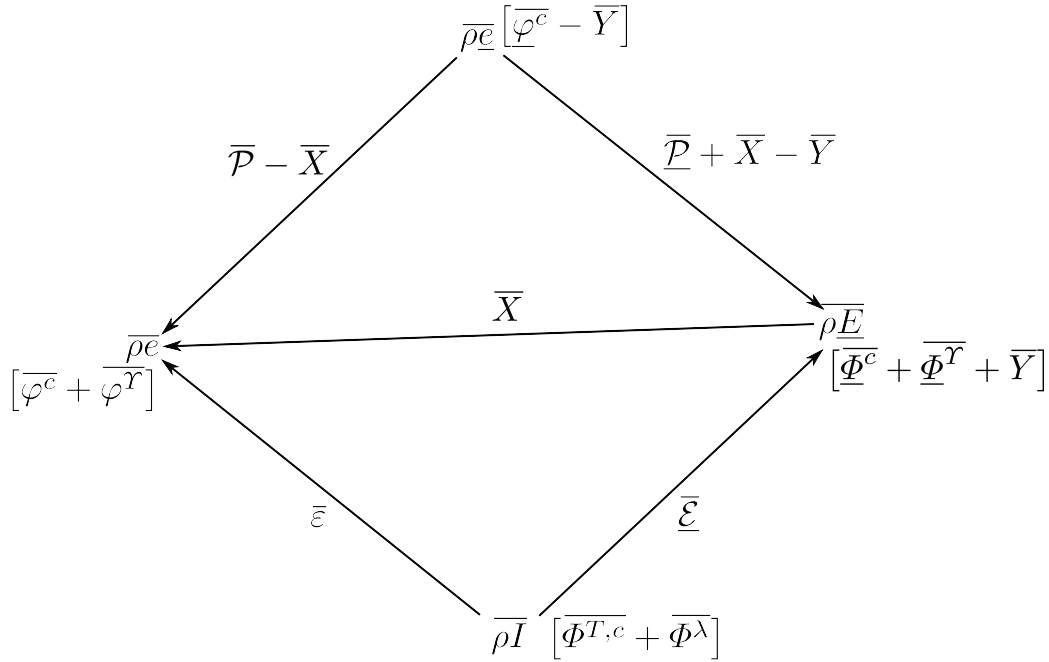


Figure 3.2 – Schematic representation of the energy exchanges between the four parts of total kinetic energy according to the formulation of Chassaing *et al.* [50]. Refer to the caption of figure 4.1 for some indications on how to read this diagram.

kinetic energy.

The formulation of Chassaing [47] is due to these two differences more similar to the classical incompressible representation of the energy exchanges, in which the term \overline{Y} appears in the evolution equation of the mean kinetic energy and where there is a direct energy exchange between turbulence kinetic energy and mean kinetic energy. However, some elements suggest that the present formulation is more physical. Indeed, it associates a full convective term to each part of kinetic energy. We consider this as necessary as it is part of the material derivative. Besides, the formulation is more symmetrical with regard to the manner it deals with fluctuations and statistically averaged quantities. The formulation is not modified if the statistical average operator and the fluctuating part operator are substituted in equations (3.13) to (3.22) and in the definitions of $\overline{\rho E}$, $\overline{\rho e}$ and $\overline{\rho I}$. Finally, the formulation may be used to consider the instantaneous energy exchanges as it does not rely on simplifications only valid in the statistically averaged case. This ensures the consistency of the formulation, in the sense that the energy exchanges in both the instantaneous and statistically averaged cases are well-defined and are not conflicting. This consistency is important to give a physical interpretation to the energy exchange, as this lets us consider the statistically averaged energy exchanges as the statistical average of the associated instantaneous energy exchanges.

3.2.2.3 Two-stage formulation

The ternary decomposition of kinetic energy is taken further with the decomposition of density into a mean and fluctuating part $\rho = \overline{\rho} + \rho'$. Namely, total energy $\rho(E + I)$ is

decomposed into a mean density part $\bar{\rho}(E+I)$ and a fluctuating density part $\rho'(E+I)$. Similarly, the mean kinetic energy $\rho\bar{E}$, the turbulence kinetic energy ρe , the mixed kinetic energy $\rho\bar{e}$ and the internal energy per unit volume ρI are decomposed into a mean density part, $\bar{\rho}\bar{E}$, $\bar{\rho}e$, $\bar{\rho}\bar{e}$ and $\bar{\rho}I$ respectively, and a fluctuating density part, $\rho'\bar{E}$, $\rho'e$, $\rho'\bar{e}$ and $\rho'I$ respectively. This results in a eightfold decomposition of total energy.

In this eightfold decomposition of total energy, the terms of the ternary formulation are decomposed further in a mean and fluctuating density part. Any term α identified in the one-stage formulation is split into two terms in the two-stage formulation: α_0 , associated with the mean density part of total energy and α_1 , associated with the fluctuating density part of total energy. Moreover, additional terms appear that represent an interaction between the mean and fluctuating density part of total energy.

The energy exchanges between the eight parts of total energy may be written as:

$$\frac{\partial \bar{\rho}\bar{E}}{\partial t} = \bar{\Phi}_0^c + \bar{\Phi}_0^r + \bar{\mathcal{P}}_0 + \bar{\mathcal{Z}}^c + \bar{\mathcal{Z}}^r + \bar{\mathcal{E}}_0, \quad (3.29)$$

$$\frac{\partial \rho'\bar{E}}{\partial t} = \bar{\Phi}_1^c + \bar{\Phi}_1^r + \bar{\mathcal{P}}_1 - \bar{\mathcal{Z}}^c - \bar{\mathcal{Z}}^r + \bar{\mathcal{E}}_1, \quad (3.30)$$

$$\frac{\partial \bar{\rho}e}{\partial t} = \bar{\varphi}_0^c + \bar{\varphi}_0^r + \bar{\mathcal{P}}_0 + \bar{\zeta}^c + \bar{\zeta}^r + \bar{\varepsilon}_0, \quad (3.31)$$

$$\frac{\partial \rho'e}{\partial t} = \bar{\varphi}_1^c + \bar{\varphi}_1^r + \bar{\mathcal{P}}_1 - \bar{\zeta}^c - \bar{\zeta}^r + \bar{\varepsilon}_1, \quad (3.32)$$

$$\frac{\partial \bar{\rho}\bar{e}}{\partial t} = \bar{\varphi}_0^c - \bar{\mathcal{P}}_0 - \bar{\mathcal{P}}_0 + \bar{\zeta}^c, \quad (3.33)$$

$$\frac{\partial \rho'\bar{e}}{\partial t} = \bar{\varphi}_1^c - \bar{\mathcal{P}}_1 - \bar{\mathcal{P}}_1 - \bar{\zeta}^c, \quad (3.34)$$

$$\frac{\partial \bar{\rho}I}{\partial t} = \bar{\Phi}_0^{T,c} + \bar{\Phi}_0^\lambda + \bar{\mathcal{Z}}^{T,c} + \bar{\mathcal{Z}}^\lambda - \bar{\mathcal{E}}_0 - \bar{\varepsilon}_0, \quad (3.35)$$

$$\frac{\partial \rho'I}{\partial t} = \bar{\Phi}_1^{T,c} + \bar{\Phi}_1^\lambda - \bar{\mathcal{Z}}^{T,c} - \bar{\mathcal{Z}}^\lambda - \bar{\mathcal{E}}_1 - \bar{\varepsilon}_1, \quad (3.36)$$

with

$$\begin{aligned} \bar{\Phi}_0^c &= -\frac{\partial \bar{\rho}U_j\bar{E}}{\partial x_j}, & \bar{\Phi}_1^c &= -\frac{\partial \rho'U_j\bar{E}}{\partial x_j}, \\ \bar{\varphi}_0^c &= -\frac{\partial \bar{\rho}U_j e}{\partial x_j}, & \bar{\varphi}_1^c &= -\frac{\partial \rho'U_j e}{\partial x_j}, \\ \bar{\varphi}_0^c &= -\frac{\partial \bar{\rho}U_j\bar{e}}{\partial x_j}, & \bar{\varphi}_1^c &= -\frac{\partial \rho'U_j\bar{e}}{\partial x_j}, \\ \bar{\Phi}_0^{T,c} &= -\frac{\partial \bar{\rho}U_j I}{\partial x_j}, & \bar{\Phi}_1^{T,c} &= -\frac{\partial \rho'U_j I}{\partial x_j}, \\ \bar{\Phi}_0^r &= \frac{\partial}{\partial x_j} \left(\frac{\Upsilon_{ij}}{\rho} \bar{\rho} \bar{U}_i \right), & \bar{\Phi}_1^r &= \frac{\partial}{\partial x_j} \left(\frac{\Upsilon_{ij}}{\rho} \rho' \bar{U}_i \right), \\ \bar{\varphi}_0^r &= \frac{\partial}{\partial x_j} \left(\frac{\Upsilon_{ij}}{\rho} \bar{\rho} u'_i \right), & \bar{\varphi}_1^r &= \frac{\partial}{\partial x_j} \left(\frac{\Upsilon_{ij}}{\rho} \rho' u'_i \right), \\ \bar{\Phi}_0^\lambda &= \frac{\partial}{\partial x_j} \left(\frac{\bar{\rho}}{\rho} \lambda \frac{\partial T}{\partial x_j} \right), & \bar{\Phi}_1^\lambda &= \frac{\partial}{\partial x_j} \left(\frac{\rho'}{\rho} \lambda \frac{\partial T}{\partial x_j} \right), \end{aligned}$$

$$\begin{aligned}
\mathcal{P}_0 &= -\bar{\rho}u'_iU_j\frac{\partial\bar{U}_i}{\partial x_j} + \overline{\bar{\rho}u'_iU_j}\frac{\partial u'_i}{\partial x_j} - \bar{\rho}u'_i\frac{1}{\rho}\frac{\partial\overline{\mathcal{Y}_{ij}}}{\partial x_j}, \\
\mathcal{P}_1 &= -\rho'u'_iU_j\frac{\partial\bar{U}_i}{\partial x_j} + \overline{\rho'u'_iU_j}\frac{\partial u'_i}{\partial x_j} - \rho'u'_i\frac{1}{\rho}\frac{\partial\overline{\mathcal{Y}_{ij}}}{\partial x_j}, \\
\underline{\mathcal{P}}_0 &= -\bar{\rho}\bar{U}_iU_j\frac{\partial u'_i}{\partial x_j} + \bar{\rho}\bar{U}_i\left(U_j\frac{\partial U_i}{\partial x_j}\right)' - \bar{\rho}\bar{U}_i\left(\frac{1}{\rho}\frac{\partial\overline{\mathcal{Y}_{ij}}}{\partial x_j}\right)', \\
\underline{\mathcal{P}}_1 &= -\rho'\bar{U}_iU_j\frac{\partial u'_i}{\partial x_j} + \rho'\bar{U}_i\left(U_j\frac{\partial U_i}{\partial x_j}\right)' - \rho'\bar{U}_i\left(\frac{1}{\rho}\frac{\partial\overline{\mathcal{Y}_{ij}}}{\partial x_j}\right)', \\
\underline{\varepsilon}_0 &= -\frac{\bar{\rho}\overline{\mathcal{Y}_{ij}}}{\rho}\frac{\partial\bar{U}_i}{\partial x_j}, & \underline{\varepsilon}_1 &= -\frac{\rho'\overline{\mathcal{Y}_{ij}}}{\rho}\frac{\partial\bar{U}_i}{\partial x_j}, \\
\varepsilon_0 &= -\frac{\bar{\rho}\overline{\mathcal{Y}_{ij}}}{\rho}\frac{\partial u'_i}{\partial x_j}, & \varepsilon_1 &= -\frac{\rho'\overline{\mathcal{Y}_{ij}}}{\rho}\frac{\partial u'_i}{\partial x_j},
\end{aligned}$$

and where we identify the following terms:

- the energy dilatation correlation Z^c ,

$$Z^c = (E + I)\frac{\partial\bar{\rho}U_j - \bar{\rho}\bar{U}_j}{\partial x_j}, \quad (3.37)$$

decomposed into: \underline{Z}^c associated with the mean kinetic energy, ζ^c associated with the turbulence kinetic energy, $\underline{\zeta}^c$ associated with the mixed kinetic energy and $Z^{T,c}$ associated with the internal energy,

$$\underline{Z}^c = \underline{E}\frac{\partial\bar{\rho}U_j - \bar{\rho}\bar{U}_j}{\partial x_j}, \quad (3.38)$$

$$\zeta^c = e\frac{\partial\bar{\rho}U_j - \bar{\rho}\bar{U}_j}{\partial x_j}, \quad (3.39)$$

$$\underline{\zeta}^c = \underline{e}\frac{\partial\bar{\rho}U_j - \bar{\rho}\bar{U}_j}{\partial x_j}, \quad (3.40)$$

$$Z^{T,c} = I\frac{\partial\bar{\rho}U_j - \bar{\rho}\bar{U}_j}{\partial x_j}, \quad (3.41)$$

- the interaction between the mean and fluctuating density part of total energy by the total stress Z^r ,

$$Z^r = -\overline{\mathcal{Y}_{ij}U_i}\frac{\partial}{\partial x_j}\left(\frac{\bar{\rho}}{\rho}\right), \quad (3.42)$$

decomposed into: \underline{Z}^r associated with the mean kinetic energy and ζ^r associated with the turbulence kinetic energy,

$$\underline{Z}^r = -\overline{\mathcal{Y}_{ij}\bar{U}_i}\frac{\partial}{\partial x_j}\left(\frac{\bar{\rho}}{\rho}\right), \quad (3.43)$$

$$\zeta^r = -\overline{\mathcal{Y}_{ij}u'_i}\frac{\partial}{\partial x_j}\left(\frac{\bar{\rho}}{\rho}\right), \quad (3.44)$$

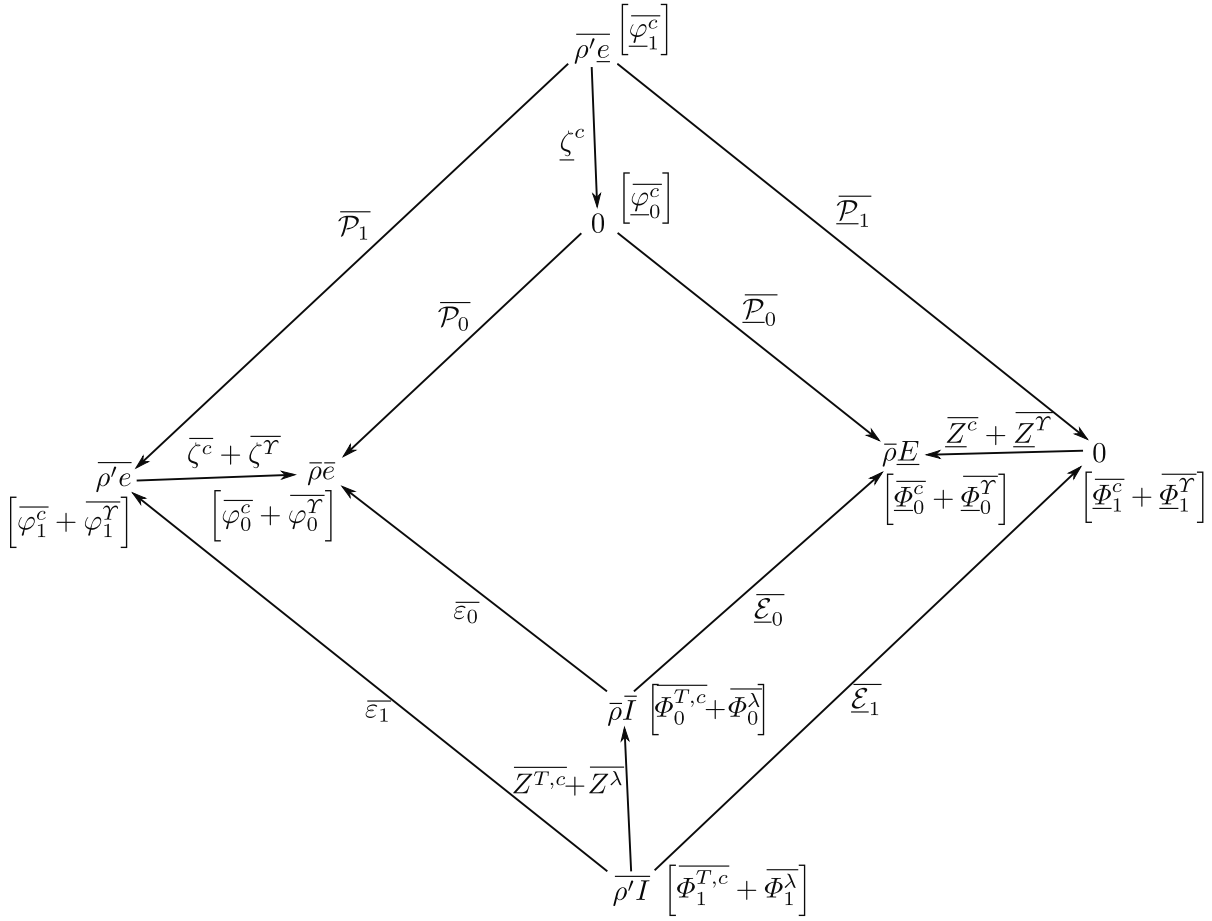


Figure 3.3 – Schematic representation of the energy exchanges between the eight parts of total kinetic energy (in the two-stage formulation). Refer to the caption of figure 4.1 for some indications on how to read this diagram.

- the interaction between the mean and fluctuating density part of total energy by conduction Z^λ .

$$Z^\lambda = -\lambda \frac{\partial T}{\partial x_j} \frac{\partial}{\partial x_j} \left(\frac{\bar{\rho}}{\rho} \right). \quad (3.45)$$

This set of equations is represented in a schematic form in figure 4.2.

The two-stage formulation includes the mean density turbulence kinetic energy. In the remaining part of the paper, we will establish its evolution equation in the spectral domain.

3.2.3 Spectral equation of the mean density turbulence kinetic energy

The investigation of the mean density turbulence kinetic energy evolution equation provides information on the energy exchanges associated with this quantity in the spatial direction. The study may be extended to the spectral domain by establishing its spectral evolution equation. This investigation permits to give the effect of the

energy exchanges with regard to the size of the turbulent structures.

In order to write the spectral equation, we need to consider a flow with at least one direction of homogeneity. Without loss of generality, we consider a turbulent flow with two homogeneous and periodic directions, x and z . The inhomogeneous direction is denoted y . The dimensions of the domain in the x , y and z directions are denoted L_x , L_y and L_z respectively. Since the flow is periodic in the x and z directions, we perform the Fourier transform in the x and z directions only and leave the y direction untransformed. Any physical quantity $g(x, y, z)$ can be expressed as a Fourier series,

$$g(\mathbf{x}, y, t) = \sum_{p, q = -\infty}^{\infty} \widehat{g}(\mathbf{k}_{p, q}, y, t) e^{i\mathbf{k}_{p, q} \cdot \mathbf{x}}, \quad (3.46)$$

where p and q are positive or negative integers, $\mathbf{x} = (x, z)$ is the position vector in the xOz plane and $\mathbf{k}_{p, q} = \mathbf{k} = (k_x, k_z) = (\frac{2\pi p}{L_x}, \frac{2\pi q}{L_z})$ is the position vector in the $k_x Ok_z$ plane. The Fourier coefficients of the Fourier series expansion of g are denoted with the hat operator ($\widehat{}$) and are given by [173]:

$$\widehat{g}(\mathbf{k}, y, t) = \frac{1}{L_x L_z} \int_0^{L_x} \int_0^{L_z} g(\mathbf{x}, y, t) e^{-i\mathbf{k} \cdot \mathbf{x}} d\mathbf{x}. \quad (3.47)$$

The half-trace of the velocity fluctuation correlation tensor \bar{e} is equal to half the correlation

$$C(\mathbf{r}, y, t) = \overline{u'_i(\mathbf{r}, y, t) u'_i(\mathbf{x} + \mathbf{r}, y, t)} \quad (3.48)$$

in the particular case $\mathbf{r} = 0$, that is $\bar{e}(y, t) = \frac{1}{2} C(\mathbf{0}, y, t)$. We can express C as a Fourier series from (3.46). The Fourier coefficients \widehat{C} can be written as [173, 235]

$$\widehat{C}(\mathbf{k}, y, t) = \overline{\widehat{u}'_i{}^*(\mathbf{k}, y, t) \widehat{u}'_i(\mathbf{k}, y, t)}, \quad (3.49)$$

where the asterisk (*) denotes the complex conjugate. Henceforth, we denote $\bar{\bar{e}}$ and call spectral equivalent of \bar{e} the half of the spectral correlation \widehat{C} ,

$$\bar{\bar{e}} = \frac{1}{2} \widehat{u}'_i{}^* \widehat{u}'_i. \quad (3.50)$$

From similar arguments, we shall associate to each term of the evolution equation of the half-trace of the velocity fluctuation correlation tensor a spectral equivalent.

Spectral equations of the turbulence kinetic energy were given by Domaradzki *et al.* [83], Marati *et al.* [188], Dunn and Morrison [85], Bolotnov *et al.* [28], Lee and Moser [165], Mizuno [197] in the incompressible case and Aulery *et al.* [10] in the variable density case. The present decomposition gives a clear one-to-one correspondence between the terms of the spectral and spatial decompositions. To this end, a purely spectral term with no spatial contribution has to be considered. The decomposition is similar to the decomposition of Mizuno [197] at the incompressible limit.

The spectral evolution equation of the mean density turbulence kinetic energy may be written as:

$$\frac{\partial \bar{\bar{e}}}{\partial t} = \bar{\bar{\varphi}}_0^c + \bar{\bar{\varphi}}_0^r + \bar{\bar{\mathcal{P}}}_0 + \bar{\bar{\zeta}}^c + \bar{\bar{\zeta}}^r + \bar{\bar{\varepsilon}}_0, \quad (3.51)$$

where we identify the following terms:

- the convection $\overline{\varphi}_0^c$, associated with the spatial convection $\overline{\varphi}_0^c$,

$$\overline{\varphi}_0^c = -\text{Re} \left(-\frac{1}{2} \overline{\frac{\partial \widehat{\rho u}_i^* \widehat{u}_i U_j}{\partial x_j}} \right), \quad (3.52)$$

- the transfer by the total stress $\overline{\varphi}_0^{\mathcal{R}}$, associated with the spatial transfer by the total stress $\overline{\varphi}_0^{\mathcal{R}}$,

$$\overline{\varphi}_0^{\mathcal{R}} = \text{Re} \left(\overline{\frac{\partial \widehat{\rho u}_i^* \widehat{\Upsilon}_{ij}}{\partial x_j} \frac{1}{\rho}} \right), \quad (3.53)$$

- the interaction with mixed kinetic energy $\overline{\mathcal{P}}_0$, associated with the spatial interaction with mixed kinetic energy $\overline{\mathcal{P}}_0$,

$$\overline{\mathcal{P}}_0 = \text{Re} \left(-\overline{\widehat{\rho u}_i^* \widehat{u}_j \frac{\partial \overline{U}_i}{\partial x_j}} \right), \quad (3.54)$$

- the kinetic energy dilation correlation $\overline{\zeta}^c$, associated with the spatial kinetic energy dilation correlation $\overline{\zeta}^c$,

$$\overline{\zeta}^c = \text{Re} \left(\overline{\frac{1}{2} \widehat{u}_i^* \widehat{u}_i \frac{\partial \overline{\rho U}_j - \overline{\rho U}_j}{\partial x_j}} \right), \quad (3.55)$$

- the interaction with fluctuating density kinetic energy by the total stress $\overline{\zeta}^{\mathcal{R}}$, associated with the spatial interaction with fluctuating density kinetic energy by the total stress $\overline{\zeta}^{\mathcal{R}}$,

$$\overline{\zeta}^{\mathcal{R}} = \text{Re} \left(\overline{\widehat{u}_i^* \widehat{\Upsilon}_{ij} \frac{\partial}{\partial x_j} \left(\frac{\widehat{\rho}}{\rho} \right)} \right), \quad (3.56)$$

- the interaction between kinetic energy and internal energy $\overline{\varepsilon}_0$, associated with the spatial interaction with internal energy $\overline{\varepsilon}_0$,

$$\overline{\varepsilon}_0 = \text{Re} \left(-\overline{\widehat{\rho} \frac{\partial \widehat{u}_i^* \widehat{\Upsilon}_{ij}}{\partial x_j} \frac{1}{\rho}} \right), \quad (3.57)$$

- the purely spectral term $\overline{\Xi}$, with no contribution in the spatial domain,

$$\overline{\Xi} = \text{Re} \left(\overline{\frac{1}{2} \frac{\partial \widehat{\rho u}_i^*}{\partial x_j} \widehat{u}_i \widehat{u}_j} - \overline{\frac{1}{2} \widehat{u}_i^* \widehat{u}_j \frac{\partial \widehat{\rho u}_i}{\partial x_j}} \right), \quad (3.58)$$

where Re denotes the real part operator.

The terms are decomposed in order to have a one-to-one correspondence with the terms of the spatial decomposition. The inverted hat operator ($\widehat{\cdot}$) is used to indicate

the spectral equivalent of a spatial term. The spectral and spatial terms are tied closely. Given a spectral term written in the form $\text{Re}(\widehat{u}_i^* \widehat{a})$, for any a , the associated spatial term is $\overline{u'_i a}$. The spectral term comes from the Fourier coefficients of the spatial two-point correlation between u'_i and a [173].

The purely spectral term $\overline{\Xi}$ has no associated spatial term. The summation over the whole wavenumber space of its spectra is zero. In other words, this term has no effect on the spatial balance of kinetic energy but contributes to the interscale redistribution of kinetic energy.

3.2.4 Conclusion

The ternary decomposition of kinetic energy gives another angle of approach to the study of energy exchanges in turbulent flows. Based on the classical Reynolds averaging, the decomposition leads to the definition of a turbulence kinetic energy, a mean kinetic energy and a mixed kinetic energy. This new term, specific to the formulation, is related to the interaction between the turbulent motion and the mean motion. In the formulation, any energy exchange between the turbulence kinetic energy and the mean kinetic energy goes through the mixed term, which adds its contribution to the exchange. The formulation is decomposed further in order to include the mean density turbulence kinetic energy, product of the mean density and the half-trace of the velocity fluctuation correlation tensor. This is done by splitting the density in a mean part and a fluctuating part. Contrary to the turbulence kinetic energy, the equation of the mean density turbulence kinetic energy can easily be extended to the spectral domain. This associates a spectral equivalent to each spatial term and adds a purely spectral term to the decomposition.

Bibliography

- [10] F. Aulery, A. Toutant, F. Bataille, and Y. Zhou. Energy transfer process of anisothermal wall-bounded flows. *Physics Letters A*, 379(24):1520–1526, 2015.
- [11] F. Aulery, D. Dupuy, A. Toutant, F. Bataille, and Y. Zhou. Spectral analysis of turbulence in anisothermal channel flows. *Computers & Fluids*, 151:115–131, 2017.
- [13] B. Aupoix. Introduction to turbulence modelling for compressible flows. *VKI lecture series*, 4:H1–H64, 2000.
- [15] F. Bataille, R. Rubinstein, and M. Y. Hussaini. Eddy viscosity and diffusivity modeling. *Physics Letters A*, 346(1):168–173, 2005.
- [16] G. K. Batchelor. *The theory of homogeneous turbulence*. Cambridge university press, 1953.
- [17] P. T. Bauer, G. W. Zumwalt, and L. J. Fila. A numerical method and an extension of the korst jet mixing theory for multispecie turbulent jet mixing. AIAA paper 68 (112). In *6th Aerospace Sciences Meeting, New York*, 1968.
- [28] I. A. Bolotnov, R. T. Lahey, D. A. Drew, K. E. Jansen, and A. A. Oberai. Spectral analysis of turbulence based on the DNS of a channel flow. *Computers & Fluids*, 39(4): 640–655, 2010.
- [47] P. Chassaing. Une alternative à la formulation des équations du mouvement turbulent d'un fluide à masse volumique variable. *Journal de mécanique théorique et appliquée*, 4 (3):375–389, 1985.

- [49] P. Chassaing. The modeling of variable density turbulent flows. a review of first-order closure schemes. *Flow, Turbulence and Combustion*, 66(4):293–332, 2001.
- [50] P. Chassaing, R. A. Antonia, F. Anselmet, L. Joly, and S. Sarkar. *Variable density fluid turbulence*. Springer Science & Business Media, 2013.
- [59] A. Cimarelli, E. De Angelis, and C. M. Casciola. Paths of energy in turbulent channel flows. *J. Fluid Mech.*, 715:436–451, 2013.
- [60] A. Cimarelli, G. Cocconi, B. Frohnapfel, and E. De Angelis. Spectral enstrophy budget in a shear-less flow with turbulent/non-turbulent interface. *Phys. Fluids*, 27(12):125106, 2015.
- [61] A. Cimarelli, E. De Angelis, P. Schlatter, G. Brethouwer, A. Talamelli, and C. M. Casciola. Sources and fluxes of scale energy in the overlap layer of wall turbulence. *J. Fluid Mech.*, 771:407–423, 2015.
- [62] A. Cimarelli, E. De Angelis, J. Jiménez, and C. M. Casciola. Cascades and wall-normal fluxes in turbulent channel flows. *J. Fluid Mech.*, 796:417–436, 2016. ISSN 1469-7645.
- [68] A. W. Cook and Y. Zhou. Energy transfer in Rayleigh-Taylor instability. *Phys. Rev. E*, 66:026312, 2002.
- [70] J. Cousteix and B. Aupoix. Turbulence models for compressible flows. In *Special Course Three-Dimensional Supersonic and Hypersonic Flows Including Separation*. AGARD/FDP-VKI Special course, 1989.
- [73] X. Daguene-Frick, A. Toutant, F. Bataille, and G. Olalde. Numerical investigation of a ceramic high-temperature pressurized-air solar receiver. *Solar Energy*, 90(0):164–178, 2013. ISSN 0038-092X.
- [81] J. A. Domaradzki and R. S. Rogallo. Local energy transfer and nonlocal interactions in homogeneous, isotropic turbulence. *Physics of Fluids A: Fluid Dynamics*, 2(3):413–426, 1990.
- [83] J. A. Domaradzki, W. Liu, C. Hartel, and L. Kleiser. Energy transfer in numerically simulated wall-bounded turbulent flows. *Phys. Fluids*, 6(4):1583–1599, 1994.
- [85] D. C. Dunn and J. F. Morrison. Analysis of the energy budget in turbulent channel flow using orthogonal wavelets. *Computers & Fluids*, 34(2):199–224, 2005.
- [94] A. Favre. The equations of compressible turbulent gases. Technical Report AD0622097, DTIC Document, 1965.
- [95] A. Favre. Statistical equations of turbulent gases. *Problems of Hydrodynamics and Continuum Mechanics*, pages 231–266, 1969.
- [96] A. Favre. Turbulence: Space-time statistical properties and behavior in supersonic flows. *Phys. Fluids*, 26(10):2851–2863, 1983.
- [109] E. Garnier, N. Adams, and P. Sagaut. *Large eddy simulation for compressible flows*. Springer Science & Business Media, 2009.
- [110] T. B. Gatski and J. P. Bonnet. *Compressibility, turbulence and high speed flow*. Academic Press, 2013.
- [120] S. E. Guarini, R. D. Moser, K. Shariff, and A. Wray. Direct numerical simulation of a supersonic turbulent boundary layer at Mach 2.5. *J. Fluid Mech.*, 414:1–33, 2000.
- [122] H. Ha Minh, B. E. Launder, and J. MacInnes. A new approach to the analysis of turbulent mixing in variable density flows. In *3rd Turbulent Shear Flow Symp. p*, volume 19, 1981.
- [123] H. Ha Minh, B. E. Launder, and J. MacInnes. The turbulence modelling of variable density flows—a mixed-weighted decomposition. In *Turbulent Shear Flows 3*, pages 291–308. Springer, 1982.
- [127] P. G. Huang, G. N. Coleman, and P. Bradshaw. Compressible turbulent channel flows: DNS results and modelling. *J. Fluid Mech.*, 305:185–218, 1995.
- [144] S. Kida and S. A. Orszag. Energy and spectral dynamics in decaying compressible turbulence. *Journal of Scientific Computing*, 7(1):1–34, 1992. ISSN 0885-7474.

- [165] M. Lee and R. D. Moser. Spectral analysis on reynolds stress transport equation in high firewall-bounded turbulence. In *International Symposium on Turbulence and Shear Flow Phenomena (TSFP-9)*, Melbourne, pages 4A–3, 2006.
- [168] S. K. Lele. Compressibility effects on turbulence. *Annu. Rev. Fluid Mech.*, 26(1):211–254, 1994.
- [173] M. Lesieur. *Turbulence in Fluids*. Fluid Mechanics and Its Applications. Springer, 2008. ISBN 9781402064357.
- [183] J. L. Lumley. Spectral energy budget in wall turbulence. *Phys. Fluids*, 7(2):190–196, 1964.
- [185] T. Maeder, N. A. Adams, and L. Kleiser. Direct simulation of turbulent supersonic boundary layers by an extended temporal approach. *J. Fluid Mech.*, 429:187–216, 2001.
- [188] N Marati, CM Casciola, and R Piva. Energy cascade and spatial fluxes in wall turbulence. *J. Fluid Mech.*, 521:191–215, 2004.
- [191] L. Mathelin, F. Bataille, and Y. Zhou. Theoretical investigation of some thermal effects in turbulence modeling. *Theoretical and Computational Fluid Dynamics*, 22(6):471–483, 2008.
- [197] Y. Mizuno. Spectra of energy transport in turbulent channel flows for moderate reynolds numbers. *J. Fluid Mech.*, 805:171–187, 2016.
- [201] M. V. Morkovin. *The Mechanics of Turbulence*. Gordon and Breach, 1964.
- [212] F. Nicoud. Conservative high-order finite-difference schemes for low-Mach number flows. *J. Comput. Phys.*, 158(1):71–97, 2000.
- [233] S. Pirozzoli, F. Grasso, and T. B. Gatski. Direct numerical simulation and analysis of a spatially evolving supersonic turbulent boundary layer at $M=2.25$. *Phys. Fluids*, 16(3):530–545, 2004.
- [235] S. B. Pope. *Turbulent Flows*. Cambridge University Press, 2000.
- [245] O. Reynolds. On the dynamical theory of incompressible viscous fluids and the determination of the criterion. *Proceedings of the Royal Society of London*, 56(336-339):40–45, 1894.
- [247] A. J. L. Rodriguez and G. Emanuel. Compressible rotational flows generated by the substitution principle. *Phys. Fluids*, 31:1058–1063, 1988.
- [264] S. Serra, A. Toutant, and F. Bataille. Thermal large eddy simulation in a very simplified geometry of a solar receiver. *Heat Transfer Engineering*, 33(6):505–524, 2012.
- [265] S. Serra, A. Toutant, F. Bataille, and Y. Zhou. High-temperature gradient effect on a turbulent channel flow using thermal large-eddy simulation in physical and spectral spaces. *J. Turbulence*, 13:N49, 2012.
- [266] S. Serra, A. Toutant, F. Bataille, and Y. Zhou. Turbulent kinetic energy spectrum in very anisothermal flows. *Physics Letters A*, 376(45):3177–3184, 2012.
- [272] G. S. Sidharth, A. Kartha, and G. V. Candler. Filtered velocity based LES of mixing in high speed recirculating shear flow. In *46th AIAA Fluid Dynamics Conference*, page 3184, 2016.
- [290] A. Toutant and F. Bataille. Turbulence statistics in a fully developed channel flow submitted to a high temperature gradient. *International Journal of Thermal Sciences*, 74:104–118, 2013.
- [291] A. Toutant, E. Labourasse, O. Lebaigue, and O. Simonin. DNS of the interaction between a deformable buoyant bubble and a spatially decaying turbulence: a priori tests for LES two-phase flow modelling. *Computers & Fluids*, 37(7):877–886, 2008.
- [312] D. C. Wilcox. *Turbulence modeling for CFD*, volume 2. DCW industries La Canada, CA, 1998.
- [318] C.-S. Yih. Exact solutions for steady two-dimensional flow of a stratified fluid. *J. Fluid Mech.*, 9(02):161–174, 1960.

- [324] Y. Zhou. Degrees of locality of energy transfer in the inertial range. *Physics of Fluids A: Fluid Dynamics*, 5(5):1092–1094, 1993.
- [325] Y. Zhou. Interacting scales and energy transfer in isotropic turbulence. *Physics of Fluids A: Fluid Dynamics*, 5(10):2511–2524, 1993.

3.3 Conclusion of chapter 3

Using the Reynolds average, a new representation of the energy exchanges in variable density flows is established. The formulation is developed in the context of a monophasic non-reactive flow without gravity, limiting the energy exchanges to the interaction between kinetic energy and internal energy. These hypotheses are relevant to the flows found in high-temperature solar receivers. The representation can be complemented in more complex flows to take into account additional effects, for instance the chemical potential in reactive flows or the gravitational potential energy if gravity is not neglected. The representation can also be simplified to take into account further approximations. In low Mach number flows, the effect on internal energy of the interaction between kinetic energy and internal energy is neglected. Low Mach number flows therefore approximately obey to another description of the energy exchanges in which kinetic energy is destructed rather than converted into internal energy. The internal energy per unit volume is time dependent but constant in space.

The Reynolds decomposition of density provides a theoretical basis to the study of the mean density turbulence kinetic energy in a variable density setting. This is crucial to the further investigations of the energy exchanges as we are able to give the energy exchanges associated with the mean density turbulence kinetic energy in the spectral domain. The only other possible approach found in the literature is based on a density square-root weighting of the velocity [318]. Each spatial energy exchange is associated with a spectral energy exchange and a purely spectral term representing the interscale transport of kinetic energy is added. The correspondence between the spatial and spectral energy exchanges implies that the expression of the spatial term can be recovered from the associated spectral term and vice versa. In addition, the spatial terms can be computed from the summation of the associated spectral term over the whole wavenumber space. The arguments for this property are well known in the literature [see e.g. 173] and reported in appendix A.

A modified version of the representation of the energy exchanges is used in the two following chapters to investigate from direct numerical simulations the energy exchanges associated with the half-trace of the velocity fluctuation correlation tensor and improve our understanding of the influence of the temperature gradient and the Reynolds number on the energy exchanges. Using the direct numerical simulations presented in section 1.3, the most significant terms are identified and their physical effect in the spatial and spectral domain is analysed.

Chapter 4

Turbulence kinetic energy exchanges in flows with highly variable fluid properties

4.1 Introduction of chapter 4

In the flows found in solar receivers, and in the strongly anisothermal turbulent channel flows investigated, the temperature dependence of the fluid properties with temperature is significant. This modifies the energy exchanges and invalidates the passive scalar approach of dealing with temperature [145, 138, 139, 234]. The variations of the fluid properties modifies the velocity profile, thereby not well described by incompressible scaling laws and turbulence models [127, 124]. In addition, strongly anisothermal turbulent channel flows exhibit an asymmetric character absent from most studies of the energy exchanges in flows with variable fluid properties [215, 222, 224, 223, 225]. In this chapter, the energy exchanges associated with the half-trace of the velocity fluctuation correlation tensor are investigated from direct numerical simulations.

The study of the half-trace of the velocity fluctuation correlation tensor is justified by a decomposition of kinetic energy very similar to the decomposition of chapter 3. Using a decomposition of density in a constant and variable part instead of the Reynolds decomposition replaces the mean density parts of total energy by the constant density parts. Within this paradigm, the half-trace of the velocity fluctuation correlation tensor is up to a constant scalar factor the constant density turbulence kinetic energy, which appears in the formulation in place of the mean density turbulence kinetic energy. This allows us to identify the physically relevant groupings of its evolution equation in variable density flows. Compared to the incompressible case, there is a new energy exchange between the constant and variable density part of kinetic energy. The energy exchanges found in the incompressible case keep their physical meaning but their mathematical expression is modified. The energy exchanges are decomposed to isolate the terms formally identical to the terms remaining in incompressible flows with constant fluid properties and the terms specific to compressible flows with variable fluid properties. This highlights the explicit contributions of the flow dilatation, the fluctuations of the fluid properties and the mean variations of the fluid proper-

ties to the energy exchanges. Though, in general, the so-called incompressible terms are also affected by the temperature gradient given the temperature velocity coupling. The result of these decompositions is given in this chapter and used to analyse the energy exchanges associated with the half-trace of the velocity fluctuation correlation tensor from direct numerical simulations. The detailed derivation of this alternative formulation of the energy exchanges and its decomposition is given in appendix B.

The energy exchanges are investigated from the direct numerical simulations of fully developed channel flows at $Re_\tau = 180$ presented in section 1.3, namely an incompressible isothermal channel and an anisothermal channel. The main objective is to study the effect of the temperature gradient on the energy exchanges. The contribution of each term of the above-described decompositions to the energy exchanges is assessed to identify the terms that can be neglected. In particular, the importance of some terms specific to flows with variable fluid properties is emphasised. The energy exchange related to the streamwise volume force in the channel is also considered and is found negligible. The spatial and spectral behaviour of the energy exchanges is then discussed. The study of the energy exchanges shows the statistically averaged effect of the energy exchanges on the half-trace of the velocity correlation fluctuation tensor. The effect of the variations of the fluid properties is inferred from the comparison of the behaviour in the incompressible isothermal configuration and at the hot and cold side in the anisothermal configuration.

4.2 Paper 2

This section reproduces the paper D. Dupuy, A. Toutant, and F. Bataille. Turbulence kinetic energy exchanges in flows with highly variable fluid properties. *Journal of Fluid Mechanics*, 834:5–54, 2018 [91].

Abstract

This paper investigates the energy exchanges associated with the half-trace of the velocity fluctuation correlation tensor in a strongly anisothermal low Mach fully developed turbulent channel flow. The study is based on direct numerical simulations of the channel within the low Mach number hypothesis and without gravity. The overall flow behaviour is governed by the variable fluid properties. The temperature of the two channel walls are imposed at 293 K and 586 K to generate the temperature gradient. The mean friction Reynolds number of the simulation is 180. The analysis is carried out in the spatial and spectral domains. The spatial and spectral studies use the same decomposition of the terms of the evolution equation of the half-trace of the velocity fluctuation correlation tensor. The importance of each term of the decomposition in the energy exchanges is assessed. This lets us identify the terms associated with variations or fluctuations of the fluid properties that are not negligible. Then, the behaviour of the terms is investigated. The spectral energy exchanges are first discussed in the incompressible case since the analysis is not present in the literature with the decomposition used in this study. The modification of the energy

exchanges by the temperature gradient is then investigated in the spatial and spectral domains. The temperature gradient generates an asymmetry between the two sides of the channel. The asymmetry can in a large part be explained by the combined effect of the mean local variations of the fluid properties and a Reynolds number effect.

4.2.1 Introduction

This paper provides a numerical analysis of the energy exchanges associated with the half-trace of the velocity fluctuation correlation tensor in a low Mach turbulent channel flow subjected to a strong temperature gradient. The investigation is relevant to the study of wall-bounded turbulent flows with variable fluid properties, provided that acoustic effects are small. Flows subjected to a large temperature gradient are characterised by a strong coupling between temperature and turbulence [264, 290]. The statistics of velocity and temperature means and fluctuations are modified by the temperature gradient, as an asymmetry between the turbulence statistics at both walls is generated. This asymmetry is more complex than a Reynolds number effect, as the scaled statistics of turbulence do not collapse with those of the isothermal channels at the turbulence Reynolds number corresponding to either wall of the anisothermal channel [265]. The energy exchanges between the different parts of total energy are insightful for the fundamental understanding of the behaviour of flows subjected to a strong temperature gradient. They include in particular the energy exchanges associated with turbulence kinetic energy. The use of flow fields from direct numerical simulations has demonstrated its relevance to the investigation of energy exchanges. Indeed, this requires the knowledge of the instantaneous three-dimensional velocity, pressure and temperature fields, which cannot be easily obtained experimentally.

In incompressible flows with constant fluid properties, direct numerical simulations of homogeneous isotropic turbulence have validated Kolmogorov's hypothesis on the locality of the energy transfer [81] and interacting scales [324, 325]. Reliable statistics of the terms of the evolution equation of the turbulence kinetic energy in a channel flow have been provided in the spatial domain by various authors, including Kim *et al.* [146], Moser *et al.* [203], Abe *et al.* [2], Del Álamo and Jiménez [79], Hoyas and Jiménez [126], Kozuka *et al.* [149] and more recently Vreman and Kuerten [305]. The analysis of the energy transfer processes in the incompressible channel flow has been pursued in the space of scales through the analysis of the second-order structure function by Marati *et al.* [188], Cimarelli *et al.* [59, 61, 62], Cimarelli and De Angelis [58] and in the spectral domain by Domaradzki *et al.* [83], Bolotnov *et al.* [28]. In compressible flows with highly variable fluid properties, the turbulence kinetic energy may be defined in several manners according to the chosen decomposition of total energy. The main approaches are the density-weighted averaging decomposition [94], the mixed-weighted decomposition [17], the density square-root-weighted decomposition [318] and the classical averaging decomposition [47]. The reader may find more details on these decompositions in Cousteix and Aupoix [70], Aupoix [13], Chassaing *et al.* [50], Gatski and Bonnet [110], Chassaing *et al.* [50]. Numerical analyses of the turbulence energetic behaviour may be carried out using any of the above-mentioned definitions of turbulence kinetic energy. Notable works include Ha Minh *et al.* [123] for the mixed-weighted decomposition and Kida and Orszag [144], Cook and Zhou [68]

for the density square-root-weighted decomposition. To the knowledge of the authors, there is no such reference numerical analysis based on the classical averaging decomposition. By contrast, the density-weighted averaging decomposition has been used by many authors. In particular, the energy exchanges associated with turbulence kinetic energy in compressible channel flows with a high Mach number have been investigated extensively [127, 120, 185, 161, 233, 269, 268]. The density-weighted averaging is indeed well suited to the physics of compressible flows. The low Mach channel flow subjected to a strong temperature gradient has received less attention from the literature. The sole analysis has been carried out in the spectral domain with the density square-root-weighted decomposition by Aulery *et al.* [10, 11] at a mean friction Reynolds number of 180 and 395. The two studies use a decomposition of the terms of the evolution equation of turbulence kinetic energy based on the work of Bolotnov *et al.* [28]. The literature thus lacks a detailed study of the effect of the temperature gradient on the spatial profiles of the energy exchanges associated with turbulence kinetic energy.

Thereupon, this paper analyses the energy exchanges associated with the half-trace of the velocity fluctuation correlation tensor using a decomposition of turbulence kinetic energy based on the classical averaging. One of the main advantages of the classical averaging is that it is the usual way to extend the study into the spectral domain. Within the formulation used, each term of the evolution equation of the half-trace of the velocity fluctuation correlation tensor is associated with an energy exchange. In that sense, each term is given a physical meaning. Each term is then decomposed in the particular case of a fully developed channel flow to isolate the parts that are formally identical to the terms remaining in flows with constant fluid properties, and the terms specific to flows with variable fluid properties. These terms are related to the flow dilatation, the variation or the fluctuation of the fluid properties or the presence of a mean wall-normal velocity. The decomposition is carried out in both the spatial and spectral domains. There is a one-to-one correspondence between the terms of the spatial and spectral decompositions.

In this paper, we use this property to investigate the energy exchanges associated with the half-trace of the velocity fluctuation correlation tensor in the spatial and spectral domains in a consistent manner. This ensures that the integration of the spectral term is exactly equal to the associated spatial term. To compute the terms, we carry out two direct numerical simulations of a fully developed low Mach turbulent channel flow: one isothermal and one anisothermal. In both cases, the mean friction Reynolds number of the simulation is 180. The effects of gravity are neglected. In the anisothermal simulation, the temperatures of the two channel walls are 293 K and 586 K. Compared to the isothermal simulation, the only new physical phenomenon is the variations of density, viscosity and conductivity with temperature. The numerical set-up is validated in the isothermal configuration with the data of Moser *et al.* [203], Bolotnov *et al.* [28] and Vreman and Kuerten [305]. The spatial and spectral amplitudes of each term are assessed. This allows us to determine the relative importance of each term, and in particular evaluate the importance of the terms specific to flows with variable fluid properties. Then, we study the effect of the temperature gradient on the energy exchanges. In the spatial domain, the results extend the existing literature in the isothermal configuration to the anisothermal configuration. In the spectral domain, the analysis provides new insights into the spectral energy exchanges in both the isothermal and anisothermal configurations, since the energy exchanges have not

been studied with the same decomposition in the incompressible literature.

The ternary representation of the energy exchanges used in this paper is summarised in section 4.2.2. The detailed channel flow configuration, the numerical set-up and the data acquisition are presented in section 4.2.3. The results are discussed and analysed in section 4.2.4.

4.2.2 Energy exchanges associated with the half-trace of the velocity fluctuation correlation tensor in the ternary decomposition

The ternary representation of the energy exchanges is based on the decomposition of velocity into a mean and fluctuating part with the classical (non-density-weighted) averaging [245]. Let us denote $(\overline{\quad})$ the statistical average operator and (\prime) the fluctuating part operator. The velocity is decomposed as $U_i = \overline{U}_i + u'_i$, where U_i the i -th component of the velocity. We use a lowercase u' for the velocity fluctuation for a better visual differentiation but there is no further underlying differences. The instantaneous total energy per unit volume is the sum of the instantaneous kinetic energy per unit volume ρE and the internal energy per unit volume ρI , with ρ the density, I the internal energy per unit mass and E the half-trace of the instantaneous velocity correlation tensor $E = \frac{1}{2}U_i U_i$. The classical averaging decomposition of velocity leads to the decomposition of kinetic energy into three terms:

- the mean kinetic energy $\rho \underline{E} = \frac{1}{2}\rho \overline{U}_i \overline{U}_i$ related to the mean motion;
- the turbulence kinetic energy $\rho e = \frac{1}{2}\rho u'_i u'_i$ related to the turbulent motion; and
- the mixed kinetic energy $\rho \underline{e} = \rho u'_i \overline{U}_i$ related to the interaction between the mean and turbulent motion.

Namely, we obtain $\rho E = \rho \underline{E} + \rho e + \rho \underline{e}$, that is [47]

$$\frac{1}{2}\rho U_i U_i = \frac{1}{2}\rho \overline{U}_i \overline{U}_i + \frac{1}{2}\rho u'_i u'_i + \rho u'_i \overline{U}_i \quad (4.1)$$

The total energy per unit volume is a conservative quantity. However, the four parts of total energy, ρI , $\rho \underline{E}$, ρe and $\rho \underline{e}$, are not conservative. The non-conservative terms of the evolution equation of each part of total energy each can be interpreted as an energy exchange between two parts of total energy. The energy exchanges between the four parts of total energy are represented in a schematic form in figure 4.1. They are of three different kinds. The terms $\underline{\mathcal{E}}$ and ε represent an interaction between kinetic energy and internal energy. The terms $\underline{\mathcal{P}}$ and \mathcal{P} are associated with an interaction between two parts of kinetic energy. The conservative energy transfer terms are convective or diffusive terms that account for a portion of the total energy transfer. The terms $\underline{\Phi}^c$, φ^c , $\Phi^{T,c}$ and Φ^λ are convective terms. The term Φ^λ is the transfer by conduction and the terms $\underline{\Phi}^r$ and φ^r represent transfers by external force.

In order to obtain the evolution equation of the half-trace of the velocity fluctuation correlation tensor within this formulation, we further decompose the three parts of

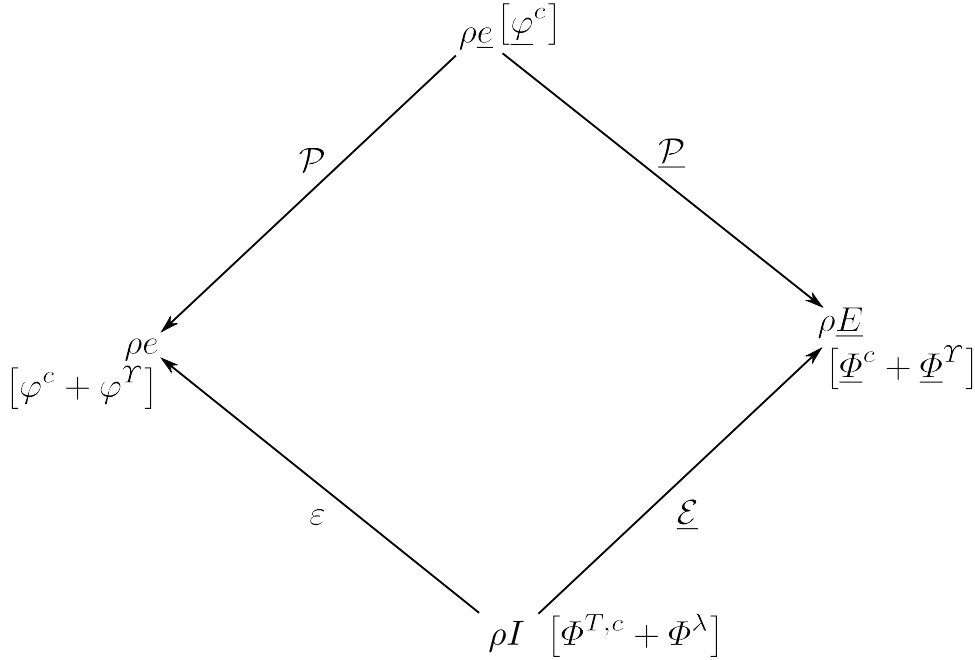


Figure 4.1 – Schematic representation of the energy exchanges between the four parts of total kinetic energy in the ternary representation. An arrow represents an interaction between two quantities.

kinetic energy and internal energy in a constant and variable density part. We split to this intent the density ρ into a constant part ρ_0 and a variable part ρ_1 , $\rho(\mathbf{x}, t) = \rho_0 + \rho_1(\mathbf{x}, t)$, where \mathbf{x} is the position vector and t the time. We consider the resulting decomposition of total energy into $\rho_0 \underline{E}$, $\rho_0 e$, $\rho_0 \underline{e}$, $\rho_0 I$, $\rho_1 \underline{E}$, $\rho_1 e$, $\rho_1 \underline{e}$ and $\rho_1 I$. The energy exchanges between the eight parts of total energy include a new interaction, between the constant and variable density part of total energy. The formulation includes up to the constant scalar factor ρ_0 the half-trace of the velocity fluctuation correlation tensor e , as defined and extensively studied in the incompressible literature. This quantity is directly related to the Reynolds stress and the turbulence kinetic energy since $\overline{\rho u'_i u'_i} \approx \overline{\bar{\rho} u'_i u'_i}$ under Morkovin's hypothesis [201], which is valid in the flow considered in this paper. It has a spectral equivalent, $\rho_0 \check{e} = \frac{1}{2} \rho_0 \widehat{u'_i}^* \widehat{u'_i}$, which will be investigated in this paper. From now on, we will focus on the energy exchanges associated with its evolution equation. The formulation gives the relevant groupings of the terms of its evolution equation in the variable density case: the conservative energy transfers, φ^c and φ^r ; the interaction with internal energy ε ; the interaction with the other parts of kinetic energy \mathcal{P} and the interaction with variable density kinetic energy, ζ^c and ζ^r . The first three are present in the incompressible case though with a simpler mathematical expression. The latter is unique to flows with variable density. We use the same notations for the constant density part of the energy exchanges as for the complete terms to avoid more cumbersome notations. The interaction with internal energy ε , the interaction with the other parts of kinetic energy ζ^r and the transfer by external force φ^r can be seen as the sum of a viscous and pressure contribution. In particular, splitting the stress tensor \mathcal{T} into the pressure and viscous stress leads to a clearly reversible pressure contribution, the pressure dilatation correlation [260], that

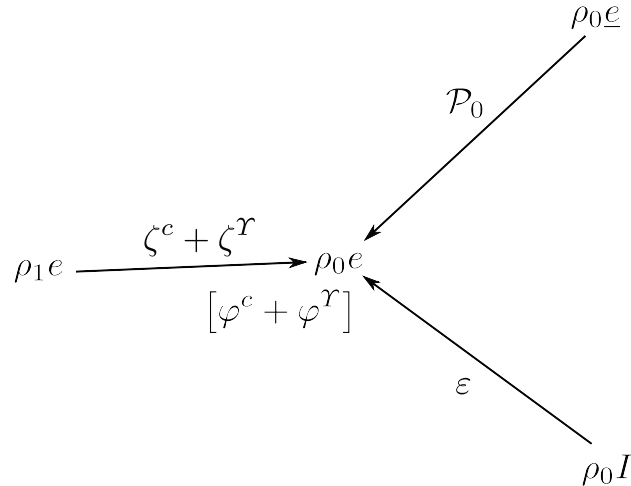


Figure 4.2 – Schematic representation of the energy exchanges associated with the “constant density turbulence kinetic energy” $\rho_0 e$, identical to the half-trace of the velocity fluctuation correlation tensor e up to the constant scalar factor ρ_0 .

exchanges energy in either direction, and an irreversible viscous contribution, called dissipation, which always transfers kinetic energy into internal energy. The energy exchanges associated with $\rho_0 e$ are represented in figure 4.2.

In this paper, the statistical average of these instantaneous energy exchanges are considered. This ensures the consistency of the formulation, in the sense that the energy exchanges in both the instantaneous and statistically averaged cases are well defined and are not conflicting. This consistency is important to give a physical interpretation to the energy exchange, as this lets us consider the statistically averaged energy exchanges as the statistical average of the associated instantaneous energy exchanges. The schematic representation of the energy exchanges in the statistically averaged case is not presented as it is identical, albeit with the addition of the statistical average.

The energy exchanges associated with the half-trace of the velocity fluctuation correlation tensor are decomposed in the particular case of a fully developed channel flow to recover the terms remaining in flows with constant fluid properties (here denoted with subscript I). The terms specific to flows with variable fluid properties (here denoted with subscript I) arise from the flow compressibility, the variations or fluctuations of the fluid properties and the presence of a mean wall-normal velocity. The mean wall-normal velocity \bar{U}_y differs from zero in the compressible variable density channel with the classical averaging because it is in balance with the turbulent mass flux, $\bar{\rho}\bar{U}_y = -\overline{\rho' u'_y}$. With a mass-weighted averaging, the mean wall-normal velocity is equal to zero. The study is then extended to the spectral domain. Since the flow is periodic in the streamwise and spanwise directions, any physical quantity $g(x, y, z)$ can be expressed as a Fourier series. We define and denote with the hat operator ($\hat{\cdot}$) the Fourier coefficients of the Fourier series expansion of g [see e.g. 173]:

$$\hat{g}(\mathbf{k}, y, t) = \frac{1}{L_x L_z} \int_0^{L_x} \int_0^{L_z} g(\mathbf{x}, y, t) e^{-i\mathbf{k}\cdot\mathbf{x}} d\mathbf{x}. \quad (4.2)$$

where $\mathbf{x} = (x, z)$ is the position vector in the xOz plane and $\mathbf{k} = (k_x, k_z)$ is the position vector in the $k_x Ok_z$ plane. In the spectral domain, we study the terms of the evolution

equation of

$$\check{e} = \frac{1}{2} \widehat{u'_i}^* \widehat{u'_i}, \quad (4.3)$$

The spectral analysis extends each term of the spatial decomposition to the spectral domain, associating each of them with a corresponding term of the spectral decomposition. In addition, a purely spectral term is identified in the spectral decomposition, that is a spectral term with no spatial contribution.

To summarise the spatial and spectral decompositions, let us compare below the evolution equation of the half-trace of the velocity fluctuation correlation tensor in the spatial and spectral domains. It is given in the spatial domain by

$$\begin{aligned} \frac{\partial \bar{e}}{\partial t} &= \bar{\varphi} + \bar{\mathcal{P}} + \bar{\zeta} + \bar{\varepsilon} \\ &= \bar{\varphi}_I + \bar{\varphi}_\Gamma + \bar{\mathcal{P}}_I + \bar{\mathcal{P}}_{\bar{U}_y} + \bar{\zeta} + \bar{\varepsilon}_I + \bar{\varepsilon}_\Gamma \end{aligned} \quad (4.4)$$

and in the spectral domain by

$$\begin{aligned} \frac{\partial \check{e}}{\partial t} &= \check{\varphi} + \check{\mathcal{P}} + \check{\zeta} + \check{\varepsilon} + \check{\Xi}, \\ &= \check{\varphi}_I + \check{\varphi}_\Gamma + \check{\mathcal{P}}_I + \check{\mathcal{P}}_{\check{U}_y} + \check{\zeta} + \check{\varepsilon}_I + \check{\varepsilon}_\Gamma + \check{\Xi}, \end{aligned} \quad (4.5)$$

with

$$\begin{aligned} \bar{\varphi}_I &= \bar{\varphi}_I^c + \bar{\varphi}_I^p + \bar{\varphi}_{I,1}^\nu + \bar{\varphi}_{I,2}^\nu & \check{\varphi}_I &= \check{\varphi}_I^c + \check{\varphi}_I^p + \check{\varphi}_{I,1}^\nu + \check{\varphi}_{I,2}^\nu \\ \bar{\varepsilon}_I &= \bar{\varepsilon}_{I,1}^\nu + \bar{\varepsilon}_{I,2}^\nu & \check{\varepsilon}_I &= \check{\varepsilon}_{I,1}^\nu + \check{\varepsilon}_{I,2}^\nu \\ \bar{\varphi}_\Gamma &= \bar{\varphi}_{\bar{U}_y}^c + \bar{\varphi}_{\partial \bar{\rho}}^p + \bar{\varphi}_{\rho'}^p + \bar{\varphi}_{\rho',2}^\nu \\ &\quad + \bar{\varphi}_{\partial \bar{v},1}^\nu + \bar{\varphi}_{\partial \bar{v},2}^\nu + \bar{\varphi}_{\nu',1}^\nu \\ &\quad + \bar{\varphi}_{\nu',2}^\nu + \bar{\varphi}_\Theta^\nu & \check{\varphi}_\Gamma &= \check{\varphi}_{\bar{U}_y}^c + \check{\varphi}_{\partial \bar{\rho}}^p + \check{\varphi}_{\rho'}^p + \check{\varphi}_{\rho',2}^\nu \\ & & &\quad + \check{\varphi}_{\partial \bar{v},1}^\nu + \check{\varphi}_{\partial \bar{v},2}^\nu + \check{\varphi}_{\nu',1}^\nu \\ & & &\quad + \check{\varphi}_{\nu',2}^\nu + \check{\varphi}_\Theta^\nu \\ \bar{\zeta} &= \bar{\zeta}_\Theta^c + \bar{\zeta}_{\rho'}^c + \bar{\zeta}_{\partial \rho}^p + \bar{\zeta}_{\partial \rho,1}^\nu \\ &\quad + \bar{\zeta}_{\partial \rho,2}^\nu + \bar{\zeta}_\Theta^\nu & \check{\zeta} &= \check{\zeta}_\Theta^c + \check{\zeta}_{\rho'}^c + \check{\zeta}_{\partial \rho}^p + \check{\zeta}_{\partial \rho,1}^\nu \\ & & &\quad + \check{\zeta}_{\partial \rho,2}^\nu + \check{\zeta}_\Theta^\nu \\ \bar{\varepsilon}_\Gamma &= \bar{\varepsilon}_{\rho'}^p + \bar{\varepsilon}_{\nu',1}^\nu + \bar{\varepsilon}_{\nu',2}^\nu + \bar{\varepsilon}_\Theta^\nu & \check{\varepsilon}_\Gamma &= \check{\varepsilon}_{\rho'}^p + \check{\varepsilon}_{\nu',1}^\nu + \check{\varepsilon}_{\nu',2}^\nu + \check{\varepsilon}_\Theta^\nu \end{aligned}$$

and:

$$\begin{aligned} \bar{\varphi}_I^c &= -\frac{\partial \overline{e u'_y}}{\partial y} & \check{\varphi}_I^c &= \text{Re} \left(-\frac{1}{2} \frac{\partial \widehat{u'_i}^* \widehat{u'_i} \widehat{u'_y}}{\partial y} \right) \\ \bar{\varphi}_{\bar{U}_y}^c &= -\frac{\partial \bar{e} \bar{U}_y}{\partial y} & \check{\varphi}_{\bar{U}_y}^c &= -\frac{\partial \bar{U}_y \check{e}}{\partial y} \\ \bar{\varphi}_I^p &= -\frac{1}{\bar{\rho}} \frac{\partial}{\partial y} \overline{u'_y P} & \check{\varphi}_I^p &= \text{Re} \left(-\frac{1}{\bar{\rho}} \frac{\partial}{\partial y} \widehat{u'_y}^* \widehat{P} \right) \\ \bar{\varphi}_{\partial \bar{\rho}}^p &= \frac{\overline{u'_y P}}{\bar{\rho}^2} \frac{\partial \bar{\rho}}{\partial y} & \check{\varphi}_{\partial \bar{\rho}}^p &= \text{Re} \left(\frac{\widehat{u'_y}^* \widehat{P}}{\bar{\rho}^2} \frac{\partial \bar{\rho}}{\partial y} \right) \end{aligned}$$

$$\begin{aligned}
\overline{\varphi_{\rho'}^p} &= \overline{\frac{\partial u'_y P \rho'}{\partial y \bar{\rho}(\bar{\rho} + \rho')}} & \overline{\check{\varphi}_{\rho'}^p} &= \operatorname{Re} \left(\overline{\frac{\partial \widehat{u}'_y{}^* P \rho'}{\partial y \widehat{\rho}(\widehat{\rho} + \rho')}} \right) \\
\overline{\varphi_{I,1}^\nu} &= \bar{\nu} \frac{\partial^2 \bar{e}}{\partial y^2} & \overline{\check{\varphi}_{I,1}^\nu} &= \operatorname{Re} \left(\bar{\nu} \frac{\partial^2 \bar{e}}{\partial y^2} \right) \\
\overline{\varphi_{I,2}^\nu} &= \bar{\nu} \frac{\partial^2 \overline{u'_y u'_y}}{\partial y^2} & \overline{\check{\varphi}_{I,2}^\nu} &= \operatorname{Re} \left(\bar{\nu} \frac{\partial^2 \widehat{u}'_y{}^* \widehat{u}'_y}{\partial y^2} \right) \\
\overline{\varphi_{\vartheta',2}^\nu} &= -\bar{\nu} \frac{\partial}{\partial y} \overline{u'_y \frac{\partial u'_i}{\partial x_i}} & \overline{\check{\varphi}_{\vartheta',2}^\nu} &= \operatorname{Re} \left(-\bar{\nu} \frac{\partial}{\partial y} \overline{\widehat{u}'_i{}^* \widehat{u}'_y} \right) \\
\overline{\varphi_{\partial \bar{\nu},1}^\nu} &= \frac{\partial \bar{e}}{\partial y} \frac{\partial \bar{\nu}}{\partial y} & \overline{\check{\varphi}_{\partial \bar{\nu},1}^\nu} &= \operatorname{Re} \left(\frac{\partial \bar{e}}{\partial y} \frac{\partial \bar{\nu}}{\partial y} \right) \\
\overline{\varphi_{\partial \bar{\nu},2}^\nu} &= u'_i \frac{\partial u'_y}{\partial x_i} \frac{\partial \bar{\nu}}{\partial y} & \overline{\check{\varphi}_{\partial \bar{\nu},2}^\nu} &= \operatorname{Re} \left(\widehat{u}'_i{}^* \frac{\partial \widehat{u}'_y}{\partial x_i} \frac{\partial \bar{\nu}}{\partial y} \right) \\
\overline{\varphi_{\nu',1}^\nu} &= \frac{\partial}{\partial y} \left(\overline{\nu' u'_i \frac{\partial U_i}{\partial y}} \right) & \overline{\check{\varphi}_{\nu',1}^\nu} &= \operatorname{Re} \left(\frac{\partial}{\partial y} \left(\widehat{u}'_i{}^* \nu' \frac{\partial U_i}{\partial y} \right) \right) \\
\overline{\varphi_{\nu',2}^\nu} &= \frac{\partial}{\partial y} \left(\overline{\nu' u'_i \frac{\partial U_y}{\partial x_i}} \right) & \overline{\check{\varphi}_{\nu',2}^\nu} &= \operatorname{Re} \left(\frac{\partial}{\partial y} \left(\widehat{u}'_i{}^* \nu' \frac{\partial U_y}{\partial x_i} \right) \right) \\
\overline{\varphi_{\Theta}^\nu} &= -\frac{\partial}{\partial y} \left(\overline{\frac{2\nu}{3} u'_y \frac{\partial U_i}{\partial x_i}} \right) & \overline{\check{\varphi}_{\Theta}^\nu} &= \operatorname{Re} \left(\frac{\partial}{\partial y} \left(-\frac{2}{3} \widehat{u}'_y{}^* \nu \frac{\partial U_i}{\partial x_i} \right) \right) \\
\overline{\mathcal{P}_I} &= -\overline{u'_x u'_y} \frac{\partial \bar{U}_x}{\partial y} & \overline{\check{\mathcal{P}}_I} &= \operatorname{Re} \left(-\widehat{u}'_x{}^* \widehat{u}'_y \frac{\partial \bar{U}_x}{\partial y} \right) \\
\overline{\mathcal{P}_{\bar{U}_y}} &= -\overline{u'_y u'_y} \frac{\partial \bar{U}_y}{\partial y} & \overline{\check{\mathcal{P}}_{\bar{U}_y}} &= \operatorname{Re} \left(-\widehat{u}'_y{}^* \widehat{u}'_y \frac{\partial \bar{U}_y}{\partial y} \right) \\
\overline{\zeta_{\Theta}^c} &= \bar{e} \frac{\partial \bar{U}_j}{\partial x_j} & \overline{\check{\zeta}_{\Theta}^c} &= \bar{e} \frac{\partial \bar{U}_j}{\partial x_j} \\
\overline{\zeta_{\vartheta'}^c} &= e \frac{\partial u'_j}{\partial x_j} & \overline{\check{\zeta}_{\vartheta'}^c} &= \operatorname{Re} \left(\frac{1}{2} \widehat{u}'_i{}^* u'_i \frac{\partial u'_j}{\partial x_j} \right) \\
\overline{\zeta_{\partial \rho}^p} &= -\frac{\overline{u'_i P}}{\rho^2} \frac{\partial \rho}{\partial x_i} & \overline{\check{\zeta}_{\partial \rho}^p} &= \operatorname{Re} \left(-\widehat{u}'_i{}^* \frac{\widehat{P}}{\rho^2} \frac{\partial \rho}{\partial x_i} \right) \\
\overline{\zeta_{\partial \rho,1}^\nu} &= \frac{\nu}{\rho} \frac{\partial \rho}{\partial x_j} \overline{u'_i \frac{\partial U_i}{\partial x_j}} & \overline{\check{\zeta}_{\partial \rho,1}^\nu} &= \operatorname{Re} \left(\widehat{u}'_i{}^* \frac{\nu}{\rho} \frac{\partial \rho}{\partial x_j} \frac{\partial U_i}{\partial x_j} \right) \\
\overline{\zeta_{\partial \rho,2}^\nu} &= \frac{\nu}{\rho} \frac{\partial \rho}{\partial x_j} \overline{u'_i \frac{\partial U_j}{\partial x_i}} & \overline{\check{\zeta}_{\partial \rho,2}^\nu} &= \operatorname{Re} \left(\widehat{u}'_i{}^* \frac{\nu}{\rho} \frac{\partial \rho}{\partial x_j} \frac{\partial U_j}{\partial x_i} \right) \\
\overline{\zeta_{\Theta}^\nu} &= -\frac{2\nu}{3\rho} \frac{\partial \rho}{\partial x_i} \overline{u'_i \frac{\partial U_j}{\partial x_j}} & \overline{\check{\zeta}_{\Theta}^\nu} &= \operatorname{Re} \left(-\widehat{u}'_i{}^* \frac{2\nu}{3\rho} \frac{\partial \rho}{\partial x_i} \frac{\partial U_j}{\partial x_j} \right)
\end{aligned}$$

$$\begin{aligned}
\overline{\varepsilon_{\vartheta'}^p} &= \frac{\overline{P \partial u'_i}}{\rho \partial x_i} & \overline{\varepsilon_{\vartheta'}^p} &= \text{Re} \left(\overline{\frac{\partial u'_i}{\partial x_i} \frac{\widehat{P}}{\rho}} \right) \\
\overline{\varepsilon_{I,1}^\nu} &= -\overline{\nu \frac{\partial u'_i}{\partial x_j} \frac{\partial u'_i}{\partial x_j}} & \overline{\varepsilon_{I,1}^\nu} &= \text{Re} \left(-\overline{\nu \frac{\partial u'_i}{\partial x_j} \frac{\partial u'_i}{\partial x_j}} \right) \\
\overline{\varepsilon_{I,2}^\nu} &= -\overline{\nu \frac{\partial u'_i}{\partial x_j} \frac{\partial u'_j}{\partial x_i}} & \overline{\varepsilon_{I,2}^\nu} &= \text{Re} \left(-\overline{\nu \frac{\partial u'_i}{\partial x_j} \frac{\partial u'_j}{\partial x_i}} \right) \\
\overline{\varepsilon_{\nu',1}^\nu} &= -\overline{\nu' \frac{\partial u'_i}{\partial x_j} \frac{\partial U_i}{\partial x_j}} & \overline{\varepsilon_{\nu',1}^\nu} &= \text{Re} \left(-\overline{\frac{\partial u'_i}{\partial x_j} \nu' \frac{\partial U_i}{\partial x_j}} \right) \\
\overline{\varepsilon_{\nu',2}^\nu} &= -\overline{\nu' \frac{\partial u'_i}{\partial x_j} \frac{\partial U_j}{\partial x_i}} & \overline{\varepsilon_{\nu',2}^\nu} &= \text{Re} \left(-\overline{\frac{\partial u'_i}{\partial x_j} \nu' \frac{\partial U_j}{\partial x_i}} \right) \\
\overline{\varepsilon_\Theta^\nu} &= \frac{\overline{2\nu \partial u'_i \partial U_j}}{3 \partial x_i \partial x_j} & \overline{\varepsilon_\Theta^\nu} &= \text{Re} \left(\overline{\frac{\partial u'_i}{\partial x_i} \frac{2\nu \partial U_j}{3 \partial x_j}} \right) \\
&& \overline{\Xi} &= \text{Re} \left(\overline{\frac{1}{2} \frac{\partial u'_i}{\partial x_j} u'_i u'_j - \frac{1}{2} \widehat{u'_i}^* u'_j \frac{\partial u'_i}{\partial x_j}} \right)
\end{aligned}$$

The terms are expressed using the symmetries of the flow and its homogeneity in the streamwise and spanwise directions to simplify the writing ($\frac{\partial \bar{\cdot}}{\partial x} = \frac{\partial \bar{\cdot}}{\partial z} = 0$ and $\bar{U}_z = 0$). In particular, only the terms that do not have a zero theoretical value are considered. For instance, we only take into account the terms ($i = x, j = y$) and ($i = y, j = y$) of the production $\bar{\mathcal{P}} = -\overline{u'_i u'_j \frac{\partial \bar{U}_i}{\partial x_j}}$, since the other terms are theoretically equal to zero.

In the incompressible case, only the incompressible terms remain. The evolution equation of the half-trace of the velocity fluctuation correlation tensor reduces in the spatial domain to

$$\frac{\partial \bar{\varepsilon}}{\partial t} = \bar{\varphi}_I^c + \bar{\varphi}_I^p + \bar{\varphi}_{I,1}^\nu + \bar{\varphi}_{I,2}^\nu + \bar{\mathcal{P}}_I + \bar{\varepsilon}_{I,1}^\nu + \bar{\varepsilon}_{I,2}^\nu \quad (4.6)$$

and in the spectral domain to

$$\frac{\partial \bar{\varepsilon}}{\partial t} = \bar{\varphi}_I^c + \bar{\varphi}_I^p + \bar{\varphi}_{I,1}^\nu + \bar{\varphi}_{I,2}^\nu + \bar{\mathcal{P}}_I + \bar{\varepsilon}_{I,1}^\nu + \bar{\varepsilon}_{I,2}^\nu + \bar{\Xi}. \quad (4.7)$$

In flows with highly variable fluid properties, additional terms appear. Nevertheless, they originate from distinct flow characteristics. The thermal terms may appear because of the addition of a wall-normal mean velocity \bar{U}_y , come from the flow dilatation Θ , or lie in variations or fluctuations of the fluid properties, namely the viscosity and the density.

4.2.3 Study configuration

To provide the data necessary to compute the terms of the evolution equation of the half-trace of the velocity fluctuation correlation tensor, a direct numerical simulation

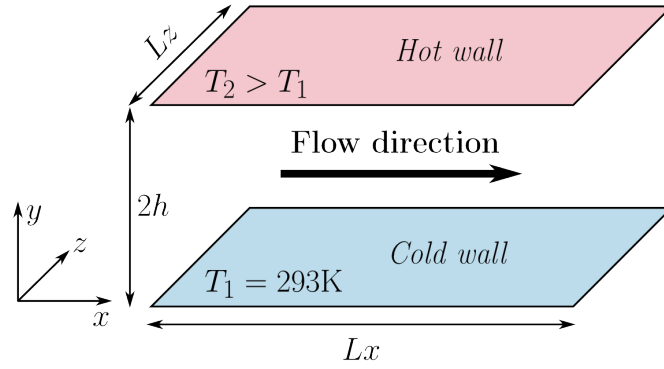


Figure 4.3 – Biperiodic anisothermal channel flow

of a fully developed channel flow is carried out. In the following, we describe the flow, the geometry, the numerical settings and the numerical tools used. Then, we validate the numerical method in the incompressible case.

4.2.3.1 Channel flow configuration

We consider a fully developed turbulent air flow under a strong temperature gradient in a rectangular channel, as represented in figure 4.3. The channel is periodic in both the streamwise (x) and spanwise (z) directions. The channel walls are at constant temperature. The temperature of the hot wall is $T_2 = 586$ K and the temperature of the cold wall is $T_1 = 293$ K. This creates a temperature gradient in the wall-normal direction (y). The flow is fully developed despite non-adiabatic wall conditions because the heat flux at the hot and cold wall exactly balance out. The mean friction Reynolds number is $Re_\tau = 180$. Let us define this quantity. The friction Reynolds number at each wall is defined as

$$Re_\tau = \frac{U_\tau h}{\nu_\omega}, \quad (4.8)$$

with h the half-height of the channel, ν_ω the cinematic viscosity at the wall and U_τ the friction velocity

$$U_\tau = \sqrt{\nu_\omega \left(\frac{\partial \bar{U}_x}{\partial y} \right)_\omega}. \quad (4.9)$$

The friction Reynolds numbers at the hot and cold wall are different, since the value of the friction velocity and the properties of the fluid differ. The mean friction Reynolds number is defined as the average of the friction Reynolds number computed at the cold and hot side.

The same channel is also studied in the isothermal case. In that case, both walls are at the cold temperature. The same friction Reynolds number is considered. This results in a 20% lower mass flow rate. Hereafter, we will refer to the channel flow configuration in which the channel is subjected to a strong temperature gradient as the anisothermal configuration and the configuration in which both walls are at the same temperature as the isothermal configuration.

4.2.3.2 Governing equations

The above-described flow is weakly turbulent. The mean Mach number is 0.008. Compressibility effects due to velocity are therefore negligible. Large variations of the fluid properties are generated by the temperature gradient. These considerations let us use Paolucci's method [219] to remove acoustic effects from the Navier–Stokes equations. Each variable of the Navier–Stokes equations is written as a power series of the squared Mach number. Then, the smaller-order terms of each equation are kept. The resulting low Mach number equations split the pressure in two parts: the thermodynamical pressure P_0 and the mechanical pressure P . The constant in space thermodynamical pressure P_0 is the mean pressure in the domain. The mechanical pressure is the pressure induced by momentum variations. The effects of gravity are neglected and air is considered as an ideal gas for the purpose of this study.

Since the channel flow is periodic in the streamwise direction, no pressure gradient appears through the boundary conditions to balance out the dissipative forces. A streamwise volume force f is added to the momentum conservation equation in order to replicate the effect of a pressure gradient.

Given the above considerations, we use the following set of equations:

- Mass conservation equation

$$\frac{\partial \rho}{\partial t} + \frac{\partial \rho U_j}{\partial x_j} = 0, \quad (4.10)$$

- Momentum conservation equation

$$\frac{\partial \rho U_i}{\partial t} + \frac{\partial \rho U_j U_i}{\partial x_j} = -\frac{\partial P}{\partial x_i} + \frac{\partial}{\partial x_j} \left[\mu \left(\frac{\partial U_i}{\partial x_j} + \frac{\partial U_j}{\partial x_i} \right) \right] - \frac{2}{3} \frac{\partial}{\partial x_i} \left(\mu \frac{\partial U_j}{\partial x_j} \right) + f \delta_{ix}, \quad (4.11)$$

- Energy conservation equation

$$\rho C_p \left(\frac{\partial T}{\partial t} + U_j \frac{\partial T}{\partial x_j} \right) = \frac{\partial P_0}{\partial t} + \frac{\partial}{\partial x_j} \left(\lambda \frac{\partial T}{\partial x_j} \right), \quad (4.12)$$

- Ideal gas law

$$P_0 = \rho r T, \quad (4.13)$$

- Thermodynamical pressure homogeneity

$$\frac{\partial P_0}{\partial x_i} = 0, \quad (4.14)$$

with ρ the density, T the temperature, μ the dynamic viscosity, λ the thermal conductivity, C_p the heat capacity at constant pressure, r the ideal gas specific constant, t the time, P the mechanical pressure, P_0 the thermodynamical pressure, U_i the i -th component of velocity and x_i the Cartesian coordinate in i -direction. Einstein summation convention is used and δ_{ij} is the Kronecker delta.

We use Sutherland's law [287] to compute the fluid properties

$$\mu(T) = \mu_0 \left(\frac{T}{T_0} \right)^{\frac{3}{2}} \frac{T_0 + S}{T + S}, \quad (4.15)$$

$$\lambda(T) = \frac{C_p}{Pr} \mu(T), \quad (4.16)$$

with $\mu_0 = 1.716 \cdot 10^{-5}$ Pa s, $S = 110.4$ K and $T_0 = 273.15$ K. The Prandtl number and the heat capacity at constant pressure are assumed constant, with $Pr = 0.76$ and $C_p = 1005$ J kg⁻¹ K⁻¹. The ideal gas specific constant is $r = 287$ J kg⁻¹ K⁻¹.

4.2.3.3 Numerical setting

The mesh is regular in both homogeneous directions and follows a hyperbolic tangent law in the wall-normal direction. The wall-normal grid coordinates are symmetrical with respect to the plane $y = h$. In the first half of the channel, they are given by

$$y_k = h \left(1 + \frac{1}{a} \tanh \left[\left(\frac{k-1}{N_y-1} - 1 \right) \tanh^{-1}(a) \right] \right), \quad (4.17)$$

where a is the mesh dilatation constant and N_y the number of grid points in the wall-normal direction.

The same mesh is used in the anisothermal and isothermal simulations. It contains $384 \times 266 \times 384$ cells. The resulting cell sizes in wall units are $\Delta_x^+ = 5.8$, $\Delta_y^+ = 0.085$ at the wall and 2.9 at the centre and $\Delta_z^+ = 2.9$ in the isothermal case; $\Delta_x^+ = 8.5$, $\Delta_y^+ = 0.13$ at the wall and 4.2 at the centre and $\Delta_z^+ = 4.2$ in the anisothermal case. Given the mesh precision, a no-slip boundary condition is used at the walls. The domain size is: $L_x = 4\pi h$, $L_y = 2h$ and $L_z = 2\pi h$ with $h = 15$ mm.

To solve the set of equations (4.10)–(4.14), we use a finite difference method written in a divergence form in a staggered grid system [200, 212]. The time scheme is a third-order Runge–Kutta [313]. A fourth-order centred scheme is used for momentum convection and a third-order upstream scheme is used for temperature convection [170]. This is performed using the TrioCFD software [38]. This software was used in many direct numerical simulations of fluid flow coupled with other physical phenomena [291, 36, 44, 290].

The value of the volume force f is adjusted through a control loop to keep the mass flow rate constant,

$$f_{t+1} = f_t + C_0 \frac{D_{\text{target}} - 2D_t + D_{t-1}}{\Delta t}, \quad (4.18)$$

with C_0 a damping constant, D the mass flow rate, D_{target} the targeted mass flow rate and $t-1$, t and $t+1$ indices related to the previous, current and next time step respectively. A term associated with the forcing term $u'_x f / \rho$ appears in the transport equation of the half-trace of the velocity fluctuation correlation tensor. This term has been computed from the result of the direct numerical simulation and was found to be insignificant.

4.2.3.4 Data acquisition

The data acquisition is carried out in two steps because the computation of different terms of the evolution equation of the half-trace of the velocity fluctuation correlation tensor requires knowledge of mean and fluctuating quantities. First, statistics on the mean velocities, temperature and pressure are acquired. Full convergence is attained after a total duration of 3.59 s in the isothermal case (29 characteristic time h/U_τ) and 2.86 s in the anisothermal case (34 characteristic time, using the cold wall friction velocity). Once this prior step completed, the data collection is carried out and spans over a total duration of 7.95 s in the isothermal case (64 characteristic time) and 3.16 s in the anisothermal case (37 characteristic time).

To compute the spectral terms, we use the discrete two-dimensional Fourier transform

$$\widehat{g}(k_{x,m}, y, k_{z,n}) = \frac{1}{N_x N_z} \sum_{p=0}^{N_x-1} \sum_{k=0}^{N_z-1} g(x_p, y, z_k) \exp\left(-2\pi i \left(\frac{mp}{N_x} + \frac{kn}{N_z}\right)\right). \quad (4.19)$$

The Fourier transform is carried out in the streamwise and spanwise directions only. The time averaged spectral terms depends on the three parameters k_x , y and k_z . In order to simplify the interpretation of the terms, only the dependence on the wavenumber norm at each wall-normal coordinate will be considered. This removes from the scope of this study the spectral directionality of the energy transfers.

4.2.3.5 Wavenumber bin

The two-dimensional spectral results are analysed using wavenumber bins following Bolotnov *et al.* [28]. The procedure used is as follows: the wavenumber space is divided in N_b annulus-shaped wavenumber bins. The bin $\#i$ contains every wavenumber vector \mathbf{k} whose norm k ranges between k_i and k_{i+1} , the lower and upper bound of the bin $\#i$. For each term, we then assign to the bin $\#i$ (at its wavenumber centre $k_{c,i}$) the sum of the values of the term computed at each wavenumber contained in the bin.

Wavenumber bins kill any directionality of the energy transfers since only the wavenumber norm is taken into account. This is only correctly done if the bin contains a large number of wavenumber vectors and the distribution of the wavenumber vectors is isotropic. Since the distribution of wavenumber bins is logarithmic and the distribution of wavenumber vectors is not, the number of wavenumber vectors per bin grows exponentially with the wavenumber bin number. This results in a low number of wavenumber vector per bin at low wavenumbers. To address this issue, a low pass filter was applied to the spectral data. This improves the quality of the statistics at low wavenumbers.

The use of wavenumber bins should be taken into account in the interpretation of the results. The values obtained are uniformly distributed on a logarithmic scale and integration over the wavenumber space is done by simple summation of the values. The use of wavenumber bins also reduces the dependence of the results on the domain size and mesh. On the other hand, the results are entirely determined by the bins construction.

Bin number	Lower bound k_i	Bin centre $k_{c,i}$	Upper bound k_{i+1}
1	1.00000	1.09350	1.19574
2	1.19574	1.30755	1.42981
3	1.42981	1.56349	1.70968
4	1.70968	1.86954	2.04434
5	2.04434	2.23549	2.44451
6	2.44451	2.67308	2.92301
7	2.92301	3.19632	3.49518
8	3.49518	3.82198	4.17934
9	4.17934	4.57011	4.99742
10	4.99742	5.46469	5.97564
11	5.97564	6.53437	7.14534
12	7.14534	7.81344	8.54400
13	8.54400	9.34288	10.21645
14	10.21645	11.17170	12.21626
15	12.21626	13.35850	14.60753
16	14.60753	15.97335	17.46688
17	17.46688	19.10005	20.88592
18	20.88592	22.83878	24.97423
19	24.97423	27.30935	29.86280
20	29.86280	32.65501	35.70829
21	35.70829	39.04705	42.69800
22	42.69800	46.69031	51.05590
23	51.05590	55.82969	61.04982
24	61.04982	66.75805	73.00000

Table 4.1 – Construction of the wavenumber bins.

Thereupon, in order to compare our results with Bolotnov *et al.* [28], we use the same wavenumber bins. We define $N_b = 24$ wavenumber bins of uniform length in logarithmic scale, with

$$k_i = k_{\min} \left(\frac{k_{\max}}{k_{\min}} \right)^{\frac{i}{N_b}}, \quad (4.20)$$

where $k_{\min} = 1 \text{ m}^{-1}$ and $k_{\max} = 73 \text{ m}^{-1}$ are the minimum and maximum bound across all bins. The bounds and centre of the wavenumber bins are given in table 4.1. Note that since the wavenumber bins are constructed with respect to the domain and mesh sizes of the direct numerical simulation of Trofimova *et al.* [296] used by Bolotnov *et al.* [28], they do not span over our entire computable wavenumber space. This excludes very small and very large wavenumbers. Nonetheless, we verified that no energy exchanges were located outside of the range of wavenumber bins.

4.2.3.6 Validation

The numerical set-up is validated in the isothermal configuration through a mesh convergence study. The simulation is carried out with three meshes later referred to as coarse mesh, medium mesh and fine mesh. The coarse mesh has $192 \times 118 \times 96$ cells. The cell sizes in wall units are $\Delta_x^+ = 11.5$, $\Delta_y^+ = 0.17$ at the wall and 6.7 at the

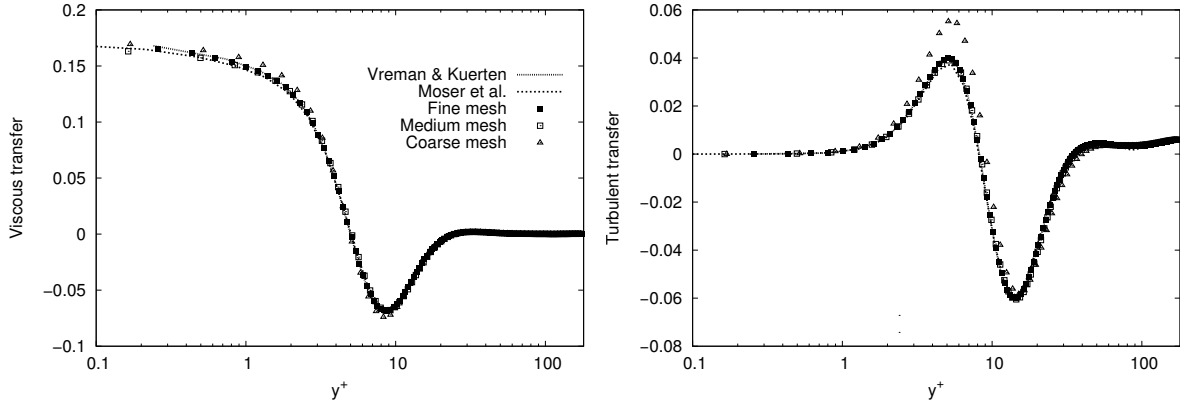


Figure 4.4 – Validation of the profile of the viscous transfer $\bar{\nu} \frac{\partial^2 \bar{e}}{\partial y^2}$ (left) and of the turbulent transfer $-\frac{\partial \overline{e u_y}}{\partial y}$ (right).

centre and $\Delta_z^+ = 11.5$. The medium mesh has $384 \times 190 \times 288$ cells. The cell sizes in wall units are $\Delta_x^+ = 5.8$, $\Delta_y^+ = 0.16$ at the wall and 3.7 at the centre and $\Delta_z^+ = 3.9$. The fine mesh is described in section 4.2.3.3. The results are compared to the three following references from the literature: Moser *et al.* [203] and Vreman and Kuerten [305] in the spatial domain and Bolotnov *et al.* [28] in the spectral domain. The three references are at the same friction Reynolds number of 180. The consistency of the spectral results is ensured by making sure that the integrated spectral data reduces to the correct spatial value.

Validation of the spatial turbulence kinetic energy terms

The turbulence kinetic energy is given in the incompressible case by the half-trace of the velocity fluctuation correlation tensor. The viscous transfer and the turbulent transfer, two terms of its evolution equation, are compared in the isothermal case to the results of Moser *et al.* [203] and Vreman and Kuerten [305] in figure 4.4. The values are scaled by U_τ^4 / ν_ω , where U_τ is the friction velocity and ν_ω the cinematic viscosity at the wall. The results show two things. First, the profiles associated with the medium and fine meshes are very close, indicating that the mesh convergence is attained. Second, the fine mesh profiles are nearly identical to the reference profiles of Vreman and Kuerten [305]. The profiles of Moser *et al.* [203] deviate slightly from the profiles of Vreman and Kuerten [305] for the viscous transfer near to the wall. The results of Vreman and Kuerten [305] are believed to be the most accurate as they use a finer mesh and a longer averaging time. Hence, the data of Vreman and Kuerten [305] will from now on be used exclusively for the validation of the spatial terms.

The mesh convergence study shows similar results for the other terms (not shown here). The comparison of the fine mesh profiles with the results of Vreman and Kuerten [305] is shown for each term in figure 8.3. The profile of each term is equal to the reference profile. This validates the spatial profiles of the terms of the evolution equation of the half-trace of the velocity fluctuation correlation tensor at the incompressible limit.

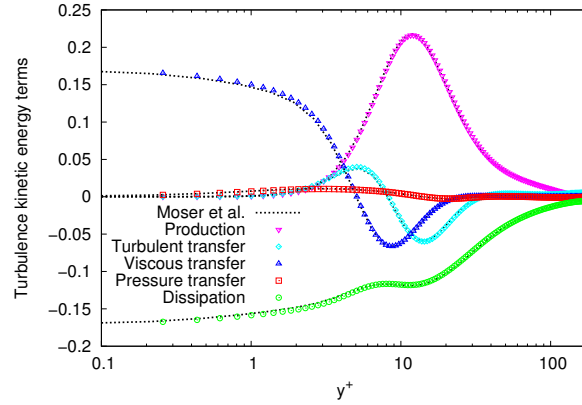


Figure 4.5 – Validation of the spatial turbulence kinetic energy terms. The terms are: the production $-\overline{u'_x u'_y} \frac{\partial \overline{U}_x}{\partial y}$, the turbulent transfer $-\frac{\partial \overline{e u'_y}}{\partial y}$, the viscous transfer $\overline{\nu} \frac{\partial^2 \overline{e}}{\partial y^2}$, the pressure transfer $-\frac{1}{\rho} \frac{\partial}{\partial y} \overline{P u'_y}$ and the dissipation $-\overline{\nu} \frac{\partial u'_i}{\partial x_j} \frac{\partial u'_i}{\partial x_j}$.

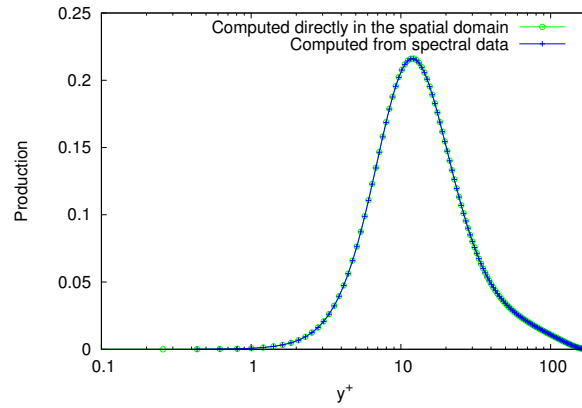


Figure 4.6 – Production profile computed directly in the spatial domain, $-\overline{u'_x u'_y} \frac{\partial \overline{U}_x}{\partial y}$, and computed from the spectral data, $\text{Re} \left(-\widehat{u'_x}^* \widehat{u'_y} \frac{\partial \overline{U}_x}{\partial y} \right)$.

Validation of the spectral turbulence kinetic energy terms

The numerical properties of the discrete Fourier transform used ensure that the summation of over all wavenumber bins of a spectral term for a given wall-normal coordinate y is equal to the value of the associated spatial term. This property is used to verify the consistency of the spectral and spatial data. The profiles of production computed from the spectral data and computed directly in the spatial domain are compared in figure 4.6 and are shown to be identical. This was verified to be true for all terms in the isothermal case and in the anisothermal case.

The spectral data are compared in the isothermal case to the results provided by Bolotnov *et al.* [28]. The figure 4.7 compares the spectral profiles of the production computed from the coarse, medium and fine meshes with Bolotnov *et al.* [28] at a distance of 10 in wall units from the wall. The fine and medium profiles are very close showing a good convergence of the production statistical profile in the spectral domain. The results are in agreement with those of Bolotnov *et al.* [28]. The spectral profiles have the same shape and predict the same spectral location of the maximum value.

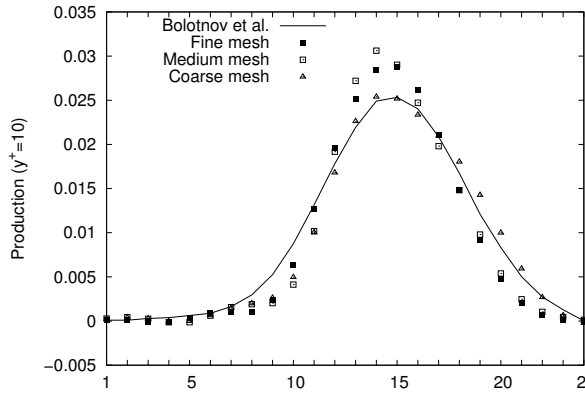


Figure 4.7 – Validation of the spectral profile at $y^+ = 10$ of the production, $\text{Re} \left(\overline{-u'_x u'_y \frac{\partial \bar{U}_x}{\partial y}} \right)$.

There are however some differences. The profile of Bolotnov *et al.* [28] has a lower amplitude and is more spread out in wavenumber. This leads to a very similar total integrated value, though not exactly identical. Unfortunately, there are no further data on the spectral turbulence kinetic energy terms in the literature to decide between the two profiles. Therefore, we compare the spatial integrated value of the two spectra. There is 3.5%–4% difference between the spatial integrated value of Bolotnov *et al.* [28] and the results of Moser *et al.* [203] or Vreman and Kuerten [305], whereas the difference is less than 1% for our spectrum. Our results are thus more accurate with regard to their total integrated value.

This applies to all wall-normal positions and all terms investigated by Bolotnov *et al.* [28], as shown by the comparison of the two-dimensional spectra of the production in figure 4.8, the interplane triadic transfer in figure 4.9, the inplane triadic transfer in figure 4.10, the inplane triadic transfer in figure 4.10, the interplane dissipation in figure 4.11, the inplane dissipation in figure 4.12 and the viscous transfer in figure 4.13. In each case, both plot uses the same normalisation and the colour scales are identical. For each plot, our results agree very closely with the results of Bolotnov *et al.* [28]. The two spectra follow the same general behaviour. They also are in a very good agreement on the spatial and spectral location of the terms. Nevertheless, there are some differences. The results of Bolotnov *et al.* [28] tends to have a lower amplitude and be more spread out in wavenumber. This is the same behaviour as previously discussed for the spectral profile of production and the same remarks may apply.

4.2.4 Results

The numerical results with regard to the terms of the evolution equation of the half-trace of the velocity fluctuation correlation tensor are discussed in this section.

The energy exchanges associated with the half-trace of the velocity fluctuation correlation tensor are investigated in the spatial and spectral domains. In both cases, the analysis is carried out in two configurations as described in section 4.2.3.1: the isothermal configuration and the anisothermal configuration. In the isothermal configuration, the flow is incompressible as there is no temperature gradient. In the anisothermal configuration, the strong temperature gradient generates large variations of the fluid

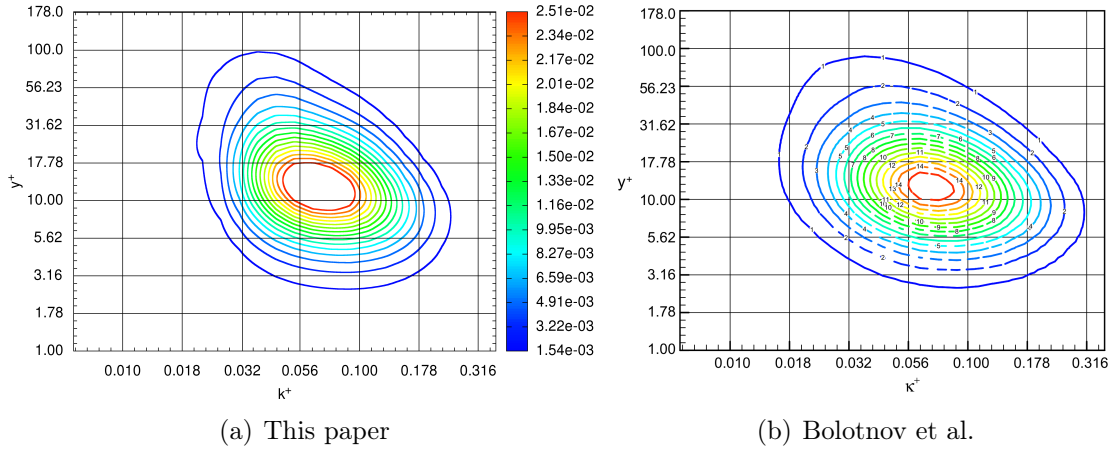


Figure 4.8 – Production, $\text{Re} \left(-\widehat{u'_x}^* \widehat{u'_y} \frac{\partial \overline{U_x}}{\partial y} \right)$.

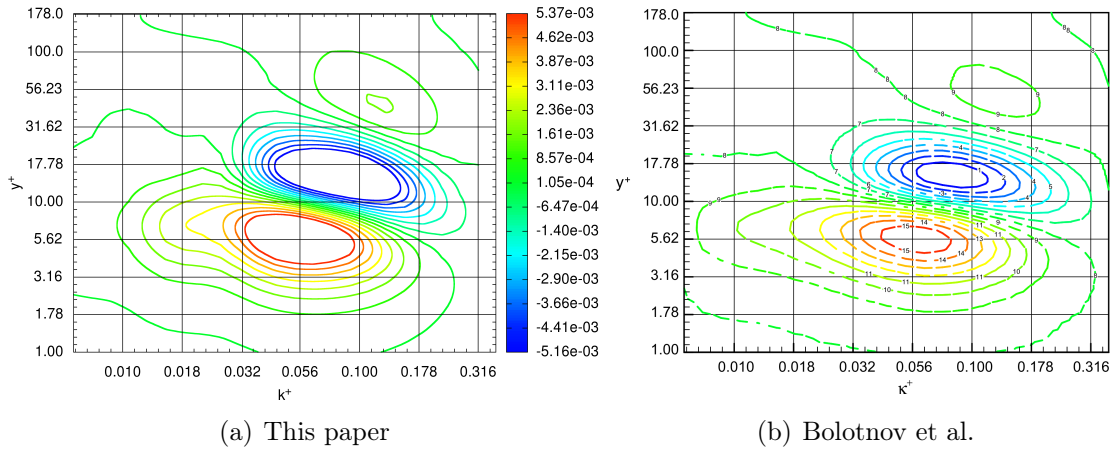


Figure 4.9 – Interplane triadic, $\text{Re} \left(-\widehat{u'_i}^* \frac{\partial \widehat{u'_i} u'_y}{\partial y} \right)$.

properties. In the spatial domain, the terms of the half-trace of the velocity fluctuation correlation tensor have been studied in the literature in the isothermal configuration [see e.g. 203, 305], but has not been documented in the anisothermal configuration. In the spectral domain, the analysis is novel in both the isothermal and anisothermal configurations with the decomposition used in this study. The spatial results in the isothermal configuration are used solely to validate the numerical method. In this section, we discuss the results in the isothermal configuration in the spectral domain and in the anisothermal configuration in both the spatial and spectral domains.

The effect of the temperature gradient on the terms of the evolution equation of the half-trace of the velocity fluctuation correlation tensor is decomposed in two separate effects. The first effect is the behaviour modification of the terms of the incompressible evolution equation, here called incompressible terms. The second effect is the addition of terms specific to flows with variable fluid properties, here called thermal terms. Each term is associated with an energy exchange, that is either a conservative energy transfer or an interaction with another part of total energy. The incompressible energy

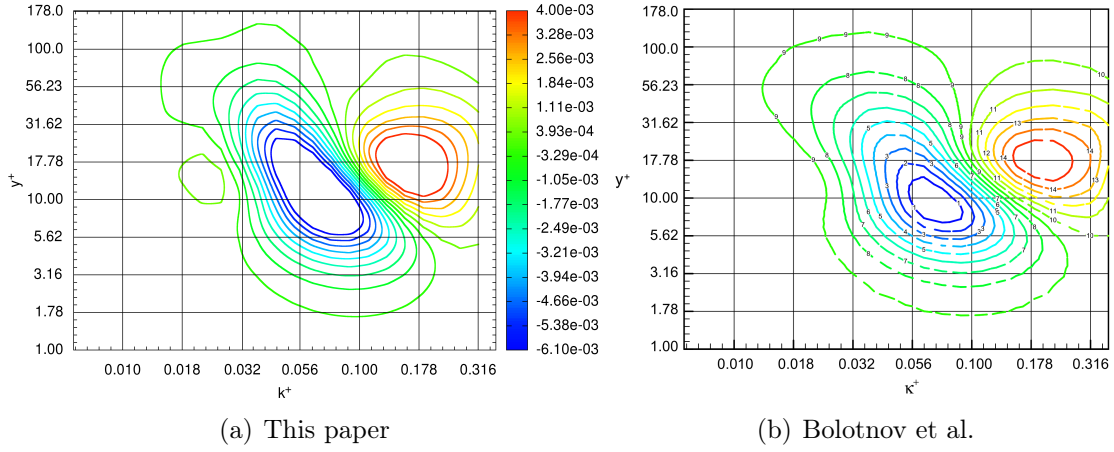


Figure 4.10 – Inplane triadic, $\text{Re} \left(-\widehat{u}_i^* \frac{\partial \widehat{u}'_i u'_x}{\partial x} - \widehat{u}_i^* \frac{\partial \widehat{u}'_i u'_z}{\partial z} \right)$.

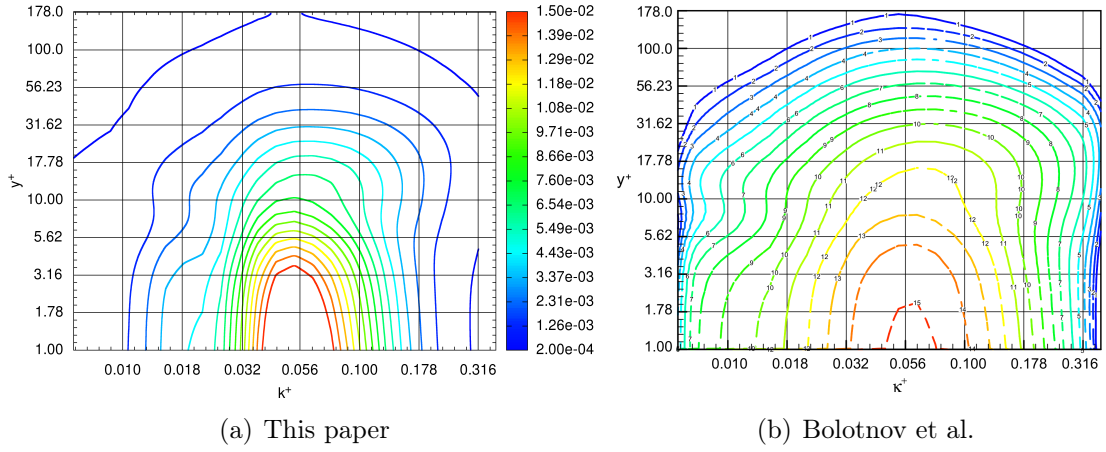


Figure 4.11 – Interplane dissipation, $\text{Re} \left(-\bar{\nu} \frac{\partial \widehat{u}'_i}{\partial y} \frac{\partial \widehat{u}'_i}{\partial y} \right)$.

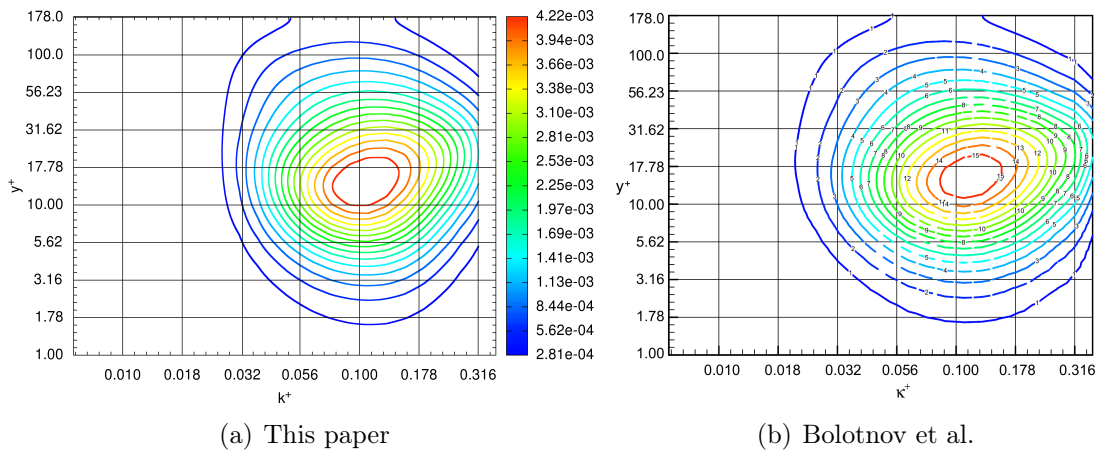


Figure 4.12 – Inplane dissipation, $\text{Re} \left(-\bar{\nu} \frac{\partial \widehat{u}'_i}{\partial x} \frac{\partial \widehat{u}'_i}{\partial x} - \bar{\nu} \frac{\partial \widehat{u}'_i}{\partial z} \frac{\partial \widehat{u}'_i}{\partial z} \right)$.

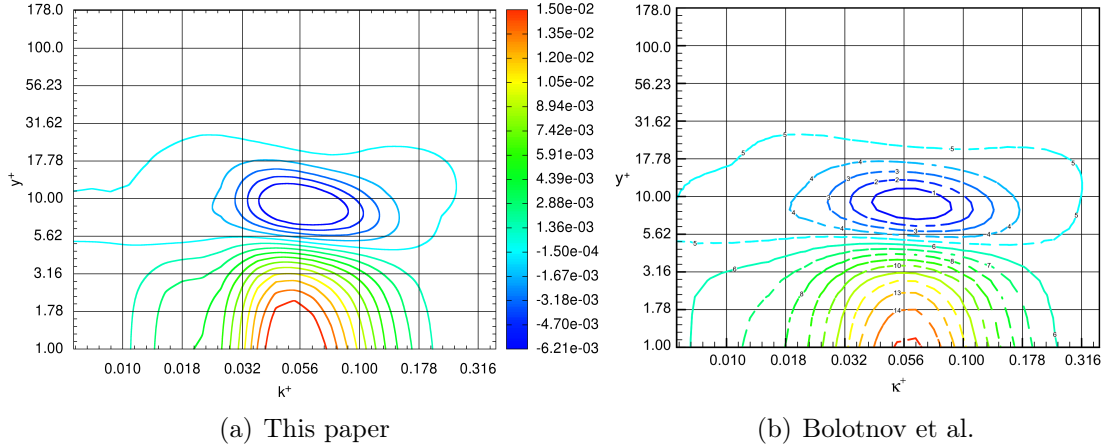


Figure 4.13 – Viscous transfer, $\text{Re} \left(\bar{\nu} \frac{\partial^2 \bar{e}}{\partial y^2} \right)$.

exchanges are modified by the temperature gradient both through the incompressible terms and the addition of thermal terms to their expression. Additionally, a new thermal energy exchange is added, composed only of thermal terms.

In both the spatial and spectral domains, the analysis of the energy exchanges in the anisothermal configuration first investigates the effect of the temperature gradient on the incompressible energy exchanges. Then, we investigate the contribution of the thermal terms to the energy exchanges. This analysis includes the thermal terms of the incompressible energy exchanges and of the thermal energy exchange.

4.2.4.1 Scalings

For later use, we define here the four following scalings: the constant scaling, the classical scaling, the semi-local scaling and the integral scaling. With the constant scaling, all profiles are scaled identically thus keeping the same relative behaviour as the raw profiles. The scaling uses a combination of the friction velocity U_τ° and the cinematic viscosity at the wall ν_ω° in the isothermal configuration. This scaling uses the results of the isothermal configuration even for profiles in the anisothermal case since the scaling should always be the same. The constant scaling is denoted with a superscript circle ($^\circ$),

$$y^\circ = \frac{yU_\tau^\circ}{\nu_\omega^\circ}, \quad (4.21)$$

$$k^\circ = \frac{k\nu_\omega^\circ}{U_\tau^\circ}, \quad (4.22)$$

$$\mathbf{U}^\circ = \frac{\mathbf{U}}{U_\tau^\circ}, \quad (4.23)$$

$$e^\circ = \frac{e}{U_\tau^{\circ 2}}, \quad (4.24)$$

$$\left(\frac{\partial e}{\partial t} \right)^\circ = \frac{1}{U_\tau^{\circ 4} / \nu_\omega^\circ} \left(\frac{\partial e}{\partial t} \right). \quad (4.25)$$

With the classical scaling, the profiles are scaled using the results at the same side

of the channel. All quantities are scaled by a combination of the friction velocity U_τ and the cinematic viscosity ν_ω at the closest wall. The classical scaling is denoted with a superscript plus sign (+),

$$y^+ = \frac{yU_\tau}{\nu_\omega}, \quad (4.26)$$

$$k^+ = \frac{k\nu_\omega}{U_\tau}, \quad (4.27)$$

$$\mathbf{U}^+ = \frac{\mathbf{U}}{U_\tau}, \quad (4.28)$$

$$e^+ = \frac{e}{U_\tau^2}, \quad (4.29)$$

$$\left(\frac{\partial e}{\partial t}\right)^+ = \frac{1}{U_\tau^4/\nu_\omega} \left(\frac{\partial e}{\partial t}\right). \quad (4.30)$$

With the semi-local scaling, the profiles takes into account the mean local fluid properties instead of the fluid properties at the wall. The semi-local scaling is denoted with a superscript asterisk (*),

$$y^* = \frac{yU_\tau^*}{\bar{\nu}(y)}, \quad (4.31)$$

$$k^* = \frac{k\bar{\nu}(y)}{U_\tau^*}, \quad (4.32)$$

$$\mathbf{U}^* = \frac{\mathbf{U}}{U_\tau^*}, \quad (4.33)$$

$$e^* = \frac{e}{U_\tau^{*2}}, \quad (4.34)$$

$$\left(\frac{\partial e}{\partial t}\right)^* = \frac{1}{U_\tau^{*4}/\bar{\nu}(y)} \left(\frac{\partial e}{\partial t}\right), \quad (4.35)$$

with,

$$U_\tau^* = \sqrt{\frac{\mu_\omega}{\bar{\rho}(y)} \left(\frac{\partial \bar{U}_x}{\partial y}\right)_\omega}. \quad (4.36)$$

The semi-local scaling is part of the current paradigm of scalings for compressible wall turbulence [293]. While it was first proposed using heuristic arguments [249, 127, 67], two different mathematical frameworks were developed recently to support the validity of the semi-local scaling by Patel *et al.* [222] and Trettel and Larsson [293].

With the integral scaling, the profiles are scaled using an integral length scale as in Brun *et al.* [37]. The integral scaling is denoted with a superscript (B),

$$y^B = \int_0^{y^+} \frac{\mu_\omega}{\bar{\mu}(y)} dy^+ \quad (4.37)$$

$$\mathbf{U}^B = \frac{\mathbf{U}}{U_\tau^B} \quad (4.38)$$

$$e^B = \frac{e}{U_\tau^{B2}} \quad (4.39)$$

$$\left(\frac{\partial e}{\partial t}\right)^B = \frac{1}{U_\tau^{B^4}/\nu_\omega} \left(\frac{\partial e}{\partial t}\right) \quad (4.40)$$

$$(4.41)$$

with,

$$U_\tau^B = \frac{y^B \bar{\mu}(y)}{y^+ \mu_\omega} \sqrt{\frac{\rho_\omega}{\bar{\rho}(y)}} U_\tau. \quad (4.42)$$

In particular, note that the terms of the evolution equation of the half-trace of the velocity fluctuation correlation tensor are scaled by $U_\tau^{\circ 4}/\nu_\omega^\circ$ with the constant scaling, U_τ^4/ν_ω with the classical scaling, $U_\tau^{*4}/\bar{\nu}(y)$ with the semi-local scaling and $U_\tau^{B^4}/\nu_\omega$ with the integral scaling.

We remark that the values of U_τ^4/ν_ω at the hot and cold sides are the same within 0.5% accuracy. The classical scaling thus does not modify the relative amplitude of the hot and cold sides. We do not see any physical reason for the equality of U_τ^4/ν_ω at the two sides, that is of the relation

$$\nu_{\omega_1} \left(\frac{\partial \bar{U}_x}{\partial y}\right)_{\omega_1}^2 = \nu_{\omega_2} \left(\frac{\partial \bar{U}_x}{\partial y}\right)_{\omega_2}^2 \quad (4.43)$$

where the subscript ω_1 denotes the value at the cold wall and the subscript ω_2 the value at the hot wall. Further analyses at different friction Reynolds number and temperature ratios are required to verify the possible generality of the property.

4.2.4.2 Assessment of the amplitude of the terms

The maximum amplitude of each term of the evolution equation of the half-trace of the velocity fluctuation correlation tensor is reported in table 4.2. The purpose of this is twofold. First, this gives an estimate of the relative importance of each term. Second, the importance of each term compared to the balance term indicates whether the term has reliable statistics.

The most significant terms in the low Mach anisothermal channel flow remain the incompressible terms, namely terms that do not vanish in the incompressible case. For each energy exchange, the most important term of the decomposition is an incompressible term, with the obvious exception of the interaction with variable density kinetic energy which vanishes in the incompressible case. The only incompressible terms that have a very low maximum amplitude are the two terms $\overline{\varepsilon_{I,2}^\nu}$ and $\overline{\varphi_{I,2}^\nu}$, which cancel each other out in the incompressible case. The purely spectral term is found to be a major part of the energy exchanges in the spectral domain.

The amplitudes of the thermal terms do not follow those of the associated incompressible terms. For instance, while the incompressible production is the term with the highest amplitude, the thermal production is one of the smallest terms. Instead, it depends primarily on the underlying physical origin of the terms. The most significant thermal terms are terms associated with the viscous shear stress, and more specifically the part associated with the product with the velocity gradient. Though, they differ in the energy exchange they are associated with (conservative energy transfer, interaction with internal energy or with variable density kinetic energy) and the source of their

Term of the equation of the Spatial equation	half-trace of the velocity fluctuation correlation Associated energy exchange	Maximum value	
		Spatial	Spectral
$\overline{\mathcal{P}_I} = -\overline{u'_x u'_y} (\partial_y \overline{U}_x)$	Production (I)	$2.3 \cdot 10^{-1}$	$3.4 \cdot 10^{-2}$
$\overline{\varepsilon_{I,1}^\nu} = -\overline{\bar{\nu}} (\partial_j u'_i) (\partial_j u'_i)$	Interaction with IE, dissipation (I)	$1.8 \cdot 10^{-1}$	$2.0 \cdot 10^{-2}$
$\overline{\varphi_{I,1}^\nu} = \overline{\bar{\nu}} (\partial_y \partial_y \bar{e})$	Conservative energy transfer, viscous transfer (I)	$1.7 \cdot 10^{-1}$	$2.0 \cdot 10^{-2}$
$\overline{\varphi_I^e} = -\partial_y \overline{e u'_y}$	Conservative energy transfer, convection (I)	$6.5 \cdot 10^{-2}$	$7.7 \cdot 10^{-3}$
$\overline{\varphi_{\nu',1}^\nu} = \partial_y \overline{\nu' u'_i \partial_y U_i}$	Conservative energy transfer, viscous transfer	$2.4 \cdot 10^{-2}$	$2.6 \cdot 10^{-3}$
$\overline{\zeta_{\partial\rho,1}^\nu} = \overline{(\nu/\rho)} (\partial_j \rho) u'_i (\partial_j U_i)$	Interaction with VDKE, viscous contribution	$1.6 \cdot 10^{-2}$	$1.7 \cdot 10^{-3}$
$\overline{\varepsilon_{\nu',1}^\nu} = -\overline{\nu'} (\partial_j u'_i) (\partial_j U_i)$	Interaction with IE, dissipation	$1.5 \cdot 10^{-2}$	$1.7 \cdot 10^{-3}$
$\overline{\varphi_{\partial\bar{\nu},1}^\nu} = \overline{(\partial_y \bar{e}) (\partial_y \bar{\nu})}$	Conservative energy transfer, viscous transfer	$1.2 \cdot 10^{-2}$	$1.4 \cdot 10^{-3}$
$\overline{\varphi_I^p} = -\overline{(1/\bar{\rho})} (\partial_y u'_y P)$	Conservative energy transfer, pressure transfer (I)	$9.0 \cdot 10^{-3}$	$1.2 \cdot 10^{-3}$
$\overline{\zeta_{\bar{y}}^c} = \overline{\bar{e}} (\partial_j \overline{U}_j)$	Interaction with VDKE, kinetic energy dilatation	$3.8 \cdot 10^{-3}$	$4.1 \cdot 10^{-4}$
$\overline{\Xi} = 0$	Purely spectral term (I)	$3.6 \cdot 10^{-3}$	$1.2 \cdot 10^{-2}$
$\overline{\zeta_{\bar{y}'}^c} = \overline{e (\partial_j u'_j)}$	Interaction with VDKE, kinetic energy dilatation	$2.7 \cdot 10^{-3}$	$2.9 \cdot 10^{-4}$
$\overline{\varphi_{\overline{U}_y}^c} = -\partial_y (\overline{\bar{e} U}_y)$	Conservative energy transfer, convection	$2.6 \cdot 10^{-3}$	$3.4 \cdot 10^{-4}$
$\overline{\varepsilon_{I,2}^\nu} = -\overline{\bar{\nu}} (\partial_j u'_i) (\partial_i u'_j)$	Interaction with IE, dissipation (I)	$2.6 \cdot 10^{-3}$	$3.1 \cdot 10^{-4}$
$\overline{\varphi_{I,2}^\nu} = \overline{\bar{\nu}} (\partial_y \partial_y u'_y u'_y)$	Conservative energy transfer, viscous transfer (I)	$2.4 \cdot 10^{-3}$	$3.1 \cdot 10^{-4}$
$\overline{\zeta^p} = -\overline{(u'_i P / \rho^2)} (\partial_i \bar{\rho})$	Interaction with VDKE, pressure contribution	$1.2 \cdot 10^{-3}$	$1.5 \cdot 10^{-4}$
	<i>Balance term</i>	$1.0 \cdot 10^{-3}$	$2.6 \cdot 10^{-4}$
$\overline{\varphi_{\partial\bar{\rho}}^p} = \overline{(u'_y P / \bar{\rho}^2)} (\partial_y \bar{\rho})$	Conservative energy transfer, pressure transfer	$7.0 \cdot 10^{-4}$	$8.9 \cdot 10^{-5}$
$\overline{\varphi_{\rho'}^p} = \partial_y \overline{u'_y P \rho'} / (\bar{\rho} (\bar{\rho} + \rho'))$	Conservative energy transfer, pressure transfer	$4.0 \cdot 10^{-4}$	$7.8 \cdot 10^{-5}$
$\overline{\varepsilon^p} = \overline{(P/\rho)} (\partial_i u'_i)$	Interaction with IE, pressure dilatation	$3.4 \cdot 10^{-4}$	$5.0 \cdot 10^{-5}$
$\overline{\varphi_{\partial\bar{\nu},2}^\nu} = \overline{u'_i (\partial_i u'_i) (\partial_y \bar{\nu})}$	Conservative energy transfer, viscous transfer	$3.0 \cdot 10^{-4}$	$4.0 \cdot 10^{-5}$
$\overline{\zeta_{\partial\rho,2}^\nu} = \overline{(\nu/\rho)} (\partial_j \rho) u'_i (\partial_i U_j)$	Interaction with VDKE, viscous contribution	$1.9 \cdot 10^{-4}$	$2.3 \cdot 10^{-5}$
$\overline{\varphi_{\nu',2}^\nu} = \partial_y \overline{\nu' u'_i (\partial_i U}_y)$	Conservative energy transfer, viscous transfer	$1.5 \cdot 10^{-4}$	$1.7 \cdot 10^{-5}$
$\overline{\mathcal{P}_{\overline{U}_y}} = -\overline{u'_y u'_y} (\partial_y \overline{U}_y)$	Production	$1.4 \cdot 10^{-4}$	$1.7 \cdot 10^{-5}$
$\overline{\varepsilon_{\nu',2}^\nu} = -\overline{\nu'} (\partial_j u'_i) (\partial_i U_j)$	Interaction with IE, dissipation	$1.0 \cdot 10^{-4}$	$1.1 \cdot 10^{-5}$
$\overline{\varphi_{\nu',2}^\nu} = -\overline{\bar{\nu}} (\partial_y u'_y \partial_i u'_i)$	Conservative energy transfer, viscous transfer	$2.5 \cdot 10^{-5}$	$1.1 \cdot 10^{-5}$
$\overline{\varphi_{\Theta}^\nu} = -\partial_y \overline{(2\nu/3) u'_y (\partial_i U_i)}$	Conservative energy transfer, viscous transfer	$1.8 \cdot 10^{-5}$	$2.6 \cdot 10^{-6}$
$\overline{\varepsilon_{\Theta}^\nu} = \overline{(2\nu/3)} (\partial_i u'_i) (\partial_j U_j)$	Interaction with IE, dissipation	$2.1 \cdot 10^{-6}$	$1.2 \cdot 10^{-7}$
$\overline{\zeta_{\Theta}^\nu} = -\overline{(2\nu/3\rho)} (\partial_i \rho) u'_i (\partial_j U_j)$	Interaction with VDKE, viscous contribution	$1.9 \cdot 10^{-6}$	$2.0 \cdot 10^{-7}$

Table 4.2 – Maximum value of the terms of the evolution equation of the half-trace of the velocity fluctuation correlation tensor in the spatial and spectral domain. For the sake of conciseness, the expression of each term is given in the spatial domain only. The type of each term refers to the four energy exchanges associated with the half-trace of the velocity fluctuation correlation tensor according to the ternary representation: the conservative energy transfer, the interaction with internal energy (IE), the production, interaction with the other parts of kinetic energy, and the interaction with variable density kinetic energy (VDKE). The symbol (I) is appended to the terms that do not vanish in the incompressible case. The results are given with the classical scaling.

thermal character (fluctuation of the viscosity, variation of the mean viscosity or of the density). With regard to the terms associated with the other parts of the viscous shear stress, the terms associated with the product with the transpose of the velocity gradient are very small compared to the terms associated with the product with the velocity gradient. The terms associated with the product with the velocity divergence are the smallest terms of all. This is only true for the viscous terms as the kinetic energy dilatation correlation and to a lesser extent the pressure dilatation correlation have larger amplitude.

Hence, the effect of the thermal terms with regard to the energy exchanges is the largest on the conservative energy transfer and the interaction with internal energy. The two most significant terms of the thermal conservative energy transfer $\overline{\varphi_\Gamma}$ are $\overline{\varphi_{\nu',1}^\nu}$ and $\overline{\varphi_{\partial\nu,1}^\nu}$, both part of the thermal viscous transfer. In the thermal interaction with internal energy $\overline{\varepsilon_\Gamma}$, the term $\overline{\varepsilon_{\nu',1}^\nu}$ predominates. The additional energy exchange with variable density kinetic energy $\overline{\zeta}$ is substantial. It acts primarily through its viscous contribution and secondly through the kinetic energy dilatation correlation. For the three interactions, the pressure contribution is not significant. Note however that the data provided in the table are mute towards the local importance of the terms, which may be larger or lower than what the maximum amplitude make it appears to be.

For the purpose of this paper, a term is considered statistically reliable if its maximum amplitude is at least ten times larger than the maximum amplitude of the kinetic energy balance. This leaves the eight following statistically reliable terms:

- $\overline{\mathcal{P}_I}$, the incompressible production,
- $\overline{\varepsilon_{I,1}^\nu}$, a part of the incompressible dissipation,
- $\overline{\varphi_{I,1}^\nu}$, a part of the incompressible viscous transfer,
- $\overline{\varphi_I^c}$, the convection by turbulent motion,
- $\overline{\varphi_{\nu',1}^\nu}$, a part of viscosity fluctuation viscous transfer,
- $\overline{\zeta_{\partial\rho,1}^\nu}$, a part of the density variation viscous interaction with variable density kinetic energy,
- $\overline{\varepsilon_{\nu',1}^\nu}$, a part of the viscosity fluctuation dissipation,
- $\overline{\varphi_{\partial\nu,1}^\nu}$, a part of the mean viscosity variation viscous transfer,

In the following, the behaviour of those eight terms is analysed. The remaining 18 terms are not discussed individually as their amplitude is too low to ensure that their profile is correctly described. In particular, the pressure transfer and the pressure contribution to the interaction with variable density kinetic energy and the interaction with internal energy will not be studied.

4.2.4.3 Results in the spatial domain

In this section, we investigate the energy exchanges associated with the half-trace of the velocity fluctuation correlation tensor in the spatial domain. The analysis is carried

out in three steps. First, we study the total effect of the temperature gradient on the incompressible energy exchanges, through the combined effect of the modification of the behaviour of the incompressible terms and the addition of thermal terms. In particular, we study the effect of the Reynolds number variations across the channel. Then, we focus on the contribution of the modification of the incompressible terms to the alteration of the incompressible energy exchanges. Finally, we investigate the profiles of the thermal terms.

Profiles of the incompressible energy exchanges in the anisothermal configuration

The four energy exchanges associated with the half-trace of the velocity fluctuation correlation tensor are the production, the conservative energy transfer, the interaction with variable density kinetic energy and the interaction with internal energy. The production represented in figure 4.14, the conservative energy transfer in figure 4.15 and the interaction with internal energy in figure 4.16. The interaction with variable density kinetic energy is discussed later since, as a thermal energy exchange, its behaviour is particular. We also provide the profile of the relevant parts of each term. The viscous transfer is given in figure 4.17 and the turbulent transfer in figure 4.18. The pressure transfer is not discussed because it is not statistically reliable in the anisothermal configuration. The dissipation is given by the profile of the interaction with internal energy, since the pressure dilatation is negligible.

For each term, the profiles at the hot and cold sides are compared to each other and to the corresponding profile in the isothermal configuration. The results are given with the constant scaling, the classical scaling, the semi-local scaling and the integral scaling. The three scalings show an asymmetry between the hot and cold profiles, though of different nature. Some generalities are found in the manner in which the temperature gradient manifests itself as summarised in the following.

The constant scaling shows the effect of the temperature gradient when not correcting the friction velocity and viscosity differences between the isothermal and anisothermal case. The general behaviour of the profiles is never drastically modified. However, the amplitudes in absolute value are increased considerably at the hot and cold side compared to the isothermal results. The amplitudes at the cold side are larger than the amplitudes at the hot side. Meanwhile, the positions of the local or global extrema are shifted closer to the wall at the cold side compared to the isothermal profile and closer to the centre of the channel at the hot side. Since the wall-normal coordinate axis is logarithmic, this shift comes with an increase of the spatial range of the term at the hot side and a decrease at the cold side. In particular, the effect of the amplitude and spatial extent modification offset each other for the production, such that the total integrated production is the same at the hot and cold side. Within 1% error, this remark may also be applied to the interaction with internal energy

The classical scaling shows the effect of the temperature gradient when scaled by the friction velocity and the viscosity at the wall. With the classical scaling, the anisothermal profiles have the same order of magnitude as the isothermal profile. This proves that most of the amplitude differences seen with the constant scaling are due to the increased friction velocity on the anisothermal configuration. The scaled amplitude

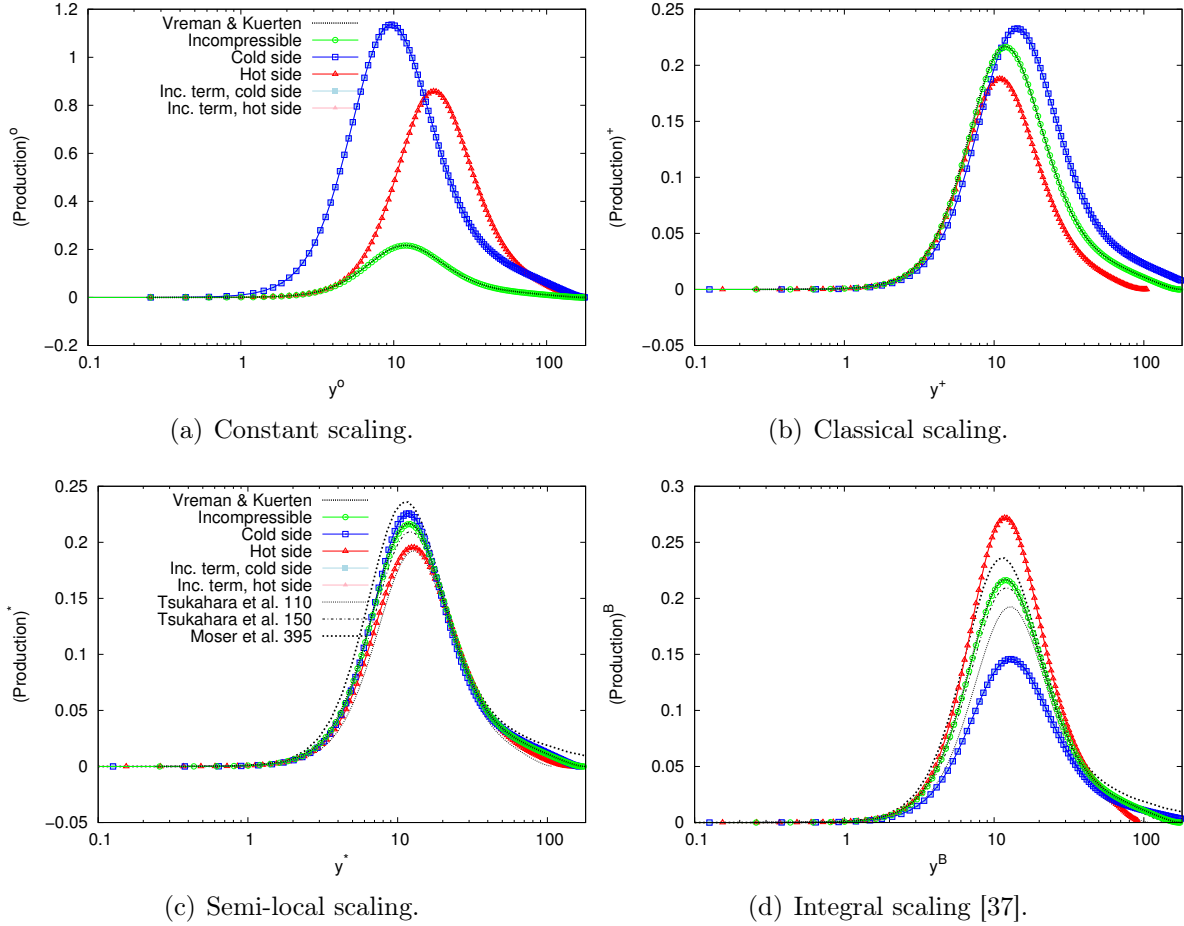


Figure 4.14 – Production, total $\overline{\mathcal{P}}$ and incompressible $\overline{\mathcal{P}}_I$.

at the cold side is increased compared to the isothermal profile and decreased at the hot side. We recall that the classical scaling has no effect on the relative amplitude of the terms at the hot and cold side since the value of U_τ^4/ν_ω is the same at both sides of the channel. In other words, the classical scaling successfully explains the differences between the isothermal amplitudes and the anisothermal amplitudes but is silent towards the difference between the hot and cold sides. The relative position of the local or global extrema of the hot, cold and isothermal profiles are swapped by the classical scaling. Now, the extrema are seen shifted closer to the wall in wall units at the hot side compared to the isothermal profile and closer to the centre of the channel at the cold side. A good explanation is that the classical scaling takes into account the viscosity at the wall thus overcorrects the position closer to the centre of the channel where the viscosity is similar at both sides of the channel.

To address this, the semi-local scaling takes into account the mean local variations of the fluid properties. With the semi-local scaling, there is no position differences between the hot, cold and isothermal profiles. This result shows the physical relevance of the semi-local scaling, which is able to explain the positional shift of the hot and cold profiles compared to the isothermal profile. However, the amplitude differences are not modified.

A possible explanation of these amplitude differences could be a Reynolds number

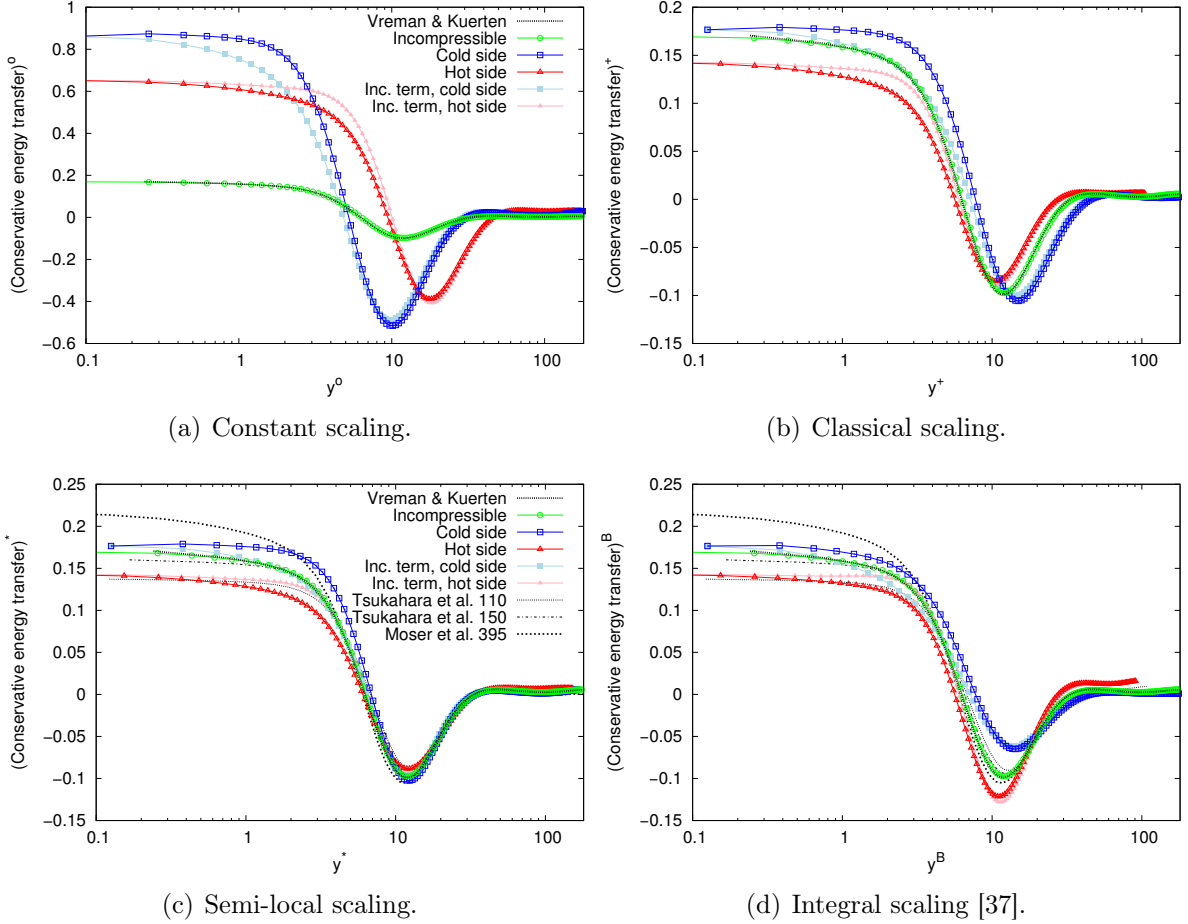


Figure 4.15 – Conservative energy transfer, total $\bar{\varphi}$ and incompressible $\bar{\varphi}_I$.

effect, that is the local variations of the friction Reynolds number across the channel between the hot and cold sides. Indeed, the temperature gradient creates variations of the local friction Reynolds number (figure 4.19), that we define as $U_\tau^*(y)h/\bar{\nu}(y)$ following the semi-local scaling. The local friction Reynolds number spans between 107 at the hot wall and 260 at the cold wall. Within this Reynolds number range, the scaled isothermal profiles depend on the Reynolds number. This makes the semi-local scaling harder to interpret, as it would prevent the hot and cold profiles to collapse. To study the Reynolds number effect, we compare the effect of the temperature gradient to the effect of Reynolds number variations in the isothermal configuration. We use to this intent the data of Tsukahara *et al.* [298] at the friction Reynolds numbers 110 and 150, the isothermal results at $Re_\tau = 180$ and the data of Moser *et al.* [203] at $Re_\tau = 395$ (considering the lack of available data between 180 and 395).

The semi-locally scaled profiles of production (figure 4.14(c)) follow very closely a Reynolds number effect. We use the empirical relation between the maximum of production and the friction Reynolds number of Laadhari [154] to compute the peak of production in the isothermal configuration associated with the friction Reynolds number of the peak of production in the anisothermal configuration (around 121 at the hot side and 215 at the cold side). The results agree within 1% accuracy to the anisothermal results. Therefore, we can conclude that the effect of the temperature gradient on production is to a very large extent a Reynolds number effect. A mathematical ar-

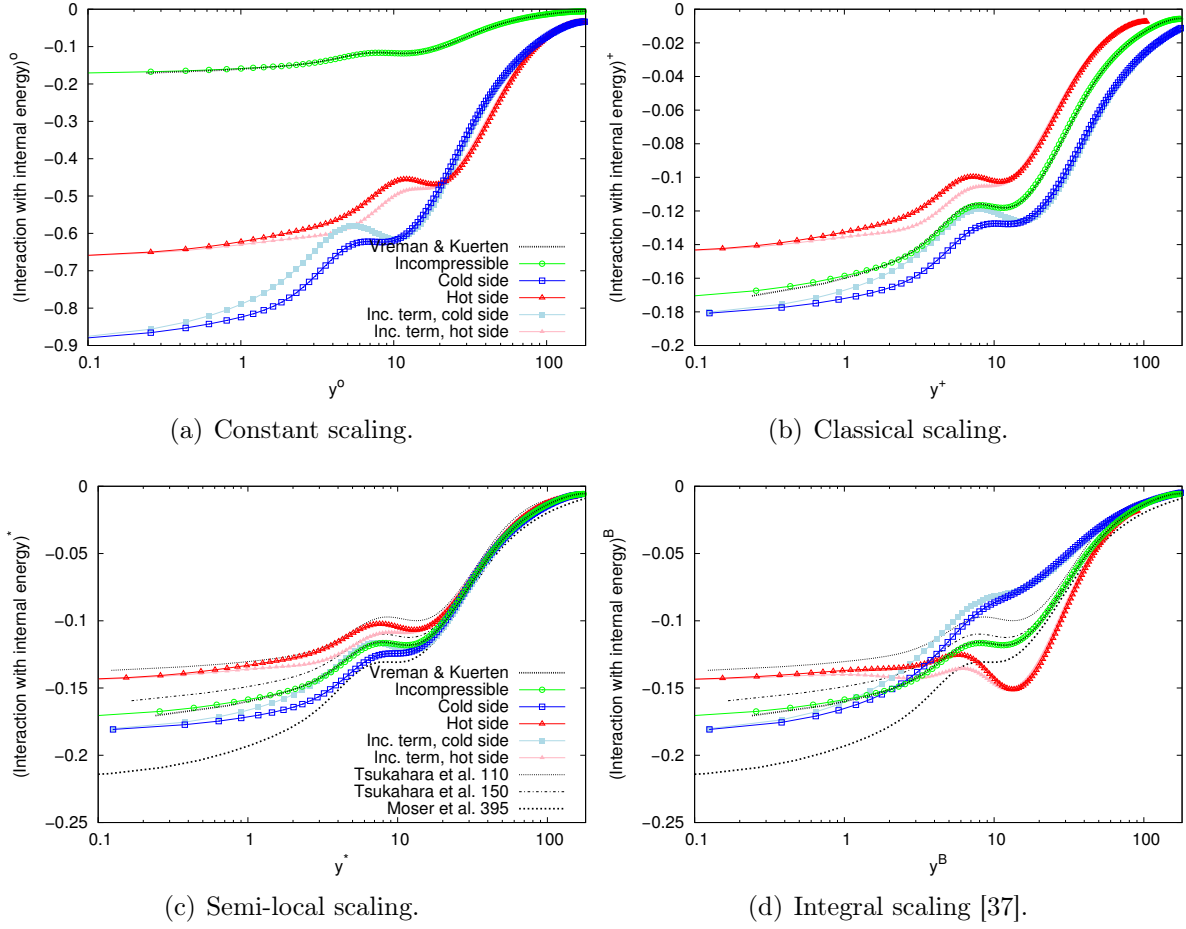


Figure 4.16 – Interaction with internal energy, total $\bar{\varepsilon}$ and incompressible $\bar{\varepsilon}_I^v$.

argument supporting this fact can be inferred from the mean streamwise momentum balance, which may be rewritten with the semi-local scaling as

$$\overline{u_x^* u_y^*} + \frac{\partial \bar{U}_x^*}{\partial y^*} = \left(1 - \frac{y^*}{Re_\tau^*}\right), \quad (4.44)$$

assuming that $\overline{\rho u_x' u_y'} \approx \bar{\rho} \overline{u_x' u_y'}$ and $\overline{\mu \frac{\partial U_x}{\partial y}} \approx \bar{\mu} \frac{\partial \bar{U}_x}{\partial y}$. The semi-locally scaled incompressible production $\overline{\mathcal{P}_I^*}$ is thus equal to

$$\overline{\mathcal{P}_I^*} = -\overline{u_x^* u_y^*} \frac{\partial \bar{U}_x^*}{\partial y^*} = \left(\frac{\partial \bar{U}_x^*}{\partial y^*}\right)^2 - \frac{\partial \bar{U}_x^*}{\partial y^*} \left(1 - \frac{y^*}{Re_\tau^*}\right). \quad (4.45)$$

This expression is identical to the expression of the production in the incompressible case with the semi-local scaling substituting the classical scaling, hinting that the semi-local scaling is an appropriate scaling for the production in the variable property case.

While the effect of the temperature gradient on the interaction with internal energy (figure 4.16(c)), the viscous transfer (figure 4.17(c)) and the convection (figure 4.18(c)) is also in a large part due to a Reynolds number effect, this explanation is not sufficient to explain the effect of the temperature gradient on these terms. The value of the interaction with internal energy (figure 4.16(c)) at the hot wall is comprised between

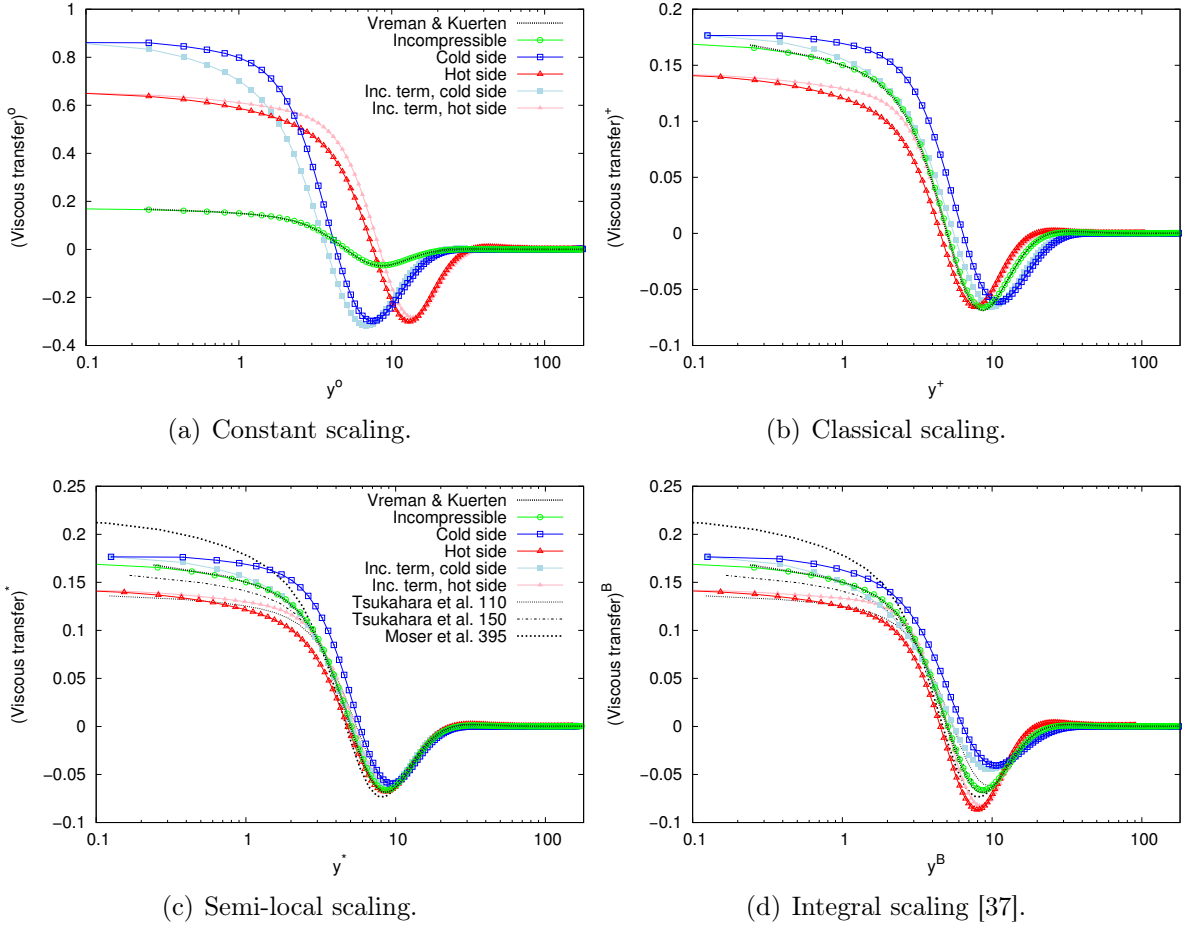


Figure 4.17 – Viscous transfer (part of the conservative energy transfer), total $\overline{\varphi^V}$ and incompressible $\overline{\varphi_I^V}$.

the value at the wall in the isothermal configuration at $Re_\tau = 110$ and $Re_\tau = 150$, despite being associated with a friction Reynolds number of 107. The semi-locally scaled profile of the viscous transfer (4.17(c)) deviates noticeably from all isothermal profiles from $y^* = 10$ to the wall. In particular, while the semi-local profiles of the viscous transfer in the four isothermal configurations ($Re_\tau = 110, 150, 180, 395$) pass through the same point at $y^* = 3.5$, the hot and cold anisothermal profiles deviate from this point significantly. The difference amounts to 20% of the maximum value of the viscous transfer throughout the channel. The semi-locally scaled hot and cold profiles of the convection (figure 4.18(c)) are farther from the isothermal profiles at the negative extremum than at the positive extremum, closer from the wall, which is the opposite of what a Reynolds number effect would imply. The effect of the temperature gradient is from these simple observations proven inconsistent with a sole Reynolds number effect. This shows that there is an additional effect that is not taken into account by the semi-local scaling and a Reynolds number effect. This effect is related to the variations of the fluid properties since it is the only new physical phenomenon in the anisothermal channel compared to the isothermal simulation. Judging from the failure of the semi-local scaling, based on the mean local value of the fluid properties, we may presume that the mean local value of the fluid properties do not explain the entirety of the effect of the temperature gradient. It may thus be necessary to take into account

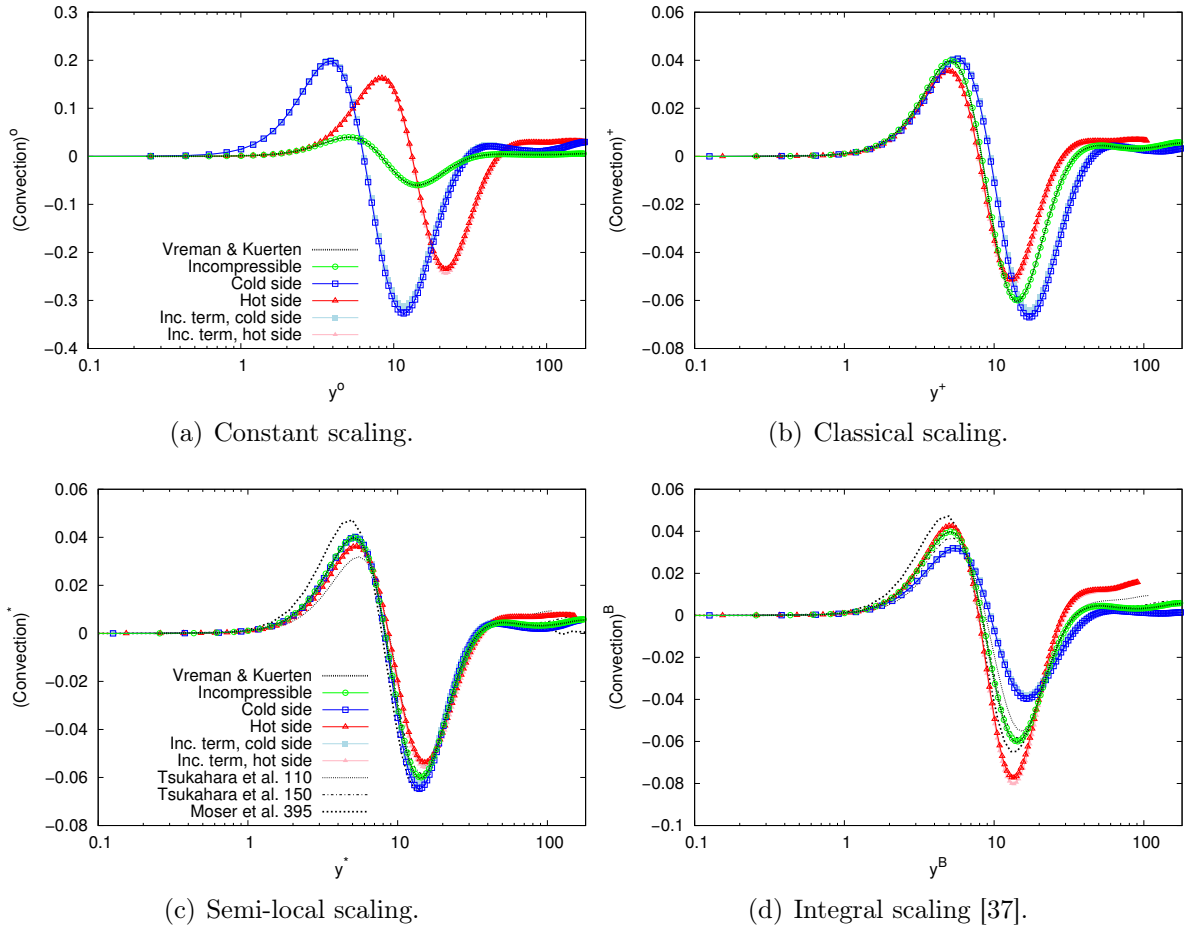


Figure 4.18 – Convection (part of the conservative energy transfer), total $\overline{\varphi^c}$ and incompressible $\overline{\varphi_I^c}$.

the fluctuations of the fluid properties to explain this effect. This is consistent with the previous study of Serra *et al.* [265] which showed this effect through the analysis of the isotropic component of the velocity fluctuation correlation tensor, out of which the half-trace is governed by the energy exchanges studied here.

The integral scaling is another approach to scale the profile using the mean fluid properties. The integral scaling significantly reduces the position asymmetry of the classical scaling for the production (figure 4.14(d)). However, the scaling overcorrects the amplitude difference between the hot and cold sides and swaps their positions. The amplitude difference with the integral scaling is thus no longer consistent with a Reynolds number effect. Moreover, the integral scaling gives very unsatisfying results for the terms with non-zero value at the wall, in particular the interaction with internal energy (figure 4.16(d)), since the ordering of the profiles at the wall is not changed. Since the integral scaling appears less appropriate, this scaling will not be discussed further in the remaining part of the paper.

All in all, the effect of the temperature gradient on the profiles at the hot and cold sides is characterised by a twofold asymmetry. The asymmetry in the position of the extrema is explained by the mean local variations of the fluid properties. The asymmetry in the amplitudes is in part due to the local variations of the friction

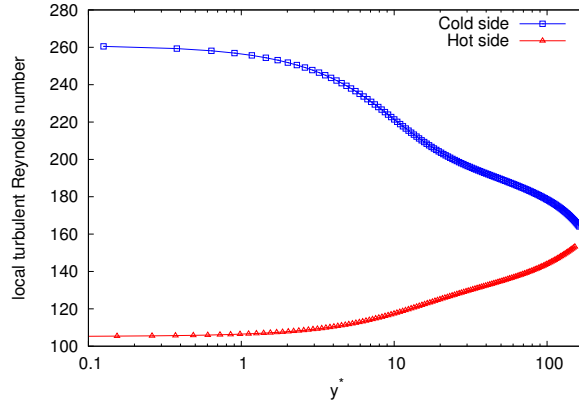


Figure 4.19 – Local friction Reynolds number $\frac{U_\tau^* h}{\bar{\nu}(y)}$ as a function of the distance to the wall with the semi-local scaling.

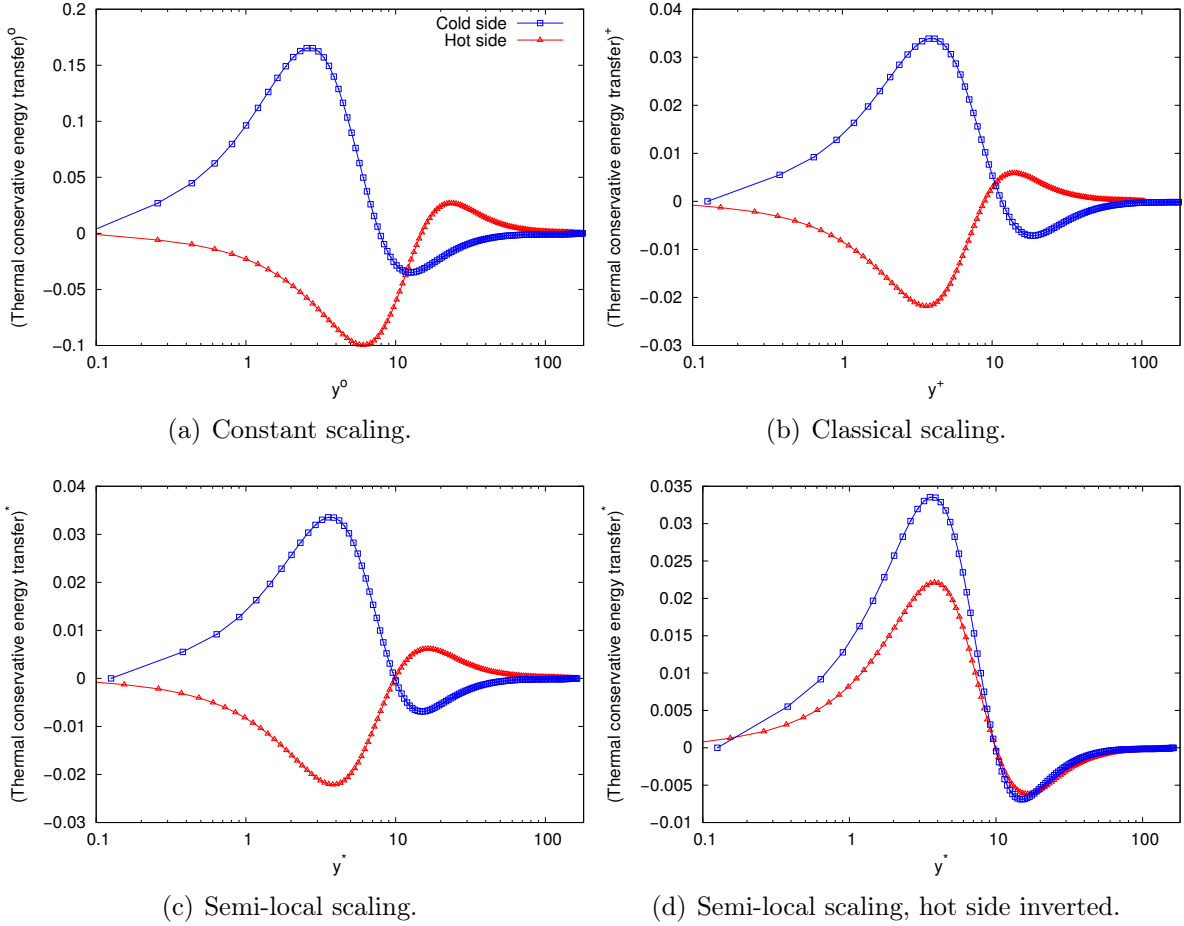
Reynolds number and in part due to the local fluctuations of the fluid properties.

Profiles of the incompressible terms in the anisothermal configuration

The effect of the temperature gradient on the profiles takes place both through the addition of thermal terms to the energy exchanges and the alteration of the profile of the incompressible terms. To assess the two phenomena, the set of figures 4.14 to 4.18 provides a comparison of the total energy exchanges to their incompressible part, that we recall are formally identical to the terms in the incompressible case.

In agreements with the conclusions of the analysis of the maximum amplitude of the terms in section 4.2.4.2, the production and the convection are not modified significantly by the addition of the corresponding thermal terms. However, the profiles of the interaction with internal energy, the viscous transfer and hence the conservative energy transfer are noticeably modified. With semi-local scaling, the changes are restricted to an area that arises very near to the wall and ends around $y^* = 20$. The scaled profile of the incompressible terms are much closer to the isothermal profile than the total term. The addition of the thermal terms separates the three profiles more clearly, moving the hot and cold profiles further away from each other and from the isothermal profile. In other words, taking into account only the incompressible terms leads to results closer to the isothermal profile than the true anisothermal profiles.

While the hot and cold profiles of the viscous transfer have a different behaviour than the isothermal profiles, the hot and cold profiles of the incompressible viscous transfer are more similar (figure 4.17(c)). In particular, the hot and cold profiles of the incompressible viscous transfer pass through the point at $y^* = 3.5$ as the profiles of the viscous transfer in the four isothermal configurations ($Re_\tau = 110, 150, 180, 395$). At the hot side, the profile of the incompressible term is in line with a Reynolds number effect. The difference between the incompressible term and the total term thus represents the more complex interaction between temperature and turbulence.

Figure 4.20 – Thermal conservative energy transfer $\overline{\varphi_T}$.

Profiles of the thermal terms in the anisothermal configuration

We study here the thermal terms of the energy exchanges. This includes the thermal terms of the production, of the conservative energy transfer and of the interaction with internal energy and the total profile of the interaction with variable density kinetic energy since this energy exchange does not have an incompressible part. The thermal conservative energy transfer is represented in figure 4.20, the interaction with variable density kinetic energy in figure 4.21 and the thermal interaction with internal energy in figure 4.22. The behaviour of the thermal production is not discussed as its amplitude was found too low.

The three profiles share an interesting characteristic unknown to any of the incompressible terms. The profile at the hot and cold sides are of opposite signs. For most terms, the sign inversion can be understood from their mathematical expression. For instance, $\partial_y (\overline{\nu' u'_x} \partial_y \overline{U}_x)$, the leading term of the thermal conservative energy transfer undergoes a sign inversion as both $\overline{\nu' u'_x}$ and $\partial_y \overline{U}_x$ undergo a sign inversion, which implies that the derivative of their product also does. Because of the sign inversion, we give, in addition to the profiles with the three scalings, the profile with the semi-local scaling with sign of the term at the hot side inverted. This allows a more convenient comparison of the hot and cold profiles when ignoring the sign difference.

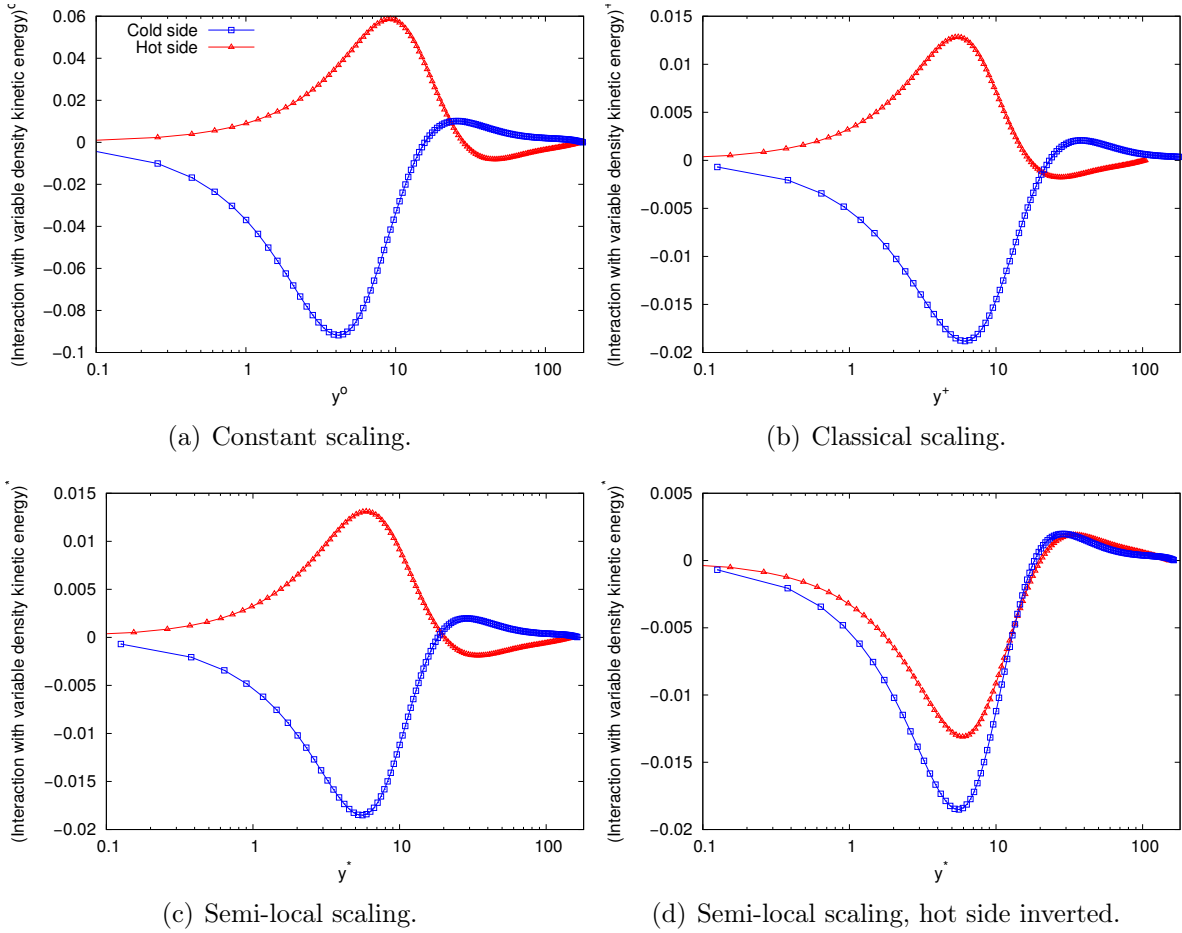
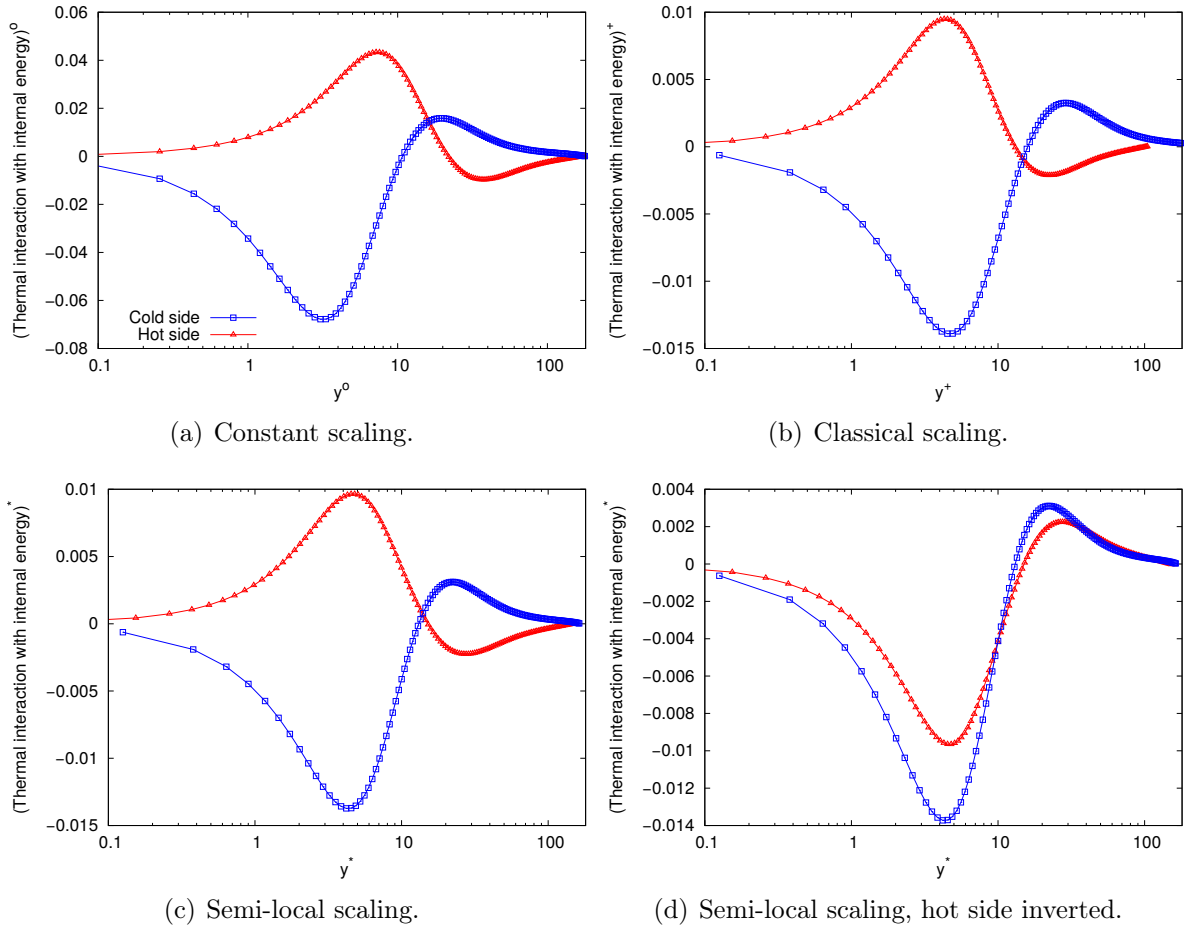


Figure 4.21 – Interaction with variable density kinetic energy $\bar{\zeta}$.

The shape of the three thermal terms is similar. This is rather unexpected as the three terms are related to different energy exchanges and have different associated incompressible profiles. Besides, the interaction with variable density kinetic energy is interpreted as a new interaction whereas the thermal interaction with internal energy and the thermal conservative energy transfer are seen as the thermal part of a larger energy exchange. The hot and cold profiles both tend to zero at the wall and at the centre of the channel. Between these two points, both profiles have two extrema, one positive and one negative. The first extremum has a larger amplitude than the second extremum but the second extremum has a larger spatial range. In the thermal conservative energy transfer (figure 4.20), the two extrema have the same integral. This term transfers the energy from the extremum close to the wall towards the centre of the channel at the hot side, and conversely towards the wall at the cold side. On the other hand, the first extremum has a smaller integral than the second extremum for the thermal interaction with internal energy (figure 4.22). The effect of this term is an energy loss at the extremum close to the wall at the cold side and a gain closer to the centre of the channel at the cold side, and vice versa at the hot side. This can be thought of as a pseudo-transfer in the opposite direction to the thermal conservative energy transfer. However, this effect is accompanied by a net energy gain at the cold side and loss at the hot side. The same remark may be applied to the interaction with variable density kinetic energy (figure 4.21), but the transfer occurs in the opposite

Figure 4.22 – Thermal interaction with internal energy $\bar{\varepsilon}_T$.

direction. The amplitude of the extrema is always larger at the cold side than at the hot side, and to a greater extent for the first extremum than for the second extremum. As for the incompressible energy exchanges, the spatial extent of the term is at the same time larger at the hot side compared to the cold side. As just previously noted, the significant part of the thermal terms is limited to an area that excludes the near vicinity of the wall and the centre of the channel. This can be explained as the velocity and temperature fluctuations are zero at the wall and the temperature gradient is low at the centre of the channel.

The signs of the extrema are the same for the two non-conservative thermal terms, and are of opposite signs for the thermal conservative energy transfer. Hence, the sum of the non-conservative terms and the sum of the conservative terms are of opposite signs. With regard to the total energy exchanges, the sum of the non-conservative terms is equal to the opposite of the conservative energy transfer. We may wonder if this property holds for the thermal terms as the thermal conservative and non-conservative terms may interact with each other only or also with the incompressible terms. To answer this question, the sum of all thermal terms is represented in figure 4.23. The profile is of the same order of magnitude as the thermal terms, proving that the thermal terms do not cancel out. It is composed of three extrema where, like the individual term, the profiles at the hot and cold side are of opposite sign. The integral of the positive extrema is larger than the integral of the negative extrema at both the hot

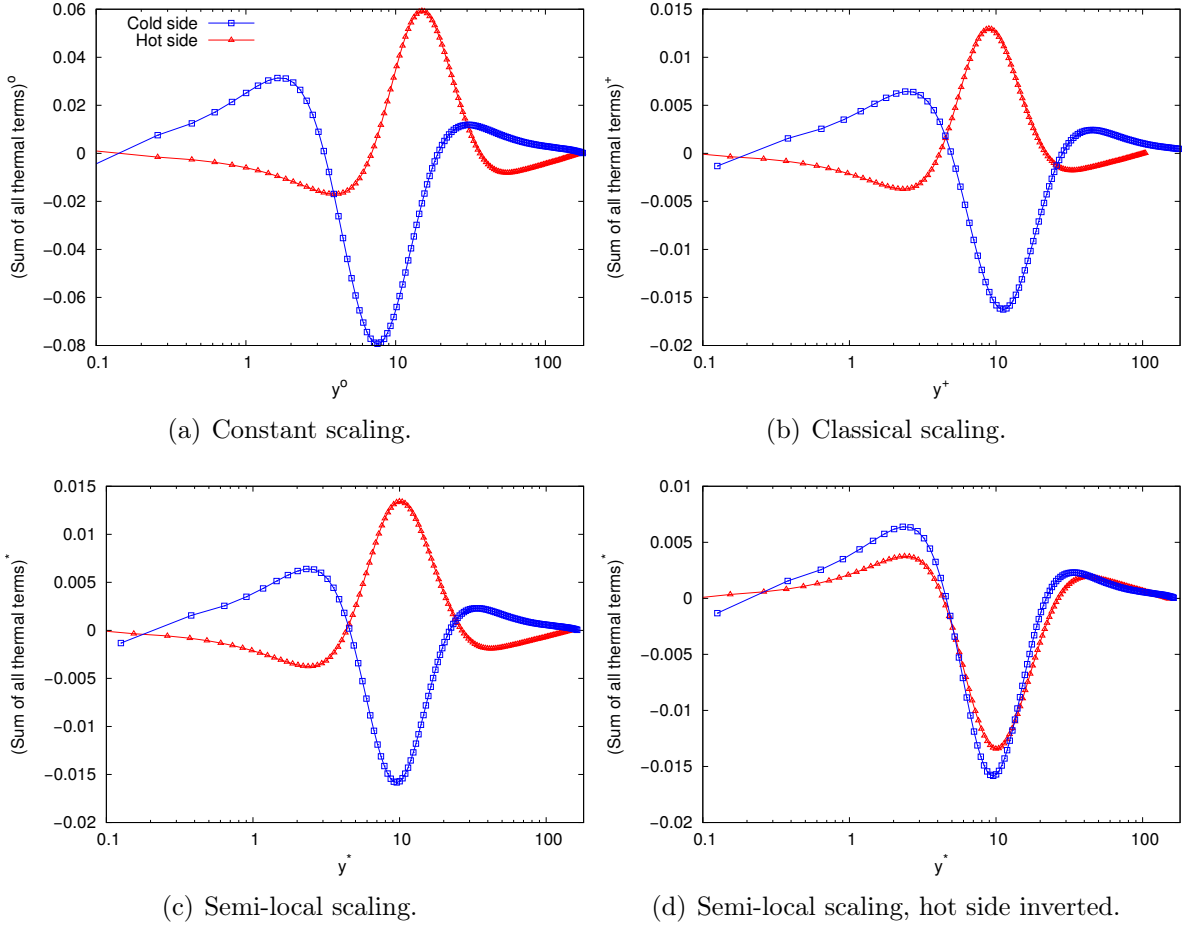


Figure 4.23 – Sum of all thermal terms $\overline{\varphi_T} + \overline{\zeta} + \overline{\varepsilon_T}$.

and cold sides, resulting in a net energy gain overall.

The profiles of the thermal terms are modified by the classical scaling and the semi-local scaling in a similar way to the terms that do not vanish in the incompressible case. With the constant scaling, an extremum is always closer to the wall at the cold side than at the hot side. The classical scaling reduces the position differences between the hot and cold side, and swaps their relative position. Indeed, by contrast with the constant scaling, an extremum is always closer to the wall in wall units at the hot side than at the cold side. The difference is very slight for the first extremum, but larger for the second extremum. This is in agreement with the proposed interpretation of this result given in the previous section.

With the semi-local scaling, there is no position differences between the extrema of kinetic energy gain/loss at the hot and cold sides. Additionally, the areas where the hot and cold profiles are of the same sign are removed. Therefore, any kinetic energy loss coincides with a kinetic energy gain at the same position at the other side of the channel. The semi-locally scaled hot and cold profiles can thus be considered to always be of opposite sign and completely symmetric if not for the amplitude differences, which are left largely unchanged. This shows that the amplitude difference cannot be solely explained by the mean local variations of the fluid properties.

4.2.4.4 Results in the spectral domain

In this section, the spectral behaviour of the terms of the evolution equation of the half-trace of the velocity fluctuation correlation tensor is discussed. The spectra of the energy exchanges are not documented in the literature with the decomposition used in this study. Thereupon, we first describe the spectral behaviour of the energy exchanges in the isothermal configuration. Then, we study the effect of the temperature gradient on the spectra of the incompressible energy exchanges. Finally, we analyse the spectra of the thermal terms separately.

Spectra of the incompressible energy exchanges in the isothermal configuration

In the incompressible case, the four main spectral energy terms are the production, the conservative energy transfer, the purely spectral transfer and the interaction with internal energy. They are represented in the isothermal configuration in figure 4.24(c), 4.25(c), 4.26(c) and 4.27(c) respectively. We recall that for each plot, the amplitude is given by the integration of the spectral density of the term over a wavenumber bin, as described in section 4.2.3.5. The spectra give the total statistically averaged effect of the term, that is the statistical balance of the energy taken and given at each wall-normal coordinate and wavenumber. This may hide some physical phenomena from the analysis.

The production (figure 4.24(c)) generates turbulence kinetic energy from mean kinetic energy in a limited area in both the spectral and spatial domains. The area is roughly circular but slanted so that large eddies contribute to the production farther from the wall and small eddies closer to the wall. This is consistent with the spatial profile of production (figure 4.14) which consists of a single peak. The maximum of production is located at ($y^\circ = 12; k^\circ = 0.07$).

The conservative energy transfer (figure 4.25(c)) transfers the energy from an area centred on the position of the maximum of production, with a very large wavenumber range. The energy is transferred towards the wall and slightly towards large scales. This is consistent with the spatial profile of the conservative energy transfer (figure 4.15).

The purely spectral transfer (figure 4.26(c)) redistributes the energy among scales with no effect in the spatial domain. The energy is taken from an area very close to the maximum of production but slightly farther from the wall and redistributed towards both large scales and small scales, with few spatial position shifts. The spectrum is slanted and involves smaller eddies closer to the wall and larger eddies away from the wall. The positive area at small scales has a twice as large amplitude than the positive area at large scales. The purely spectral transfer thus primarily moves the energy towards small scales. The spectrum highlights the complex redistribution of scales in wall-bounded flows through both direct and inverse energy cascades.

The interaction with internal energy (figure 4.27(c)) dissipates kinetic energy into internal energy very near to the wall. This is consistent with its spatial profile (figure 4.16). The extremum of its spectrum is at the same position as the positive area of the spectrum of the conservative energy transfer. However, its spatial extent is significantly

larger, going much closer to the centre of the channel. When away from the wall, the scales that contribute to the interaction with internal energy are smaller. This is the opposite behaviour of the production peak described above. Since the production and the dissipation have opposite effect, the consequences are similar.

The conservative energy transfer is the sum of three contributions: the convection, the viscous transfer and the pressure transfer. We study here individually the spectra of the viscous transfer (figure 4.28(c)) and the convection (figure 4.29(c)). The pressure transfer is not discussed as its amplitude is too small for its spectrum to be statistically reliable in the anisothermal configuration (see section 4.2.4.2).

The viscous transfer (figure 4.28(c)) transfers the energy from an area around $y^\circ = 10$ to the wall with no scale shift. The transfer does not occur only in the spatial direction, since the wavenumber range of the positive area is larger than the wavenumber range of the negative area.

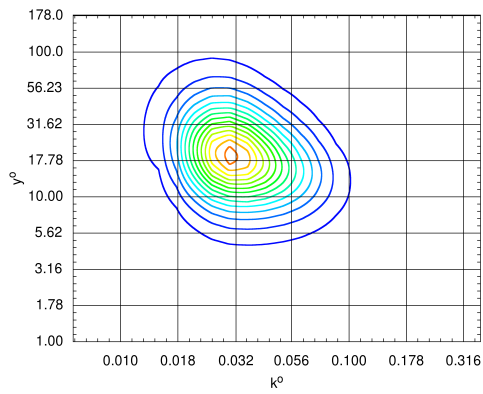
The convection (figure 4.29(c)) is characterised by transfers in both the spatial and spectral domains. The energy is taken from an area located at the same wall-normal coordinate as the maximum of production but at smaller scales and transferred both towards the wall at larger scales and towards the centre of the channel at smaller scales. The former of these two effects is however far more significant.

The overall spectral behaviour of the energy exchanges in a wall-bounded flow is as follows. Mean kinetic energy is transformed into turbulence kinetic energy around a particular point in the spatial and spectral domains. The energy is primarily redistributed towards small scales; transferred with few scale shift towards the wall, then transformed into internal energy.

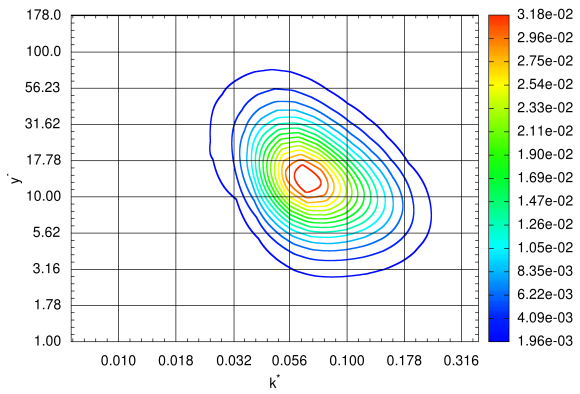
Spectra of the incompressible energy exchanges in the anisothermal configuration

We now focus on the effect of the temperature gradient on the terms of the evolution equation of the half-trace of the velocity fluctuation correlation tensor, investigated above in the isothermal configuration. The production is represented in figure 4.24, the conservative energy transfer in figure 4.25, the purely spectral transfer in figure 4.26, the interaction with internal energy in figure 4.27, the viscous transfer in figure 4.28 and the convection in figure 4.29. Let us recall that in flows with variable fluid properties, the interaction with internal energy is the sum of two contributions: the dissipation and the pressure dilatation correlation. Since the pressure dilatation correlation is negligible, the spectra of the interaction with internal energy also give the spectra of the dissipation.

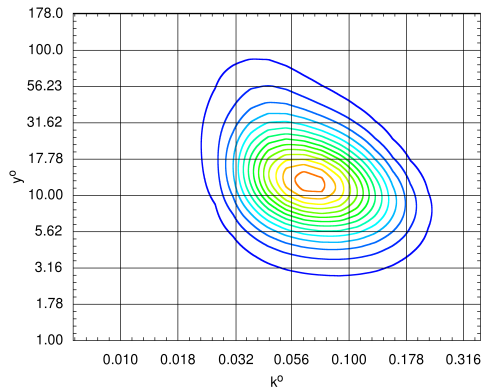
For each term, we give the spectra obtained with the constant scaling and with the semi-local scaling. As shown by the analysis in the spatial domain, the classical scaling overcorrects the position of the maxima in the wall-normal direction because of the large variations of the fluid properties. In the spectral domain, the classical scaling was found to provide no further information over the constant scaling and the semi-local scaling as this behaviour holds. For similar reasons, the results with the integral scaling are not shown. For each scaling, we compare the spectra at the hot and cold sides in the anisothermal configuration and the spectra in the isothermal configuration.



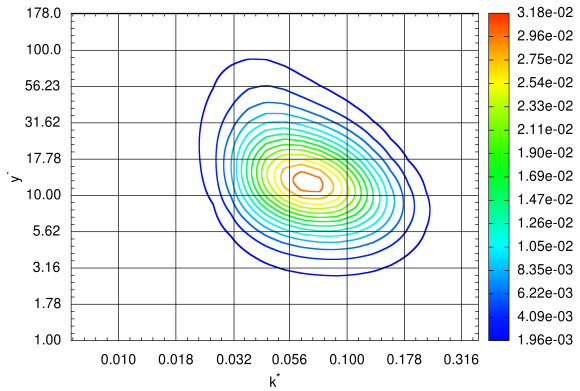
(a) Hot side, constant scaling.



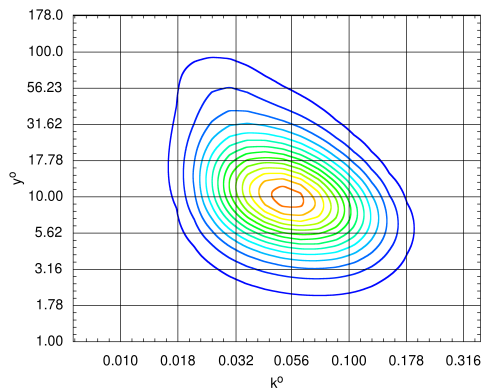
(b) Hot side, semi-local scaling.



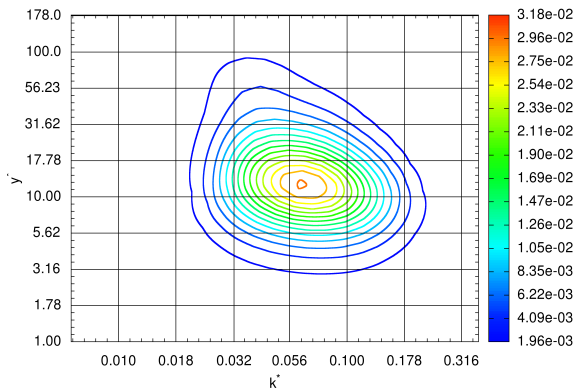
(c) Isothermal, constant scaling.



(d) Isothermal, semi-local scaling.



(e) Cold side, constant scaling.



(f) Cold side, semi-local scaling.

Figure 4.24 – Production \bar{P} .

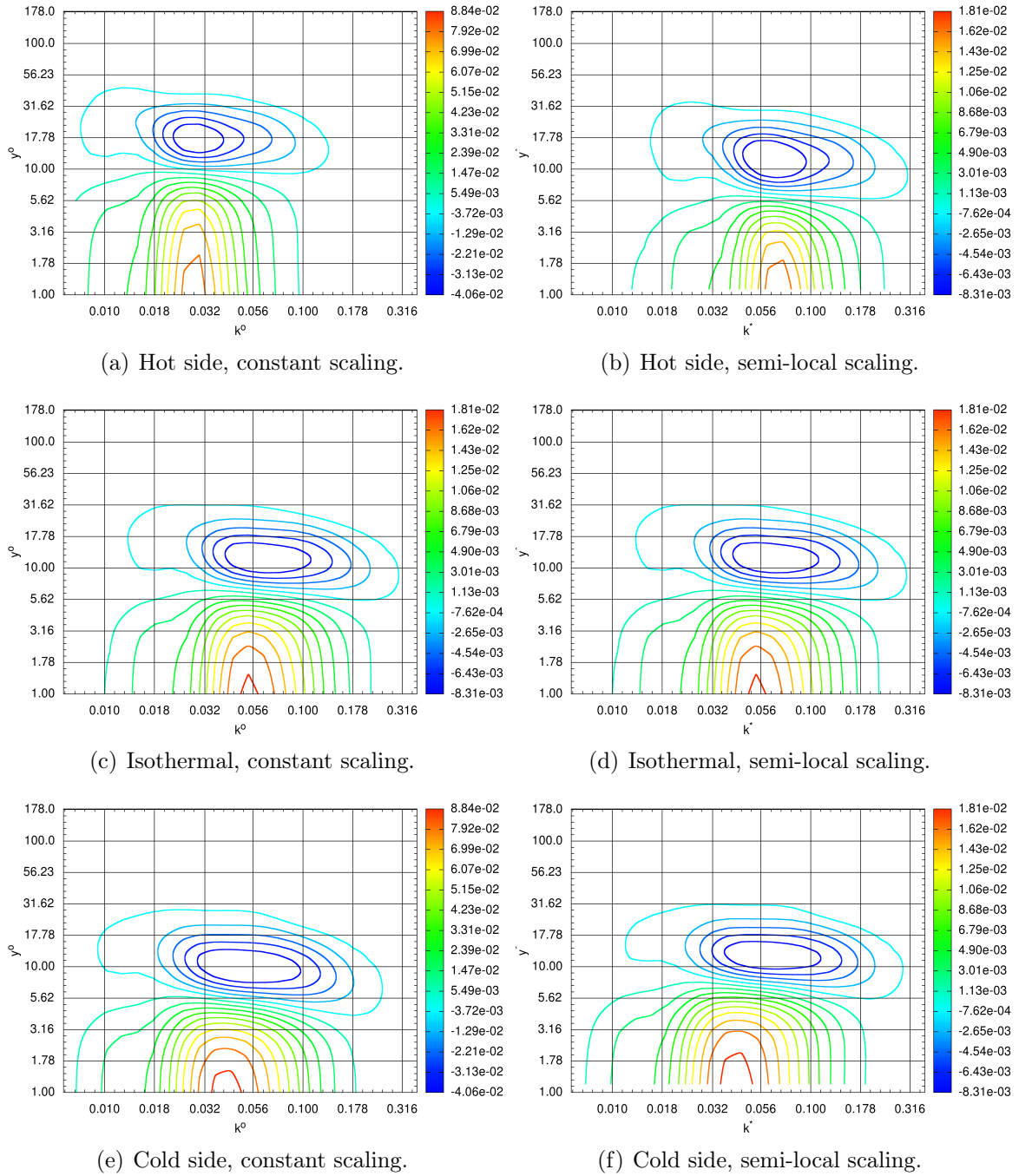


Figure 4.25 – Conservative energy transfer $\bar{\varphi}$.

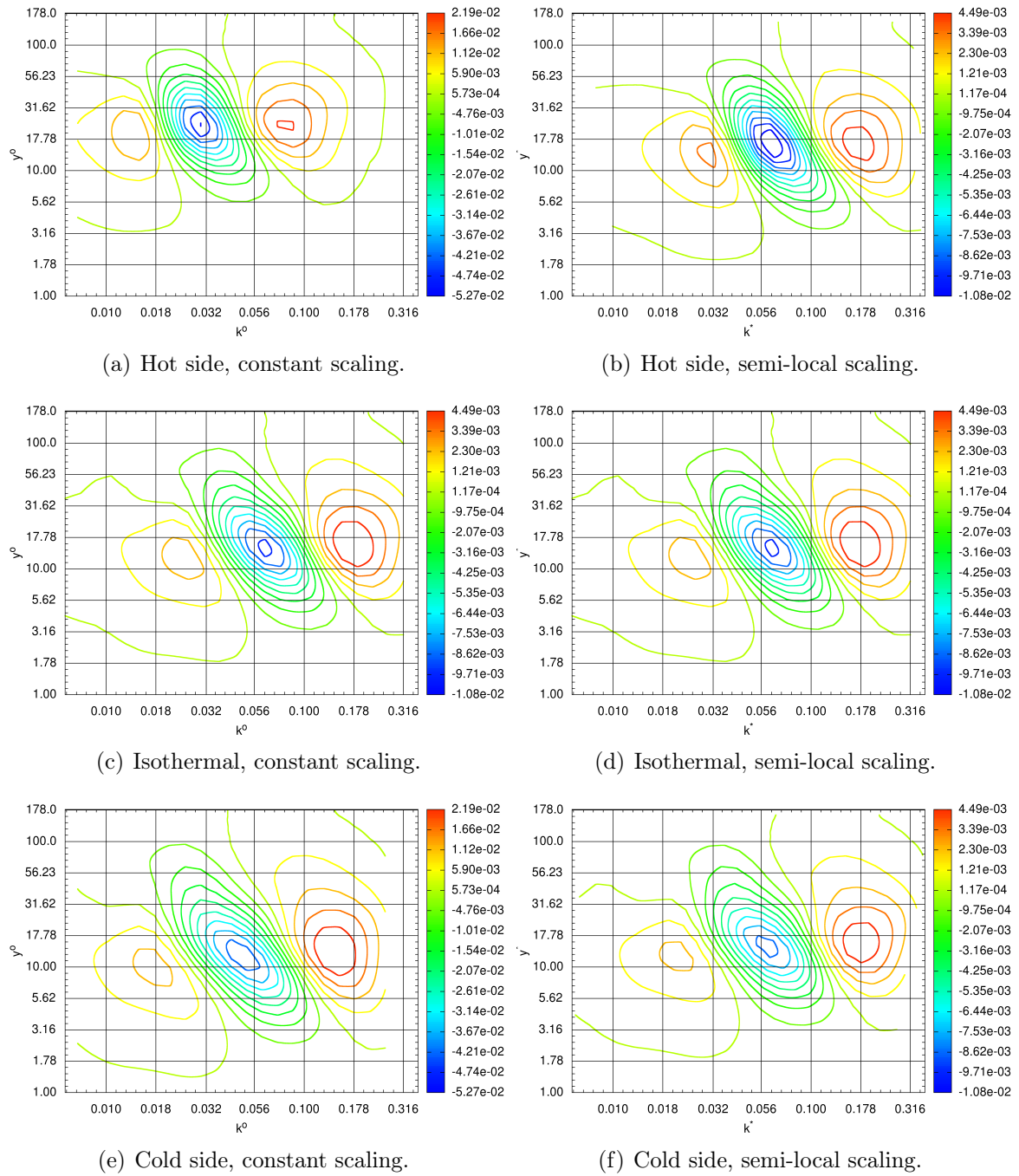
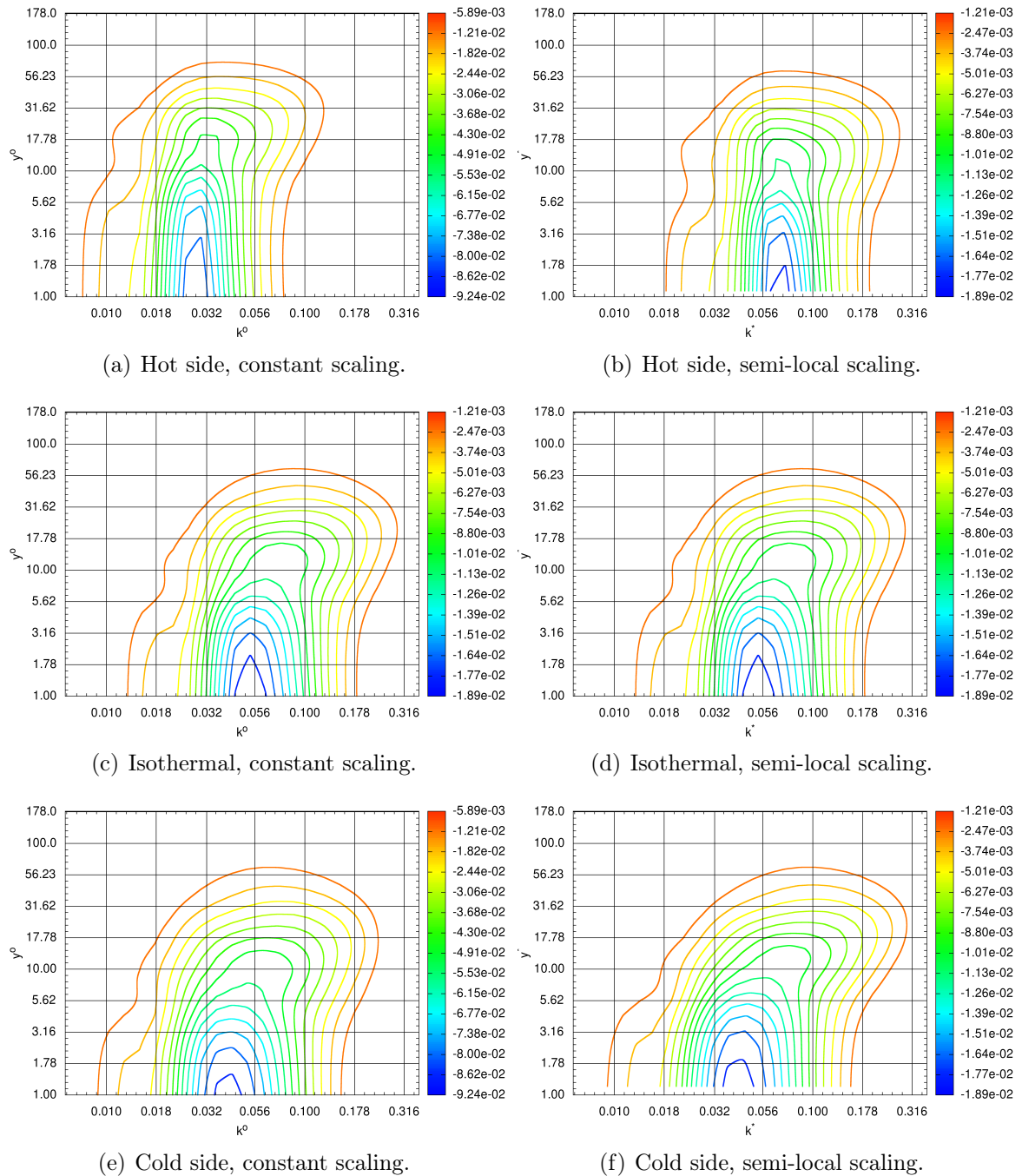


Figure 4.26 – Purely spectral transfer $\bar{\Xi}$.

Figure 4.27 – Interaction with internal energy $\bar{\epsilon}$.

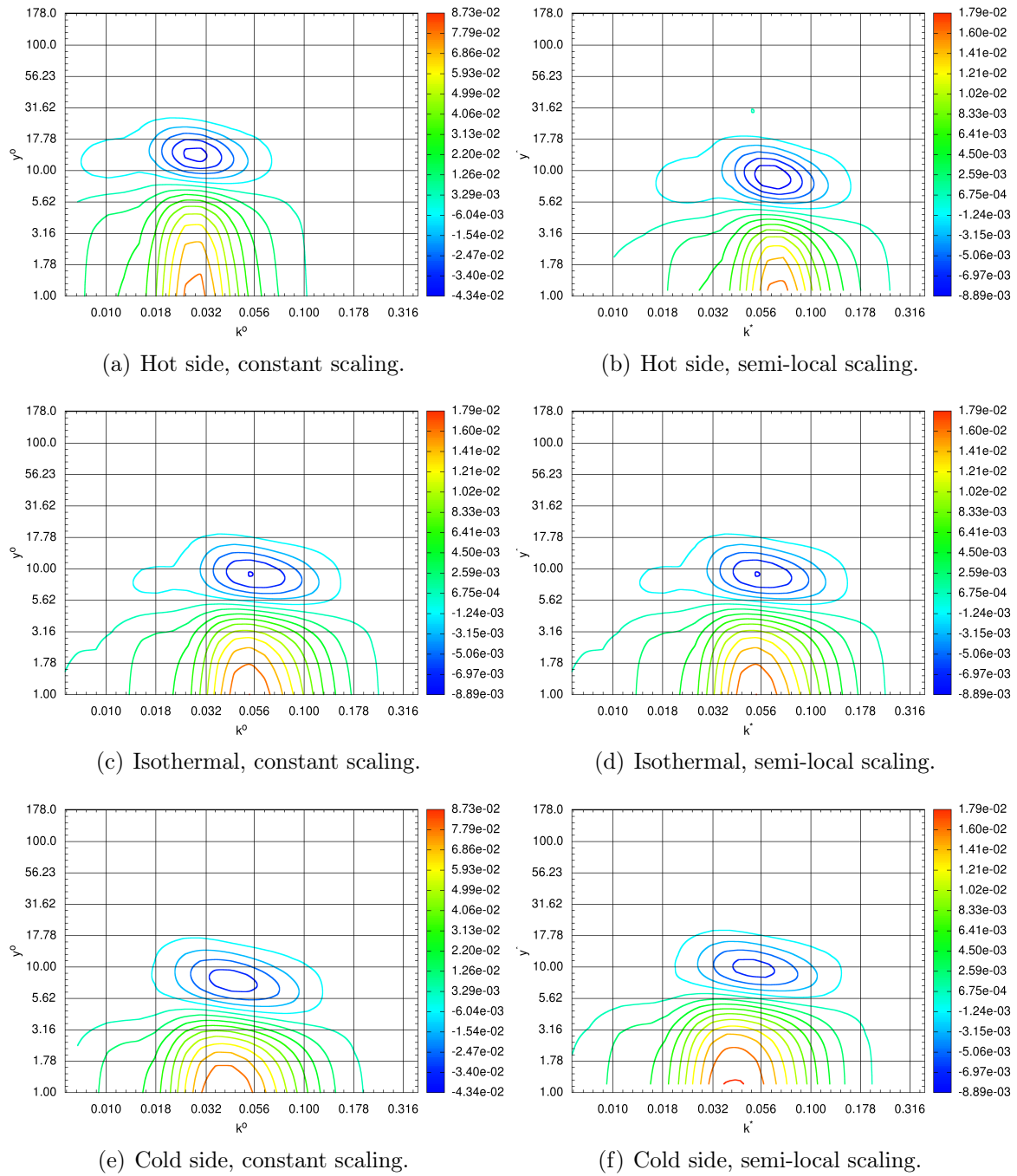


Figure 4.28 – Viscous transfer (part of the conservative energy transfer) $\overline{\varphi^v}$.

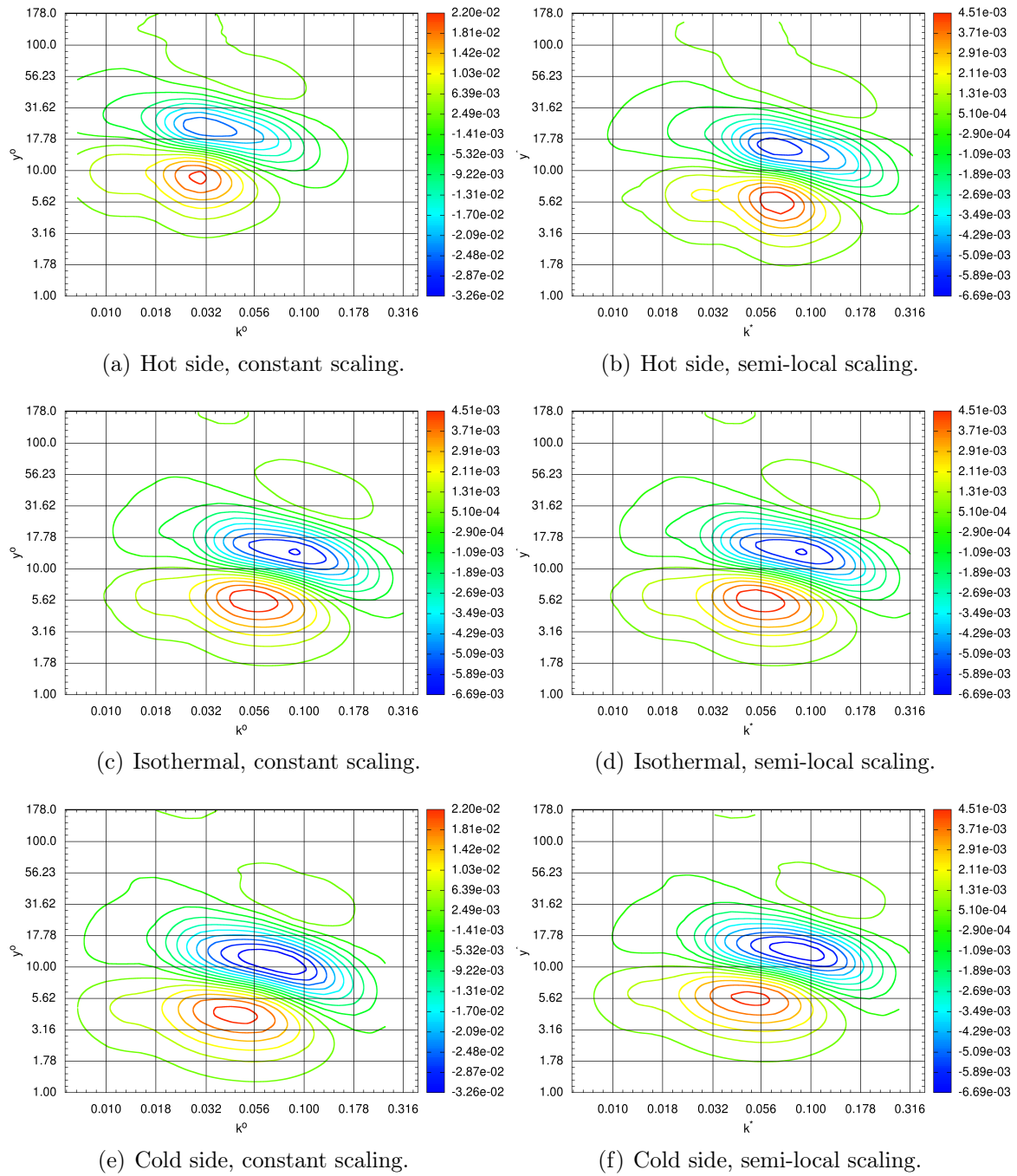


Figure 4.29 – Convection (part of the conservative energy transfer) $\overline{\varphi^c}$.

The effect of the temperature gradient is less universal in the spectral domain than in the spatial domain. With the constant scaling, the spatial position of the spectral extrema is modified for each term as described in the spatial domain. Namely, it is shifted closer to the wall at the cold side and farther at the hot side. The spectral position of the extrema is shifted towards large scales at both the hot and cold sides compared to the isothermal spectra. The shift is small at the cold side and large at the hot side. This creates an additional asymmetry between the hot and cold sides. The amplitude of the extrema is larger at the hot side than at the cold side. This is counterintuitive because the extrema in the spatial domain are larger at the cold side. This apparent contradiction is explained by a difference in the range of scales handled. The energy exchanges take place over a wider range of scales at the cold side and are restricted to a smaller wavenumber range at the hot side. In other words, the larger spatial amplitudes at the cold side do not root in larger spectral amplitudes but in a larger number of scales handled.

In agreement with the analysis in the spatial domain, there is no spatial position difference between the hot and cold sides with the semi-local scaling. The effect of the semi-local scaling on the spectral position differences is not the same for each term.

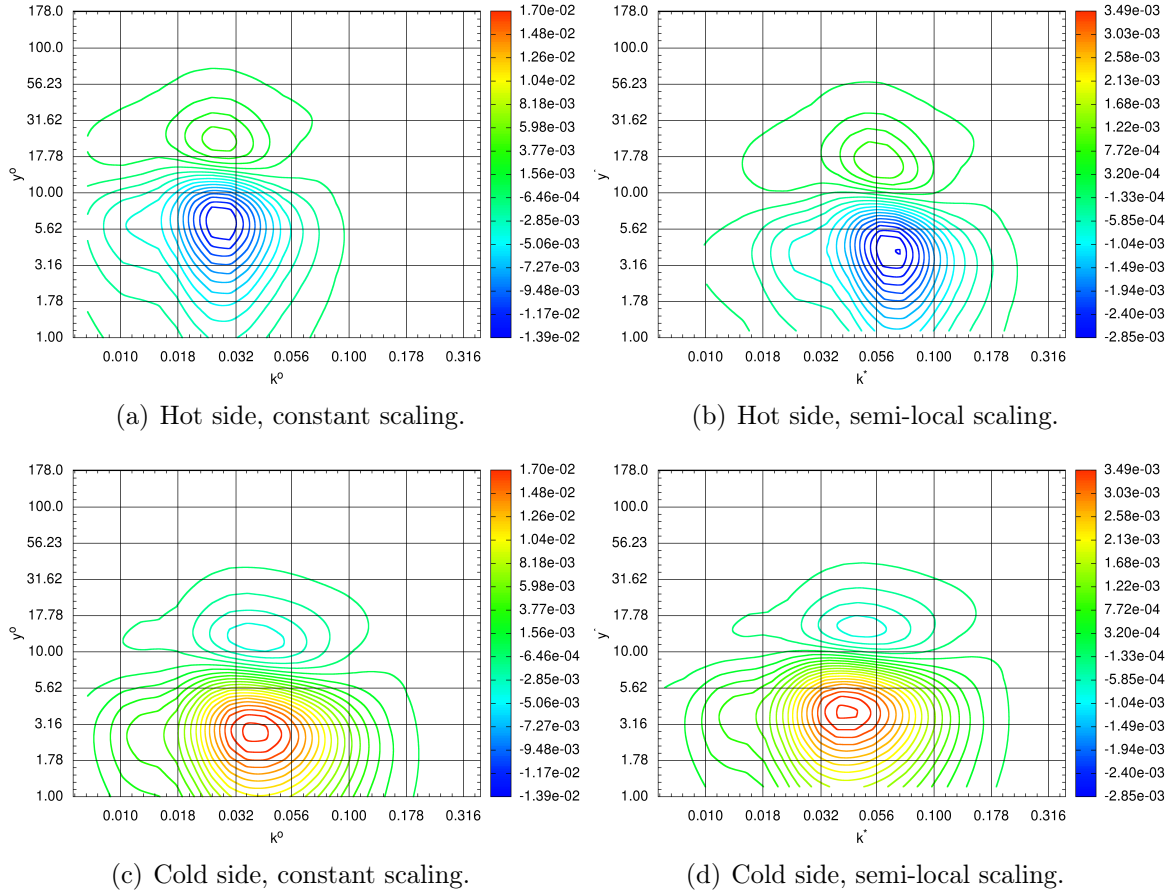
With the semi-local scaling, there is no longer a spectral position difference between the hot and cold sides of the maximum of production (figure 4.24).

This is also true for the negative area of the spectra of the conservative energy transfer (figure 4.25), which hence stays centred on the maximum of production. The positive area also stays centred on the extremum of dissipation, which as will be described later means that the spectral positions of the extrema at the hot and cold sides remain different. As a result of the inconsistency between the behaviour of the two areas, the pseudo-transfer from the negative area to the positive area appears to be almost entirely towards the wall at the hot side and both towards the wall and towards large scales at the cold side.

With regard to the purely spectral transfer (figure 4.26), the spectral position difference between the hot and cold sides disappears for the negative area and the positive area at small scales but remains for the positive area at large scales at the hot side. The inverse energy cascade hence is modified by the complex interaction between temperature and turbulence.

The extremum of the interaction with internal energy (figure 4.27) is not at the same spectral position at the hot and cold sides. The relative positions of the hot and cold extrema is swapped compared to the constant scaling. The extremum at the hot side appears closer to the smallest scales than in the isothermal configuration, and closer to the largest scales at the cold side. We previously identified that smaller scales contribute to the interaction with internal energy away from the wall. This behaviour almost vanishes at the hot side but is strengthened at the cold side. Taking into account the mean local variations of the fluid properties with semi-local scaling, the effect appears stronger.

The spectral position difference between the hot and cold sides observed with the constant scaling remains for some extrema but vanishes for others with the semi-local scaling. If the difference vanishes, it suggests that the spectral position asymmetry is a direct consequence of the spatial position asymmetry, through the mean local variations of the viscosity. If the difference remains, it suggests that the asymmetry additionally

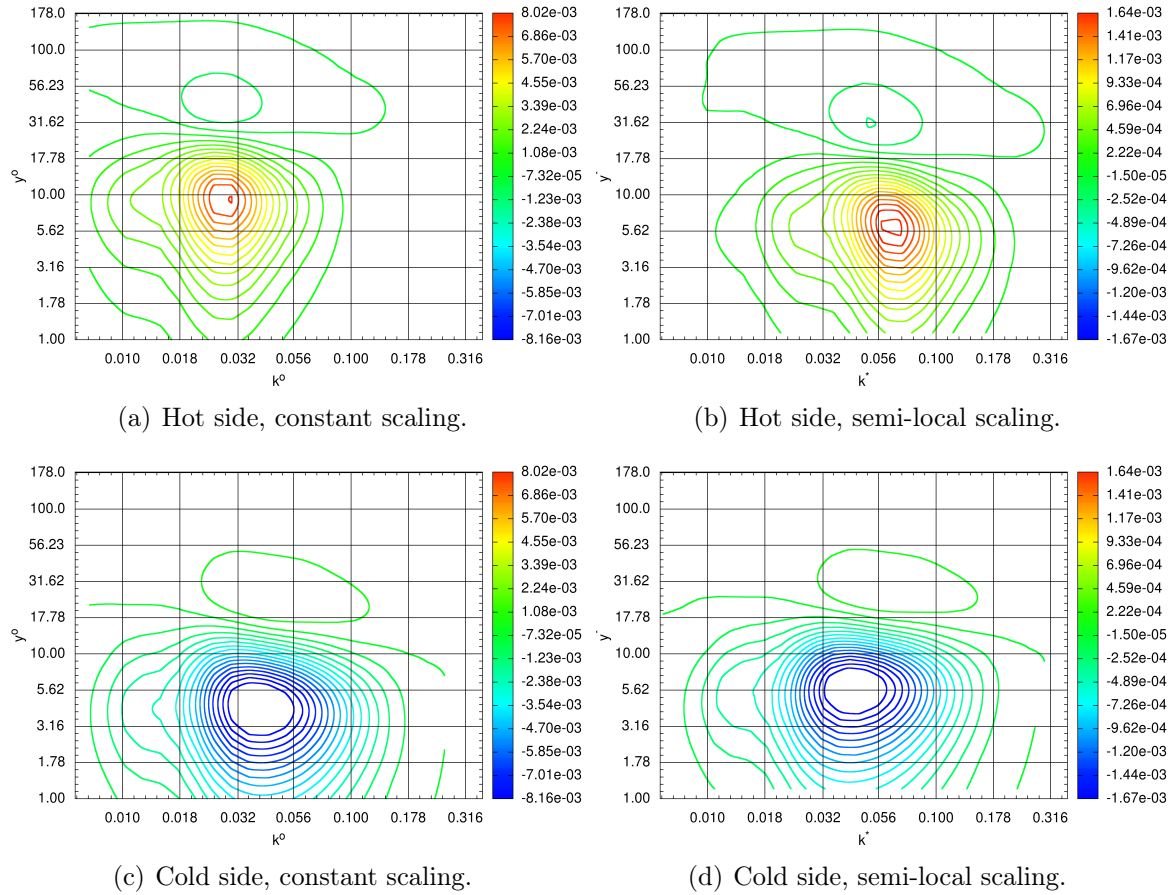
Figure 4.30 – Thermal conservative energy transfer $\overline{\varphi}_T$.

lies in more complex phenomena, namely the combined effect of local Reynolds number variations and of the local fluctuations of the fluid properties.

Spectra of the thermal terms in the anisothermal configuration

The thermal terms are the thermal part of the above-investigated terms and the total profile of the interaction with variable density kinetic energy, a thermal energy exchange. We only discuss here the terms that have a statistically reliable spectra from our direct numerical simulation. The thermal conservative energy transfer is represented in figure 4.30, the interaction with variable density kinetic energy in figure 4.31 and the thermal interaction with internal energy in figure 4.32. The thermal production is not discussed as its effect is negligible and the purely spectral transfer has no thermal contribution.

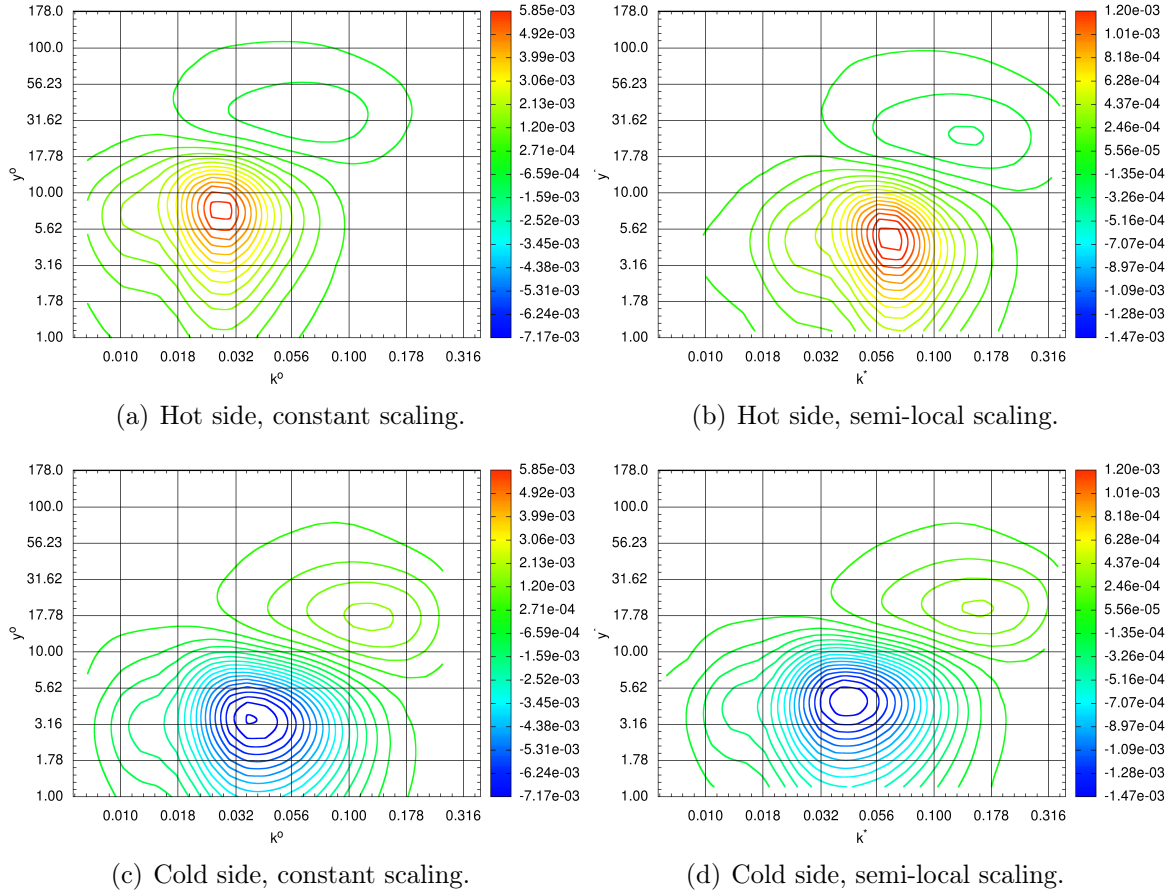
The three terms were shown to have a similar spatial profile. The similarities also appear in the spectral domain. As could be induced from the spatial profiles, the spectra are composed of two areas of opposite signs at each side, that are also of opposite sign between the hot and cold sides. That is, a kinetic energy gain (respectively loss) at one side of the channel occurs with a kinetic energy loss (respectively gain) at the other side of the channel. The extrema close to the wall have a significantly larger spectral amplitude than the second extrema. The spectral amplitude in absolute value

Figure 4.31 – Interaction with variable density kinetic energy ζ .

of an extremum is larger at the cold side than the hot side. This may seem obvious from the spatial profiles but contrasts with the spectra of the incompressible energy exchanges. In agreement with the other spectra, the extrema with the constant scaling are closer to the large scales at the hot side and spans over a wider range of scales at the cold side. Hence, the larger spatial amplitudes at the cold side come both from a larger spectral amplitude and a larger number of scales handled.

The spectral position of the extrema closer to the wall is identical for the three terms at both the hot and cold sides. The spectral position of the extrema close to the centre of the channel is identical for the thermal conservative energy transfer and the interaction with variable density kinetic energy, but different for the thermal interaction with internal energy. In the former case, its spectral position with the constant scaling is the same as the extremum close to the wall. In the latter case, it is located at smaller scales.

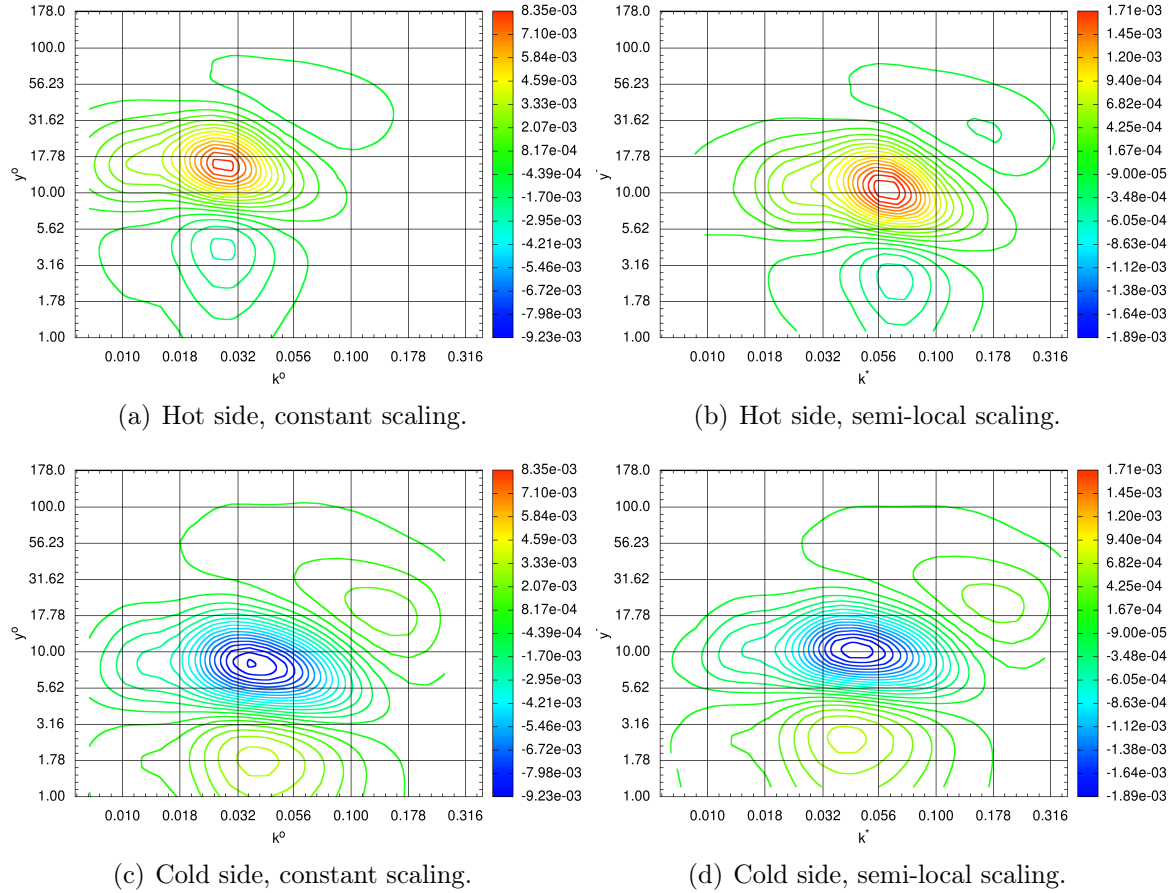
For the thermal conservative energy transfer and the interaction with variable density kinetic energy, the semi-local scaling creates a spectral position shift between the two extrema. For the interaction with variable density kinetic energy, the already existing shift is increased at the cold side and reduced at the hot side. The semi-local scaling fails to nullify the spectral position difference between the hot and cold sides for all extrema of the thermal terms. With the semi-local scaling, an extremum appears closer to the small scales at the hot side. This behaviour is similar to the behaviour of

Figure 4.32 – Thermal interaction with internal energy $\bar{\varepsilon}_T$.

some extrema of the previously discussed total terms.

The combined effect of the thermal terms is rather unobvious because of the spatial and spectral position differences between the three terms. The spectra of the sum of all thermal terms, represented in figure 4.33, are composed of three areas of opposite sign between the hot and cold sides. This is in agreement with the spatial profiles (figure 4.23). The first two areas are located at the same wavenumber as the extrema closer to the wall of the separate spectra. The third area more or less corresponds to the extremum close to the centre of the channel of the thermal interaction with internal energy. It is thus located at smaller scales than the first two areas. The spectra show complex interactions both in the spatial and spectral directions and between the two sides of the channel.

The semi-local scaling retains in the anisothermal configuration a large part of the overall spectral behaviour of the energy exchanges found in the isothermal configuration. The production and redistribution among scales of turbulence kinetic energy are not significantly modified. However, the kinetic energy transfer towards the wall and the dissipation are modified. In particular, the scales involved differ between the hot and cold sides. They are shifted towards large scales at the cold side and towards small scales at the hot side.

Figure 4.33 – Sum of all thermal terms $\overline{\varphi}_T + \overline{\zeta} + \overline{\varepsilon}_T$.

4.2.5 Conclusion

The energy exchanges associated with the half-trace of the velocity fluctuation correlation tensor are investigated in the spatial and spectral domains from two direct numerical simulations of a fully developed turbulent channel flow: one isothermal and one anisothermal, in which the flow is subjected to a strong temperature gradient. The flow in the anisothermal channel is mainly an incompressible flow with variable fluid properties. The most significant thermal terms are associated with the rate of deformation part of the viscous shear stress while the viscous terms associated with dilatation are very small. The temperature gradient generates an asymmetry between the profiles of the energy exchanges between the hot and cold sides. This asymmetry consists of: (1) an asymmetry in the position of the extrema explained by the mean local variations of the fluid properties and (2) an asymmetry in the amplitude of the extrema, explained with, in addition, the combined effect of local Reynolds number variations and of the local fluctuations of the fluid properties. The asymmetry originates both from the subtle modification of the behaviour of the incompressible terms compared to the isothermal configuration and the addition of thermal terms. Both effects are found necessary to obtain the correct behaviour of the energy exchanges for the interaction with internal energy, the viscous transfer and hence the conservative energy transfer.

The spectral evolution equation of the half-trace of the velocity fluctuation correla-

tion tensor allows us to carry on the analysis of the energy exchanges into the spectral domain. In the isothermal configuration, the purely spectral term is found to represent a significant part of the spectral energy exchanges. It redistributes the energy among scales through both direct and inverse cascades. The extension of the spectral decomposition to the anisothermal configuration shows that the larger spatial amplitudes at the cold side come from a larger number of scales handled in the spectral domain. Additionally, an asymmetry in the wavenumber position of the spectral extrema is observed near the wall. This additional effect moves the cold side to the large scales and the hot side to the small scales.

Acknowledgments

The authors gratefully acknowledge the CEA for the development of the TRUST platform and TrioCFD. This work was granted access to the computer resources of CINES under the allocation 2016-c20162a5099 made by GENCI. We are grateful to I. Bolotnov for providing us the exact limits of his wavenumber bins and T. Tsukahara for providing us his data on the turbulence kinetic energy budget.

Bibliography

- [2] H. Abe, H. Kawamura, and Y. Matsuo. Direct numerical simulation of a fully developed turbulent channel flow with respect to the Reynolds number dependence. *Journal of Fluids Engineering*, 123(2):382–393, 2001.
- [10] F. Aulery, A. Toutant, F. Bataille, and Y. Zhou. Energy transfer process of anisothermal wall-bounded flows. *Physics Letters A*, 379(24):1520–1526, 2015.
- [11] F. Aulery, D. Dupuy, A. Toutant, F. Bataille, and Y. Zhou. Spectral analysis of turbulence in anisothermal channel flows. *Computers & Fluids*, 151:115–131, 2017.
- [13] B. Aupoix. Introduction to turbulence modelling for compressible flows. *VKI lecture series*, 4:H1–H64, 2000.
- [17] P. T. Bauer, G. W. Zumwalt, and L. J. Fila. A numerical method and an extension of the korst jet mixing theory for multispecie turbulent jet mixing. AIAA paper 68 (112). In *6th Aerospace Sciences Meeting, New York*, 1968.
- [28] I. A. Bolotnov, R. T. Lahey, D. A. Drew, K. E. Jansen, and A. A. Oberai. Spectral analysis of turbulence based on the DNS of a channel flow. *Computers & Fluids*, 39(4):640–655, 2010.
- [36] G. Brillant, S. Husson, F. Bataille, and F. Ducros. Study of the blowing impact on a hot turbulent boundary layer using thermal large eddy simulation. *Intl. J. Heat Fluid Flow*, 29(6):1670–1678, 2008.
- [37] C. Brun, M. Petrovan Boiarciuc, M. Haberkorn, and P. Comte. Large eddy simulation of compressible channel flow. *Theoretical and Computational Fluid Dynamics*, 22(3):189–212, 2008.
- [38] C. Calvin, O. Cueto, and P. Emonot. An object-oriented approach to the design of fluid mechanics software. *ESAIM: Mathematical Modelling and Numerical Analysis*, 36(05):907–921, 2002.
- [44] M. Chandesris, A. d’Hueppe, B. Mathieu, D. Jamet, and B. Goyeau. Direct numerical simulation of turbulent heat transfer in a fluid-porous domain. *Phys. Fluids*, 25(12):125110, 2013.

- [47] P. Chassaing. Une alternative à la formulation des équations du mouvement turbulent d'un fluide à masse volumique variable. *Journal de mécanique théorique et appliquée*, 4 (3):375–389, 1985.
- [50] P. Chassaing, R. A. Antonia, F. Anselmet, L. Joly, and S. Sarkar. *Variable density fluid turbulence*. Springer Science & Business Media, 2013.
- [58] A. Cimarelli and E. De Angelis. The physics of energy transfer toward improved subgrid-scale models. *Phys. Fluids*, 26(5):055103, 2014.
- [59] A. Cimarelli, E. De Angelis, and C. M. Casciola. Paths of energy in turbulent channel flows. *J. Fluid Mech.*, 715:436–451, 2013.
- [61] A. Cimarelli, E. De Angelis, P. Schlatter, G. Brethouwer, A. Talamelli, and C. M. Casciola. Sources and fluxes of scale energy in the overlap layer of wall turbulence. *J. Fluid Mech.*, 771:407–423, 2015.
- [62] A. Cimarelli, E. De Angelis, J. Jiménez, and C. M. Casciola. Cascades and wall-normal fluxes in turbulent channel flows. *J. Fluid Mech.*, 796:417–436, 2016. ISSN 1469-7645.
- [67] G. N. Coleman, J. Kim, and R. D. Moser. A numerical study of turbulent supersonic isothermal-wall channel flow. *J. Fluid Mech.*, 305:159–183, 1995.
- [68] A. W. Cook and Y. Zhou. Energy transfer in Rayleigh-Taylor instability. *Phys. Rev. E*, 66:026312, 2002.
- [70] J. Cousteix and B. Aupoix. Turbulence models for compressible flows. In *Special Course Three-Dimensional Supersonic and Hypersonic Flows Including Separation*. AGARD/FDP-VKI Special course, 1989.
- [79] J. C. Del Álamo and J. Jiménez. Spectra of the very large anisotropic scales in turbulent channels. *Phys. Fluids*, 15(6):L41–L44, 2003.
- [81] J. A. Domaradzki and R. S. Rogallo. Local energy transfer and nonlocal interactions in homogeneous, isotropic turbulence. *Physics of Fluids A: Fluid Dynamics*, 2(3):413–426, 1990.
- [83] J. A. Domaradzki, W. Liu, C. Hartel, and L. Kleiser. Energy transfer in numerically simulated wall-bounded turbulent flows. *Phys. Fluids*, 6(4):1583–1599, 1994.
- [94] A. Favre. The equations of compressible turbulent gases. Technical Report AD0622097, DTIC Document, 1965.
- [110] T. B. Gatski and J. P. Bonnet. *Compressibility, turbulence and high speed flow*. Academic Press, 2013.
- [120] S. E. Guarini, R. D. Moser, K. Shariff, and A. Wray. Direct numerical simulation of a supersonic turbulent boundary layer at Mach 2.5. *J. Fluid Mech.*, 414:1–33, 2000.
- [123] H. Ha Minh, B. E. Launder, and J. MacInnes. The turbulence modelling of variable density flows—a mixed-weighted decomposition. In *Turbulent Shear Flows 3*, pages 291–308. Springer, 1982.
- [126] S. Hoyas and J. Jiménez. Scaling of the velocity fluctuations in turbulent channels up to $Re_\tau = 2003$. *Phys. Fluids*, 18(1):011702, 2006.
- [127] P. G. Huang, G. N. Coleman, and P. Bradshaw. Compressible turbulent channel flows: DNS results and modelling. *J. Fluid Mech.*, 305:185–218, 1995.
- [144] S. Kida and S. A. Orszag. Energy and spectral dynamics in decaying compressible turbulence. *Journal of Scientific Computing*, 7(1):1–34, 1992. ISSN 0885-7474.
- [146] J. Kim, P. Moin, and R. Moser. Turbulence statistics in fully developed channel flow at low Reynolds number. *J. Fluid Mech.*, 177:133–166, 1987.
- [149] M. Kozuka, Y. Seki, and H. Kawamura. DNS of turbulent heat transfer in a channel flow with a high spatial resolution. *Intl. J. Heat Fluid Flow*, 30(3):514–524, 2009.
- [154] F. Laadhari. On the evolution of maximum turbulent kinetic energy production in a channel flow. *Phys. Fluids*, 14(10):L65–L68, 2002.
- [161] R. Lechner, J. Sesterhenn, and R. Friedrich. Turbulent supersonic channel flow. *J. Turbulence*, 2(1):001–001, 2001.

- [170] B. P. Leonard. A stable and accurate convective modelling procedure based on quadratic upstream interpolation. *Computer Methods in Applied Mechanics and Engineering*, 19(1):59–98, 1979.
- [173] M. Lesieur. *Turbulence in Fluids*. Fluid Mechanics and Its Applications. Springer, 2008. ISBN 9781402064357.
- [185] T. Maeder, N. A. Adams, and L. Kleiser. Direct simulation of turbulent supersonic boundary layers by an extended temporal approach. *J. Fluid Mech.*, 429:187–216, 2001.
- [188] N. Marati, CM Casciola, and R Piva. Energy cascade and spatial fluxes in wall turbulence. *J. Fluid Mech.*, 521:191–215, 2004.
- [200] Y. Morinishi, T. S. Lundhomas, O. V. Vasilyev, and P. Moin. Fully conservative higher order finite difference schemes for incompressible flow. *J. Comput. Phys.*, 143(1):90–124, 1998.
- [201] M. V. Morkovin. *The Mechanics of Turbulence*. Gordon and Breach, 1964.
- [203] R. D. Moser, J. Kim, and N. N. Mansour. Direct numerical simulation of turbulent channel flow up to $Re_\tau = 590$. *Phys. Fluids*, 11(4):943–945, 1999.
- [212] F. Nicoud. Conservative high-order finite-difference schemes for low-Mach number flows. *J. Comput. Phys.*, 158(1):71–97, 2000.
- [219] S. Paolucci. On the filtering of sound from the Navier–Stokes equations. Technical Report SAND82-8257, Sandia National Labs., Livermore, CA (USA), 1982.
- [222] A. Patel, J. Peeters, B. Boersma, and R. Pecnik. Semi-local scaling and turbulence modulation in variable property turbulent channel flows. *Phys. Fluids*, 27(9):095101, 2015.
- [233] S. Pirozzoli, F. Grasso, and T. B. Gatski. Direct numerical simulation and analysis of a spatially evolving supersonic turbulent boundary layer at $M=2.25$. *Phys. Fluids*, 16(3):530–545, 2004.
- [245] O. Reynolds. On the dynamical theory of incompressible viscous fluids and the determination of the criterion. *Proceedings of the Royal Society of London*, 56(336-339):40–45, 1894.
- [249] J. C. Rotta. Über den Einfluß der Machschen Zahl und des Wärmeübergangs auf das Wandgesetz turbulenter Strömung. *Z. Flugwiss.*, 7:264–274, 1959.
- [260] S. Sarkar. The pressure–dilatation correlation in compressible flows. *Physics of Fluids A: Fluid Dynamics*, 4(12):2674–2682, 1992.
- [264] S. Serra, A. Toutant, and F. Bataille. Thermal large eddy simulation in a very simplified geometry of a solar receiver. *Heat Transfer Engineering*, 33(6):505–524, 2012.
- [265] S. Serra, A. Toutant, F. Bataille, and Y. Zhou. High-temperature gradient effect on a turbulent channel flow using thermal large-eddy simulation in physical and spectral spaces. *J. Turbulence*, 13:N49, 2012.
- [268] M. S. Shadloo, A. Hadjadj, and F. Hussain. Statistical behavior of supersonic turbulent boundary layers with heat transfer at $M=2$. *International Journal of Heat and Fluid Flow*, 53:113–134, 2015.
- [269] M. F. Shahab, G. Lehnasch, T. B. Gatski, and P. Comte. Statistical characteristics of an isothermal, supersonic developing boundary layer flow from DNS data. *Flow, Turbulence and Combustion*, 86(3-4):369–397, 2011.
- [287] W. Sutherland. The viscosity of gases and molecular force. *The London, Edinburgh, and Dublin Philosophical Magazine and Journal of Science*, 36(223):507–531, 1893.
- [290] A. Toutant and F. Bataille. Turbulence statistics in a fully developed channel flow submitted to a high temperature gradient. *International Journal of Thermal Sciences*, 74:104–118, 2013.
- [291] A. Toutant, E. Labourasse, O. Lebaigue, and O. Simonin. DNS of the interaction between a deformable buoyant bubble and a spatially decaying turbulence: a priori tests for LES two-phase flow modelling. *Computers & Fluids*, 37(7):877–886, 2008.

- [293] A. Trettel and J. Larsson. Mean velocity scaling for compressible wall turbulence with heat transfer. *Phys. Fluids*, 28(2):026102, 2016.
- [296] A. V. Trofimova, A. E. Tejada-Martínez, K. E. Jansen, and R. T. Lahey Jr. Direct numerical simulation of turbulent channel flows using a stabilized finite element method. *Computers & Fluids*, 38(4):924–938, 2009. ISSN 0045-7930.
- [298] T. Tsukahara, T. Seki, H. Kawamura, and D. Tochio. DNS of turbulent channel flow at very low Reynolds numbers. In *Proc. of the Fourth International Symposium on Turbulence and Shear Flow Phenomena*, pages 935–940. Begel House Inc., 2005.
- [305] A. W. Vreman and J. G. M. Kuerten. Comparison of direct numerical simulation databases of turbulent channel flow at $Re_\tau = 180$. *Phys. Fluids*, 26(1):015102, 2014.
- [313] J. H. Williamson. Low-storage Runge-Kutta schemes. *J. Comput. Phys.*, 35(1):48–56, 1980.
- [318] C.-S. Yih. Exact solutions for steady two-dimensional flow of a stratified fluid. *J. Fluid Mech.*, 9(02):161–174, 1960.
- [324] Y. Zhou. Degrees of locality of energy transfer in the inertial range. *Physics of Fluids A: Fluid Dynamics*, 5(5):1092–1094, 1993.
- [325] Y. Zhou. Interacting scales and energy transfer in isotropic turbulence. *Physics of Fluids A: Fluid Dynamics*, 5(10):2511–2524, 1993.

4.3 Conclusion of chapter 4

The ternary decomposition of total energy and the decomposition of density in a constant and variable part give physical groundings to the study of the energy exchanges associated with the half-trace of the velocity fluctuation correlation tensor in the spatial and spectral domains. The energy exchanges are very different from the energy exchanges found in homogeneous isotropic turbulence. The dissipation does not occur at smaller scales than the production but at similar scales. The interscale transport of kinetic energy towards small scales is supplemented by an interscale transport towards large scales and a significant amount of kinetic energy is transferred to the near-wall region. The temperature gradient creates an asymmetry between the energy exchanges at the hot and cold sides, which are different and deviate from the energy exchanges in the incompressible isothermal configuration. The asymmetry can be interpreted as the combined influence of the addition of thermal terms and the behaviour modification of the incompressible terms. The most significant thermal terms are associated with the rate of deformation part of the viscous shear stress. The other thermal terms do not have a large effect in the flow investigated. The significant thermal terms show some universality in their behaviour and thus in their effect on the flow, mainly characterised by a net energy transfer towards or away from the wall.

The use of a semi-local scaling taking into account the variations of the mean local fluid properties successfully predicts a large part of the asymmetry. However, it does not entirely explain the amplitude differences as the energy exchanges have with the semi-local scaling a larger spatial amplitude at the cold side than at the hot side. In the spectral domain, the energy exchanges also handle with the semi-local scaling a larger number of scales at the cold side and, for some terms, a wavenumber asymmetry is observed. This suggests that a nontrivial portion of the asymmetry between the hot and cold sides is tied to more complex effects of the temperature gradient. A low Reynolds number effect has been identified, given by the variations of the local friction

Reynolds number across the channel. While this further explain a large part of the asymmetry, the results are inconsistent with a sole Reynolds number effect. In the next chapter, the analysis will be extended with the direct numerical simulation of the anisothermal channel at $Re_\tau = 395$ to investigate the effect of the mean friction Reynolds number on the asymmetry.

Chapter 5

Effect of the Reynolds number on turbulence kinetic energy exchanges

5.1 Introduction of chapter 5

The direct numerical simulations of the strongly anisothermal channel flow at the mean friction Reynolds number of $Re_\tau = 180$ and $Re_\tau = 395$ enable the study of the effect of the Reynolds number on the energy exchanges associated with the half-trace of the velocity fluctuation correlation tensor. At $Re_\tau = 180$, the effect of the temperature gradient on the energy exchanges has been investigated in the previous chapter. This chapter focuses on the effect of the mean friction Reynolds number on the energy exchanges and on the influence of the temperature gradient. The same method is used to analyse the energy exchanges and the study is based on the same decomposition of kinetic energy [89, 91]. Namely, the energy exchanges are decomposed into incompressible terms and thermal terms. The incompressible terms are formally identical to the terms present in the incompressible isothermal configuration. The thermal terms are specific to flows with variable fluid properties. The energy exchanges composed of at least one non-zero incompressible term are called incompressible energy exchanges. The energy exchanges composed only of thermal terms are called thermal energy exchanges.

5.2 Results

The energy exchanges associated with the half-trace of the velocity fluctuation correlation tensor are investigated using the semi-local scaling [127], which is an appropriate scaling for the energy exchanges [91][see also 224, 225, 91]. In contrast with the classical scaling, based only on wall values, the semi-local scaling is based on a velocity scale U_τ^* and a length scale \bar{v}/U_τ^* defined using the wall shear-stress and the mean local fluid properties. This leads to a semi-local wall coordinate y^* , a semi-local wavenumber k^* , a semi-local velocity \mathbf{U}^* and a semi-local friction Reynolds number Re_τ^* ,

$$y^* = \frac{yU_\tau^*}{\bar{v}(y)}, \quad (5.1)$$

$$k^* = \frac{k\bar{v}(y)}{U_\tau^*}, \quad (5.2)$$

$$\mathbf{U}^* = \frac{\mathbf{U}}{U_\tau^*}, \quad (5.3)$$

$$Re_\tau^* = \frac{U_\tau^* h}{\bar{v}(y)}, \quad (5.4)$$

with,

$$U_\tau^* = \sqrt{\frac{\mu_\omega}{\bar{\rho}(y)} \left(\frac{\partial \bar{U}_x}{\partial y} \right)_\omega}, \quad (5.5)$$

where the subscript ω denotes the value at the wall. The terms of the evolution equation of the half-trace of the velocity fluctuation correlation tensor are scaled by $U_\tau^{*4}/\bar{v}(y)$.

The energy exchanges are investigated in the spatial and spectral domains. In both cases, the analysis is carried out in two steps. First, we study the effect of the mean friction Reynolds number on the incompressible energy exchanges, through the combined effect of incompressible terms and thermal terms. Then, we study its effect on the incompressible terms and the thermal terms separately.

5.2.1 Effect of the Reynolds number in the spatial domain

5.2.1.1 Profiles of the incompressible energy exchanges in the anisothermal configuration

The temperature gradient creates at $Re_\tau = 180$ and $Re_\tau = 395$ an asymmetry between spatial profiles at the hot and cold sides of the three incompressible energy exchanges associated with the half-trace of the velocity fluctuation correlation tensor: the production, the conservative energy transfer and the interaction with internal energy. The energy exchanges have a greater magnitude at the cold side than at the hot side, but occur over a narrower spatial range and closer to the wall. These effects of the temperature gradient are Reynolds number dependent.

The spatial profiles at $Re_\tau = 180$ and $Re_\tau = 395$ of the three incompressible energy exchanges is provided in figure 5.1 with the semi-local scaling. The profiles of the two most significant parts of the conservative energy transfer, the viscous transfer and the convection, are also given. At higher mean friction Reynolds number, the asymmetry between the hot and cold sides is reduced. This is consistent with the assumption that the asymmetry between the hot and cold sides is mainly due to two separate contributions [91]:

- the variations of the local velocity and length scales due to the variations of the local fluid properties, to some extent taken into account by the semi-local scaling;
- a varying low Reynolds number effect between the hot and cold sides depending on the semi-local friction Reynolds number (not taken into account by the semi-local scaling).

Indeed, the profiles of the energy exchanges exhibit low Reynolds number effects in the incompressible isothermal case within the Reynolds number range of this study. A

lower Reynolds number decreases the amplitude of the energy exchanges and shifts the profiles farther from the wall. This Reynolds number dependence is more pronounced for the interaction with internal energy and the viscous transfer than for the production and the convection. In the anisothermal channel, the semi-local friction Reynolds number varies across the channel due to the temperature gradient. At $Re_\tau = 180$, the semi-local friction Reynolds number ranges from 105 at the hot wall to 260 at the cold wall. At $Re_\tau = 395$, the semi-local friction Reynolds number ranges from 227 at the hot wall to 556 at the cold wall. The profiles are therefore subjected to a varying low Reynolds number effect between the hot and cold sides, which cannot be expected to be taken into account by any scaling based on the local fluid properties, given that the classical wall scaling does not collapse the incompressible isothermal profiles at various friction Reynolds number.

As at $Re_\tau = 180$ [91], the semi-local scaling properly account for the effect of the variations of the local fluid properties on the profile of production (figure 5.1(a)) at $Re_\tau = 395$. This is shown by the fact that the maximum of production with the semi-local scaling follows a low Reynolds number effect according to the empirical relation of Laadhari [154]. While the semi-local scaling is also relevant for the other energy exchanges, the profiles of the conservative energy transfer (figure 5.1(b)) and the interaction with internal energy (figure 5.1(c)) show evidence that the approximation of the semi-local scaling does not perfectly take into account the effect of the variations of the local fluid properties. The value of the interaction with internal energy (figure 5.1(c)) at the wall is not equal to that of the incompressible isothermal profile at the wall semi-local friction Reynolds number. The hot and cold profiles of the viscous transfer (figure 5.1(d)) deviates from all incompressible isothermal profiles, even at the point near $y^* = 3.5$ where they pass through the same points. The asymmetry between the hot and cold profiles of the convection (figure 5.1(e)) is very small compared to a low Reynolds number effect, especially at the positive extremum, closer from the wall. These results confirms previous findings at $Re_\tau = 180$ [91].

Hence, the asymmetry between the hot and cold sides is reduced at $Re_\tau = 395$ compared to $Re_\tau = 180$ because low Reynolds number effects are smaller the higher the Reynolds number. This only affects one component of the effect of the temperature gradient however. While a simulation at even higher Reynolds number would be free of low Reynolds number effects, the results suggest that the hot and cold profiles would still not collapse because the approximation of the semi-local scaling does not perfectly account for the effect of the variations of the local fluid properties. This is investigated further by decomposing the energy exchanges into incompressible terms and thermal terms.

5.2.1.2 Profiles of the incompressible terms in the anisothermal configuration

The spatial profiles with the semi-local scaling of the incompressible terms follows for the most part the same general behaviour as the total incompressible energy exchanges and are subject to a similar effect of the Reynolds number (figure 5.1). The incompressible production is identical to the total production because the thermal production is negligible (figure 5.1(a)). At $Re_\tau = 180$, the profiles of the incompressible conservative energy transfer (figure 5.1(b)) and the incompressible interaction with in-

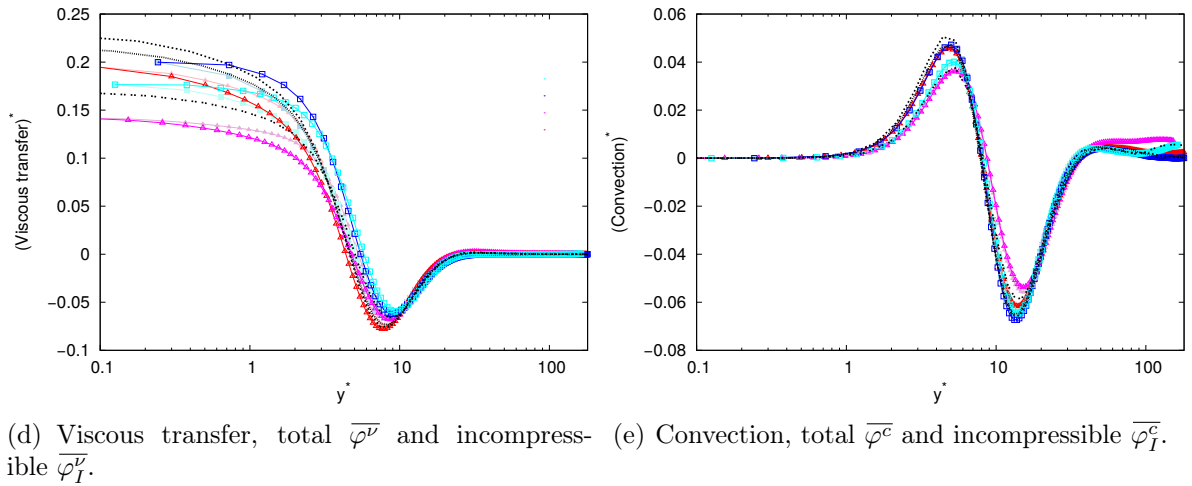
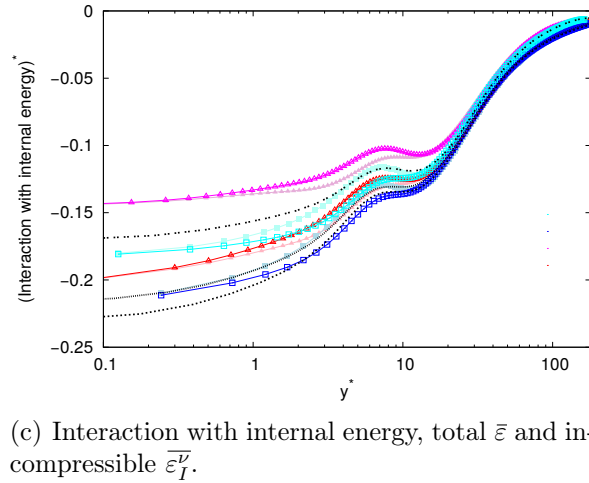
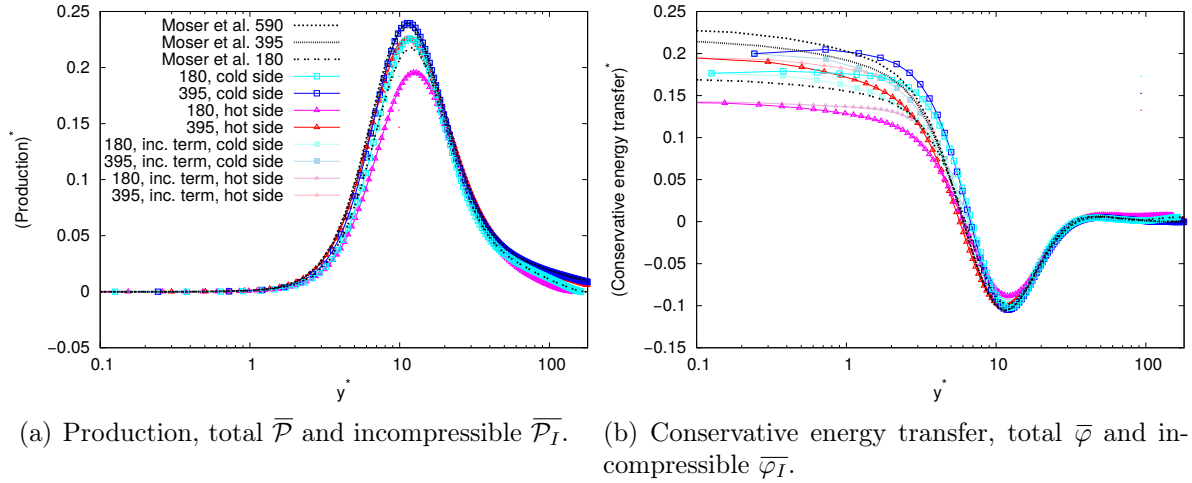


Figure 5.1 – Profiles of the terms of the budget of the half-trace of the velocity fluctuation correlation tensor with the semi-local scaling at $Re_\tau = 180$ and $Re_\tau = 395$. The profiles of the two most significant parts of the conservative energy transfer are also given, The results are compared to the reference data of Moser *et al.* [203] for an incompressible isothermal channel flow at the friction Reynolds numbers 180, 395 and 590. The viscous transfer and the convection are the two most significant parts of the conservative energy transfer.

ternal energy (figure 5.1(c)) at the hot and cold sides are closer to each other and to the incompressible isothermal profiles, especially in an area around $y^* = 4$ but not at the wall where the incompressible and total terms are identical. At $Re_\tau = 395$, the effect is similar but goes further, inverting the ordering of the hot and cold profiles at some parts of the channel, leading to a larger amplitude at the hot side. This is due to the reduced asymmetry of the energy exchanges between the hot and cold sides.

5.2.1.3 Profiles of the thermal terms in the anisothermal configuration

We provide in figure 5.2 the spatial profiles with the semi-local scaling of the three most significant thermal terms at $Re_\tau = 180$ and $Re_\tau = 395$: the thermal conservative energy transfer (figure 5.2(a)), the interaction with variable density kinetic energy (figure 5.2(b)) and the thermal interaction with internal energy (figure 5.2(c)). The interaction with variable density kinetic energy is a thermal energy exchange while the thermal conservative energy transfer and the thermal interaction with internal energy are parts of incompressible exchanges specific to flows with variable fluid properties. The thermal production is not discussed because it is negligible compared to the incompressible production. The three investigated thermal terms show some similarity as their profile is composed of two peaks which are of opposite sign at the hot and cold sides, and have a larger magnitude at the cold side than at the hot side.

The profiles of the thermal terms at the two mean friction Reynolds number are very similar. The effects of the Reynolds number on the thermal terms, very small, are given hereafter. At $Re_\tau = 395$, the position of the extrema is shifted towards the wall compared to $Re_\tau = 180$, reducing the position asymmetry between the hot and cold sides for the extremum closer to the centre of the channel. The amplitude of the extremum closer to the wall is increased slightly whereas the amplitude of the extremum closer to the centre of the channel is decreased. These effects are not significant and do not affect notably the amplitude asymmetry between the hot and cold sides. All in all, the Reynolds number dependence of the thermal terms is very slight, suggesting that the profiles are almost universal within the Reynolds number range of this study. Therefore, we may infer the approximate conclusion that low Reynolds number effects only affect the incompressible terms but are negligible on thermal terms. In other words, the thermal terms are functions of the variations of the mean local fluid properties only and do not substantially depend on the Reynolds number. This shows the relevance of the decomposition of the energy exchanges into incompressible terms and thermal terms.

Since the magnitude of the incompressible terms increases with the mean friction Reynolds number while thermal terms are largely unaffected, the relative contributions of the thermal terms to the energy exchanges decline at high Reynolds number. On the other hand, the relative importance of the thermal terms on the asymmetry between the hot and cold sides become larger, given that the asymmetry between the hot and cold sides is reduced for the incompressible terms. This follows from the assumption that a varying low Reynolds number effect is a significant part of the effect of the temperature gradient on the incompressible terms whereas the thermal terms are only tied to the variations of the mean local fluid properties. Increasing the mean friction Reynolds number reduces the low Reynolds number effects, which gives less weight to the incompressible terms on the asymmetry between the hot and cold sides. However,

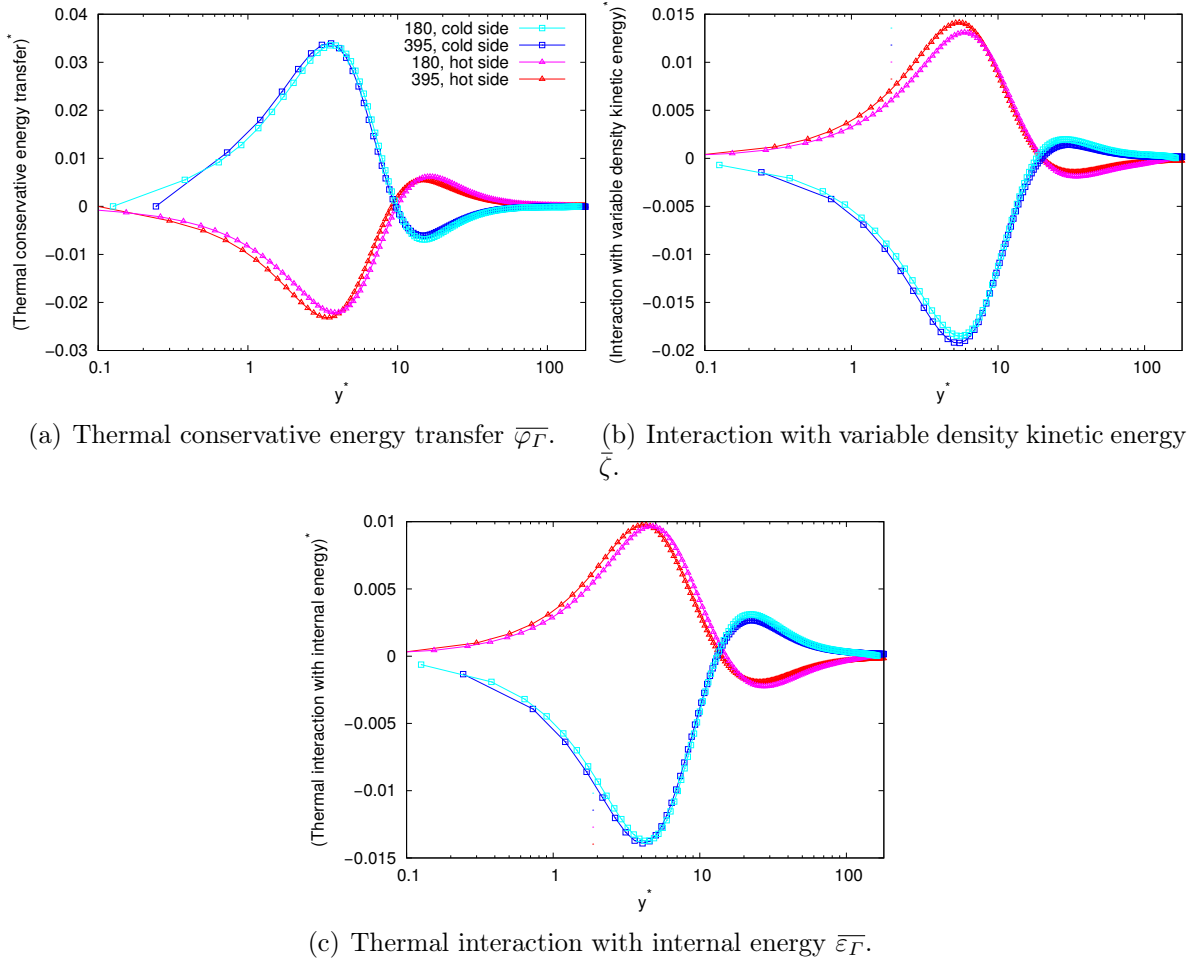


Figure 5.2 – Profiles of the thermal terms of the budget of the half-trace of the velocity fluctuation correlation tensor with the semi-local scaling at $Re_\tau = 180$ and $Re_\tau = 395$.

as noted above, the incompressible terms are also in a large part related to the variations of the local fluid properties since the decomposition does not completely separate the two effects.

5.2.2 Effect of the Reynolds number in the spectral domain

5.2.2.1 Spectra of the incompressible energy exchanges in the anisothermal configuration

The effect of the mean friction Reynolds number on the spectral energy exchanges is investigated. The spectral behaviour of the energy exchanges has been described in Dupuy *et al.* [91] in the incompressible isothermal case and in the anisothermal case. The half-trace of the velocity fluctuation correlation tensor is in the spectral domain predominantly governed by four incompressible spectral energy exchanges: the production, the interscale transport, the conservative energy transfer and the interaction with internal energy. The production of turbulence kinetic energy occurs around $y^* = 12$ and $k^* = 0.07$. The interscale transport redistributes the produced energy among scales, mainly towards small scales but also towards large scales. The energy is, in ad-

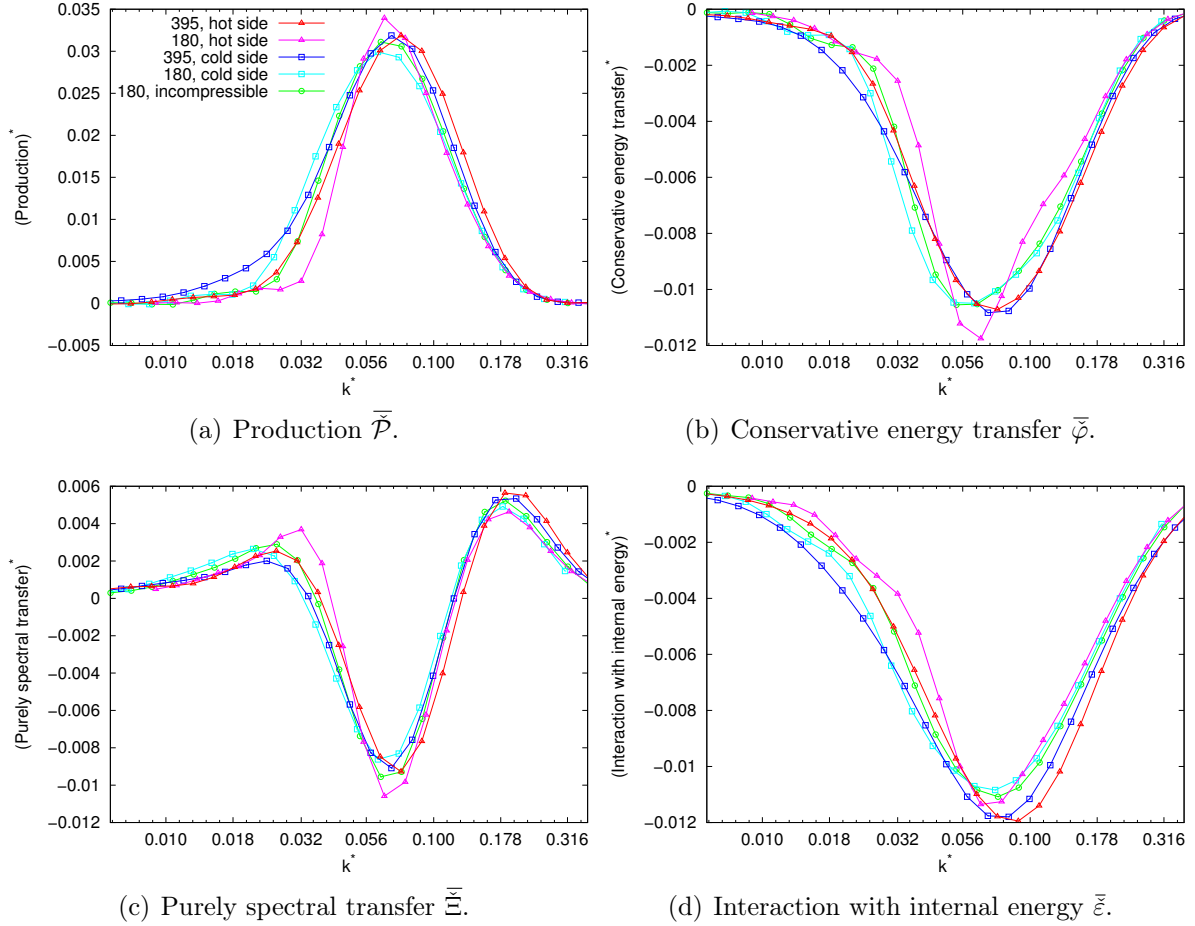


Figure 5.3 – Profiles of the terms of the budget of the half-trace of the velocity fluctuation correlation tensor with the semi-local scaling at $Re_\tau = 180$ and $Re_\tau = 395$ as a function of wavenumber at the location of the spatial peak of production ($y^* \approx 12$).

dition, transferred away and towards the wall by the conservative energy transfer, with a limited scale shift from production. A cut of the spectra at the location of the spatial peak of production (figure 5.3) show that no energy exchange predominates. The produced energy is split almost evenly in three energy processes: its transfer towards the wall, its redistribution towards large and small scales and its conversion into internal energy. Near the wall, takes place most of the interaction with internal energy, that is the conversion of turbulence kinetic energy into internal energy. The production and the purely spectral transfer are negligible. The interaction with internal energy and the conservative energy transfer are thus in balance and occurs at the same wavenumber (figure 5.4). At the center of the channel, the production is negligible. The energy coming from the production area is transported towards small scales where it is dissipated. The conservative energy transfer and the interaction with internal energy thus do not occur at the same wavenumber (figure 5.5). The temperature gradient alters the energy exchanges. They have a lower spectral magnitude at the cold side than at the hot side, but occur at smaller wavenumbers, closer to the wall and handle a larger range of scales.

The spectra of the four incompressible energy exchanges are provided in the set of figures 5.6 to 5.9 with the semi-local scaling. The spectra of the viscous transfer and the

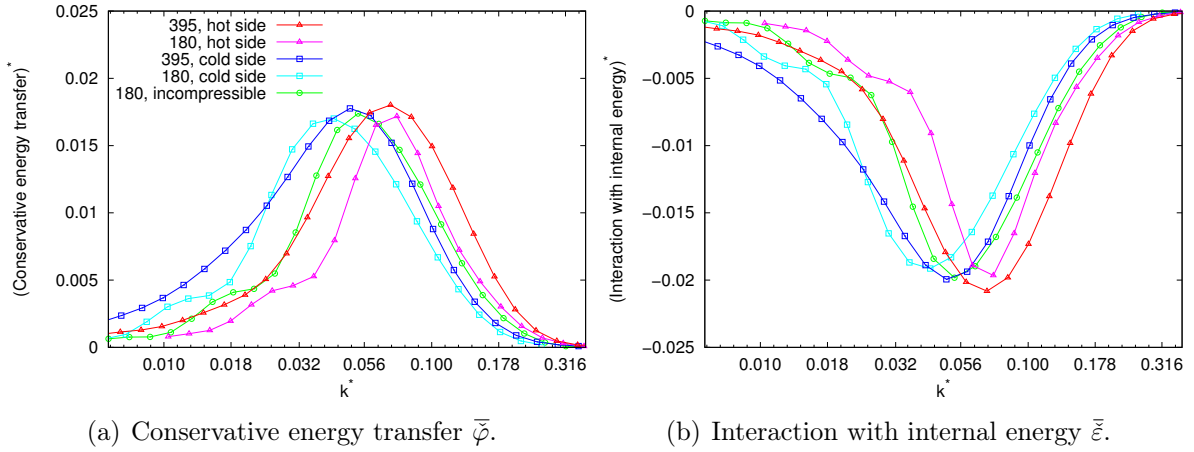


Figure 5.4 – Profiles of the terms of the budget of the half-trace of the velocity fluctuation correlation tensor with the semi-local scaling at $Re_\tau = 180$ and $Re_\tau = 395$ as a function of wavenumber very near to the wall (at $Re_\tau = 180$, $y^* = 0.25$ for the incompressible profile, $y^* = 0.38$ at the cold side and $y^* = 0.15$ at the hot side; at $Re_\tau = 395$, $y^* = 0.73$ at the cold side and $y^* = 0.30$ at the hot side). The production and the purely spectral transfer are negligible.

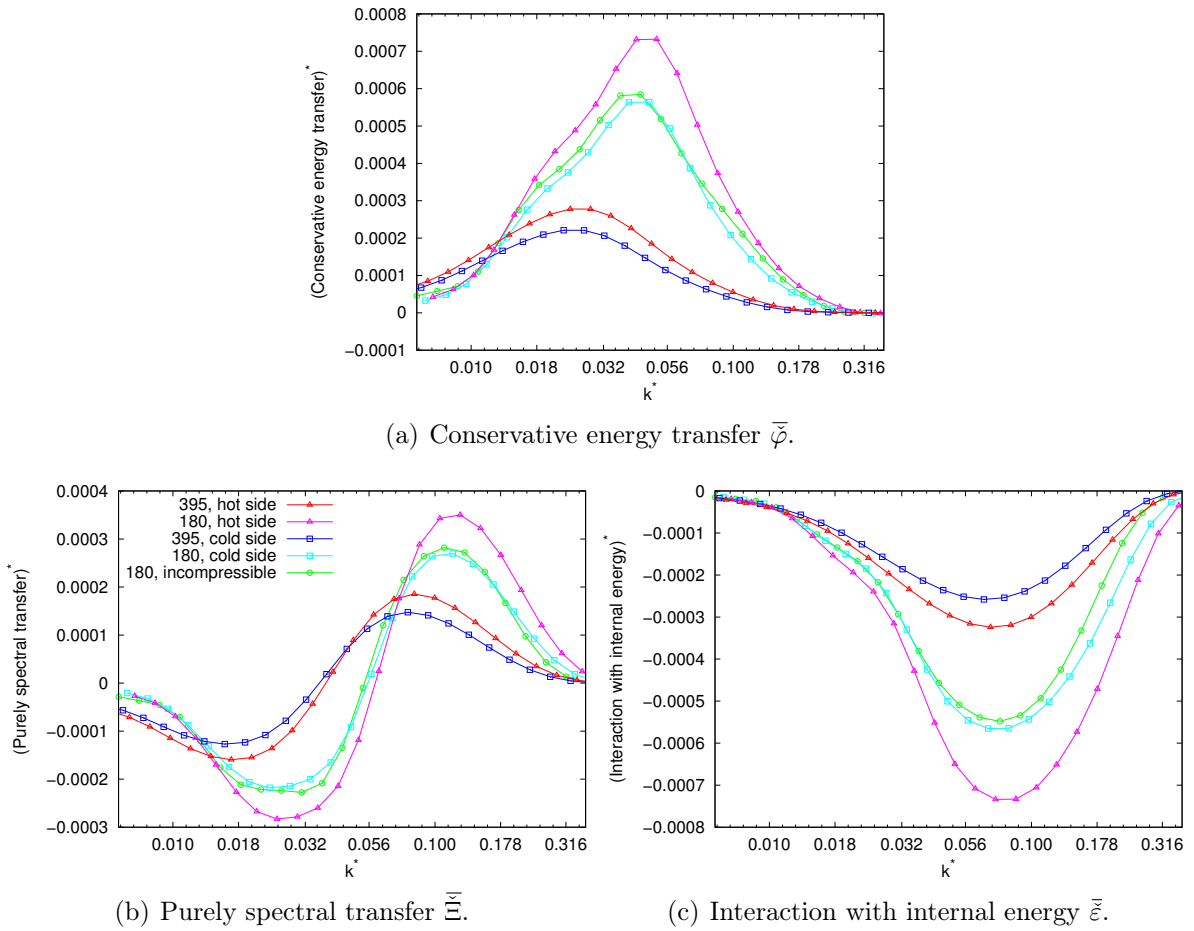


Figure 5.5 – Profiles of the terms of the budget of the half-trace of the velocity fluctuation correlation tensor with the semi-local scaling at $Re_\tau = 180$ and $Re_\tau = 395$ as a function of wavenumber at the center of the channel. The production is negligible.

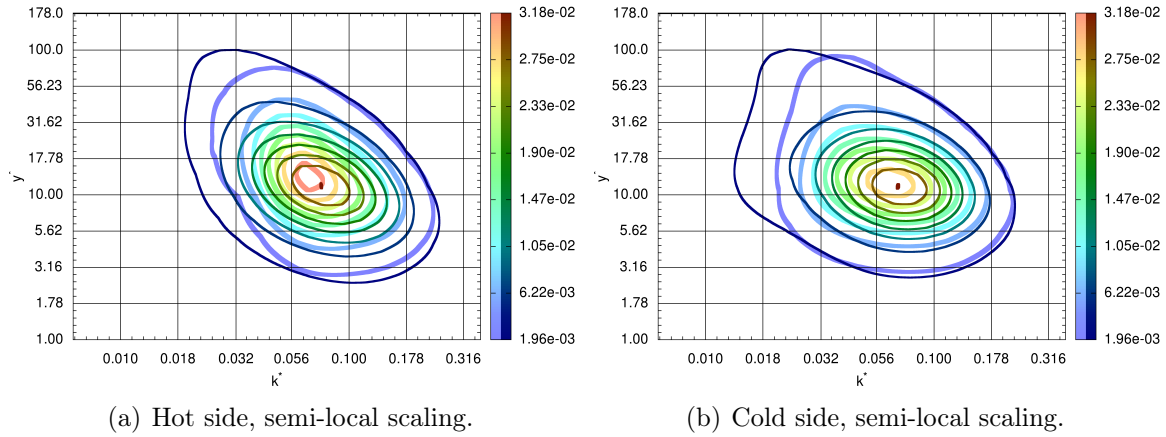


Figure 5.6 – Spectra of the production $\bar{\mathcal{P}}$ with semi-local scaling at $Re_\tau = 180$ (thick lines, light colour) and $Re_\tau = 395$ (thin line, dark colour).

convection, the two most significant parts of the conservative energy transfer, are given in figures 5.10 and 5.11. In addition, the spatial and spectral position and the amplitude of the peaks of each energy exchange are provided in table 5.1. With the semi-local scaling, the general behaviour of the spectral energy exchanges are similar at $Re_\tau = 180$ and $Re_\tau = 395$. As in the spatial domain, we consider that the spectral energy exchanges in the anisothermal configuration are in a large part due to the combination of the variations of the local fluid properties and a varying low Reynolds number effect. These two effects also influence the scales handled by the energy exchanges. A large part of the wavenumber asymmetry related to the variations of the local fluid properties is taken into account by the semi-local scaling. In accordance with the spatial results, the spectral extrema are closer to the wall at higher mean friction Reynolds number. This also applies to the interscale transport (figure 5.8), which has no contribution in the spatial domain. The spectra also suggest that the range of scales handled by the energy exchanges increases with the mean friction Reynolds number, both at large and small scales. This differs from the classical theory of homogeneous isotropic turbulence [254, 288], verified experimentally [108], which predicts a modification of the spectra only at small scales. Possible explanations of this behaviour include an effect of flow anisotropy due to the wall, the numerical procedure and the periodic boundary conditions. A similar behaviour has been obtained by Schiavo *et al.* [262] in incompressible isothermal straight and convergent-divergent channels.

Besides these general effects relevant to all energy exchanges, the production peak (figure 5.6) is shifted towards small scales at $Re_\tau = 395$ compared to $Re_\tau = 180$ at the hot and cold sides. Its amplitude is increased at the cold side and decreased at the hot side, reducing the asymmetry between the hot and cold sides in terms of spectral magnitude. The negative peak of the conservative energy transfer (figure 5.7) follows the same pattern, thereby staying centred on the peak of production. The positive peak behaves like the extremum of the interaction with internal energy, described later. The negative extremum of the interscale transport (figure 5.8) is shifted towards small scales at the higher mean friction Reynolds number while the maximum at large scales is shifted towards large scales at the hot side and towards small scales at the cold side, reducing the asymmetry between the hot and cold sides. The negative area and the

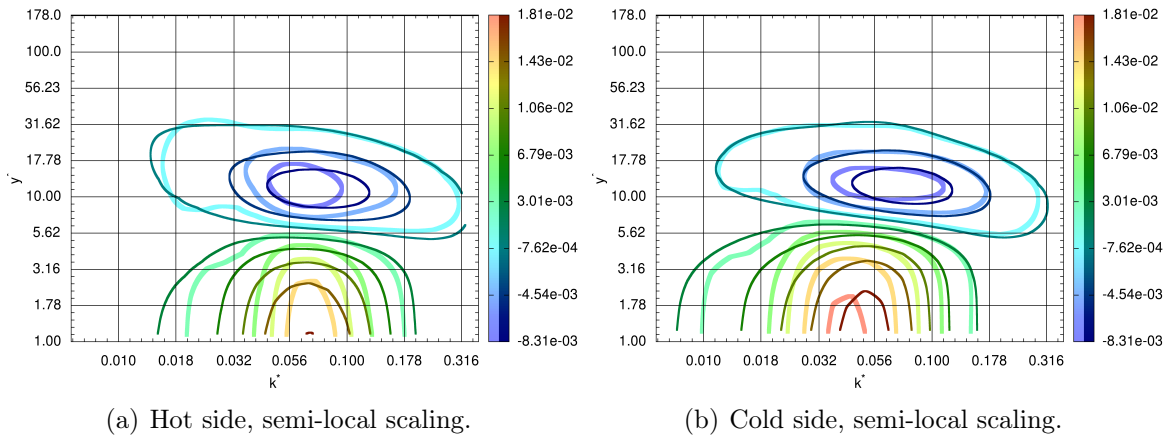


Figure 5.7 – Spectra of the conservative energy transfer $\bar{\varphi}$ with semi-local scaling at $Re_\tau = 180$ (thick lines, light colour) and $Re_\tau = 395$ (thin line, dark colour).

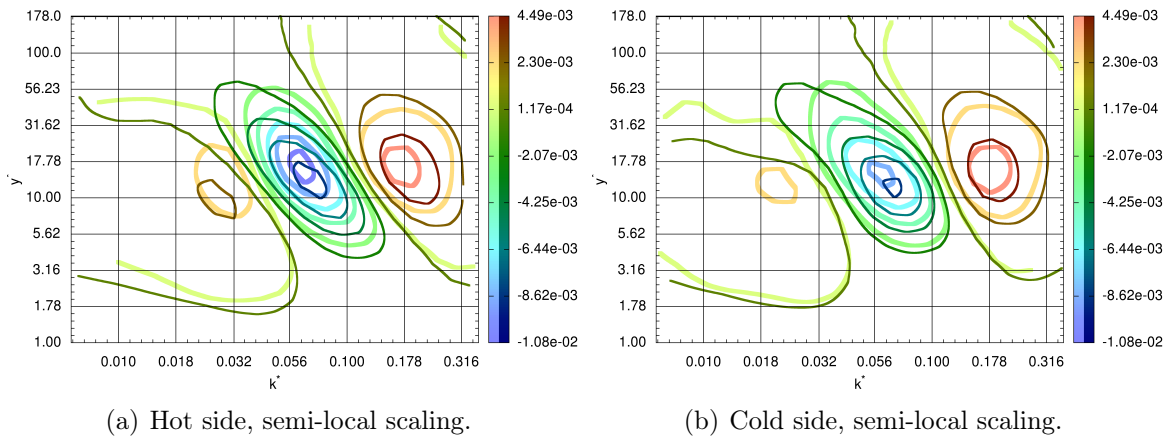


Figure 5.8 – Spectra of the purely spectral transfer $\bar{\Xi}$ with semi-local scaling at $Re_\tau = 180$ (thick lines, light colour) and $Re_\tau = 395$ (thin line, dark colour).

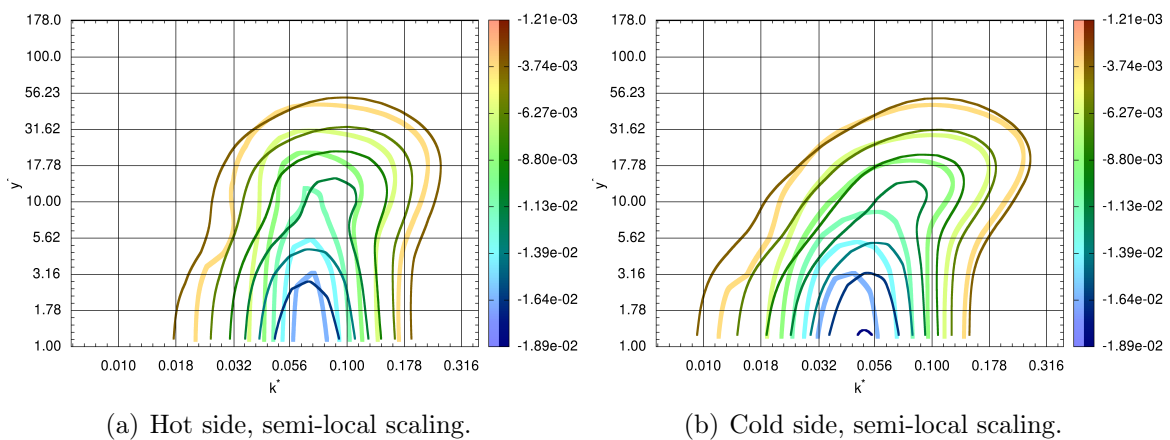


Figure 5.9 – Spectra of the interaction with internal energy $\bar{\varepsilon}$ with semi-local scaling at $Re_\tau = 180$ (thick lines, light colour) and $Re_\tau = 395$ (thin line, dark colour).

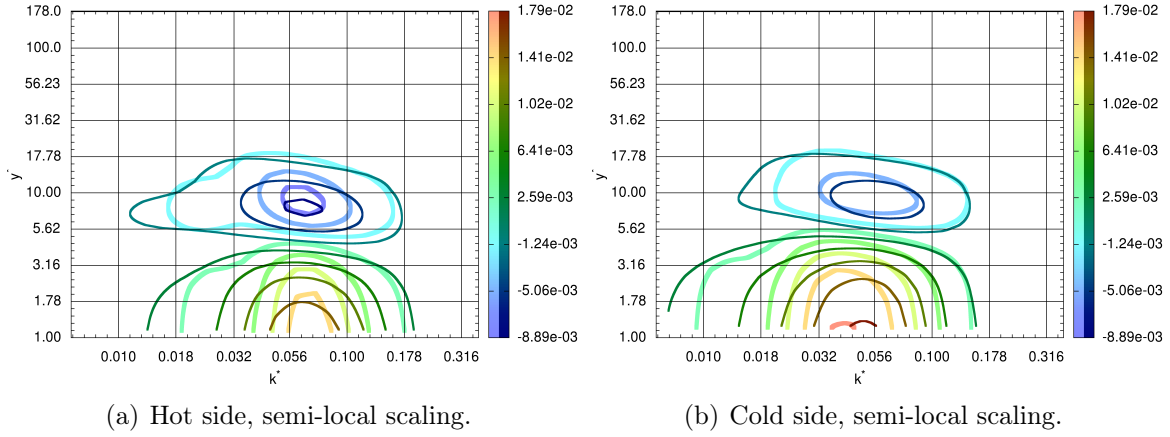


Figure 5.10 – Spectra of the viscous transfer (part of the conservative energy transfer) $\overline{\varphi^v}$ with semi-local scaling at $Re_\tau = 180$ (thick lines, light colour) and $Re_\tau = 395$ (thin line, dark colour).

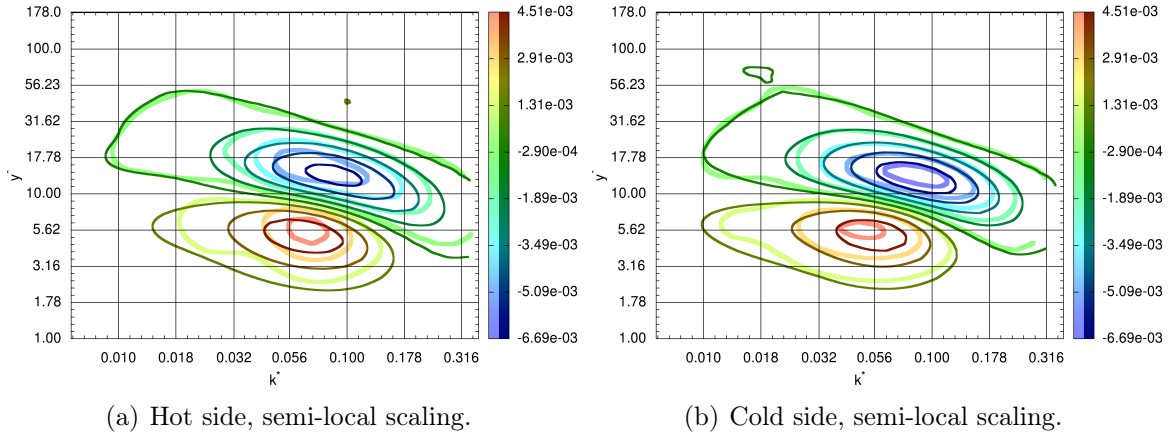


Figure 5.11 – Spectra of the convection (part of the conservative energy transfer) $\overline{\varphi^c}$ with semi-local scaling at $Re_\tau = 180$ (thick lines, light colour) and $Re_\tau = 395$ (thin line, dark colour).

positive area at large scales have a smaller amplitude at $Re_\tau = 395$ than at $Re_\tau = 180$ whereas the positive area at small scales has a larger amplitude. The direct interscale transport towards small scales is therefore strengthened compared to the transport towards large scales. The extremum of the interaction with internal energy (figure 5.9) has a larger amplitude at the higher mean friction Reynolds number. It is also shifted towards large scales at the hot side and towards small scales at the cold side, reducing the wavenumber asymmetry between the hot and cold side. This suggests that the wavenumber asymmetry between the hot and cold sides at $Re_\tau = 180$ results in part from a low Reynolds number effect, that is from the semi-local friction Reynolds number asymmetry between the hot and cold side. The same remark can be made regarding the amplitude asymmetry of the production peak and the wavenumber asymmetry of the positive area at large scales of the interscale transport, although carefulness is required. A more precise knowledge of the different effects of the friction Reynolds number on the spectra in the incompressible isothermal case would be required for a more accurate separation of the different effects of the temperature gradient.

	Side	$Re_\tau = 180$			$Re_\tau = 395$		
		k^*	y^*	Amplitude	k^*	y^*	Amplitude
Production	C	0.062	12.4	3.00×10^{-2}	0.069	11.2	3.19×10^{-2}
	H	0.065	13.5	3.42×10^{-2}	0.076	11.6	3.19×10^{-2}
Conservative energy transfer	C	0.043	0.64	1.92×10^{-2}	0.050	1.21	1.97×10^{-2}
	H	0.074	0.26	1.93×10^{-2}	0.070	0.50	2.00×10^{-2}
	C	0.052	12.4	-1.05×10^{-2}	0.070	11.7	-1.08×10^{-2}
	H	0.066	11.9	-1.18×10^{-2}	0.076	11.2	-1.07×10^{-2}
Purely spectral transfer	C	0.021	12.4	2.65×10^{-3}	0.023	9.76	2.25×10^{-3}
	H	0.032	13.5	3.73×10^{-3}	0.026	10.4	2.59×10^{-3}
	C	0.063	14.0	-9.13×10^{-3}	0.070	11.7	-9.08×10^{-3}
	H	0.064	16.5	-1.21×10^{-2}	0.075	12.4	-9.33×10^{-3}
Interaction with internal energy	C	0.186	14.6	5.29×10^{-3}	0.174	14.8	5.77×10^{-3}
	H	0.187	15.8	5.07×10^{-3}	0.181	15.3	6.24×10^{-3}
	C	0.043	0.38	-1.91×10^{-2}	0.049	0.73	-1.99×10^{-2}
	H	0.074	0.15	-1.97×10^{-2}	0.070	0.30	-2.08×10^{-2}
Viscous transfer	C	0.043	0.64	1.88×10^{-2}	0.050	1.21	1.84×10^{-2}
	H	0.074	0.26	1.90×10^{-2}	0.070	0.50	1.91×10^{-2}
	C	0.050	9.56	-7.81×10^{-3}	0.056	8.80	-7.50×10^{-3}
	H	0.067	8.71	-1.06×10^{-2}	0.065	7.95	-9.45×10^{-3}
Convection	C	0.047	5.58	4.75×10^{-3}	0.054	5.48	5.51×10^{-3}
	H	0.070	5.62	5.20×10^{-3}	0.067	5.15	5.62×10^{-3}
	C	0.090	13.5	-7.29×10^{-3}	0.084	13.2	-8.09×10^{-3}
	H	0.064	15.8	-6.52×10^{-3}	0.089	13.6	-7.30×10^{-3}
Thermal conservative energy transfer	C	0.038	3.87	3.77×10^{-3}	0.052	3.59	3.33×10^{-3}
	H	0.071	4.03	-3.08×10^{-3}	0.057	3.51	-2.49×10^{-3}
	C	0.045	15.1	-9.19×10^{-4}	0.059	13.8	-6.94×10^{-4}
	H	0.053	16.5	9.90×10^{-4}	0.052	14.5	6.51×10^{-4}
Interaction with variable density kinetic energy	C	0.040	5.94	-2.04×10^{-3}	0.054	5.48	-1.88×10^{-3}
	H	0.069	5.92	1.80×10^{-3}	0.066	5.44	1.51×10^{-3}
	C	0.057	27.5	2.09×10^{-4}	0.075	27.2	1.73×10^{-4}
	H	0.050	31.6	-2.56×10^{-4}	0.059	30.3	-1.66×10^{-4}
Thermal interaction with internal energy	C	0.039	4.53	-1.55×10^{-3}	0.052	4.07	-1.37×10^{-3}
	H	0.070	4.79	1.34×10^{-3}	0.056	4.30	1.05×10^{-3}
	C	0.160	19.6	3.53×10^{-4}	0.150	19.8	3.15×10^{-4}
	H	0.150	24.8	-2.39×10^{-4}	0.147	22.7	-2.22×10^{-4}

Table 5.1 – Wavenumber, wall-normal coordinate and amplitude of the local spectral extrema of each term of the equation of the half-trace of the velocity fluctuation correlation tensor with the semi-local scaling at the hot (H) and cold (C) sides at $Re_\tau = 180$ and $Re_\tau = 395$ in the anisothermal configuration.

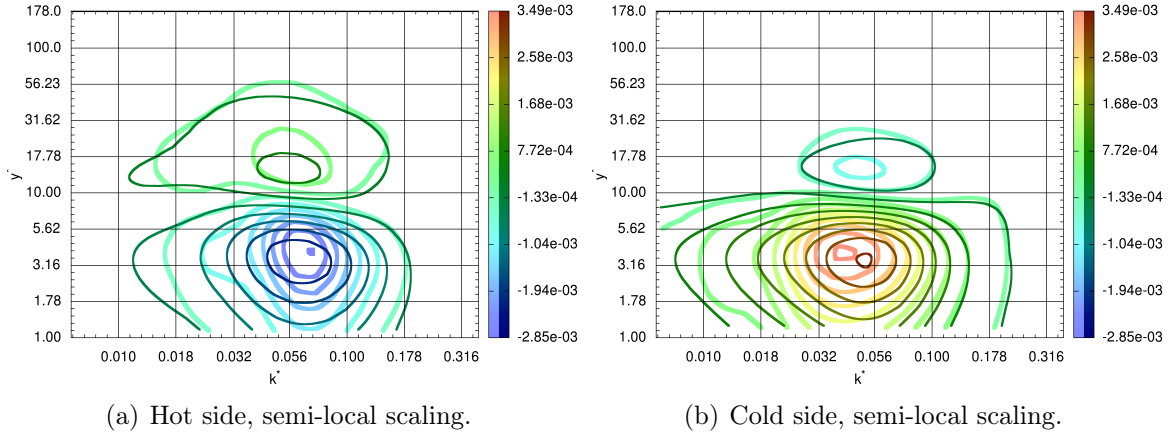


Figure 5.12 – Spectra of the thermal conservative energy transfer $\overline{\varphi}_T$ with semi-local scaling at $Re_\tau = 180$ (thick lines, light colour) and $Re_\tau = 395$ (thin line, dark colour).

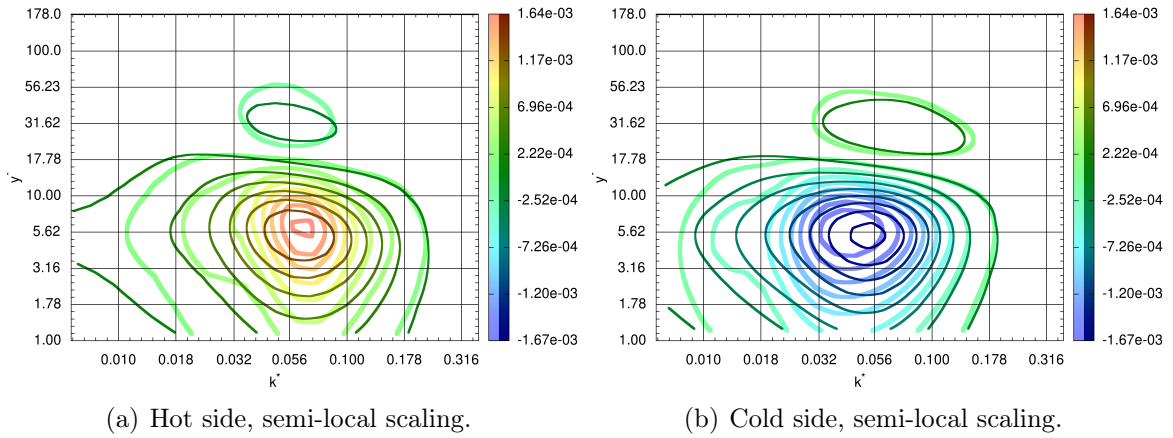


Figure 5.13 – Spectra of the interaction with variable density kinetic energy $\overline{\zeta}$ with semi-local scaling at $Re_\tau = 180$ (thick lines, light colour) and $Re_\tau = 395$ (thin line, dark colour).

5.2.2.2 Spectra of the thermal terms in the anisothermal configuration

The spectra of the three most significant thermal terms include the spectra of the interaction with variable density kinetic energy, a thermal energy exchange, and the thermal conservative energy transfer and the thermal interaction with internal energy, the thermal parts of incompressible energy exchanges. They are given with the semi-local scaling at $Re_\tau = 180$ and $Re_\tau = 395$ in the set of figures 5.12 to 5.14. The effect of the mean friction Reynolds number on the spatial profiles of the thermal terms was found to be small. In the spectral domain, more differences are identified. For the three thermal terms (figures 5.12 to 5.14), the amplitude of the extremum close to the wall is decreased at the hot and cold sides at $Re_\tau = 395$ compared to $Re_\tau = 180$, by around 20% at the hot side and by around 10% at the cold side. This is rather unexpected since the amplitude of the spatial profiles is largely unaffected by the mean friction Reynolds number. The lower spectral magnitude are counterbalanced by the larger range of scales handled. In addition to a spatial shift towards the wall affecting all terms, the extremum close to the wall is shifted towards large scales at the hot side and towards small scales at the cold side. This reduces the wavenumber asymmetry

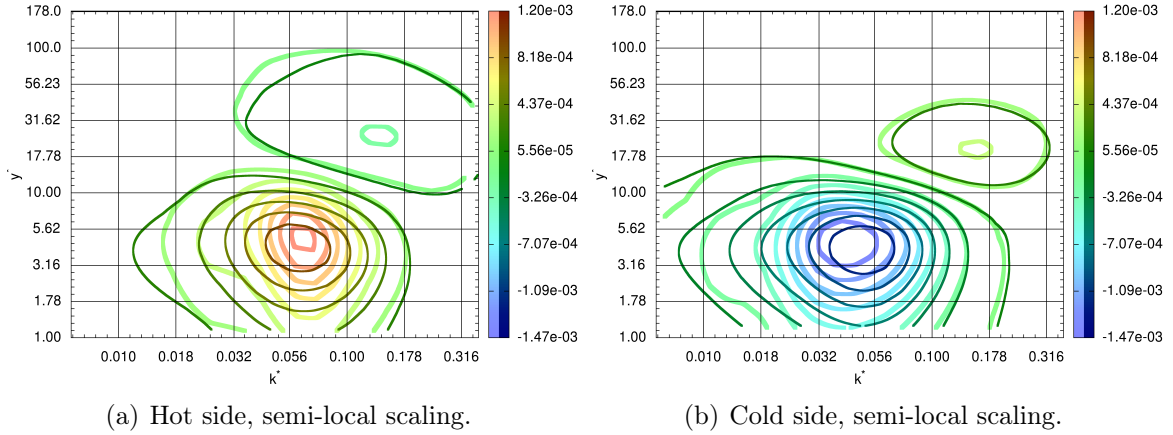


Figure 5.14 – Spectra of the thermal interaction with internal energy $\overline{\varepsilon_T}$ with semi-local scaling at $Re_\tau = 180$ (thick lines, light colour) and $Re_\tau = 395$ (thin line, dark colour).

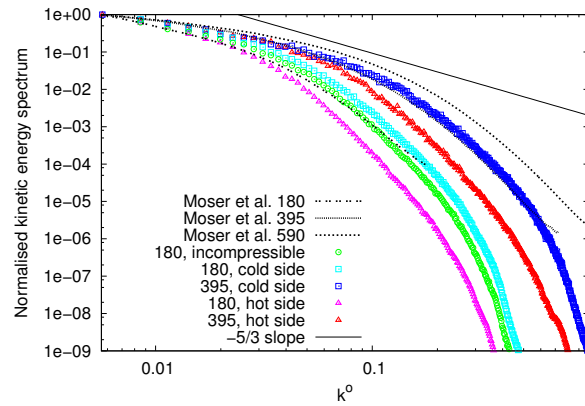


Figure 5.15 – Normalised streamwise spectrum of the half-trace of the velocity fluctuation correlation tensor at $Re_\tau = 180$ and $Re_\tau = 395$ at the location of the spatial peak of production ($y^* \approx 12$).

between the hot and cold sides and suggests that this asymmetry is tied to a low Reynolds number effect. The mean friction Reynolds number seems to modify the spectral behaviour of the thermal terms but does not alter significantly their spatial profiles within the Reynolds number range of this study.

5.2.2.3 Kinetic energy spectrum

The energy exchanges drive the spectrum of the half-trace of the velocity fluctuation correlation tensor, which is also asymmetrised between the hot and cold sides. Figure 5.15 gives the streamwise spectra in the anisothermal channels at $Re_\tau = 180$ and $Re_\tau = 395$ at the location of the spatial peak of production. To compare the slope of the different spectra at the hot and cold sides, the spectra are normalised to one at the smallest wavenumber common to all simulations. The slope of the spectrum is increased at the hot side and decreased at the cold side. The effect is consistent with an effect of the semi-local friction Reynolds number as shown by the reference data of Moser *et al.* [203]. We are not able to distinguish an effect of the variations of the fluid properties on the slope of the spectrum. The variations of the fluid properties may

have a small but insignificant effect on the slope or only affect the amplitude of the spectrum.

5.3 Conclusion of chapter 5

The effect of the Reynolds number on the energy exchanges associated with the half-trace of the velocity fluctuation correlation tensor are investigated in the spatial and spectral domains in a strongly anisothermal low Mach fully developed turbulent channel flow. The study is based on the direct numerical simulation of the channel at the mean friction Reynolds number of $Re_\tau = 180$ and $Re_\tau = 395$. The temperature gradient creates an asymmetry between the energy exchanges at the hot and cold side. The asymmetry can be attributed to the combined effect of the variations of the local fluid properties and a varying low Reynolds number effect, based on the semi-local friction Reynolds number which varies across the channel. The effect of the variations of the local fluid properties is to some extent taken into account by the semi-local scaling, defined using the wall shear-stress and the mean local fluid properties. The low Reynolds number effects, not taken into account by the semi-local scaling, are investigated using reference data in the incompressible isothermal channel. The effects of the semi-local friction Reynolds number variations are smaller at higher mean friction Reynolds number, reducing the asymmetry between the hot and cold sides. With the semi-local scaling, the energy exchanges occur closer to the wall at $Re_\tau = 395$ than at $Re_\tau = 180$, handle a larger range of scales and have a larger spatial amplitude. The energy exchanges are decomposed to isolate the terms specific to flows with variable fluid properties, called thermal terms. The mean friction Reynolds number modifies the spectral behaviour of the thermal terms but does not affect significantly their spatial profile, showing the usefulness of the decomposition.

Chapter 6

Conclusion of part I

The energy exchanges associated with turbulence kinetic energy have been investigated in isothermal and anisothermal low Mach number turbulent channel flows. Chapter 3 addressed the decomposition of kinetic energy to define turbulence kinetic energy using the Reynolds average. The approach has been used to study the energy exchanges associated with turbulence kinetic energy in the spatial and spectral domain. Chapter 4 examined the energy exchanges using the direct numerical simulations of the isothermal and anisothermal channel at $Re_\tau = 180$. The study focused on the effect of the temperature gradient on the energy exchanges and on the asymmetry between the two sides of the channel. Chapter 5 used the direct numerical simulation of the anisothermal channel at $Re_\tau = 395$ to analyse the effect of the Reynolds number on the energy exchanges. The results show the combined influence of all physical phenomena governing the energy exchanges.

In strongly anisothermal channel flows, the energy exchanges associated with turbulence kinetic energy are determined by the walls, the mass flow rate and the temperature gradient. The walls create an inhomogeneity in the wall-normal direction which drives the anisotropy of the flow and the physics of the energy exchanges. The mass flow rate dictates the mean friction Reynolds number. The temperature gradient creates an asymmetry between the energy exchanges at the hot and cold sides. The asymmetry is due to the variations of the local fluid properties and low Reynolds number effects. The variations of the local fluid properties are to some extent taken into account by the semi-local scaling and modify the velocity and length scales of turbulence. The low Reynolds number effects are given by the variations of the semi-local friction Reynolds number and are dependent on the mean friction Reynolds number. Prandtl number variations are neglected and thus out of the scope of the study.

The results suggest that at higher mean friction Reynolds number, the asymmetry between the hot and cold sides can in a large part be predicted by the semi-local scaling. The approximation is relevant as long as the Reynolds number dependence of the scaled profiles is negligible in the incompressible isothermal case. In practice, the knowledge of the semi-local variables may not be sufficient as dimensioned variables are more relevant. In contrast to the classical incompressible scaling, which only involves the friction velocity, the semi-local requires the knowledge of the mean local fluid properties. The reconstruction of the dimensioned profiles from the scaled profiles and the simulation parameters involves in strongly anisothermal flows the friction velocity

and the friction temperature. The experimental verification of the results requires the full development of the flow with regard to velocity and temperature. In particular, the flow should not receive or give any heat to the constant temperature walls, which requires a very long channel.

The energy exchanges associated with turbulence kinetic energy are relevant to Reynolds-averaged Navier–Stokes (RANS) modelling and large-eddy simulation (LES) modelling. RANS simulations are based on the modelling of the Reynolds stress. Following isotropy assumptions, the spatial energy exchanges associated with turbulence kinetic energy are most commonly used for this purpose. Large-eddy simulations are based on the modelling of the small scales of turbulence. This may be thought as the approximation of the small-scale part of the spectral energy exchanges associated with kinetic energy. In homogeneous isotropic incompressible turbulence, the small-scale region is the realm of dissipation. This lead to the construction of purely dissipative models. In strongly anisothermal wall-bounded flows reign many types of energy exchanges in the small-scale region. This makes the large-eddy simulation of these flows more complex.

Part II

Large-eddy simulation

Chapter 7

Introduction of part II

The computational complexity of direct numerical simulation hinders the numerical simulation of three-dimensional turbulent flows in complex geometries [209]. The total number of operations typically grows as the cube of Reynolds number, a finer spatial and temporal discretisation being required to capture the wide range of scales of turbulence [270]. In most practical applications, the Reynolds number is too large to resolve all scales of motion in reasonable time. Hence arises the idea of large-eddy simulation (LES), where the larger scales of motion are resolved and the small scales only considered with regard to their effect on the larger scales [276, 169, 77, 78, 100]. The scale separation may be formalised using spatiotemporal filter to decompose the fields of velocity and of the state variables into large-scale and small-scale part [169]. The large-scale fields are referred to as resolved or filtered. The small-scale fields are referred to as unresolved, subfilter or subgrid.

Large-eddy simulation is based on the assumption of universality of small scales, that is their independence from large-scale driving mechanisms [246, 148]. Small-scale motions are independent from large scales and macroscopic boundary conditions. They are relatively isotropic, self-similar and contain a minority of kinetic energy. Compared to Reynolds-averaged Navier–Stokes modelling, less need to be modelled and more is resolved. It is more computationally expensive and intrinsically unsteady, thus requiring additional computational time for the averaging of the turbulence statistics. However, it gives more detailed flow data and has become a widely recognised and acknowledged turbulence modelling method for engineering applications [241, 204, 217].

Most authors [155] follow an implicit filtering approach, based on the resolution of the equations governing the evolution of the filtered variables. The strategy is similar to an under-resolved numerical simulation with a subgrid-scale model to express the effect of the subgrid-scale on the filtered variables. No actual filtering is carried out, the filter being implicitly determined by the equations resolved, the mesh, the numerical method and the subgrid-scale model [190, 207, 115, 150, 97, 55, 220, 196]. By contrast, in the explicit filtering approach [169, 184, 121, 31, 275], the convective term is filtered explicitly to reduce the number of scales of the solution. The procedure explicitly defines a filter length and significantly reduces the dependency of the method on the grid and numerical errors. However, it also reduces the range of resolved scales as the filter length must be larger than the local cell size. Large-eddy simulation is sometimes also coupled with other modelling approaches. In particular, detached-eddy simulation

[278, 292, 285, 279] and constrained large-eddy simulation [51, 133, 158] combines large-eddy simulation modelling and Reynolds-averaged Navier–Stokes (RANS) modelling.

This introduction gives briefly the main ideas of large-eddy simulation filtering and modelling. This will be useful for the investigation of the large-eddy simulation of strongly anisothermal turbulent flows carried out in the following chapters and introduced at the end of this section.

7.1 Filtering

The separation of the large-scale motions and the small-scales motion may be modelled by the spatiotemporal filtering of the instantaneous flow variables [169]. It is customary to define the low-pass filter as a convolution in an unbounded domain. For any field ψ , the filtered field $\bar{\psi}$ is defined as

$$\bar{\psi}(x, t) = \int_{-\infty}^{\infty} \int_{-\infty}^{\infty} \psi(\xi, \tau) G(x - \xi, t - \tau, x, t) d\xi d\tau, \quad (7.1)$$

where G is the convolution kernel, associated with a characteristic filter time $\bar{\Delta}_t$ and filter length $\bar{\Delta}$. Almost universally, the time filtering is neglected in equation (7.1) [253]. Large-eddy simulation based on time filtering has been investigated by some authors [74, 75, 40, 41, 237, 240, 238]. We here follows the more popular approach based on spatial filtering, the spatial filter implicitly inducing a time filtering. The filter verifies the following fundamental properties:

- conservation of constants, that is the filter normalisation,

$$\bar{1} = 1; \quad (7.2)$$

- linearity, i.e. for any two fields ψ_1 and ψ_2 and constants a_1 and a_2 ,

$$\overline{a_1\psi_1 + a_2\psi_2} = a_1\bar{\psi}_1 + a_2\bar{\psi}_2. \quad (7.3)$$

In general, the filter is in however not idempotent, hence $\overline{\bar{\psi}} \neq \bar{\psi}$ and $\overline{\psi_1\psi_2} \neq \bar{\psi}_1\bar{\psi}_2$. The commutation of the filter with spatial derivation is also not assumed, $\overline{\partial_x\psi} \neq \partial_x\bar{\psi}$.

Three spatial filters are most classically employed in large-eddy simulation in the one-dimensional case [102]:

- The box filter, also called rectangular or top-hat filter, is a weighted volume average. Its filter kernel is given by

$$G(x - \xi) = \frac{1}{\bar{\Delta}} [|x - \xi| < \bar{\Delta}]. \quad (7.4)$$

where $[\cdot]$ are Iverson brackets, evaluating to 1 if the proposition within bracket is satisfied and 0 otherwise. It is associated with a sinc transfer function \hat{G} in the spectral domain,

$$\hat{G}(k) = \frac{\sin(k\bar{\Delta}/2)}{k\bar{\Delta}/2}. \quad (7.5)$$

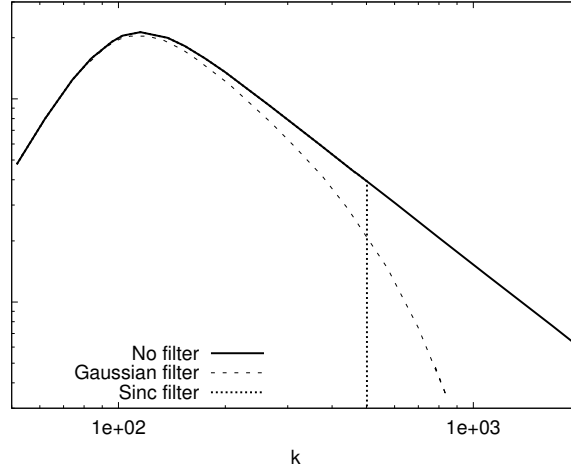


Figure 7.1 – Typical spectra of the turbulence kinetic energy of non-filtered and filtered solutions in homogeneous isotropic incompressible turbulence. The Gaussian and sinc filters have the same filter length, such that $k_c = \pi/\bar{\Delta} = 500$. The scales are arbitrary. From Sagaut [253].

- The sinc filter, also called spectral or sharp cutoff filter, removes frequencies beyond the cutoff frequency $\pi/\bar{\Delta}$ without affecting lower frequencies. Its filter kernel is a sinc function in the spatial domain,

$$G(x - \xi) = \frac{\sin(\pi(x - \xi)/\bar{\Delta})}{\pi(x - \xi)/\bar{\Delta}}. \quad (7.6)$$

It is associated with a rectangular transfer function,

$$\hat{G}(k) = [|k| < \pi/\bar{\Delta}]. \quad (7.7)$$

- The Gaussian filter, also called generalised Weierstrass transform, is based on the normal distribution

$$G(x - \xi) = \sqrt{\frac{\gamma}{\pi\bar{\Delta}^2}} e^{-\frac{\gamma|x-\xi|^2}{\bar{\Delta}^2}}, \quad (7.8)$$

with γ is a constant. The value $\gamma = 6$ is commonly used [253]. The associated spectral transfer function is also a Gaussian function,

$$\hat{G}(k) = e^{-\frac{\bar{\Delta}^2 k^2}{4\gamma}}. \quad (7.9)$$

The modification of the energy spectrum by the Gaussian and sinc filter are compared on figure 7.1. The box filter has a compact support in the physical domain but is nonlocal in the spectral domain. Conversely, the sinc filter is nonlocal in the spatial domain and local in the spectral domain. The Gaussian filter is nonlocal both the spatial and spectral domains. The sinc filter is idempotent, thus non-invertible. Besides, the sinc filter is not positive. Therefore, it does not ensure positivity of the subgrid-scale variance $\overline{\psi^2} - \bar{\psi}^2$ for any field ψ , and of the subgrid-scale kinetic energy in particular [308]. These three continuous filters are ideal, and are approximated in practice.

Multidimensional filtering may be expressed as a sequence of one-dimensional filters on the condition that the filter is separable [25],

$$\bar{\psi} = \overline{\overline{\psi}^{xyz}}, \quad (7.10)$$

where $\overline{\cdot}^x$, $\overline{\cdot}^y$ and $\overline{\cdot}^z$ are one-dimensional filters. This form is computationally advantageous compared to a three-dimensional filter.

7.2 Modelling

The evolution equation of the filtered variables cannot be inferred from the flow governing equations because the filter does not, in general, commute with spatial derivation and multiplication. The non-commutations can be represented with the introduction of subgrid terms. To close the system of equations, the subgrid terms are modelled using an algorithm computable in a large-eddy simulation. The models are called subgrid-scales models. The addition of the subgrid-scale models should not violate the symmetry properties of Navier–Stokes equations [280, 216, 242], including Galilean invariance [107], and the laws of thermodynamics. It is also desirable that the models have no effects in flows without subgrid-scale generation, and conversely in flows with an interscale energy transport towards subgrid scales [304]. In wall-bounded flows, the consistency of the asymptotic near-wall behaviour of the model with the exact subgrid term is considered very important [213, 214]. An excellent review of the physical properties of some subgrid-scale models may be found in Silvis *et al.* [273].

The filter-derivative non-commutation subgrid terms are proportional to the local filter length [300, 301]. Therefore, the filter and the derivative generally only commute for space-independent filter length in an unbounded domain [116]. However, many flows exhibit large variations of length scales, rendering the use of the space-independent filter length computationally impracticable. In that case, the use of specifically designed filters, commuting with the derivative up to an arbitrary order, has been suggested [300, 302]. The modelling of the filter-derivative non-commutation subgrid term may also be considered [117]. More often however, the filter-derivative non-commutation subgrid terms are simply neglected to simplify the expression of the filtered governing equations [169].

In the incompressible isothermal case, the filtering of the Navier–Stokes equations only involve one filter-multiplication non-commutation subgrid term, related to the momentum convection, and often called subgrid-scale tensor,

$$F_{U_j U_i} = \overline{U_j U_i} - \overline{U_j} \overline{U_i}. \quad (7.11)$$

As will be discussed in the following chapters, the filtering leads to additional subgrid terms in strongly anisothermal turbulent flows. This will not be discussed further in this introduction because most modelling strategies are in common. The modelling of the subgrid-scale tensor has received a lot of attention from the literature. Several modelling strategies have been developed. Algebraic or zero-equation models express the subgrid-scale model as a function of the filtered variables and the filter length scales. They differ from models requiring the resolution of one or more additional transport equations to compute the subgrid-scale model [253, 181]. This thesis focus only on algebraic models, of the form

$$F_{U_j U_i} \approx \tau_{ij}^{\text{mod}}(\overline{\mathbf{U}}, \overline{\Delta}), \quad (7.12)$$

where the function $\tau_{ij}^{\text{mod}}(\mathbf{U}, \overline{\Delta})$ is a subgrid-scale model. Orthogonal to this distinction is the classification of subgrid-scale models into structural and functional models [253].

7.2.1 Structural models

Structural models approximate the effect of the filter without assumptions on the physical nature of the effect of the subgrid term. A review of structural models is given by Lu and Rutland [181]. We here describe the two most popular zero-equation approaches:

Gradient Model

The gradient model [169, 64] is based on a Taylor series expansion of the filter. Equation (7.1) may be approximated as

$$\bar{\psi} = \sum_{n=1}^{\infty} \gamma_{2n} \frac{\partial^{2n} \psi}{\partial x^{2n}}, \quad (7.13)$$

for an even filter kernel. The coefficients are given by $\gamma_n = \bar{\Delta}^n / (2^n (n+1)!)$ for a box filter and $\gamma_n = (n-1)! \bar{\Delta}^n / (12^{n/2} n!)$ for a gaussian filter [137]. The Van Cittert iterative deconvolution [299, 283, 284], gives a series expansion of the inverse of the filter,

$$G^{-1} = \sum_{n=1}^{\infty} (1-G)^n. \quad (7.14)$$

Using (7.13) and (7.14), an approximation of the subgrid-scale tensor can be obtained from

$$\overline{U_j U_i} - \bar{U}_j \bar{U}_i = \overline{\overline{U_j}^{-1} \overline{U_i}^{-1}} - \bar{U}_j \bar{U}_i. \quad (7.15)$$

At the second order, this expression leads to

$$\tau_{ij}^{\text{Grad.}}(\bar{\mathbf{U}}, \bar{\Delta}) = \frac{1}{12} G_{ij}(\bar{\mathbf{U}}, \bar{\Delta}) = \frac{\bar{\Delta}_k^2}{12} \frac{\partial \bar{U}_i}{\partial x_k} \frac{\partial \bar{U}_j}{\partial x_k}, \quad (7.16)$$

with the box and gaussian filter. We will use the generalised definition

$$\tau_{ij}^{\text{Grad.}}(\bar{\mathbf{U}}, \bar{\Delta}) = \frac{C^{\text{Grad.}}}{12} G_{ij}(\bar{\mathbf{U}}, \bar{\Delta}) = C^{\text{Grad.}} \frac{\bar{\Delta}_k^2}{12} \frac{\partial \bar{U}_i}{\partial x_k} \frac{\partial \bar{U}_j}{\partial x_k}. \quad (7.17)$$

The classical gradient model is recovered using $C^{\text{Grad.}} = 1$.

Scale-similarity model

The scale-similarity model [14, 180] assumes that structure of subgrid scales is similar to the structure of the smallest resolved scales. Using a test filter ($\widehat{\cdot}$), explicitly computed in a large-eddy simulation, the subgrid-scale tensor is approximated as

$$\tau_{ij}^{\text{Simil.}}(\bar{\mathbf{U}}, \bar{\Delta}) = C^{\text{Simil.}} L_{ij}(\bar{\mathbf{U}}) = C^{\text{Simil.}} \left(\widehat{\overline{U_j U_i}} - \widehat{\bar{U}_j} \widehat{\bar{U}_i} \right), \quad (7.18)$$

The original version of the model uses a second application of the large-eddy simulation filter and $C^{\text{Simil.}} = 1$ [14]. Introducing the Taylor series expansion (7.13) of the filter in this scale-similarity model is equivalent to the gradient model (7.16) at the second order [42, 314]. However, the two methods are not identical since the higher-order terms are different.

7.2.2 Functional models

Functional models, also called eddy-viscosity models, assume that the effect of subgrid scales is similar to viscous effects, hence strictly dissipative. The main action of subgrid scales is the dissipation of the energy they receive from large scales, thus they may be modelled with a subgrid-scale model ensuring the dissipation of the energy that should have been transported from large scales to small scales [98]. These models rely on the energy cascade model of homogeneous isotropic turbulence, challenged as seen in part I in wall-bounded turbulent flows, the wall adding a spatial energy transfer to the energy exchanges and an inverse energy cascade, towards large scales, to the interscale transport. The prediction of the inverse energy cascade is required for an accurate estimation of the subgrid-scale dissipation but can lead to numerical instabilities [82, 135, 194, 7, 58, 311].

Eddy-viscosity models assume that the subgrid term is aligned with the rate of deformation tensor [32],

$$\tau_{ij}^{\text{mod}}(\mathbf{U}, \overline{\Delta}) = -2\nu_e^{\text{mod}} \left(S_{ij} - \frac{1}{3} S_{kk} \right), \quad (7.19)$$

with $S_{ij} = \frac{1}{2} (\partial_j \bar{U}_i + \partial_i \bar{U}_j)$ the rate of deformation tensor and ν_e^{mod} the eddy-viscosity, whose expression depends on the particular model used. Most authors consider that only the deviatoric part of the subgrid term is modelled,

$$\tau_{ij} - \frac{1}{3} \tau_{kk} = -2\nu_e^{\text{mod}} \left(S_{ij} - \frac{1}{3} S_{kk} \right), \quad (7.20)$$

as the right-hand side of equation (7.20) has zero trace. The modelling of the isotropic part of the subgrid-scale tensor τ_{kk} has been suggested by Yoshizawa [320][see also 281, 189] but is either neglected or ignored by most authors, on the basis that it can be included as part of the filtered pressure. In practice, this is equivalent to the use of (7.19), modifying only the interpretation of the results.

The first and most well-known eddy-viscosity model is the Smagorinsky model [276]. This model gives satisfactory results in homogeneous isotropic incompressible turbulence [187] but does not generalise well to more complex geometries. A fundamental problem of the Smagorinsky model [276] is that it is based on an invariant that does not asymptotically vanish near walls. Various alternative eddy-viscosity models have been proposed in the literature. The list includes the Smagorinsky model [276], the WALE model [213], the Vreman model [304], the Kobayashi model [147] the shear-improved Smagorinsky model [174], the Sigma model [214], the QR model [303], the VSS model [252], the S3PQR model [294], the AMD model [250], and the vortex-stretching model [273]. In addition, damping function and wall models can be used to improve the asymptotic near-wall behaviour of the model [230, 231, 228, 227].

7.2.3 Mixed models

Mixed models combine structural and functional models. The goal is to combine the perceived advantages of both type of modelling, namely the capture of the structure and anisotropy of the subgrid term for structural models, and the prediction of the interscale energy transport between resolved scales and subgrid scales for functional models. The main family of mixed models, introduced by Bardina *et al.* [14], expresses

the subgrid term as a linear combination of a structural model and a functional model, often the Smagorinsky model [276]. The multiplicative mixed models of Ghaisas and Frankel [113, 114] may also be seen as mixed models.

7.2.4 Dynamic models

Most algebraic models involve a multiplicative constant, determined theoretically or empirically, whose optimal value might depend on the physics of the flow investigated. Germano *et al.* [112] proposed a method to dynamically adjust the value of this multiplicative constant, reducing the number of parameters of the model. The method is essentially an algorithm that allow the construction from any algebraic model $\tau_{ij}^{\text{mod}}(\mathbf{U}, \overline{\Delta})$ of a new model $\tau_{ij}^{\text{dyn,mod}}(\mathbf{U}, \overline{\Delta})$, referred to as the dynamic version of the model,

$$\tau_{ij}^{\text{dyn,mod}}(\overline{\mathbf{U}}, \overline{\Delta}) = C^{\text{dyn}} \tau_{ij}^{\text{mod}}(\overline{\mathbf{U}}, \overline{\Delta}). \quad (7.21)$$

The determination of the parameter C^{dyn} is carried out using a test filter ($\widehat{\cdot}$) and the assumption, following the scale-similarity hypothesis, that the above formula holds with the same parameter C^{dyn} at both the level of the large-eddy simulation filter and the level of the test filter,

$$\overline{U_j U_i} - \overline{U_j} \overline{U_i} \approx C^{\text{dyn}} \tau_{ij}^{\text{mod}}(\overline{\mathbf{U}}, \overline{\Delta}), \quad (7.22)$$

$$\widehat{\overline{U_j U_i}} - \widehat{\overline{U_j}} \widehat{\overline{U_i}} \approx C^{\text{dyn}} \tau_{ij}^{\text{mod}}(\widehat{\overline{\mathbf{U}}}, \widehat{\overline{\Delta}}). \quad (7.23)$$

The value of $\widehat{\overline{\Delta}}$ is best approximated as $\widehat{\overline{\Delta}} = (\overline{\Delta}_i + \widehat{\Delta}_i)^{1/2}$ for Gaussian and box filters [111, 307]. Filtering (7.22), and assuming

$$\widehat{\overline{C^{\text{dyn}} \tau_{ij}^{\text{mod}}(\overline{\mathbf{U}}, \overline{\Delta})}} = C^{\text{dyn}} \widehat{\overline{\tau_{ij}^{\text{mod}}(\overline{\mathbf{U}}, \overline{\Delta})}}, \quad (7.24)$$

it follows that

$$L_{ij}(\overline{\mathbf{U}}) \approx C^{\text{dyn}} m_{ij}(\overline{\mathbf{U}}, \overline{\Delta}), \quad (7.25)$$

where $L_{ij}(\overline{\mathbf{U}})$ is given by equation (7.18) and

$$m_{ij}(\overline{\mathbf{U}}, \overline{\Delta}) = \tau_{ij}^{\text{mod}}(\widehat{\overline{\mathbf{U}}}, \widehat{\overline{\Delta}}) - \widehat{\overline{\tau_{ij}^{\text{mod}}(\overline{\mathbf{U}}, \overline{\Delta})}}. \quad (7.26)$$

The parameter C^{dyn} may be determined from relation (7.25) as all terms are computable in a large-eddy simulation. Dynamic procedures aim to minimise the residual

$$E_{ij}(\overline{\mathbf{U}}, \overline{\Delta}) = L_{ij}(\overline{\mathbf{U}}) - C^{\text{dyn}} m_{ij}(\overline{\mathbf{U}}, \overline{\Delta}). \quad (7.27)$$

This relation needs to be contracted to determine a single value of the parameter. The non-contraction of equation (7.27) defines tensorial parameters C_{ij}^{dyn} , extending the dynamic procedure to the construction of models of the form

$$\tau_{ij}^{\text{ten,dyn,mod}}(\overline{\mathbf{U}}, \overline{\Delta}) = C_{ij}^{\text{dyn}} \tau_{ij}^{\text{mod}}(\overline{\mathbf{U}}, \overline{\Delta}), \quad (7.28)$$

where no implicit summations over i and j are assumed.

The computed parameter exhibits a large spatiotemporal variability and may take negative values. To increase the robustness of the parameter calculation, a clipping procedure or a local, global or Lagrangian averaging should be introduced [118, 195, 221].

A non-global averaging may be used to adapt the model to the local structure of the flow and improve its asymptotic near-wall behaviour, particularly in the case of the Smagorinsky model [276]. However, this is numerically unstable if the subgrid-scale model has already a proper asymptotic near-wall behaviour [19]. Global averaging may then be used [321, 162, 19, 274], following Park *et al.* [221] who extended previous dynamic procedure and suggested a new method based on the global equilibrium hypothesis [71].

We here describe three approaches, given as follows:

Scalar dynamic method

Following the approach of Lilly [177], the parameter is computed to minimise the variance of the residual,

$$\frac{\partial \langle E_{kl} E_{kl} \rangle}{\partial C^{\text{dyn}}} = 0, \quad (7.29)$$

leading to

$$C^{\text{dyn}} = \frac{\langle m_{ij}(\bar{\mathbf{U}}, \bar{\mathbf{\Delta}}) L_{ij}(\bar{\mathbf{U}}) \rangle}{\langle m_{mn}(\bar{\mathbf{U}}, \bar{\mathbf{\Delta}}) m_{mn}(\bar{\mathbf{U}}, \bar{\mathbf{\Delta}}) \rangle}. \quad (7.30)$$

Tensorial dynamic method

As in the (scalar) dynamic method, the tensorial parameter of the model is computed dynamically to minimise for all i and j the variance of the residual [1],

$$\frac{\partial \langle E_{kl} E_{kl} \rangle}{\partial C_{ij}^{\text{dyn}}} = 0 \quad \text{for all } i \text{ and } j, \quad (7.31)$$

leading to

$$C_{ij}^{\text{dyn}} = \frac{\langle m_{ij}(\bar{\mathbf{U}}, \bar{\mathbf{\Delta}}) L_{ij}(\bar{\mathbf{U}}) \rangle}{\langle m_{ij}(\bar{\mathbf{U}}, \bar{\mathbf{\Delta}}) m_{ij}(\bar{\mathbf{U}}, \bar{\mathbf{\Delta}}) \rangle}. \quad (7.32)$$

where no implicit summations over i and j are assumed.

Zero-residual dynamic method

The tensorial parameter of the model is computed dynamically to zero for all i and j the statistical average of the residual,

$$\langle E_{ij} \rangle = 0 \quad \text{for all } i \text{ and } j, \quad (7.33)$$

leading to

$$C_{ij}^{\text{dyn}} = \frac{\langle m_{ij}(\bar{\mathbf{U}}, \bar{\mathbf{\Delta}}) L_{ij}(\bar{\mathbf{U}}) \rangle}{\langle m_{ij}(\bar{\mathbf{U}}, \bar{\mathbf{\Delta}}) m_{ij}(\bar{\mathbf{U}}, \bar{\mathbf{\Delta}}) \rangle}. \quad (7.34)$$

where no implicit summations over i and j are assumed.

The average $\langle \cdot \rangle$ may be computed as an averaging over the homogeneous directions or as a volume average for a global determination of the parameter [221]. The formula needs to be adapted if a mixed model is used [199] or if only the deviatoric part of the subgrid term is modelled.

7.3 Objectives of this work

We investigate the large-eddy simulation of strongly anisothermal turbulent flows. The validation of subgrid-scale models is carried out using a priori tests and a posteriori tests. A priori tests compare the subgrid-scale models to the subgrid term computed from the filtering of experimental or numerical three-dimensional flow fields. A posteriori tests investigate the predictions of large-eddy simulations implementing the subgrid-scale models. It is difficult to assess the consequence of the errors found in a priori tests with regard the predictive capability of the models in large-eddy simulation. For instance, it is well-known that the gradient model [169] and the scale-similarity model [14] give poor performances used alone in a posteriori tests despite being well correlated with the exact subgrid term in a priori tests [14, 253, 259, 24, 141]. On the other hand, the a posteriori evaluation of subgrid-scale models is complicated by the strong dependence of the results of the large-eddy simulations on the numerical method. Besides, it is often difficult to assess from the results of a posteriori tests the underlying cause of the failure of the models [253].

The analysis is carried out within the context of the simulation of strongly anisothermal turbulent channel flows with the low Mach number equations. Chapter 8 studies the filtering of the low Mach number equations from the direct numerical simulations presented in section 1.3 to identify the relevant subgrid terms. The coupling between temperature and turbulence leads to additional subgrid terms. Chapter 9 addresses their modelling of strongly anisothermal turbulent flows from a priori tests, also using the results of the direct numerical simulations presented in section 1.3 Chapter 10 carries on the study of the subgrid-scale modelling from a posteriori tests at $Re_\tau = 180$ and $Re_\tau = 395$.

Chapter 8

Study of the large-eddy simulation subgrid terms of a low Mach number anisothermal channel flow

8.1 Introduction of chapter 8

The large-eddy simulation of strongly anisothermal low Mach number flows involve additional specific subgrid terms compared to the incompressible isothermal configuration because of the variations of the fluid properties. The interaction between temperature and turbulence creates density-velocity correlations and nonlinearities related to the viscous shear-stress and the conductive heat flux, which might require modelling. The scale separation can be approached from the filtering of any formulation of the Navier–Stokes equations or appropriate approximation of the Navier–Stokes equations. In this chapter, we investigate the filtering of the low Mach number equations, suited to the flows found in solar receivers. The subgrid terms arising from the filtering of the low Mach number equations are classified to identify the most significant filter-derivative non-commutation subgrid terms and filter-multiplication non-commutation subgrid terms. The analysis is carried out with different formulations of the filtered low Mach number equations. This strategy seeks to identify the most well-suited formulation.

The subgrid terms of the low Mach number equations depend on the set of variables resolved in the large-eddy simulation. In compressible flows, most authors use a change of variable in which the filtered variables are weighted by density. This density-weighted filter is called Favre filter. The unweighted filter is called classical filter. The expression of the filtered governing equations in terms of Favre-filtered variables removes the subgrid terms related to density-velocity correlations. However, its relevance is not clear for the low Mach number equations from a modelling perspective because the velocity appears without the density in the energy conservation equation. The assessment of the relevance of the classical filter and the Favre filter should take into account the manner the equations are arranged upon filtering. To make the comparison of the two approaches as fair as possible, we investigate both the filtering of the momentum conservation equation, in which the velocity appears along with density, and the filtering of the velocity transport equation, in which the velocity appears without the density.

The filtering of the low Mach number equations is investigated from the results of the direct numerical simulations of fully developed strongly anisothermal channel flows at $Re_\tau = 180$ and $Re_\tau = 395$ presented in section 1.3. The strength of the subgrid terms is compared according to their quadratic mean. The filtering is carried out with box filters of various filter widths. The box filter is simple, fits well with the intuitive idea of spatial averaging and is an approximation of the implicit filter associated with finite differences methods [248, 263]. The spectral filter is more appropriate to represent the implicit filter associated with spectral methods. The Gaussian filter has a non-compact support and would need to be approximated with a windowed Gaussian filter. We verified that the results were similar using the second-order Taylor series expansion (7.13) of the filter up to filter length six times as large as the local cell size, suggesting that the dependence of the analysis on the choice of the filter is not strong.

8.2 Paper 3

This section reproduces the paper D. Dupuy, A. Toutant, and F. Bataille. Study of the large-eddy simulation subgrid terms of a low mach number anisothermal channel flow. *International Journal of Thermal Sciences*, 135:221–234, 2018 [90].

Abstract

The subgrid terms of the low Mach number equations are investigated in a strongly anisothermal low Mach number flow. The filtered low Mach number equations are established in three formulations in order to compare the unweighted classical filter and the density-weighted Favre filter on the one hand, and the filtering of the momentum conservation equation and the velocity transport equation on the other hand. In the three formulations, we establish the filtered equations of mass conservation, momentum conservation, energy conservation, of the ideal gas law and of the resolved kinetic energy transport equation. The magnitude of all subgrid terms is assessed a priori in the three formulations using the results of direct numerical simulations of a strongly anisothermal fully developed turbulent channel flow. The classification of the subgrid terms gives the relevance of various effects of the temperature gradient.

8.2.1 Introduction

In solar power towers, the solar flux is concentrated towards the solar receiver, wherethrough its energy is transferred to the heat transfer fluid. The optimisation of the internal geometry of the solar receiver is a key challenge for the efficiency of solar power towers. The thermal exchange towards the fluid should be maximised while the pressure loss should be minimised. This long-term goal would benefit from accurate numerical simulations of the low Mach number strongly anisothermal turbulent flows found in solar receivers [265]. However, high numerical costs prevent the direct numerical simulation (DNS) of all scales of turbulence in the conditions of a real solar receiver. An effective alternative is the thermal large-eddy simulation (LES). The LES

resolves the largest scales of the flow and models the effect of the small scales on the large scales. The method requires subgrid-scale models suited to low Mach number strongly anisothermal turbulent flows [10, 11, 91].

The subgrid terms can be investigated a priori from high-resolution three-dimensional flow fields. A priori tests were carried out with particle image velocimetry measurements [180, 43] and DNS results, in incompressible isotropic homogeneous turbulence [64, 1], rotating turbulence [182], channel flows [229, 175], in two phase divergence-free flows [291], in passive and active scalar decaying homogeneous turbulence [56, 113] and in flows with purely compressible effects, in a temporal shear layer [309, 310, 306] and in freely decaying homogeneous isotropic turbulence [189]. In flows with variable fluid properties, the analysis can be carried out using two large-eddy simulation filters, the unweighted classical filter and the density-weighted Favre filter [94]. The Favre filter is used by most authors in compressible flows [109]. The classical filter has been employed by Yoshizawa [320], Sun and Lu [286], Boersma and Lele [27], Bodony and Lele [26] and Sidharth *et al.* [272]. In addition, the set of subgrid terms to model depends on the formulation of the filtered governing equations, of the energy equation in particular but also of the momentum equation [271]. Using a priori tests, Vreman *et al.* [309] and Martín *et al.* [189] assessed the amplitude of all subgrid terms involved in the compressible Navier–Stokes equations for different formulations of the energy conservation equation.

In the literature, the subgrid terms have not been investigated for low Mach number strongly anisothermal turbulent flows. In this paper, we extend the analysis to this configuration. In strongly anisothermal flows, the large temperature differences require taking into account the variations of the fluid properties. If in addition the flow is turbulent, the variations of the fluid properties are related to the velocity fluctuations. The figure 8.2 is an illustration of the correlation between the velocity and temperature. The isosurface of figure 8.2 is not only an isotherm but also a surface of isodensity, isoviscosity and isoconductivity. Both the velocity and temperature profiles are turbulent and exhibit a wide range of length scales. The correlations between velocity and temperature lead to additional subgrid terms associated with the nonlinearities of the viscous term and of the heat flux. In the literature, these additional subgrid terms are always neglected (see for example [265, 317, 4, 52, 264, 258, 176]). However, to the best of our knowledge, there is no study to justify this assumption in low Mach number flows. We investigate whether these additional subgrid terms may be neglected. This study is essential for the flows found in solar receivers, characterised by a strong coupling between turbulence and temperature, along with high variations of the fluid properties (density, viscosity and thermal conductivity) with temperature [290].

We study the subgrid terms using the results of direct numerical simulations of a strongly anisothermal fully developed turbulent channel flow. The investigation is based on a particular form of the Navier–Stokes equations under the low Mach number hypothesis, called low Mach number equations [87]. The filtering of the low Mach number equations gives rise to specific subgrid terms. Three formulations of the filtered low Mach number equations are investigated, which leads to three specific sets of subgrid terms. The analysis is carried out using the classical filter and the Favre filter. With the classical filter, we compare the filtering of the momentum conservation equation to the filtering of the velocity transport equation. We assess the magnitude

of each term in the three formulations. This provides insights on the asymmetry of the subgrid and non-subgrid terms between the two sides of the channel and on the relative importance of the various competing physical processes. The study takes into account both the subgrid terms associated with non-commutation of the filter with the derivative and the nonlinearities arising from the large variations of the fluid properties. The objective is to identify the subgrid terms that can be neglected and the subgrid terms that should be modelled in the three formulations.

We describe the low Mach number equations in section 2. In section 3, we study the filtering of the low Mach number equations in three formulations. The subgrid terms derived in the general case are then estimated in the channel flow configuration. The detailed channel flow configuration can be found in section 4 as well as the numerical method used to compute the subgrid terms. The results are discussed in section 5.

8.2.2 Low Mach number equations

We consider a turbulent flow at low Mach number ($Ma < 0.3$). The low Mach number hypothesis let us use Paolucci's method [219] to remove acoustic effects from the Navier–Stokes equations. Each variable of the Navier–Stokes equations is written as a power series of the squared Mach number. Keeping only the smaller-order terms leads to the so-called low Mach number equations. The pressure is split in two parts: the thermodynamical pressure P , mean pressure in the domain, and the mechanical pressure P_0 , associated with momentum variations. The thermodynamical pressure is constant in space. The gas is air, an ideal gas for the purpose of this study. The effects of gravity are neglected.

Those considerations lead to the low Mach number equations, given by:

- Mass conservation equation

$$\frac{\partial \rho}{\partial t} + \frac{\partial \rho U_j}{\partial x_j} = 0, \quad (8.1)$$

- Momentum conservation equation

$$\frac{\partial \rho U_i}{\partial t} = - \frac{\partial \rho U_j U_i}{\partial x_j} - \frac{\partial P}{\partial x_i} + \frac{\partial \Sigma_{ij}}{\partial x_j}, \quad (8.2)$$

- Energy conservation equation

$$\frac{\partial U_j}{\partial x_j} = - \frac{1}{\gamma P_0} \left[(\gamma - 1) \frac{\partial Q_j}{\partial x_j} - \frac{\partial P_0}{\partial t} \right], \quad (8.3)$$

- Ideal gas law

$$T = \frac{P_0}{\rho r}, \quad (8.4)$$

with ρ the density, T the temperature, Σ_{ij} the shear-stress tensor, Q_j the conductive heat flux, γ the heat capacity ratio, r the ideal gas specific constant, t the time, P the mechanical pressure, P_0 the thermodynamical pressure, U_i the i -th component

of velocity and x_i the Cartesian coordinate in i -th direction. Einstein summation convention is used and δ_{ij} is the Kronecker delta.

In the low Mach number equations, the energy conservation equation has a distinctive form. The local conservation of energy is imposed by a constraint on the divergence of the velocity. Namely, the dilatation of the fluid is proportional to the difference between the conductive heat flux and the global variation of thermodynamical pressure. To obtain equation (9.3), we use the low Mach number hypothesis to approximate the compressible energy conservation equation in enthalpy form as [212]

$$\frac{\partial \rho C_p T}{\partial t} + \frac{\partial \rho U_j C_p T}{\partial x_j} = \frac{\partial P_0}{\partial t} - \frac{\partial Q_j}{\partial x_j}, \quad (8.5)$$

where C_p is the heat capacity at constant pressure. We then use the ideal gas law (9.4) to substitute in this equation ρT with P_0/r . Using the fact that the thermodynamical pressure is constant in space, we isolate the divergence of the velocity and combine the two temporal terms.

We assume that air is a Newtonian fluid to compute the shear-stress tensor,

$$\Sigma_{ij} = \mu(T) \left(\frac{\partial U_i}{\partial x_j} + \frac{\partial U_j}{\partial x_i} \right) - \frac{2}{3} \mu(T) \frac{\partial U_k}{\partial x_k} \delta_{ij}. \quad (8.6)$$

The heat flux is given by

$$Q_j = -\lambda(T) \frac{\partial T}{\partial x_j}. \quad (8.7)$$

The variations of viscosity with temperature are accounted for by the Sutherland's law [287],

$$\mu(T) = \mu_0 \left(\frac{T}{T_0} \right)^{\frac{3}{2}} \frac{T_0 + S}{T + S}, \quad (8.8)$$

with $\mu_0 = 1.716 \cdot 10^{-5}$ Pa s, $S = 110.4$ K and $T_0 = 273.15$ K. The thermal conductivity is deduced from the Prandtl number Pr and the heat capacity at constant pressure C_p , both assumed constant with $Pr = 0.76$ and $C_p = 1005$ J kg⁻¹ K⁻¹. The ideal gas specific constant is $r = 287$ J kg⁻¹ K⁻¹.

We will study the filtering of the low Mach number equations in three formulations that we shall call the Classical formulation, the Favre formulation and the Velocity formulation.

8.2.3 Filtering of the low Mach number equations

The large-eddy simulation is based on the idea of scale separation. Theoretically, the separation is carried out by the application of a filter, denoted $(\overline{\cdot})$, on the Navier–Stokes equations. We restrict our discussion in this paper to a spatial filter. The filter is taken to verify the properties of conservation of constants, $\overline{a} = a$ with a a constant, and of linearity, $\overline{\phi + \psi} = \overline{\phi} + \overline{\psi}$ for any ϕ and ψ [253]. Note however that the filter may be inhomogeneous and thus not commute with derivation. In the following, this spatial filter will be referred to as the classical filter. The formulation of the filtered low Mach number equations involves two kinds of subgrid terms. The first kind arises from the

non-commutation of the filter with the derivative and are related to the variations of filter width, that is from the LES mesh inhomogeneity. They are denoted in the form C_α^β . The second kind arises from nonlinearities, that is from the non-commutation between the filtering and the multiplication operator. They are denoted in the form F_α . Most of them are related to the large variations of the fluid properties, with the notable exception of the subgrid term associated with momentum convection.

8.2.3.1 Classical formulation

In the Classical formulation, the low Mach number equations are filtered with the classical filter and expressed in terms of classical-filtered variables. The filtered low Mach number equations in the Classical formulation are given by:

- Mass conservation equation

$$\frac{\partial \bar{\rho}}{\partial t} + \frac{\partial}{\partial x_j} (\bar{\rho} \bar{U}_j + F_{\rho U_j}) + C_{\rho U_j}^j = 0, \quad (8.9)$$

- Momentum conservation equation

$$\begin{aligned} \frac{\partial}{\partial t} (\bar{\rho} \bar{U}_i + F_{\rho U_i}) = & - \frac{\partial}{\partial x_j} (\bar{\rho} \bar{U}_j \bar{U}_i + F_{\rho U_j U_i}) - C_{\rho U_j U_i}^j - \frac{\partial \bar{P}}{\partial x_i} - C_P^i \\ & + \frac{\partial}{\partial x_j} (\check{\Sigma}_{ij} + F_{\Sigma_{ij}}) + C_{\Sigma_{ij}}^j, \end{aligned} \quad (8.10)$$

- Energy conservation equation

$$\frac{\partial \bar{U}_j}{\partial x_j} + C_{U_j}^j = - \frac{\gamma - 1}{\gamma P_0} \left[\frac{\partial}{\partial x_j} (\check{Q}_j + F_{Q_j}) + C_{Q_j}^j \right] - \frac{1}{\gamma P_0} \frac{\partial P_0}{\partial t}, \quad (8.11)$$

- Ideal gas law

$$\bar{T} = \frac{P_0}{r} \left(\frac{1}{\bar{\rho}} + F_{1/\rho} \right), \quad (8.12)$$

with the classical filter counterparts of the shear-stress tensor and of the heat flux given by

$$\check{\Sigma}_{ij} = \mu(\bar{T}) \left(\frac{\partial \bar{U}_i}{\partial x_j} + \frac{\partial \bar{U}_j}{\partial x_i} \right) - \frac{2}{3} \mu(\bar{T}) \frac{\partial \bar{U}_k}{\partial x_k} \delta_{ij}, \quad (8.13)$$

$$\check{Q}_j = -\lambda(\bar{T}) \frac{\partial \bar{T}}{\partial x_j}, \quad (8.14)$$

with μ the dynamic viscosity, λ the thermal conductivity and the following subgrid terms:

$$C_{\rho U_j}^j = \frac{\partial \overline{\rho U_j}}{\partial x_j} - \frac{\partial \bar{\rho} \bar{U}_j}{\partial x_j} \quad (8.15)$$

$$C_{\rho U_j U_i}^j = \frac{\partial \overline{\rho U_j U_i}}{\partial x_j} - \frac{\partial \bar{\rho} \bar{U}_j \bar{U}_i}{\partial x_j} \quad (8.16)$$

$$C_P^i = \frac{\partial \bar{P}}{\partial x_i} - \frac{\partial \bar{P}}{\partial x_i} \quad (8.17) \quad F_{\rho U_j} = \overline{\rho U_j} - \bar{\rho} \bar{U}_j \quad (8.21)$$

$$F_{\rho U_i} = \overline{\rho U_i} - \bar{\rho} \bar{U}_i \quad (8.22)$$

$$C_{\Sigma_{ij}}^i = \frac{\partial \overline{\Sigma_{ij}}}{\partial x_j} - \frac{\partial \overline{\Sigma_{ij}}}{\partial x_j} \quad (8.18) \quad F_{\rho U_j U_i} = \overline{\rho U_j U_i} - \bar{\rho} \bar{U}_j \bar{U}_i \quad (8.23)$$

$$F_{\Sigma_{ij}} = \overline{\Sigma_{ij}} - \check{\Sigma}_{ij} \quad (8.24)$$

$$C_{U_j}^j = \frac{\partial \bar{U}_j}{\partial x_j} - \frac{\partial \bar{U}_j}{\partial x_j} \quad (8.19) \quad F_{Q_j} = \overline{Q_j} - \check{Q}_j \quad (8.25)$$

$$C_{Q_j}^j = \frac{\partial \overline{Q_j}}{\partial x_j} - \frac{\partial \overline{Q_j}}{\partial x_j} \quad (8.20) \quad F_{1/\rho} = \frac{\bar{1}}{\rho} - \frac{1}{\bar{\rho}} \quad (8.26)$$

In addition, it is useful to express the transport equation of the resolved kinetic energy $\bar{\rho} \underline{E} = \frac{1}{2} \bar{\rho} \bar{U}_i \bar{U}_i$. Indeed, the total energy conservation is not explicitly stated in the system of equations (8.9)–(8.12) but implied by the momentum conservation equation (8.10) and the energy conservation equation (8.11). The resolved kinetic energy transport equation is the part of total energy conservation related to the momentum conservation. It is obtained from equation (8.10) multiplied by \bar{U}_i and equation (8.9),

$$\begin{aligned} & \frac{\partial \bar{\rho} \underline{E}}{\partial t} - \frac{\partial \underline{E} F_{\rho U_j}}{\partial x_j} + F_{\rho U_j} \frac{\partial \underline{E}}{\partial x_j} - \underline{E} C_{\rho U_j}^j + \frac{\partial \bar{U}_i F_{\rho U_i}}{\partial t} - F_{\rho U_i} \frac{\partial \bar{U}_i}{\partial t} \\ &= - \frac{\partial}{\partial x_j} (\bar{\rho} \bar{U}_j \underline{E} + \bar{U}_i F_{\rho U_j U_i}) + F_{\rho U_j U_i} \frac{\partial \bar{U}_i}{\partial x_j} - \bar{U}_i C_{\rho U_j U_i}^j - \frac{\partial \bar{U}_i \bar{P}}{\partial x_i} + \bar{P} \frac{\partial \bar{U}_i}{\partial x_i} - \bar{U}_i C_P^i \\ & \quad + \frac{\partial}{\partial x_j} (\bar{U}_i \check{\Sigma}_{ij} + \bar{U}_i F_{\Sigma_{ij}}) - (\check{\Sigma}_{ij} + F_{\Sigma_{ij}}) \frac{\partial \bar{U}_i}{\partial x_j} + \bar{U}_i C_{\Sigma_{ij}}^j. \end{aligned} \quad (8.27)$$

This equation gives the contribution of the subgrid terms of the filtered momentum conservation equation to the balance of the resolved kinetic energy. It will be used to assess the magnitude of their energetic contribution. The contribution of the subgrid terms with regard to total energy is given by the subgrid terms of the resolved kinetic energy transport equation (8.27) and the energy conservation equation (8.11).

8.2.3.2 Favre formulation

The use of the Favre filter ($\tilde{\cdot}$) is common when working with variable density flows. It is a variable change in which filtered variables are weighted by density. For any variable ϕ , the Favre-filtered variable $\tilde{\phi}$ is defined as $\tilde{\phi} = \overline{\rho \phi} / \bar{\rho}$. With the Favre filter, we avoid the subgrid terms associated with the nonlinearities of the form $\rho \phi$ in the convective term of the mass conservation equation, the time derivative term of the momentum conservation equation and the ideal gas law. On the other hand, a subgrid term is added when a variable ϕ appears without the density, as the velocity in the energy conservation equation. The subgrid terms associated with the nonlinearities of the shear-stress tensor and of the conductive heat flux are modified by the use of the Favre filter, but it is not obvious to what extent this affects the behaviour and importance of the subgrid terms. Finally, the subgrid terms associated with the non-commutation of the filter with the derivative are not modified by the use of the Favre filter.

In the Favre formulation, the low Mach number equations are filtered with the classical filter and expressed in terms of Favre-filtered variables. The filtered low Mach

number equations in the Favre formulation are given by:

- Mass conservation equation

$$\frac{\partial \bar{\rho}}{\partial t} + \frac{\partial \bar{\rho} \tilde{U}_j}{\partial x_j} + C_{\rho U_j}^j = 0, \quad (8.28)$$

- Momentum conservation equation

$$\begin{aligned} \frac{\partial \bar{\rho} \tilde{U}_i}{\partial t} = & - \frac{\partial}{\partial x_j} \left(\bar{\rho} \tilde{U}_j \tilde{U}_i + \bar{\rho} G_{U_j U_i} \right) - C_{\rho U_j U_i}^j - \frac{\partial \bar{P}}{\partial x_i} - C_P^i \\ & + \frac{\partial}{\partial x_j} \left(\hat{\Sigma}_{ij} + G_{\Sigma_{ij}} \right) + C_{\Sigma_{ij}}^j, \end{aligned} \quad (8.29)$$

- Energy conservation equation

$$\frac{\partial}{\partial x_j} \left(\tilde{U}_j + \bar{\rho} G_{U_j/\rho} \right) + C_{U_j}^j = - \frac{\gamma - 1}{\gamma P_0} \left[\frac{\partial}{\partial x_j} \left(\hat{Q}_j + G_{Q_j} \right) + C_{Q_j}^j \right] - \frac{1}{\gamma P_0} \frac{\partial P_0}{\partial t}, \quad (8.30)$$

- Ideal gas law

$$\tilde{T} = \frac{P_0}{\bar{\rho} r}, \quad (8.31)$$

with the Favre filter counterparts of the shear-stress tensor and of the heat flux given by

$$\hat{\Sigma}_{ij} = \mu(\tilde{T}) \left(\frac{\partial \tilde{U}_i}{\partial x_j} + \frac{\partial \tilde{U}_j}{\partial x_i} \right) - \frac{2}{3} \mu(\tilde{T}) \frac{\partial \tilde{U}_k}{\partial x_k} \delta_{ij}, \quad (8.32)$$

$$\hat{Q}_j = -\lambda(\tilde{T}) \frac{\partial \tilde{T}}{\partial x_j}, \quad (8.33)$$

and the following subgrid terms specific to the Favre formulation:

$$G_{U_j U_i} = \widetilde{U_j U_i} - \tilde{U}_j \tilde{U}_i \quad (8.34) \quad G_{U_j/\rho} = \widetilde{U_j/\rho} - \tilde{U}_j/\bar{\rho} \quad (8.36)$$

$$G_{\Sigma_{ij}} = \overline{\Sigma_{ij}} - \hat{\Sigma}_{ij} \quad (8.35) \quad G_{Q_j} = \overline{Q_j} - \hat{Q}_j \quad (8.37)$$

The subgrid terms $F_{\rho U_j}$ and $G_{U_j/\rho}$ are closely related,

$$\frac{F_{\rho U_j}}{\bar{\rho}} = -\bar{\rho} G_{U_j/\rho}. \quad (8.38)$$

These two subgrid terms express explicitly the correlation between density and velocity.

The resolved kinetic energy transport equation is obtained from equation (8.29) multiplied by \tilde{U}_i and equation (8.28),

$$\begin{aligned} & \frac{\partial \bar{\rho} \underline{E}}{\partial t} - \underline{E} C_{\rho U_j}^j \\ & = - \frac{\partial}{\partial x_j} \left(\bar{\rho} \tilde{U}_j \underline{E} + \bar{\rho} \tilde{U}_i G_{U_j U_i} \right) + \bar{\rho} G_{U_j U_i} \frac{\partial \tilde{U}_i}{\partial x_j} - \tilde{U}_i C_{\rho U_j U_i}^j - \frac{\partial \tilde{U}_i \bar{P}}{\partial x_i} + \bar{P} \frac{\partial \tilde{U}_i}{\partial x_j} - \tilde{U}_i C_P^i \\ & + \frac{\partial}{\partial x_j} \left(\tilde{U}_i \hat{\Sigma}_{ij} + \tilde{U}_i G_{\Sigma_{ij}} \right) - \left(\hat{\Sigma}_{ij} + G_{\Sigma_{ij}} \right) \frac{\partial \tilde{U}_i}{\partial x_j} + \tilde{U}_i C_{\Sigma_{ij}}^j. \end{aligned} \quad (8.39)$$

Compared to the Classical formulation, the Favre formulation is a priori more suited to the momentum conservation equation, the mass conservation equation and the ideal gas law but is less appropriate for the energy conservation equation.

8.2.3.3 Velocity formulation

The Velocity formulation is based on the velocity filtering approach suggested by Sidharth and Candler [271], Sidharth *et al.* [272]. The momentum conservation equation in the low Mach number equations is rewritten before filtering as the velocity transport equation,

$$\frac{\partial U_i}{\partial t} = -\frac{\partial U_j U_i}{\partial x_j} + U_i \frac{\partial U_j}{\partial x_j} - \frac{1}{\rho} \frac{\partial P}{\partial x_i} + \frac{1}{\rho} \frac{\partial \Sigma_{ij}}{\partial x_j}. \quad (8.40)$$

The equations are then filtered with the classical filter and expressed in terms of classical-filtered variables. The filtered low Mach number equations in the Velocity formulation are given by the mass conservation equation (8.9), the energy conservation equation (8.11), the ideal gas law (8.12) and the velocity transport equation:

$$\begin{aligned} \bar{\rho} \frac{\partial \bar{U}_i}{\partial t} = & -\bar{\rho} \frac{\partial}{\partial x_j} (\bar{U}_j \bar{U}_i + F_{U_j U_i}) - \bar{\rho} C_{U_j U_i}^j + \bar{\rho} \bar{U}_i \frac{\partial \bar{U}_j}{\partial x_j} + \bar{\rho} F_{U_i \partial_j U_j} + \bar{\rho} \bar{U}_i C_{U_j}^j \\ & - \frac{\partial \bar{P}}{\partial x_i} - C_P^i - \bar{\rho} F_{\partial_i P / \rho} + \frac{\partial}{\partial x_j} (\check{\Sigma}_{ij} + F_{\Sigma_{ij}}) + C_{\Sigma_{ij}}^j + \bar{\rho} F_{\partial_j \Sigma_{ij} / \rho}, \end{aligned} \quad (8.41)$$

with the following subgrid terms:

$$C_{U_j U_i}^j = \frac{\overline{\partial U_j U_i}}{\partial x_j} - \frac{\partial \bar{U}_j \bar{U}_i}{\partial x_j} \quad (8.42)$$

$$F_{U_j U_i} = \overline{U_j U_i} - \bar{U}_j \bar{U}_i \quad (8.43)$$

$$F_{U_i \partial_j U_j} = \overline{U_i \frac{\partial U_j}{\partial x_j}} - \bar{U}_i \frac{\partial \bar{U}_j}{\partial x_j} \quad (8.44)$$

$$F_{\partial_i P / \rho} = \frac{\overline{1 \frac{\partial P}{\partial x_i}}}{\rho} - \frac{1}{\bar{\rho}} \frac{\partial \bar{P}}{\partial x_i} \quad (8.45)$$

$$F_{\partial_j \Sigma_{ij} / \rho} = \frac{\overline{1 \frac{\partial \Sigma_{ij}}{\partial x_j}}}{\rho} - \frac{1}{\bar{\rho}} \frac{\partial \bar{\Sigma}_{ij}}{\partial x_j} \quad (8.46)$$

Upon filtering, the velocity transport equation gives rise to different subgrid terms than the momentum conservation equation. The time derivative of the velocity density product subgrid term $F_{\rho U_i}$ does not appear in the Velocity formulation. However, there is three additional subgrid terms associated with the divergence of the velocity and the correlation of the density with other terms of the equation.

The resolved kinetic energy transport equation is given by

$$\begin{aligned} \bar{\rho} \frac{\partial \bar{E}}{\partial t} = & -\bar{\rho} \frac{\partial}{\partial x_j} (\bar{U}_j \bar{E} + F_{U_j U_i} \bar{U}_i) + \bar{\rho} F_{U_j U_i} \frac{\partial \bar{U}_i}{\partial x_j} - \bar{\rho} \bar{U}_i C_{U_j U_i}^j \\ & + \bar{\rho} \bar{E} \frac{\partial \bar{U}_j}{\partial x_j} + \bar{\rho} \bar{U}_i F_{U_i \partial_j U_j} + 2\bar{\rho} \bar{E} C_{U_j}^j \\ & - \frac{\partial \bar{P} \bar{U}_i}{\partial x_i} + \bar{P} \frac{\partial \bar{U}_i}{\partial x_i} - \bar{U}_i C_P^i - \bar{\rho} \bar{U}_i F_{\partial_i P / \rho} \\ & + \frac{\partial}{\partial x_j} (\check{\Sigma}_{ij} \bar{U}_i + F_{\Sigma_{ij}} \bar{U}_i) - (\check{\Sigma}_{ij} + F_{\Sigma_{ij}}) \frac{\partial \bar{U}_i}{\partial x_j} + \bar{U}_i C_{\Sigma_{ij}}^j + \bar{\rho} \bar{U}_i F_{\partial_j \Sigma_{ij} / \rho}. \end{aligned} \quad (8.47)$$

This equation is obtained from equation (8.41) multiplied by \bar{U}_i and equation (8.9).

8.2.4 Numerical study configuration

8.2.4.1 Channel flow configuration

We consider a fully developed three-dimensional anisothermal channel flow, as shown in figure 9.1. This geometry is one of the simpler that reproduces the distinctive features of low Mach number strongly anisothermal turbulent flows. It is therefore well suited to the study of the subgrid scale specificities of these flows.

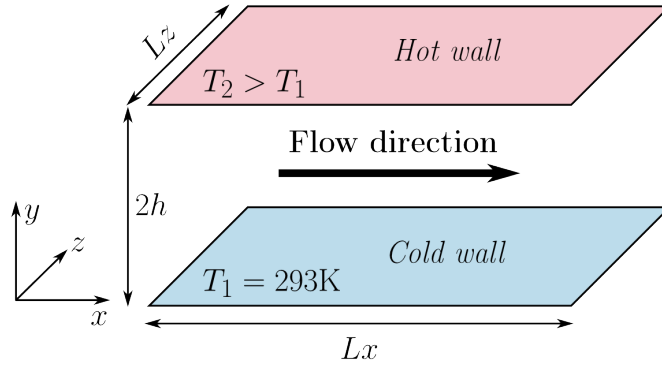


Figure 8.1 – Biperiodic anisothermal channel flow.

The channel is periodic in both the streamwise (x) and spanwise (z) directions. The temperatures of the two plane channel walls are $T_2 = 586$ K at the hot wall and $T_1 = 293$ K at the cold wall. This creates the temperature gradient in the wall-normal direction (y). Two mean friction Reynolds number are considered, $Re_\tau = 180$ and $Re_\tau = 395$, where Re_τ is defined as the average of the friction Reynolds numbers $Re_{\tau,\omega}$ calculated at the hot and cold wall,

$$Re_{\tau,\omega} = \frac{U_\tau h}{\nu_\omega}, \quad (8.48)$$

with $U_\tau = \nu_\omega (\partial_y \bar{U}_x)_\omega^{0.5}$ the friction velocity and ν_ω the wall kinematic viscosity. We show in figure 8.2 an isotherm and the velocity magnitude on a plane for a given timestep at $Re_\tau = 180$.

8.2.4.2 Numerical settings

To provide the data required to compute the subgrid terms of the low Mach number equations, direct numerical simulations of the fully developed channel flow described in 4.1 are carried for the two selected friction Reynolds number (180 and 395). At $Re_\tau = 180$, the domain size is $4\pi h \times 2h \times 2\pi h$, and the mesh used contains $384 \times 266 \times 384$ grid points. At $Re_\tau = 395$, the domain size is $4\pi h \times 2h \times 4/3\pi h$ and the mesh used contains $768 \times 512 \times 512$ grid points. In both cases, the mesh is regular in both homogeneous directions and follow a hyperbolic tangent law in the wall-normal coordinate direction. The wall-normal grid coordinates are given by

$$y_k = L_y \left(1 + \frac{1}{a} \tanh \left[\left(\frac{k-1}{N_y-1} - 1 \right) \tanh^{-1}(a) \right] \right), \quad (8.49)$$

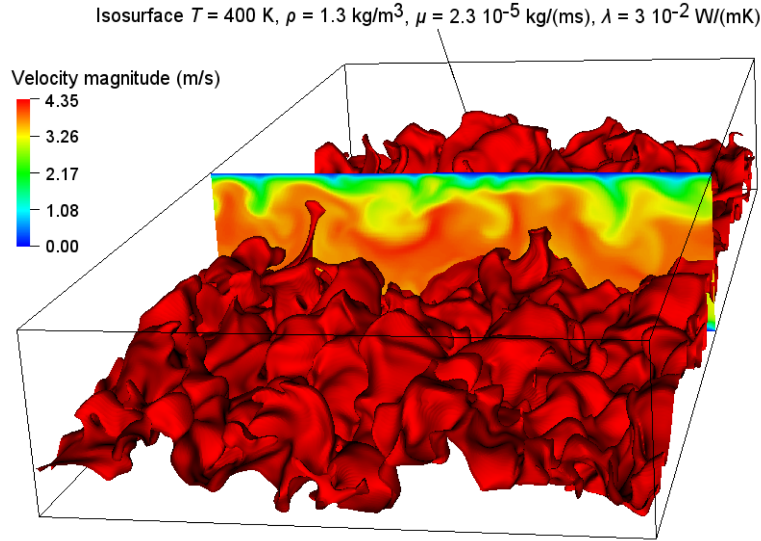


Figure 8.2 – Surface of the 400 K isotherm and velocity magnitude in a plane normal to the flow direction ($Re_\tau = 180$).

with a the mesh dilatation parameter and N_y the number of grid points in the wall-normal direction. The cell sizes in wall units are $\Delta_x^+ = 8.5$, $\Delta_y^+ = 0.13 - 4.2$ and $\Delta_z^+ = 4.2$ at $Re_\tau = 180$; $\Delta_x^+ = 9.1$, $\Delta_y^+ = 0.25 - 4.1$ and $\Delta_z^+ = 4.7$ at $Re_\tau = 395$. The two meshes have the same level of refinement. The small differences are due to the constraints of the numerical method (multigrid solver) and parallelism. A finite volume method is used with a third-order Runge–Kutta time scheme and a fourth-order centred momentum convection scheme. This is performed using the TrioCFD software [38]. The numerical set-up is validated through a mesh convergence study and by comparison of our results in the incompressible case to the reference data of Moser *et al.* [203] and Vreman and Kuerten [305]. These numerical results have been validated against experimental data [63, 92, 151, 9]. We provide in figure 8.3 a comparison of the spatial turbulence kinetic energy terms computed by our numerical procedure to the reference data of Vreman and Kuerten [305] at $Re_\tau = 180$. Similarly, the results have been compared to the reference data of Moser *et al.* [203] at $Re_\tau = 395$ (not shown here). This validates our numerical method at the incompressible limit. In the anisothermal configuration, the same code has been validated against experimental data for a similar friction Reynolds number and temperature gradient by Bellec *et al.* [21].

8.2.4.3 Filtering process

To compute the subgrid terms a priori, we filter explicitly the DNS flow field. At $Re_\tau = 180$, three filters of varying width are investigated, from now on called “filter A”, “filter B” and “filter C”. The three filters are three-dimensional box filter, also known as top-hat filter, of uniform width in both homogeneous directions and nonuniform width in the wall-normal direction. The filter sizes in wall units and the number of grid points corresponding to the filters are,

- filter A: $\overline{\Delta}_x^+ = 43$, $\overline{\Delta}_y^+ = 0.8 - 21$, $\overline{\Delta}_z^+ = 21$ and $77 \times 53 \times 77$ grid points;

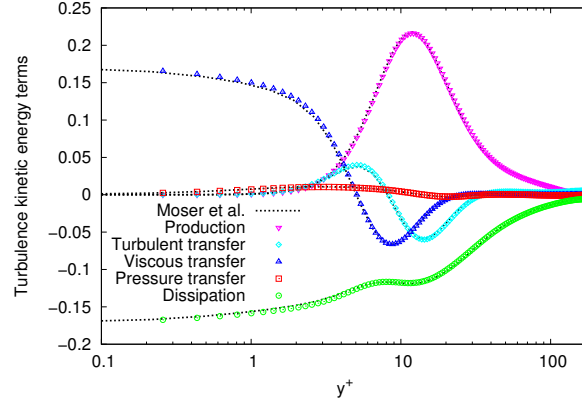


Figure 8.3 – Validation of the spatial turbulence kinetic energy terms.

- filter B: $\bar{\Delta}_x^+ = 68$, $\bar{\Delta}_y^+ = 0.5 - 25$, $\bar{\Delta}_z^+ = 34$ and $48 \times 50 \times 48$ grid points;
- filter C: $\bar{\Delta}_x^+ = 91$, $\bar{\Delta}_y^+ = 0.13 - 43$, $\bar{\Delta}_z^+ = 45$ and $36 \times 40 \times 36$ grid points.

At $Re_\tau = 395$, only filter A is examined. The filter sizes in wall units are $\bar{\Delta}_x^+ = 47$, $\bar{\Delta}_y^+ = 1.5 - 21$ and $\bar{\Delta}_z^+ = 24$. This corresponds to a mesh with $154 \times 102 \times 102$ grid points.

The filter A corresponds to an average over five DNS cells in the three directions. It is computed using the following discrete approximation of the box filter:

$$\bar{\phi}(x_i, y_k, z_j, t) = \frac{1}{25(y_{k'+3} - y_{k'-2})} \sum_{i'=i-2}^{i+2} \sum_{k'=k-2}^{k+2} \sum_{j'=j-2}^{j+2} \phi(x_{i'}, y_{k'}, z_{j'}, t) (y_{k'+1} - y_{k'}). \quad (8.50)$$

The variations of the filter width in the wall-normal direction follow those of the DNS mesh.

The filters B and C are constructed to follow a hyperbolic tangent law (8.49) in the wall-normal direction. We cannot use the same method as for filter A to compute the filters B and C because the filter width is a non-integer multiple of the DNS cell size. In order to carry out the filtering with an arbitrary filter length, the DNS data are first interpolated using a cubic spline. Then, the top-hat filter is computed from the interpolated values without mesh restrictions. The spline interpolation adds an additional filtering to the box filter. However, this additional filter can be neglected given the resolution of the direct numerical simulation. The interpolation and filtering are not computed in three dimensions but sequentially in the three spatial directions. This is possible because the box filter is separable, that is, can be expressed as the product of three one-dimensional filters. Using the filter width of filter A, the method given similar results to equation (8.50).

The filtered quantities are not computed very close the domain boundary, where not enough points are available to apply the filter. This is justified by the fact that in practice, the large-eddy simulation of the channel would be carried out with DNS precision very close to the wall.

8.2.5 Results and discussion

We assess the importance of the subgrid terms in the Classical formulation, the Favre formulation and the Velocity formulation. This provides valuable data to determine which terms can be neglected and which terms should be modelled. The strength of the subgrid terms are investigated according to their quadratic mean, or root mean square, compared to the non-subgrid terms. Numerically, the quadratic mean is computed by an average on the two homogeneous directions and on 100 non-consecutive time steps that cover all thermodynamic configurations of the flow. The results are converged as the mean computed on 50 time steps is identical to the mean computed on 100 time steps. Since the flow is homogeneous in the streamwise and spanwise directions, the analysis is carried out as a function of the wall-normal coordinate y , scaled by the height of the channel and in the classical wall scaling

$$y^+ = Re_\tau \frac{y}{h} = \frac{yU_\tau}{\nu_\omega}. \quad (8.51)$$

The subgrid terms are first investigated with the filter A. Then, the effect of the filter width on the results is examined.

8.2.5.1 Magnitude of the subgrid terms

In this section, the magnitude of subgrid terms is assessed at $Re_\tau = 180$ and $Re_\tau = 395$ with the filter A. The results at $Re_\tau = 180$ and $Re_\tau = 395$ are identical with regard to the classification of the subgrid terms. We thus only provide the results with the filter A at $Re_\tau = 180$, for the mass conservation equation (figure 8.4), the streamwise momentum conservation equation or the streamwise velocity transport equation (figure 8.5), the spanwise momentum conservation equation or the spanwise velocity transport equation (figure 8.6), the wall-normal momentum conservation equation or the wall-normal velocity transport equation (figure 8.7), the resolved kinetic energy transport equation (figure 8.8), the energy conservation equation (figure 8.9), and the ideal gas law (figure 8.10). In each case, the results are given in the entire channel with a linear abscissa and at the cold side with a logarithmic abscissa, to emphasise the near-wall region. Only the cold side is shown with the logarithmic abscissa because a large-eddy simulation of the channel would be less resolved at the cold side than at the hot side.

Indeed, given the dependence of density, viscosity and conductivity on temperature, the temperature gradient generates an asymmetry between the hot and cold sides of the channel. The dynamic viscosity and the friction velocity are higher at the hot wall and the friction Reynolds number is larger at the cold side. All terms of the mass conservation equation, momentum conservation equation, resolved kinetic energy transport equation and energy conservation equation have a larger amplitude at the cold side than at the hot side. In addition, the local maxima of the profiles of most subgrid terms are closer to the wall at the cold side than at the hot side. This asymmetry can in a large part be explained by the local variations of the mean fluid properties [290]. The profiles are also subject to a low Reynolds number effect [91]. Since the three filters used are symmetric with respect to the centre of the channel, the cold side is less resolved in wall units than the hot side. This contributes to the fact that the subgrid terms have a larger amplitude at the cold side than at the hot side

in the mass conservation equation, momentum conservation equation, resolved kinetic energy transport equation and energy conservation equation.

Mass conservation equation

The mass conservation equation (figure 8.4) gives a relationship between the time derivative of density and the divergence of the mass flux. With the classical filter (Classical or Velocity formulation), the subgrid term associated with the density-velocity correlation $\partial_j F_{\rho U_j}$ is very small at the centre of the channel and remains one order of magnitude smaller than the non-subgrid terms near the wall, where it is the most significant. The filter-derivative non-commutation subgrid term $C_{\rho U_j}^j$ has a smaller amplitude in most part of the channel but has the same order of magnitude at the wall. With the Favre filter, it is the only subgrid term in the mass conservation equation.

Since the statistical average of the time derivative of density is zero, the divergence of the resolved mass flux $\partial_j \bar{\rho U_j}$ is in balance with the subgrid terms. With the classical filter, the statistical average of the density-velocity correlation subgrid term has the same order of magnitude as the divergence of the resolved mass flux, while the filter-derivative non-commutation subgrid term is negligible. The modelling of the subgrid term $\partial_j \bar{\rho U_j}$ is necessary to take this behaviour into account in a large-eddy simulation. Therefore, we consider that with the classical filter, the modelling of the density-velocity correlation subgrid term $\partial_j F_{\rho U_j}$ is more important than the modelling of the filter-derivative non-commutation subgrid term $C_{\rho U_j}^j$.

Momentum conservation equation

To study the subgrid terms related to the momentum conservation, we investigate the subgrid terms as they appear in the streamwise, spanwise and wall-normal momentum conservation equations (figures 8.5, 8.6 and 8.7 respectively), or velocity transport equation in the case of the Velocity formulation, and the energetic contribution of the subgrid terms from the resolved kinetic energy transport equation (figure 8.9). In either case, the time derivative term and the convective term predominate at the centre of the channel. Nevertheless, these two terms in a large part cancel each other out. To be considered negligible, a subgrid term should thus at least be negligible compared to the third largest non-subgrid term, namely the pressure term.

Two non-subgrid terms are negligible throughout the entire channel, namely the velocity-dilatation product in the spanwise and wall-normal velocity transport equations and the pressure-dilatation product in the resolved kinetic energy transport equation. The velocity-dilatation product in the streamwise velocity transport equation is also small but is not negligible. This shows the small influence of dilatation on the flow dynamics in low Mach number strongly anisothermal flows. This is consistent with the negligible effect of dilatation on the turbulence kinetic energy budget [91].

In the momentum conservation equation (figures 8.5, 8.6 and 8.7), the most significant subgrid term in the three formulations is the subgrid term associated with momentum or velocity convection, $\partial_j F_{\rho U_j U_i}$, $\partial_j \bar{\rho} G_{U_j U_i}$ and $\partial_j F_{U_j U_i}$. It is larger than viscous term in the bulk and cannot be neglected at the wall. This subgrid term has a larger amplitude at the centre of the channel in the Classical formulation than in

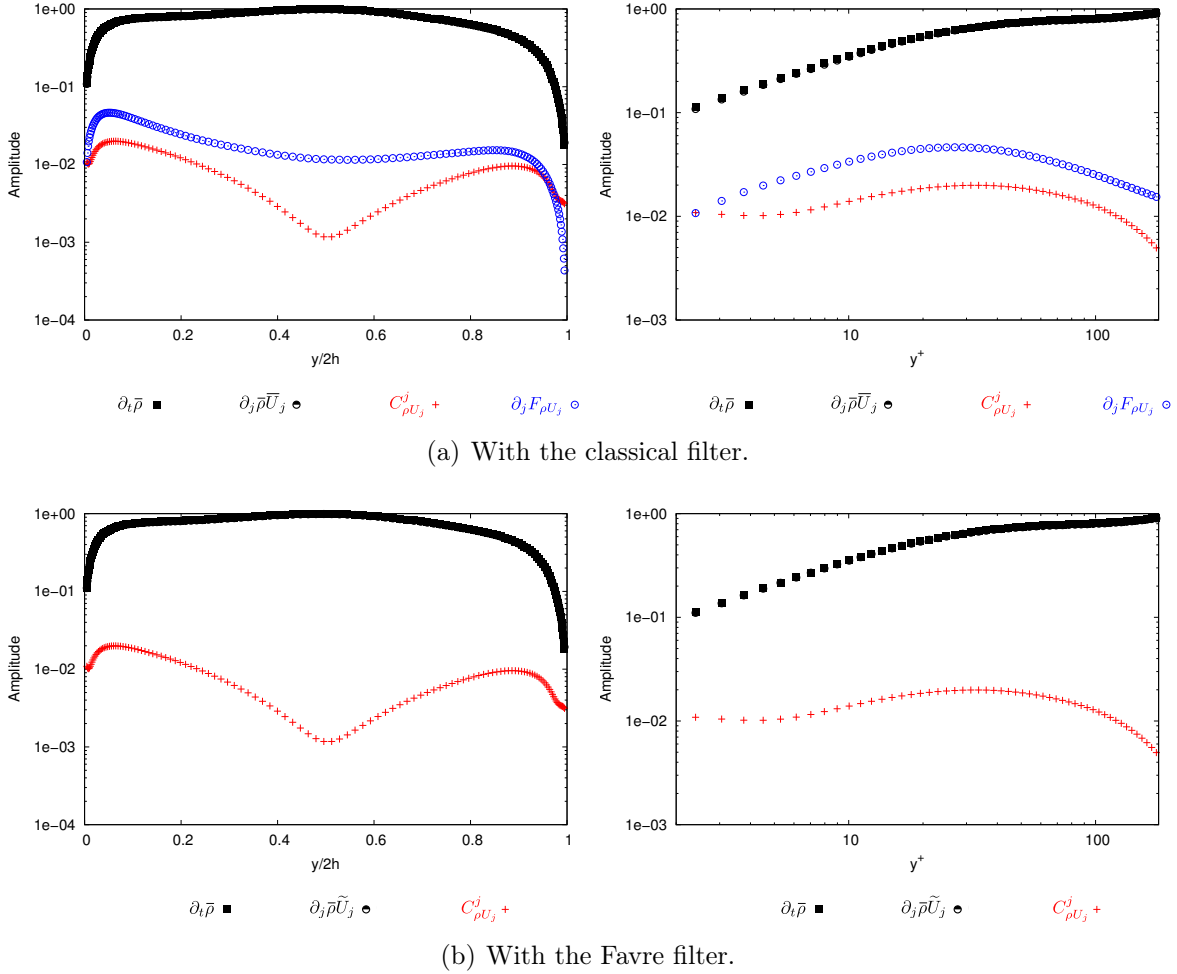
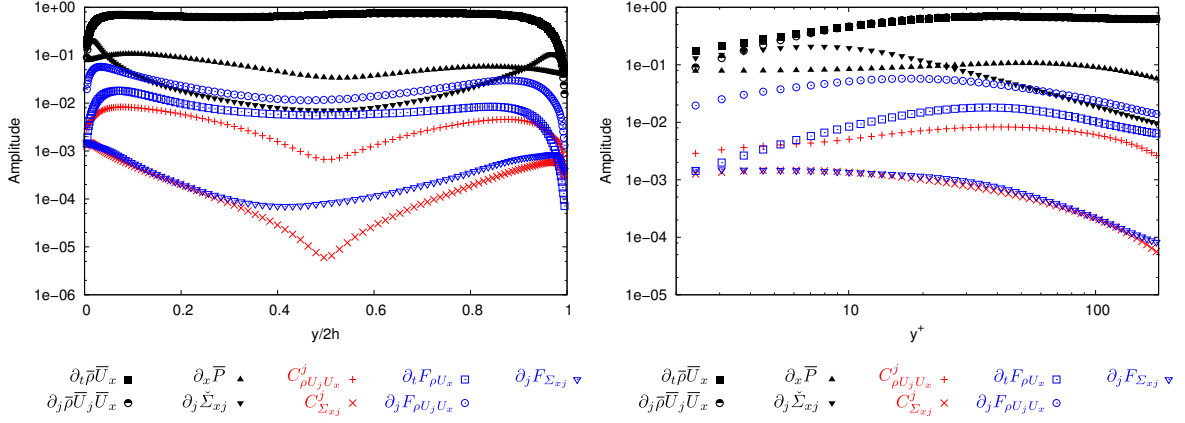


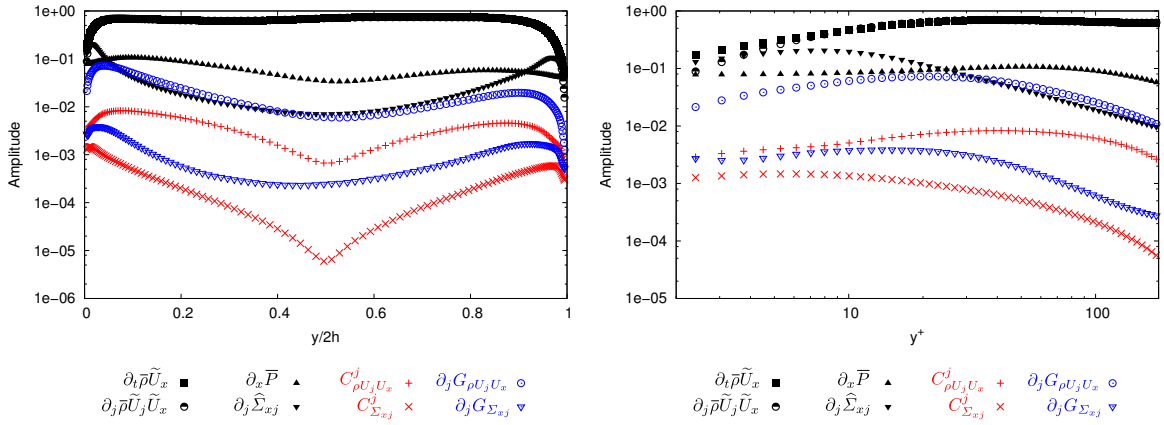
Figure 8.4 – Root mean square of the terms of the mass conservation equation as a function of the wall-normal coordinate in the Classical and Velocity formulations (a) and in the Favre formulation (b) at $Re_\tau = 180$ with the filter A. The amplitude is scaled by the maximum value in the domain in the three formulations.

the Favre and Velocity formulations but a slightly lower amplitude near the wall. It is harder to model in the Classical formulation since it is a triple correlation whereas it is a double correlation in the Favre and Velocity formulations.

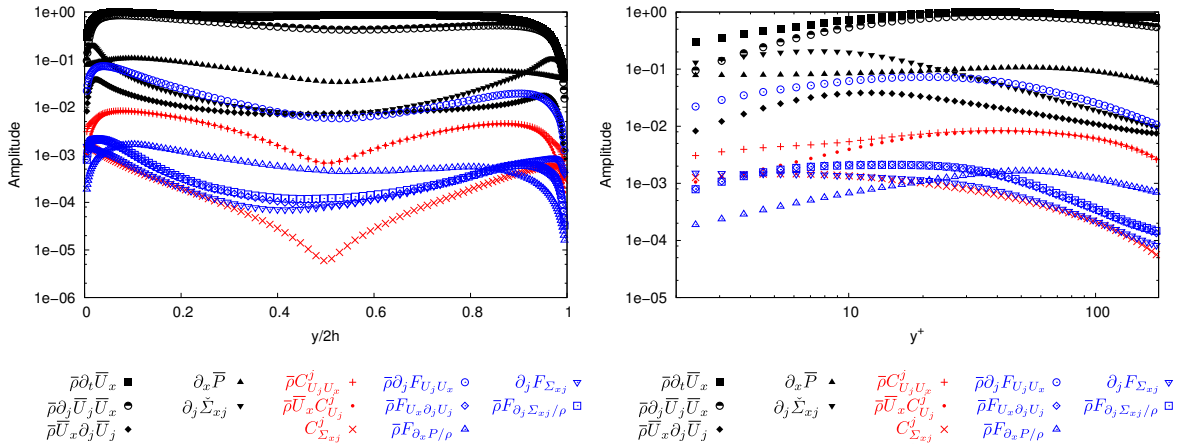
Three subgrid terms have a medium-sized amplitude. In the Classical formulation, the time derivative subgrid term $\partial_t F_{\rho U_i}$ is the second most significant subgrid term. In particular, it has the same order of magnitude as the viscous term at the centre of the channel. Present in the three formulations, the filter-derivative non-commutation subgrid term associated with the convective term, $C_{\rho U_j U_i}^j$ or $C_{U_j U_i}^j$, has a lower amplitude than any non-negligible non-subgrid term but by less than one order of magnitude. It appears very small in the spanwise and wall-normal directions, but is more significant in the streamwise momentum equation. In the Velocity formulation, this subgrid term is followed by the velocity divergence filter-derivative non-commutation subgrid term $C_{U_j}^j$, which has a similar behaviour. Since the subgrid terms $C_{U_j U_i}^j$ and $C_{U_j}^j$ appear with opposite sign in the velocity transport equation, the subgrid terms associated with the filter-derivative non-commutation are less significant in the Velocity formulation.



(a) In the Classical formulation.

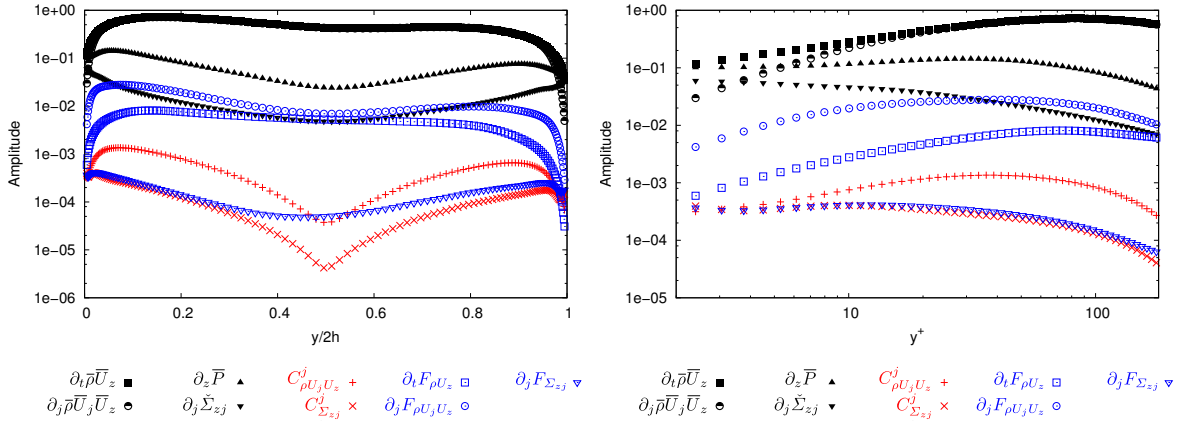


(b) In the Favre formulation.

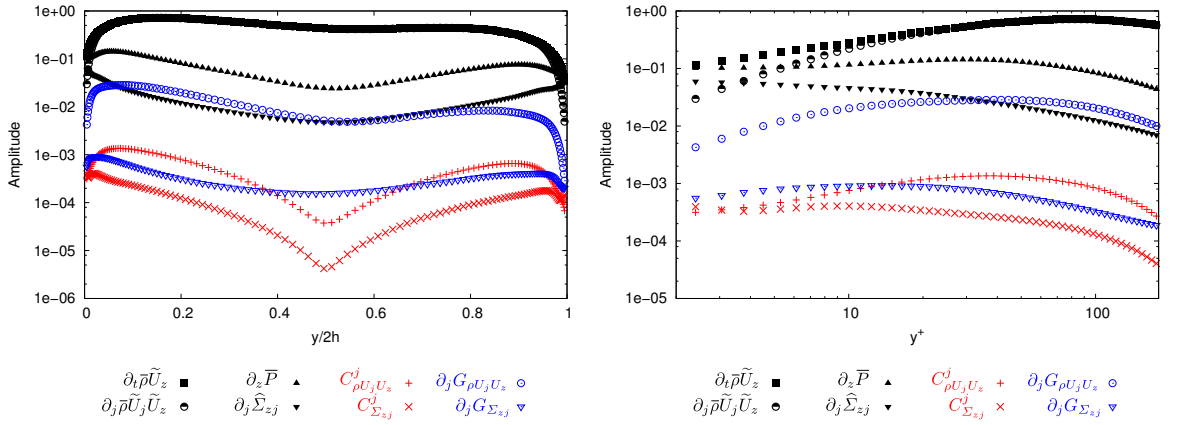


(c) In the Velocity formulation.

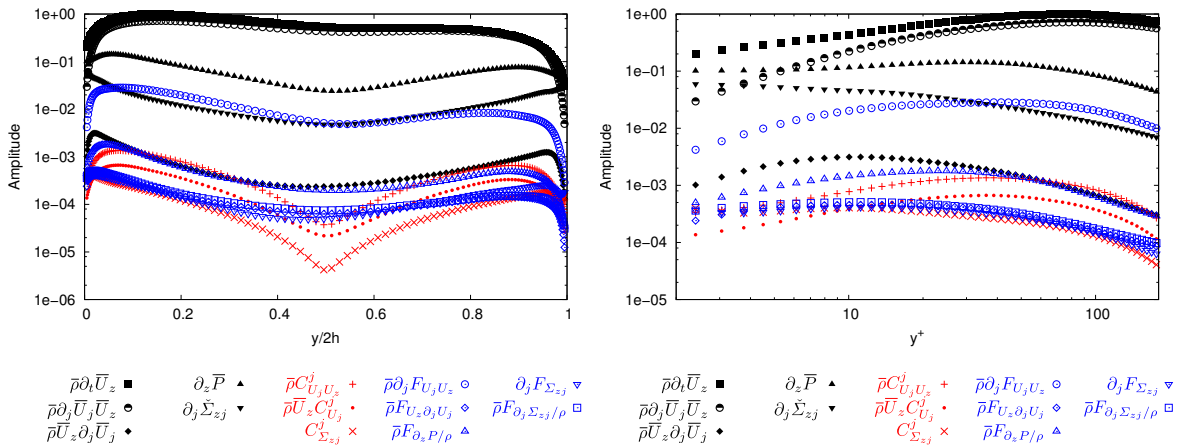
Figure 8.5 – Root mean square of the terms of the streamwise momentum conservation equation as a function of the wall-normal coordinate in the Classical formulation (a), in the Favre formulation (b) and of the terms of the streamwise velocity transport equation in the Velocity formulation (c) at $Re_{\tau} = 180$ with the filter A. The amplitude is scaled by the maximum value in the domain in the three formulations.



(a) In the Classical formulation.



(b) In the Favre formulation.



(c) In the Velocity formulation.

Figure 8.6 – Root mean square of the terms of the spanwise momentum conservation equation as a function of the wall-normal coordinate in the Classical formulation (a), in the Favre formulation (b) and of the terms of the spanwise velocity transport equation in the Velocity formulation (c) at $Re_\tau = 180$ with the filter A. The amplitude is scaled by the maximum value in the domain in the three formulations.

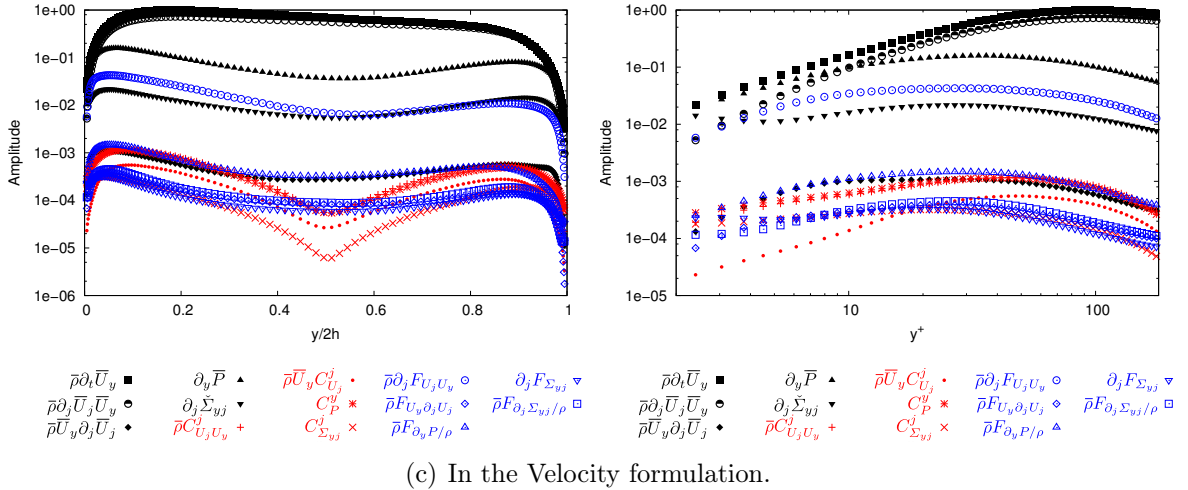
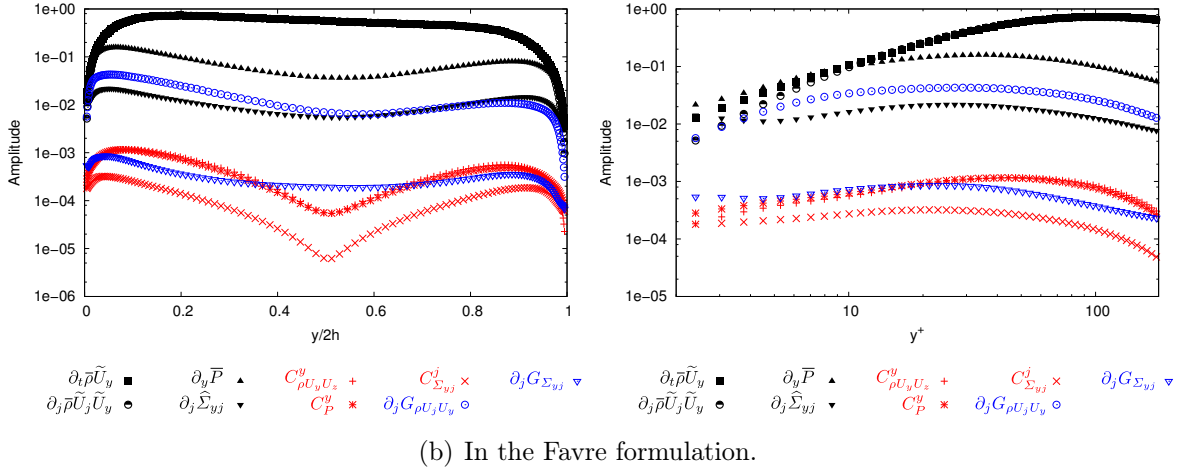
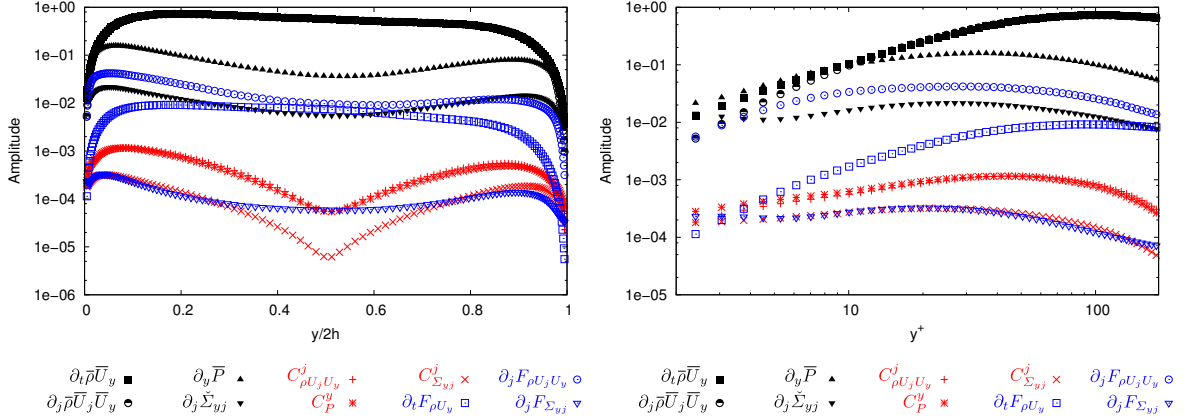
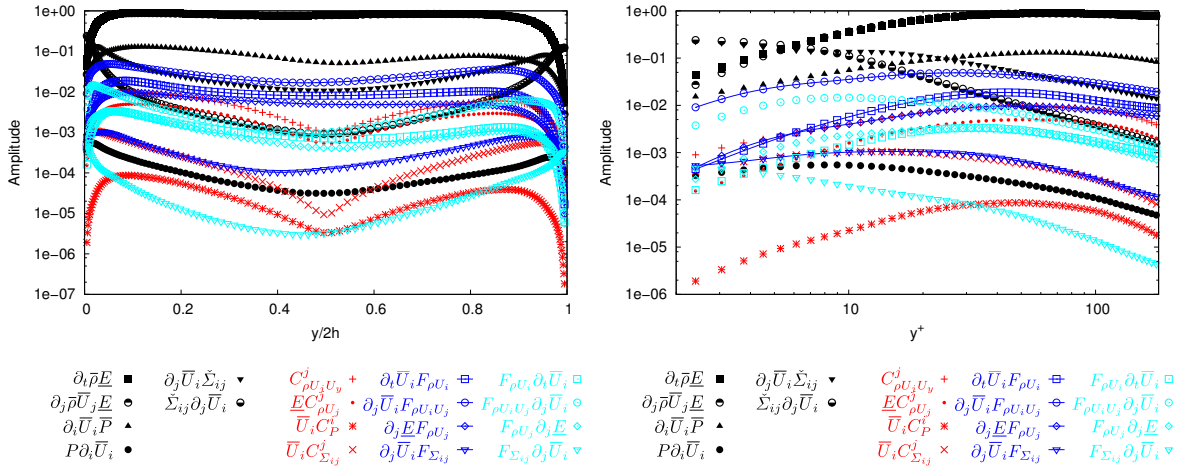
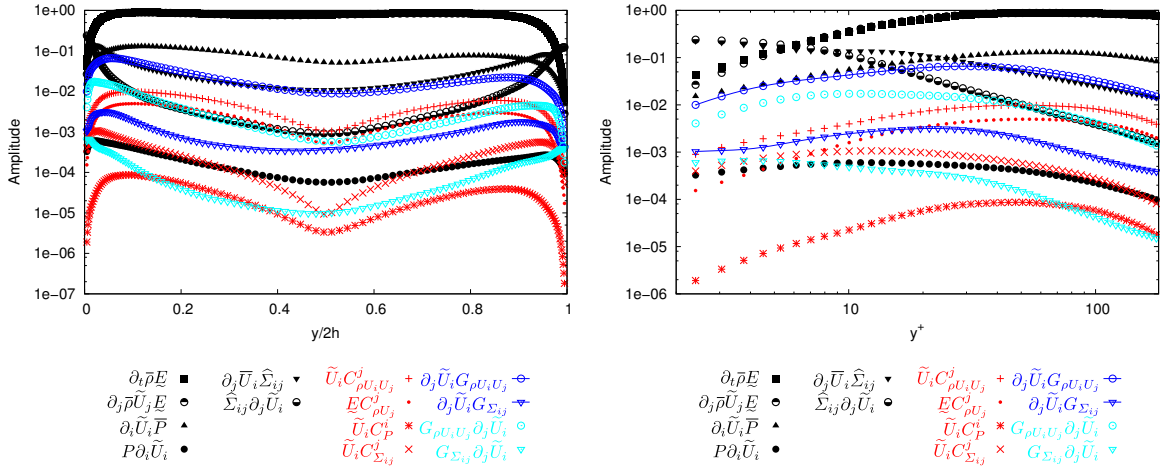


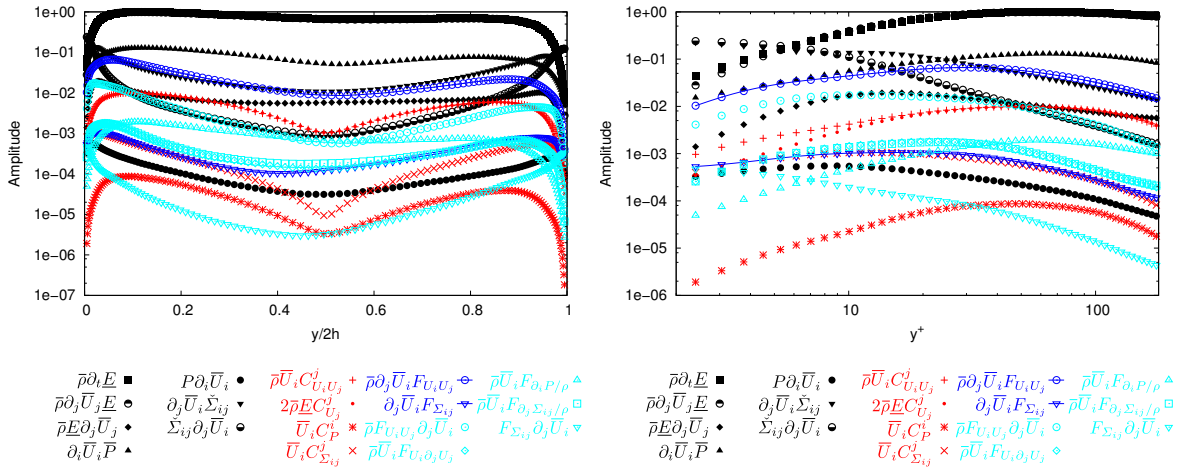
Figure 8.7 – Root mean square of the terms of the wall-normal momentum conservation equation as a function of the wall-normal coordinate in the Classical formulation (a), in the Favre formulation (b) and of the terms of the wall-normal velocity transport equation and in the Velocity formulation (c) at $Re_\tau = 180$ with the filter A. The amplitude is scaled by the maximum value in the domain in the three formulations.



(a) In the Classical formulation.



(b) In the Favre formulation.



(c) In the Velocity formulation.

Figure 8.8 – Root mean square of the terms of the resolved kinetic energy transport equation as a function of the wall-normal coordinate in the Classical formulation (a), in the Favre formulation (b) and in the Velocity formulation (c) at $Re_\tau = 180$ with the filter A. The amplitude is scaled by the maximum value in the domain in the three formulations.

The subgrid term associated with the nonlinearities of the viscous diffusion, $\partial_j F_{\Sigma_{ij}}$ and $G_{\Sigma_{ij}}$, can be considered insignificant in the three formulations. Its amplitude is increased by around one order of magnitude in the Favre formulation but remains one order of magnitude smaller than any non-subgrid term in the entire channel. Assuming that the small-scale variations of velocity are significant, this suggests that the influence of small-scale variations of viscosity on the behaviour of the flow is negligible. The filter-derivative non-commutation subgrid term associated with the pressure and viscous terms C_P^i and $C_{\Sigma_{ij}}^i$ are also negligible. All three of the additional subgrid terms in the Velocity formulation, $F_{U_i \partial_j U_j}$, $F_{\partial_i P / \rho}$ and $F_{\partial_j \Sigma_{ij} / \rho}$, are also found to have a very small amplitude. The most significant of the three is the subgrid term $F_{\partial_i P / \rho}$. The Velocity formulation thus appears more interesting than the classical formulation with regard to the subgrid-scale modelling as the time derivative subgrid term is replaced with three negligible subgrid terms.

The resolved kinetic energy transport equation (figure 8.9) confirms the classification of the subgrid terms in the momentum conservation equation. The most significant subgrid term in the momentum conservation equation have a significant energetic contribution, reaffirming the importance of the subgrid terms associated with momentum or velocity convection, $\partial_j F_{\rho U_j U_i}$, $\partial_j \bar{\rho} G_{U_j U_i}$ and $\partial_j F_{U_j U_i}$, and, in the Classical formulation, of the subgrid term associated with the time derivative term, $\partial_t F_{\rho U_i}$.

Energy conservation equation

Omitting the time derivative of the thermodynamical pressure, constant in space, the energy conservation equation (figure 8.9) expresses the equality, up to a constant scalar factor, of the divergence of the velocity and of the heat flux. The difference between the divergence of the resolved velocity and heat flux represents the effect of the subgrid terms. With the classical filter (Classical or Velocity formulation), the only significant subgrid term is the filter-derivative non-commutation subgrid term $C_{U_j}^j$ associated with the divergence of the velocity. The subgrid terms $\partial_j F_{Q_j}$ and $C_{Q_j}^j$ associated with the heat flux are at least 50 times smaller than the non-subgrid terms throughout the entire channel. This is consistent with the assumption that the variations of conductivity over a small control volume can be neglected. With the Favre filter, the additional subgrid term associated with the density-velocity correlation $G_{U_j / \rho}$ has a large amplitude, of the same magnitude as the non-subgrid terms. In other words, the divergence of the Favre-filtered velocity is a poor approximation of the divergence of the velocity because of the small-scale variations of density and velocity. The density-velocity correlation is more significant in the energy conservation equation in the Favre formulation than in mass or momentum conservation equation in the Classical or Velocity formulations. The nonlinearity error $\partial_j G_{Q_j}$ associated with the heat flux is significantly larger with the Favre filter than with the classical filter but remains rather small.

Ideal gas law

The ideal gas law (figure 8.10) is used to compute the filtered temperature from the filtered density. With the Favre filter, there is theoretically no subgrid term in the

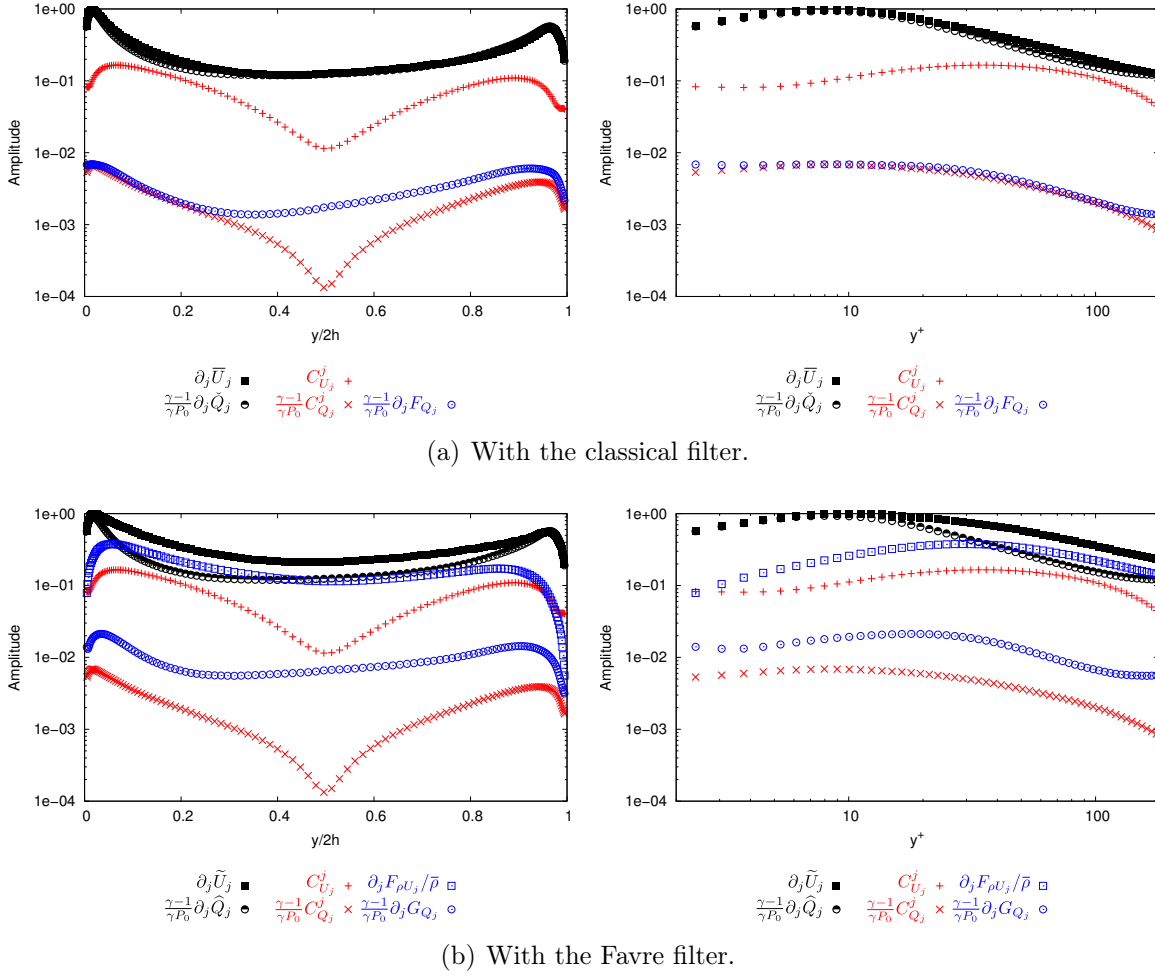
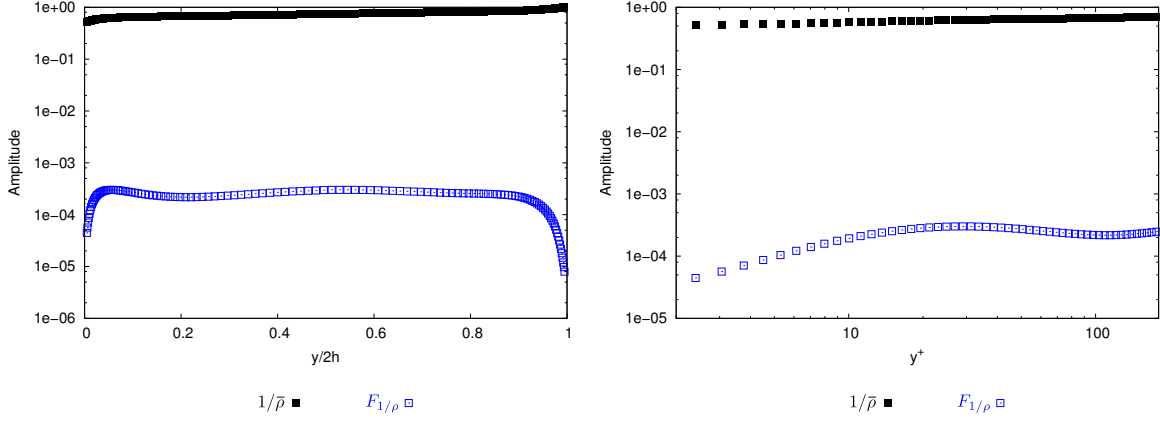


Figure 8.9 – Root mean square of the terms of the energy conservation equation as a function of the wall-normal coordinate in the Classical and Velocity formulations (a) and in the Favre formulation (b) at $Re_\tau = 180$ with the filter A. The amplitude is scaled by the maximum value in the domain in the three formulations.

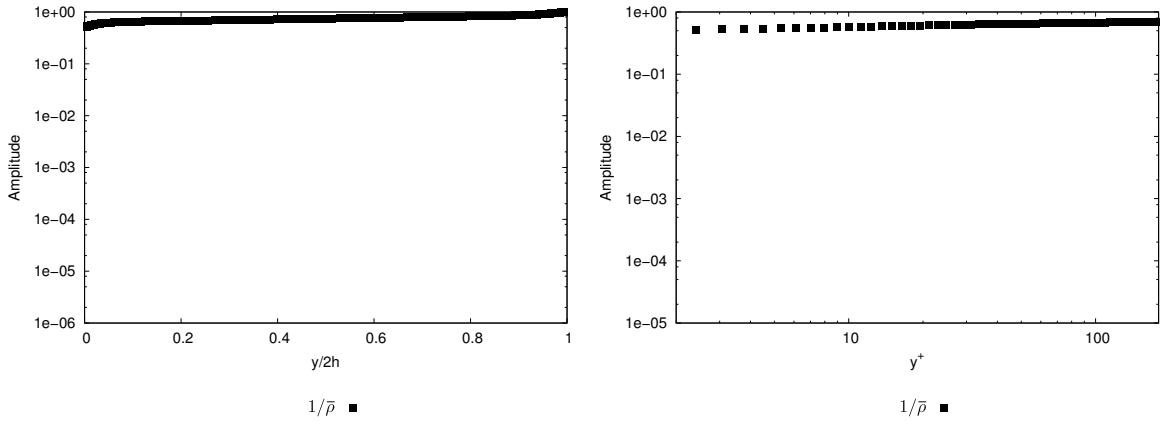
ideal gas law. With the classical filter (Classical or Velocity formulation), the subgrid term $F_{1/\rho}$ it is found negligible. The ideal gas law can thus be used without model with both the classical and Favre filter.

Summary

The subgrid terms are classified according to their quadratic average in table 8.1. The large subgrid terms are the most significant subgrid terms, and should be modelled first. The medium subgrid terms have a smaller amplitude. The modelling of the small or very small subgrid terms should only be considered after all large and medium subgrid terms are modelled, and may not be recommended as their amplitude may not be larger than even the modelling error of the larger subgrid terms.



(a) With the classical filter.



(b) With the Favre filter.

Figure 8.10 – Root mean square of the terms of the ideal gas law as a function of the wall-normal coordinate in the Classical and Velocity formulations (a) and in the Favre formulation (b) at $Re_\tau = 180$ with the filter A. The amplitude is scaled by the maximum value in the domain in the three formulations.

Equation	Formulation	Large	Medium	Small or very small
Mass	Classical, Velocity		$\partial_j F_{\rho U_j}, C_{\rho U_j}^j$	
	Favre		$C_{\rho U_j}^j$	
Momentum	Classical	$\partial_j F_{\rho U_j U_i}$	$\partial_t F_{\rho U_i}, C_{\rho U_j U_i}^j$	$C_P^i, \partial_j F_{\Sigma_{ij}}, C_{\Sigma_{ij}}^i$
	Favre	$\partial_j \bar{\rho} G_{U_j U_i}$	$C_{\rho U_j U_i}^j$	$C_P^i, \partial_j G_{\Sigma_{ij}}, C_{\Sigma_{ij}}^i$
	Velocity	$\bar{\rho} \partial_j F_{U_j U_i}$	$\bar{\rho} C_{U_j U_i}^j, \bar{\rho} \bar{U}_i C_{U_j}^j$	$\bar{\rho} F_{U_i \partial_j U_j}, \bar{\rho} F_{\partial_i P / \rho}, C_P^i, \bar{\rho} F_{\partial_j \Sigma_{ij} / \rho}, \partial_j F_{\Sigma_{ij}}, C_{\Sigma_{ij}}^i$
Energy	Classical, Velocity		$C_{U_j}^j$	$\partial_j F_{Q_j}, C_{Q_j}^j$
	Favre	$G_{U_j / \rho}$	$C_{U_j}^j$	$\partial_j G_{Q_j}, C_{Q_j}^j$
Ideal gas law	Classical, Velocity			$F_{1/\rho}$
	Favre			

Table 8.1 – Classification of the subgrid terms in the three formulations.

8.2.5.2 Effect of the filter width

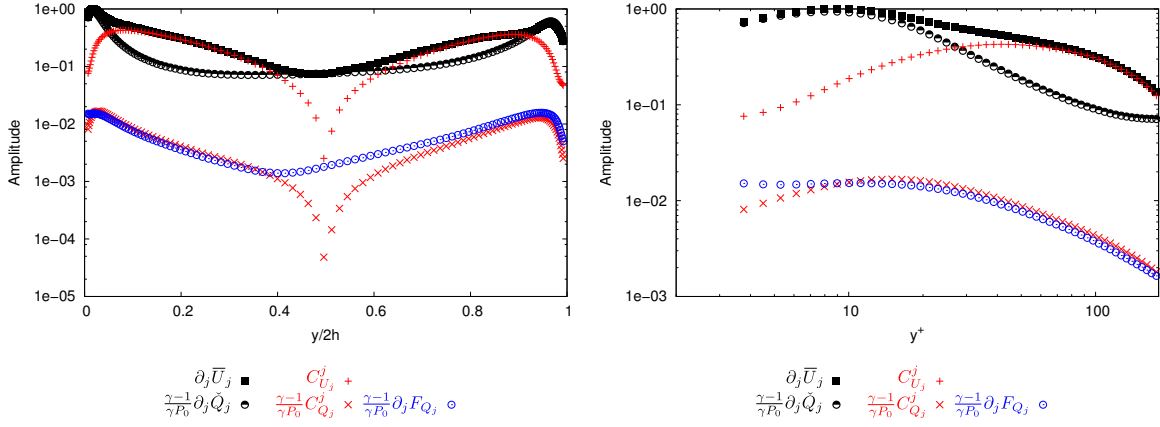
The effect of the filter width on the subgrid term is investigated at $Re_\tau = 180$ by comparing the amplitude of the subgrid terms with the filters A, B and C. As the filter size is increased, the magnitude of all subgrid term is increased compared to the non-subgrid terms. In the mass conservation equation, the momentum conservation equation and the ideal gas law, the increase is not sufficient to affect the conclusions of the classification of the subgrid terms, since the order of magnitude of the subgrid terms remains similar for the three filters. This supports the assumption that, while the variations across the channel of viscosity and thermal conductivity have a significant impact on turbulence [264], the effects of their small-scale variations on the flow are negligible.

In the energy conservation equation, the filter width has a strong influence on the magnitude of the filter-derivative non-commutation subgrid term $C_{U_j}^j$ associated with the divergence of the velocity. While the magnitude of this subgrid term is moderate with the filter A (figure 8.9), it is very large with the filter C (figure 8.11), as its amplitude is larger than that of the resolved heat flux from the logarithmic region to near the centre of the channel. The results with the filter B (not presented here) are in-between. The differences are primarily due to the increased anisotropy of the filter when the filter width is increased. The three filters follow a hyperbolic tangent law in the wall-normal coordinate direction, with a larger dilatation parameter the larger the filter width. With the filter C, the subgrid term $C_{U_j}^j$ is rather small in the viscous sublayer and becomes very large farther from the wall. This suggests that a filter more uniform in the logarithmic region is preferable to limit the influence of this subgrid term.

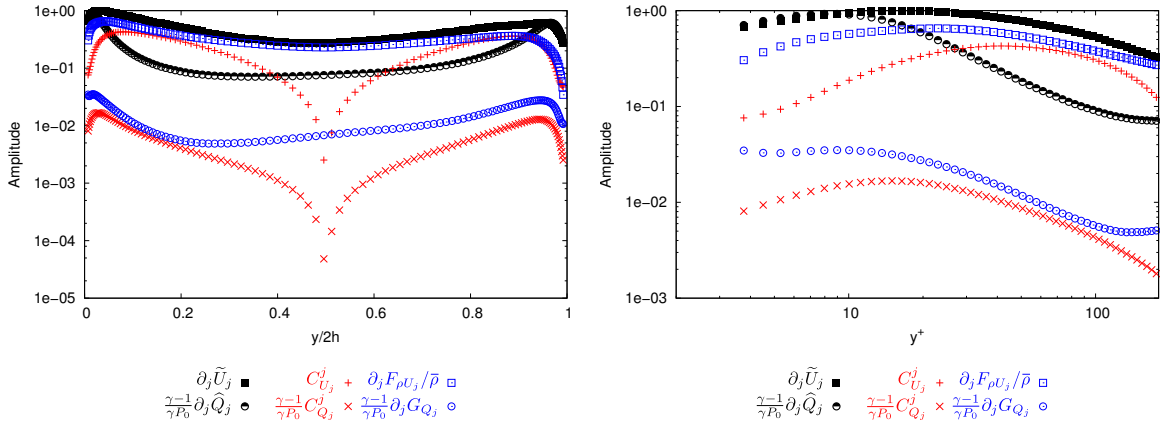
The conclusions of the classification of the subgrid terms (8.1) are valid for the filter A and B. For the filter C, $C_{U_j}^j$ is a large subgrid term. We consider its modelling necessary.

8.2.6 Conclusion

The low Mach number equations are suited to turbulent flows with a low Mach number but subjected to large variations of the fluid properties. They are characterised by a distinctive form of the energy conservation equation, that does not let us categorically choose between the classical filter and the Favre filter. In this study, we filter the low Mach number equations and identify the specific subgrid terms. Then, we investigate a priori the magnitude of all subgrid terms using the flow field from direct numerical simulations of a strongly anisothermal turbulent channel flow. The temperature gradient creates an asymmetry between the hot and cold sides regarding the amplitude and position of the maxima of the subgrid terms, explained by the local variations of the mean fluid properties and a low Reynolds number effect. Regardless of the formulation, more than half of the subgrid terms are found negligible. In particular, the effect of small-scale variations of viscosity and thermal conductivity may be neglected. The two most significant subgrid terms are the subgrid terms associated with momentum convection and with the density-velocity correlation. Due to the mesh inhomogeneity, the modelling of some filter-derivative non-commutation



(a) With the classical filter.



(b) With the Favre filter.

Figure 8.11 – Root mean square of the terms of the energy conservation equation as a function of the wall-normal coordinate in the Classical and Velocity formulations (a) and in the Favre formulation (b) at $Re_\tau = 180$ with the filter C. The amplitude is scaled by the maximum value in the domain in the three formulations.

may also need to be considered, depending on the width of the selected filter. The classical filter is found more appropriate if the momentum equation is expressed as the velocity transport equation. The Favre filter removes the need for the modelling of the density-velocity correlation from the mass conservation equation but requires the modelling of an additional subgrid term in the energy equation, which has a very significant amplitude. The density-velocity correlation thus needs to be modelled in both cases.

Acknowledgment

The authors gratefully acknowledge the CEA for the development of the TRUST platform. This work was granted access to the HPC resources of CINES under the allocations 2016-c20162a5099 and 2017-A0022A05099 made by GENCI.

Bibliography

- [1] A. Abba, A. C. Cercignani, and L. Valdetaro. Analysis of subgrid scale models. *Comput. Math. Appl.*, 46(4):521–535, 2003.
- [4] N. Al-Zurfi and A. Turan. LES of rotational effects on film cooling effectiveness and heat transfer coefficient in a gas turbine blade with one row of air film injection. *International Journal of Thermal Sciences*, 99:96–112, 2016.
- [9] R. A. Antonia, M. Teitel, J. Kim, and L. W. B. Browne. Low-reynolds-number effects in a fully developed turbulent channel flow. *Journal of Fluid mechanics*, 236:579–605, 1992.
- [10] F. Aulery, A. Toutant, F. Bataille, and Y. Zhou. Energy transfer process of anisothermal wall-bounded flows. *Physics Letters A*, 379(24):1520–1526, 2015.
- [11] F. Aulery, D. Dupuy, A. Toutant, F. Bataille, and Y. Zhou. Spectral analysis of turbulence in anisothermal channel flows. *Computers & Fluids*, 151:115–131, 2017.
- [21] M. Bellec, A. Toutant, and G. Olalde. Large eddy simulations of thermal boundary layer developments in a turbulent channel flow under asymmetrical heating. *Computers & Fluids*, 151:159–176, 2017.
- [26] D. J. Bodony and S. J. Lele. On using large-eddy simulation for the prediction of noise from cold and heated turbulent jets. *Phys. Fluids*, 17(8):085103, 2005.
- [27] B. J. Boersma and S. K. Lele. Large eddy simulation of compressible turbulent jets. *Center for Turbulence Research, Annual Research Briefs*, pages 365–377, 1999.
- [38] C. Calvin, O. Cueto, and P. Emonot. An object-oriented approach to the design of fluid mechanics software. *ESAIM: Mathematical Modelling and Numerical Analysis*, 36(05):907–921, 2002.
- [43] M. A. Carper and F. Porté-Agel. Subfilter-scale fluxes over a surface roughness transition. part ii: A priori study of large-eddy simulation models. *Boundary-Layer Meteorology*, 127(1):73–95, 2008.
- [52] S. C. P. Cheung and G. H. Yeoh. A fully-coupled simulation of vortical structures in a large-scale buoyant pool fire. *International Journal of Thermal Sciences*, 48(12):2187–2202, 2009.
- [56] S. G. Chumakov and C. J. Rutland. Dynamic structure subgrid-scale models for large eddy simulation. *International Journal for Numerical Methods in Fluids*, 47(8-9):911–923, 2005.
- [63] J. A. Clark. A study of incompressible turbulent boundary layers in channel flow. *Journal of Basic Engineering*, 90(4):455–467, 1968.
- [64] R. A. Clark, J. H. Ferziger, and W. C. Reynolds. Evaluation of subgrid-scale models using an accurately simulated turbulent flow. *J. Fluid Mech.*, 91(1):1–16, 1979.
- [87] D. Dupuy, A. Toutant, and F. Bataille. Study of the sub-grid terms of the large-eddy simulation of a low Mach strongly anisothermal channel flow. In *Eurotherm Seminar 106, Paris, France*, 2016.
- [91] D. Dupuy, A. Toutant, and F. Bataille. Turbulence kinetic energy exchanges in flows with highly variable fluid properties. *Journal of Fluid Mechanics*, 834:5–54, 2018.
- [92] H. Eckelmann. The structure of the viscous sublayer and the adjacent wall region in a turbulent channel flow. *Journal of Fluid Mechanics*, 65(3):439–459, 1974.
- [94] A. Favre. The equations of compressible turbulent gases. Technical Report AD0622097, DTIC Document, 1965.
- [109] E. Garnier, N. Adams, and P. Sagaut. *Large eddy simulation for compressible flows*. Springer Science & Business Media, 2009.
- [113] N. S. Ghaisas and S. H. Frankel. A priori evaluation of large eddy simulation subgrid-scale scalar flux models in isotropic passive-scalar and anisotropic buoyancy-driven homogeneous turbulence. *J. Turbulence*, 15(2):88–121, 2014.

- [151] H.-P. Kreplin and H. Eckelmann. Behavior of the three fluctuating velocity components in the wall region of a turbulent channel flow. *The Physics of Fluids*, 22(7):1233–1239, 1979.
- [175] C. Li. *A-priori analysis of LES subgrid scale models applied to wall turbulence with pressure gradients*. PhD thesis, Ecole Centrale de Lille, 2013.
- [176] W. Li, X. Li, J. Ren, and H. Jiang. Large eddy simulation of compound angle hole film cooling with hole length-to-diameter ratio and internal crossflow orientation effects. *International Journal of Thermal Sciences*, 121:410–423, 2017.
- [180] S. Liu, C. Meneveau, and J. Katz. On the properties of similarity subgrid-scale models as deduced from measurements in a turbulent jet. *J. Fluid Mech.*, 275:83–119, 1994.
- [182] H. Lu, C. J. Rutland, and L. M. Smith. A priori tests of one-equation LES modeling of rotating turbulence. *J. Turbulence*, (8):N37, 2007.
- [189] M. Pino Martín, U. Piomelli, and G. V. Candler. Subgrid-scale models for compressible large-eddy simulations. *Theoretical and Computational Fluid Dynamics*, 13(5):361–376, 2000.
- [203] R. D. Moser, J. Kim, and N. N. Mansour. Direct numerical simulation of turbulent channel flow up to $Re_\tau = 590$. *Phys. Fluids*, 11(4):943–945, 1999.
- [212] F. Nicoud. Conservative high-order finite-difference schemes for low-Mach number flows. *J. Comput. Phys.*, 158(1):71–97, 2000.
- [219] S. Paolucci. On the filtering of sound from the Navier–Stokes equations. Technical Report SAND82-8257, Sandia National Labs., Livermore, CA (USA), 1982.
- [229] U. Piomelli, P. Moin, and J. H. Ferziger. Model consistency in large eddy simulation of turbulent channel flows. *Phys. Fluids*, 31(7):1884–1891, 1988.
- [253] P. Sagaut. *Large eddy simulation for incompressible flows: an introduction*. Springer Science & Business Media, 2006.
- [258] M. Sanchez, F. Aulery, A. Toutant, and F. Bataille. Large eddy simulation of thermal boundary layer spatial development in a turbulent channel flow. *Journal of Fluids Engineering*, 136(6):060906, 2014.
- [264] S. Serra, A. Toutant, and F. Bataille. Thermal large eddy simulation in a very simplified geometry of a solar receiver. *Heat Transfer Engineering*, 33(6):505–524, 2012.
- [265] S. Serra, A. Toutant, F. Bataille, and Y. Zhou. High-temperature gradient effect on a turbulent channel flow using thermal large-eddy simulation in physical and spectral spaces. *J. Turbulence*, 13:N49, 2012.
- [271] G. S. Sidharth and G. V. Candler. Stretched-vortex based subgrid-scale modeling for variable-density flows. In *45th AIAA Fluid Dynamics Conference*, page 2782, 2015.
- [272] G. S. Sidharth, A. Kartha, and G. V. Candler. Filtered velocity based LES of mixing in high speed recirculating shear flow. In *46th AIAA Fluid Dynamics Conference*, page 3184, 2016.
- [286] X.-B. Sun and X.-Y. Lu. A large eddy simulation approach of compressible turbulent flow without density weighting. *Phys. Fluids*, 18(11):118101, 2006.
- [287] W. Sutherland. The viscosity of gases and molecular force. *The London, Edinburgh, and Dublin Philosophical Magazine and Journal of Science*, 36(223):507–531, 1893.
- [290] A. Toutant and F. Bataille. Turbulence statistics in a fully developed channel flow submitted to a high temperature gradient. *International Journal of Thermal Sciences*, 74:104–118, 2013.
- [291] A. Toutant, E. Labourasse, O. Lebaigue, and O. Simonin. DNS of the interaction between a deformable buoyant bubble and a spatially decaying turbulence: a priori tests for LES two-phase flow modelling. *Computers & Fluids*, 37(7):877–886, 2008.
- [305] A. W. Vreman and J. G. M. Kuerten. Comparison of direct numerical simulation databases of turbulent channel flow at $Re_\tau = 180$. *Phys. Fluids*, 26(1):015102, 2014.

- [306] B. Vreman. *Direct and large-eddy simulation of the compressible turbulent mixing layer*. PhD thesis, University of Twente, 1995.
- [309] B. Vreman, B. Geurts, and H. Kuerten. A priori tests of large eddy simulation of the compressible plane mixing layer. *Journal of Engineering Mathematics*, 29(4):299–327, 1995.
- [310] B. Vreman, B. Geurts, and H. Kuerten. Subgrid-modelling in LES of compressible flow. *Applied Scientific Research*, 54(3):191–203, 1995.
- [317] S. M. Yahya, S. F. Anwer, and S. Sanghi. Turbulent forced convective flow in an anisothermal channel. *International Journal of Thermal Sciences*, 88:84–95, 2015.
- [320] A. Yoshizawa. Statistical theory for compressible turbulent shear flows, with the application to subgrid modeling. *Phys. Fluids*, 29(7):2152–2164, 1986.

8.3 Conclusion of chapter 8

The estimation of relative importance of the subgrid terms from their quadratic mean is used to identify the subgrid terms that can be neglected and the subgrid terms that should be modelled for large-eddy simulation of the low Mach number equations. The formulation of the low Mach number equations upon filtering is tied to the choice of resolved variables. The filtering of the momentum conservation equation is more adequate if the equations are expressed in terms of Favre-filtered variables. The filtering of the velocity transport equation is more adequate if the equations are expressed in terms of classical-filtered variables. However, the classification of the subgrid terms does not provide sufficient evidences of the better suitability of either the classical filter or the Favre filter for the large-eddy simulation of the low Mach number equations. The filter-derivative non-commutation subgrid terms are mostly independent of the choice of the formulation. The subgrid terms associated with the nonlinearities of the shear-stress tensor and of the conductive heat flux have a larger amplitude with the Favre filter but are small in both formulations. The subgrid term associated with momentum convection has a similar amplitude with the Favre filter and the classical filter. The subgrid term associated with the density-velocity correlation appears in the energy conservation equation with the Favre filter and in the mass conservation equation with the classical filter. It has a larger quadratic mean with the Favre filter compared to the other terms of the energy conservation equation than with the classical filter compared to the other terms of the mass conservation equation. However, the density-velocity correlation subgrid term may has a significant statistical average contribution to the mass conservation equation with the classical filter.

The use of three filters of varying width shows the robustness of the results to moderate variations of the filter width. A larger filter width increases the amplitude of all subgrid terms but particularly affects the filter-derivative non-commutation subgrid terms. The more uneven the filter, the more the filter-derivative non-commutation subgrid terms are significant. This is especially concerning for the filter-derivative non-commutation subgrid term associated with the divergence of the velocity in the energy conservation equation. With the largest filter used, the subgrid term has a large amplitude and should be taken into account.

In the next chapter, we assess the modelling of the two most significant subgrid terms of the filtered low Mach number equations, the momentum convection subgrid

term and the density-velocity correlation subgrid term. The analysis follows a similar approach, based on the direct numerical simulations of strongly anisothermal turbulent channel flows presented in section 1.3.

Chapter 9

A priori tests of subgrid-scale models in an anisothermal turbulent channel flow at low Mach number

9.1 Introduction of chapter 9

The eddy-viscosity modelling of the filter-multiplication non-commutation subgrid term associated with momentum convection encompass a variety of models with different properties, sharing only the fundamental hypothesis that the effect of subgrid scales is analogous to viscous diffusion [32]. The popularity of this class of model is attributed to its robustness and low computational complexity. [253, 294] The main shortcoming of eddy-viscosity models is the assumption that the action of the subgrid term is purely dissipative, preventing a local inverse energy cascade from small to large scales, or backscatter. The suitability of this assumption is not clear in strongly anisothermal turbulent channel flows, but can also be perceived as an advantage since this property is desirable for numerical stability. Assuming a constant subgrid-scale Prandtl or Schmidt number, eddy-viscosity modelling can be extended to subgrid terms associated with the correlation of velocity and a scalar with the simple gradient-diffusion hypothesis [253]. The resulting models are called eddy-diffusivity models. Alternative procedures such as generalised gradient-diffusion hypothesis [76, 131], algebraic flux model [140] and differential flux model [159] provide improvements in Reynolds-averaged Navier–Stokes simulations [316, 33] and can be adapted to large-eddy simulation [315]. They are not investigated here. In this chapter, we investigate the eddy-viscosity modelling of the momentum convection subgrid term and the eddy-diffusivity modelling of the density-velocity correlation subgrid term, the two most significant subgrid terms arising from the from the filtering of the low Mach number equations.

A priori tests of subgrid-scale models from the filtering of three-dimensional flow fields may be carried out following different approaches. Ideally, the subgrid-scale models should give the best possible prediction in a large-eddy simulation that is achieve a statistical correspondence between the fields of large-eddy simulation and the filtered fields of direct numerical simulation. It is reasonable to assume that the predictive capability of a subgrid-scale model is related to some measure of the closeness between the subgrid-scale model and the exact subgrid term. This is not as simple as it might

appear, for the subgrid-scale model is in practice applied to the resolved variables of a large-eddy simulation, corresponding to the filtered variables of a direct numerical simulation only ideally [173, 156, 253, 235, 236]. Structural models aim to reproduce the local structure of the exact subgrid term from the reconstruction of unresolved scales, suggesting that the local error between the exact subgrid term and the subgrid-scale model should be investigated. The quadratic error is natural to quantify this performance [156]. Functional models aim to globally reproduce the interscale energy transport between resolved scales and subgrid scales, suggesting that the subgrid dissipation should be investigated. Considering that the constant of the models can be arbitrarily adjusted to obtain the correct total subgrid dissipation over the volume, the models should have the ability to provide a representative profile of the statistical average of the subgrid dissipation.

The subgrid-scale models are investigated from the direct numerical simulation of the anisothermal channel flows at $Re_\tau = 180$ presented in section 1.3. The analysis is carried out whether the subgrid terms are expressed in terms of Favre-filtered variables or in terms of classical-filtered variables. Using tools from linear regression analysis and the direct comparison of the statistical average, we study the contribution of the subgrid-scale models in the filtered low Mach number equations and the contribution of the subgrid-scale models to the subgrid dissipation. As a basis of comparison, each model is scaled in order to match the correct level of total subgrid dissipation over the volume. In addition to the models from the literature, two new eddy-viscosity and eddy-diffusivity models are proposed and investigated.

9.2 Paper 4

This section reproduces the paper D. Dupuy, A. Toutant, and F. Bataille. A priori tests of subgrid-scale models in an anisothermal turbulent channel flow at low mach number. (Submitted for publication) [86].

Abstract

The subgrid-scale modelling of a low Mach number strongly anisothermal turbulent flow is investigated using direct numerical simulations. The study is based on the filtering of the low Mach number equations, suited to low Mach number flows with highly variable fluid properties. The results are relevant to formulations of the filtered low Mach number equations established with the classical filter or the Favre filter. The two most significant subgrid terms of the filtered low Mach number equations are considered. They are associated with the momentum convection and the density-velocity correlation. We focus on eddy-viscosity and eddy-diffusivity models. Subgrid-scale models from the literature are analysed and two new models are proposed. The subgrid-scale models are compared to the exact subgrid term using the instantaneous flow field of the direct numerical simulation of a strongly anisothermal fully developed turbulent channel flow. There is no significant differences between the use of the classical and Favre filter regarding the performance of the models. We

suggest that the models should take into account the asymptotic near-wall behaviour of the filter length. Eddy-viscosity and eddy-diffusivity models are able to represent the energetic contribution of the subgrid term but not its effect in the flow governing equations. The AMD and scalar AMD models are found to be in better agreement with the exact subgrid terms than the other investigated models in the a priori tests.

9.2.1 Introduction

This paper addresses the large-eddy simulation subgrid-scale modelling of low Mach number strongly anisothermal turbulent flows. Flows subjected to a strong temperature gradient are prevalent in many industrial processes, such as heat exchangers, propulsion systems or solar power towers [265]. They are characterised by strong coupling between turbulence and temperature, along with high variations of the fluid properties (density, viscosity and thermal conductivity) with temperature [290, 11, 91]. In many cases, the direct numerical simulation (DNS) of strongly anisothermal turbulent flows is unpracticable because too many scales of temperature and velocity are produced and not enough resolution is available to resolve all the relevant scales. In order to predict the large-scale behaviour of low Mach number strongly anisothermal turbulent flows, thermal large-eddy simulation (LES) is an effective alternative. Large-eddy simulation is based on the explicit resolution of the large scales of turbulence and the use of subgrid-scale models to account for the effect of the smaller scales on the large scales. The scale separation may be represented by the application of a low-pass spatial filter on the flow governing equations.

The filtering of the low Mach number equations gives rise to specific subgrid terms. Using a priori tests, Dupuy *et al.* [90] assessed the amplitude of all subgrid terms in several formulations. The expression of the filtered low Mach equations with the unweighted classical filter and the density-weighted Favre filter [94] leads to two different set of equations involving the same non-negligible subgrid terms [87, 88, 90]. The two most significant subgrid terms are associated with the momentum convection and the density-velocity correlation. The adequate modelling of these subgrid terms is required for the large-eddy simulation of low Mach number strongly anisothermal turbulent flows.

Various modelling strategies have been devised to represent the subgrid terms. Two main types of model are found: structural models, established with no prior knowledge of the nature of the effect of the subgrid term, and functional models, which assume that the effect of the subgrid term is similar to molecular diffusion and therefore acts as a dissipative action [253]. The subgrid-scale models should be consistent with important mathematical and physical properties of the Navier–Stokes equations and the turbulent stresses [273]. With regard to the subgrid term associated with momentum convection, the functional eddy-viscosity models are by far the most used because they are simple, inexpensive and robust. A review of eddy-viscosity models may be found in [253, 294, 273]. The eddy-viscosity assumption can be extended to the density-velocity correlation subgrid term using the constant subgrid-scale Prandtl or Schmidt number assumption. This is referred to as eddy-diffusivity models.

In this paper, we assess the subgrid-scale models a priori using the flow field from the

direct numerical simulation of a strongly anisothermal turbulent channel flow. In the literature, a priori studies of the subgrid-scale models have been carried out in incompressible flows [64, 1, 182, 229, 175], two phase divergence-free flows [291, 141], passive and active scalar decaying homogeneous turbulence [56, 113] and in flows with purely compressible effects, in a temporal shear layer [309, 310, 306], a multi-species mixing layer [29], and in freely decaying homogeneous isotropic turbulence [189]. The analysis is here extended to low Mach number strongly anisothermal turbulent flows. We focus on eddy-viscosity and eddy-diffusivity models. Structural models, such as the scale-similarity [14] and gradient model [169], are known to display high degrees of correlation with the exact subgrid term in a priori tests despite easily leading to instabilities when used in an actual large-eddy simulation [14, 253, 259, 24, 141]. Eddy-viscosity models, which assume that the subgrid term is aligned with the rate of deformation tensor or the scalar gradient, are purely dissipative and have desirable property for numerical stability. Besides, by restricting the study to a single family of models, we may hope that the a priori tests have a more easy-to-interpret relevance for a posteriori results. The subgrid-scale models investigated are the Smagorinsky model [276], the WALE model [213], the Vreman model [304], the Sigma model [214], the AMD model [250], the scalar AMD model [3], the VSS model [252] and the Kobayashi model [147]. In addition, two new eddy-viscosity and eddy-diffusivity models are proposed and investigated, the Anisotropic Smagorinsky model, which attempts to improve anisotropy of the Smagorinsky model by involving three filter length scales instead of one, and the MMG model, which may be viewed as multiplicative mixed model.

The filtering of the low Mach number equations is described in section 2. The subgrid-scale models are presented in section 3. The channel flow configuration and the numerical method are given in section 4. The section 5 discusses the asymptotic near-wall behaviour of the models. The results are analysed in section 6.

9.2.2 Filtering of the low Mach number equations

The low Mach number equations are an approximation of the Navier–Stokes equations suited to turbulent flows with a low Mach number ($Ma < 0.3$) but subjected to large variations of the fluid properties. Using Paolucci’s method [219], each variable of the Navier–Stokes equations is written as a power series of the squared Mach number. Neglecting all but the smaller-order terms, the pressure is split in two parts: The thermodynamical pressure P (constant in space), which represents the mean pressure in the domain, and the mechanical pressure P_0 , associated with the momentum variations. The resulting equations are free from acoustic waves.

Considering in addition an ideal gas and neglecting gravity, the low Mach number equations are given by:

- Mass conservation equation

$$\frac{\partial \rho}{\partial t} + \frac{\partial \rho U_j}{\partial x_j} = 0, \quad (9.1)$$

- Momentum conservation equation

$$\frac{\partial \rho U_i}{\partial t} = -\frac{\partial \rho U_j U_i}{\partial x_j} - \frac{\partial P}{\partial x_i} + \frac{\partial \Sigma_{ij}(\mathbf{U}, T)}{\partial x_j}, \quad (9.2)$$

- Energy conservation equation

$$\frac{\partial U_j}{\partial x_j} = -\frac{1}{\gamma P_0} \left[(\gamma - 1) \frac{\partial Q_j(T)}{\partial x_j} + \frac{\partial P_0}{\partial t} \right], \quad (9.3)$$

- Ideal gas law

$$T = \frac{P_0}{\rho r}, \quad (9.4)$$

with ρ the density, T the temperature, $\Sigma_{ij}(\mathbf{U}, T)$ the shear-stress tensor, $Q_j(T)$ the conductive heat flux, γ the heat capacity ratio, r the ideal gas specific constant, t the time, P the mechanical pressure, P_0 the thermodynamical pressure, U_i the i -th component of velocity and x_i the Cartesian coordinate in i -th direction. Einstein summation convention is used. The low Mach number equations impose the local energy conservation by a constraint (9.3) on the divergence of the velocity [212].

The filtering of the low Mach number equations may lead to different formulations of the filtered low Mach number equations depending on the variables we express the equations with and the manner the equations are arranged upon filtering. Two formulations of the filtered low Mach number equations are selected, the Velocity formulation and the Favre formulation. In the Velocity formulation, a spatial filter ($\overline{\cdot}$, classical filter) is applied on the low Mach number equations with the momentum conservation equation rewritten as the velocity transport equation. The equations are then expressed in terms of classical-filtered variables. The Favre formulation is based on the use of a density-weighted filter ($\widetilde{\cdot}$, Favre filter), defined for any ϕ , as $\widetilde{\phi} = \overline{\rho\phi}/\bar{\rho}$. In the Favre formulation, the low Mach number equations are filtered with the classical filter and expressed in terms of Favre-filtered variables.

Retaining only the most significant subgrid terms [87, 88, 90], the filtered low Mach number equations are given in the Velocity formulation by:

$$\frac{\partial \bar{\rho}}{\partial t} + \frac{\partial}{\partial x_j} (\bar{\rho} \bar{U}_j + F_{\rho U_j}) = 0, \quad (9.5)$$

$$\frac{\partial \bar{U}_i}{\partial t} = -\frac{\partial}{\partial x_j} (\bar{U}_j \bar{U}_i + F_{U_j U_i}) + \bar{U}_i \frac{\partial \bar{U}_j}{\partial x_j} - \frac{1}{\bar{\rho}} \frac{\partial \bar{P}}{\partial x_i} + \frac{1}{\bar{\rho}} \frac{\partial \Sigma_{ij}(\bar{\mathbf{U}}, \bar{T})}{\partial x_j}, \quad (9.6)$$

$$\frac{\partial \bar{U}_j}{\partial x_j} = -\frac{1}{\gamma P_0} \left[(\gamma - 1) \frac{\partial Q_j(\bar{T})}{\partial x_j} + \frac{\partial P_0}{\partial t} \right], \quad (9.7)$$

$$\bar{T} = \frac{P_0}{r \bar{\rho}}, \quad (9.8)$$

and in the Favre formulation by:

$$\frac{\partial \bar{\rho}}{\partial t} + \frac{\partial \bar{\rho} \widetilde{U}_j}{\partial x_j} = 0, \quad (9.9)$$

$$\frac{\partial \bar{\rho} \widetilde{U}_i}{\partial t} = -\frac{\partial}{\partial x_j} (\bar{\rho} \widetilde{U}_j \widetilde{U}_i + \bar{\rho} G_{U_j U_i}) - \frac{\partial \bar{P}}{\partial x_i} + \frac{\partial \Sigma_{ij}(\widetilde{\mathbf{U}}, \widetilde{T})}{\partial x_j}, \quad (9.10)$$

$$\frac{\partial}{\partial x_j} (\widetilde{U}_j + \bar{\rho} G_{U_j/\rho}) = -\frac{1}{\gamma P_0} \left[(\gamma - 1) \frac{\partial Q_j(\widetilde{T})}{\partial x_j} + \frac{\partial P_0}{\partial t} \right], \quad (9.11)$$

$$\tilde{T} = \frac{P_0}{\bar{\rho}r}, \quad (9.12)$$

with the subgrid terms:

$$F_{U_j U_i} = \overline{U_j U_i} - \bar{U}_j \bar{U}_i \quad (9.13)$$

$$G_{U_j U_i} = \widetilde{U_j U_i} - \tilde{U}_j \tilde{U}_i \quad (9.14)$$

$$F_{\rho U_j} = \overline{\rho U_j} - \bar{\rho} \bar{U}_j \quad (9.15)$$

$$G_{U_j/\rho} = \widetilde{U_j/\rho} - \tilde{U}_j/\bar{\rho} \quad (9.16)$$

The Velocity and Favre formulations both involve a subgrid term associated with the momentum convection, $F_{U_j U_i}$ or $G_{U_j U_i}$, and a subgrid term associated with the density-velocity correlation, $F_{\rho U_j}$ or $G_{U_j/\rho}$, such that

$$\frac{F_{\rho U_j}}{\bar{\rho}} = -\bar{\rho} G_{U_j/\rho}. \quad (9.17)$$

The use of the Favre filter removes the need for the modelling of the density-velocity correlation from the mass conservation equation but requires the modelling of an additional subgrid term in the energy conservation equation [87, 88, 90].

The fluid (air) is assumed to be Newtonian to compute the shear-stress tensor,

$$\Sigma_{ij}(\mathbf{U}, T) = \mu(T) \left(\frac{\partial U_i}{\partial x_j} + \frac{\partial U_j}{\partial x_i} \right) - \frac{2}{3} \mu(T) \frac{\partial U_k}{\partial x_k} \delta_{ij}, \quad (9.18)$$

with $\mu(T)$ the dynamic viscosity and δ_{ij} the Kronecker delta. The heat flux is given by

$$Q_j(T) = -\lambda(T) \frac{\partial T}{\partial x_j}, \quad (9.19)$$

with $\lambda(T)$ the thermal conductivity. The variations of viscosity with temperature are accounted for by Sutherland's law [287],

$$\mu(T) = \mu_0 \left(\frac{T}{T_0} \right)^{\frac{3}{2}} \frac{T_0 + S}{T + S}, \quad (9.20)$$

with $\mu_0 = 1.716 \cdot 10^{-5}$ Pa s, $S = 110.4$ K and $T_0 = 273.15$ K. The conductivity is deduced from the Prandtl number Pr and the heat capacity at constant pressure C_p , both assumed constant with $Pr = 0.76$ and $C_p = 1005$ J kg⁻¹ K⁻¹. The ideal gas specific constant is $r = 287$ J kg⁻¹ K⁻¹.

9.2.3 Subgrid-scale models

The subgrid terms of the Velocity and Favre formulations are formally similar. Accordingly, the same modelling procedure is used in both cases. To formalise this, we may express the subgrid-scale models as a function of the filter length scales and of the filtered velocity and density in the two formulations:

$$F_{U_j U_i} \approx \tau_{ij}^{\text{mod}}(\bar{\mathbf{U}}, \bar{\Delta}), \quad (9.21)$$

$$G_{U_j U_i} \approx \tau_{ij}^{\text{mod}}(\tilde{\mathbf{U}}, \bar{\Delta}), \quad (9.22)$$

$$F_{\rho U_j} \approx \pi_j^{\text{mod}}(\bar{\mathbf{U}}, \bar{\rho}, \bar{\Delta}), \quad (9.23)$$

$$G_{U_j/\rho} \approx \pi_j^{\text{mod}}(\tilde{\mathbf{U}}, 1/\bar{\rho}, \bar{\Delta}), \quad (9.24)$$

where the functions $\tau_{ij}^{\text{mod}}(\mathbf{U}, \bar{\Delta})$ and $\pi_j^{\text{mod}}(\mathbf{U}, \phi, \bar{\Delta})$ are model-dependent but do not depend on the formulation.

Eddy-viscosity models for the subgrid term associated with momentum convection may be written in the form

$$\tau_{ij}^{\text{mod}}(\mathbf{U}, \bar{\Delta}) = -2\nu_e^{\text{mod}}(\mathbf{g}, \bar{\Delta})S_{ij}, \quad (9.25)$$

with $S_{ij} = \frac{1}{2}(g_{ij} + g_{ji})$ the rate of deformation tensor and \mathbf{g} the velocity gradient, defined by $g_{ij} = \partial_j U_i$. Notice that $\tau_{ij}^{\text{mod}}(\mathbf{U}, \bar{\Delta})$ may be considered traceless without loss of generality, even in the incompressible case, since the trace can be included as part of the filtered pressure \bar{P} . The eddy-viscosity $\nu_e^{\text{mod}}(\mathbf{g}, \bar{\Delta})$ is given by the model used. The following models from the literature are investigated:

$$\text{Smagorinsky model [276]: } \nu_e^{\text{Smag.}}(\mathbf{g}, \bar{\Delta}) = (C^{\text{Smag.}}\bar{\Delta})^2 |\mathbf{S}|, \quad (9.26)$$

$$\text{WALE model [213]: } \nu_e^{\text{WALE}}(\mathbf{g}, \bar{\Delta}) = (C^{\text{WALE}}\bar{\Delta})^2 \frac{(\mathcal{S}_{ij}^d \mathcal{S}_{ij}^d)^{\frac{3}{2}}}{(S_{mn} S_{mn})^{\frac{5}{2}} + (\mathcal{S}_{mn}^d \mathcal{S}_{mn}^d)^{\frac{5}{4}}}, \quad (9.27)$$

$$\text{Vreman model [304]: } \nu_e^{\text{Vreman}}(\mathbf{g}, \bar{\Delta}) = C^{\text{Vreman}} \sqrt{\frac{\text{II}_G}{g_{mn} g_{mn}}}, \quad (9.28)$$

$$\text{Sigma model [214]: } \nu_e^{\text{Sigma}}(\mathbf{g}, \bar{\Delta}) = (C^{\text{Sigma}}\bar{\Delta})^2 \frac{\sigma_3 (\sigma_1 - \sigma_2) (\sigma_2 - \sigma_3)}{\sigma_1^2}, \quad (9.29)$$

$$\text{AMD model [250]: } \nu_e^{\text{AMD}}(\mathbf{g}, \bar{\Delta}) = C^{\text{AMD}} \frac{\max(0, -G_{ij} S_{ij})}{g_{mn} g_{mn}}, \quad (9.30)$$

$$\text{VSS model [252]: } \nu_e^{\text{VSS}}(\mathbf{g}, \bar{\Delta}) = (C^{\text{VSS}}\bar{\Delta})^2 \frac{(R_{ij} R_{ij})^{\frac{3}{2}}}{(S_{mn} S_{mn})^{\frac{5}{2}}}, \quad (9.31)$$

$$\text{Kobayashi model [147]: } \nu_e^{\text{Koba.}}(\mathbf{g}, \bar{\Delta}) = C^{\text{Koba.}} \bar{\Delta}^2 |F_g|^{\frac{3}{2}} (1 - F_g) |\mathbf{S}|, \quad (9.32)$$

where $|\mathbf{S}| = \sqrt{2S_{ij}S_{ij}}$ is a norm of \mathbf{S} , $\mathcal{S}_{ij}^d = \frac{1}{2}(g_{ik}g_{kj} + g_{jk}g_{ki}) - \frac{1}{3}g_{kp}g_{pk}\delta_{ij}$ the traceless symmetric part of the squared velocity gradient tensor, $\sigma_1 \geq \sigma_2 \geq \sigma_3$ the three singular values of \mathbf{g} , $G_{ij} = \bar{\Delta}_k^2 g_{ik}g_{jk}$ the gradient model for the subgrid term associated with momentum convection [169], $\text{II}_G = \frac{1}{2}(\text{tr}^2(G) - \text{tr}(G^2))$ its second invariant, $R_{ij} = \beta_i g_{jj}$ the volumetric strain-stretching, with $\beta = (S_{23}, S_{13}, S_{12})$, and $F_g = (\Omega_{ij}\Omega_{ij} - S_{ij}S_{ij}) / (\Omega_{mn}\Omega_{mn} + S_{mn}S_{mn})$ the coherent structure function, with $\Omega_{ij} = \frac{1}{2}(g_{ij} - g_{ji})$ the spin tensor or rate of rotation tensor. Only constant coefficient versions of eddy-viscosity and eddy-diffusivity models are considered. The typical value of the coefficients from the literature is $C^{\text{Smag.}} = 0.10$, $C^{\text{WALE}} = 0.55$, $C^{\text{Vreman}} = 0.07$, $C^{\text{Sigma}} = 1.5$, $C^{\text{AMD}} = 0.3$, $C^{\text{VSS}} = 1.3$ and $C^{\text{Koba.}} = 0.045$. The corresponding dynamic versions of these models are not considered in order to assess the relevance of the

models before any dynamic correction [112, 177, 221]. The filter length scale is computed following Deardorff [77] as $\bar{\Delta} = (\bar{\Delta}_x \bar{\Delta}_y \bar{\Delta}_z)^{1/3}$. A review of alternative possible definitions may be found in Trias *et al.* [295].

Following the same rationale, eddy-diffusivity models for the density-velocity correlation subgrid term may be written in the form

$$\pi_j^{\text{mod}}(\mathbf{U}, \phi, \bar{\Delta}) = -2\kappa_e^{\text{mod}}(\mathbf{g}, \mathbf{d}, \bar{\Delta})d_j. \quad (9.33)$$

with \mathbf{d} the scalar gradient, defined by $d_j = \partial_j \phi$. It is common to express the eddy-diffusivity $\kappa_e^{\text{mod}}(\mathbf{g}, \bar{\Delta})$ using the constant subgrid-scale Prandtl or Schmidt number assumption,

$$\kappa_e^{\text{mod}}(\mathbf{g}, \mathbf{d}, \bar{\Delta}) = \frac{1}{Pr_t} \nu_e^{\text{mod}}(\mathbf{g}, \bar{\Delta}), \quad (9.34)$$

where Pr_t is the subgrid-scale Prandtl or Schmidt number. This provides a corresponding eddy-diffusivity model for each eddy-viscosity of equations (9.26–9.32). The dimensionless number Pr_t corresponds to a subgrid-scale Schmidt number in the Velocity formulation and a subgrid-scale Prandtl number in the Favre formulation. Given the formal similarity between the density-velocity correlation subgrid term in the Velocity and Favre formulation and the ideal gas law (9.4) which relates density and temperature, it is presumed that the same value may be used in the two formulations.

Alternatively, some specific eddy-diffusivity models have been suggested in the literature [113, 3]. We investigate one,

$$\text{Scalar AMD model [3]:} \quad \kappa_e^{\text{SAMD}}(\mathbf{g}, \mathbf{d}, \bar{\Delta}) = C^{\text{SAMD}} \frac{\max(0, -D_j d_j)}{d_m d_m}, \quad (9.35)$$

with $D_j = \bar{\Delta}_k^2 g_{jk} d_k$ the gradient model for the density-velocity correlation subgrid term.

In addition, we suggest and investigate two new models. First, the Anisotropic Smagorinsky model is a modified version of the Smagorinsky model, associated with a single filter length scale, devised to involve the three filter length scales. This aims to improve the anisotropy of the model. The model is obtained by substituting in equations (9.25) and (9.33) the velocity gradient \mathbf{g} and respectively the scalar gradient \mathbf{d} by the scaled velocity gradient \mathbf{g}^a , defined by $g_{ij}^a = (\bar{\Delta}_j / \bar{\Delta}) \partial_j U_i$, and respectively the scaled scalar gradient \mathbf{d}^a , defined by $d_j^a = (\bar{\Delta}_j / \bar{\Delta}) \partial_j \phi$. Namely,

$$\tau_{ij}^{\text{An.Smag.}}(\mathbf{U}, \bar{\Delta}) = -2\nu_e^{\text{Smag.}}(\mathbf{g}^a, \bar{\Delta}) S_{ij}^a, \quad (9.36)$$

$$\pi_j^{\text{An.Smag.}}(\mathbf{U}, \phi, \bar{\Delta}) = -2\kappa_e^{\text{Smag.}}(\mathbf{g}^a, \mathbf{d}^a, \bar{\Delta}) d_j^a, \quad (9.37)$$

with $S_{ij}^a = \frac{1}{2}(g_{ij}^a + g_{ji}^a)$ the scaled rate of deformation tensor. The eddy-viscosity and eddy-diffusivity are computed using equations (9.26) and (9.34). A similar procedure could be applied to obtain an anisotropic version of the WALE, Sigma, VSS and Kobayashi models.

Besides, we study the multiplicative mixed model based on the gradient model (MMG model), a functional model constructed such that its magnitude is determined by the gradient model [169] and its orientation is aligned with the rate of deformation

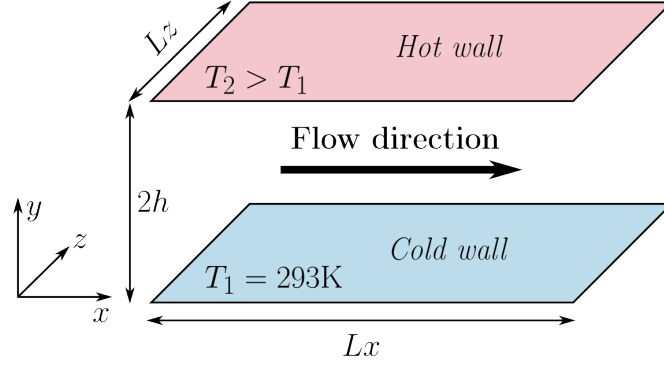


Figure 9.1 – Biperiodic anisothermal channel flow.

tensor or the scalar gradient depending on the subgrid term. This procedure is reminiscent of the multiplicative mixed model of Ghaisas and Frankel [113, 114] which had an opposite purpose. The eddy-viscosity and eddy-diffusivity according to the MMG model are given by,

$$\text{MMG model:} \quad \nu_e^{\text{MMG}}(\mathbf{g}, \overline{\Delta}) = -C^{\text{MMG}} \frac{G_{kk}}{|\mathbf{S}|}, \quad (9.38)$$

$$\text{Scalar MMG model:} \quad \kappa_e^{\text{SMMG}}(\mathbf{g}, \mathbf{d}, \overline{\Delta}) = -C^{\text{SMMG}} \frac{\sqrt{D_i D_i}}{\sqrt{d_m d_m}}. \quad (9.39)$$

A similar procedure can be applied to other structural models, such as the scale-similarity model [14]. We may also view the MMG model as a multiplicative mixed model. Using the the Smagorinsky model and the isotropic part modelling of Yoshizawa [320],

$$\tau_{mm}^{\text{Yosh.}}(\mathbf{U}, \overline{\Delta}) = 2C^{\text{Yosh.}} \overline{\Delta}^2 |\mathbf{S}|^2, \quad (9.40)$$

the MMG model $\tau_{ij}^{\text{MMG}}(\mathbf{U}, \overline{\Delta}) = -2\nu_e^{\text{MMG}}(\mathbf{g}, \overline{\Delta}) S_{ij}$ can be reformulated as

$$\tau_{ij}^{\text{MMG}}(\mathbf{U}, \overline{\Delta}) = G_{kk} \frac{\tau_{ij}^{\text{Smag.}}(\mathbf{U}, \overline{\Delta})}{\tau_{mm}^{\text{Yosh.}}(\mathbf{U}, \overline{\Delta})} \quad (9.41)$$

emphasising that the MMG model combines the magnitude of the gradient model and the structure of the Smagorinsky model. This leads by identification $C^{\text{MMG}} = (C^{\text{Smag.}})^2 / (2C^{\text{Yosh.}})$. Note that the Vreman, AMD and scalar AMD models also directly involve the gradient model [169].

9.2.4 Numerical study configuration

9.2.4.1 Channel flow configuration

We consider a fully developed three-dimensional anisothermal channel flow, as represented in figure 9.1. This geometry is one of the simpler that reproduces the distinctive features of low Mach number strongly anisothermal turbulent flows. The channel is periodic in the streamwise (x) and spanwise (z) directions. The wall-normal direction

is denoted (y). The domain size is $4\pi h \times 2h \times 2\pi h$, with $h = 15$ mm. The temperature at the channel walls is imposed at $T_1 = 293$ K at the cold wall ($y = 0$) and $T_2 = 586$ K at the hot wall ($y = 2h$). This creates a temperature gradient in the wall-normal direction. The mean friction Reynolds number is $Re_\tau = 180$, where Re_τ is defined as the average of the friction Reynolds numbers $Re_{\tau,\omega}$ calculated at the hot and cold wall,

$$Re_{\tau,\omega} = \frac{U_\tau h}{\nu_\omega}, \quad (9.42)$$

with $U_\tau = \nu_\omega (\partial_y \bar{U}_x)_\omega^{0.5}$ the friction velocity and ν_ω the wall kinematic viscosity.

9.2.4.2 Numerical settings

The mesh contains $384 \times 266 \times 384$ grid points and is regular in the homogeneous directions. It follows a hyperbolic tangent law in the wall-normal coordinate direction. The wall-normal grid coordinates are symmetrical with respect to the plane $y = h$. In the first half of the channel, they are given by

$$y_k = h \left(1 + \frac{1}{a} \tanh \left[\left(\frac{k-1}{N_y-1} - 1 \right) \tanh^{-1}(a) \right] \right), \quad (9.43)$$

with $a = 0.97$ the mesh dilatation parameter and N_y the number of grid points in the wall-normal direction. The cell sizes in wall units are $\Delta_x^+ = 8.5$, $\Delta_y^+ = 0.13$ at the wall and 4.2 at the centre of the channel and $\Delta_z^+ = 4.2$. A finite volume method is used with a third-order Runge–Kutta time scheme and a fourth-order centred momentum convection scheme. This is performed using the TrioCFD software [38].

9.2.4.3 Filtering process

The subgrid terms and the models are computed from the filtering of the instantaneous DNS data at the resolution of a large-eddy simulation mesh. The filter corresponds to a mesh with $48 \times 50 \times 48$ grid points ($\Delta_x^+ = 68$; $\Delta_y^+ = 0.5 - 25$; $\Delta_z^+ = 34$) constructed as the DNS mesh. Due to the inhomogeneity of the mesh, the filter width is variable in the wall-normal direction.

A top-hat filter is used. In one dimension, it is given in the physical space by

$$\bar{\psi}(x) = \frac{1}{\bar{\Delta}(x)} \int_{x-\frac{1}{2}\bar{\Delta}(x)}^{x+\frac{1}{2}\bar{\Delta}(x)} \psi(\xi) d\xi. \quad (9.44)$$

Multidimensional filtering is carried out by sequentially applying the one-dimensional filter in the three spatial directions. In order to carry out the filtering with an arbitrary filter length, the DNS data are first interpolated using a cubic spline. The top-hat filter is then computed from the interpolated value without mesh restrictions.

The discretisation of the differential operator of the models is carried out on the DNS grid, thus using data not available in an a posteriori large-eddy simulation [180]. This assesses the relevance of the models without regard to numerical errors. The data from 100 uncorrelated timesteps were averaged in order to obtain a satisfactory convergence of the results.

9.2.5 Asymptotic near-wall behaviour of the models

The WALE, Sigma, VSS and Kobayashi models have been designed to have an eddy-viscosity with a proper asymptotic near-wall behaviour for the subgrid term associated with momentum convection. While the components of the subgrid terms have different wall orders, the preferable asymptotic near-wall behaviour of the eddy-viscosity is cubic with respect to the distance to the wall, that is $\nu_e^{\text{mod}}(\mathbf{g}, \bar{\Delta})|_{\omega} = \mathcal{O}(y^3)$. A reason is that it is the order that the eddy-viscosity should have for the near-wall behaviour of the subgrid kinetic energy dissipation to be consistent with the exact subgrid kinetic energy dissipation. The asymptotic near-wall behaviour of the models given in the literature [213, 214, 294, 273] considers the behaviour of the differential operator the models are based on, assuming that the filter length does not tend to zero at the wall, $\bar{\Delta}|_{\omega} = \mathcal{O}(y^0)$. The near-wall order of the models can be obtained from the Taylor series expansion of the velocity and the scalar (density or inverse of density) [45, 253, 53, 214]:

$$U_x|_{\omega} = \mathcal{O}(y^1), \quad (9.45)$$

$$U_y|_{\omega} = \mathcal{O}(y^2), \quad (9.46)$$

$$U_z|_{\omega} = \mathcal{O}(y^1), \quad (9.47)$$

$$\phi|_{\omega} = \mathcal{O}(y^0). \quad (9.48)$$

The quadratic behaviour of the wall-normal velocity follows from the mass conservation equation, provided that the density is constant at the walls. This assumption is valid in our case if the time variations of thermodynamical pressure are neglected, since the wall temperatures are imposed. The filter is considered to not alter the asymptotic near-wall behaviour of the variables. This assumption is valid for a top-hat filter as defined in equation (9.44) with varying filter width. The cubic asymptotic near-wall behaviour of the subgrid term can be recovered, for the “ xy ” component, from the linear near-wall order of the streamwise velocity and the quadratic near-wall order of the wall-normal velocity [253, 273].

We find that this procedure is not satisfactory for the density-velocity correlation subgrid term. Indeed, it is not able to take into account the fact that $F_{\rho U_j} = \overline{\rho U_j} - \bar{\rho} \bar{U}_j$ cannot have a near-wall order below 2 because the filter used, given in equation (9.44), preserves constant and linear functions. To determine the asymptotic near-wall behaviour of the subgrid terms, we carry out a Taylor series expansion of the filter, leading to the gradient model [169]. Next, the near-wall order of the gradient model is expressed considering a filter with a non-zero order at the wall. For a continuous filter whose size in the wall-normal direction (y) tends to zero at the wall, it is natural to consider

$$\bar{\Delta}_x|_{\omega} = \mathcal{O}(y^0), \quad (9.49)$$

$$\bar{\Delta}_y|_{\omega} = \mathcal{O}(y^1), \quad (9.50)$$

$$\bar{\Delta}_z|_{\omega} = \mathcal{O}(y^0). \quad (9.51)$$

It follows

$$\bar{\Delta}|_{\omega} = \mathcal{O}(y^{1/3}). \quad (9.52)$$

Note also that the near-wall order of the streamwise and spanwise derivatives of the scalar is at least $\mathcal{O}(y^1)$ under the hypothesis of constant density at the walls. With

Subgrid-scale model	With $\bar{\Delta}_y _\omega = \mathcal{O}(y^0)$	With $\bar{\Delta}_y _\omega = \mathcal{O}(y^1)$
Smagorinsky model [276]	$\mathcal{O}(y^0)$	$\mathcal{O}(y^2)$
WALE model [213]	$\mathcal{O}(y^3)$	$\mathcal{O}(y^{11/3})$
Vreman model [304]	$\mathcal{O}(y^1)$	$\mathcal{O}(y^{3/2})$
Sigma model [214]	$\mathcal{O}(y^3)$	$\mathcal{O}(y^{11/3})$
AMD model [250]	$\mathcal{O}(y^1)$	$\mathcal{O}(y^3)$
Scalar AMD model [3]	$\mathcal{O}(y^0)$	$\mathcal{O}(y^3)$
VSS model [252]	$\mathcal{O}(y^3)$	$\mathcal{O}(y^{11/3})$
Kobayashi model [147]	$\mathcal{O}(y^3)$	$\mathcal{O}(y^{11/3})$
Anisotropic Smagorinsky model	$\mathcal{O}(y^0)$	$\mathcal{O}(y^2)$
MMG model	$\mathcal{O}(y^0)$	$\mathcal{O}(y^2)$
Scalar MMG model	$\mathcal{O}(y^0)$	$\mathcal{O}(y^2)$

Table 9.1 – Asymptotic near-wall behaviour of the models, for a constant and linear near-wall behaviour of the filter width. The expected order is $\mathcal{O}(y^3)$ for the subgrid term associated with momentum convection and the density-velocity correlation subgrid term.

these assumptions, the expected asymptotic near-wall behaviour of the eddy-diffusivity for models of the density-velocity correlation subgrid term is also cubic with respect to the distance to the wall, $\kappa_e^{\text{mod}}(\mathbf{g}, \mathbf{d}, \bar{\Delta})|_\omega = \mathcal{O}(y^3)$. This ensures that the order of the subgrid squared scalar dissipation corresponds to that of the exact subgrid term. For the subgrid term associated with momentum convection, the results are consistent with the literature since it leads to the same near-wall order for each component as the Taylor series expansion of the velocity tensor product.

The asymptotic near-wall behaviour of the investigated subgrid-scale models is given in table 9.1 for a filter width of order $\mathcal{O}(y^0)$ at the wall and a filter which obeys equations (9.49–9.51). With $\bar{\Delta}_y|_\omega = \mathcal{O}(y^0)$, the WALE, Sigma, VSS and Kobayashi models have the proper asymptotic near-wall behaviour. With $\bar{\Delta}_y|_\omega = \mathcal{O}(y^1)$, the AMD and scalar AMD models have the proper asymptotic near-wall behaviour.

9.2.6 Results and discussion

The performance of the subgrid-scale models is assessed from the comparison of the models and the subgrid terms computed from the DNS data. It is customary [see e.g. 64, 309, 30, 189, 239, 1, 182, 113, 141] to compare the model to the exact subgrid terms using a linear regression analysis. The correlation coefficient is an index scaled to between -1 and 1 which measures the linear correlation between two variables, that is the closeness of the relationship between the two variables with a linear relationship. A value of -1 indicates a perfect negative linear relationship, 0 no linear relationship and 1 a perfect positive linear relationship. Let us note b a model for the subgrid term of exact value a . The correlation coefficient between a and b is defined by,

$$\text{Corr}(a, b) = \frac{\langle ab \rangle - \langle a \rangle \langle b \rangle}{\sqrt{(\langle a^2 \rangle - \langle a \rangle^2)(\langle b^2 \rangle - \langle b \rangle^2)}}, \quad (9.53)$$

where the angle brackets $\langle \cdot \rangle$ denote an ensemble averaging. The regression coefficient gives the slope of the linear relationship,

$$\text{Regr}(a, b) = \frac{\langle ab \rangle - \langle a \rangle \langle b \rangle}{\langle a^2 \rangle - \langle a \rangle^2}. \quad (9.54)$$

The concordance correlation coefficient [178] is a correlation-like index scaled to between -1 and 1 which measure the agreement between two variables, that is the closeness of the relationship between the two variables with identity,

$$\text{Conc}(a, b) = \frac{\langle ab \rangle - \langle a \rangle \langle b \rangle}{\langle a^2 \rangle - \langle a \rangle^2 + \langle b^2 \rangle - \langle b \rangle^2 + (\langle a \rangle - \langle b \rangle)^2}. \quad (9.55)$$

The correlation coefficient between the model and the exact subgrid term may be interpreted as the ability of the model to capture the correct flow structure and the regression coefficient of the correct magnitude level. The concordance correlation coefficient combines the two types of information. The optimal value of the correlation coefficient, the regression coefficient and the concordance correlation coefficient is 1 . However, only a concordance correlation coefficient of 1 implies that the model and the exact subgrid term are identical.

Given the homogeneity of the flow in the streamwise and spanwise directions, the analysis is carried out as a function of the wall-normal coordinate. The ensemble averaging $\langle \cdot \rangle$ is computed as an average over time and the two homogeneous directions and the linear relationship assessed for each value of y . Notice that the addition for any value of y of a constant scaling factor to the model does not modify the correlation coefficient, multiply the regression coefficient by the constant and has a non-trivial effect on the concordance correlation coefficient.

We first present some general results regarding the performance of the models. Then, the subgrid-scale models are assessed for the subgrid term associated with momentum convection and the density-velocity correlation subgrid term.

9.2.6.1 General results

The subgrid-scale modelling in the Velocity and Favre formulations are compared from the study of the subgrid terms and the models with the classical filter and with the Favre filter. The results show no differences between the classical and Favre filter with regard to the performance of the models. For instance, the correlation coefficient between the Smagorinsky model and the exact momentum convection subgrid term with the classical filter and with the Favre filter are very similar (figure 9.2). The a priori study of the subgrid-scale models thus does not let us select between the Velocity and Favre formulations of the filtered low Mach number equations. Thereafter, the subgrid-scale models are assessed in the Velocity formulation, using the classical filter, but the results also apply to the Favre formulation.

The temperature gradient generates an asymmetry between the hot and cold sides with regard to the performance of the models. This is highlighted in figure 9.3 by comparing in the case of the Smagorinsky model the results with an isothermal simulation performed with the same mesh, numerical settings, friction Reynolds number and filtering. The correlation coefficient is larger at the hot side than in the isothermal

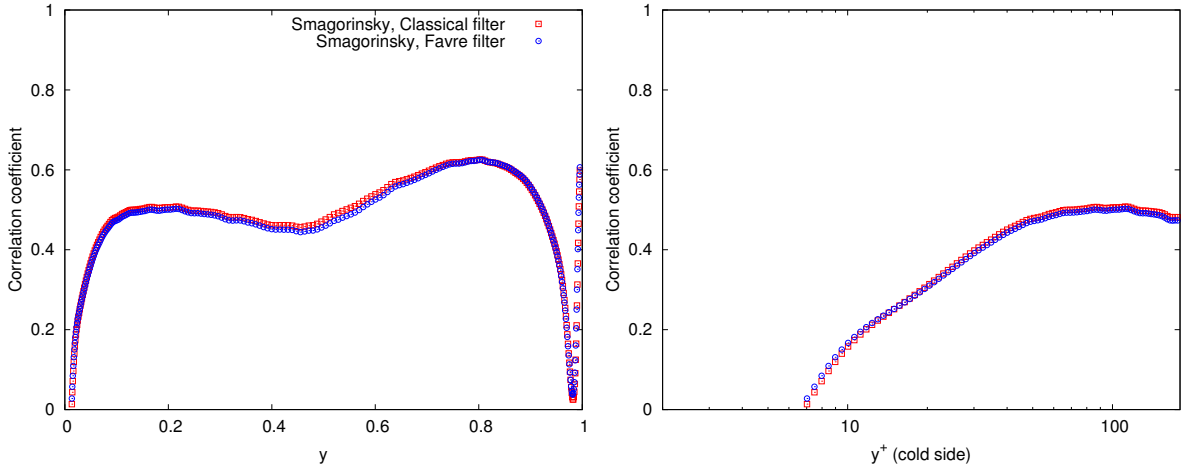


Figure 9.2 – Correlation coefficient between the exact momentum convection subgrid term and the Smagorinsky model for the term that appears in the streamwise velocity transport equation (9.6) in the Velocity formulation, $\text{Corr}(\partial_j F_{U_j U_x}, \partial_j \tau_{xj}^{\text{Smag}}(\bar{\mathbf{U}}, \bar{\mathbf{\Delta}}))$, and in the streamwise momentum conservation equation (9.10) in the Favre formulation, $\text{Corr}(\partial_j \bar{\rho} G_{U_j U_x}, \partial_j \bar{\rho} \tau_{ij}^{\text{Smag}}(\tilde{\mathbf{U}}, \bar{\mathbf{\Delta}}))$.

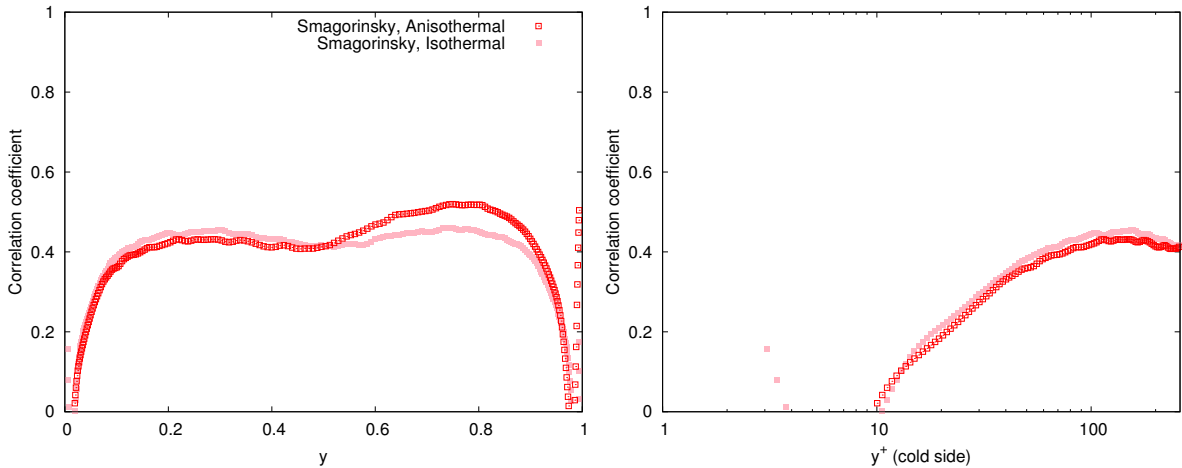


Figure 9.3 – Correlation coefficient between the divergence of the streamwise-related part of the exact momentum convection subgrid term and the Smagorinsky model, $\text{Corr}(\partial_j F_{U_j U_x}, \partial_j \tau_{xj}^{\text{Smag}}(\bar{\mathbf{U}}, \bar{\mathbf{\Delta}}))$, in the isothermal and anisothermal configurations.

configuration, and lower at the cold side. The asymmetry may be attributed to an asymmetry of filtering resolution compared to the turbulence intensity. Indeed, due to the variations of the fluid properties with temperature, the local friction Reynolds number varies across the channel, from 105 at the hot wall to 261 at the cold wall, leading to a lower turbulence intensity level at the hot side than in the isothermal configuration, and higher at the cold side.

9.2.6.2 Subgrid term associated with momentum convection

The models for the subgrid term associated with momentum convection are assessed as it appears in the streamwise velocity transport equation in figure 9.4, in the spanwise velocity transport equation in figure 9.5, and in the wall-normal velocity transport

equation in figure 9.6. The figure 9.7 addresses the subgrid kinetic energy dissipation $\bar{\rho}F_{U_j U_i} S_{ij}$, an important part of the contribution of the subgrid term to the kinetic energy exchanges. In each case, the profiles of the correlation coefficient, the regression coefficient and the concordance correlation coefficient are given as a function of the wall-normal coordinate y , scaled by the height of the channel, and in the classical wall scaling

$$y^+ = Re_\tau \frac{y}{h} = \frac{yU_\tau}{\nu_\omega}. \quad (9.56)$$

As a basis of comparison, each model is scaled in order to match the correct level of total subgrid kinetic energy dissipation in the volume. This is equivalent to setting the constant of the models to

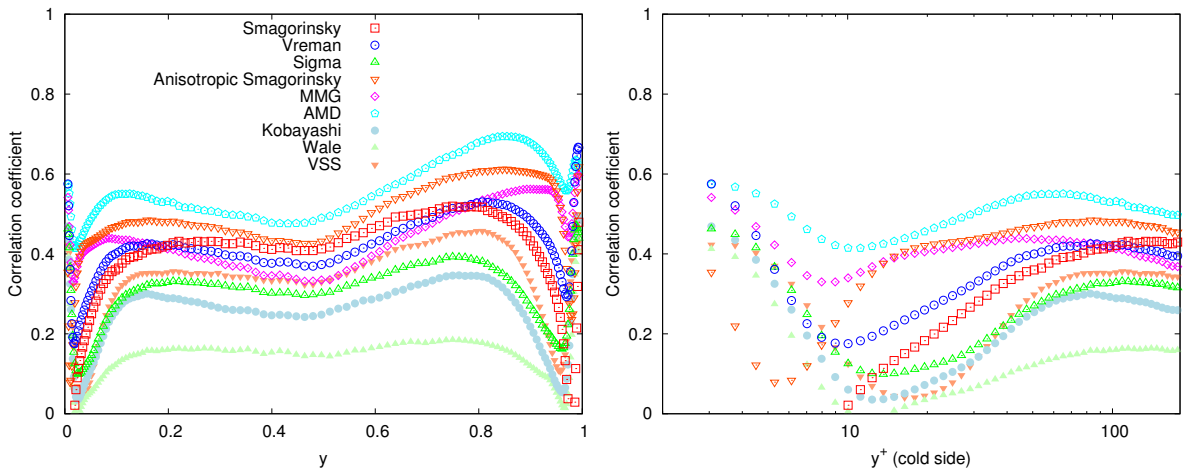
$$C^{\text{mod}} = \frac{\int_T \int_V \bar{\rho}F_{U_j U_i} S_{ij} dx dy dz dt}{\int_T \int_V \bar{\rho}\tau_{ij}^{\text{mod}}(\mathbf{U}, \mathbf{\Delta}) S_{ij} dx dy dz dt}, \quad (9.57)$$

where V denotes the entire domain and T the integration time.

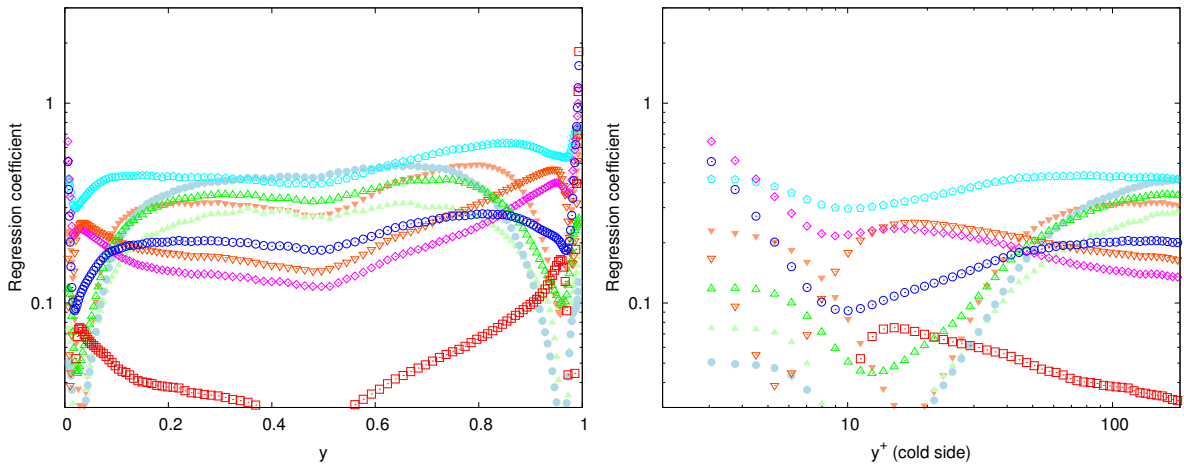
All the investigated subgrid-scale models correlates rather poorly with the exact subgrid term as it occurs in the velocity transport equation (figures 9.4(a), 9.5(a), 9.6(a)). This is consistent with previous findings which showed that the exact subgrid term correlates poorly with the rate of deformation tensor [182, 64, 180], and reflects the limits of the eddy-viscosity assumption. The models are however better-correlated with the exact subgrid term for the subgrid kinetic energy dissipation (figure 9.7(a)), with correlation coefficients higher than 0.7–0.8 throughout the channel for the best models. Accordingly, the regression coefficient at the centre of the channel appears too low for all models in the three components of the velocity transport equation (figures 9.4(b), 9.5(b), 9.6(b)), but around an adequate level for the subgrid kinetic energy dissipation (figure 9.7(b)). This discrepancy is related to the intrinsic nature of the models and may not be easily corrected as increasing the magnitude level of the models to a sufficient amplitude in the velocity transport equation would make the models overdissipative in the kinetic energy transport equation.

The AMD model is significantly more well-correlated with the exact subgrid term than the other investigated models (figures 9.4(a), 9.5(a), 9.6(a), 9.7(a)). The Vreman, Anisotropic Smagorinsky and MMG models also have a high level of correlation throughout the channel. In the streamwise velocity transport equation (figure 9.4(a)), the WALE model has a very low correlation coefficient (< 0.2) in the bulk of the channel but gives better results at the wall. In the kinetic energy transport equation (figure 9.7(a)), it is the opposite. To a lesser extent, the Sigma, VSS and Kobayashi models obey to the same pattern.

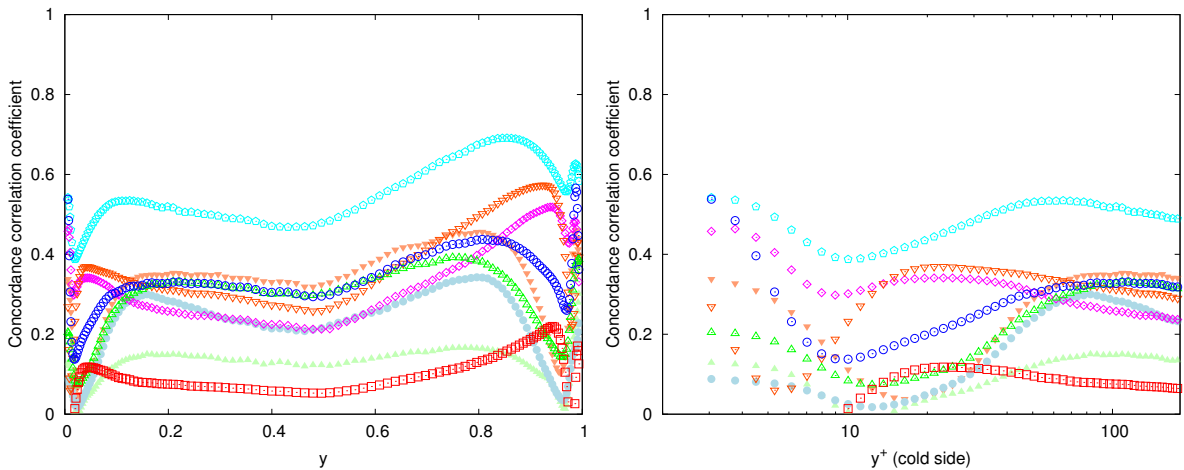
Near the wall, the correlation of the Smagorinsky model deteriorates and its amplitude increases dramatically because the differential operator it is based on does not vanish in near-wall regions, which conflicts with the near-wall behaviour of the exact subgrid term. The Anisotropic Smagorinsky model is able to improve greatly the near-wall behaviour of the Smagorinsky model, the filter lengths in the Anisotropic Smagorinsky model acting akin to a damping function. The Vreman, Anisotropic Smagorinsky and MMG models vanish at the wall but with a lower order than the exact subgrid term (table 9.1). Their magnitude compared to the exact subgrid term is increased near the wall. Nevertheless, their regression coefficient is subject to less



(a) Correlation coefficient.

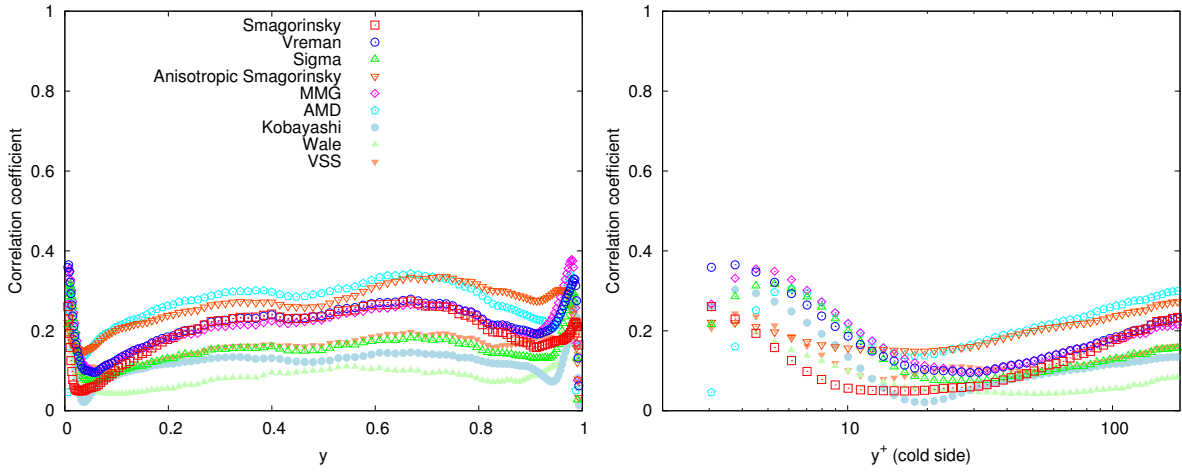


(b) Regression coefficient.

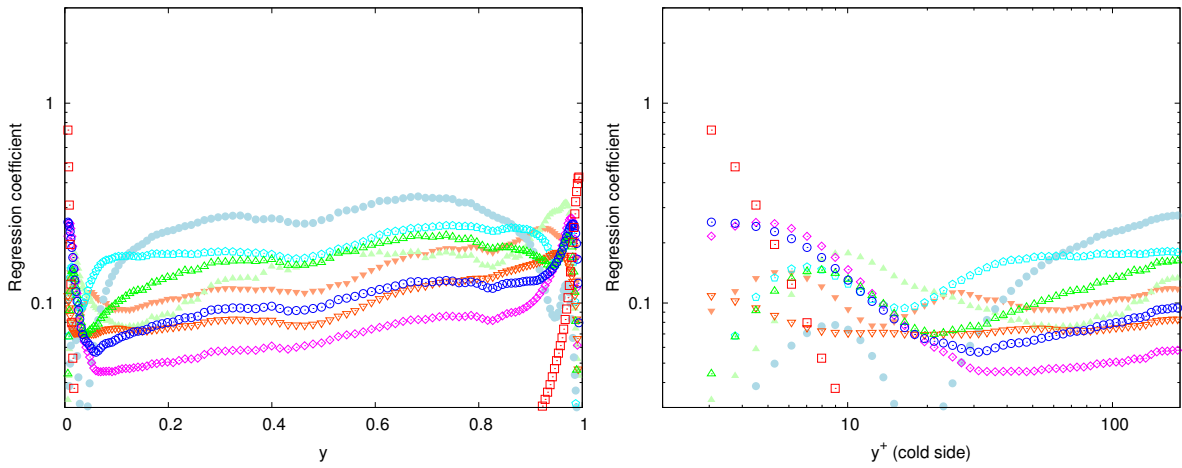


(c) Concordance correlation coefficient.

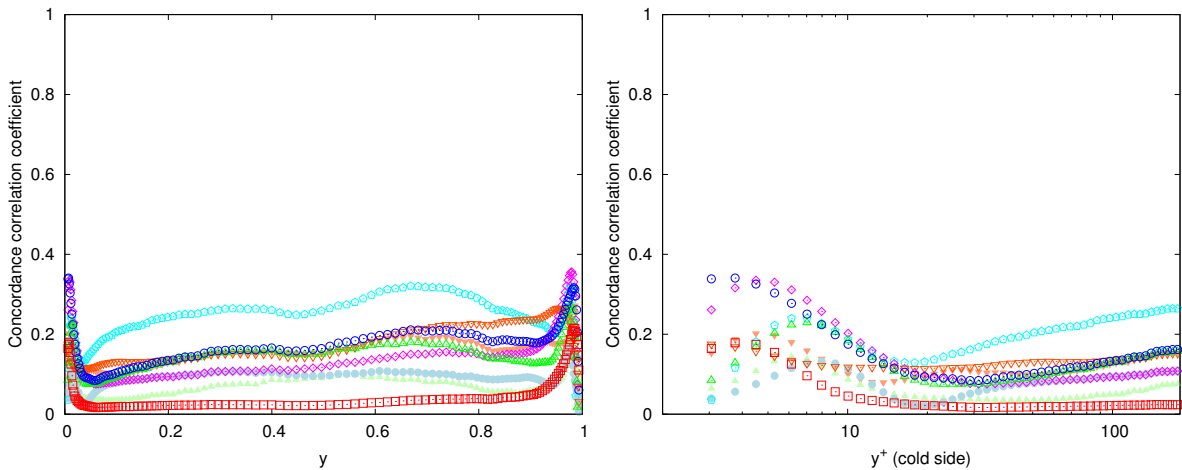
Figure 9.4 – Correlation coefficient, regression coefficient, and concordance correlation coefficient between the divergence of the streamwise-related part of the exact momentum convection subgrid term $\partial_j F_{U_j U_x}$ and eddy-viscosity models $\partial_j \tau_{xj}^{\text{mod}}(\bar{U}, \bar{\Delta})$.



(a) Correlation coefficient.

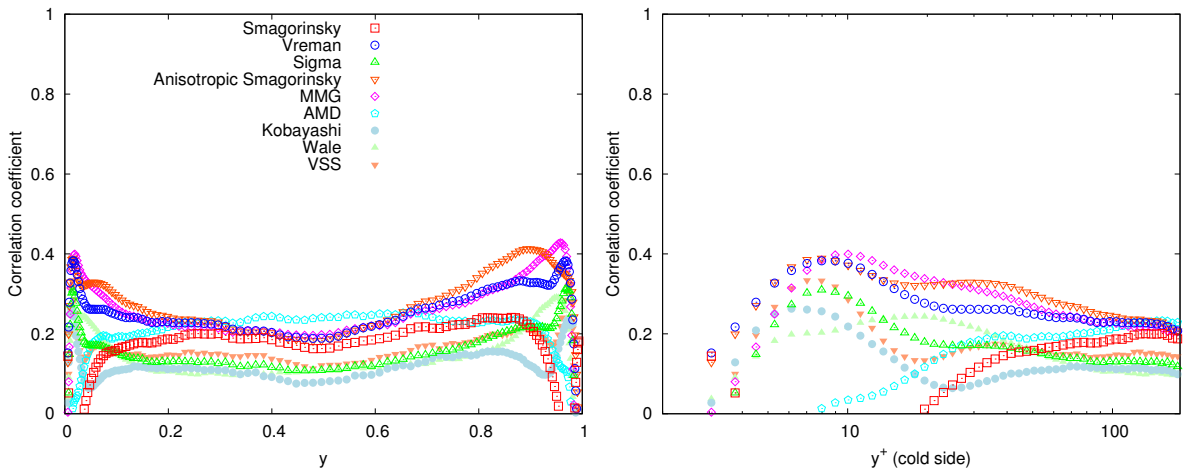


(b) Regression coefficient.

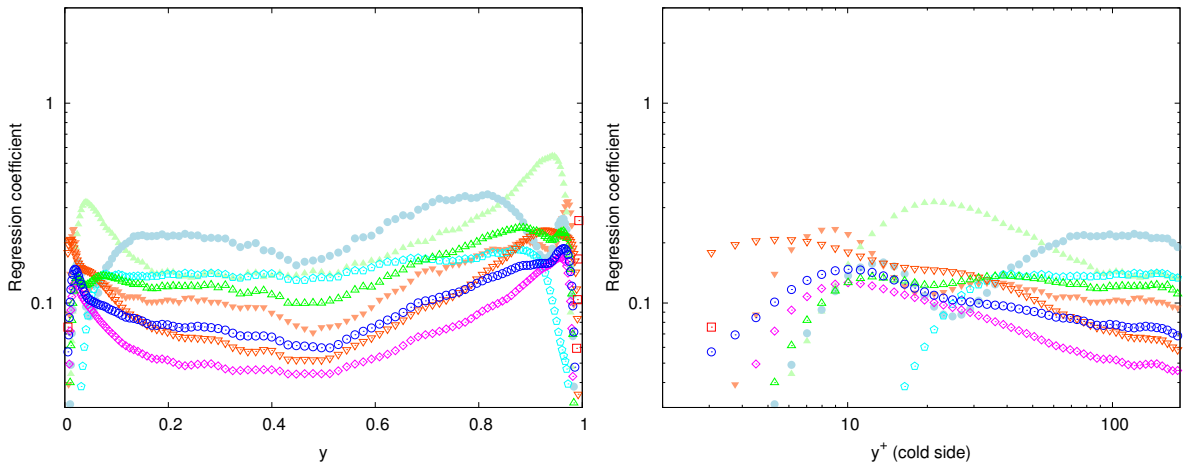


(c) Concordance correlation coefficient.

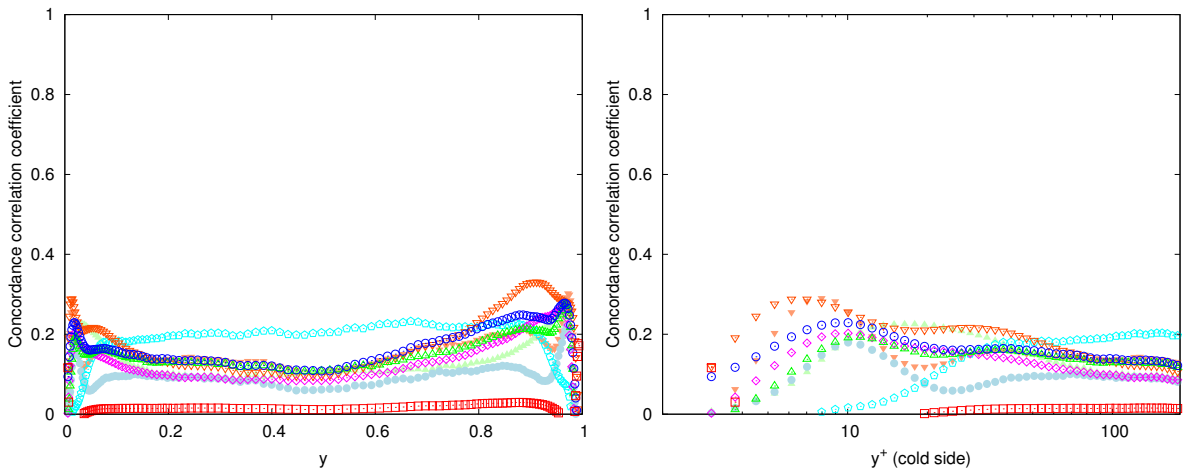
Figure 9.5 – Correlation coefficient, regression coefficient, and concordance correlation coefficient between the divergence of the spanwise-related part of the exact momentum convection subgrid term $\partial_j F_{U_j U_z}$ and eddy-viscosity models $\partial_j \tau_{zj}^{\text{mod}}(\bar{U}, \bar{\Delta})$.



(a) Correlation coefficient.

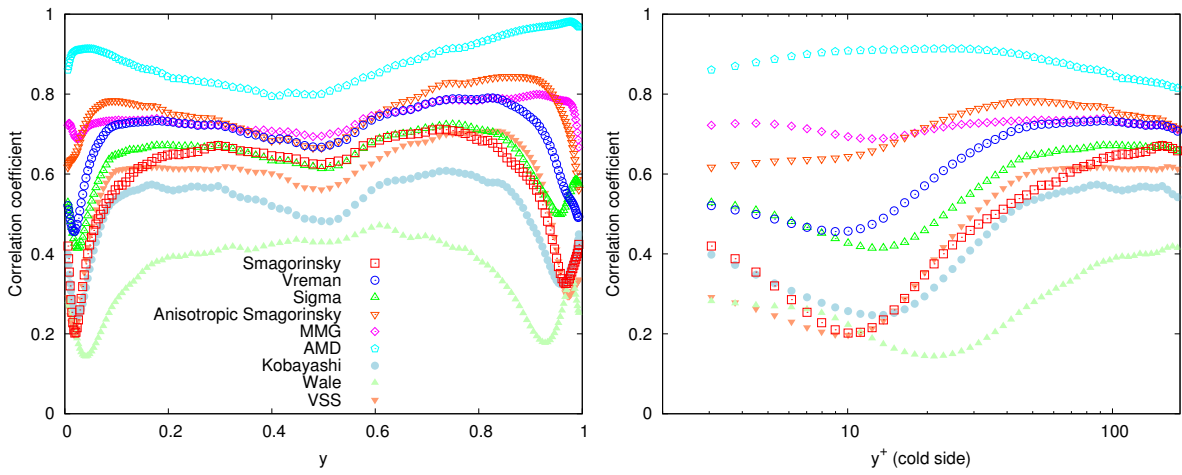


(b) Regression coefficient.

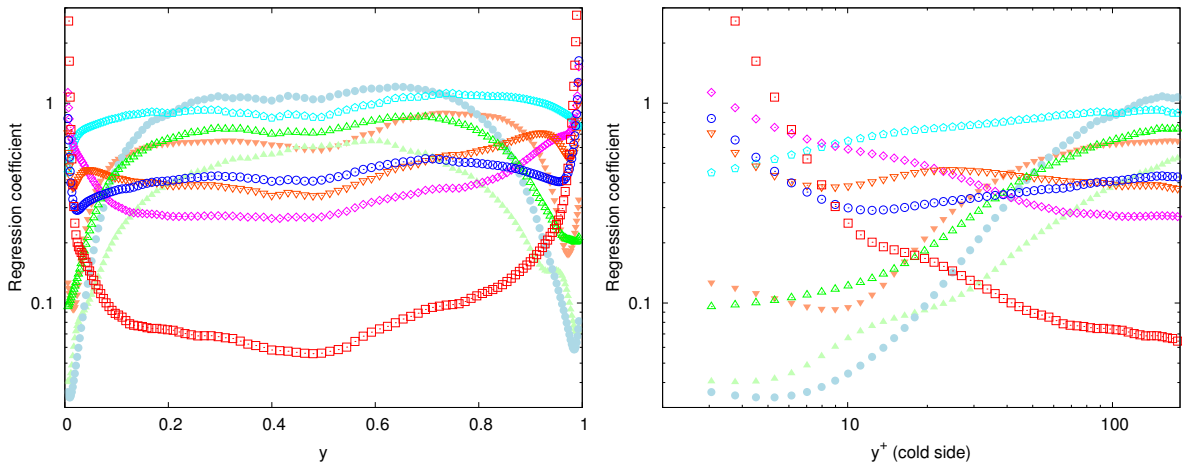


(c) Concordance correlation coefficient.

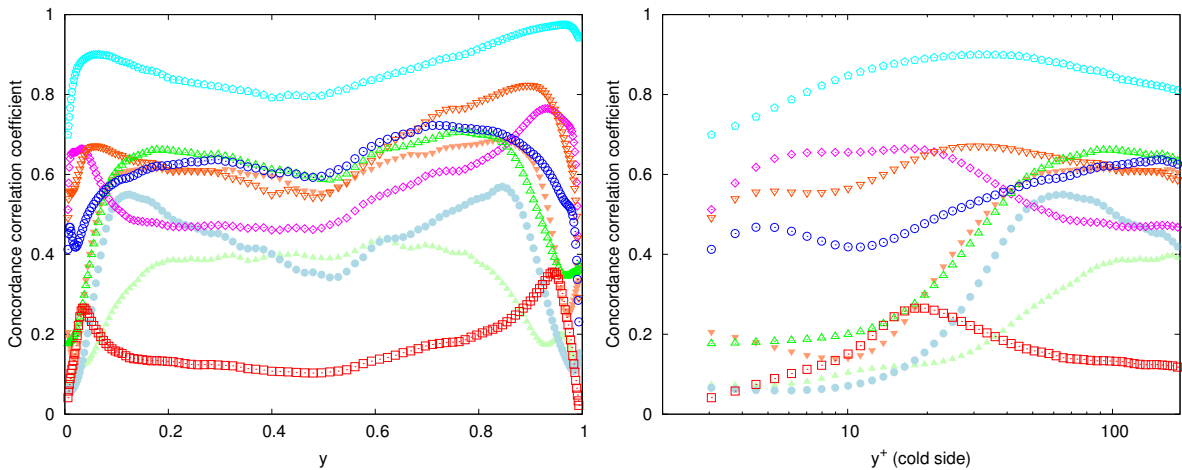
Figure 9.6 – Correlation coefficient, regression coefficient, and concordance correlation coefficient between the divergence of the wall-normal-related part of the exact momentum convection subgrid term $\partial_j F_{U_j U_y}$ and eddy-viscosity models $\partial_j \tau_{yj}^{\text{mod}}(\bar{U}, \bar{\Delta})$.



(a) Correlation coefficient.



(b) Regression coefficient.



(c) Concordance correlation coefficient.

Figure 9.7 – Correlation coefficient, regression coefficient, and concordance correlation coefficient between the subgrid kinetic energy dissipation of the exact momentum convection subgrid term $\bar{\rho}F_{U_j U_i} S_{ij}$ and eddy-viscosity models $\bar{\rho}\tau_{ij}^{\text{mod}}(\bar{U}, \bar{\Delta}) S_{ij}$.

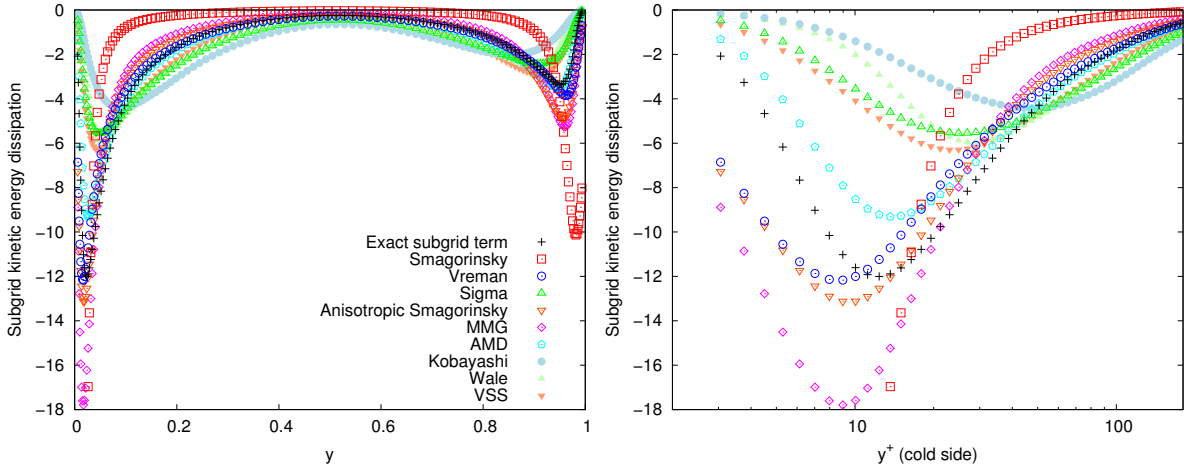


Figure 9.8 – Profile of the statistical average of the subgrid kinetic energy dissipation of the exact momentum convection subgrid term $\bar{\rho} F_{U_j U_i} S_{ij}$ and eddy-viscosity models $\bar{\rho} \tau_{ij}^{\text{mod}}(\bar{\mathbf{U}}, \bar{\mathbf{\Delta}}) S_{ij}$.

variations across throughout the channel than the WALE, Sigma, VSS and Kobayashi models (figures 9.4(b), 9.5(b), 9.6(b), 9.7(b)), up to the first point of the LES mesh that the filter represents.

The profile of the subgrid kinetic energy dissipation is given in figure 9.8. Compared to the exact subgrid term, the Smagorinsky, Vreman, Anisotropic Smagorinsky and MMG models are overdissipative in the near-wall region and underdissipative at the centre of the channel, while the WALE, Sigma, VSS and Kobayashi models dissipates more at the centre of the channel and less near the wall. This corresponds to the models theoretically predicted to lead to, respectively, a lower and a higher near-wall order than the exact subgrid term with a filter such that $\bar{\Delta}_y|_{\omega} = \mathcal{O}(y^1)$ (table 9.1).

The maximum of subgrid kinetic energy dissipation is located at $y^+ = 12$ at the cold side and $y^+ = 10$ at the hot side, in the range of the turbulence kinetic energy production [91]. Its location is mispredicted towards the centre of the channel by the WALE, Sigma, VSS and Kobayashi models and towards the wall by the Vreman, Anisotropic Smagorinsky and MMG models. The AMD model predicts quite accurately the location of the maximum of subgrid kinetic energy dissipation. It is underdissipative at the cold side and slightly overdissipative at the hot side, meaning that the asymmetry between the hot and cold side is not fully captured by the model.

Eddy-viscosity models are by construction purely dissipative. They represent relatively well the exact subgrid term for the negative values of the subgrid kinetic energy dissipation, which corresponds to a kinetic energy transfer from the resolved to subgrid scales, but cannot represent positive values of the subgrid kinetic energy dissipation. This readily appears in the probability density function of the subgrid kinetic energy dissipation, given in figure 9.9. While this is a desirable characteristic for numerical stability, this is inconsistent with the behaviour of the exact subgrid term which locally transfer the energy from the subgrid to resolved scales. The backscatter region amounts to 21% of the points in the domain.

Overall, the models in better agreement with the exact subgrid term are the AMD model, followed by the Vreman, Anisotropic Smagorinsky and MMG models (figures

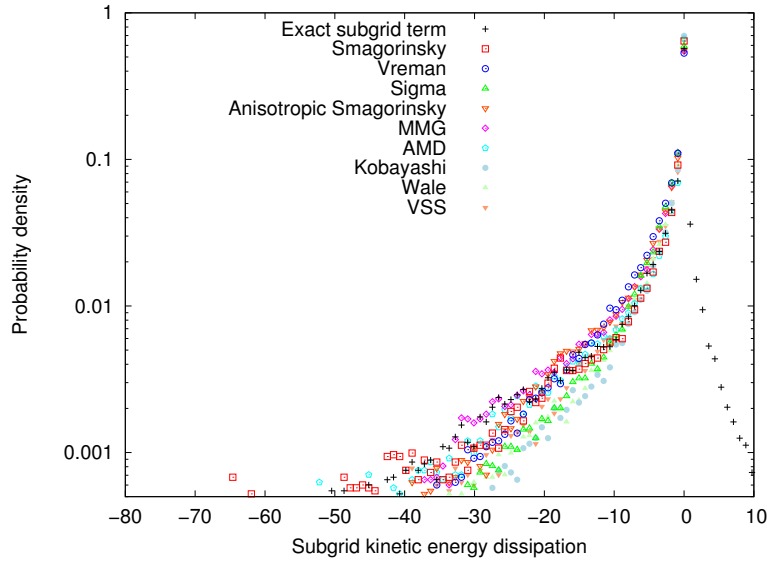


Figure 9.9 – Probability density function of the subgrid kinetic energy dissipation of the exact momentum convection subgrid term $\bar{\rho}F_{U_j U_i} S_{ij}$ and eddy-viscosity models $\bar{\rho}\tau_{ij}^{\text{mod}}(\bar{\mathbf{U}}, \bar{\mathbf{\Delta}})S_{ij}$.

9.4(c), 9.5(c), 9.6(c), 9.7(c)). Note that in the a priori tests, the performance of the AMD model is not significantly undermined by the clipping of negative viscosity or diffusivity.

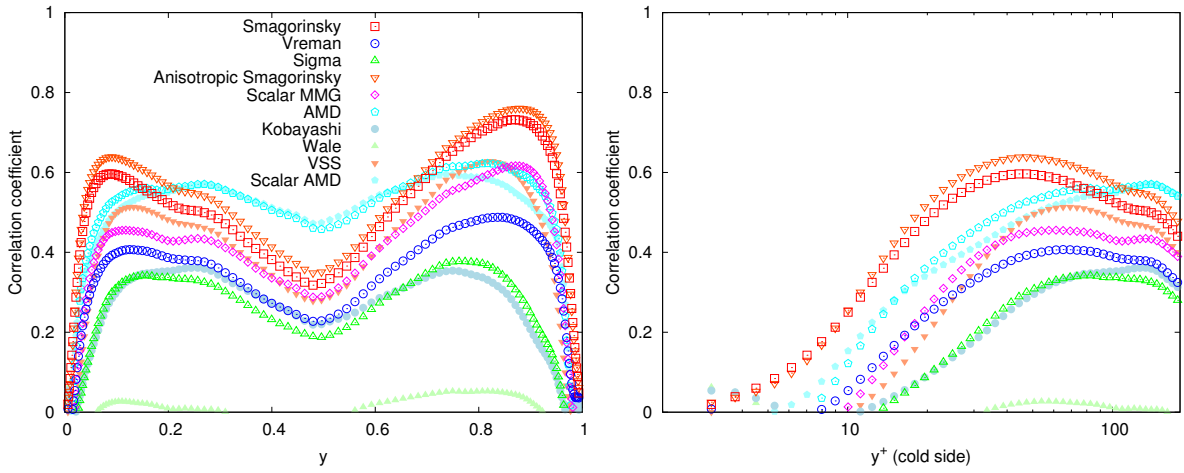
9.2.6.3 Density velocity correlation subgrid term

The models for the density-velocity correlation subgrid term are assessed as it appears in the mass conservation equation in figure 9.10 and the subgrid squared scalar dissipation $F_{\rho U_j} d_j$ is addressed in figure 9.11. As a basis of comparison, each model is scaled in order to match the correct level of total subgrid squared scalar dissipation in the volume. This is equivalent to a modification of the subgrid-scale Prandtl or Schmidt number, or to setting the constant of the models to

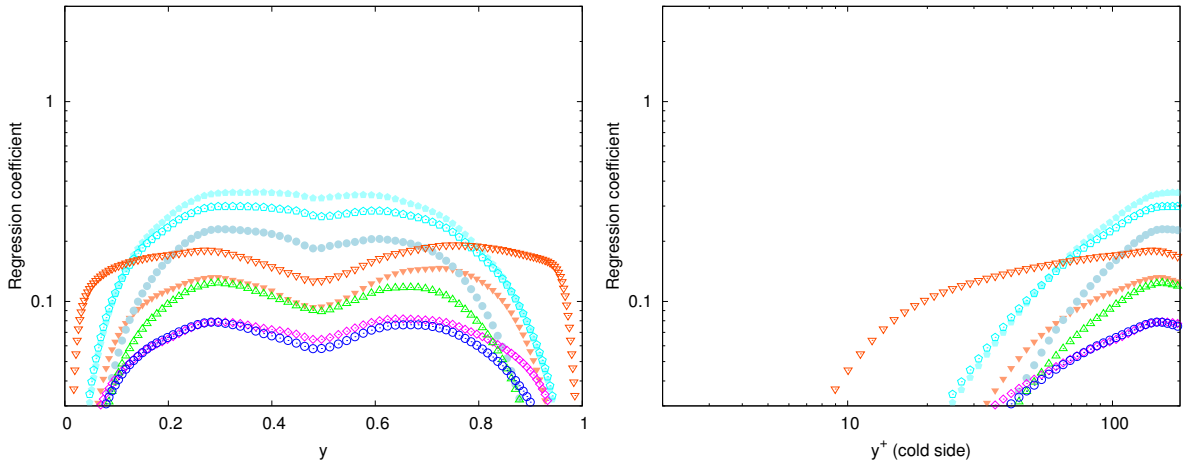
$$C^{\text{mod}} = \frac{\int_T \int_V F_{\rho U_j} d_j dx dy dz dt}{\int_T \int_V \pi_j^{\text{mod}}(\bar{\mathbf{U}}, \bar{\rho}, \bar{\mathbf{\Delta}}) d_j dx dy dz dt}, \quad (9.58)$$

with $Pr_t = 1$.

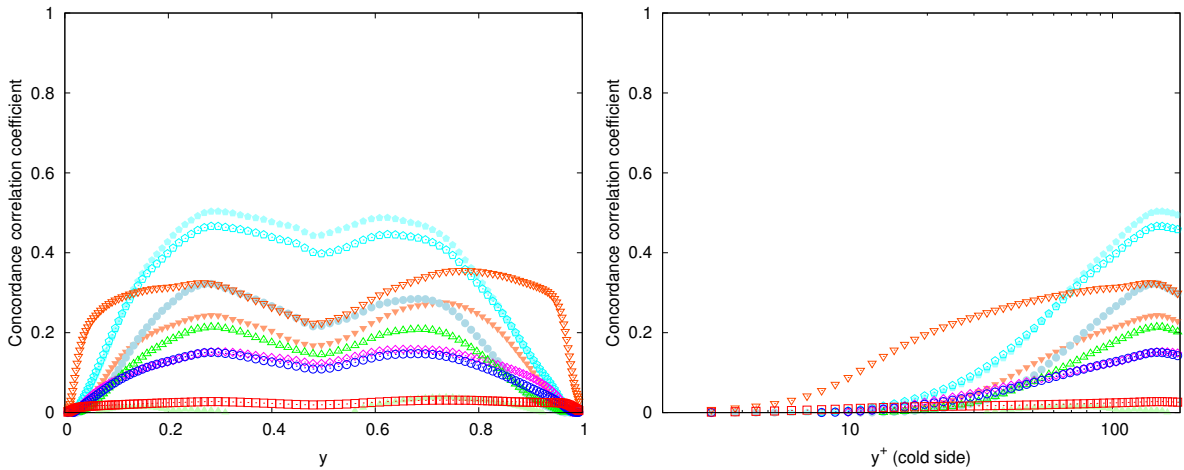
The correlation coefficient of the most models with the exact subgrid term as it appears in the mass conservation equation (figure 9.10(a)) reaches a maximum in the range 0.3–0.6, is lower at the centre of the channel and falls to or below zero near the wall. The WALE model is here an exception as its correlation with the exact subgrid term is very poor in the entire channel. At the centre of the channel, the AMD and scalar AMD models have the largest correlation coefficient. This may indicate their relevance in far-from-wall flows. Within the influence of the wall, the most well-correlated models are the Smagorinsky model and the Anisotropic Smagorinsky model, which is able to slightly improve the correlation of the Smagorinsky model. As the correlation coefficient, the regression coefficient declines from the logarithmic layer to the wall (figure 9.10(b)), meaning that the investigated subgrid-scale models fall too rapidly to zero at the wall. The drop occurs nearer to the wall with the Anisotropic



(a) Correlation coefficient.

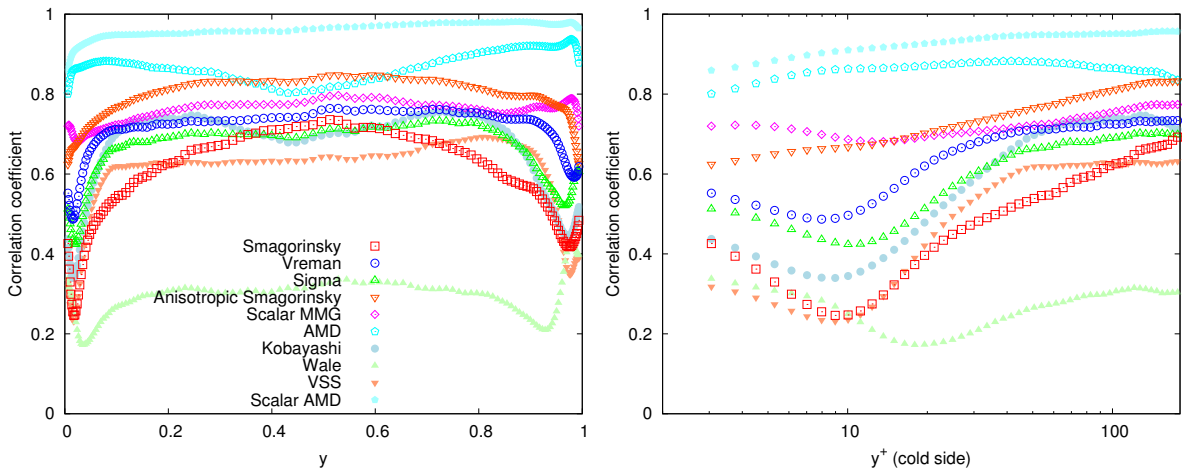


(b) Regression coefficient.

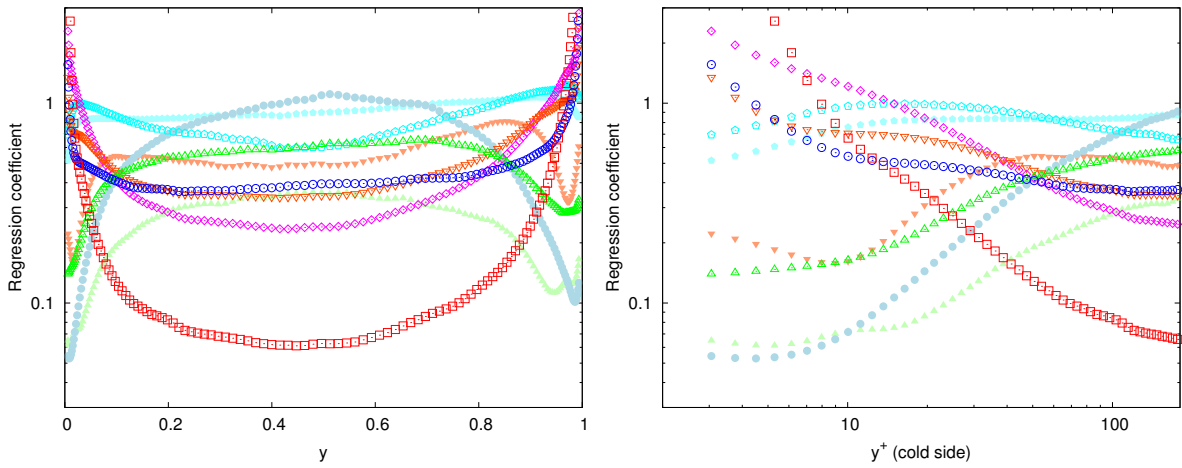


(c) Concordance correlation coefficient.

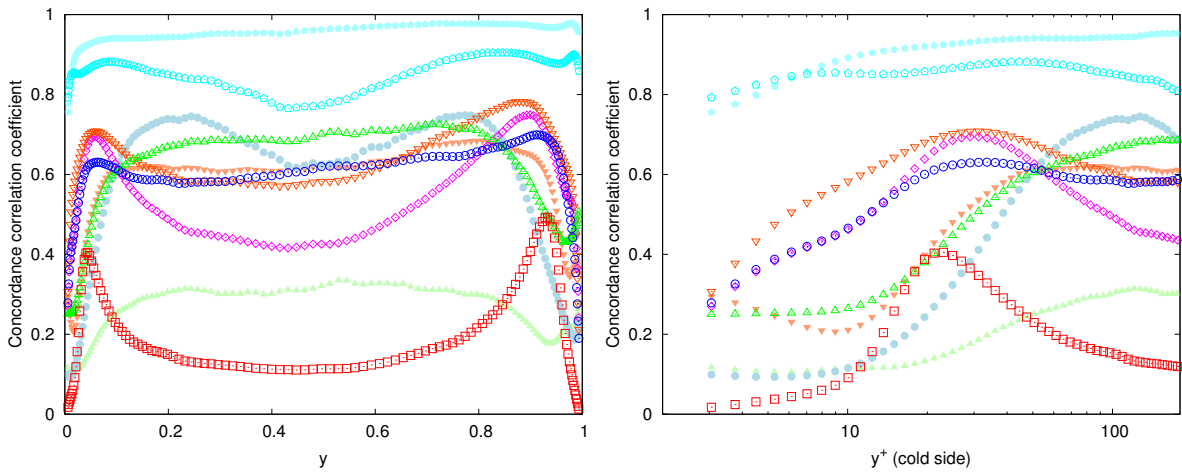
Figure 9.10 – Correlation coefficient, regression coefficient, and concordance correlation coefficient between the divergence of the exact density-velocity correlation subgrid term $\partial_j F_{\rho U_j}$ and eddy-diffusivity models $\partial_j \pi_j^{\text{mod}}(\bar{U}, \bar{\rho}, \bar{\Delta})$.



(a) Correlation coefficient.



(b) Regression coefficient.



(c) Concordance correlation coefficient.

Figure 9.11 – Correlation coefficient, regression coefficient, and concordance correlation coefficient between the subgrid squared scalar dissipation of the exact density-velocity correlation subgrid term $F_{\rho U_j} d_j$ and eddy-diffusivity models $\pi_j^{\text{mod}}(\overline{U}, \overline{\rho}, \overline{\Delta}) d_j$.

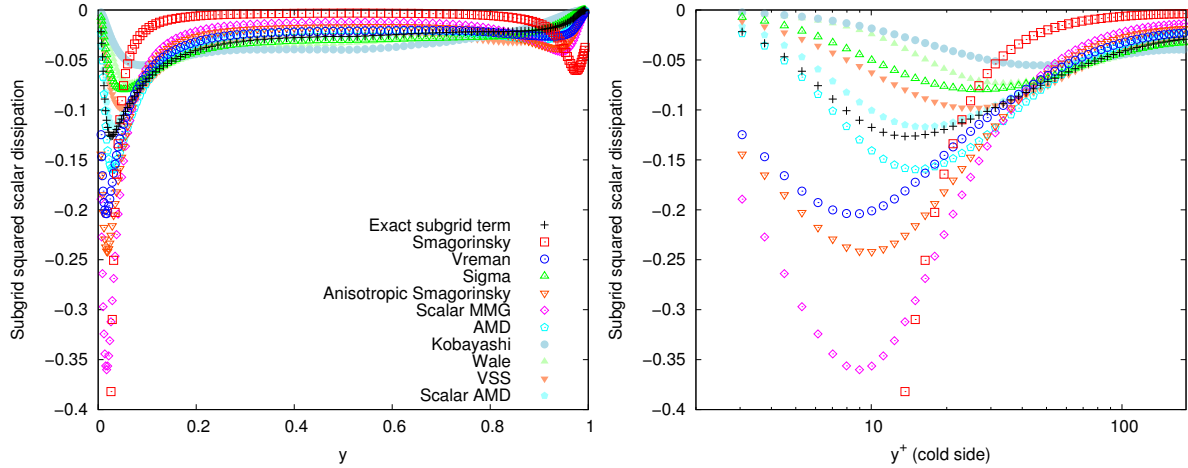


Figure 9.12 – Profile of the statistical average of the subgrid squared scalar dissipation of the exact density-velocity correlation subgrid term $F_{\rho U_j} d_j$ and eddy-diffusivity models $\pi_j^{\text{mod}}(\bar{\mathbf{U}}, \bar{\rho}, \bar{\Delta}) d_j$.

Smagorinsky model. The Anisotropic Smagorinsky, AMD and scalar AMD models are overall in a better agreement with the exact subgrid term (figure 9.10(c)).

Similarly to eddy-viscosity models, larger correlation coefficients are found for the subgrid squared scalar dissipation (figure 9.11(a)). The AMD and scalar AMD models are clearly the models that represent the more accurately the exact subgrid squared scalar dissipation (figure 9.11(c)), with in the entire channel a correlation coefficient over 0.8 (figure 9.11(a)) and a regression coefficient in the range 0.5–1 (figure 9.11(b)). The scalar AMD model provides an improvement compared to the AMD model developed for the momentum convection subgrid term. An increase of the regression coefficient of the Smagorinsky, Vreman, Anisotropic Smagorinsky and MMG models is observed near the wall, while the regression coefficient of the WALE, Sigma, VSS and Kobayashi models stabilises to a low value (figure 9.11(b)). The profile of the subgrid squared scalar dissipation (figure 9.12) shows that the Smagorinsky, Vreman, Anisotropic Smagorinsky and MMG models are overdissipative in the near-wall region and underdissipative at the centre of the channel compared to the exact subgrid term, and conversely for the WALE, Sigma, VSS and Kobayashi models. These results are identical to the results obtained for the subgrid kinetic energy dissipation. The profile of the ratio of the subgrid kinetic energy dissipation and the subgrid squared scalar dissipation (figure 9.13) shows that they have the same near-wall order. The results are thus consistent with our theoretical analysis of the asymptotic near-wall behaviour of the subgrid terms.

The eddy-diffusivity assumption is as appropriate as the eddy-viscosity assumption, in the sense the same amount of backscatter is observed for the subgrid squared scalar dissipation than for the subgrid kinetic energy dissipation, as can be seen in the probability density function of the subgrid squared scalar dissipation (figure 9.14). However, it may be argued that the behaviour of the subgrid squared scalar dissipation is less critical than the subgrid kinetic energy dissipation for the numerical stability of a numerical simulation, suggesting that more emphasis should be placed on the relevance of the model as it appears in the mass conservation equation.

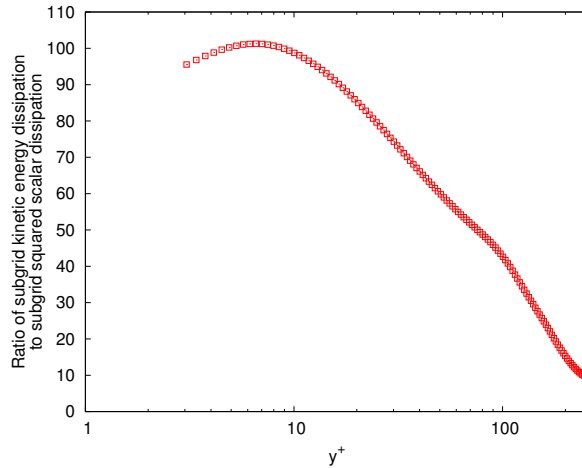


Figure 9.13 – Profile of the ratio of the statistical average of the subgrid kinetic energy dissipation and the subgrid squared scalar dissipation, $[\bar{\rho} F_{U_j U_i} S_{ij}] / [F_{\rho U_j} d_j]$.

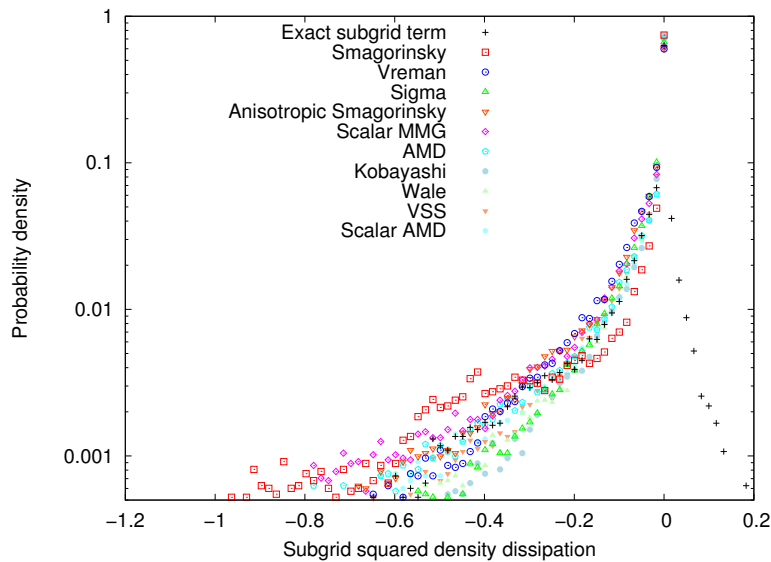


Figure 9.14 – Probability density function of the subgrid squared scalar dissipation of the exact density-velocity correlation subgrid term $F_{\rho U_j} d_j$ and eddy-diffusivity models $\pi_j^{\text{mod}}(\bar{U}, \bar{\rho}, \bar{\Delta}) d_j$.

Overall, the models in better agreement with the exact subgrid term are the AMD and scalar AMD models, followed by the Vreman, Anisotropic Smagorinsky and MMG models (figures 9.10(c), 9.11(c)). They are the same models than for the subgrid term associated with momentum convection.

9.2.7 Conclusion

The filtering of the low Mach number equations with the unweighted classical filter or the density-weighted Favre filter leads to specific subgrid terms. The two most significant subgrid terms are the subgrid terms associated with the momentum convection and the density-velocity correlation. They are compared to subgrid-scale models using the flow field from direct numerical simulations of a strongly anisothermal turbulent

channel flow. Classical and Favre filter are found to have no influence on the performance of the models. Eddy-viscosity and eddy-diffusivity models are shown to be in better agreement with the subgrid kinetic energy dissipation and the subgrid squared scalar dissipation respectively than with the contribution of the subgrid terms in the filtered low Mach number equations. However, eddy-viscosity and eddy-diffusivity models are not able to account for backscatter, present in a fifth of the points in the domain. The AMD and scalar AMD models perform better than the other investigated models with regard to the correlation coefficient, regression coefficient and concordance correlation coefficient with the exact subgrid term. This may be attributed to the strong link between the AMD and scalar AMD models and the gradient model. The AMD and scalar AMD inherit from the gradient model a similarity with the exact subgrid term but, unlike the gradient model, are purely dissipative and should not lead to numerical stability issues.

Acknowledgment

The authors gratefully acknowledge the CEA for the development of the TRUST platform. This work was granted access to the HPC resources of CINES under the allocations 2017-A0022A05099 and 2018-A0042A05099 made by GENCI.

Bibliography

- [1] A. Abba, A. C. Cercignani, and L. Valdetaro. Analysis of subgrid scale models. *Comput. Math. Appl.*, 46(4):521–535, 2003.
- [3] M. Abkar, H. J. Bae, and P. Moin. Minimum-dissipation scalar transport model for large-eddy simulation of turbulent flows. *Physical Review Fluids*, 1(4):041701, 2016.
- [11] F. Aulery, D. Dupuy, A. Toutant, F. Bataille, and Y. Zhou. Spectral analysis of turbulence in anisothermal channel flows. *Computers & Fluids*, 151:115–131, 2017.
- [14] J. Bardina, J. Ferziger, and W. C. Reynolds. Improved subgrid-scale models for large-eddy simulation. In *13th Fluid and Plasma Dynamics Conference*, page 1357, 1980.
- [24] L. C. Berselli, T. Iliescu, and W. J. Layton. *Mathematics of large eddy simulation of turbulent flows*. Springer Science & Business Media, 2005.
- [29] G. Borghesi and J. Bellan. A priori and a posteriori investigations for developing large eddy simulations of multi-species turbulent mixing under high-pressure conditions. *Physics of Fluids*, 27(3):035117, 2015.
- [30] V. Borue and S. A. Orszag. Local energy flux and subgrid-scale statistics in three-dimensional turbulence. *Journal of Fluid Mechanics*, 366:1–31, 1998.
- [38] C. Calvin, O. Cueto, and P. Emonot. An object-oriented approach to the design of fluid mechanics software. *ESAIM: Mathematical Modelling and Numerical Analysis*, 36(05):907–921, 2002.
- [45] D. R. Chapman and G. D. Kuhn. The limiting behaviour of turbulence near a wall. *Journal of Fluid Mechanics*, 170:265–292, 1986.
- [53] M. S. Chong, J. P. Monty, C. Chin, and I. Marusic. The topology of skin friction and surface vorticity fields in wall-bounded flows. *Journal of Turbulence*, (13):N6, 2012.
- [56] S. G. Chumakov and C. J. Rutland. Dynamic structure subgrid-scale models for large eddy simulation. *International Journal for Numerical Methods in Fluids*, 47(8-9):911–923, 2005.

- [64] R. A. Clark, J. H. Ferziger, and W. C. Reynolds. Evaluation of subgrid-scale models using an accurately simulated turbulent flow. *J. Fluid Mech.*, 91(1):1–16, 1979.
- [77] J. W. Deardorff. A numerical study of three-dimensional turbulent channel flow at large reynolds numbers. *Journal of Fluid Mechanics*, 41(2):453–480, 1970.
- [87] D. Dupuy, A. Toutant, and F. Bataille. Study of the sub-grid terms of the large-eddy simulation of a low Mach strongly anisothermal channel flow. In *Eurotherm Seminar 106, Paris, France*, 2016.
- [88] D. Dupuy, A. Toutant, and F. Bataille. étude de l'équation d'énergie pour le développement de modèles sous-maillages adaptés aux écoulements fortement anisothermes. In *Congrès SFT, Marseille, France*, 2017.
- [90] D. Dupuy, A. Toutant, and F. Bataille. Study of the large-eddy simulation subgrid terms of a low mach number anisothermal channel flow. *International Journal of Thermal Sciences*, 135:221–234, 2018.
- [91] D. Dupuy, A. Toutant, and F. Bataille. Turbulence kinetic energy exchanges in flows with highly variable fluid properties. *Journal of Fluid Mechanics*, 834:5–54, 2018.
- [94] A. Favre. The equations of compressible turbulent gases. Technical Report AD0622097, DTIC Document, 1965.
- [112] M. Germano, U. Piomelli, P. Moin, and W. H. Cabot. A dynamic subgrid-scale eddy viscosity model. *Physics of Fluids A: Fluid Dynamics*, 3(7):1760–1765, 1991.
- [113] N. S. Ghaisas and S. H. Frankel. A priori evaluation of large eddy simulation subgrid-scale scalar flux models in isotropic passive-scalar and anisotropic buoyancy-driven homogeneous turbulence. *J. Turbulence*, 15(2):88–121, 2014.
- [114] N. S. Ghaisas and S. H. Frankel. Dynamic gradient models for the sub-grid scale stress tensor and scalar flux vector in large eddy simulation. *Journal of Turbulence*, 17(1):30–50, 2016.
- [141] S. Ketterl and M. Klein. A-priori assessment of subgrid scale models for large-eddy simulation of multiphase primary breakup. *Computers & Fluids*, 165:64–77, 2018.
- [147] H. Kobayashi. The subgrid-scale models based on coherent structures for rotating homogeneous turbulence and turbulent channel flow. *Physics of Fluids*, 17(4):045104, 2005.
- [169] A. Leonard. Energy cascade in large eddy simulations of turbulent fluid flows. *Advances in Geophysics*, 18A:237–248, 1974.
- [175] C. Li. *A-priori analysis of LES subgrid scale models applied to wall turbulence with pressure gradients*. PhD thesis, Ecole Centrale de Lille, 2013.
- [177] D. K. Lilly. A proposed modification of the germano subgrid-scale closure method. *Physics of Fluids A: Fluid Dynamics*, 4(3):633–635, 1992.
- [178] L. I.-K. Lin. A concordance correlation coefficient to evaluate reproducibility. *Biometrics*, pages 255–268, 1989.
- [180] S. Liu, C. Meneveau, and J. Katz. On the properties of similarity subgrid-scale models as deduced from measurements in a turbulent jet. *J. Fluid Mech.*, 275:83–119, 1994.
- [182] H. Lu, C. J. Rutland, and L. M. Smith. A priori tests of one-equation LES modeling of rotating turbulence. *J. Turbulence*, (8):N37, 2007.
- [189] M. Pino Martín, U. Piomelli, and G. V. Candler. Subgrid-scale models for compressible large-eddy simulations. *Theoretical and Computational Fluid Dynamics*, 13(5):361–376, 2000.
- [212] F. Nicoud. Conservative high-order finite-difference schemes for low-Mach number flows. *J. Comput. Phys.*, 158(1):71–97, 2000.
- [213] F. Nicoud and F. Ducros. Subgrid-scale stress modelling based on the square of the velocity gradient tensor. *Flow, Turbulence and Combustion*, 62(3):183–200, 1999. ISSN 1386-6184.
- [214] F. Nicoud, H. Baya Toda, O. Cabrit, S. Bose, and J. Lee. Using singular values to build a subgrid-scale model for large eddy simulations. *Physics of Fluids*, 23(8):085106, 2011.

- [219] S. Paolucci. On the filtering of sound from the Navier–Stokes equations. Technical Report SAND82-8257, Sandia National Labs., Livermore, CA (USA), 1982.
- [221] N. Park, S. Lee, J. Lee, and H. Choi. A dynamic subgrid-scale eddy viscosity model with a global model coefficient. *Physics of Fluids*, 18(12):125109, 2006.
- [229] U. Piomelli, P. Moin, and J. H. Ferziger. Model consistency in large eddy simulation of turbulent channel flows. *Phys. Fluids*, 31(7):1884–1891, 1988.
- [239] C. D. Pruett and N. A. Adams. A priori analyses of three subgrid-scale models for one-parameter families of filters. *Physics of Fluids*, 12(5):1133–1142, 2000.
- [250] W. Rozema, H.J. Bae, P. Moin, and R. Verstappen. Minimum-dissipation models for large-eddy simulation. *Physics of Fluids*, 27(8):085107, 2015.
- [252] S. Ryu and G. Iaccarino. A subgrid-scale eddy-viscosity model based on the volumetric strain-stretching. *Physics of Fluids*, 26(6):065107, 2014.
- [253] P. Sagaut. *Large eddy simulation for incompressible flows: an introduction*. Springer Science & Business Media, 2006.
- [259] F. Sarghini, U. Piomelli, and E. Balaras. Scale-similar models for large-eddy simulations. *Physics of Fluids*, 11(6):1596–1607, 1999.
- [265] S. Serra, A. Toutant, F. Bataille, and Y. Zhou. High-temperature gradient effect on a turbulent channel flow using thermal large-eddy simulation in physical and spectral spaces. *J. Turbulence*, 13:N49, 2012.
- [273] M. H. Silvis, R. A. Remmerswaal, and R. Verstappen. Physical consistency of subgrid-scale models for large-eddy simulation of incompressible turbulent flows. *Physics of Fluids*, 29(1):015105, 2017.
- [276] J. Smagorinsky. General circulation experiments with the primitive equations: I. the basic experiment. *Monthly weather review*, 91(3):99–164, 1963.
- [287] W. Sutherland. The viscosity of gases and molecular force. *The London, Edinburgh, and Dublin Philosophical Magazine and Journal of Science*, 36(223):507–531, 1893.
- [290] A. Toutant and F. Bataille. Turbulence statistics in a fully developed channel flow submitted to a high temperature gradient. *International Journal of Thermal Sciences*, 74:104–118, 2013.
- [291] A. Toutant, E. Labourasse, O. Lebaigue, and O. Simonin. DNS of the interaction between a deformable buoyant bubble and a spatially decaying turbulence: a priori tests for LES two-phase flow modelling. *Computers & Fluids*, 37(7):877–886, 2008.
- [294] F. X. Trias, D. Folch, A. Gorobets, and A. Oliva. Building proper invariants for eddy-viscosity subgrid-scale models. *Physics of Fluids*, 27(6):065103, 2015.
- [295] F. X. Trias, A. Gorobets, M. H. Silvis, R. W. C. P. Verstappen, and A. Oliva. A new subgrid characteristic length for turbulence simulations on anisotropic grids. *Physics of Fluids*, 29(11):115109, 2017.
- [304] A. W. Vreman. An eddy-viscosity subgrid-scale model for turbulent shear flow: Algebraic theory and applications. *Physics of fluids*, 16(10):3670–3681, 2004.
- [306] B. Vreman. *Direct and large-eddy simulation of the compressible turbulent mixing layer*. PhD thesis, University of Twente, 1995.
- [309] B. Vreman, B. Geurts, and H. Kuerten. A priori tests of large eddy simulation of the compressible plane mixing layer. *Journal of Engineering Mathematics*, 29(4):299–327, 1995.
- [310] B. Vreman, B. Geurts, and H. Kuerten. Subgrid-modelling in LES of compressible flow. *Applied Scientific Research*, 54(3):191–203, 1995.
- [320] A. Yoshizawa. Statistical theory for compressible turbulent shear flows, with the application to subgrid modeling. *Phys. Fluids*, 29(7):2152–2164, 1986.

9.3 Tensorial models

9.3.1 Definition

To complement the analysis of eddy-viscosity models, we investigate a priori the modelling of the subgrid term associated with momentum convection with tensorial eddy-viscosity models. Tensorial models aim to take into account the anisotropy of the flow by weighting of each component of a subgrid-scale model. Tensorial eddy-viscosity models are tensorial models based on the eddy-viscosity assumption. They are motivated by the fact that the relevance of the eddy-viscosity assumption is not the same for each component of the subgrid term. In general, we may construct from any algebraic model $\tau_{ij}^{\text{mod}}(\mathbf{U}, \overline{\Delta})$, and second-order tensors $H_{ij}^{(k)}$ tensorial models $\tau_{ij}^{H^{(k)\text{mod}}}(\mathbf{U}, \overline{\Delta})$ of the form

$$\tau_{ij}^{H^{(k)\text{mod}}}(\mathbf{U}, \overline{\Delta}) = H_{ij}^{(k)} \tau_{ij}^{\text{mod}}(\mathbf{U}, \overline{\Delta}), \quad (9.59)$$

where no implicit summations over i and j are assumed. We define for this purpose the tensors $H_{ij}^{(1)} = [i \neq j]$, $H_{ij}^{(2)} = [\chi_{ij}^{xy}]$, $H_{ij}^{(3)} = [\neg \chi_{ij}^{yy}]$, $H_{ij}^{(4)} = [\chi_{ij}^{xy} \vee \chi_{ij}^{xz}]$, $H_{ij}^{(5)} = [\chi_{ij}^{xy} \vee \chi_{ij}^{yz}]$, $H_{ij}^{(6)} = [i = x \vee j = x]$ et $H_{ij}^{(7)} = [\chi_{ij}^{xx} \vee \chi_{ij}^{xy}]$, where $[\cdot]$ are Iverson brackets, evaluating to 1 if the proposition within bracket is satisfied and 0 otherwise, \neg the logical negation (NOT), \wedge the logical conjunction (AND), \vee the logical disjunction (OR) and with the notation $\chi_{ij}^{ab} = (i = a \wedge j = b) \vee (i = b \wedge j = a)$. More explicitly, we have

$$H_{ij}^{(1)} = \begin{pmatrix} 0 & 1 & 1 \\ 1 & 0 & 1 \\ 1 & 1 & 0 \end{pmatrix}, \quad (9.60) \quad H_{ij}^{(5)} = \begin{pmatrix} 0 & 1 & 0 \\ 1 & 0 & 1 \\ 0 & 1 & 0 \end{pmatrix}, \quad (9.64)$$

$$H_{ij}^{(2)} = \begin{pmatrix} 0 & 1 & 0 \\ 1 & 0 & 0 \\ 0 & 0 & 0 \end{pmatrix}, \quad (9.61) \quad H_{ij}^{(6)} = \begin{pmatrix} 1 & 1 & 1 \\ 1 & 0 & 0 \\ 1 & 0 & 0 \end{pmatrix}, \quad (9.65)$$

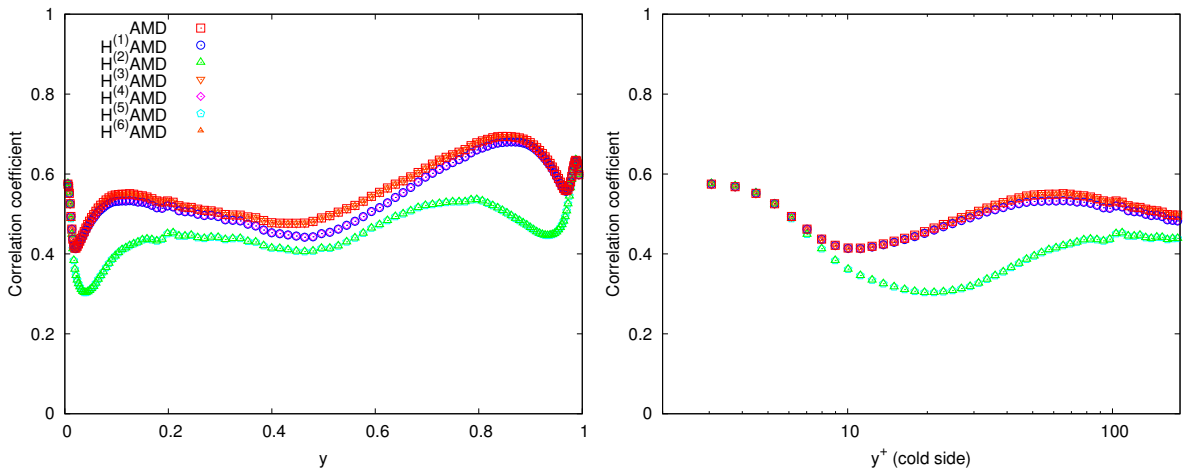
$$H_{ij}^{(3)} = \begin{pmatrix} 1 & 1 & 1 \\ 1 & 0 & 1 \\ 1 & 1 & 1 \end{pmatrix}, \quad (9.62) \quad H_{ij}^{(7)} = \begin{pmatrix} 1 & 1 & 0 \\ 1 & 0 & 0 \\ 0 & 0 & 0 \end{pmatrix}. \quad (9.66)$$

$$H_{ij}^{(4)} = \begin{pmatrix} 0 & 1 & 1 \\ 1 & 0 & 0 \\ 1 & 0 & 0 \end{pmatrix}, \quad (9.63)$$

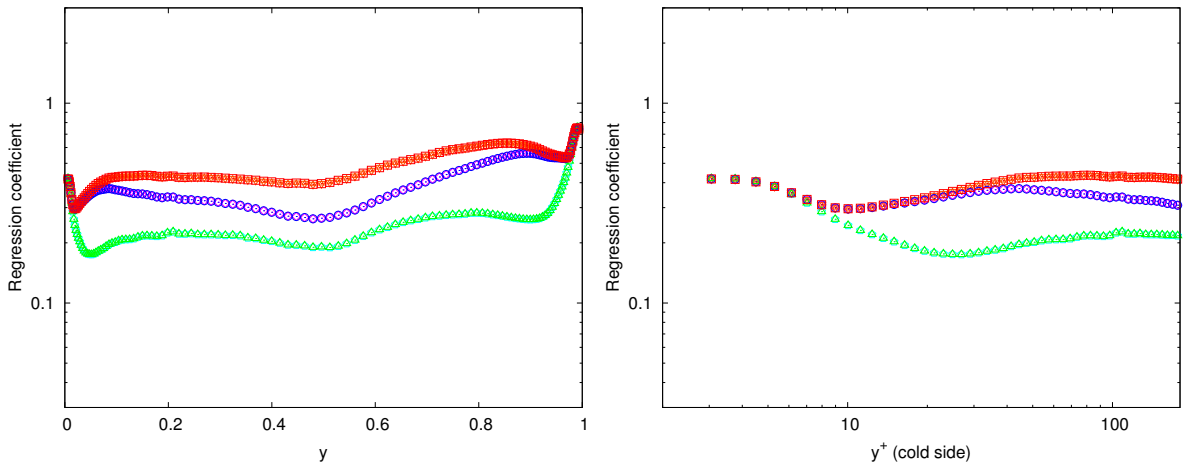
9.3.2 A priori tests

Using the same method as in provided in section 9.2, we assess a priori the relevance of tensorial eddy-viscosity models based on the AMD model for the momentum convection subgrid term as it appears in the streamwise velocity transport equation in figure 9.15, in the spanwise velocity transport equation in figure 9.16, in the wall-normal velocity transport equation in figure 9.17 and with regard to the subgrid kinetic energy dissipation $\bar{\rho} F_{U_j U_i} S_{ij}$ in figure 9.18. As a basis of comparison, the same constant as the AMD model is used to compute all tensorial AMD models.

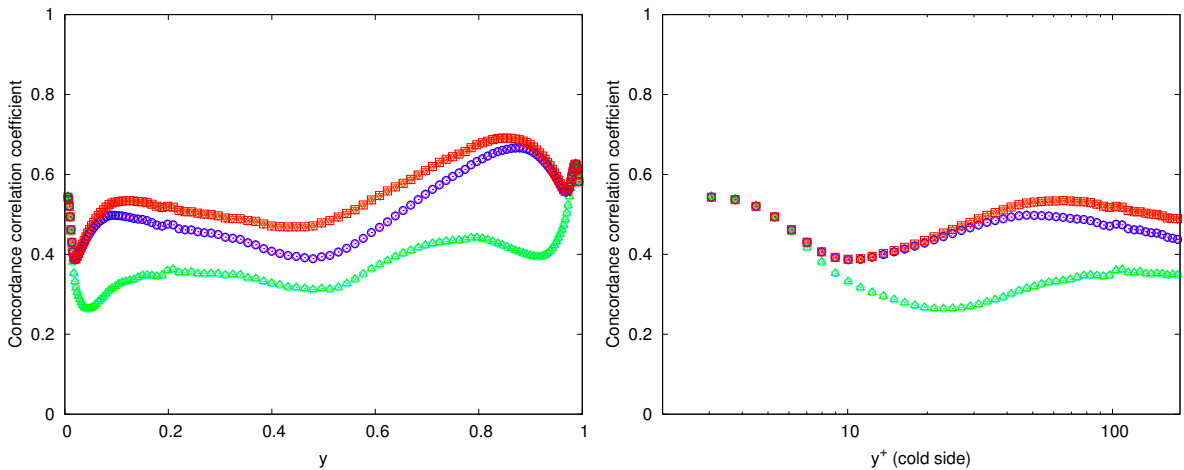
All the investigated tensorial AMD models have a lower correlation coefficient,



(a) Correlation coefficient.

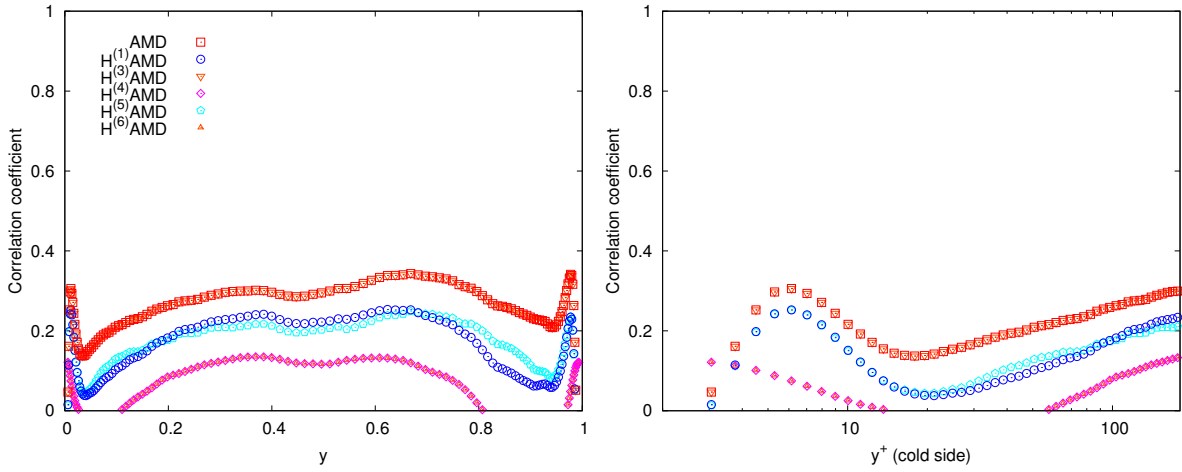


(b) Regression coefficient.

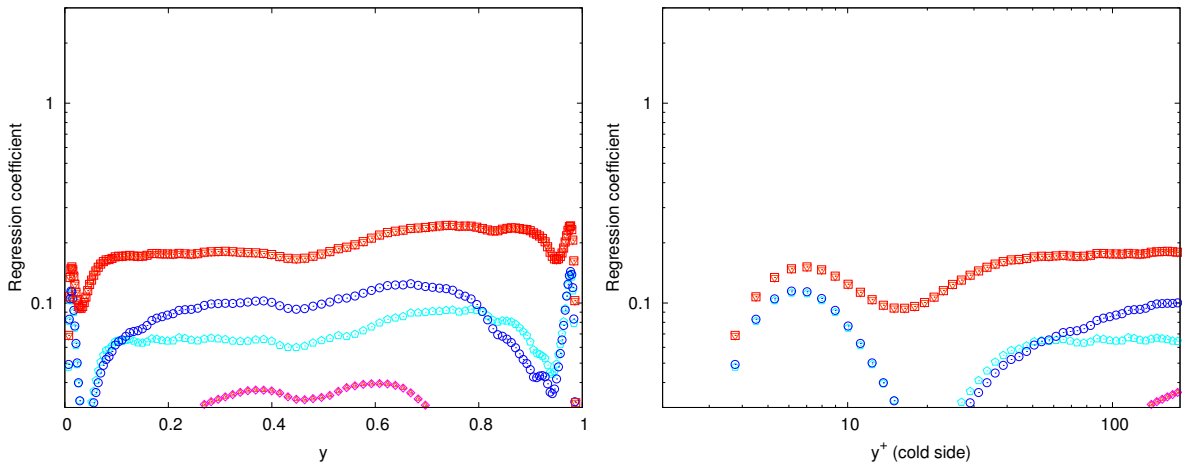


(c) Concordance correlation coefficient.

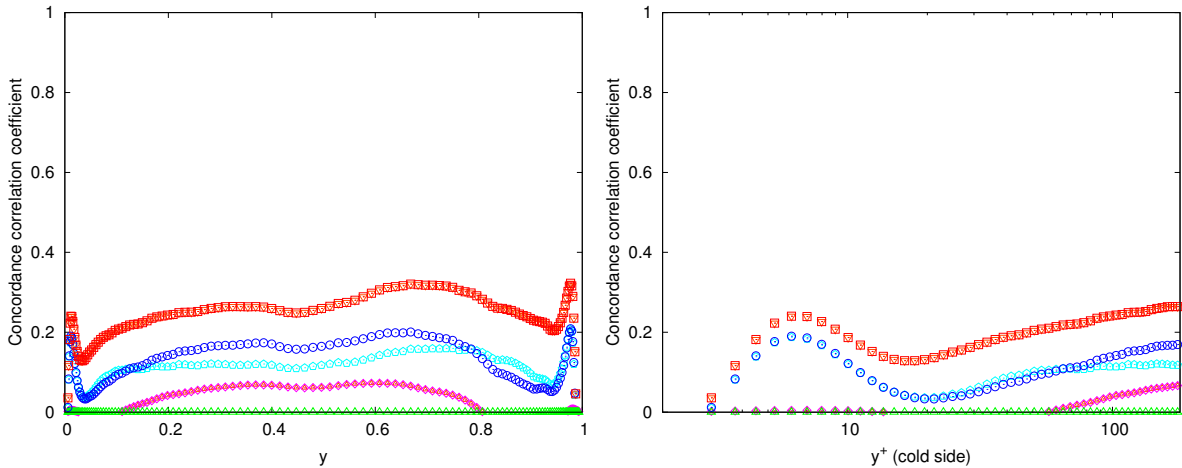
Figure 9.15 – Correlation coefficient, regression coefficient, and concordance correlation coefficient between the divergence of the streamwise-related part of the exact momentum convection subgrid term $\partial_j F_{U_j U_x}$ and tensorial AMD models $\partial_j \tau_{x_j}^{H^{(k)} \text{AMD}}(\bar{U}, \bar{\Delta})$.



(a) Correlation coefficient.

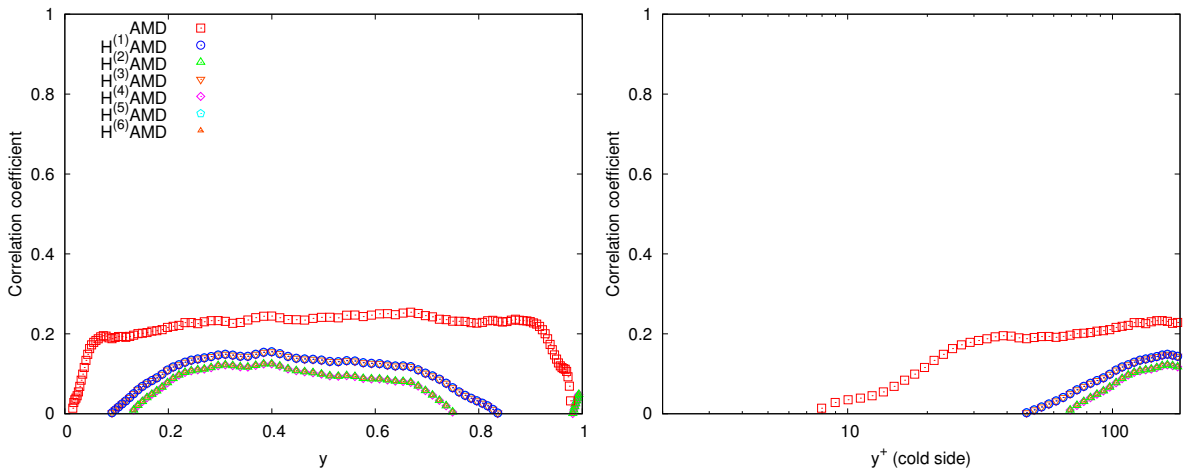


(b) Regression coefficient.

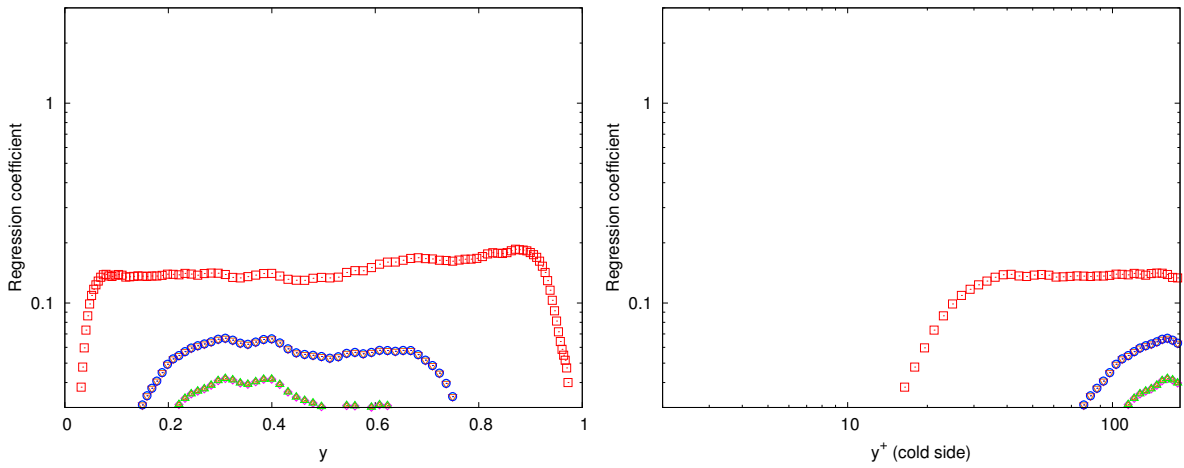


(c) Concordance correlation coefficient.

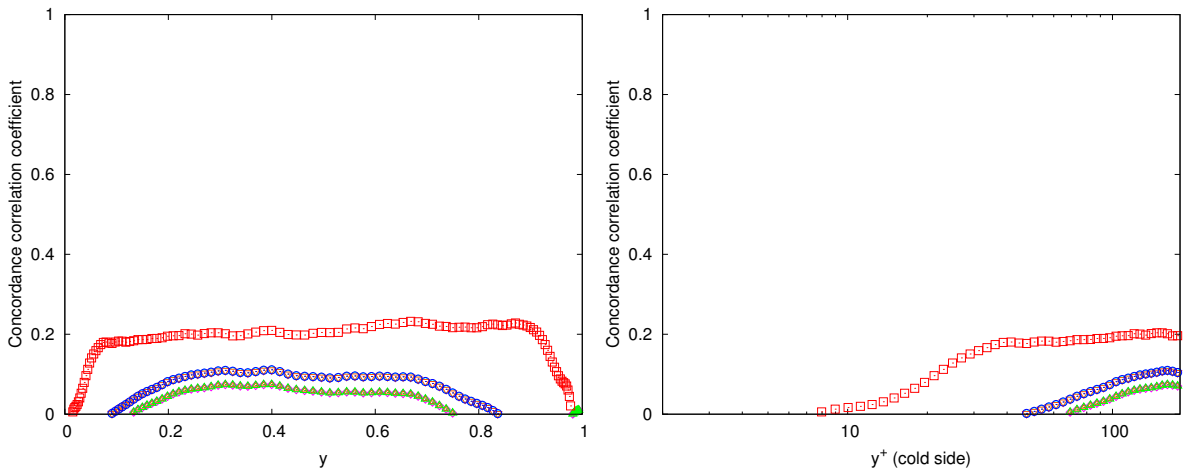
Figure 9.16 – Correlation coefficient, regression coefficient, and concordance correlation coefficient between the divergence of the spanwise-related part of the exact momentum convection subgrid term $\partial_j F_{U_j U_z}$ and tensorial AMD models $\partial_j \tau_{zj}^{H^{(k)} \text{AMD}}(\bar{U}, \bar{\Delta})$.



(a) Correlation coefficient.

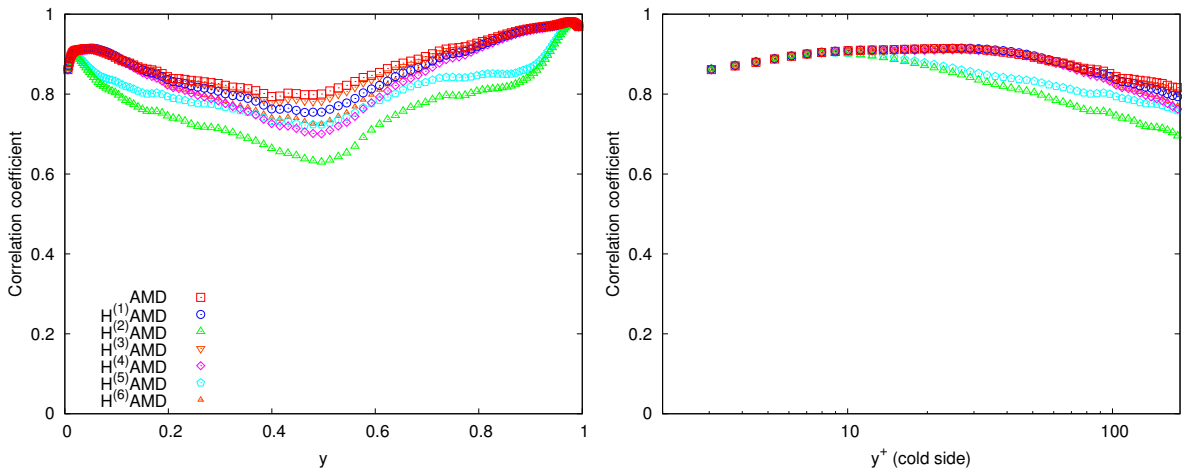


(b) Regression coefficient.

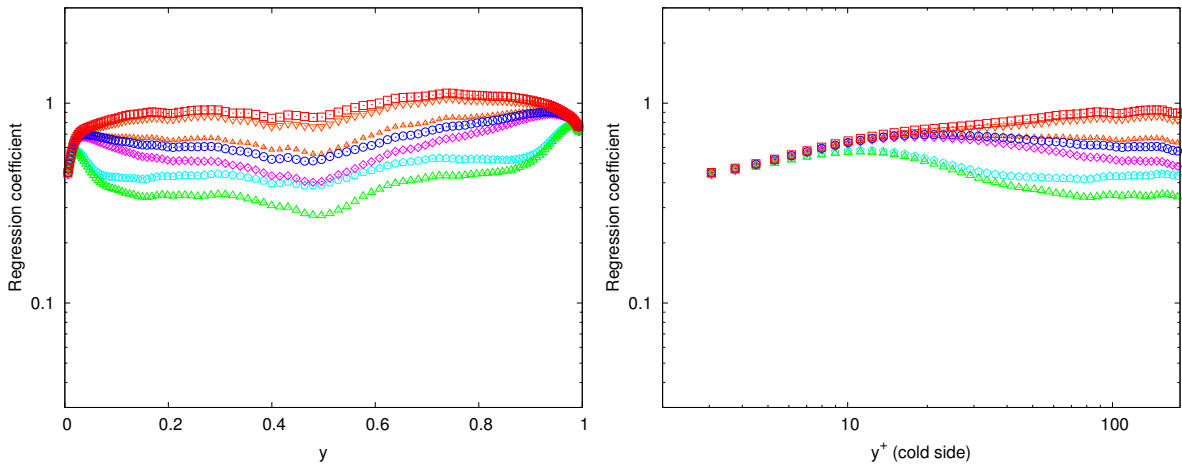


(c) Concordance correlation coefficient.

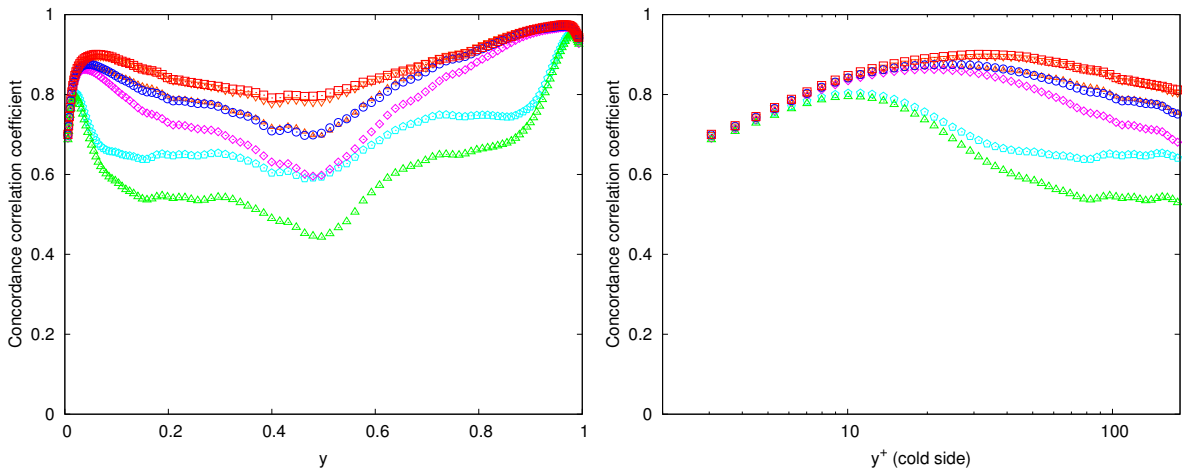
Figure 9.17 – Correlation coefficient, regression coefficient, and concordance correlation coefficient between the divergence of the wall-normal-related part of the exact momentum convection subgrid term $\partial_j F_{U_j U_y}$ and tensorial AMD models $\partial_j \tau_{yj}^{H^{(k)} \text{AMD}}(\bar{U}, \bar{\Delta})$.



(a) Correlation coefficient.



(b) Regression coefficient.



(c) Concordance correlation coefficient.

Figure 9.18 – Correlation coefficient, regression coefficient, and concordance correlation coefficient between the subgrid kinetic energy dissipation of the exact momentum convection subgrid term $\bar{\rho} F_{U_j U_i} S_{ij}$ and tensorial AMD models $\bar{\rho} \tau_{ij}^{H^{(k)} \text{AMD}}(\bar{\mathbf{U}}, \bar{\mathbf{\Delta}}) S_{ij}$.

regression coefficient and concordance correlation coefficient with the exact subgrid term than the scalar AMD model. In a priori tests, tensorial AMD models thus show no benefit over the scalar AMD model. Nevertheless, the “xy” and “xz” components of the AMD model are sufficient to provide a level of concordance with the exact subgrid term similar to the AMD model in the streamwise velocity transport equation (figure 9.15(c)) and in the kinetic energy transport equation (figure 9.18(c)). This excludes the tensorial models based on the $H^{(2)}$ and $H^{(5)}$ tensors. The significance of the other components of the AMD model and their effect on the flow is crucial to the relevance of tensorial AMD models in large-eddy simulation. Results with tensorial eddy-viscosity models based on the Sigma and Anisotropic Smagorinsky models may be found in appendix C and lead to similar conclusions.

9.4 Conclusion of chapter 9

In a fully developed three-dimensional strongly anisothermal channel flow, backscatter occurs in approximately a fifth of the points in the domain. This value is similar for the momentum convection subgrid term and the density-velocity correlation subgrid term, the two most significant subgrid terms of the filtered low Mach number equations. The modelling of these subgrid terms with eddy-viscosity or eddy-diffusivity models assumes the alignment of the subgrid term and the rate of deformation tensor, implying an absence of backscatter. Nevertheless, the a priori tests of subgrid-scale models suggest a larger correspondence between the subgrid term and the subgrid-scale model with regard to subgrid dissipation than to the contribution of the subgrid term in the filtered low Mach number equations. The comparison of the performance of various subgrid-scale models for a given total subgrid dissipation over the volume seems to indicate that better agreements are found with the AMD and scalar AMD models than the other investigated models. This holds for both the classical and Favre filters and for both the momentum convection and density-velocity correlation subgrid terms. In order to analyse the results, the asymptotic near-wall behaviour of the subgrid-scale models and of the exact subgrid term is investigated for a continuous filter whose size in the wall-normal direction (y) tends to zero at the wall. While the study seems to be consistent with the results, note that the filter used follows a hyperbolic tangent law in the wall-normal coordinate direction which does not tend to zero at the wall.

Tensorial eddy-viscosity models do not seem to provide any improvement over scalar eddy-viscosity models in a priori tests. The two new proposed eddy-viscosity and eddy-diffusivity models, the Anisotropic Smagorinsky model and the MMG model, have a high level of correlation with the exact subgrid term. In particular, the Anisotropic Smagorinsky model improves the correlation of the Smagorinsky model and its near-wall behaviour. The two models are overdissipative near to the wall as they have a lower wall order than both exact subgrid terms. Overall, they provide promising results nonetheless, outperformed only by the AMD, scalar AMD and Vreman models. The next chapter investigates a posteriori the subgrid-scale modelling of strongly anisothermal turbulent channel flows with the low Mach number equations, allowing the verification of the a priori performance of the subgrid-scale models.

Chapter 10

A posteriori tests of subgrid-scale models in an anisothermal turbulent channel flow at low Mach number

10.1 Introduction of chapter 10

The accuracy of a large-eddy simulation is determined by the physical relevance of the subgrid-scale models used with regard to the filtering operation and the numerical method. Within the low Mach number hypothesis, large-eddy simulations may be carried out using the Velocity and Favre formulations. In both cases, the two most significant subgrid terms are the momentum convection subgrid term and the density-velocity correlation subgrid term. The effect of these subgrid terms and their modelling is crucial for the prediction of the turbulent fields. In this chapter, we investigate a posteriori the modelling of the momentum convection subgrid term and the density-velocity correlation subgrid term in isothermal and anisothermal turbulent channel flows. The anisothermal channel reproduces the distinctive features of low Mach number strongly anisothermal turbulent flows. Hence, we expect the results to be relevant to the simulation of a high-temperature solar receiver.

We will focus on the effect of the models on the turbulence statistics. To assess the performance of the large-eddy simulations, the results are compared to a direct numerical simulation filtered at the resolution of the large-eddy simulations. This allows the direct comparison of the results of the large-eddy simulations and of the direct numerical simulations. The analysis is based on the LES formalism introduced by Leonard [169]. In this paradigm, the large-eddy simulation aims to provide resolved fields whose statistics correspond to the statistics of a filtered direct numerical simulation. Note that the comparison with filtered direct numerical simulation is not systematically carried out in the literature since other approaches are possible [236]. For practical applications, the knowledge of the filtered variables may not be sufficient as nonfiltered variables are more relevant. This implies that a reconstruction of the nonfiltered fields from the results of the large-eddy simulation is required. As a first step, we assume that since we use an invertible filter, an accurate prediction of the nonfiltered statistics can be obtained from the large-eddy simulation, provided that the simulation provides an accurate prediction of the filtered statistics.

The filtered DNS fields are obtained from the direct numerical simulations of fully developed channel flows at $Re_\tau = 180$ and $Re_\tau = 395$ presented in section 1.3. Using these data, we investigate the large-eddy simulation of the isothermal channel at $Re_\tau = 180$ and of the anisothermal channel at $Re_\tau = 180$ and $Re_\tau = 395$. We address the effect of functional eddy-viscosity or eddy-diffusivity models, structural models, tensorial eddy-viscosity models, mixed models, tensorial mixed models and dynamic versions of these models. However, the analysis is restricted to zero-equation algebraic models without wall function or wall model. Each model is studied using the numerical method described in section 1.2. The robustness of the models to variations of the grid resolution and of the Reynolds numbers is considered.

We give the resolved equations in section 10.2 and the subgrid-scale models investigated in section 10.3. The channel flow configuration and the numerical method are given in section 10.4. The results are discussed in section 10.5.

10.2 Filtered low Mach number equations

As in chapter 9, we consider the large-eddy simulation of the low Mach number equations in two formulations. The Velocity formulation expresses the filtered low Mach number equations in terms of variables filtered with the unweighted classical filter ($\overline{\cdot}$). The Favre formulation expresses the filtered low Mach number equations using Favre-filtered variables, that is based on the density-weighted Favre filter ($\widetilde{\cdot}$) defined for any field ψ as $\widetilde{\psi} = \overline{\rho\psi}/\bar{\rho}$. The two formulations involve a different set of subgrid terms. However, the two most significant subgrid terms are similar in the two formulations [87, 88, 90]. In both cases, a subgrid term is related to the nonlinearity of momentum convection and another related to the correlation of density and velocity. Excluding all other subgrid term, the filtered low Mach number equations are given in the Velocity formulation by:

- Mass conservation equation

$$\frac{\partial \bar{\rho}}{\partial t} + \frac{\partial}{\partial x_j} (\bar{\rho} \bar{U}_j + F_{\rho U_j}) = 0, \quad (10.1)$$

- Velocity transport equation

$$\frac{\partial \bar{U}_i}{\partial t} = -\frac{\partial}{\partial x_j} (\bar{U}_j \bar{U}_i + F_{U_j U_i}) + \bar{U}_i \frac{\partial \bar{U}_j}{\partial x_j} - \frac{1}{\bar{\rho}} \frac{\partial \bar{P}}{\partial x_i} + \frac{1}{\bar{\rho}} \frac{\partial \Sigma_{ij}(\bar{\mathbf{U}}, \bar{T})}{\partial x_j}, \quad (10.2)$$

- Energy conservation equation

$$\frac{\partial \bar{U}_j}{\partial x_j} = -\frac{1}{\gamma P_0} \left[(\gamma - 1) \frac{\partial Q_j(\bar{T})}{\partial x_j} + \frac{\partial P_0}{\partial t} \right], \quad (10.3)$$

- Ideal gas law

$$\bar{T} = \frac{P_0}{r \bar{\rho}}, \quad (10.4)$$

and in the Favre formulation by:

- Mass conservation equation

$$\frac{\partial \bar{\rho}}{\partial t} + \frac{\partial \bar{\rho} \tilde{U}_j}{\partial x_j} = 0, \quad (10.5)$$

- Momentum conservation equation

$$\frac{\partial \bar{\rho} \tilde{U}_i}{\partial t} = -\frac{\partial}{\partial x_j} \left(\bar{\rho} \tilde{U}_j \tilde{U}_i + \bar{\rho} G_{U_j U_i} \right) - \frac{\partial \bar{P}}{\partial x_i} + \frac{\partial \Sigma_{ij}(\tilde{\mathbf{U}}, \tilde{T})}{\partial x_j}, \quad (10.6)$$

- Energy conservation equation

$$\frac{\partial}{\partial x_j} \left(\tilde{U}_j + \bar{\rho} G_{U_j/\rho} \right) = -\frac{1}{\gamma P_0} \left[(\gamma - 1) \frac{\partial Q_j(\tilde{T})}{\partial x_j} + \frac{\partial P_0}{\partial t} \right], \quad (10.7)$$

- Ideal gas law

$$\tilde{T} = \frac{P_0}{\bar{\rho} r}, \quad (10.8)$$

with ρ the density, T the temperature, γ the heat capacity ratio, r the ideal gas specific constant, t the time, P the mechanical pressure, P_0 the thermodynamical pressure, U_i the i -th component of velocity and x_i the Cartesian coordinate in i -th direction. Einstein summation convention is used. The functions $\Sigma_{ij}(\mathbf{U}, T)$ and $Q_j(T)$ are used to compute the shear-stress tensor and conductive heat flux associated with a given velocity and temperature. We assume a Newtonian fluid and Fourier's law,

$$\Sigma_{ij}(\mathbf{U}, T) = \mu(T) \left(\frac{\partial U_i}{\partial x_j} + \frac{\partial U_j}{\partial x_i} \right) - \frac{2}{3} \mu(T) \frac{\partial U_k}{\partial x_k} \delta_{ij}, \quad (10.9)$$

$$Q_j(T) = -\lambda(T) \frac{\partial T}{\partial x_j}, \quad (10.10)$$

with $\mu(T)$ the dynamic viscosity, $\lambda(T)$ the thermal conductivity and δ_{ij} the Kronecker delta.

The momentum convection subgrid term is defined as $F_{U_j U_i} = \overline{U_j U_i} - \bar{U}_j \bar{U}_i$ in the Velocity formulation and $G_{U_j U_i} = \overline{U_j U_i} - \tilde{U}_j \tilde{U}_i$ in the Favre formulation. The density-velocity correlation subgrid term is defined as $F_{\rho U_j} = \overline{\rho U_j} - \bar{\rho} \bar{U}_j$ in the Velocity formulation and $G_{U_j/\rho} = \overline{U_j/\rho} - \tilde{U}_j/\bar{\rho}$ in the Favre formulation. The two formulations are related by the relation

$$\frac{F_{\rho U_j}}{\bar{\rho}} = -\bar{\rho} G_{U_j/\rho}. \quad (10.11)$$

The fluid is air. We use Sutherland's law [287] to compute the viscosity,

$$\mu(T) = \mu_0 \left(\frac{T}{T_0} \right)^{\frac{3}{2}} \frac{T_0 + S}{T + S}, \quad (10.12)$$

with $\mu_0 = 1.716 \cdot 10^{-5}$ Pa s, $S = 110.4$ K and $T_0 = 273.15$ K. We assume a constant Prandtl number $Pr = 0.76$ and heat capacity at constant pressure $C_p = 1005$ J kg⁻¹ K⁻¹.

The conductivity is deduced from the Prandtl number, the heat capacity at constant pressure and the viscosity,

$$\lambda(T) = \frac{C_p}{Pr} \mu(T). \quad (10.13)$$

The ideal gas specific constant is $r = 287 \text{ J kg}^{-1} \text{ K}^{-1}$. These parameters are the same as in the direct numerical simulations presented in section 1.3.

10.3 Subgrid-scale models

Subgrid-scale models express the subgrid terms as functions of variables resolved in the large-eddy simulation. In order to express the models for the momentum convection subgrid term and the density-velocity correlation subgrid term in the Velocity and Favre formulations, it is useful to introduce the following formalism,

$$F_{U_j U_i} \approx \tau_{ij}^{\text{mod}}(\bar{\mathbf{U}}, \bar{\Delta}), \quad (10.14)$$

$$G_{U_j U_i} \approx \tau_{ij}^{\text{mod}}(\tilde{\mathbf{U}}, \bar{\Delta}), \quad (10.15)$$

$$F_{\rho U_j} \approx \pi_j^{\text{mod}}(\bar{\mathbf{U}}, \bar{\rho}, \bar{\Delta}), \quad (10.16)$$

$$G_{U_j/\rho} \approx \pi_j^{\text{mod}}(\tilde{\mathbf{U}}, 1/\bar{\rho}, \bar{\Delta}), \quad (10.17)$$

where the functions $\tau_{ij}^{\text{mod}}(\mathbf{U}, \bar{\Delta})$ and $\pi_j^{\text{mod}}(\mathbf{U}, \phi, \bar{\Delta})$ are model-dependent but do not depend on the formulation. We investigate zero-equation algebraic models without wall function or wall model. This includes functional models, structural models, tensorial models and tensorial mixed models. Dynamic versions of each type of modelling is also considered.

10.3.1 Constant-parameter models

Using functional eddy-viscosity or eddy-diffusivity models, the subgrid terms are modelled by analogy with molecular diffusion,

$$\tau_{ij}^{\text{mod}}(\mathbf{U}, \bar{\Delta}) = -2\nu_e^{\text{mod}}(\mathbf{g}, \bar{\Delta}) S_{ij}, \quad (10.18)$$

$$\pi_j^{\text{mod}}(\mathbf{U}, \phi, \bar{\Delta}) = -\frac{\nu_e^{\text{mod}}(\mathbf{g}, \mathbf{d}, \bar{\Delta})}{Pr_t} d_j, \quad (10.19)$$

with $S_{ij} = \frac{1}{2}(g_{ij} + g_{ji})$ the rate of deformation tensor, \mathbf{g} the velocity gradient, defined by $g_{ij} = \partial_j U_i$ and \mathbf{d} the scalar gradient, defined by $d_j = \partial_j \phi$. The expression of the eddy-viscosity depends on the model used. The subgrid-scale Prandtl or Schmidt number Pr_t , assumed constant, relates the eddy-diffusivity to the eddy-viscosity. The eddy-viscosity or eddy-diffusivity models investigated have been introduced in section 9. They are recalled here:

Smagorinsky model [276]:
$$\nu_e^{\text{Smag}}(\mathbf{g}, \bar{\Delta}) = (C^{\text{Smag}} \bar{\Delta})^2 |\mathbf{S}|, \quad (10.20)$$

WALE model [213]:
$$\nu_e^{\text{WALE}}(\mathbf{g}, \bar{\Delta}) = (C^{\text{WALE}} \bar{\Delta})^2 \frac{(\mathcal{S}_{ij}^d \mathcal{S}_{ij}^d)^{\frac{3}{2}}}{(S_{mn} S_{mn})^{\frac{5}{2}} + (\mathcal{S}_{mn}^d \mathcal{S}_{mn}^d)^{\frac{5}{4}}}, \quad (10.21)$$

$$\text{Sigma model [214]:} \quad \nu_e^{\text{Sigma}}(\mathbf{g}, \bar{\Delta}) = (C^{\text{Sigma}} \bar{\Delta})^2 \frac{\sigma_3 (\sigma_1 - \sigma_2) (\sigma_2 - \sigma_3)}{\sigma_1^2}, \quad (10.22)$$

$$\text{AMD model [250]:} \quad \nu_e^{\text{AMD}}(\mathbf{g}, \bar{\Delta}) = C^{\text{AMD}} \frac{\max(0, -G_{ij} S_{ij})}{g_{mn} g_{mn}}, \quad (10.23)$$

$$\text{Scalar AMD model [3]:} \quad \nu_e^{\text{SAMD}}(\mathbf{g}, \mathbf{d}, \bar{\Delta}) = C^{\text{SAMD}} \frac{\max(0, -D_j d_j)}{d_m d_m}, \quad (10.24)$$

$$\text{Kobayashi model [147]:} \quad \nu_e^{\text{Koba.}}(\mathbf{g}, \bar{\Delta}) = C^{\text{Koba.}} \bar{\Delta}^2 |F_g|^{\frac{3}{2}} (1 - F_g) |\mathbf{S}|, \quad (10.25)$$

where $|\mathbf{S}| = \sqrt{2S_{ij}S_{ij}}$ is a norm of \mathbf{S} , $\mathcal{S}_{ij}^d = \frac{1}{2}(g_{ik}g_{kj} + g_{jk}g_{ki}) - \frac{1}{3}g_{kp}g_{pk}\delta_{ij}$ the traceless symmetric part of the squared velocity gradient tensor, $\sigma_1 \geq \sigma_2 \geq \sigma_3$ the three singular values of \mathbf{g} , $G_{ij} = \bar{\Delta}_k^2 g_{ik}g_{jk}$ the gradient model for the subgrid term associated with momentum convection, $\Pi_G = \frac{1}{2}(\text{tr}^2(G) - \text{tr}(G^2))$ its second invariant, $D_j = \bar{\Delta}_k^2 g_{jk}d_k$ the gradient model for the density-velocity correlation subgrid term, $R_{ij} = \beta_i g_{jj}$ the volumetric strain-stretching, with $\beta = (S_{23}, S_{13}, S_{12})$, and $F_g = (\Omega_{ij}\Omega_{ij} - S_{ij}S_{ij}) / (\Omega_{mn}\Omega_{mn} + S_{mn}S_{mn})$ the coherent structure function, with $\Omega_{ij} = \frac{1}{2}(g_{ij} - g_{ji})$ the spin tensor or rate of rotation tensor. The Smagorinsky, WALE, Sigma, AMD, and Kobayashi models have been initially devised for the momentum convection subgrid term and have been adapted to the density-velocity correlation subgrid term. The scalar AMD model has been devised specifically for the density-velocity correlation subgrid term.

Anisotropic eddy-viscosity or eddy-diffusivity models involve one length scale per direction instead of a single length scale. Anisotropic versions of the Smagorinsky WALE, Sigma and Kobayashi models can be devised. The AMD and Scalar AMD are already anisotropic. We define the Anisotropic Smagorinsky model [86] as,

$$\tau_{ij}^{\text{An.Smag.}}(\mathbf{U}, \bar{\Delta}) = -2\nu_e^{\text{Smag.}}(\mathbf{g}^a, \bar{\Delta}) S_{ij}^a, \quad (10.26)$$

$$\pi_j^{\text{An.Smag.}}(\mathbf{U}, \phi, \bar{\Delta}) = -\frac{\nu_e^{\text{Smag.}}(\mathbf{g}^a, \mathbf{d}^a, \bar{\Delta})}{Pr_t} d_j^a, \quad (10.27)$$

with $S_{ij}^a = \frac{1}{2}(g_{ij}^a + g_{ji}^a)$ the scaled rate of deformation tensor, \mathbf{g}^a the scaled velocity gradient, defined by $g_{ij}^a = (\bar{\Delta}_j/\bar{\Delta})\partial_j U_i$ and \mathbf{d}^a the scaled scalar gradient, defined by $d_j^a = (\bar{\Delta}_j/\bar{\Delta})\partial_j \phi$.

Using the structural gradient model [169], the subgrid terms are modelled according to a Taylor series expansion of the filter,

$$\tau_{ij}^{\text{Grad.}}(\mathbf{U}, \bar{\Delta}) = \frac{1}{12} C^{\text{Grad.}} G_{ij}(\mathbf{U}, \bar{\Delta}) = \frac{1}{12} C^{\text{Grad.}} \bar{\Delta}_k^2 g_{ik}g_{jk}, \quad (10.28)$$

$$\pi_j^{\text{Grad.}}(\mathbf{U}, \phi, \bar{\Delta}) = \frac{1}{12} C^{\text{Grad.}} D_j(\mathbf{U}, \bar{\Delta}) = \frac{1}{12} C^{\text{Grad.}} \bar{\Delta}_k^2 g_{ik}d_k, \quad (10.29)$$

Using the structural scale-similarity model [14], the subgrid terms are modelled following the scale-similarity assumption,

$$\tau_{ij}^{\text{Simil.}}(\mathbf{U}, \bar{\Delta}) = C^{\text{Simil.}} \left(\widehat{U_j U_i} - \widehat{U_j} \widehat{U_i} \right), \quad (10.30)$$

$$\pi_j^{\text{Simil.}}(\mathbf{U}, \phi, \bar{\Delta}) = C^{\text{Simil.}} \left(\widehat{U_j \phi} - \widehat{U_j} \widehat{\phi} \right), \quad (10.31)$$

where $\hat{\cdot}$ is a test filter explicitly computed in the large-eddy simulation. The Taylor series expansion of the filter $\hat{\cdot}$ in (10.30) and (10.31) leads to

$$\tau_{ij}^{\text{Simil.}}(\mathbf{U}, \bar{\Delta}) = \frac{1}{12} C^{\text{Simil.}} G_{ij}(\mathbf{U}, \hat{\Delta}) = \frac{1}{12} C^{\text{Simil.}} \hat{\Delta}_k^2 g_{ik} g_{jk}, \quad (10.32)$$

$$\pi_j^{\text{Simil.}}(\mathbf{U}, \phi, \bar{\Delta}) = \frac{1}{12} C^{\text{Simil.}} D_j(\mathbf{U}, \hat{\Delta}) = \frac{1}{12} C^{\text{Simil.}} \hat{\Delta}_k^2 g_{ik} d_k. \quad (10.33)$$

This corresponds to the gradient model associated with the filter lengths $\hat{\Delta}_k^2$ of the test filter.

As presented in section 9.3, tensorial models can be constructed from any functional or structural model in order to apply a different weighting to each component of the subgrid-scale model. We focus on tensorial eddy-viscosity models, which use the eddy-viscosity assumption only for some specific components of the subgrid term.

Functional and structural models may also be combined to form mixed models. To be more general, we consider tensorial mixed models, which combine the two models with a different weighting for each component. This may be used to combine structural and functional models for each component or to model each component with either a functional or a structural model. Tensorial mixed models are constructed from two algebraic models $\tau_{ij}^{\text{one}}(\mathbf{U}, \bar{\Delta})$ and $\tau_{ij}^{\text{two}}(\mathbf{U}, \bar{\Delta})$, and two constant second-order tensors $H^{(k)}$ and $H^{(l)}$,

$$\tau_{ij}^{(1-H^{(k)})\text{one}+H^{(l)}\text{two}}(\bar{\mathbf{U}}, \bar{\Delta}) = (1 - H_{ij}^{(k)}) \tau_{ij}^{\text{one}}(\bar{\mathbf{U}}, \bar{\Delta}) + H_{ij}^{(l)} \tau_{ij}^{\text{two}}(\bar{\mathbf{U}}, \bar{\Delta}). \quad (10.34)$$

where no implicit summations over i and j are assumed.

Unless stated otherwise, we implicitly use the model parameters $C^{\text{Smag.}} = 0.10$, $C^{\text{WALE}} = 0.55$, $C^{\text{Sigma}} = 1.5$, $C^{\text{AMD}} = 0.3$ and $C^{\text{Koba.}} = 0.045$ and a subgrid-scale Prandtl or Schmidt number $Pr_t = 0.9$. We compute the filter length scale using $\bar{\Delta} = (\bar{\Delta}_x \bar{\Delta}_y \bar{\Delta}_z)^{1/3}$ [77]. The reader may refer to Trias *et al.* [295] for a review of alternative definitions. Numerically, the divergence-related part of the deviatoric rate of deformation tensor is neglected to compute eddy-viscosity models. In other words, we make the hypothesis

$$\tau_{ij}^{\text{mod}}(\mathbf{U}, \bar{\Delta}) = -2\nu_e^{\text{mod}} \left(S_{ij} - \frac{1}{3} S_{kk} \right) \approx -2\nu_e^{\text{mod}} S_{ij}. \quad (10.35)$$

which is exact in the incompressible isothermal case and an approximation in the anisothermal case. We verified that this approximation does not affect significantly the results of the large-eddy simulations.

10.3.2 Dynamic models

For any constant-parameter algebraic subgrid-scale model, dynamic models may be constructed using the approach introduced by Germano *et al.* [112]. For a single model, the dynamic procedures are presented in section 7.2.4 for the momentum convection subgrid term. The generalisation to the density-velocity correlation subgrid term is not presented here. In addition, dynamic mixed models can be constructed using analogous procedures. For the momentum convection subgrid term, the dynamic mixed model $\tau_{ij}^{\text{dyn,one,two}}(\mathbf{U}, \bar{\Delta})$ may be expressed from two algebraic models $\tau_{ij}^{\text{one}}(\mathbf{U}, \bar{\Delta})$ and $\tau_{ij}^{\text{two}}(\mathbf{U}, \bar{\Delta})$ as

$$\tau_{ij}^{\text{dyn,one,two}}(\bar{\mathbf{U}}, \bar{\Delta}) = C^{\text{one}} \tau_{ij}^{\text{one}}(\bar{\mathbf{U}}, \bar{\Delta}) + C^{\text{two}} \tau_{ij}^{\text{two}}(\bar{\mathbf{U}}, \bar{\Delta}). \quad (10.36)$$

The determination of the parameters C^{one} and C^{two} is carried out using a test filter ($\widehat{\cdot}$) and the assumptions

$$\overline{U_j U_i} - \overline{U_j} \overline{U_i} \approx C^{\text{one}} \tau_{ij}^{\text{one}}(\overline{\mathbf{U}}, \overline{\mathbf{\Delta}}) + C^{\text{two}} \tau_{ij}^{\text{two}}(\overline{\mathbf{U}}, \overline{\mathbf{\Delta}}), \quad (10.37)$$

$$\widehat{\overline{U_j U_i}} - \widehat{\overline{U_j}} \widehat{\overline{U_i}} \approx C^{\text{one}} \tau_{ij}^{\text{one}}(\widehat{\overline{\mathbf{U}}}, \widehat{\overline{\mathbf{\Delta}}}) + C^{\text{two}} \tau_{ij}^{\text{two}}(\widehat{\overline{\mathbf{U}}}, \widehat{\overline{\mathbf{\Delta}}}), \quad (10.38)$$

where $\widehat{\overline{\mathbf{\Delta}}}$ is best approximated as $\widehat{\overline{\mathbf{\Delta}}} = (\overline{\mathbf{\Delta}}_i + \widehat{\overline{\mathbf{\Delta}}}_i)^{1/2}$ for Gaussian and box filters [111, 307].

Filtering (10.37), and assuming

$$\overline{C^{\text{one}} \tau_{ij}^{\text{one}}(\overline{\mathbf{U}}, \overline{\mathbf{\Delta}})} = C^{\text{one}} \tau_{ij}^{\text{one}}(\overline{\mathbf{U}}, \overline{\mathbf{\Delta}}), \quad (10.39)$$

$$\overline{C^{\text{two}} \tau_{ij}^{\text{two}}(\overline{\mathbf{U}}, \overline{\mathbf{\Delta}})} = C^{\text{two}} \tau_{ij}^{\text{two}}(\overline{\mathbf{U}}, \overline{\mathbf{\Delta}}), \quad (10.40)$$

it follows that

$$L_{ij}(\overline{\mathbf{U}}) \approx C^{\text{one}} m_{ij}^{\text{one}}(\overline{\mathbf{U}}, \overline{\mathbf{\Delta}}) + C^{\text{two}} m_{ij}^{\text{two}}(\overline{\mathbf{U}}, \overline{\mathbf{\Delta}}), \quad (10.41)$$

where $L_{ij}(\overline{\mathbf{U}})$ is given by equation (7.18) and

$$m_{ij}^{\text{one}}(\overline{\mathbf{U}}, \overline{\mathbf{\Delta}}) = \tau_{ij}^{\text{one}}(\widehat{\overline{\mathbf{U}}}, \widehat{\overline{\mathbf{\Delta}}}) - \overline{\tau_{ij}^{\text{one}}(\overline{\mathbf{U}}, \overline{\mathbf{\Delta}})}, \quad (10.42)$$

$$m_{ij}^{\text{two}}(\overline{\mathbf{U}}, \overline{\mathbf{\Delta}}) = \tau_{ij}^{\text{two}}(\widehat{\overline{\mathbf{U}}}, \widehat{\overline{\mathbf{\Delta}}}) - \overline{\tau_{ij}^{\text{two}}(\overline{\mathbf{U}}, \overline{\mathbf{\Delta}})}. \quad (10.43)$$

Dynamic procedures aim to minimise the residual

$$E_{ij} = L_{ij} - C^{\text{one}} m_{ij}^{\text{one}} - C^{\text{two}} m_{ij}^{\text{two}}. \quad (10.44)$$

Several methods have been suggested to compute the parameters C^{one} and C^{two} . They are given as follows:

One-parameter dynamic mixed method

The parameter of one of the two models is arbitrarily set, for instance C^{one} , then the parameter of the other model is computed dynamically to minimise the variance of the residual [322, 307],

$$\frac{\partial \langle E_{kl} E_{kl} \rangle}{\partial C^{\text{two}}} = 0, \quad (10.45)$$

leading to

$$C^{\text{two}} = \frac{\langle m_{ij}^{\text{two}} (L_{ij} - C^{\text{one}} m_{ij}^{\text{one}}) \rangle}{\langle m_{mn}^{\text{two}} m_{mn}^{\text{two}} \rangle}. \quad (10.46)$$

The parameter of the first model C^{one} may be set to a constant. Alternatively, it may be computed with the classical dynamic method, that is without taking into consideration the second model. This has been suggested in order to improve the two-parameter dynamic procedure [8, 199].

Two-parameter dynamic mixed method

The parameters of the two models are computed dynamically to minimise the variance of the residual [256, 257, 125, 259],

$$\frac{\partial \langle E_{kl} E_{kl} \rangle}{\partial C^{\text{one}}} = 0 \quad \text{and} \quad \frac{\partial \langle E_{kl} E_{kl} \rangle}{\partial C^{\text{two}}} = 0, \quad (10.47)$$

leading to

$$C^{\text{two}} = \frac{\langle m_{ij}^{\text{one}} m_{ij}^{\text{one}} \rangle \langle L_{kl} m_{kl}^{\text{two}} \rangle - \langle m_{ij}^{\text{one}} m_{ij}^{\text{two}} \rangle \langle m_{kl}^{\text{one}} L_{kl} \rangle}{\langle m_{mn}^{\text{one}} m_{mn}^{\text{one}} \rangle \langle m_{pq}^{\text{two}} m_{pq}^{\text{two}} \rangle - \langle m_{mn}^{\text{one}} m_{mn}^{\text{two}} \rangle \langle m_{pq}^{\text{one}} m_{pq}^{\text{two}} \rangle}. \quad (10.48)$$

The parameter C^{one} may be computed from the permutation of the exponents “one” and “two” in the above expression.

A generalisation of dynamic mixed models to an arbitrary number of parameters is given by Sagaut *et al.* [255].

The dynamic procedure may be extended to the construction of a model using tensorial parameters C_{ij}^{one} and C_{ij}^{two} ,

$$\tau_{ij}^{\text{dyn,one,two}}(\bar{\mathbf{U}}, \bar{\mathbf{\Delta}}) = C_{ij}^{\text{one}} \tau_{ij}^{\text{one}}(\bar{\mathbf{U}}, \bar{\mathbf{\Delta}}) + C_{ij}^{\text{two}} \tau_{ij}^{\text{two}}(\bar{\mathbf{U}}, \bar{\mathbf{\Delta}}), \quad (10.49)$$

where no implicit summations over i and j are assumed. The dynamic methods (10.46) and (10.48) can be extended to tensorial parameters. The tensorial dynamic mixed methods are given as follows:

Tensorial one-parameter dynamic mixed method

As in the (scalar) one-parameter dynamic mixed method, the parameters of one of the two models are arbitrarily set, the parameters of the other model being computed dynamically to minimise for all i and j the variance of the residual,

$$\frac{\partial \langle E_{kl} E_{kl} \rangle}{\partial C_{ij}^{\text{two}}} = 0 \quad \text{for all } i \text{ and } j, \quad (10.50)$$

leading to

$$C_{ij}^{\text{two}} = \frac{\langle m_{ij}^{\text{two}} (L_{ij} - C^{\text{one}} m_{ij}^{\text{one}}) \rangle}{\langle m_{ij}^{\text{two}} m_{ij}^{\text{two}} \rangle}, \quad (10.51)$$

where no implicit summations over i and j are assumed. The parameter of the first model C^{one} either be set to a constant, computed using the classical tensorial or zero-residual dynamic method.

Tensorial two-parameter dynamic mixed method

As in the (scalar) two-parameter dynamic mixed method, the parameters of the two models are computed dynamically to minimise for all i and j the variance of the residual,

$$\frac{\partial \langle E_{kl} E_{kl} \rangle}{\partial C_{ij}^{\text{one}}} = 0 \quad \text{and} \quad \frac{\partial \langle E_{kl} E_{kl} \rangle}{\partial C_{ij}^{\text{two}}} = 0 \quad \text{for all } i \text{ and } j, \quad (10.52)$$

leading to

$$C_{ij}^{\text{two}} = \frac{\langle m_{ij}^{\text{one}} m_{ij}^{\text{one}} \rangle \langle L_{ij} m_{ij}^{\text{two}} \rangle - \langle m_{ij}^{\text{one}} m_{ij}^{\text{two}} \rangle \langle m_{ij}^{\text{one}} L_{ij} \rangle}{\langle m_{ij}^{\text{one}} m_{ij}^{\text{one}} \rangle \langle m_{ij}^{\text{two}} m_{ij}^{\text{two}} \rangle - \langle m_{ij}^{\text{one}} m_{ij}^{\text{two}} \rangle \langle m_{ij}^{\text{one}} m_{ij}^{\text{two}} \rangle}, \quad (10.53)$$

where no implicit summations over i and j are assumed. The parameter C^{one} may be computed from the permutation of the exponents “one” and “two” in the above expression.

Besides, two tensorial dynamic mixed methods based on the zero-residual dynamic method have been considered. Simulations with these dynamic methods were found to be unstable. They are nonetheless given below for completeness:

Zero-residual one-parameter dynamic mixed method

The parameters of one of the two models are arbitrarily set, the parameters of the other model being computed dynamically to zero for all i and j the statistical average of the residual,

$$\langle E_{ij} \rangle = 0 \quad \text{for all } i \text{ and } j, \quad (10.54)$$

leading to

$$C_{ij}^{\text{two}} = \frac{\langle L_{ij} - C_{ij}^{\text{one}} m_{ij}^{\text{one}} \rangle}{\langle m_{ij}^{\text{two}} \rangle}, \quad (10.55)$$

where no implicit summations over i and j are assumed.

Zero-residual two-parameter dynamic mixed method

The parameters of the two models are computed dynamically to zero for all i and j the statistical average of the residual and the divergence of the variance of the residual,

$$\frac{\partial \langle E_{kl} E_{kl} \rangle}{\partial C_{ij}^{\text{one}}} + \frac{\partial \langle E_{kl} E_{kl} \rangle}{\partial C_{ij}^{\text{two}}} = 0 \quad \text{and} \quad \langle E_{ij} \rangle = 0 \quad \text{for all } i \text{ and } j, \quad (10.56)$$

leading to

$$C_{ij}^{\text{two}} = \frac{\langle m_{ij}^{\text{one}} m_{ij}^{\text{one}} \rangle \langle L_{ij} \rangle - \langle m_{ij}^{\text{one}} \rangle \langle m_{ij}^{\text{one}} L_{ij} \rangle - \langle m_{ij}^{\text{one}} \rangle \langle m_{ij}^{\text{two}} L_{ij} \rangle + \langle m_{ij}^{\text{one}} \rangle \langle m_{ij}^{\text{two}} \rangle \langle L_{ij} \rangle}{\langle m_{ij}^{\text{one}} m_{ij}^{\text{one}} \rangle \langle m_{ij}^{\text{two}} \rangle - \langle m_{ij}^{\text{one}} \rangle \langle m_{ij}^{\text{one}} m_{ij}^{\text{two}} \rangle + \langle m_{ij}^{\text{two}} \rangle \langle m_{ij}^{\text{one}} m_{ij}^{\text{two}} \rangle - \langle m_{ij}^{\text{one}} \rangle \langle m_{ij}^{\text{two}} m_{ij}^{\text{two}} \rangle}, \quad (10.57)$$

where no implicit summations over i and j are assumed. The parameter C^{one} may be computed from the permutation of the exponents “one” and “two” in the above expression.

For each dynamic procedure, the average $\langle \cdot \rangle$ can be computed as a plane average, that is over the homogeneous directions, or as a global average, that is over the volume of the channel. The parameters of plane-average dynamic procedures is a function of time and the wall-normal coordinate. The parameters of global-average dynamic procedures is a function of time.

10.4 Numerical study configuration

10.4.1 Channel flow configuration

We investigate the large-eddy simulation of a fully developed three-dimensional turbulent channel flow with and without a temperature gradient. The channel has the same characteristics as the channel described in section 1.3, namely it is periodic in the

streamwise (x) and spanwise (z) directions and enclosed by two plane walls in the wall-normal direction (y). Without the temperature gradient, the flow is isothermal and incompressible. The temperature of the two walls is $T_1 = 293$ K. With the temperature gradient, the flow is strongly anisothermal and at low Mach number. The temperature of the cold wall ($y = 0$) is $T_1 = 293$ K and the temperature of the hot wall ($y = 2h$) is $T_2 = 586$ K. Large-eddy simulations of the channel are carried out at the mean friction Reynolds number $Re_\tau = 180$ and $Re_\tau = 395$, where Re_τ is the average of the friction Reynolds number at the cold and hot sides. At $Re_\tau = 180$, the domain size is $4\pi h \times 2h \times 2\pi h$, with $h = 15$ mm. At $Re_\tau = 395$, the domain size is $4\pi h \times 2h \times 4/3\pi h$.

10.4.2 Numerical settings

The channel flow presented in section 10.4.1 is simulated using three meshes at $Re_\tau = 180$, referred to as “48B”, “36C” and “24C”, and one mesh at $Re_\tau = 395$, referred to as “96B”. The meshes are rectilinear. The grid spacing is uniform in the homogeneous directions (x and z) and follows a hyperbolic tangent law in the wall-normal coordinate direction (y),

$$y_k = L_y \left(1 + \frac{1}{a} \tanh \left[\left(\frac{k-1}{N_y-1} - 1 \right) \tanh^{-1}(a) \right] \right), \quad (10.58)$$

with a the mesh dilatation parameter and N_y the number of grid points in the wall-normal direction. The number of grid points and the cell sizes of the meshes of the large-eddy simulations are given in table 10.1.

The analysis of the results of the large-eddy simulations is made with the direct numerical simulations of the same channel described in section 1.3. The direct numerical simulations use the same numerical method as the large-eddy simulations and have the same domain size.

As in the direct numerical simulations (section 1.3), a streamwise volume force f is added to balance the viscous dissipation in the large-eddy simulations. The same targeted mass flow rate is used in the large-eddy simulations and in the direct numerical simulations. The resulting wall shear stress may however be different. Accordingly, the mass enclosed in the domain is the same in all simulations but the mean thermodynamical pressure may be different. This is discussed in more detail in section 10.5.1.

10.4.3 Filtering process

In order to allow the direct comparison of the results of the large-eddy simulations and of the direct numerical simulations, we filter the instantaneous DNS data at the resolution of the LES meshes. We use a top-hat filter to perform this filtering. The top-hat filter is given in one dimension by

$$\bar{\psi}(x) = \frac{1}{\overline{\Delta}(x)} \int_{x-\frac{1}{2}\overline{\Delta}(x)}^{x+\frac{1}{2}\overline{\Delta}(x)} \psi(\xi) d\xi, \quad (10.59)$$

and in three dimensions by the sequential application of the one-dimensional filter in the three spatial directions. To carry out the box filter, we first interpolate the DNS

Re_τ	Name	Number of grid points $N_x \times N_y \times N_z$	Dimension of the domain $L_x \times L_y \times L_z$	Cell sizes in wall units $\Delta_x^+; \Delta_y^+(0) - \Delta_y^+(h); \Delta_z^+$
180	48B	$48 \times 50 \times 48$	$4\pi h \times 2h \times 2\pi h$	68 ; 0.50 – 25 ; 34
180	36C	$36 \times 40 \times 36$	$4\pi h \times 2h \times 2\pi h$	91 ; 2.0 – 22 ; 45
180	24C	$24 \times 28 \times 24$	$4\pi h \times 2h \times 2\pi h$	136 ; 2.0 – 35 ; 68
395	96B	$96 \times 100 \times 64$	$4\pi h \times 2h \times (4/3)\pi h$	73 ; 0.50 – 27 ; 36

Table 10.1 – Computational domain and grid spacing of the three meshes used at $Re_\tau = 180$ and of the mesh used at $Re_\tau = 395$. The cell sizes in wall units are computed using the friction velocity of the direct numerical simulations at the cold side. They are smaller in the isothermal channel and in the anisothermal channel at the hot side.

data using a cubic spline then compute the filter from the interpolated data, as in [86]. The cubic spline interpolation allows the computation of the filter with an arbitrary filter length and without mesh restrictions. The spline interpolation adds an additional filtering to the box filter. However, this additional filter is small compared to the box filter with the DNS meshes used and can be neglected.

Filtering is also required to compute the test filter involved in the scale-similarity model and dynamic models. These filters are computed using other methods because the spline interpolation is too computationally expensive to be used in a large-eddy simulation. The test filter of dynamic methods, referred to as “filter A” is computed as an average over three cells in the three directions. In one dimension, it is given by

$$\bar{\psi}(x_i) = \frac{\psi(x_{i+1})\Delta(x_{i+1}) + \psi(x_i)\Delta(x_i) + \psi(x_{i-1})\Delta(x_{i-1})}{\Delta(x_{i-1}) + \Delta(x_i) + \Delta(x_{i+1})}, \quad (10.60)$$

where $\Delta(x_i)$ is the local cell size around the point x_i . This approximates a top-hat filter whose width is thrice as large as the LES mesh. The test filter of the scale-similarity model has been computed using the filter A and another filter. The second filter, referred to as “filter T”, uses the Taylor series expansion of the box filter, given in one dimension by

$$\bar{\psi}(x) = \psi(x) + \frac{\Delta^2}{24} \frac{\partial^2 \psi}{\partial x^2}. \quad (10.61)$$

The second derivative is computed using a second-order centred finite difference approximation,

$$\bar{\psi}(x_i) = \psi(x_i) + \frac{[\Delta(x_i)]^2}{24} \frac{\psi(x_{i+1})\Delta(x_{i-1/2}) - \psi(x_i)[\Delta(x_{i-1/2}) + \Delta(x_{i+1/2})] + \psi(x_{i-1})\Delta(x_{i+1/2})}{\Delta(x_{i-1/2})\Delta(x_i)\Delta(x_{i+1/2})}, \quad (10.62)$$

using the local cell size as the filter width.

10.5 Results and discussion

The large-eddy simulations of the isothermal and anisothermal channel address the modelling of the two most significant subgrid terms arising from the filtering of the low

Mach number equations. The isothermal channel will be used to study the relevance of subgrid-scale models for the momentum convection subgrid term. The anisothermal channel will be used to study the relevance of subgrid-scale models for the density-velocity correlation subgrid term, of combinations of subgrid-scale models for the two subgrid terms and of the use of the Velocity and Favre formulations. Before proceeding to the comparison of the subgrid-scale models, we briefly discuss the simulation of the channel without subgrid-scale model.

To analyse the results, we define the three following scalings:

- The scaling (+), or classical scaling, based on the friction velocity U_τ , the wall kinematic viscosity ν_ω and temperature T_ω and the friction temperature T_τ ,

$$y^+ = \frac{yU_\tau}{\nu_\omega}, \quad \mathbf{U}^+ = \frac{\mathbf{U}}{U_\tau}, \quad T^+ = \frac{T - T_\omega}{T_\tau};$$

- The scaling ($^\circ$), based on the channel half-height, the average kinematic viscosity $\frac{1}{2}(\nu_1 + \nu_2)$ and the temperature difference $T_2 - T_1$,

$$y^\circ = \frac{y}{h}, \quad \mathbf{U}^\circ = \frac{\mathbf{U}h}{\frac{1}{2}(\nu_1 + \nu_2)}, \quad T^\circ = \frac{T - T_\omega}{T_2 - T_1};$$

- The scaling ($^\times$), based on the average friction velocity $\frac{1}{2}(U_{\tau,1} + U_{\tau,2})$, the average kinematic viscosity $\frac{1}{2}(\nu_1 + \nu_2)$ and the average friction temperature $\frac{1}{2}(T_{\tau,1} + T_{\tau,2})$,

$$y^\times = y^\circ, \quad \mathbf{U}^\times = \frac{\mathbf{U}}{\frac{1}{2}(U_{\tau,1} + U_{\tau,2})}, \quad T^\times = \frac{T - \frac{1}{2}(T_1 + T_2)}{\frac{1}{2}(T_{\tau,1} + T_{\tau,2})}.$$

The friction Reynolds number and heat flux of the large-eddy simulations are given in appendix D.

10.5.1 Simulation without subgrid-scale models

Simulations without subgrid-scale model are carried out with the meshes 24C, 36C and 48B. The mass flow rate of the simulations is imposed using a control loop to adjust the streamwise volume force f , as described in section 1.3. The targeted mass flow rate is the same as in the direct numerical simulations. Accordingly, the simulations have the same mass flow rate than the direct numerical simulations but predict a different wall shear stress. With the mesh 48B, the error on the friction velocity is 1% in the anisothermal channel at $Re_\tau = 180$. Imposing a constant streamwise volume force would maintain the wall shear stress at the same level as the direct numerical simulations, but results in an error of 1% on the mass flow rate. The results of simulations with constant mass flow rate and constant streamwise volume force are compared in figure 10.1 in the anisothermal channel at $Re_\tau = 180$. The scaling of the profiles takes into account the differences of mass flow rate. Nevertheless, the two approaches are not completely equivalent because the Reynolds number differences between the two methods may induce low Reynolds number effects.

The results of the simulations without subgrid-scale model are compared to direct numerical simulations filtered at the resolution of the simulation meshes. The filtering is

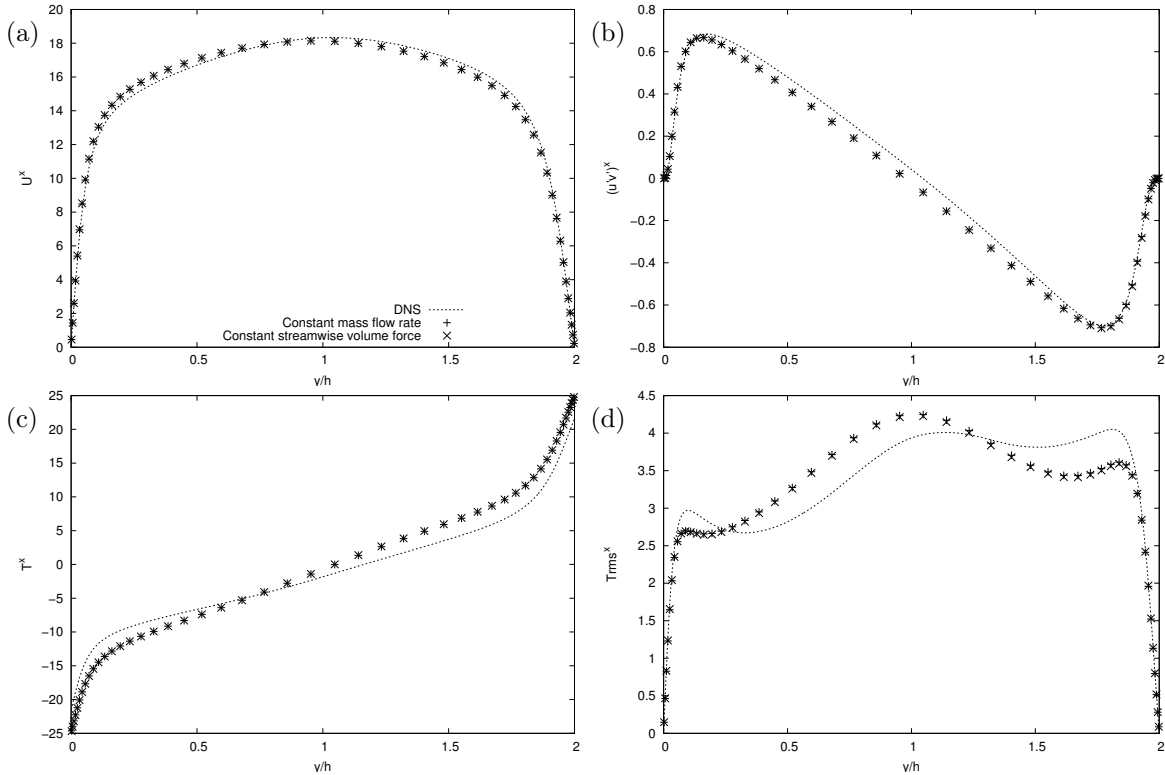


Figure 10.1 – Comparison of simulations with no subgrid-scale model with constant mass flow rate and constant streamwise volume force for the profiles of the mean streamwise velocity $\langle U_x \rangle$ (a), the covariance of streamwise and wall-normal velocity $\langle u'_x u'_y \rangle$ (b), the mean temperature $\langle T \rangle$ (c) and the standard deviation of temperature $\sqrt{\langle T'^2 \rangle}$ (d) in the anisothermal channel at $Re_\tau = 180$ with the mesh 48B.

carried out using the classical filter and the Favre filter. The two filters lead to identical results for the mean streamwise velocity, the mean temperature, the covariance of streamwise and wall-normal velocity and the standard deviation of velocity components and of temperature. The distinction is only relevant for the mean wall-normal velocity, which is different in the Velocity and Favre formulations. The mean filtered wall-normal velocity requires a longer averaging time than the other turbulence statistics and is not well-converged. We may only guess that the mean filtered wall-normal velocity has a slightly lower amplitude than the mean nonfiltered wall-normal velocity with the classical filter and a significantly lower amplitude with the Favre filter (figure 10.5).

The mean nonfiltered and filtered streamwise velocity are identical, whereas the simulation with the mesh 24C at $Re_\tau = 180$ underestimates significantly the friction velocity, and thus the mean streamwise velocity near the wall. As the mass flow rate is imposed, the mean streamwise velocity is without scaling satisfactory at the center of the channel for all simulations in the incompressible case (figure 10.2). In the anisothermal channel however (figures 10.3 and 10.4), the simulations do not capture correctly the asymmetry between the profiles at the hot and cold sides, overestimating the velocity at the cold side and underestimating the velocity at the hot side.

The heat flux at the wall is underestimated by all anisothermal simulations and by the coarser simulations in particular. This error directly impacts the mean wall-normal velocity. Indeed, without subgrid-scale models, the energy conservation equation leads

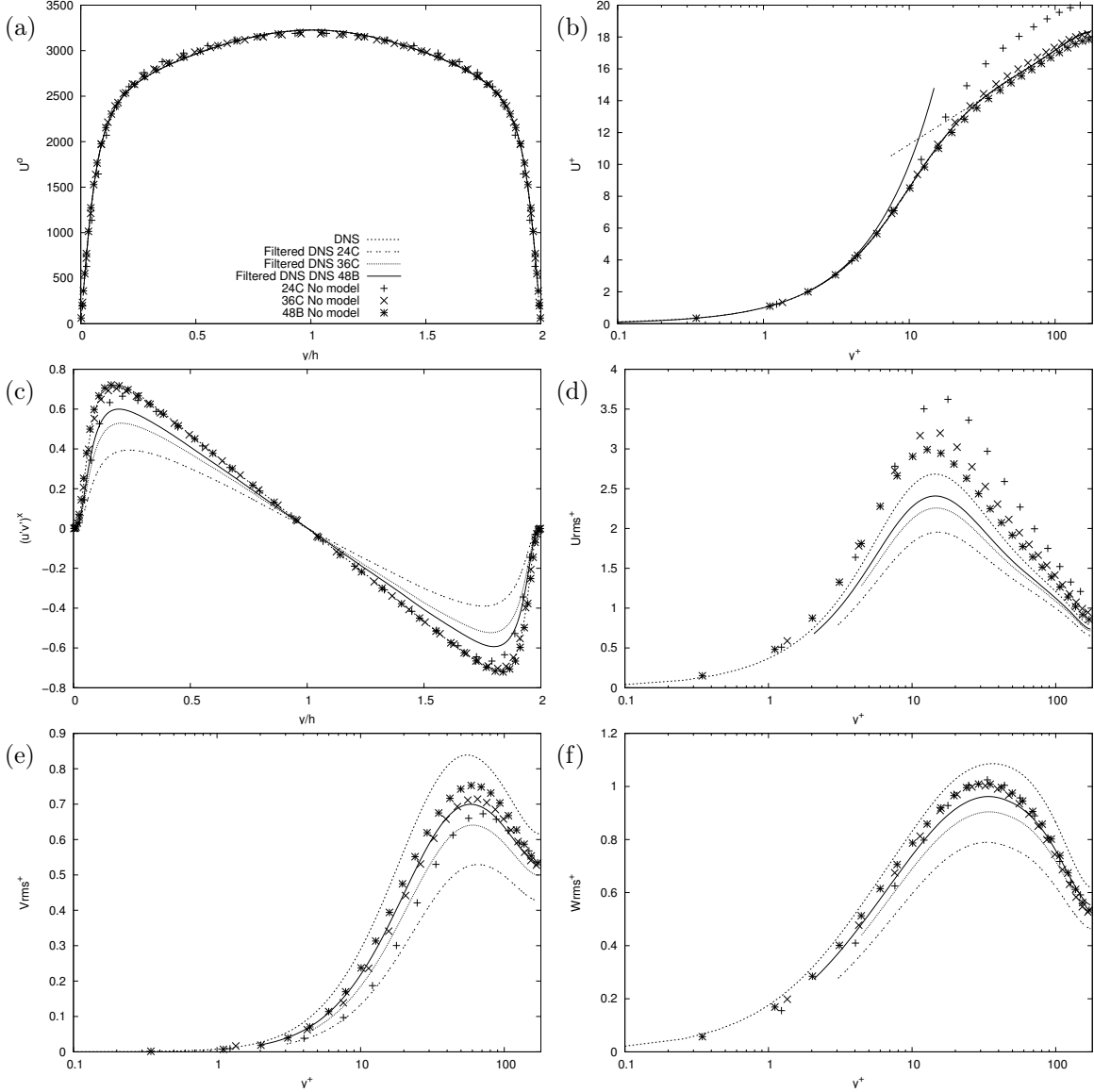


Figure 10.2 – Comparison of simulations with no subgrid-scale model with the meshes 24C, 36C and 48B for the profiles of the mean streamwise velocity $\langle U_x \rangle$ (a, b), the covariance of streamwise and wall-normal velocity $\langle u'_x u'_y \rangle$ (c), the standard deviation of streamwise velocity $\sqrt{\langle u_x'^2 \rangle}$ (d), wall-normal velocity $\sqrt{\langle u_y'^2 \rangle}$ (e) and spanwise velocity $\sqrt{\langle u_z'^2 \rangle}$ (f) in the isothermal channel at $Re_\tau = 180$.

with the low Mach number hypothesis to a balance between the mean wall-normal velocity and the mean local conductive heat flux,

$$\frac{\gamma P_0}{\gamma - 1} \langle U_y \rangle = -[\langle Q_y \rangle - Q_0], \quad (10.63)$$

where Q_0 is the conductive heat flux at $y = 0$ (cold wall). Since the heat flux at the center of the channel is well predicted by all simulations, the error on the mean wall-normal velocity is closely related to the error on the wall heat flux (figure 10.5). The mean wall-normal velocity appears underestimated if it is compared to the classical-filtered DNS data. In all simulations, the mean thermodynamical pressure is larger than in the direct numerical simulation. The error is however not significant compared

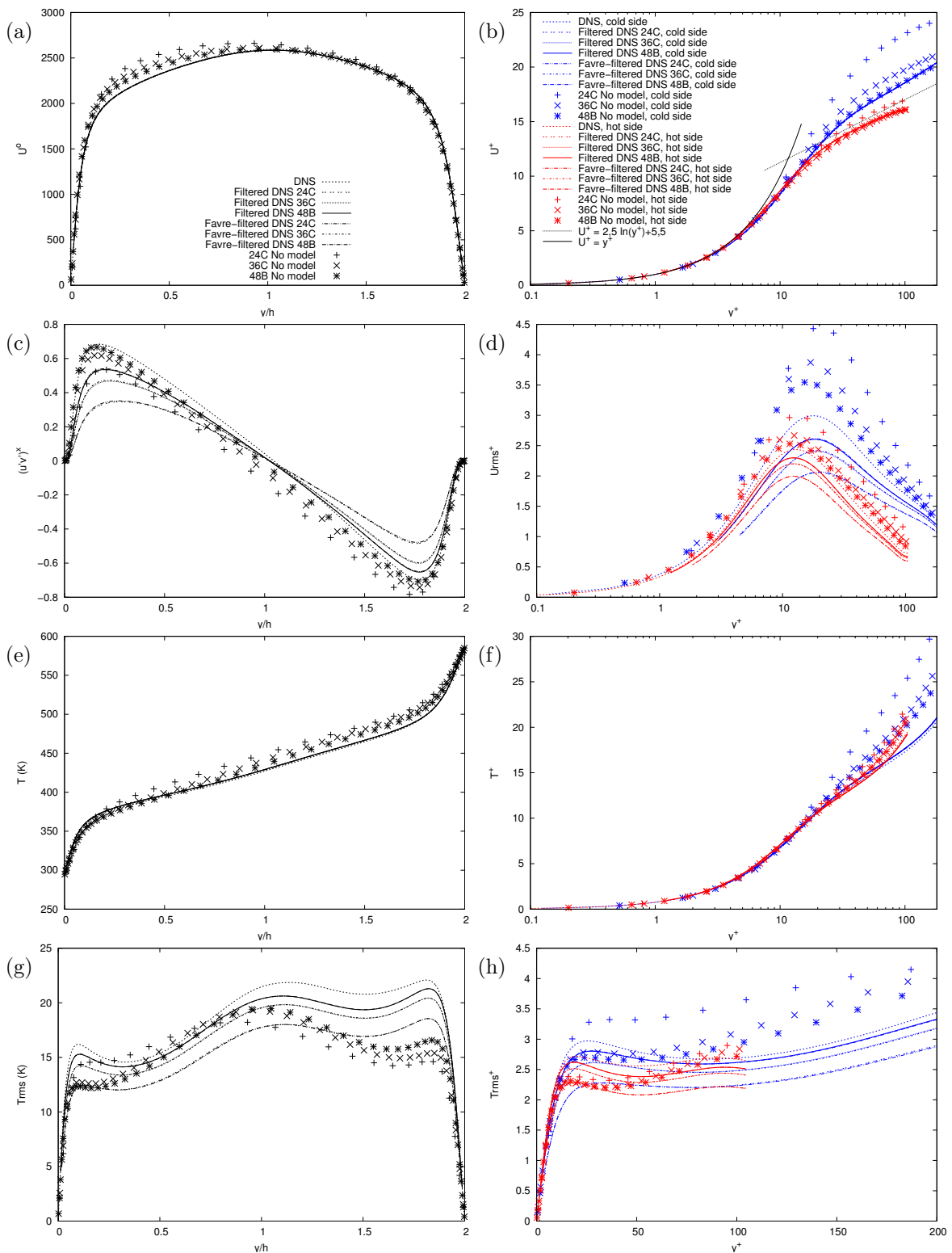


Figure 10.3 – Comparison of simulations with no subgrid-scale model with the meshes 24C, 36C and 48B for the profiles of the mean streamwise velocity $\langle U_x \rangle$ (a, b), the covariance of streamwise and wall-normal velocity $\langle u'_x u'_y \rangle$ (c), the standard deviation of streamwise velocity $\sqrt{\langle u_x'^2 \rangle}$ (d), the mean temperature $\langle T \rangle$ (e, f) and the standard deviation of temperature $\sqrt{\langle T'^2 \rangle}$ (g, h) in the anisothermal channel at $Re_\tau = 180$.

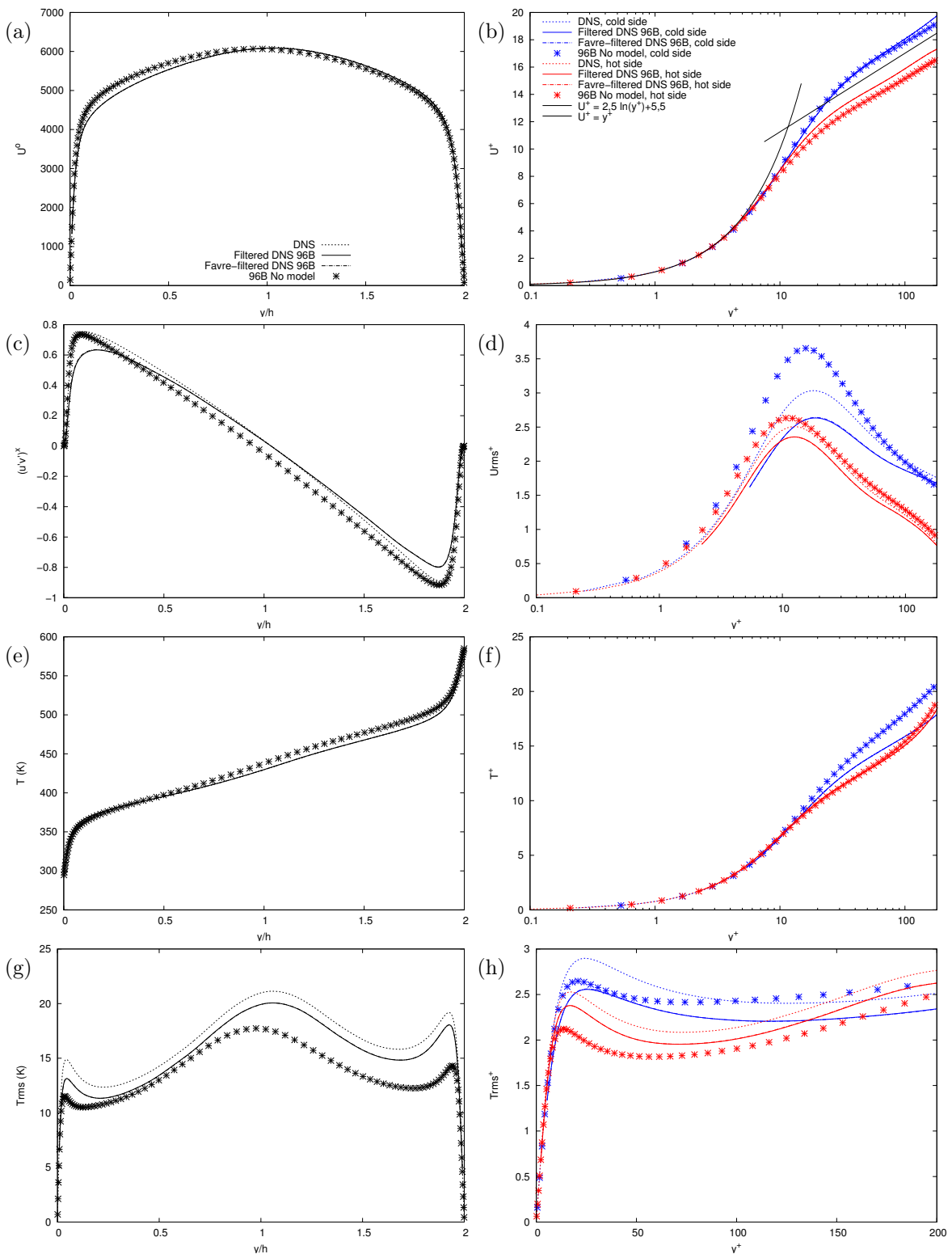


Figure 10.4 – Comparison of simulations with no subgrid-scale model with the mesh 96B for the profiles of the mean streamwise velocity $\langle U_x \rangle$ (a, b), the covariance of streamwise and wall-normal velocity $\langle u'_x u'_y \rangle$ (c), the standard deviation of streamwise velocity $\sqrt{\langle u_x'^2 \rangle}$ (d), the mean temperature $\langle T \rangle$ (e, f) and the standard deviation of temperature $\sqrt{\langle T'^2 \rangle}$ (g, h) in the anisothermal channel at $Re_\tau = 395$.

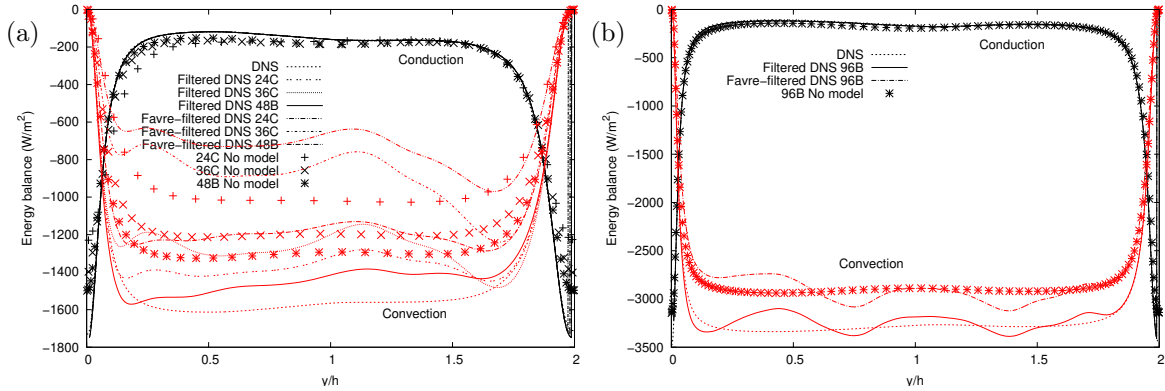


Figure 10.5 – Comparison of simulations with no subgrid-scale model for the profiles of the terms of the energy balance (10.63), namely the convective heat flux $\langle U_y(\gamma P_0)/(\gamma - 1) \rangle$ (“Convection”) and the conductive heat flux $\langle -\lambda(\partial T/\partial y) \rangle$ (“Conduction”) with the meshes 24C, 36C and 48B in the anisothermal channel at $Re_\tau = 180$ and with the mesh 96B in the anisothermal channel at $Re_\tau = 395$.

to the error on the heat flux, and does not exceed 4% with the mesh 24C at $Re_\tau = 180$.

The filtering of the DNS data decreases significantly the maximum value of the covariance of streamwise and wall-normal velocity and the standard deviation of velocity components. The decrease is larger for a larger filter width. In the isothermal channel at $Re_\tau = 180$, the decrease ranges from around 10% with the mesh 48B to around 30% with the mesh 24C. However, the simulations without model lead with the three meshes to a similar covariance of streamwise and wall-normal velocity and standard deviation of spanwise velocity, while the standard deviation of streamwise velocity increases with mesh derefinement (figure 10.2). The interpretation of these results should take into account the effect of the classical scaling, as the underestimation of the wall shear stress in the coarser simulations offsets a slight decrease the covariance of streamwise and wall-normal velocity and the standard deviation of spanwise velocity without scaling.

In the anisothermal channel, the asymmetry between the profiles of the turbulence statistics at the hot and cold sides is not captured correctly by the simulations. For instance, the amplitude asymmetry between the profiles of the standard deviation of streamwise velocity at the hot and cold sides is amplified compared to the direct numerical simulation (figure 10.3). Conversely, the asymmetry is reduced using the filtered DNS data. This reduction is due to the lower turbulence intensity level at the hot side, leading, in wall units, to an asymmetry of filtering resolution. The mean temperature is without scaling overestimated in the bulk of the channel. In other words, the temperature difference to the wall is underestimated at the hot side and overestimated at the cold side. With the classical scaling, it is overestimated at both the hot and cold sides given the error on the wall heat flux. For the same reason, the standard deviation of temperature decreases without scaling with mesh derefinement but increases at the cold side with mesh derefinement with the classical scaling.

In the isothermal channel at $Re_\tau = 180$, the error on the friction velocity is 9% with the mesh 24C, 6% with the mesh 36C and 2% with the mesh 48B. The relative accuracy of the wall shear stress with the mesh 48B is partly due to its non-monotonous convergence of the prediction with mesh refinement. As identified by Meyers and

Sagaut [196], the non-monotonous convergence allows the existence of a grid-resolution line where the error on the wall shear stress is zero. The simulation of the channel with a finer $72 \times 68 \times 72$ mesh leads to an error of 4% for the wall shear stress in the isothermal case. This is less accurate than with the mesh 48B, confirming that the mesh 48B is close to Meyers' no error line. Due to this non-monotonous convergence of the wall shear stress and the turbulence statistics, it is important to verify the robustness of the subgrid-scale models to a range of friction Reynolds numbers and grid resolutions.

In the following, we will study the simulation of the isothermal and anisothermal channels with subgrid-scale models, that is its large-eddy simulation. We first study the modelling of the subgrid term associated with momentum convection in the incompressible isothermal case. We then verify the generality of the results in the anisothermal case, extend the analysis to the modelling of the density-velocity correlation subgrid term and compare the Velocity and Favre formulations.

10.5.2 Large-eddy simulation in the incompressible isothermal case

To study the modelling of the momentum convection subgrid term, we carry out large-eddy simulations of the isothermal channel at $Re_\tau = 180$ with several functional models, structural models, tensorial models and tensorial mixed models.

10.5.2.1 Functional modelling

In this section, we investigate the functional modelling of the momentum convection subgrid term. The functional models investigated are the Smagorinsky, WALE, Sigma, AMD, Kobayashi and Anisotropic Smagorinsky models, as well as dynamic versions of these models. The results of large-eddy simulations with these models are compared in figure 10.6 with the mesh 48B. As consistently found in the literature [see e.g. 304], the Smagorinsky model does not perform well in shear flow and considerably deteriorates the profiles of the turbulence statistics. The Anisotropic Smagorinsky model improves significantly the predictions compared to the Smagorinsky model, providing similar results to the WALE, Sigma and AMD models. The WALE, Sigma, AMD, Kobayashi and Anisotropic Smagorinsky models underestimate the wall shear stress, thus do not lead to a good representation of the scaled mean streamwise velocity. The additional dissipation provided by the model is able to decrease the maximum value of the standard deviation of wall-normal and spanwise velocity, but the standard deviation of streamwise velocity is increased further away from the filtered DNS profile. The no-model simulation yields a better prediction of the friction Reynolds number, the mean streamwise velocity and the standard deviation of velocity components than the large-eddy simulations with functional models. The points discussed above are also valid for the meshes 24C and 36C. The larger filter widths amplify the reduction of the standard deviation of wall-normal and spanwise velocity following approximately the same behaviour as the filtered direct numerical simulation (figure 10.7). On the other hand, the standard deviation of streamwise velocity is even with the 24C mesh not reduced compared to the no-model simulation, further enhancing the discrepancy with the filtered direct numerical simulation. The predictions of the large-eddy simulations

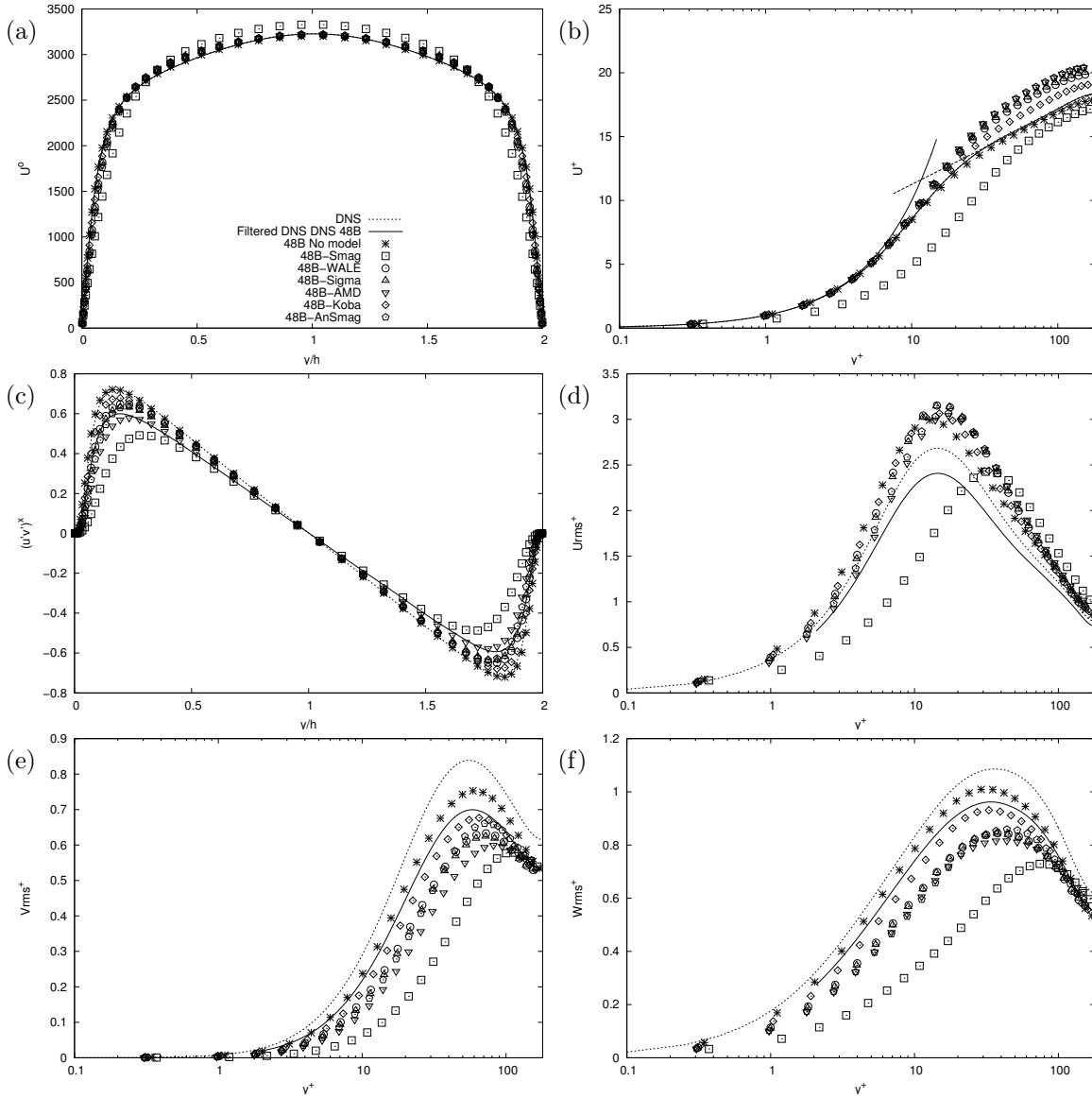


Figure 10.6 – Comparison of large-eddy simulations with the Smagorinsky, WALE, Sigma, AMD, Kobayashi and Anisotropic Smagorinsky models for the profiles of the mean streamwise velocity $\langle U_x \rangle$ (a, b), the covariance of streamwise and wall-normal velocity $\langle u'_x u'_y \rangle$ (c), the standard deviation of streamwise velocity $\sqrt{\langle u'^2_x \rangle}$ (d), wall-normal velocity $\sqrt{\langle u'^2_y \rangle}$ (e) and spanwise velocity $\sqrt{\langle u'^2_z \rangle}$ (f) in the isothermal channel at $Re_\tau = 180$ with the mesh 48B.

depend on the parameter of the model. Using the parameters given in section 10.3, a lower subgrid-scale viscosity is obtained with the Kobayashi model (figure 10.9). This leads to more accurate results with the meshes and numerical method of this study.

Dynamic models provide a less arbitrary comparison of functional models in the sense that it is not complicated by the choice of the model parameter. We study plane-average, global-average, tensorial plane-average and tensorial global-average dynamic methods. The main purpose of the plane-average dynamic method is the local adaptation of the model parameter, which may compensate an unsatisfactory asymptotic near-wall behaviour of the model [273]. This is particularly well-suited to the Smagorinsky model. The plane-average dynamic Smagorinsky model (figure 10.8) gives similar results to the non-dynamic WALE and Sigma models. With the plane-average

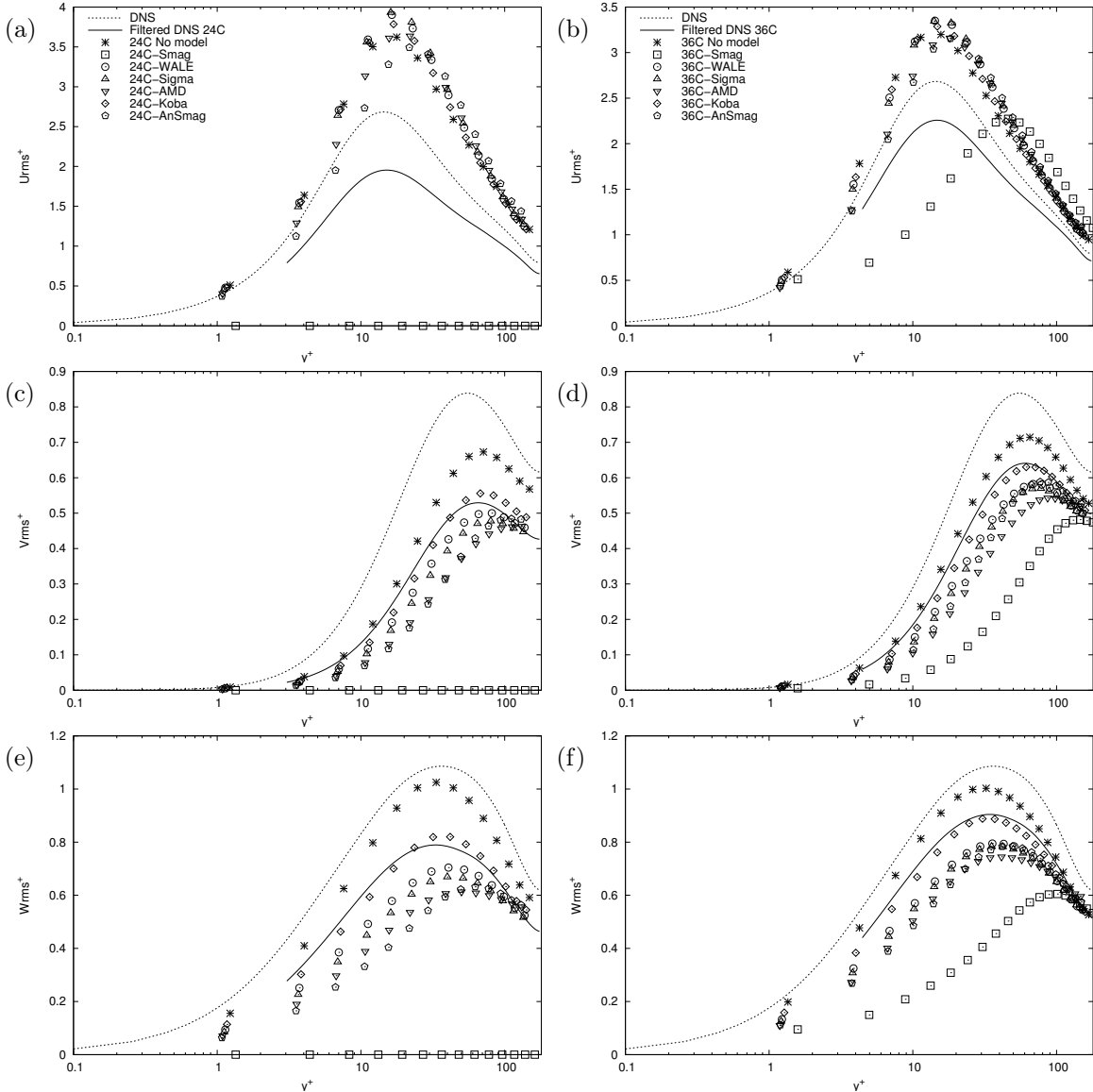


Figure 10.7 – Comparison of large-eddy simulations with the Smagorinsky, WALE, Sigma, AMD, Kobayashi and Anisotropic Smagorinsky models with the meshes 24C (left) and 36C (right) for the profiles of the standard deviation of streamwise velocity $\sqrt{\langle u_x'^2 \rangle}$ (a, b), wall-normal velocity $\sqrt{\langle u_y'^2 \rangle}$ (c, d) and spanwise velocity $\sqrt{\langle u_z'^2 \rangle}$ (e, f) in the isothermal channel at $Re_\tau = 180$.

dynamic procedure, the Anisotropic Smagorinsky model deteriorates the predictions of the Smagorinsky model. Large-eddy simulations with the plane-average dynamic WALE, Sigma, AMD and Kobayashi models are not stable. This is consistent with the observation by Baya Toda *et al.* [18] that the plane-average dynamic method might degrade subgrid-scale models with a proper asymptotic near-wall behaviour and lead to numerical instabilities.

The global-average dynamic method multiplies the subgrid-scale models by a time-dependent function without modifying the local behaviour of the model. The average and standard deviation of the dynamic parameters are given in table 10.2. The global-average dynamic procedure increases the Kobayashi and Anisotropic Smagorinsky models but reduces the WALE and AMD models, except with the mesh 24C. The

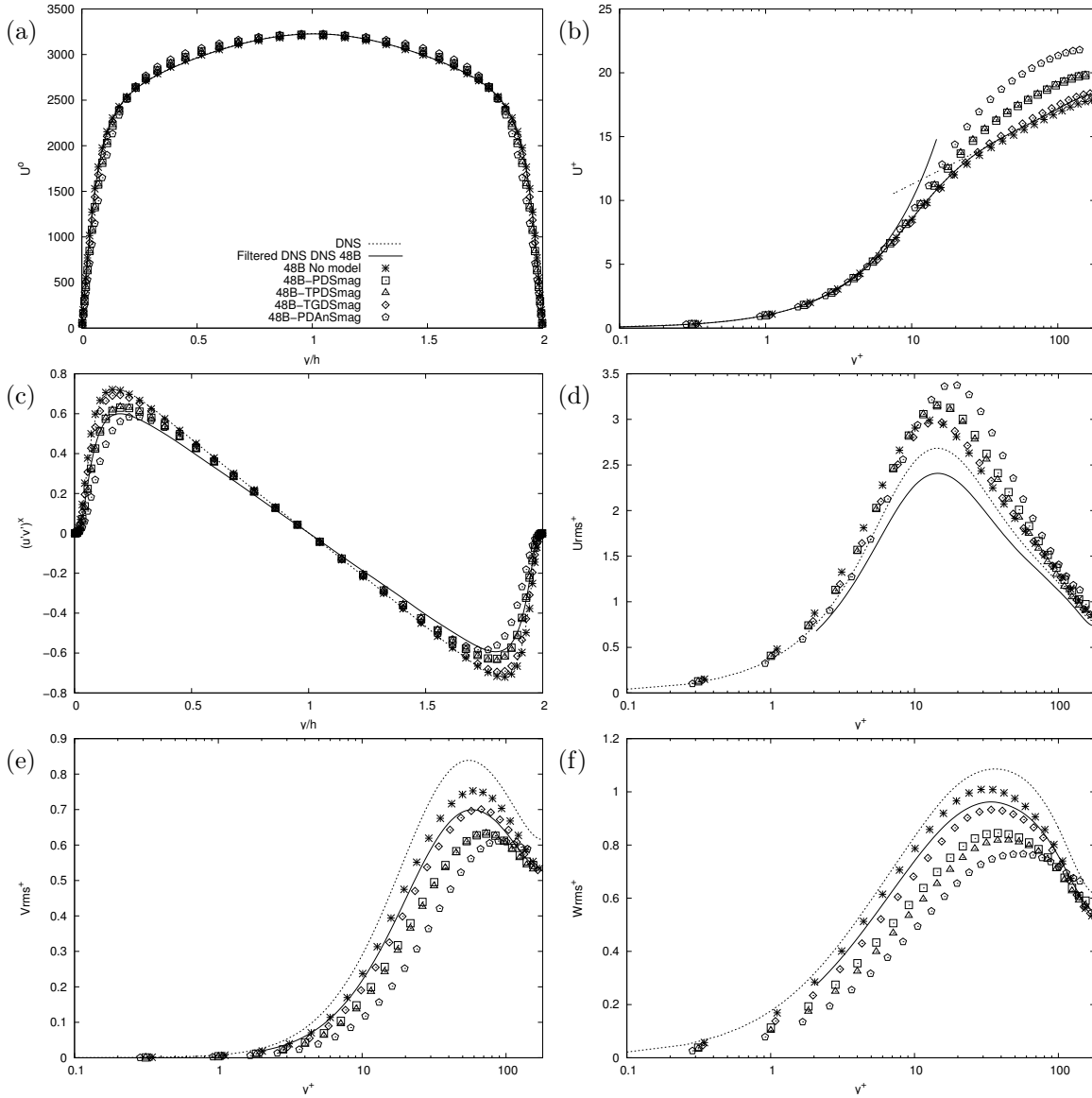


Figure 10.8 – Comparison of large-eddy simulations with the plane-average, tensorial plane-average and tensorial global-average dynamic Smagorinsky model and the plane-average dynamic Anisotropic Smagorinsky model for the profiles of the mean streamwise velocity $\langle U_x \rangle$ (a, b), the covariance of streamwise and wall-normal velocity $\langle u'_x u'_y \rangle$ (c), the standard deviation of streamwise velocity $\sqrt{\langle u'^2_x \rangle}$ (d), wall-normal velocity $\sqrt{\langle u'^2_y \rangle}$ (e) and spanwise velocity $\sqrt{\langle u'^2_z \rangle}$ (f) in the isothermal channel at $Re_\tau = 180$ with the mesh 48B.

Smagorinsky model is made negligible to prevent its detrimental near-wall influence (figure 10.9). The global-average dynamic WALE, AMD and Kobayashi models lead to a good prediction of the standard deviation of wall-normal and spanwise velocity, but the standard deviation of streamwise velocity is not improved compared to the no-model simulation (figure 10.10). The Sigma and Anisotropic Smagorinsky models do not provide good results with the global-average dynamic procedure.

The tensorial global-average dynamic method alters the relative contribution of each component of the subgrid-scale models. Excluding the Anisotropic Smagorinsky model, the tensorial global-average dynamic procedure decreases heavily the relative amplitude of the “ yy ”, “ yz ” and “ zz ” components, moderately decreases the “ xz ” com-

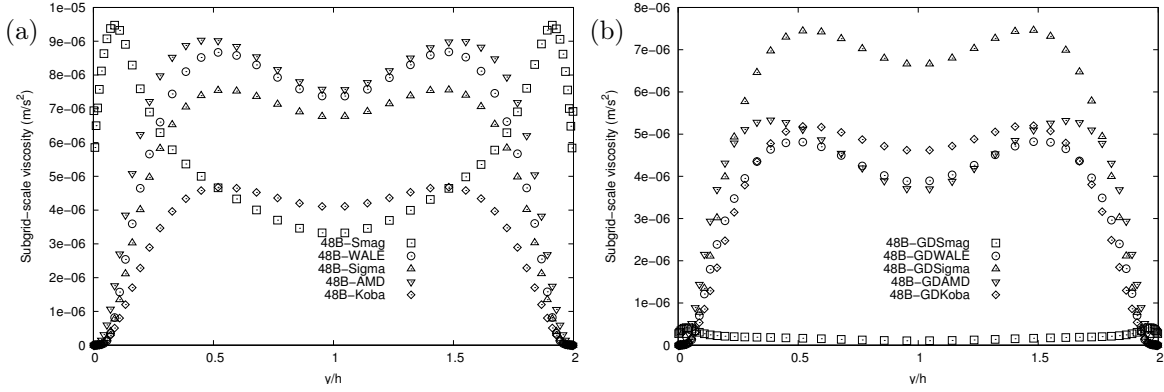


Figure 10.9 – Comparison of simulations with the constant-parameters and global-average dynamic Smagorinsky, WALE, Sigma, AMD, Kobayashi and Anisotropic Smagorinsky models for the profiles of the subgrid-scale viscosity in the isothermal channel at $Re_\tau = 180$ with the mesh 48B.

Average of the dynamic parameter (standard deviation),

	$\langle C^{\text{mod}} \rangle \left(\sqrt{\langle (C^{\text{mod}})^2 \rangle - \langle C^{\text{mod}} \rangle^2} \right)$		
	Mesh 24C	Mesh 36C	Mesh 48 B
Smag.	0.009 (0.001)	0.016 (0.001)	0.033 (0.001)
WALE	1.337 (0.554)	0.591 (0.073)	0.494 (0.038)
Sigma	1.723 (0.263)	1.182 (0.083)	0.982 (0.046)
AMD	—	—	0.455 (0.019)
Kobayashi	—	—	1.151 (0.088)
An. Smag.	0.694 (0.080)	1.008 (0.075)	1.544 (0.101)
Gradient	—	—	2.593 (0.053)

Table 10.2 – Average and normalised standard deviation of the dynamic parameter of the large-eddy simulations with the global-average dynamic Smagorinsky, WALE, Sigma, AMD, Kobayashi and Anisotropic Smagorinsky models in the isothermal channel at $Re_\tau = 180$ with the meshes 24C, 36C and 48B.

ponent and amplifies the “ xy ” (table 10.3). The effect of the tensorial global-average dynamic procedure on the “ xx ” component is strongly dependent of the model. Depending on the model and the component, negative average parameters are obtained. In other words, the models are not purely dissipative. The Sigma model is the only functional model investigated with only positive parameters. The “ xy ” and “ xz ” are positive for all models while the “ zz ” component is negative for most models. This echoes the results of a priori tests (section 9.3), which showed that the “ xy ” and “ xz ” components of functional models were the most crucial. The tensorial global-average dynamic Smagorinsky model decreases the standard deviation of wall-normal and spanwise velocity without increasing the standard deviation of streamwise velocity (figure 10.8). Similar results are obtained with the tensorial global-average dynamic WALE, AMD and Kobayashi models (figure 10.11). This is an improvement compared to the global-average dynamic procedure. The tensorial global-average dynamic AMD model is able to decrease the maximum value of the standard deviation of streamwise velocity, improving the results compared to the no-model simulation. It is the only investigated

Average of the dynamic parameter (standard deviation),

$$\langle C^{\text{mod}} \rangle (\sqrt{\langle (C^{\text{mod}})^2 \rangle - \langle C^{\text{mod}} \rangle^2})$$

	xx	xy	xz	yy	zy	zz
Smag.	6.755 (0.434)	0.028 (0.001)	0.073 (0.049)	0.269 (0.025)	-0.011 (0.005)	-0.266 (0.036)
WALE	-0.732 (0.159)	1.463 (0.093)	0.432 (0.041)	0.225 (0.066)	-0.035 (0.023)	0.418 (0.056)
Sigma	1.664 (0.267)	1.662 (0.077)	0.617 (0.069)	0.155 (0.058)	0.002 (0.030)	0.160 (0.050)
AMD	0.624 (0.097)	0.750 (0.035)	0.245 (0.038)	0.001 (0.034)	0.035 (0.022)	-0.064 (0.026)
Kobayashi	2.546 (0.274)	2.719 (0.175)	0.785 (0.133)	-0.145 (0.081)	0.048 (0.046)	-0.030 (0.067)
An. Smag.	5.435 (0.480)	1.618 (0.148)	0.275 (0.094)	1.531 (0.259)	-0.236 (0.086)	-0.323 (0.078)
Gradient	2.587 (0.061)	2.404 (0.039)	1.379 (0.039)	2.928 (0.067)	1.566 (0.041)	1.949 (0.031)

Table 10.3 – Average and normalised standard deviation of the dynamic parameters of the large-eddy simulations with the tensorial global-average dynamic Smagorinsky, WALE, Sigma, AMD, Kobayashi and Anisotropic Smagorinsky models in the isothermal channel at $Re_\tau = 180$ with the mesh 48B.

functional model with this property.

10.5.2.2 Structural modelling

In this section, we investigate the structural modelling of the momentum convection subgrid term. The structural models investigated are the gradient and scale-similarity models, as well as the dynamic versions of the gradient model. We give the results of large-eddy simulations with the gradient and scale-similarity models in figure 10.12 with the mesh 48B. The classical gradient model ($C^{\text{Grad.}} = 1$) improves slightly the standard deviation of streamwise velocity compared to the no-model simulation, but deteriorates the profiles of the standard deviation of wall-normal and spanwise velocity near the wall and the prediction of the wall shear stress. Nonetheless, the effects of the gradient model on the flow are rather small. To amplify the effects, we investigate gradient models with a parameter $C^{\text{Grad.}}$ larger than one. The simulations are not stable using large multiplicative parameters. The filtering of the gradient model improves the stability of the simulation. The resulting filtered gradient model may be seen as an alternative formulation of the rational model proposed by Galdi and Layton [106][see also 23, 129, 130, 24],

$$\widehat{\tau}_{ij}^{\text{Grad,filtered}}(\mathbf{U}, \overline{\Delta}) = \widehat{\tau}_{ij}^{\text{Grad.}}(\mathbf{U}, \overline{\Delta}) = \frac{1}{12} C^{\text{Grad.}} \overline{\Delta}_k^2 g_{ik} g_{jk}. \quad (10.64)$$

The test filter $\widehat{\cdot}$ is computed using filter A. The filtering alters the results of the simulation since with $C^{\text{Grad.}} = 2$, the predicted wall shear stress is significantly different for the nonfiltered and filtered gradient models (figure 10.12). With $C^{\text{Grad.}} = 9$, the filtered gradient model leads to a standard deviation of streamwise velocity at the level of the filtered direct numerical simulation. However, the covariance of streamwise and wall-normal velocity and the standard deviation of wall-normal and spanwise velocity are underestimated. Hence, there is no Pareto improvement compared to the classical gradient model.

The plane-average and global-average dynamic gradient models give nearly identi-

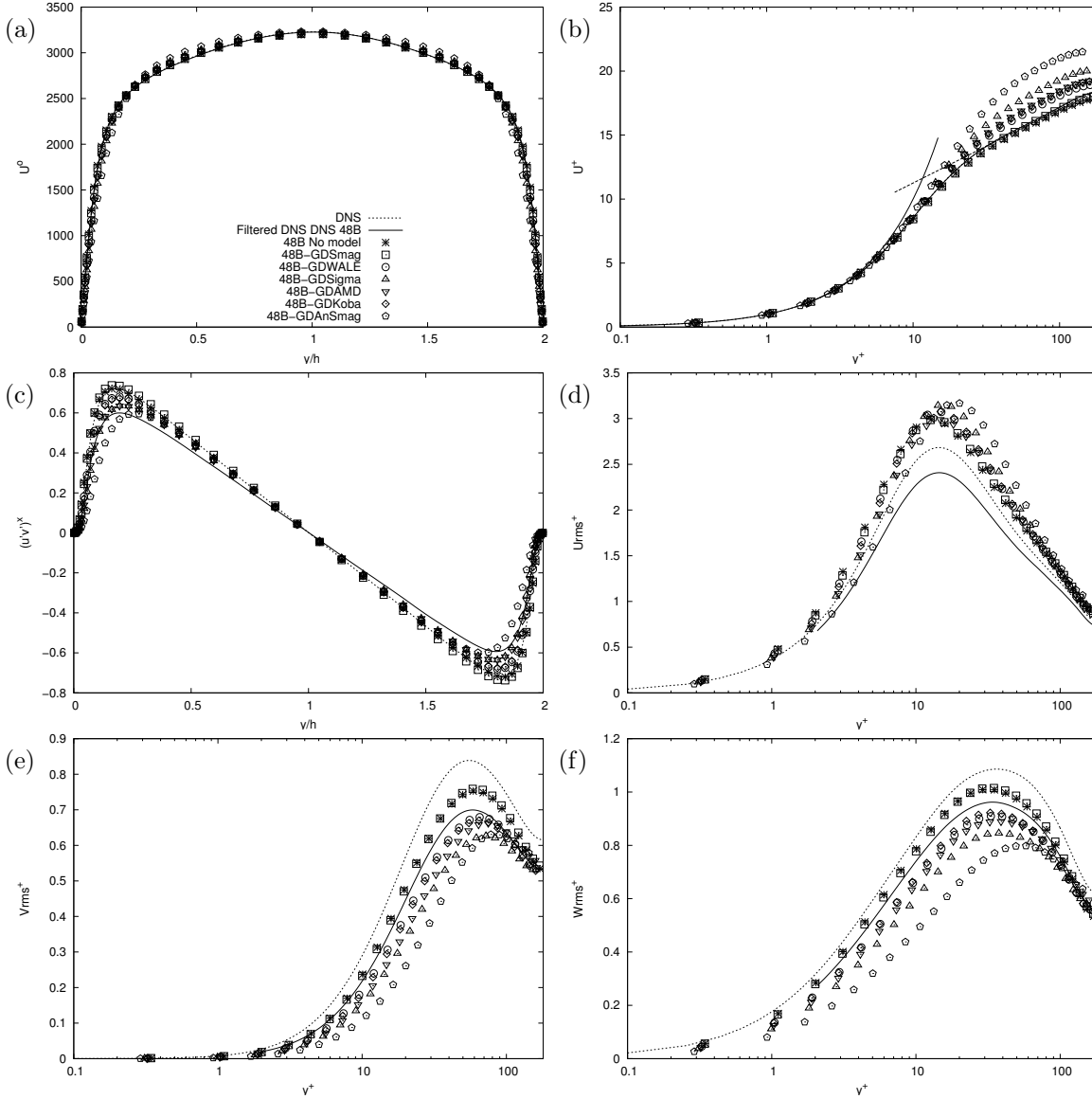


Figure 10.10 – Comparison of large-eddy simulations with the global-average dynamic Smagorinsky, WALE, Sigma, AMD, Kobayashi and Anisotropic Smagorinsky models for the profiles of the mean streamwise velocity $\langle U_x \rangle$ (a, b), the covariance of streamwise and wall-normal velocity $\langle u'_x u'_y \rangle$ (c), the standard deviation of streamwise velocity $\sqrt{\langle u'^2_x \rangle}$ (d), wall-normal velocity $\sqrt{\langle u'^2_y \rangle}$ (e) and spanwise velocity $\sqrt{\langle u'^2_z \rangle}$ (f) in the isothermal channel at $Re_\tau = 180$ with the mesh 48B.

cal results because the plane-average dynamic parameter does not strongly depend on the wall-normal coordinate (figure 10.13). They amplify on average the gradient model (table 10.2) and provide similar results to the constant-parameter simulations. The tensorial plane-average or global-average dynamic gradient model amplify each component of the gradient model but increase in particular the relative amplitude of the “ xx ”, “ xy ” and “ yy ” components (table 10.3). The tensorial dynamic gradient models, and the plane-average dynamic gradient model in particular, provide a more accurate prediction of the wall shear stress and the near-wall profile of the standard deviation of wall-normal and spanwise velocity (figure 10.13).

The results of the large-eddy simulations with the scale-similarity model depend

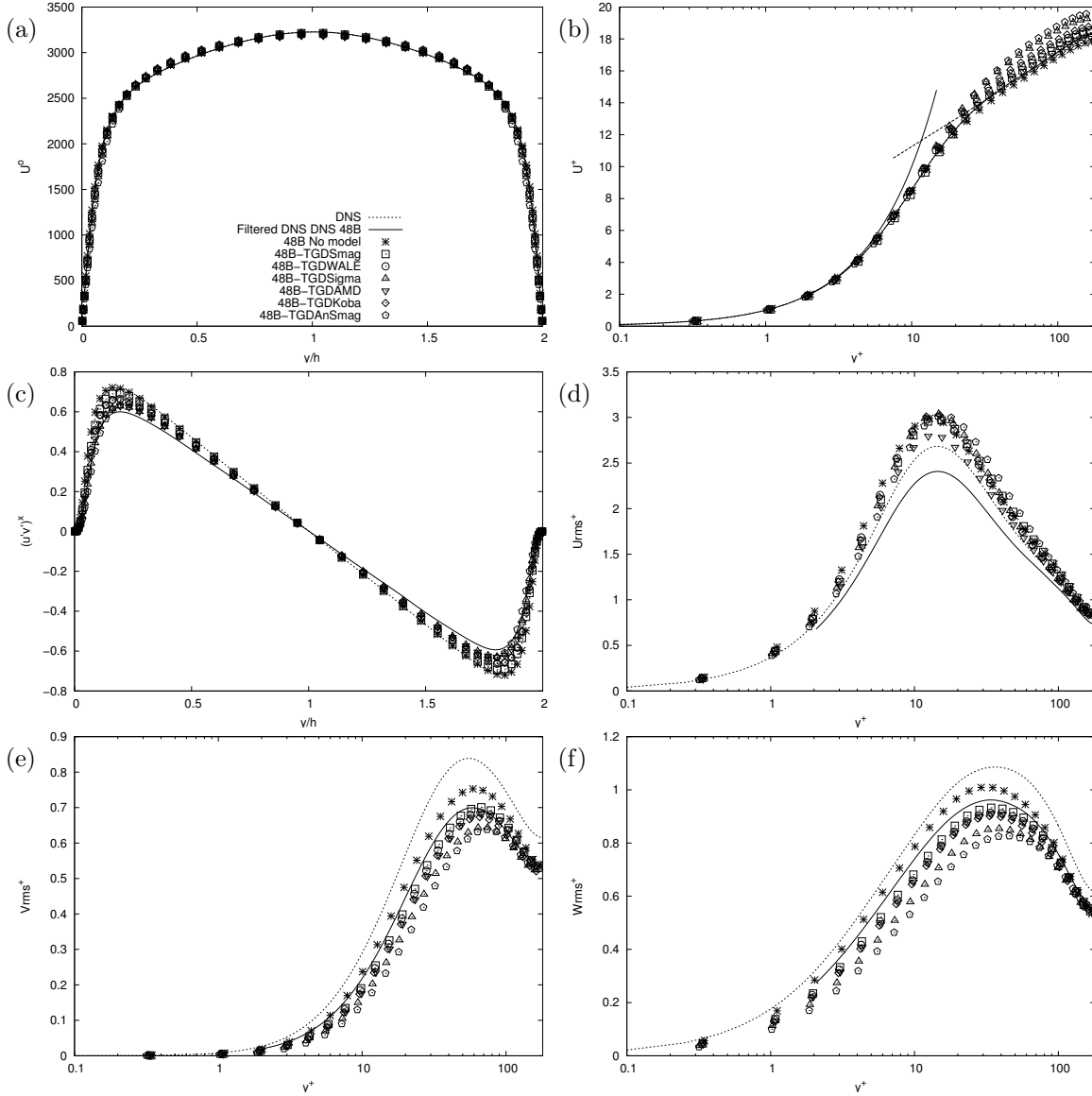


Figure 10.11 – Comparison of large-eddy simulations with the tensorial global-average dynamic Smagorinsky, WALE, Sigma, AMD, Kobayashi and Anisotropic Smagorinsky models for the profiles of the mean streamwise velocity $\langle U_x \rangle$ (a, b), the covariance of streamwise and wall-normal velocity $\langle u'_x u'_y \rangle$ (c), the standard deviation of streamwise velocity $\sqrt{\langle u_x'^2 \rangle}$ (d), wall-normal velocity $\sqrt{\langle u_y'^2 \rangle}$ (e) and spanwise velocity $\sqrt{\langle u_z'^2 \rangle}$ (f) in the isothermal channel at $Re_\tau = 180$ with the mesh 48B.

on the filter used (figure 10.12). Using filter A (10.60), the scale-similarity model is tied to the gradient model with $C^{\text{Grad.}} = 9$ according to the Taylor series expansion (10.32) of the test filter in the scale-similarity model with $\widehat{\Delta}_k^2 \approx 3\overline{\Delta}_k$. Using filter T (10.62), the scale-similarity model is tied to the gradient model with $C^{\text{Grad.}} = 1$ since $\widehat{\Delta}_k^2 \approx \overline{\Delta}_k$. However, the predictions with the scale-similarity and gradient model are not the same, suggesting that the higher-order terms are relevant. With the filter A, the scale-similarity model has with the mesh 48B an excessive impact on the flow and deteriorates the profiles of the turbulence statistics. With the filter T, the model is more similar to the original model of Bardina *et al.* [14]. The prediction of all turbulence statistics is with the mesh 48B improved compared to the no-model simulation. In

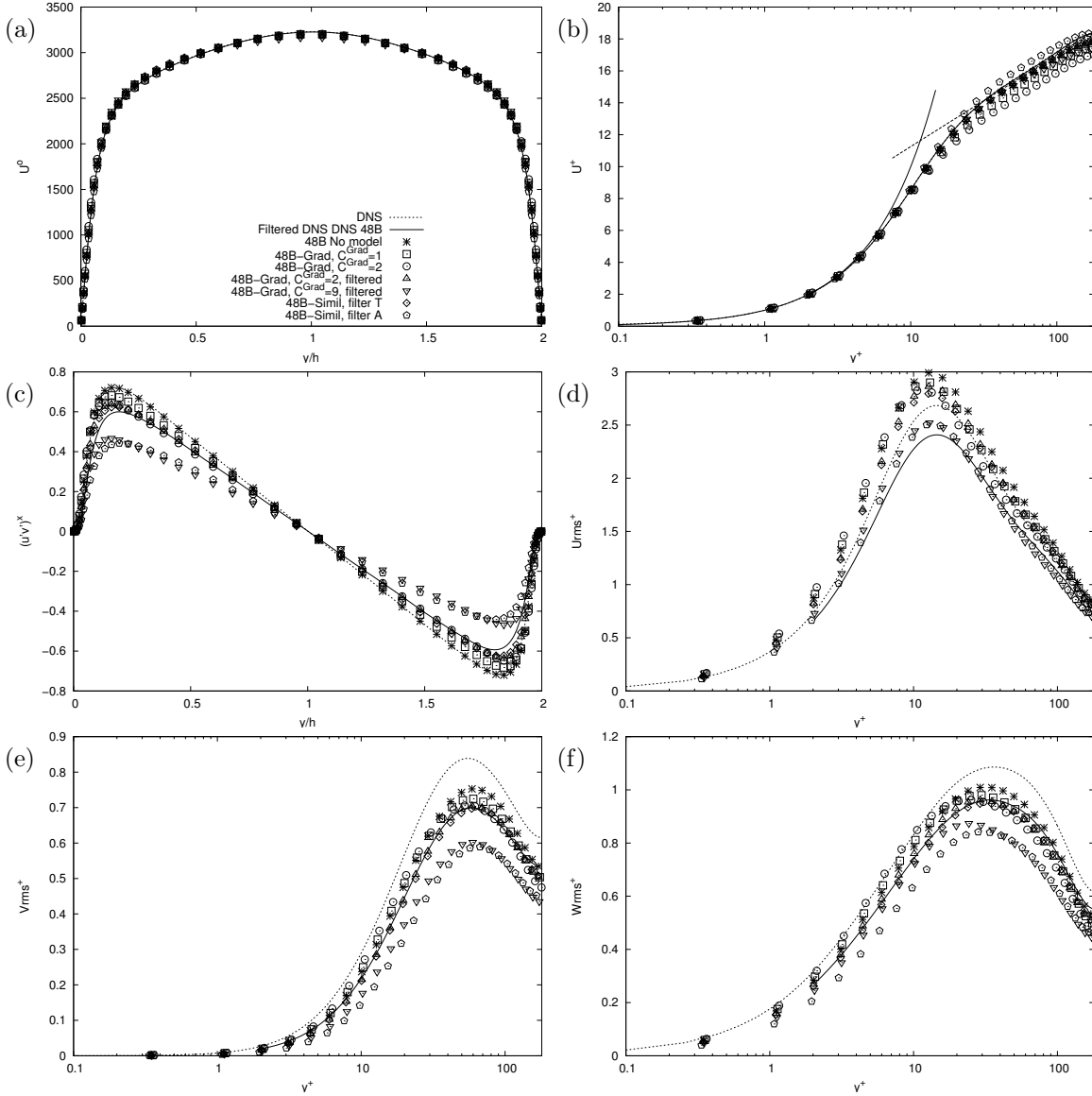


Figure 10.12 – Comparison of large-eddy simulations with the gradient model using $C^{\text{Grad.}} = 1$ and $C^{\text{Grad.}} = 2$ and the filtered gradient model using $C^{\text{Grad.}} = 2$ and $C^{\text{Grad.}} = 9$ and with the scale-similarity model using filter T and filter A for the profiles of the mean streamwise velocity $\langle U_x \rangle$ (a, b), the covariance of streamwise and wall-normal velocity $\langle u_x' u_y' \rangle$ (c), the standard deviation of streamwise velocity $\sqrt{\langle u_x'^2 \rangle}$ (d), wall-normal velocity $\sqrt{\langle u_y'^2 \rangle}$ (e) and spanwise velocity $\sqrt{\langle u_z'^2 \rangle}$ (f) in the isothermal channel at $Re_\tau = 180$ with the mesh 48B. The filtered gradient model uses the filter A.

particular, the covariance of streamwise and wall-normal velocity and the standard deviation of wall-normal and spanwise velocity are in agreement with the filtered direct numerical simulation. The standard deviation of wall-normal and spanwise velocity remains overestimated but is decreased compared to the no-model simulation. These satisfactory results do not generalise very well to the 24C and 36C meshes. Indeed, the effects of the scale-similarity model on the turbulence statistics is similar for the three meshes and does not seem to correctly take into account the variations of filter width. As a result, the covariance of streamwise and wall-normal velocity and the standard deviation of velocity components are overestimated with the meshes 24C and

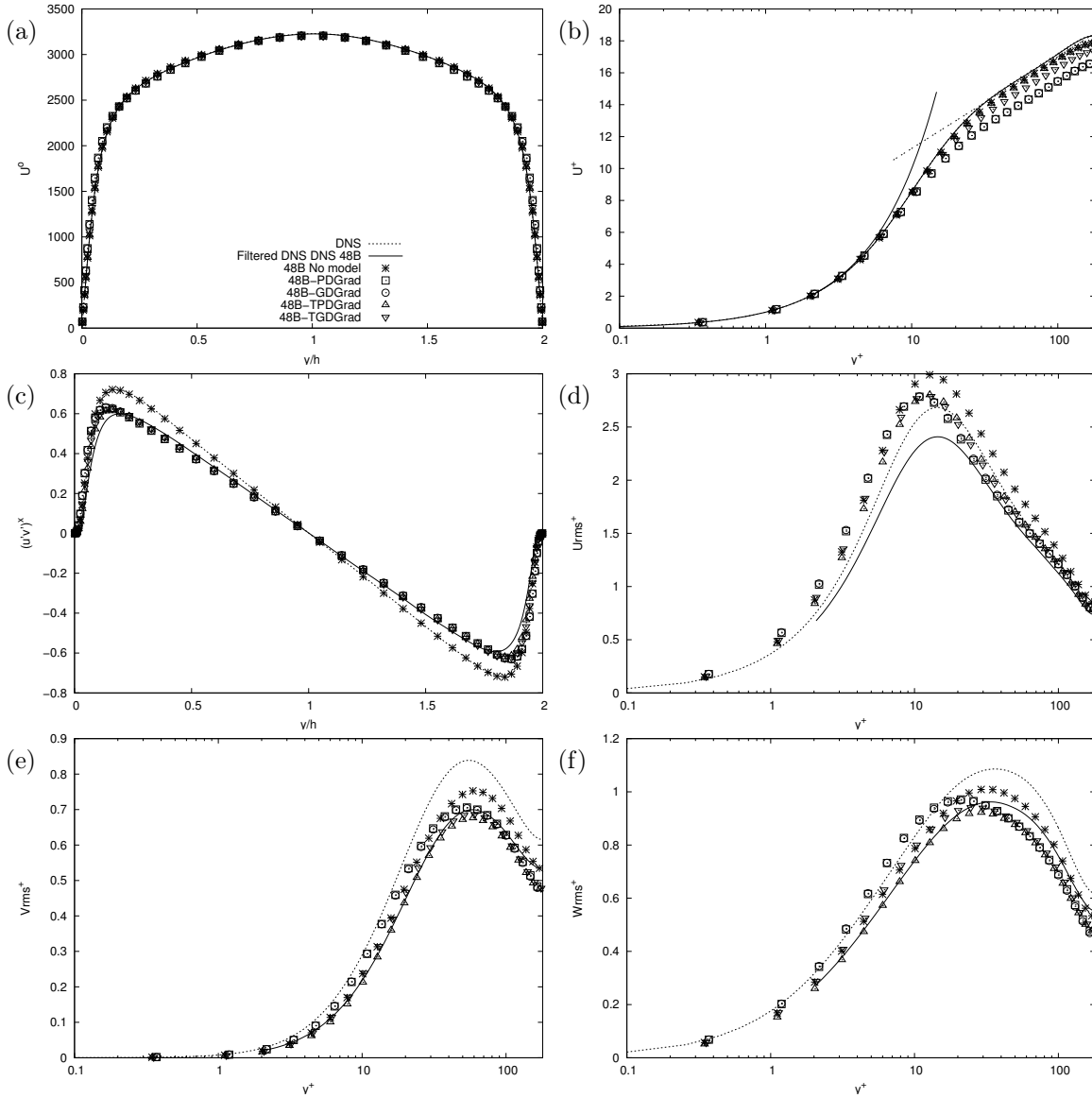


Figure 10.13 – Comparison of large-eddy simulations with the plane-average, global-average, tensorial plane-average and tensorial global-average dynamic gradient models for the profiles of the mean streamwise velocity $\langle U_x \rangle$ (a, b), the covariance of streamwise and wall-normal velocity $\langle u'_x u'_y \rangle$ (c), the standard deviation of streamwise velocity $\sqrt{\langle u'^2_x \rangle}$ (d), wall-normal velocity $\sqrt{\langle u'^2_y \rangle}$ (e) and spanwise velocity $\sqrt{\langle u'^2_z \rangle}$ (f) in the isothermal channel at $Re_\tau = 180$ with the mesh 48B.

36C (figure 10.14).

10.5.2.3 Tensorial models and tensorial mixed models

In this section, we investigate the modelling of the momentum convection subgrid term with tensorial, mixed and tensorial mixed models, as well as the dynamic versions of these models. We focus in particular on models based on the AMD model. The results of large-eddy simulations with various tensorial AMD models is compared in figure 10.15 with the mesh 48B. The models based on the $H^{(4)}$ (9.63) tensor leads to the best prediction of the wall shear stress while those based on the $H^{(2)}$ (9.61),

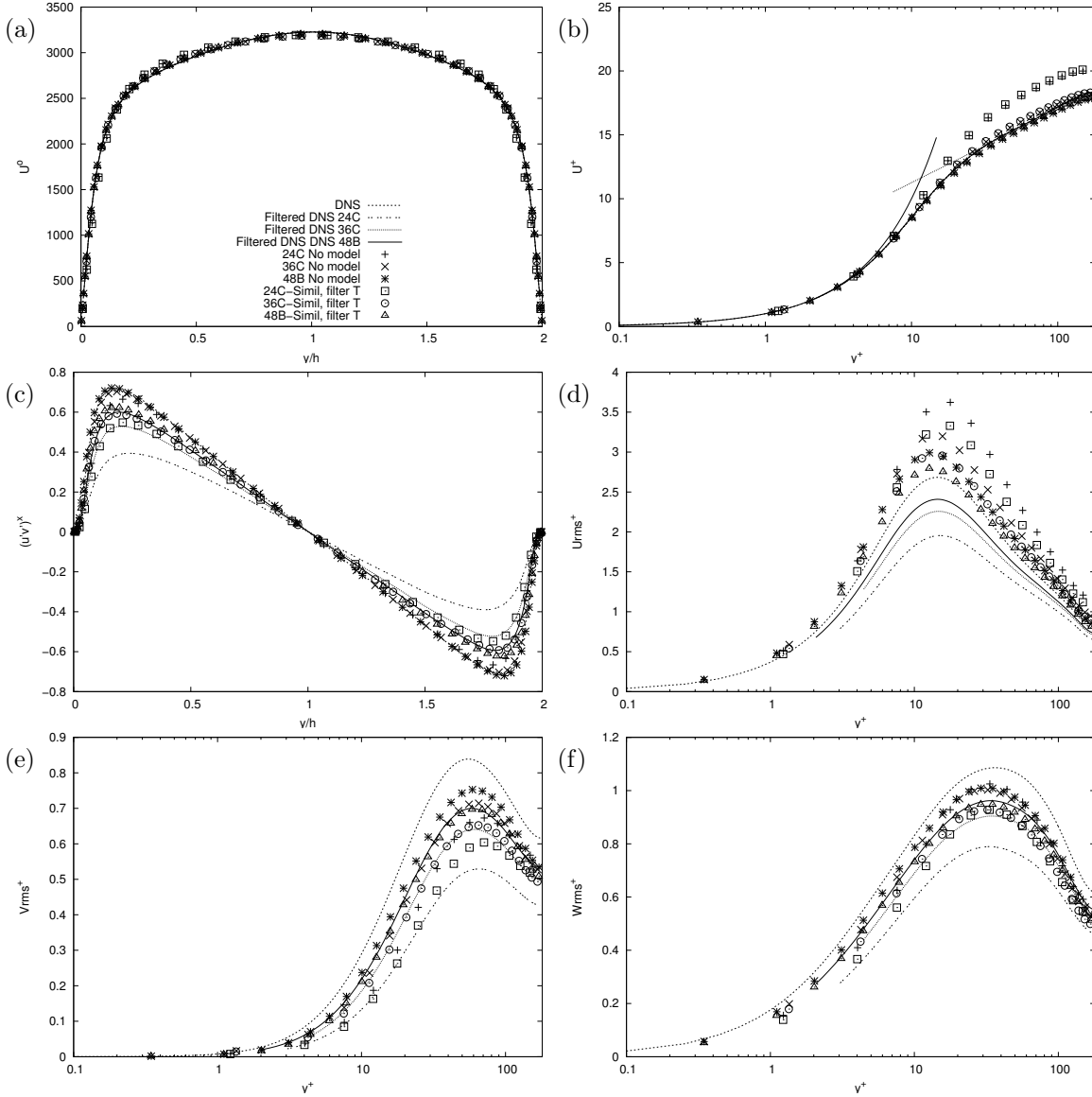


Figure 10.14 – Comparison of large-eddy simulations with the scale-similarity model using filter T with the meshes 24C, 36C and 48B for the profiles of the mean streamwise velocity $\langle U_x \rangle$ (a, b), the covariance of streamwise and wall-normal velocity $\langle u'_x u'_y \rangle$ (c), the standard deviation of streamwise velocity $\sqrt{\langle u'^2_x \rangle}$ (d), wall-normal velocity $\sqrt{\langle u'^2_y \rangle}$ (e) and spanwise velocity $\sqrt{\langle u'^2_z \rangle}$ (f) in the isothermal channel at $Re_\tau = 180$.

$H^{(3)}$ (9.62) and $H^{(6)}$ (9.65) tensors heavily underestimate or overestimate the wall shear stress. Compared to the classical AMD model, the tensorial AMD models based on the $H^{(2)}$ (9.61), $H^{(4)}$ (9.63) and $H^{(5)}$ (9.64) tensors give better predictions of the covariance of streamwise and wall-normal velocity and of the standard deviation of velocity components. Besides, while functional models were found unable to decrease the maximum value of the standard deviation of streamwise velocity compared to the no-model simulation (figure 10.6), all tensorial AMD models investigated verify this property. The behaviour of the tensorial AMD models upon mesh derefinement is as the scale-similarity model not satisfactory for the covariance of streamwise and wall-normal velocity and the standard deviation of streamwise velocity. Indeed, the reduction of the maximum amplitude is not sufficiently enhanced with the coarser

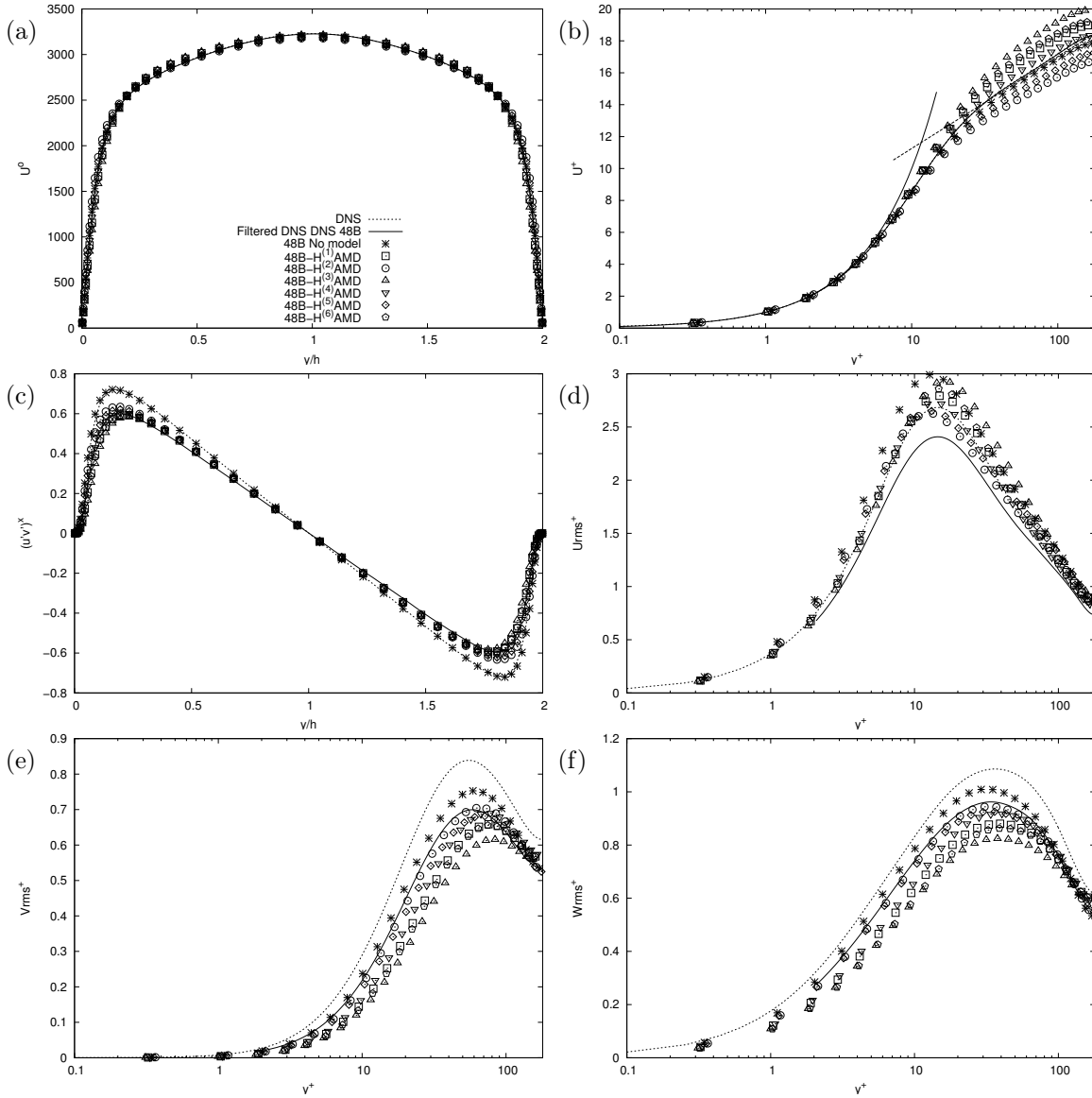


Figure 10.15 – Comparison of large-eddy simulations with tensorial AMD models for the profiles of the mean streamwise velocity $\langle U_x \rangle$ (a, b), the covariance of streamwise and wall-normal velocity $\langle u'_x u'_y \rangle$ (c), the standard deviation of streamwise velocity $\sqrt{\langle u'^2_x \rangle}$ (d), wall-normal velocity $\sqrt{\langle u'^2_y \rangle}$ (e) and spanwise velocity $\sqrt{\langle u'^2_z \rangle}$ (f) in the isothermal channel at $Re_\tau = 180$ with the mesh 48B.

meshes (figure 10.18). It is however more acceptable for the standard deviation of wall-normal and spanwise velocity in the sense that the profiles undergo the expected decrease of maximum amplitude with increased filter width.

Contrary to tensorial AMD models, the tensorial models based on the Smagorinsky, WALE or Sigma model do not decrease the maximum value standard deviation of streamwise velocity with the mesh 48B (figure 10.17). A decrease is also obtained using a tensorial Anisotropic Smagorinsky model, but the effect is smaller than with the AMD model. While the underlying explanation is not known, this is to some extent consistent with the results of tensorial global-average dynamic models (figure 10.11), in which the AMD model led to a stronger decrease of the standard deviation of streamwise velocity.

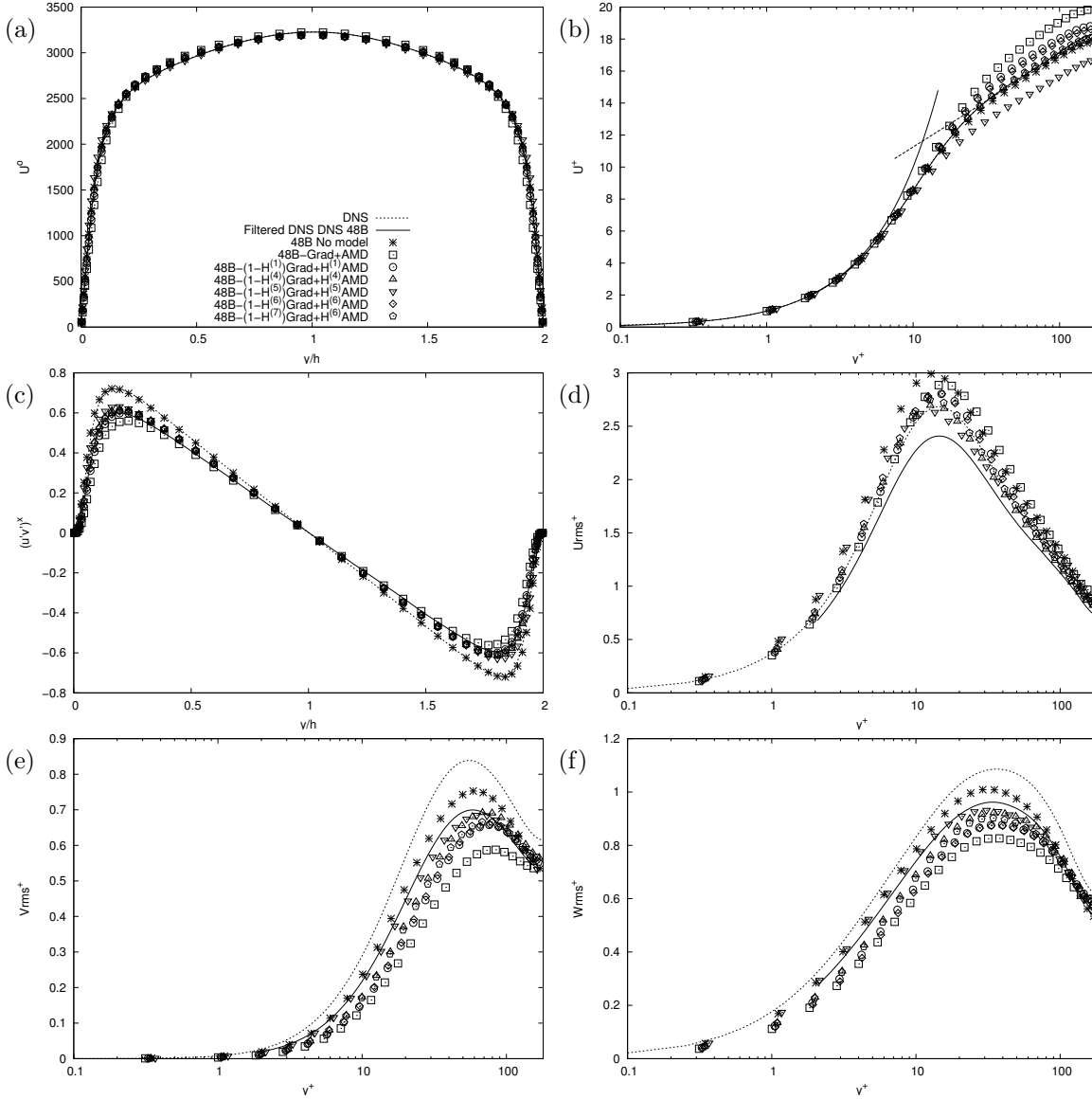


Figure 10.16 – Comparison of large-eddy simulations with the gradient-AMD mixed model and tensorial gradient-AMD mixed models for the profiles of the mean streamwise velocity $\langle U_x \rangle$ (a, b), the covariance of streamwise and wall-normal velocity $\langle u'_x u'_y \rangle$ (c), the standard deviation of streamwise velocity $\sqrt{\langle u_x'^2 \rangle}$ (d), wall-normal velocity $\sqrt{\langle u_y'^2 \rangle}$ (e) and spanwise velocity $\sqrt{\langle u_z'^2 \rangle}$ (f) in the isothermal channel at $Re_\tau = 180$ with the mesh 48B.

Tensorial gradient-AMD mixed models complement tensorial AMD models using the gradient model to model the components of the subgrid term not modelled by the AMD model. The addition of the gradient model to the AMD model has only a small effect on the turbulence statistics (figure 10.16). It decreases the estimated wall shear stress, providing an improvement for the classical AMD model and the tensorial AMD models based on the $H^{(1)}$ (9.60), $H^{(3)}$ (9.62), $H^{(4)}$ (9.63) and $H^{(6)}$ (9.65) tensors, which overestimate the wall shear stress, and a degradation for the tensorial AMD models based on the $H^{(2)}$ (9.61) and $H^{(5)}$ (9.64) tensors, which underestimate the wall shear stress.

We investigated various dynamic versions of gradient-AMD mixed models. Dynamic gradient-AMD mixed models may be based on a plane average, a global average,

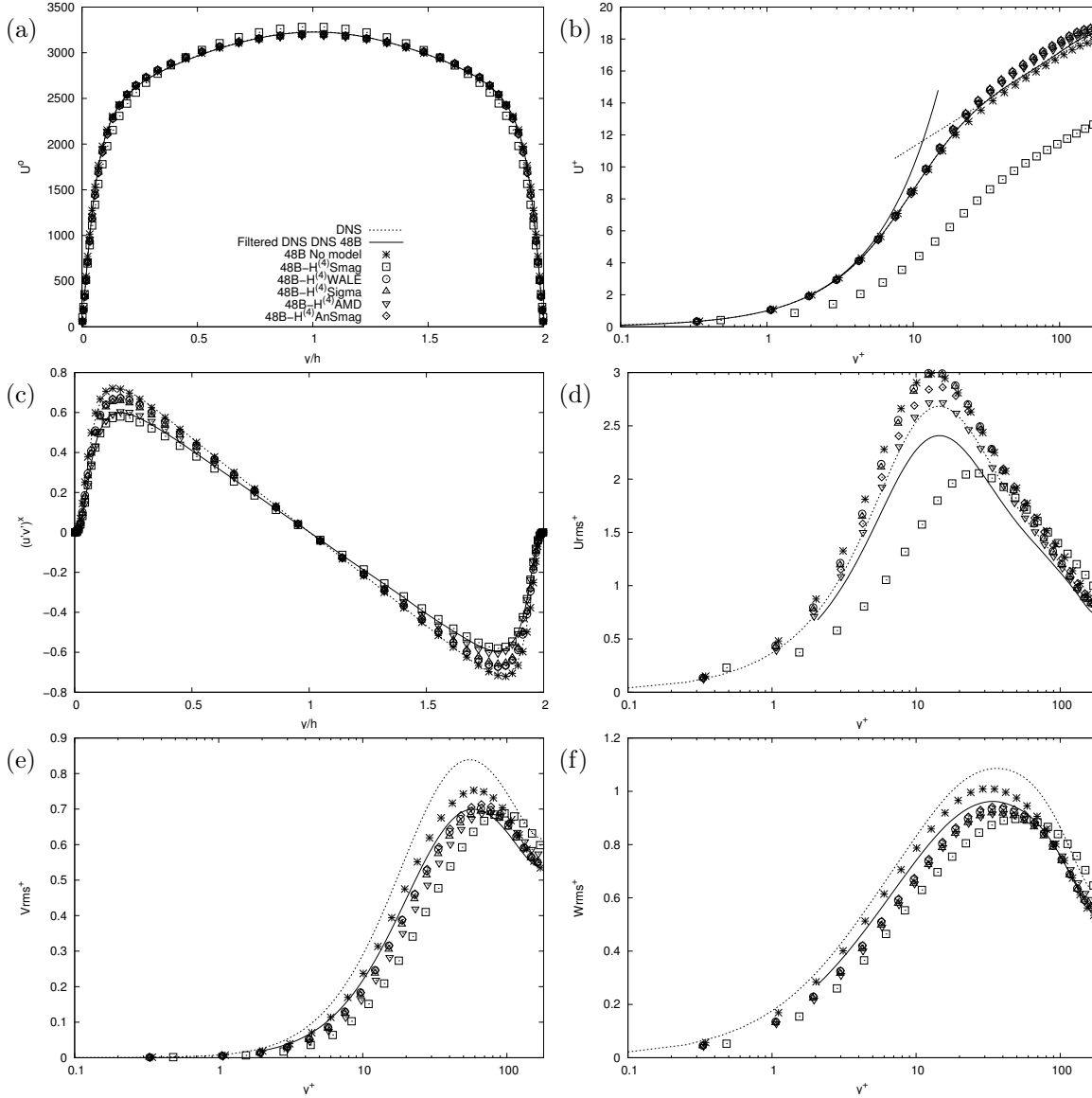


Figure 10.17 – Comparison of large-eddy simulations with tensorial gradient-Smagorinsky, gradient-WALE, gradient-Sigma, gradient-AMD and gradient-Anisotropic-Smagorinsky mixed models for the profiles of the mean streamwise velocity $\langle U_x \rangle$ (a, b), the covariance of streamwise and wall-normal velocity $\langle u_x' u_y' \rangle$ (c), the standard deviation of streamwise velocity $\sqrt{\langle u_x'^2 \rangle}$ (d), wall-normal velocity $\sqrt{\langle u_y'^2 \rangle}$ (e) and spanwise velocity $\sqrt{\langle u_z'^2 \rangle}$ (f) in the isothermal channel at $Re_\tau = 180$ with the mesh 48B.

a tensorial plane average or a tensorial global average. Some dynamic procedures are not stable. The stability of the dynamic procedures investigated is reported in table 10.4. Plane-average dynamic methods are only stable if the AMD-related part of the model is not dynamic. Global-average dynamic methods are more stable. All dynamic procedures investigated are stable if the negative values of the dynamic parameters of the AMD model are clipped. However, this makes the AMD model negligible using a global average (table 10.5) or a tensorial global average (table 10.6). If the dynamic procedure is not tensorial, the one-parameter dynamic method based on the prior computation of the AMD model with the classical dynamic procedure (P1Grad+PDAMD or G1Grad+GDAMD) and the two-parameter dynamic method (P2(Grad+AMD) or

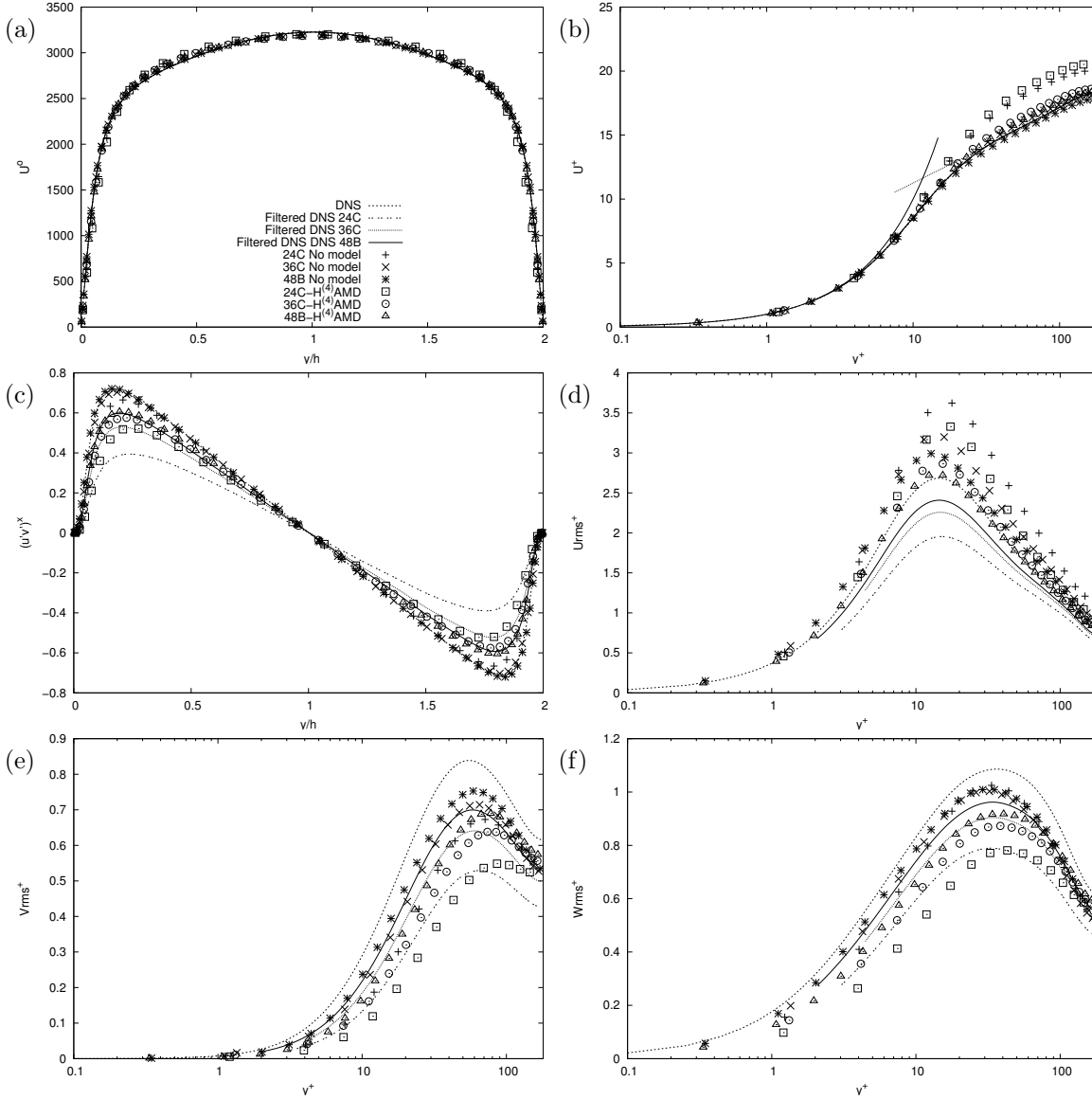


Figure 10.18 – Comparison of large-eddy simulations with the tensorial gradient-AMD mixed model based on the $H^{(4)}$ (9.63) tensor with the meshes 24C, 36C and 48B for the profiles of the mean streamwise velocity $\langle U_x \rangle$ (a, b), the covariance of streamwise and wall-normal velocity $\langle u'_x u'_y \rangle$ (c), the standard deviation of streamwise velocity $\sqrt{\langle u'^2_x \rangle}$ (d), wall-normal velocity $\sqrt{\langle u'^2_y \rangle}$ (e) and spanwise velocity $\sqrt{\langle u'^2_z \rangle}$ (f) in the isothermal channel at $Re_\tau = 180$.

G2(Grad+AMD)) give similar results. The one-parameter dynamic method based on the prior computation of the gradient model with the classical dynamic method (PDGrad+P1AMD or GDGrad+G1AMD) and the use of the classical dynamic method for the gradient and AMD models (PDGrad+PDAMD or GDGrad+GDAMD) also give similar results. We compare in figure 10.19 a selection of the best-performing models for each type of dynamic procedure. The dynamic gradient-AMD mixed models do not provide significant improvements over the constant-parameter tensorial gradient-AMD mixed models. The best results are achieved with tensorial dynamic procedures.

All in all, while none of the models investigated in the isothermal channel at $Re_\tau = 180$ is able to properly reproduce the effect of the momentum convection subgrid term

	Type of averaging	Dynamic method of each model		Stability
		Gradient	AMD	
P1Grad+AMD	Plane-average	One-parameter	Not dynamic	Stable
PDGrad+PDAMD	Plane-average	Classical	Classical	Not stable
PDGrad+P1AMD	Plane-average	Classical	One-parameter	Not stable
P1Grad+PDAMD	Plane-average	One-parameter	Classical	Not stable
P2(Grad+AMD)	Plane-average	Two-parameter	Two-parameter	Not stable
TP1Grad+AMD	Tensorial plane-average	One-parameter	Not dynamic	Stable
TPDGrad+TPDAMD	Tensorial plane-average	Classical	Classical	Not stable
TPDGrad+TP1AMD	Tensorial plane-average	Classical	One-parameter	Not stable
TP1Grad+TPDAMD	Tensorial plane-average	One-parameter	Classical	Not stable
TP2(Grad+AMD)	Tensorial plane-average	Two-parameter	Two-parameter	Not stable
G1Grad+AMD	Global-average	One-parameter	Not dynamic	Stable
GDGrad+GDAMD	Global-average	Classical	Classical	Stable
GDGrad+G1AMD	Global-average	Classical	One-parameter	Stable
G1Grad+GDAMD	Global-average	One-parameter	Classical	Not stable
G2(Grad+AMD)	Global-average	Two-parameter	Two-parameter	Not stable
TG1Grad+AMD	Tensorial global-average	One-parameter	Not dynamic	Stable
TGDGrad+TGDAMD	Tensorial global-average	Classical	Classical	Stable
TGDGrad+TG1AMD	Tensorial global-average	Classical	One-parameter	Not stable
TG1Grad+TGDAMD	Tensorial global-average	One-parameter	Classical	Stable
TG2(Grad+AMD)	Tensorial global-average	Two-parameter	Two-parameter	Not stable

Table 10.4 – Stability of the large-eddy simulations with plane-average, global-average, tensorial plane-average and tensorial global-average dynamic methods for gradient-AMD mixed models in the isothermal channel at $Re_\tau = 180$ with the mesh 48B. The clipping only concerns the negative dynamic parameters of the AMD model.

Average of the dynamic parameter (standard deviation),

	$\langle C^{\text{mod}} \rangle$	$\sqrt{\langle (C^{\text{mod}})^2 \rangle - \langle C^{\text{mod}} \rangle^2}$
	AMD-related	Gradient-related
G1Grad+AMD	—	1.760 (0.047)
GDGrad+GDAMD	0.424 (0.017)	2.245 (0.054)
GDGrad+G1AMD	0.424 (0.017)	2.208 (0.053)
G1Grad+GDAMD*	0.003 (0.007)	2.587 (0.053)
G2(Grad+AMD)*	0.003 (0.008)	2.589 (0.054)

Table 10.5 – Average and normalised standard deviation of the AMD-related and gradient-related dynamic parameters of the large-eddy simulations with global-average dynamic gradient-AMD mixed models in the isothermal channel at $Re_\tau = 180$ with the mesh 48B. An asterisk (*) indicates the clipping of the AMD-related part.

on the flow, some models improves the predictions of the simulation compared to the no-model case. We recommend the use of the scale-similarity model and the constant-parameter or dynamic tensorial AMD model, which provide the most promising results. In the next section, we study the large-eddy simulation of the anisothermal channel at $Re_\tau = 180$ and $Re_\tau = 395$.

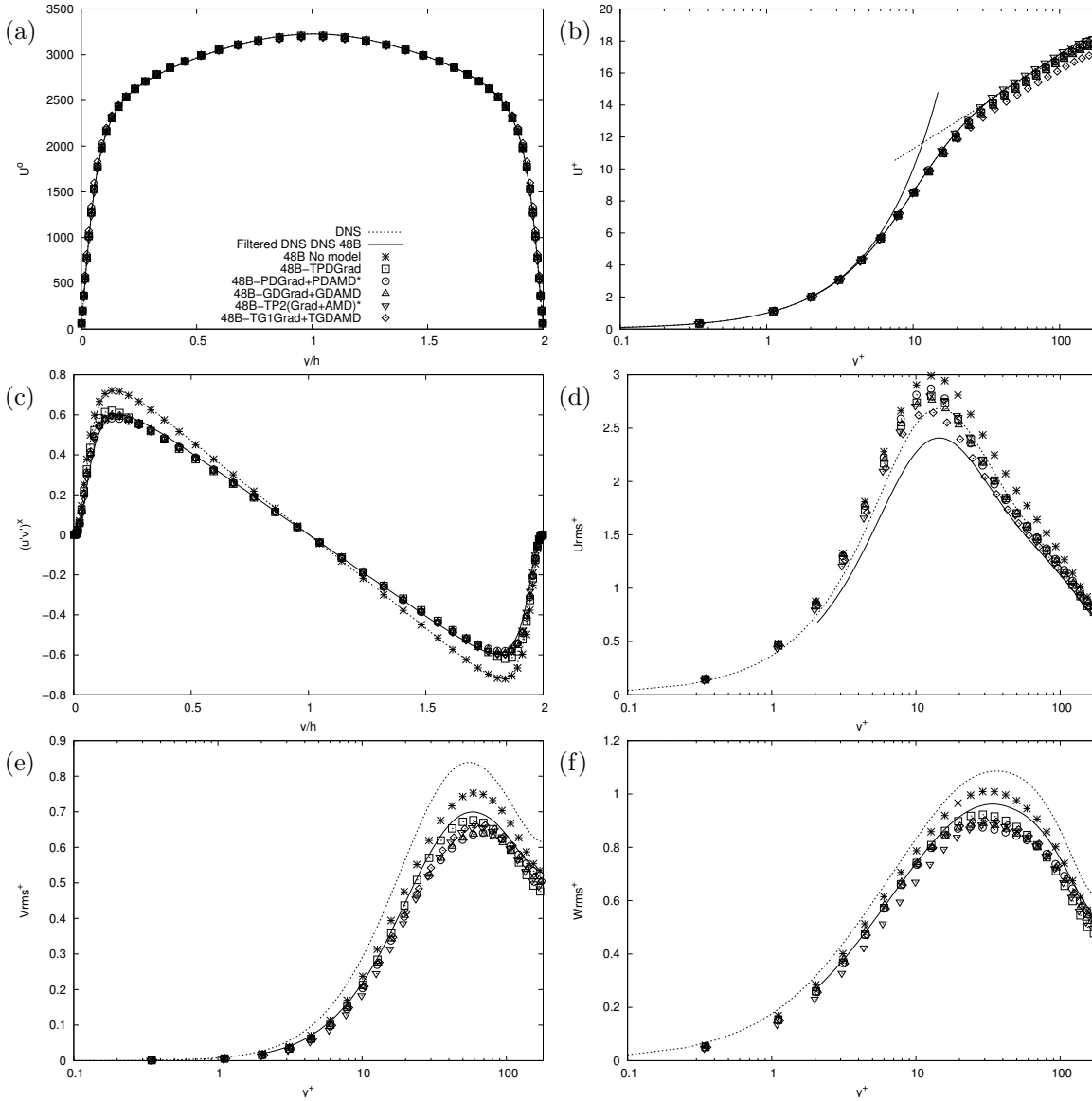


Figure 10.19 – Comparison of large-eddy simulations with dynamic gradient-AMD mixed models for the profiles of the mean streamwise velocity $\langle U_x \rangle$ (a, b), the covariance of streamwise and wall-normal velocity $\langle u'_x u'_y \rangle$ (c), the standard deviation of streamwise velocity $\sqrt{\langle u'^2_x \rangle}$ (d), wall-normal velocity $\sqrt{\langle u'^2_y \rangle}$ (e) and spanwise velocity $\sqrt{\langle u'^2_z \rangle}$ (f) in the isothermal channel at $Re_\tau = 180$ with the mesh 48B. An asterisk (*) indicates the clipping of the AMD-related part.

10.5.3 Large-eddy simulation in the anisothermal case

To investigate the large-eddy simulation of the anisothermal channel at $Re_\tau = 180$ and $Re_\tau = 395$, we separate the study of subgrid-scale models for the momentum convection subgrid term and the density-velocity correlation subgrid term. To proceed with the study of the modelling of the momentum convection subgrid term in the anisothermal case, we first perform large-eddy simulations modelling only this subgrid term. We then study the modelling of the density-velocity correlation subgrid term using the same procedure. Finally, large-eddy simulations modelling the two subgrid terms are carried out. At each phase, the Velocity and Favre formulations are compared.

Average of the dynamic parameter (standard deviation),
 $\langle C^{\text{mod}} \rangle (\sqrt{\langle (C^{\text{mod}})^2 \rangle - \langle C^{\text{mod}} \rangle^2})$

	xx	xy	xz	yy	zy	zz
TG1Grad+AMD	—	—	—	—	—	—
TGDGrad+TGDAMD	0.634 (0.080)	0.761 (0.031)	0.255 (0.037)	-0.020 (0.033)	0.049 (0.021)	-0.076 (0.025)
TGDGrad+TG1AMD*	0.000 (0.000)	0.213 (0.019)	0.125 (0.022)	0.100 (0.022)	0.003 (0.005)	0.000 (0.000)
TG1Grad+TGDAMD	0.584 (0.076)	0.799 (0.033)	0.258 (0.038)	-0.008 (0.034)	0.050 (0.021)	-0.073 (0.025)
TG2(Grad+AMD)*	0.000 (0.000)	0.327 (0.030)	0.121 (0.022)	0.101 (0.023)	0.003 (0.005)	0.000 (0.000)

(a) AMD-related dynamic parameters

	xx	xy	xz	yy	zy	zz
TG1Grad+AMD	1.818 (0.051)	0.465 (0.070)	1.244 (0.053)	2.326 (0.077)	1.466 (0.060)	1.668 (0.049)
TGDGrad+TGDAMD	2.280 (0.053)	2.271 (0.060)	1.422 (0.034)	2.681 (0.067)	1.598 (0.034)	1.853 (0.030)
TGDGrad+TG1AMD*	2.473 (0.056)	2.359 (0.060)	1.408 (0.037)	2.840 (0.066)	1.599 (0.038)	1.933 (0.030)
TG1Grad+TGDAMD	2.311 (0.055)	1.302 (0.048)	1.388 (0.035)	2.727 (0.068)	1.587 (0.035)	1.875 (0.029)
TG2(Grad+AMD)*	2.486 (0.057)	1.962 (0.061)	1.399 (0.037)	2.863 (0.067)	1.601 (0.039)	1.940 (0.031)

(b) Gradient-related dynamic parameters

Table 10.6 – Average and normalised standard deviation of the AMD-related and gradient-related dynamic parameters of the large-eddy simulations with tensorial global-average dynamic gradient-AMD mixed models in the isothermal channel at $Re_\tau = 180$ with the mesh 48B. An asterisk (*) indicates the clipping of the AMD-related part.

10.5.3.1 Modelling of the momentum convection subgrid term

In this section, we investigate the effect of subgrid-scale models for the momentum convection subgrid term in the Velocity and Favre formulations. This extends the incompressible isothermal analysis of section 10.5.2 to the anisothermal configuration in order to verify the generality of the results and study the effect of the models on temperature-related statistics. The simulations of this section do not model the density-velocity correlation subgrid term. Since the density-velocity correlation subgrid term is not modelled, the Velocity and Favre formulations are very similar. With the WALE model for instance, the Velocity and Favre formulations lead to almost identical results at $Re_\tau = 180$ (figure 10.20) and $Re_\tau = 395$. Note however that the Favre formulation tends to predict a slightly lower thermodynamical pressure and wall heat flux than the Velocity formulation for a given model.

Most of the observations made in section 10.5.2 regarding the modelling of the momentum convection subgrid term with functional, structural, tensorial or tensorial mixed models are also valid in the anisothermal channel. In addition, the asymmetry between the hot and cold sides should correctly be taken into account by the large-eddy simulation. In the anisothermal channel, a good prediction of the mean streamwise velocity without scaling at the center of the channel is not guaranteed despite the imposed mass flow rate since it requires an accurate description of the asymmetry of the velocity profile. Without model, the velocity is overestimated at the cold side and underestimated at the hot side. No functional model (figure 10.21) or structural model (figure 10.22) is able to rectify this behaviour, although some aggravate it. As seen in section 10.5.1, the symmetric filtering of the asymmetric channel leads, in wall

units, to an asymmetry of filtering resolution between the hot and cold sides. The maximum amplitude of the streamwise velocity at the cold side should be reduced to correctly handle the excessive amplitude asymmetry found in no-model simulations. In the isothermal channel, this was achieved by no functional model. In the anisothermal channel, this is achieved by the AMD model at $Re_\tau = 180$ (figure 10.21) and $Re_\tau = 395$ (figure 10.24) but the maximum is shifted towards the centre of the channel. As in the isothermal channel, this is also achieved by the tensorial global-average AMD model, the gradient and scale-similarity model and by tensorial AMD models and mixed gradient-AMD models.

Besides, the modelling of the momentum convection subgrid term has an effect on the profile of temperature. Without model, the temperature gradient at the wall is underestimated. With all functional model investigated, including dynamic versions of these models, the subgrid-scale viscosity further decreases of the temperature gradient at the wall, deteriorating the prediction of the wall heat flux further away from the filtered DNS profile. Far from the wall on the other hand, functional models improve the temperature profile compared to the no-model simulation, provided that the parameter of the model is not too strong. This holds for the meshes 24C, 36C and 48B at $Re_\tau = 180$ (figure 10.23) and the mesh 96B at $Re_\tau = 395$ (figure 10.24). This is also achieved by the plane-average dynamic Smagorinsky model, tensorial global-average dynamic models and tensorial AMD models, in particular those based on the based on the $H^{(1)}$ (9.60) or $H^{(4)}$ (9.63) tensor. The structural gradient and scale-similarity models do not have a significant effect on the wall heat flux. The misprediction of the wall heat flux directly impacts the mean wall-normal velocity. The structural models investigated decrease the mean wall-normal velocity. The functional models investigated do not have a large effect on the mean wall-normal velocity with the mesh 48B at $Re_\tau = 180$ but lead to a pronounced decrease with the mesh 24C (figure 10.23). With or without scaling, functional and structural models increase the standard deviation of temperature at the hot and cold sides. An accurate prediction of the temperature profile, if possible with the models investigated, should come from the modelling of the density-velocity correlation subgrid term.

10.5.3.2 Modelling of the density-velocity correlation subgrid term

In this section, we investigate the effect of subgrid-scale models for the density-velocity correlation subgrid term in the Velocity and Favre formulations. The models investigated are adaptations of models of section 10.5.2 to the density-velocity correlation subgrid term and the scalar AMD model, specific to this subgrid term. The simulations of this section do not model the momentum convection subgrid term. Modelling the density-velocity correlation subgrid term primarily affects temperature-related statistics, as the prediction of the wall heat flux, the mean temperature, the mean wall-normal velocity or the standard deviation of temperature. They may have a small effect on the covariance of streamwise and wall-normal velocity or the standard deviation of wall-normal and spanwise velocity but have, in general, a negligible impact on the mean streamwise velocity and the prediction of the wall shear stress. The density-velocity correlation subgrid term does not appear in the same equation in the Velocity and Favre equations. Its modelling has nevertheless a similar effect on the mean temperature and on the standard deviation of temperature in the Velocity and

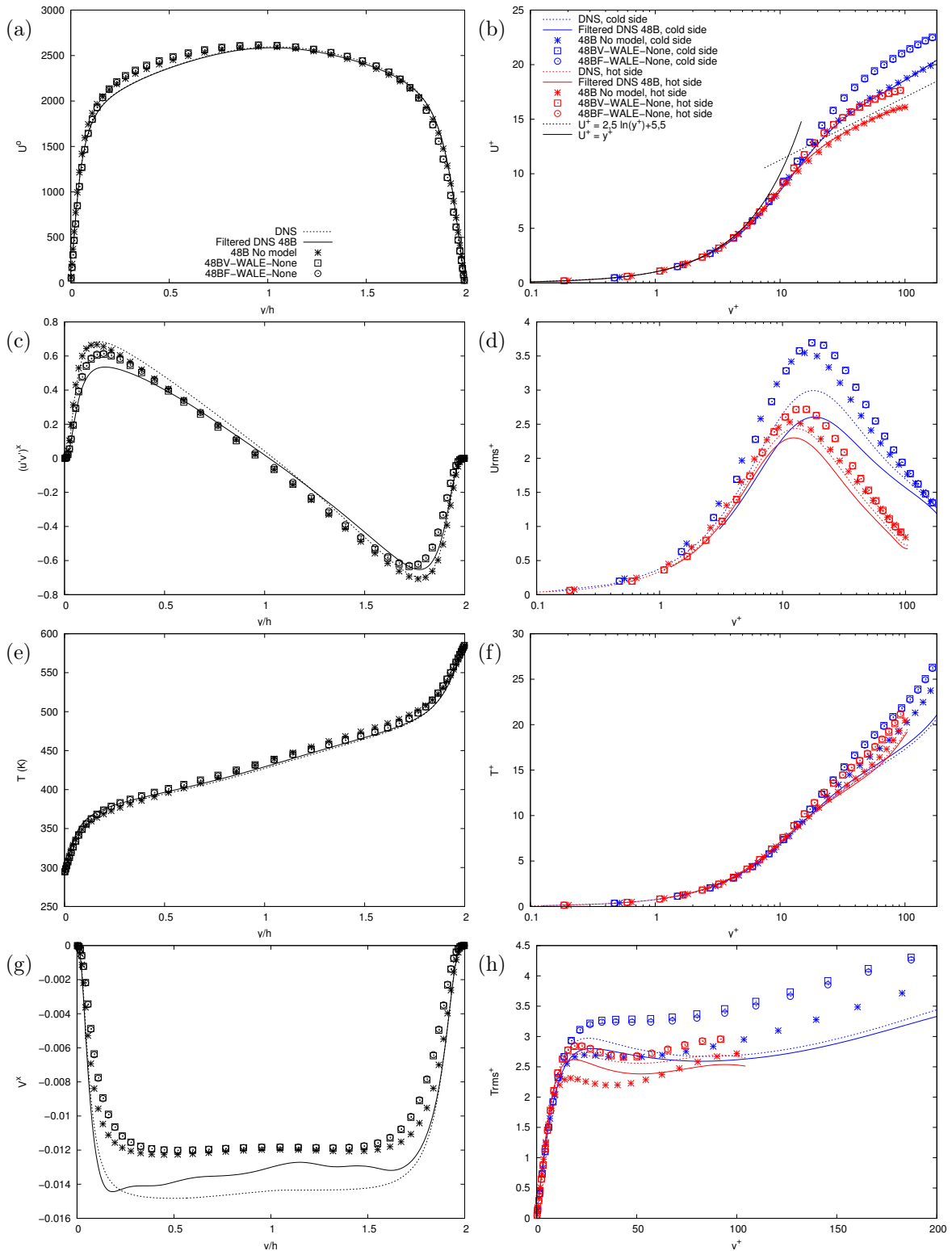


Figure 10.20 – Comparison of large-eddy simulations with the WALE model for the momentum convection subgrid term in the Velocity and Favre formulations for the profiles of the mean streamwise velocity $\langle U_x \rangle$ (a, b), the covariance of streamwise and wall-normal velocity $\langle u'_x u'_y \rangle$ (c), the standard deviation of spanwise velocity $\sqrt{\langle u_z'^2 \rangle}$ (d), the mean temperature $\langle T \rangle$ (e, f), the mean wall-normal velocity $\langle U_y \rangle$ (g) and the standard deviation of temperature $\sqrt{\langle T'^2 \rangle}$ (h) in the anisothermal channel at $Re_\tau = 180$ with the mesh 48B.

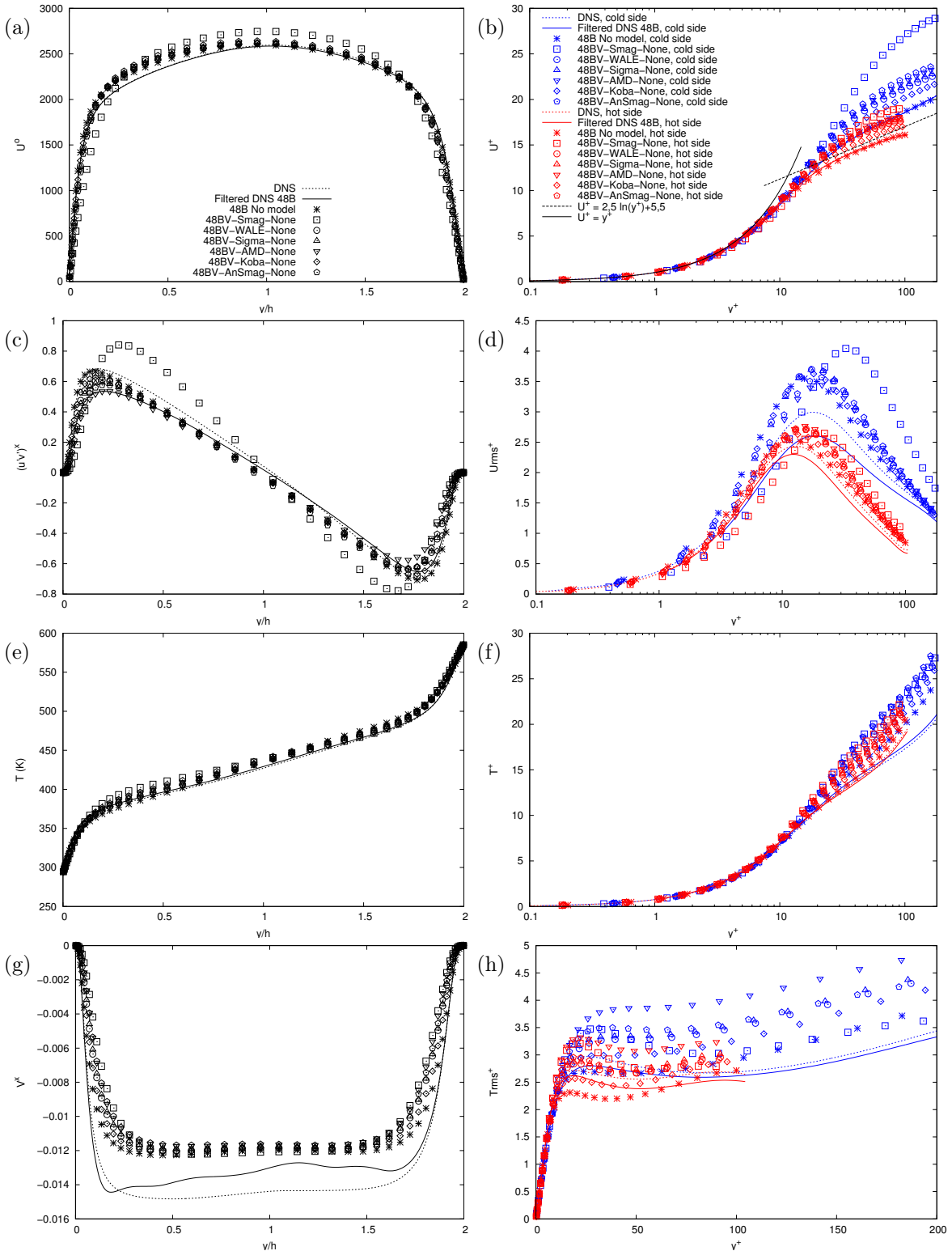


Figure 10.21 – Comparison of large-eddy simulations with the Smagorinsky, WALE, Sigma, AMD, Kobayashi and Anisotropic Smagorinsky models for the momentum convection subgrid term in the Velocity formulation for the profiles of the mean streamwise velocity $\langle U_x \rangle$ (a, b), the covariance of streamwise and wall-normal velocity $\langle u'_x u'_y \rangle$ (c), the standard deviation of spanwise velocity $\sqrt{\langle u_z'^2 \rangle}$ (d), the mean temperature $\langle T \rangle$ (e, f), the mean wall-normal velocity $\langle U_y \rangle$ (g) and the standard deviation of temperature $\sqrt{\langle T'^2 \rangle}$ (h) in the anisothermal channel at $Re_\tau = 180$ with the mesh 48B.

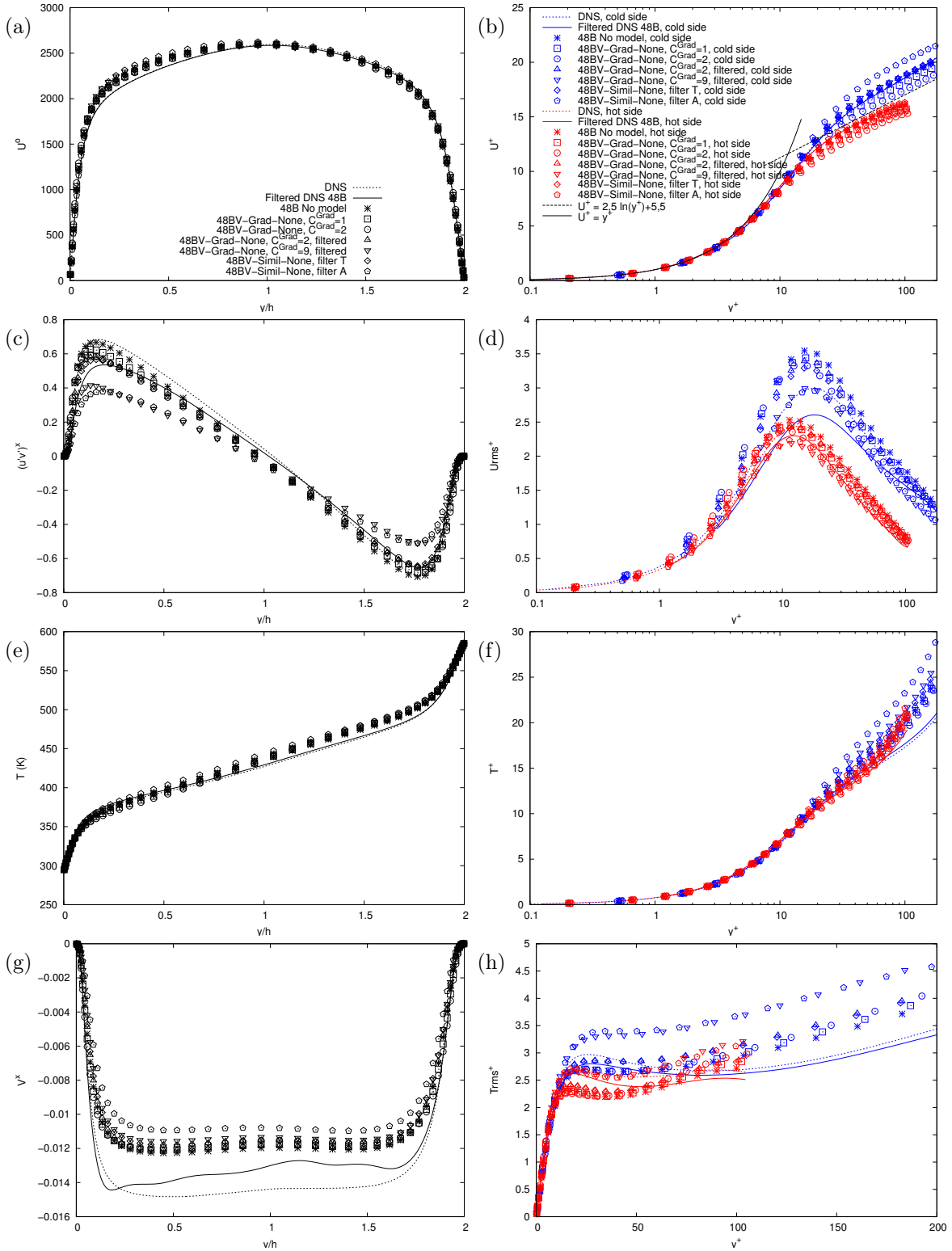


Figure 10.22 – Comparison of large-eddy simulations with the gradient model using $C^{Grad.} = 1$ and $C^{Grad.} = 2$, the filtered gradient model using $C^{Grad.} = 2$ and $C^{Grad.} = 9$ and the scale-similarity model using filter T and filter A for the momentum convection subgrid term in the Velocity formulation for the profiles of the mean streamwise velocity $\langle U_x \rangle$ (a, b), the covariance of streamwise and wall-normal velocity $\langle u'_x u'_y \rangle$ (c), the standard deviation of spanwise velocity $\sqrt{\langle u_z'^2 \rangle}$ (d), the mean temperature $\langle T \rangle$ (e, f), the mean wall-normal velocity $\langle U_y \rangle$ (g) and the standard deviation of temperature $\sqrt{\langle T'^2 \rangle}$ (h) in the anisothermal channel at $Re_\tau = 180$ with the mesh 48B. The filtered gradient model uses the filter A.

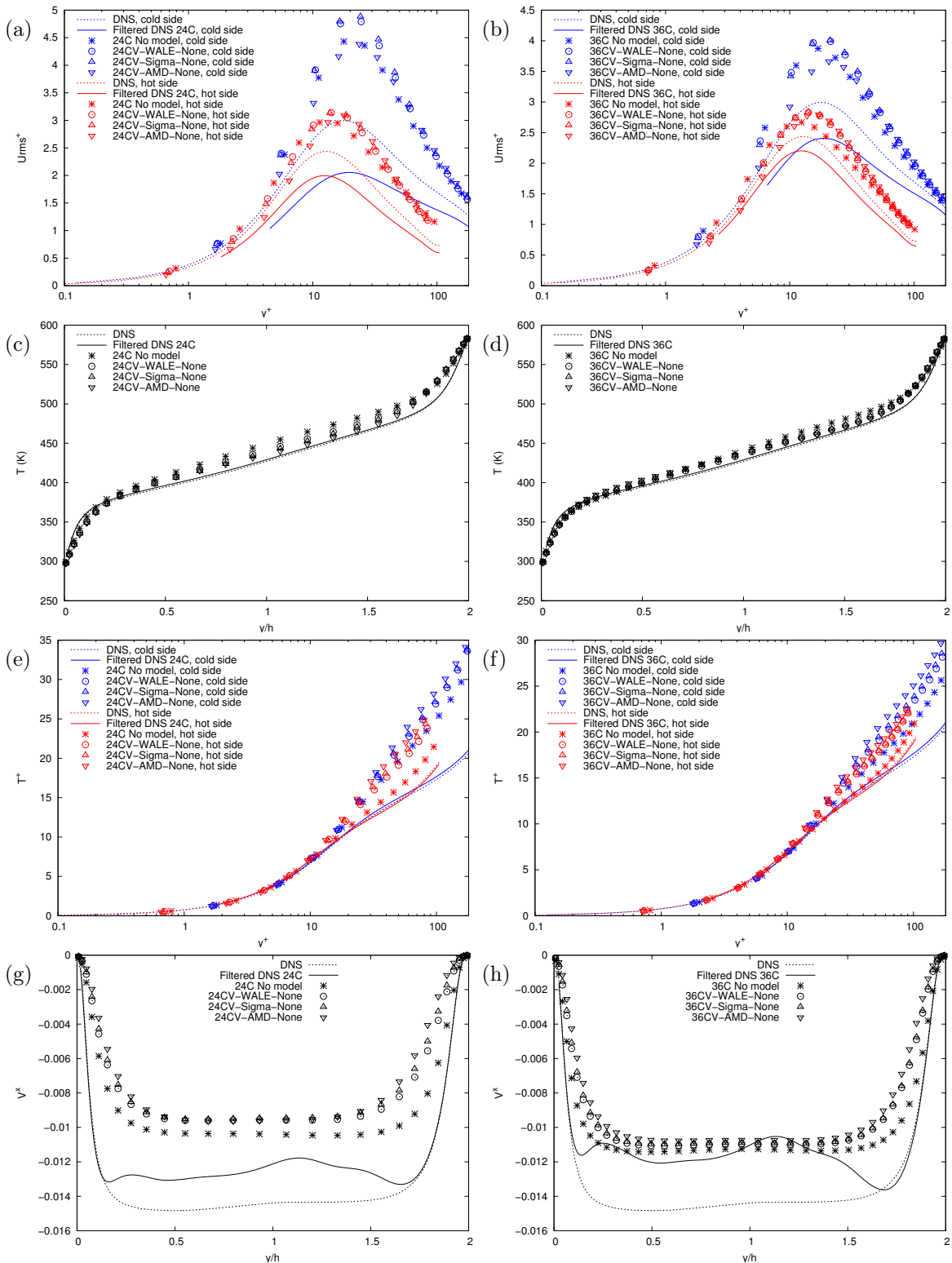


Figure 10.23 – Comparison of large-eddy simulations with the WALE, Sigma and AMD models for the momentum convection subgrid term in the Velocity formulation with the meshes 24C (left) and 36C (right) for the profiles of the standard deviation of streamwise velocity $\sqrt{\langle u_x'^2 \rangle}$ (a, b), the mean temperature $\langle T \rangle$ (c, d) and the mean wall-normal velocity $\langle U_y \rangle$ (e, f) in the anisothermal channel at $Re_\tau = 180$.

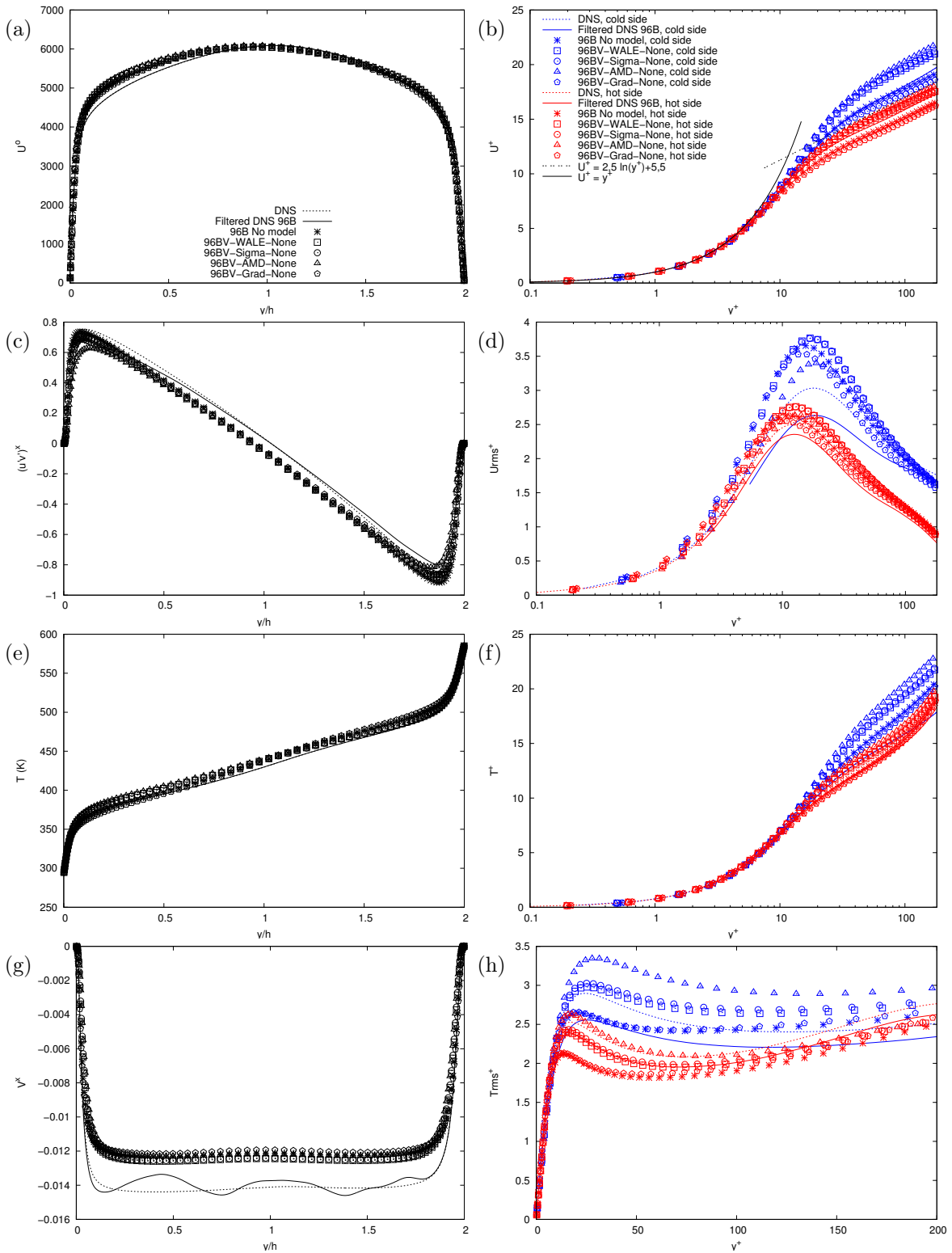


Figure 10.24 – Comparison of large-eddy simulations with the WALE, Sigma, AMD and gradient models for the momentum convection subgrid term in the Velocity formulation for the profiles of the mean streamwise velocity $\langle U_x \rangle$ (a, b), the covariance of streamwise and wall-normal velocity $\langle u'_x u'_y \rangle$ (c), the standard deviation of spanwise velocity $\sqrt{\langle u_z'^2 \rangle}$ (d), the mean temperature $\langle T \rangle$ (e, f), the mean wall-normal velocity $\langle U_y \rangle$ (g) and the standard deviation of temperature $\sqrt{\langle T'^2 \rangle}$ (h) in the anisothermal channel at $Re_\tau = 395$ with the mesh 96B.

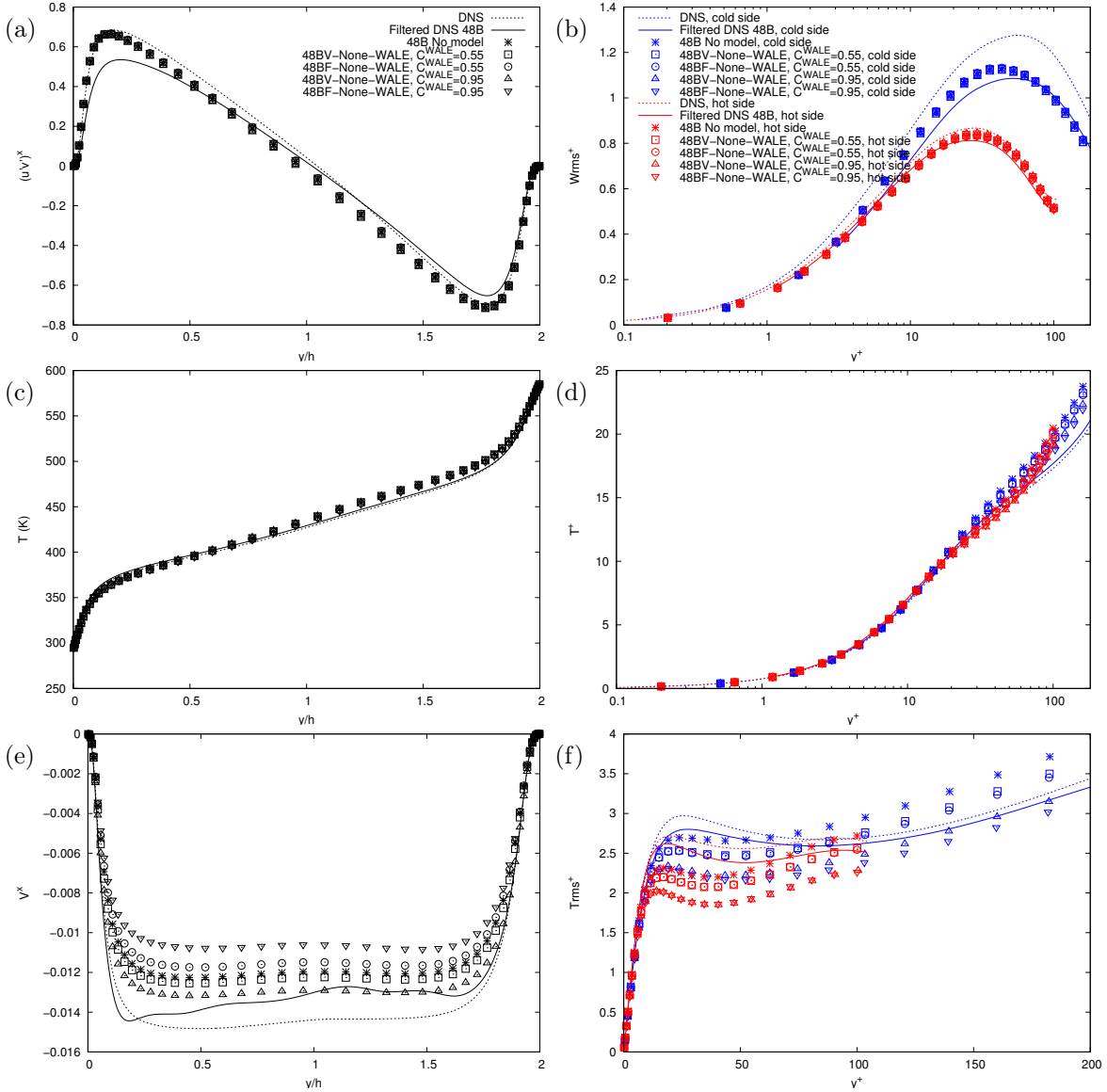


Figure 10.25 – Comparison of large-eddy simulations with the WALE model for the density-velocity correlation subgrid term in the Velocity and Favre formulations for the profiles of the covariance of streamwise and wall-normal velocity $\langle u'_x u'_y \rangle$ (a), the standard deviation of spanwise velocity $\sqrt{\langle u_z'^2 \rangle}$ (b), the mean temperature $\langle T \rangle$ (c, d), the mean wall-normal velocity $\langle U_y \rangle$ (e) and the standard deviation of temperature $\sqrt{\langle T'^2 \rangle}$ (f) in the anisothermal channel at $Re_\tau = 180$ with the mesh 48B.

Favre formulations (figure 10.25). The effect of the formulation is the greatest on the mean wall-normal velocity. This is consistent with the fact that the classical-filtered and Favre-filtered statistics are identical except for the mean wall-normal velocity.

Every model investigated increases the wall heat flux compared to the no-model simulation. This improves the results of the simulation since the wall heat flux is underestimated without model. At $Re_\tau = 180$, the increase is larger with the mesh 24C than with the mesh 48B, but not sufficiently. Indeed, the DNS wall heat flux is exceeded with the mesh 48B while still not attained with the mesh 24C using the WALE model with the parameter $C^{WALE} = 1.65$ or the scale-similarity using filter A. In addition, most models decrease the standard deviation of temperature at the hot and

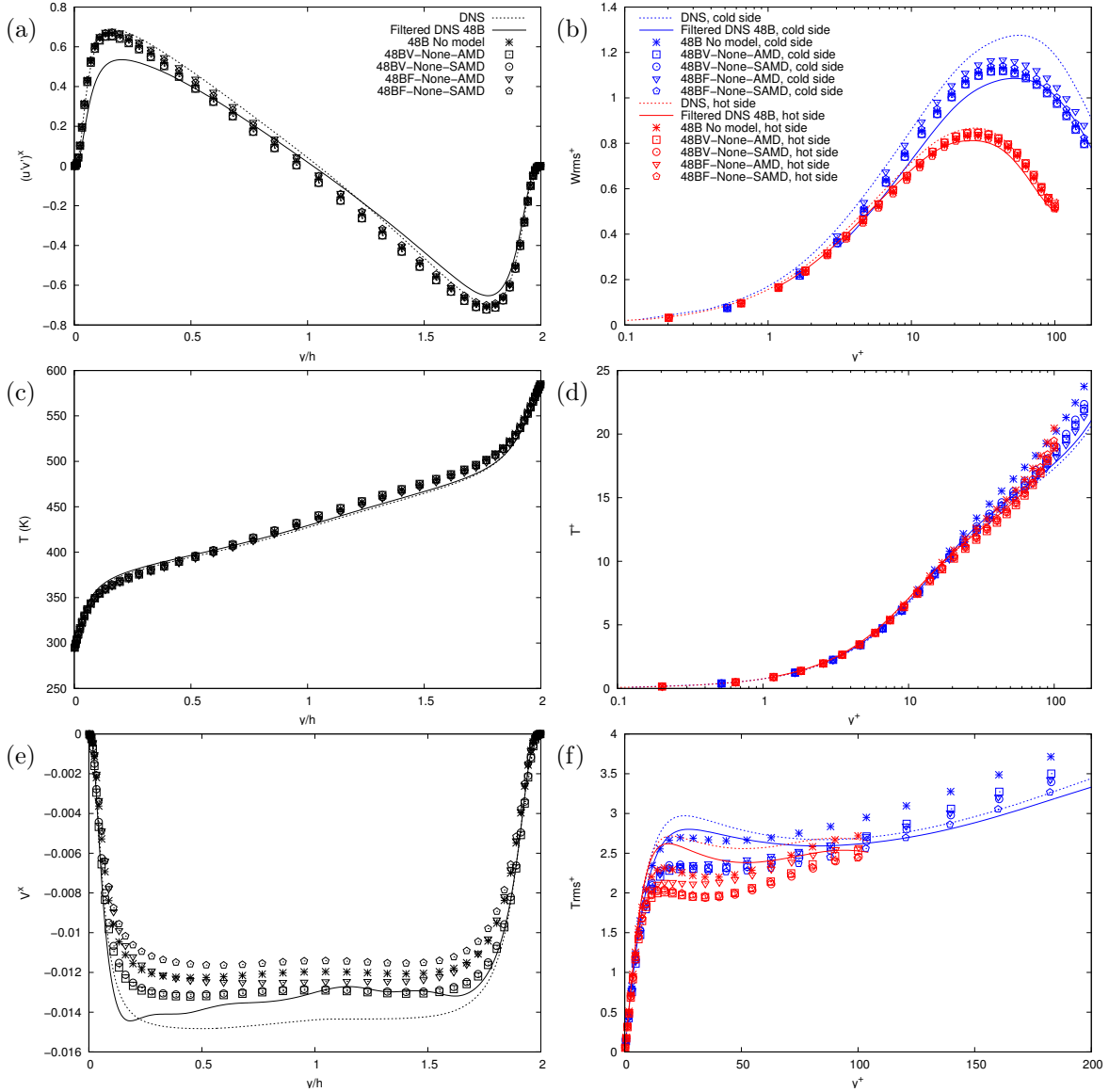


Figure 10.26 – Comparison of large-eddy simulations with the AMD model using $C^{\text{AMD}} = 0.1$, $C^{\text{AMD}} = 0.2$ and $C^{\text{AMD}} = 0.3$ for the density-velocity correlation subgrid term in the Velocity formulation for the profiles of the covariance of streamwise and wall-normal velocity $\langle u'_x u'_y \rangle$ (a), the standard deviation of spanwise velocity $\sqrt{\langle u_z'^2 \rangle}$ (b), the mean temperature $\langle T \rangle$ (c, d), the mean wall-normal velocity $\langle U_y \rangle$ (e) and the standard deviation of temperature $\sqrt{\langle T'^2 \rangle}$ (f) in the anisothermal channel at $Re_\tau = 180$ with the mesh 48B.

cold sides. The decrease occurs in the Velocity and Favre formulations but is slightly more pronounced in the Velocity formulation. These findings hold for functional and structural models. However, the effect of the models on turbulence statistics is not very strong at $Re_\tau = 180$ using the same model parameters as for the momentum convection subgrid term. Larger parameters are required. For functional models, we study parameters corresponding to a subgrid-scale Prandtl or Schmidt number $Pr_t = 0.3$. The larger parameter improves the temperature profile with the WALE model (figure 10.25). The results are identical with the Sigma model. The AMD and scalar AMD models lead to similar results in the Velocity formulation (figure 10.26). However, they differ in the Favre formulation. In particular, the AMD model

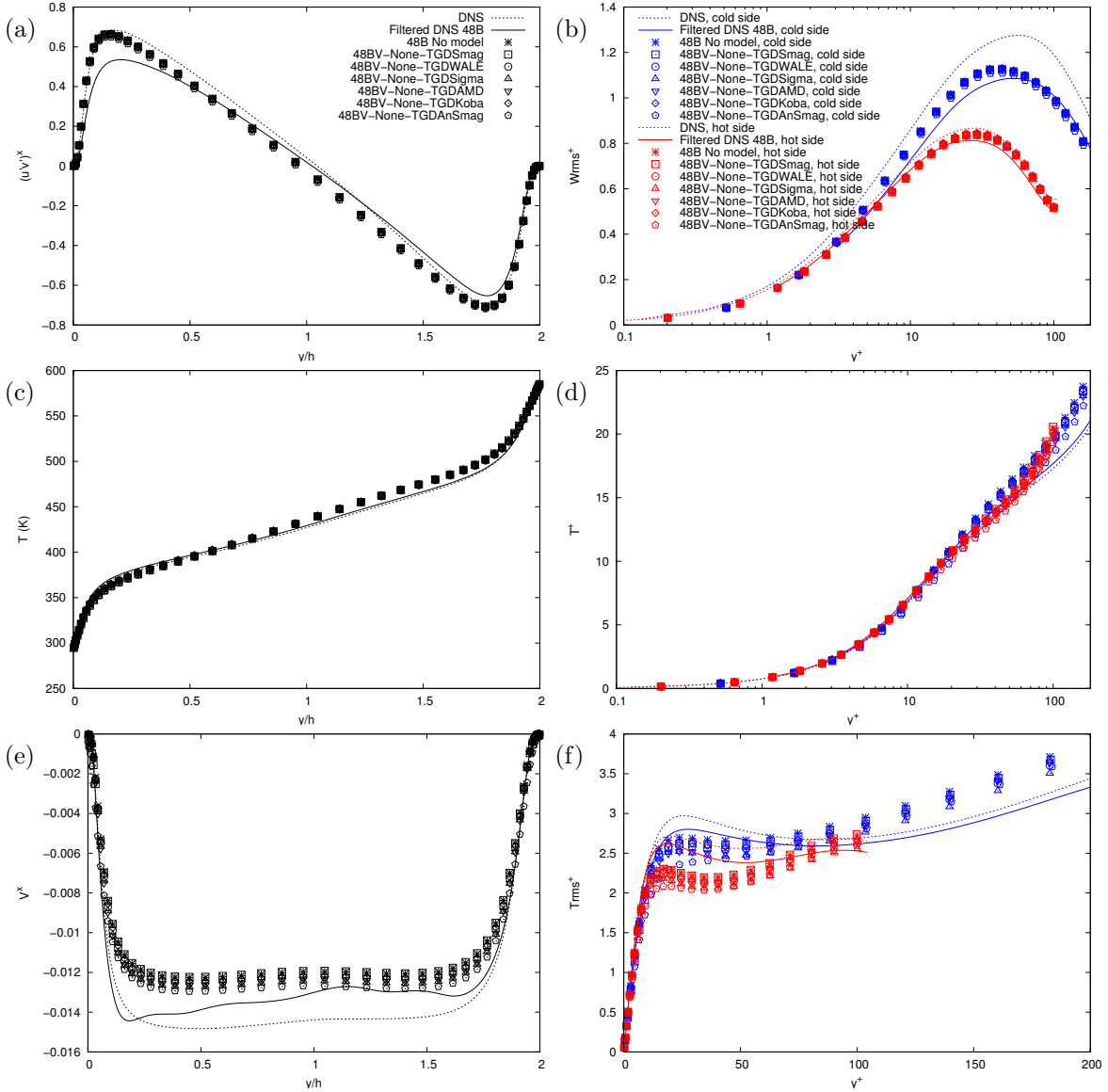


Figure 10.27 – Comparison of large-eddy simulations with the vectorial global-average dynamic Smagorinsky, WALE, Sigma, AMD, Kobayashi and Anisotropic Smagorinsky models for the density-velocity correlation subgrid term in the Velocity formulation for the profiles of the covariance of streamwise and wall-normal velocity $\langle u'_x u'_y \rangle$ (a), the standard deviation of spanwise velocity $\sqrt{\langle u_z'^2 \rangle}$ (b), the mean temperature $\langle T \rangle$ (c, d), the mean wall-normal velocity $\langle U_y \rangle$ (e) and the standard deviation of temperature $\sqrt{\langle T'^2 \rangle}$ (f) in the anisothermal channel at $Re_\tau = 180$ with the mesh 48B.

increases the mean wall-normal velocity compared to the no-model simulation while the scalar AMD model leads to a decrease. The scalar AMD model behaves as the other functional models while the AMD model is peculiar. The vectorial global-average dynamic determination of the parameters of functional models decreases the spanwise component of the models and increase the streamwise contribution (table 10.7). Similar dynamic parameters are obtained in the Velocity and Favre formulations. This does not modify significantly the effect of the model on the turbulence statistics (figure 10.27). As functional models, the classical gradient model (figure 10.28) and scale-similarity model (figure 10.29) have a limited impact on the flow. To amplify the models, we

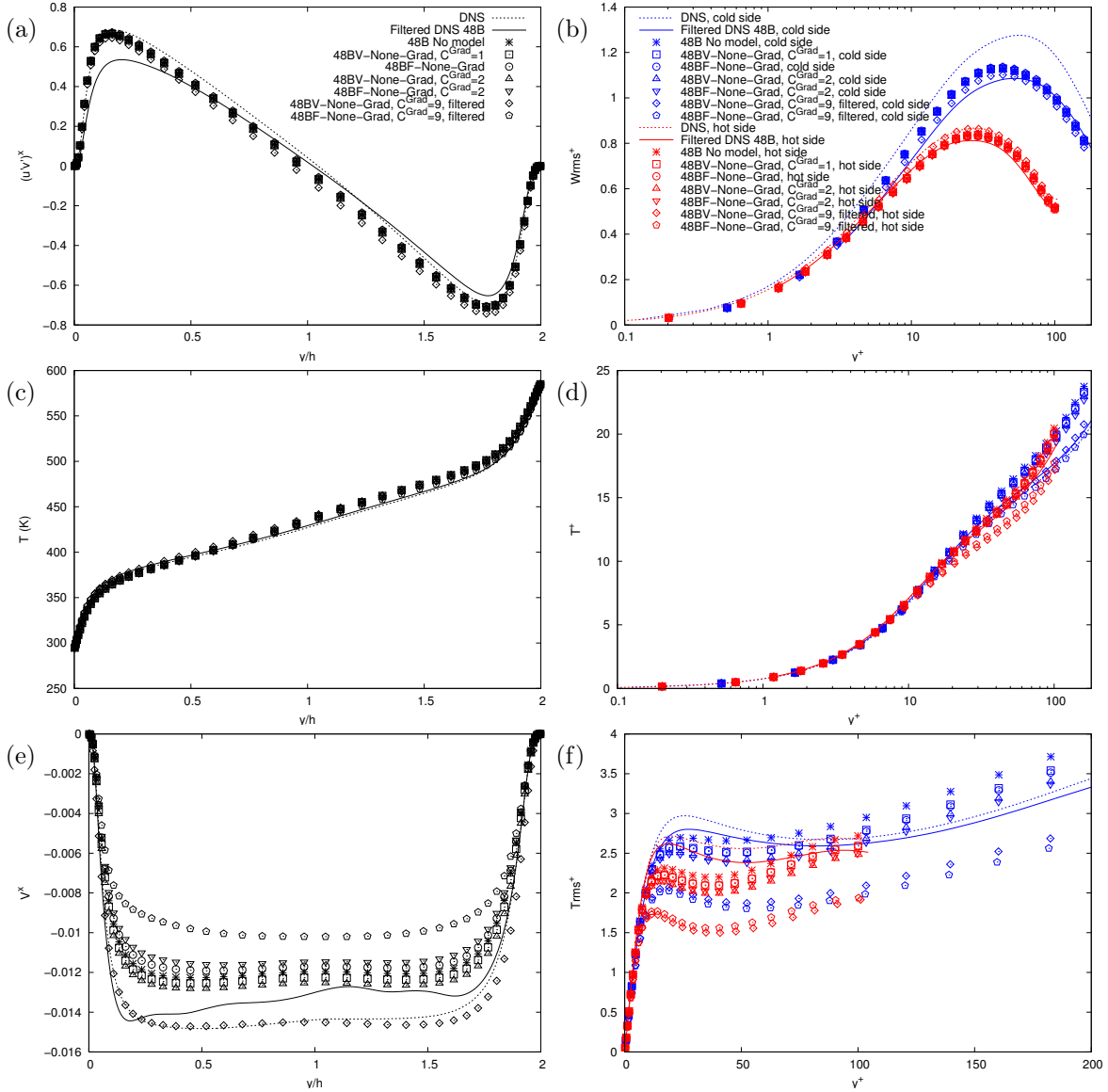


Figure 10.28 – Comparison of large-eddy simulations with the gradient model using $C^{Grad.} = 1$ and $C^{Grad.} = 2$ and the filtered gradient model using $C^{Grad.} = 2$ and $C^{Grad.} = 9$ for the density-velocity correlation subgrid term in the Velocity formulation for the profiles of the covariance of streamwise and wall-normal velocity $\langle u'_x u'_y \rangle$ (a), the standard deviation of spanwise velocity $\sqrt{\langle u_z'^2 \rangle}$ (b), the mean temperature $\langle T \rangle$ (c, d), the mean wall-normal velocity $\langle U_y \rangle$ (e) and the standard deviation of temperature $\sqrt{\langle T'^2 \rangle}$ (f) in the anisothermal channel at $Re_\tau = 180$ with the mesh 48B.

study the gradient model using $C^{Grad.} = 2$ and $C^{Grad.} = 9$ and the scale-similarity model using filter A. We obtain large increase of the wall heat flux and decrease of the standard deviation of temperature. The covariance of streamwise and wall-normal velocity and the standard deviation of wall-normal velocity are also affected. While the amplification of a functional model can be justified using a low subgrid-scale Prandtl or Schmidt number assumption, the amplification of structural models is theoretically not founded.

The above observations suggest that the model for the density-velocity correlation subgrid term is useful and necessary for an accurate prediction of the temperature

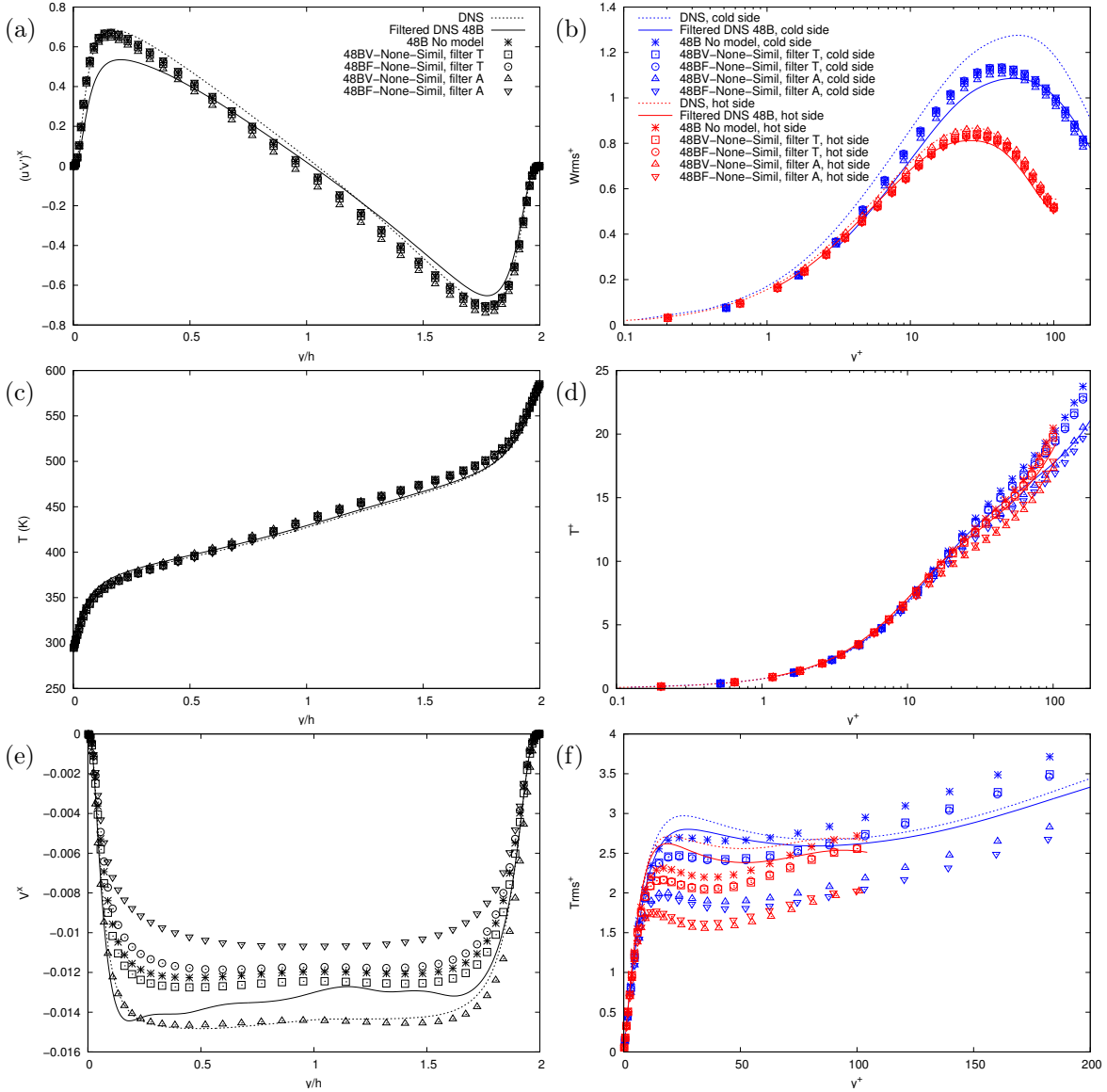


Figure 10.29 – Comparison of large-eddy simulations with the scale-similarity model using filter T and filter A for the density-velocity correlation subgrid term in the Velocity formulation for the profiles of the covariance of streamwise and wall-normal velocity $\langle u'_x u'_y \rangle$ (a), the standard deviation of spanwise velocity $\sqrt{\langle u_z'^2 \rangle}$ (b), the mean temperature $\langle T \rangle$ (c, d), the mean wall-normal velocity $\langle U_y \rangle$ (e) and the standard deviation of temperature $\sqrt{\langle T'^2 \rangle}$ (f) in the anisothermal channel at $Re_\tau = 180$ with the mesh 48B.

field. On the other hand, it cannot improve significantly the deficiencies of the section 10.5.3.1 regarding statistics not directly related to temperature.

10.5.3.3 Modelling of the momentum convection subgrid term and the density-velocity subgrid term

In this section, we investigate large-eddy simulation of the anisothermal channel combining models for the momentum convection subgrid term and models for the density-velocity correlation subgrid term. Two sets of simulations are carried out. The first set of simulations models the two subgrid terms using the same model. The second

$$\langle C^{\text{mod}} \rangle \left(\sqrt{\langle (C^{\text{mod}})^2 \rangle - \langle C^{\text{mod}} \rangle^2} \right)$$

	Velocity formulation			Favre formulation		
	x	y	z	x	y	z
Smag.	12.976 (0.841)	0.021 (0.001)	0.184 (0.061)	13.405 (0.871)	0.005 (0.000)	0.165 (0.065)
WALE	-0.737 (0.230)	0.609 (0.028)	0.165 (0.026)	-0.785 (0.289)	0.606 (0.029)	0.167 (0.027)
Sigma	2.348 (0.413)	0.840 (0.028)	0.372 (0.050)	2.415 (0.429)	0.834 (0.030)	0.366 (0.050)
AMD	2.101 (0.200)	0.356 (0.018)	0.167 (0.031)	2.237 (0.232)	0.360 (0.019)	0.156 (0.031)
SAMD	1.571 (0.262)	0.563 (0.019)	0.226 (0.029)	1.692 (0.281)	0.549 (0.020)	0.220 (0.031)
Kobayashi	5.067 (0.433)	0.747 (0.037)	0.565 (0.070)	5.125 (0.452)	0.752 (0.037)	0.561 (0.071)
An. Smag.	8.233 (0.671)	2.609 (0.126)	0.462 (0.119)	8.585 (0.729)	2.548 (0.158)	0.396 (0.129)

Table 10.7 – Average and normalised standard deviation of the dynamic parameters of the large-eddy simulations with the vectorial global-average dynamic Smagorinsky, WALE, Sigma, AMD, Scalar AMD, Kobayashi and Anisotropic Smagorinsky models in the Velocity and Favre formulations in the anisothermal channel at $Re_\tau = 180$ with the mesh 48B.

set of simulations models the momentum convection subgrid term with the tensorial AMD model based on the $H^{(4)}$ (9.63) tensor ($H^{(4)}$ AMD model) and uses another model for the density-velocity correlation subgrid term.

As suggested by the separate study of the two subgrid terms in section 10.5.3.1 and 10.5.3.2, the modelling of the two subgrid terms with a functional model is not appropriate. The WALE model for instance underestimates the wall shear stress and heat flux and overestimates the standard deviation of streamwise velocity and of temperature with the meshes 24C, 36C and 48B at $Re_\tau = 180$ (figure 10.30) or with the mesh 96B at $Re_\tau = 395$. The predictions are in this regard less accurate than with a no-model simulation. These unsatisfactory results can mainly be attributed to the functional modelling of the momentum convection subgrid term. The functional modelling of the density-velocity correlation subgrid term decreases the mean temperature and the standard deviation of temperature. This holds in the Velocity and Favre formulations. The formulation has a small effect on most turbulence statistics but has a large influence on the mean wall-normal velocity, which is different in the Velocity and Favre formulations. The global-average dynamic procedure provide a less arbitrary determination of the model parameter but the local behaviour of the model is not modified. The plane-average dynamic procedure is only applicable to the Smagorinsky model. The tensorial global-average dynamic procedure is applicable to all functional models investigated and may alter favorably the behaviour of the model. In particular, significant improvements are observed for all turbulence statistics with the AMD model compared to the constant-parameter or global-average versions (figure 10.31).

The $H^{(4)}$ AMD model is one of the most satisfactory models for the momentum convection subgrid term. This model is combined with several models for the density-velocity correlation subgrid term. As expected, the modelling of the density-velocity correlation subgrid term increases the wall heat flux and reduces the standard deviation of temperature. The effect of the model is lower than in simulation without model for the momentum convection subgrid term. At $Re_\tau = 180$, the $H^{(4)}$ AMD model decreases the prediction of the wall heat flux compared to the no-model simulation. A strong

increase from the density-velocity correlation subgrid term is thus required. This may for instance be achieved with the AMD or scalar AMD model using $C^{\text{AMD}} = 0.90$ or with the scale-similarity model using filter A. With these two models, the wall heat flux and the mean wall-normal velocity in the Velocity formulation increased dramatically up to the level of the direct numerical simulation with the meshes 48B (figure 10.32) and 36C (figure 10.33). With the mesh 24C (figure 10.34), the effect of the models is no longer sufficient to obtain an accurate prediction of the wall heat flux. At $Re_\tau = 395$, the $H^{(4)}$ AMD model increases the prediction of the wall heat flux compared to the no-model simulation. The heat flux increase provided by the AMD or scalar AMD model using $C^{\text{AMD}} = 0.90$ or the scale-similarity model using filter A is now excessive (figure 10.35). In other words, a lower parameter is preferable at $Re_\tau = 395$ compared to $Re_\tau = 180$. To address this issue, a subgrid-scale model less dependent on the friction Reynolds number should be used for the momentum convection subgrid term. The modelling of the density-velocity correlation subgrid term affects more heavily the temperature profile at the cold side in the Favre formulation than in the Velocity formulation, while the opposite is true at the hot side. Since the scaled profile of temperature is without model more accurate at the hot side than at the cold side for all simulations, the Favre formulation gives a more accurate scaled temperature profile than the Velocity formulation. In addition, the velocity is less overestimated at the cold side in the Favre formulation than in the Velocity formulation, the profile of the covariance of streamwise and wall-normal velocity is closer to the DNS profile at the center of the channel and the predicted mean thermodynamical pressure less overestimated. In both formulations, the standard deviation of temperature is decreased excessively to a lower level than the filtered DNS profile.

All in all, while none of the model combinations investigated is able to properly reproduce the asymmetry between the hot and cold sides, some improvements are achieved compared to the no-model case. Most models investigated seem suitable for the density-velocity correlation subgrid term. For instance, the scalar AMD model or scale-similarity models can be used. We recommend the use of the Favre formulation rather than the Velocity formulation.

10.6 Conclusion of chapter 10

The large-eddy simulation of a turbulent isothermal or anisothermal channel flow shows the challenge presented by the subgrid-scale modelling of shear flows. In this study, the subgrid-scale modelling is addressed from the filtering of the low Mach number equations in two formulations, the Velocity formulation and the Favre formulation. Only the two most significant subgrid terms are considered, the momentum convection subgrid term and the density-velocity correlation subgrid term. Within the Reynolds number range investigated, the functional modelling of the momentum convection subgrid term does not ameliorate some of the deficiencies of coarse-mesh simulation without model. For instance, the turbulence anisotropy is not well represented as the models insufficiently decrease the standard deviation of streamwise velocity compared to the wall-normal and spanwise components. In the anisothermal case, the models also fail to reproduce accurately the asymmetry between the hot and cold sides. Alternative modelling approaches, such as structural models, tensorial models

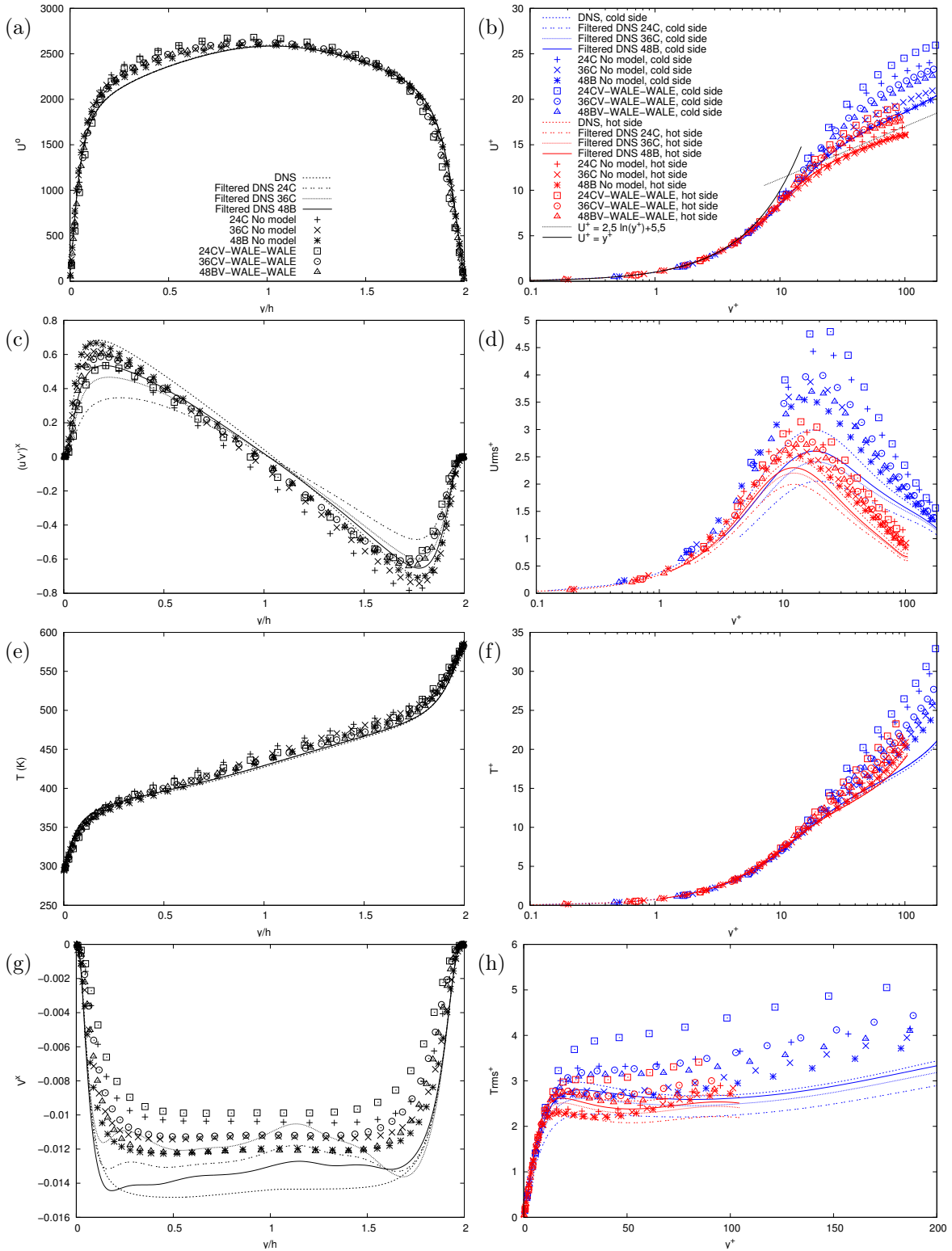


Figure 10.30 – Comparison of large-eddy simulations with the WALE model for the momentum convection subgrid term and the density-velocity correlation subgrid term with the meshes 24C, 36C and 48B in the Velocity formulation for the profiles of the mean streamwise velocity $\langle U_x \rangle$ (a, b), the covariance of streamwise and wall-normal velocity $\langle u'_x u'_y \rangle$ (c), the standard deviation of streamwise velocity $\sqrt{\langle u_x'^2 \rangle}$ (d), the mean temperature $\langle T \rangle$ (e, f), the mean wall-normal velocity $\langle U_y \rangle$ (g) and the standard deviation of temperature $\sqrt{\langle T'^2 \rangle}$ (h) in the anisothermal channel at $Re_\tau = 180$.

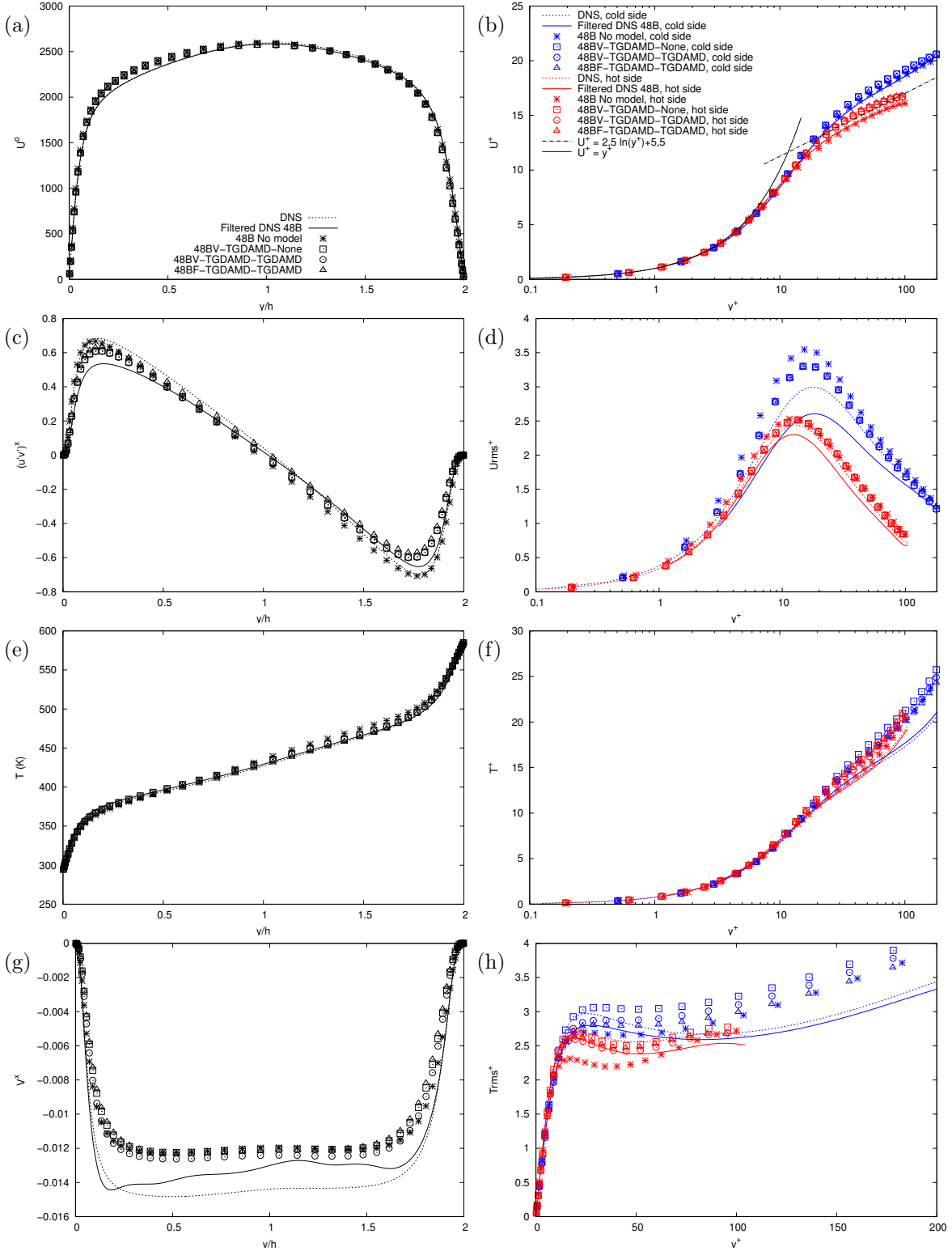


Figure 10.31 – Comparison of large-eddy simulations with the tensorial/vectorial global-average dynamic AMD model for either the momentum convection subgrid term alone or both the momentum convection subgrid term and the density-velocity correlation subgrid term in the Velocity and Favre formulations for the profiles of the mean streamwise velocity $\langle U_x \rangle$ (a, b), the covariance of streamwise and wall-normal velocity $\langle u'_x u'_y \rangle$ (c), the standard deviation of streamwise velocity $\sqrt{\langle u_x'^2 \rangle}$ (d), the mean temperature $\langle T \rangle$ (e, f), the mean wall-normal velocity $\langle U_y \rangle$ (g) and the standard deviation of temperature $\sqrt{\langle T'^2 \rangle}$ (h) in the anisothermal channel at $Re_\tau = 180$ with the mesh 48B.

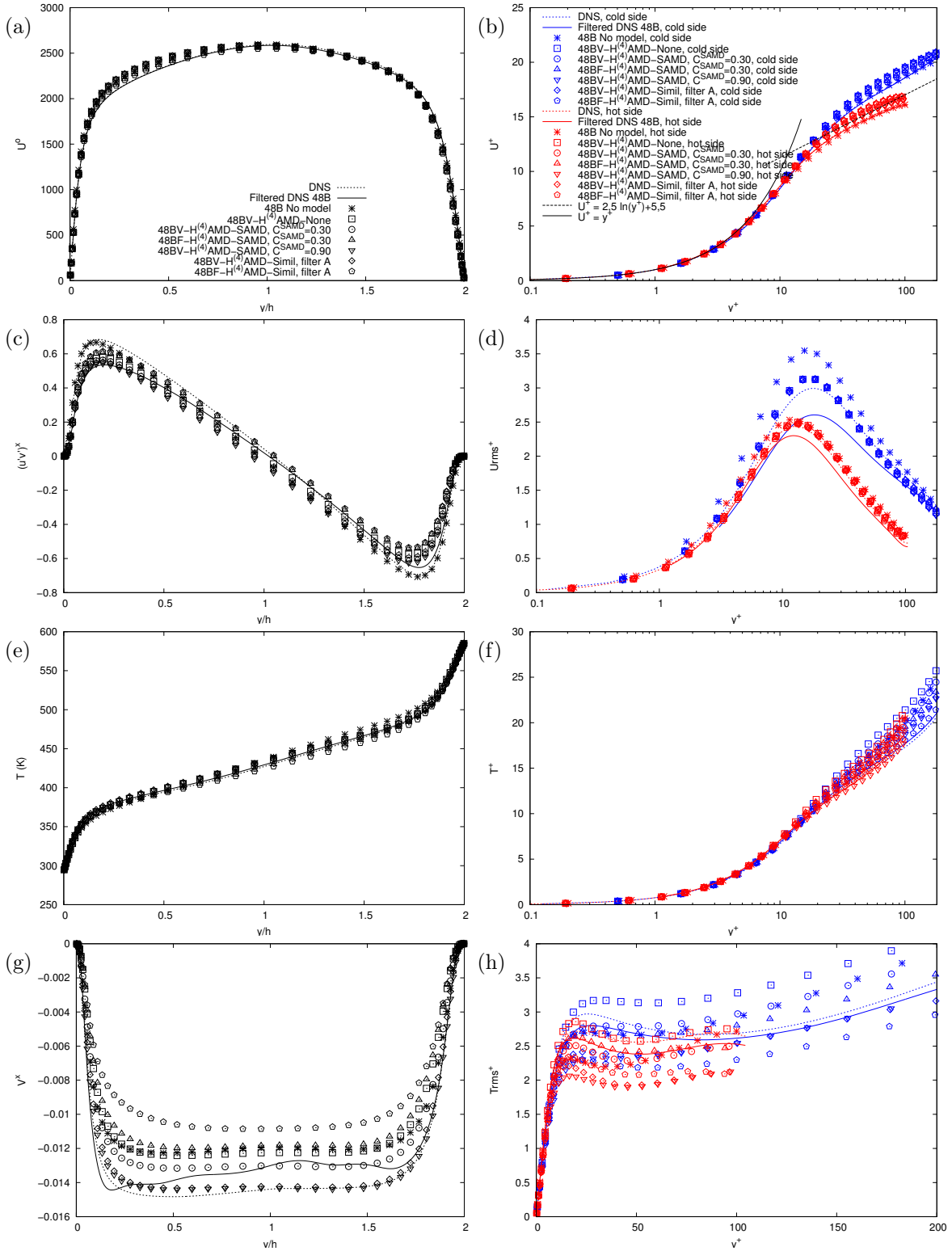


Figure 10.32 – Comparison of large-eddy simulations with the tensorial AMD model based on the $H^{(4)}$ (9.63) tensor for the momentum convection subgrid term and the scalar AMD model or the scale-similarity model using filter A for the density-velocity correlation subgrid term in the Velocity and Favre formulations for the profiles of the mean streamwise velocity $\langle U_x \rangle$ (a, b), the covariance of streamwise and wall-normal velocity $\langle u'_x u'_y \rangle$ (c), the standard deviation of streamwise velocity $\sqrt{\langle u_x'^2 \rangle}$ (d), the mean temperature $\langle T \rangle$ (e, f), the mean wall-normal velocity $\langle U_y \rangle$ (g) and the standard deviation of temperature $\sqrt{\langle T'^2 \rangle}$ (h) in the anisothermal channel at $Re_\tau = 180$ with the mesh 48B.

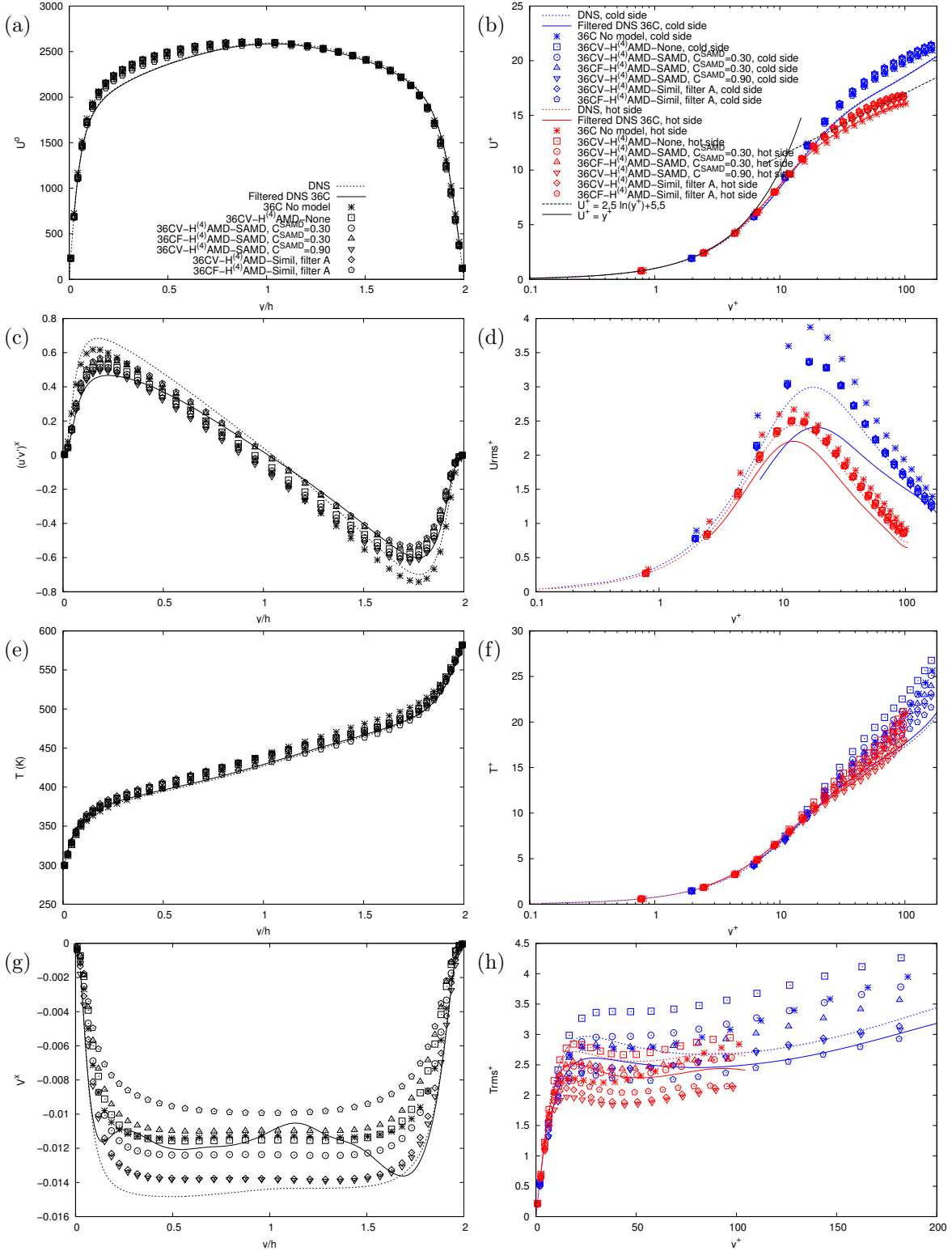


Figure 10.33 – Comparison of large-eddy simulations with the tensorial AMD model based on the $H^{(4)}$ (9.63) tensor for the momentum convection subgrid term and the scalar AMD model or the scale-similarity model using filter A for the density-velocity correlation subgrid term in the Velocity and Favre formulations for the profiles of the mean streamwise velocity $\langle U_x \rangle$ (a, b), the covariance of streamwise and wall-normal velocity $\langle u_x' u_y' \rangle$ (c), the standard deviation of streamwise velocity $\sqrt{\langle u_x'^2 \rangle}$ (d), the mean temperature $\langle T \rangle$ (e, f), the mean wall-normal velocity $\langle U_y \rangle$ (g) and the standard deviation of temperature $\sqrt{\langle T'^2 \rangle}$ (h) in the anisothermal channel at $Re_\tau = 180$ with the mesh 36C.

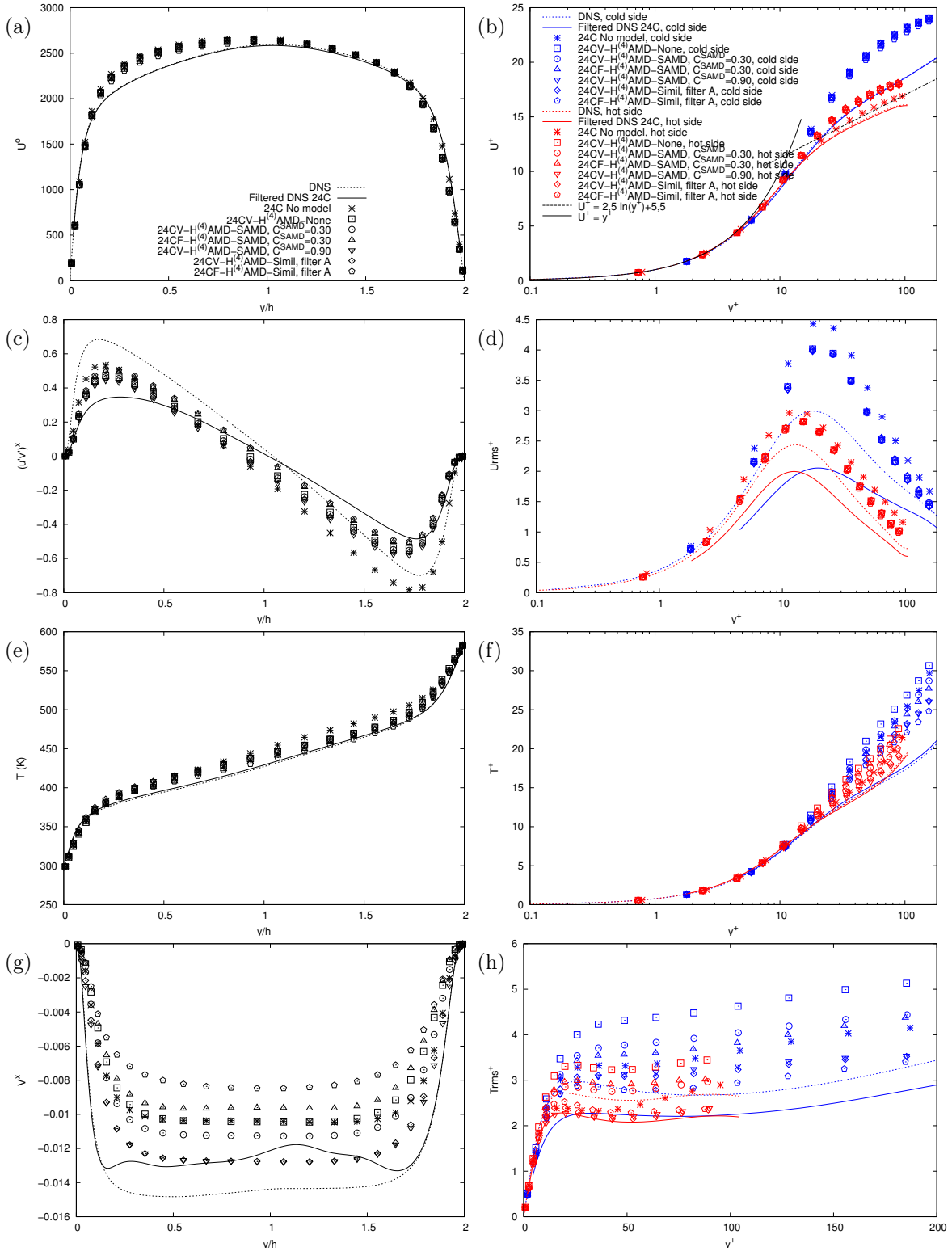


Figure 10.34 – Comparison of large-eddy simulations with the tensorial AMD model based on the $H^{(4)}$ (9.63) tensor for the momentum convection subgrid term and the scalar AMD model or the scale-similarity model using filter A for the density-velocity correlation subgrid term in the Velocity and Favre formulations for the profiles of the mean streamwise velocity $\langle U_x \rangle$ (a, b), the covariance of streamwise and wall-normal velocity $\langle u'_x u'_y \rangle$ (c), the standard deviation of streamwise velocity $\sqrt{\langle u_x'^2 \rangle}$ (d), the mean temperature $\langle T \rangle$ (e, f), the mean wall-normal velocity $\langle U_y \rangle$ (g) and the standard deviation of temperature $\sqrt{\langle T'^2 \rangle}$ (h) in the anisothermal channel at $Re_\tau = 180$ with the mesh 24C.

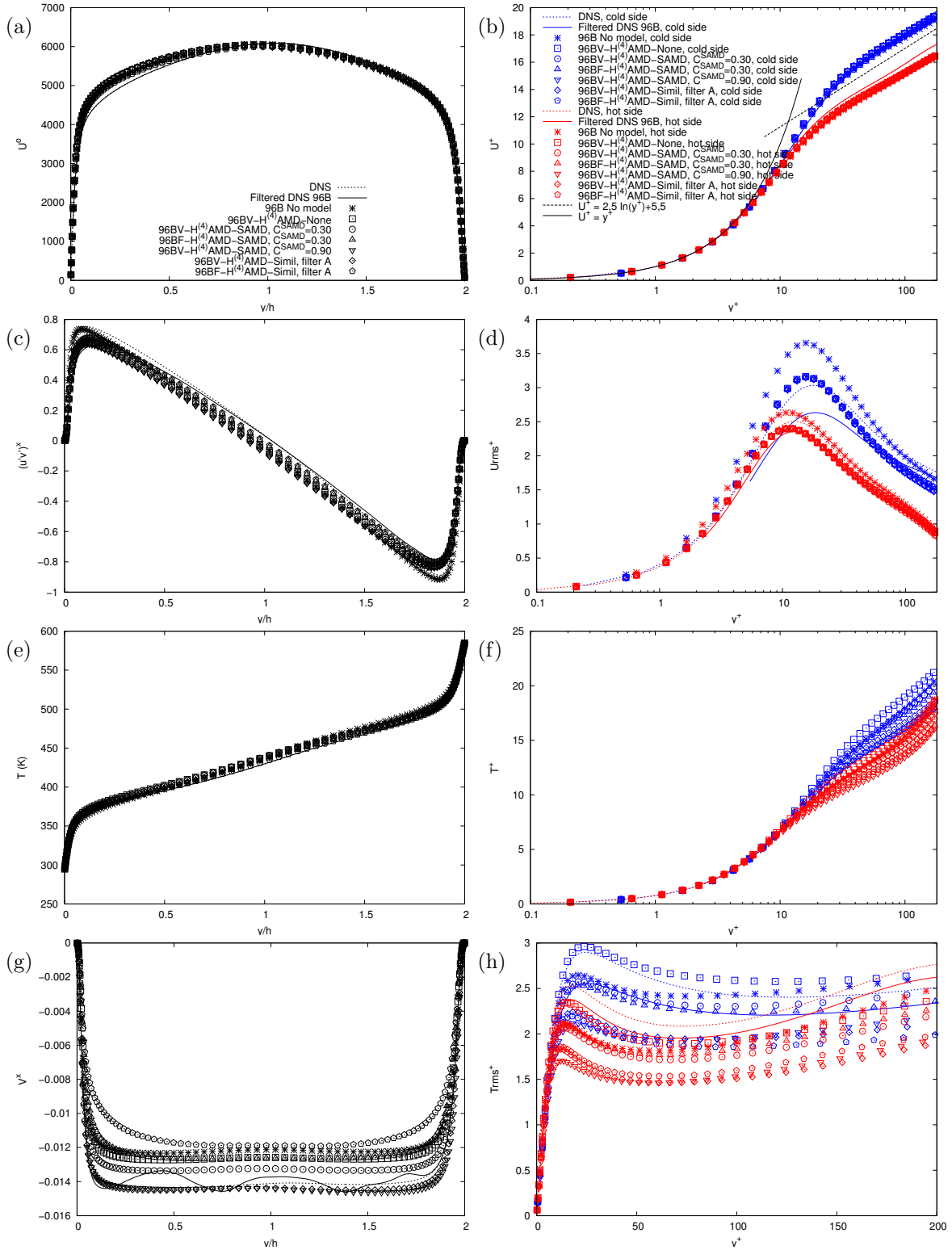


Figure 10.35 – Comparison of large-eddy simulations with the tensorial AMD model based on the $H^{(4)}$ (9.63) tensor for the momentum convection subgrid term and the scalar AMD model or the scale-similarity model using filter A for the density-velocity correlation subgrid term in the Velocity and Favre formulations for the profiles of the mean streamwise velocity $\langle U_x \rangle$ (a, b), the covariance of streamwise and wall-normal velocity $\langle u_x' u_y' \rangle$ (c), the standard deviation of streamwise velocity $\sqrt{\langle u_x'^2 \rangle}$ (d), the mean temperature $\langle T \rangle$ (e, f), the mean wall-normal velocity $\langle U_y \rangle$ (g) and the standard deviation of temperature $\sqrt{\langle T'^2 \rangle}$ (h) in the anisothermal channel at $Re_\tau = 395$ with the mesh 96B.

and tensorial global-average dynamic functional models, can improve the results. However, the effect of these models is not in full accord with the filtered direct numerical simulations and is not amplified as expected upon mesh derefinement. The modelling of the density-velocity correlation subgrid term is useful and beneficial for the prediction of temperature-related statistics but does not seem to significantly alter the velocity. It has a smaller impact on the flow than the momentum convection subgrid term. The results suggest that the Favre formulation is preferable to the Velocity formulation for an accurate prediction of the mean temperature. Functional models propose a relevant modelling approach for the density-velocity correlation subgrid term since it influences the turbulence statistics positively. Structural models are also relevant. However, the accurate prediction of the flow requires the agreement of the strength of the model with the effect of the model for the momentum convection subgrid term.

Chapter 11

Conclusion of part II

The large-eddy simulation of low Mach number equations has been investigated in isothermal and anisothermal fully developed turbulent channel flows. Chapter 8 addressed the filtering of the low Mach number equations using the direct numerical simulations of the anisothermal channel at $Re_\tau = 180$ and $Re_\tau = 395$. The subgrid terms were classified according to their magnitude in two formulations identified as relevant. Chapter 9 examined the modelling of the two most significant subgrid terms a priori, using the direct numerical simulation of the anisothermal channel at $Re_\tau = 180$. The study focused on eddy-viscosity and eddy-diffusivity models. Chapter 10 analysed the modelling of the two subgrid terms a posteriori, that is from large-eddy simulations implementing the models. The filtering of the direct numerical simulations of the isothermal and anisothermal channel at $Re_\tau = 180$ and $Re_\tau = 395$ was used to interpret the results.

The large-eddy simulation of strongly anisothermal flows show the combined influence of numerical and modelling errors. The numerical errors are related to the discretisations and numerical schemes. The modelling errors are related to the inexact correspondence of the subgrid-scale models and the subgrid terms, including the error made on neglected subgrid terms. Using the low Mach number equations, this can be performed in two formulations referred to as the Velocity formulation and the Favre formulation. The two formulations lead to similar results with regard to the number of significant subgrid terms and the a priori performance of the subgrid terms. However, the a posteriori predictions of large-eddy simulations are more accurate in the Favre formulation with the numerical schemes and discretisations used.

The modelling is responsible for the prediction of the mean flow variables, the turbulence anisotropy and the asymmetry between the hot and cold sides. The modelling of the momentum convection governs the wall shear stress and the turbulence anisotropy. The gradient model is well correlated with the subgrid term but is not as impactful in a large-eddy simulation. Eddy-viscosity models can provide an accurate description of the energetic contribution of the subgrid term but show poor structural performances. Implemented in large-eddy simulations, they are not satisfactory. Tensorial eddy-viscosity models deteriorate the a priori performance of eddy-viscosity models but can be beneficial a posteriori. However, their definitions is specific to channel flows and not directly applicable in more complex geometries without the construction of a flow-dependent coordinate system based on the velocity. Tensorial dynamic methods

are possible substitutes. The modelling of density-velocity correlations is crucial to the accurate prediction of the heat flux. Eddy-diffusivity and structural models seem suitable for this subgrid term. Since there is two subgrid terms, the analysis depends on the modelling error on the momentum convection subgrid term and it is not trivial to which extent this should be taken into account.

The large-eddy simulation of strongly anisothermal flows remains a considerable challenge. We limited our analysis to zero-equation algebraic models and assumed for maximum generality no prior knowledge of the flow. Although the models investigated are not optimal and can be improved, the difficulties encountered suggest that the large-eddy simulations may benefit from more sophisticated modelling approaches. For this purpose, large-eddy simulation can be combined with other modelling tactics, as in detached-eddy simulation [278, 292, 285, 279] or in constrained large-eddy simulation [51, 133, 158]. Besides, a detailed characterisation of numerical errors is necessary for a more complete understanding of the results of the large-eddy simulations. We may study for this purpose the influence of the numerical methods, the discretisations and the numerical schemes on the results of large-eddy simulations. The explicit filtering approach to large-eddy simulation is also useful in that regard as it allows the grid convergence of the solution, disentangling numerical and modelling errors.

General conclusion and perspectives

The objective of this thesis has been to address turbulent flows subjected to a strong temperature gradient, as found in high-temperature solar receivers. The analysis can be divided into two parts. The first part characterised the influence of the temperature gradient on the energy exchanges between the different parts of total energy within the fluid. The second part analysed the subgrid-scale modelling of these flows for large-eddy simulation.

In order to focus on the effect of temperature on the flow, we have considered a flow between two plane walls at constant temperature: a cold wall and a hot wall. The approximations made are presented in chapter 1. The fluid in the channel was modelled as a continuous medium in local thermodynamical equilibrium. Given the large variations of fluid properties and low velocities found in solar receivers, the motion of this continuous medium can be described using the low Mach number equations. In addition, the variations of fluid properties with temperature can be computed using the ideal gas law, Sutherland's law [287] and a constant Prandtl number assumption. The constant-temperature smooth walls and periodic boundary conditions of the channel are not realistic descriptions of a real solar receiver. However, the simplicity of the geometry enabled the direct numerical simulation of the channel at the friction Reynolds number $Re_\tau = 180$ and $Re_\tau = 395$. The results of the direct numerical simulations have been used throughout the thesis. In particular, we used the simulations to study the energy exchanges associated with the half-trace of the velocity fluctuation correlation tensor and the large-eddy simulation of the low Mach number equations.

We addressed the energy exchanges in strongly anisothermal channel flows. Before proceeding to a numerical study, we investigated in chapter 3 the decomposition of total energy using the Reynolds average. The Reynolds decomposition of velocity leads to a ternary decomposition of kinetic energy into turbulence kinetic energy, mean kinetic energy and mixed kinetic energy. The further decomposition of density splits each term in two parts. It is thereby possible to identify and give a physical meaning to the energy exchanges associated with the half-trace of the velocity fluctuation correlation tensor in the spatial and spectral domains. Four spectral energy exchanges have been identified: the production, the interscale transport, the conservative energy transfer and the interaction with internal energy.

We analysed these energy exchanges from the direct numerical simulations of the channel at $Re_\tau = 180$ in chapter 4. Turbulence kinetic energy is produced from mean kinetic energy at a particular spatial and spectral location. This energy is redistributed towards large and small scales and transferred towards the wall. The conversion of turbulence kinetic energy into internal energy is predominant near the wall, and occurs at similar scales to production. The temperature gradient creates an asymmetry be-

tween the energy exchanges at the hot and cold sides of the channel. A large part of the asymmetry can be explained using a semi-local scaling based on the variations of the mean local fluid properties. In addition, we identified a low Reynolds effect corresponding to the variations of the local friction Reynolds number across the channel. Nevertheless, a non-negligible part of the asymmetry between the hot and cold sides cannot be recovered from these two effects.

Using the direct numerical simulations of the channel at $Re_\tau = 395$, we examined in chapter 5 the influence of the Reynolds number on the effect of the temperature gradient. At higher Reynolds number, the low Reynolds effects are smaller. The variations of the local fluid properties have a larger relative contribution to the asymmetry between the hot and cold sides. We also decomposed the energy exchanges in order to study separately the incompressible terms, as found in the incompressible isothermal case, and the thermal terms, specific to flows with variable fluid properties. The significant thermal terms have a similar effect on the flow. Besides, low Reynolds number effects have a negligible impact on thermal terms and only affect incompressible terms.

We also addressed the large-eddy simulation of strongly anisothermal channel flows. Before proceeding to subgrid-scale model tests, we investigated in chapter 8 the filtering of the low Mach number equations. The subgrid terms involved in the filtered low Mach number equations depends on the formulation of the equations upon filtering. If the velocity transport equation is filtered, the unweighted classical filter is preferable, leading to the Velocity formulation. If the momentum conservation equations is filtered, the density-weighted Favre filter is preferable, leading to the Favre formulation. In both formulations, the same subgrid terms have been found significant: the subgrid term associated with momentum convection, the subgrid associated with the density-velocity correlation and, depending on the filter width, the subgrid terms associated with the filter-derivative non-commutation of dilatation.

We analysed the modelling of the momentum convection subgrid term and the density-velocity correlation subgrid term from the direct numerical simulations of the channel at $Re_\tau = 180$ in chapter 9. These a priori tests compared eddy-viscosity and eddy-diffusivity models to the exact subgrid terms. No differences were identified between the Velocity and Favre formulations regarding the a priori model performances. Among the new models proposed and the models from the literature investigated, the AMD and scalar AMD models are in better agreement with the exact subgrid term. However, the models only satisfactorily represent the energetic contribution of the subgrid term. A poor correspondence was found for all models for the contribution of the subgrid term in the filtered low Mach number equations.

Using simulations implementing the models at $Re_\tau = 180$ and $Re_\tau = 395$, we examined in chapter 10 the influence of the modelling in large-eddy simulations. These a posteriori tests relied on the filtering of the direct numerical simulations for the interpretation of the results. The model combinations investigated did not properly predict the turbulence anisotropy or the asymmetry between the hot and cold sides. Nonetheless, they improved the predictions of the simulations compared to the no-model case. For the momentum convection subgrid term, we recommended the use of the scale-similarity model and the constant-parameter or dynamic tensorial AMD model. For the density-velocity correlation subgrid term, several models seemed able to improve temperature-related statistics, for instance the scalar AMD model and the

scale-similarity model. More accurate results were obtained with the Favre formulation than with the Velocity formulation.

The main limitation of the study is the dependence of the analysis to the numerical errors. To refine the interpretation of the results, it would be useful to characterise the influence of the numerical schemes and discretisations used on the results of large-eddy simulations. To this end, numerical and modelling errors may be separated using an explicit filtering approach. While the zero-equation algebraic models investigated improve the results compared to a simulation without model, more sophisticated modelling approaches may be required to solve the remaining challenges. For instance, the subgrid-scale models can be combined to RANS modelling in detached-eddy simulations [278, 292, 285, 279] and constrained large-eddy simulations [51, 133, 158]. The modelling should properly reproduce the asymmetry between the hot and cold sides and the small-scale part of the spectral energy exchanges.

Appendices

Appendix A

Link between spatial and spectral correlations

In this appendix, we establish a relation between the spatial correlations and the spectral correlations. Let us denote C^{ab} the spatial two-point correlation between a and b defined as

$$C^{ab}(\mathbf{r}, y, t) = \overline{a(\mathbf{x}, y, t)b(\mathbf{x} + \mathbf{r}, y, t)}, \quad (\text{A.1})$$

with the notation $\mathbf{r} = (r_x, r_z)$. In particular, let us notice that

$$C^{ab}(\mathbf{0}, y, t) = \overline{a(\mathbf{x}, y, t)b(\mathbf{x}, y, t)}. \quad (\text{A.2})$$

We write $C^{ab}(\mathbf{0}, y)$ as a Fourier series (see equation 3.46):

$$C^{ab}(\mathbf{0}, y, t) = \sum_{p,q=-\infty}^{\infty} \widehat{C}^{ab}(\mathbf{k}_{p,q}, y, t). \quad (\text{A.3})$$

We can express the Fourier coefficients \widehat{C}^{ab} as a function of the Fourier coefficients \widehat{a} and \widehat{b} . Indeed,

$$\overline{\widehat{a}(\mathbf{k}', y, t)\widehat{b}(\mathbf{k}, y, t)} = \left(\frac{1}{L_x L_z}\right)^2 \int_0^{L_x} \int_0^{L_z} \int_0^{L_x} \int_0^{L_z} e^{-i(\mathbf{k}' \cdot \mathbf{x} + \mathbf{k} \cdot \mathbf{x}')} \overline{a(\mathbf{x}, y, t)b(\mathbf{x}', y, t)} d\mathbf{x}' d\mathbf{x}. \quad (\text{A.4})$$

With $\mathbf{x}' = \mathbf{x} + \mathbf{r}$,

$$\overline{\widehat{a}(\mathbf{k}', y, t)\widehat{b}(\mathbf{k}, y, t)} = \left(\frac{1}{L_x L_z}\right)^2 \int_0^{L_x} \int_0^{L_z} e^{-i(\mathbf{k} + \mathbf{k}') \cdot \mathbf{x}} d\mathbf{x} \int_0^{L_x} \int_0^{L_z} C^{ab}(\mathbf{r}, y) e^{-i(\mathbf{k} \cdot \mathbf{r})} d\mathbf{r}. \quad (\text{A.5})$$

We then obtain

$$\overline{\widehat{a}(\mathbf{k}', y, t)\widehat{b}(\mathbf{k}, y, t)} = \widehat{C}^{ab}(\mathbf{k}, y) \delta_{\mathbf{k} + \mathbf{k}'} \quad (\text{A.6})$$

using the properties

$$\delta_{\mathbf{k}} = \left(\frac{1}{2\pi}\right)^2 \int_0^{L_x} \int_0^{L_z} e^{-i\mathbf{k} \cdot \mathbf{x}} d\mathbf{x} \quad (\text{A.7})$$

and

$$\widehat{C}^{ab}(\mathbf{k}, y) = \left(\frac{1}{2\pi}\right)^2 \int_0^{L_x} \int_0^{L_z} C^{ab}(\mathbf{r}, y) e^{-i(\mathbf{k} \cdot \mathbf{r})} d\mathbf{r}. \quad (\text{A.8})$$

If a is real, we have the property

$$\widehat{a}^*(\mathbf{k}, y, t) = \widehat{a}(-\mathbf{k}, y, t). \quad (\text{A.9})$$

With $\mathbf{k}' = -\mathbf{k}$, the relation (A.6) becomes

$$\overline{\widehat{a}^*(\mathbf{k}, y, t)\widehat{b}(\mathbf{k}, y, t)} = \widehat{C}^{ab}(\mathbf{k}, y). \quad (\text{A.10})$$

This relation link the Fourier coefficients of the spatial two-point correlations between a and b to the spectral one-point correlation between the Fourier coefficients of a and b . By combining the result with equations (A.2) and (A.3), we obtain

$$\overline{a(\mathbf{x}, y, t)b(\mathbf{x}, y, t)} = \sum_{p,q=-\infty}^{\infty} \overline{\widehat{a}^*(\mathbf{k}_{p,q}, y, t)\widehat{b}(\mathbf{k}_{p,q}, y, t)} \quad (\text{A.11})$$

This provides a relation between the spatial one-point correlation between a and b and the spectral one-point correlation between the Fourier coefficients of a and b .

Appendix B

Formulation and decomposition of the energy exchanges

B.1 Energy exchanges with the decomposition of density in a constant and variable part

B.1.1 General considerations

In this section, we describe the formulation of the energy exchanges between the different parts of total energy obtained from the Reynolds decomposition of velocity and the decomposition of density in a constant and variable part. This formulation is used in chapter 4 and 5. We use the same physical hypotheses than in section 3.2.2.1. We will establish two formulations. In the one-stage formulation, only velocity is decomposed. In the two-stage formulation, both velocity and density are decomposed.

The one-stage formulation relies on the Reynolds decomposition of velocity $U_i = \bar{U}_i + u'_i$. The kinetic energy is decomposed into three parts: the mean kinetic energy $\rho \underline{E} = \frac{1}{2} \rho \bar{U}_i \bar{U}_i$ associated with the mean motion, the turbulence kinetic energy $\rho e = \frac{1}{2} \rho u'_i u'_i$ associated with the turbulent motion and the mixed kinetic energy $\rho \underline{e} = \rho u'_i \bar{U}_i$ associated with both the mean and turbulent motion, that is

$$\rho E = \rho \underline{E} + \rho e + \rho \underline{e}. \quad (\text{B.1})$$

This leads to the following fourfold decomposition of total energy:

$$\rho E + \rho I = \rho \underline{E} + \rho e + \rho \underline{e} + \rho I. \quad (\text{B.2})$$

The two-stage formulation relies in addition on the decomposition of the density ρ into a constant part ρ_0 and a variable part ρ_1 ,

$$\rho(\mathbf{x}, t) = \rho_0 + \rho_1(\mathbf{x}, t). \quad (\text{B.3})$$

where \mathbf{x} is the position vector. Here, ρ_1 is a turbulent function, $\rho_1 = \rho'_1 + \bar{\rho}_1$. The kinetic energy ρE is decomposed into a constant density part $\rho_0 E$ and a variable density part $\rho_1 E$. The half-trace of the velocity correlation tensor E is understood as the constant

density portion of kinetic energy up to the constant scalar factor ρ_0 . Similarly, the mean kinetic energy $\rho\bar{E}$, the turbulence kinetic energy ρe and the mixed kinetic energy $\rho\bar{e}$ are decomposed into a constant density part, $\rho_0\bar{E}$, ρ_0e and $\rho_0\bar{e}$ respectively, and a variable density part, $\rho_1\bar{E}$, ρ_1e and $\rho_1\bar{e}$ respectively. The internal energy per unit volume ρI is also decomposed into a constant density part ρ_0I and a variable density part ρ_1I . This leads to the following eightfold decomposition of total energy:

$$\rho E + \rho I = \rho_0\bar{E} + \rho_0e + \rho_0\bar{e} + \rho_0I + \rho_1\bar{E} + \rho_1e + \rho_1\bar{e} + \rho_1I. \quad (\text{B.4})$$

To devise the formulations, let us write here for latter use the evolution equation of \bar{U}_i , u'_i and I :

$$\frac{\partial \bar{U}_i}{\partial t} + U_j \frac{\partial \bar{U}_i}{\partial x_j} = \frac{1}{\rho} \frac{\partial \overline{\mathcal{Y}_{ij}}}{\partial x_j}, \quad (\text{B.5})$$

$$\frac{\partial u'_i}{\partial t} + \left(U_j \frac{\partial U_i}{\partial x_j} \right)' = \left(\frac{1}{\rho} \frac{\partial \mathcal{Y}_{ij}}{\partial x_j} \right)', \quad (\text{B.6})$$

$$\frac{\partial I}{\partial t} + U_j \frac{\partial I}{\partial x_j} = \frac{1}{\rho} \frac{\partial}{\partial x_j} \left(\lambda \frac{\partial T}{\partial x_j} \right) + \frac{1}{\rho} \mathcal{Y}_{ij} \frac{\partial U_i}{\partial x_j}. \quad (\text{B.7})$$

Equation (B.5) is obtained by dividing both sides of equation (3.2) by the density ρ then taking the statistical average. Equation (B.6) is obtained by dividing both sides of equation (3.2) by ρ then subtracting from the result equation (B.5). Equation (B.7) is obtained by dividing equation (3.3) by ρ .

B.1.2 One-stage formulation

In order to identify the energy exchanges between the different parts of the fourfold decomposition (B.2) of total kinetic energy, we shall derive the evolution equation of each of these quantities.

First, to obtain the evolution equation of the mean kinetic energy $\rho\bar{E}$, we will take the sum of two contributions. First, we multiply equation (B.5) by $\rho\bar{U}_i$,

$$\rho \frac{\partial \bar{E}}{\partial t} + \rho \bar{U}_i U_j \frac{\partial \bar{U}_i}{\partial x_j} = \rho \bar{U}_i \frac{1}{\rho} \frac{\partial \overline{\mathcal{Y}_{ij}}}{\partial x_j}. \quad (\text{B.8})$$

Next, we multiply the mass conservation equation (3.1) by \bar{E} ,

$$\bar{E} \frac{\partial \rho}{\partial t} + \bar{E} \frac{\partial \rho U_j}{\partial x_j} = 0. \quad (\text{B.9})$$

The summation of equations (B.8) and (B.9) gives:

$$\frac{\partial \rho \bar{E}}{\partial t} + \bar{E} \frac{\partial \rho U_j}{\partial x_j} + \rho \bar{U}_i U_j \frac{\partial \bar{U}_i}{\partial x_j} = \rho \bar{U}_i \frac{1}{\rho} \frac{\partial \overline{\mathcal{Y}_{ij}}}{\partial x_j}. \quad (\text{B.10})$$

Second, to obtain the evolution equation of the turbulence kinetic energy ρe , we will take the sum of two contributions. First, we multiply equation (B.6) by $\rho u'_i$,

$$\rho \frac{\partial e}{\partial t} + \rho u'_i \left(U_j \frac{\partial U_i}{\partial x_j} \right)' = \rho u'_i \left(\frac{1}{\rho} \frac{\partial \mathcal{Y}_{ij}}{\partial x_j} \right)'. \quad (\text{B.11})$$

Next, we multiply the mass conservation equation (3.1) by e ,

$$e \frac{\partial \rho}{\partial t} + e \frac{\partial \rho U_j}{\partial x_j} = 0. \quad (\text{B.12})$$

The summation of equations (B.11) and (B.12) gives:

$$\frac{\partial \rho e}{\partial t} + e \frac{\partial \rho U_j}{\partial x_j} + \rho u'_i \left(U_j \frac{\partial U_i}{\partial x_j} \right)' = \rho u'_i \left(\frac{1}{\rho} \frac{\partial \Upsilon_{ij}}{\partial x_j} \right)'. \quad (\text{B.13})$$

Third, to obtain the evolution equation of the mixed kinetic energy $\rho \underline{e}$, we will take the sum of three contributions. First, we multiply equation (B.5) by $\rho u'_i$,

$$\rho u'_i \frac{\partial \bar{U}_i}{\partial t} + \rho u'_i U_j \frac{\partial \bar{U}_i}{\partial x_j} = \rho u'_i \frac{1}{\rho} \frac{\partial \Upsilon_{ij}}{\partial x_j}. \quad (\text{B.14})$$

Next, we multiply equation (B.6) by $\rho \bar{U}_i$,

$$\rho \bar{U}_i \frac{\partial u'_i}{\partial t} + \rho \bar{U}_i \left(U_j \frac{\partial U_i}{\partial x_j} \right)' = \rho \bar{U}_i \left(\frac{1}{\rho} \frac{\partial \Upsilon_{ij}}{\partial x_j} \right)'. \quad (\text{B.15})$$

Finally, we multiply the mass conservation equation (3.1) by \underline{e} ,

$$\underline{e} \frac{\partial \rho}{\partial t} + \underline{e} \frac{\partial \rho U_j}{\partial x_j} = 0. \quad (\text{B.16})$$

The summation of equations (B.14), (B.15) and (B.16) gives:

$$\frac{\partial \rho \underline{e}}{\partial t} + \underline{e} \frac{\partial \rho U_j}{\partial x_j} + \rho u'_i U_j \frac{\partial \bar{U}_i}{\partial x_j} + \rho \bar{U}_i \left(U_j \frac{\partial U_i}{\partial x_j} \right)' = \rho u'_i \frac{1}{\rho} \frac{\partial \Upsilon_{ij}}{\partial x_j} + \rho \bar{U}_i \left(\frac{1}{\rho} \frac{\partial \Upsilon_{ij}}{\partial x_j} \right)'. \quad (\text{B.17})$$

Fourth, the evolution equation of the internal energy ρI is given by (3.3).

The equations (B.10), (B.13), (B.17) and (3.3) constitute the set of partial differential equations that embodies the instantaneous energy exchanges between the four part of total energy. However, it is not obvious from these equations how the energy exchanges between the four part of total energy must be understood. Following the criteria described in section B.1.1, it is rewritten as:

$$\frac{\partial \rho \underline{E}}{\partial t} + \frac{\partial \rho U_j \underline{E}}{\partial x_j} - \frac{\partial \Upsilon_{ij} \bar{U}_i}{\partial x_j} = -\rho \bar{U}_i U_j \frac{\partial u'_i}{\partial x_j} + \rho \bar{U}_i \left(U_j \frac{\partial U_i}{\partial x_j} \right)' - \rho \bar{U}_i \left(\frac{1}{\rho} \frac{\partial \Upsilon_{ij}}{\partial x_j} \right)' - \Upsilon_{ij} \frac{\partial \bar{U}_i}{\partial x_j}, \quad (\text{B.18})$$

$$\frac{\partial \rho e}{\partial t} + \frac{\partial \rho U_j e}{\partial x_j} - \frac{\partial \Upsilon_{ij} u'_i}{\partial x_j} = -\rho u'_i U_j \frac{\partial \bar{U}_i}{\partial x_j} + \rho u'_i U_j \frac{\partial \bar{U}_i}{\partial x_j} - \rho u'_i \frac{1}{\rho} \frac{\partial \Upsilon_{ij}}{\partial x_j} - \Upsilon_{ij} \frac{\partial u'_i}{\partial x_j}, \quad (\text{B.19})$$

$$\begin{aligned} \frac{\partial \rho \underline{e}}{\partial t} + \frac{\partial \rho U_j \underline{e}}{\partial x_j} &= \rho \bar{U}_i U_j \frac{\partial u'_i}{\partial x_j} - \rho \bar{U}_i \left(U_j \frac{\partial U_i}{\partial x_j} \right)' + \rho \bar{U}_i \left(\frac{1}{\rho} \frac{\partial \Upsilon_{ij}}{\partial x_j} \right)' \\ &\quad + \rho u'_i U_j \frac{\partial \bar{U}_i}{\partial x_j} - \rho u'_i U_j \frac{\partial \bar{U}_i}{\partial x_j} + \rho u'_i \frac{1}{\rho} \frac{\partial \Upsilon_{ij}}{\partial x_j}, \end{aligned} \quad (\text{B.20})$$

$$\frac{\partial \rho I}{\partial t} + \frac{\partial \rho U_j I}{\partial x_j} - \frac{\partial}{\partial x_j} \left(\lambda \frac{\partial T}{\partial x_j} \right) = \frac{\rho \Upsilon_{ij}}{\rho} \frac{\partial \bar{U}_i}{\partial x_j} + \Upsilon_{ij} \frac{\partial u'_i}{\partial x_j}. \quad (\text{B.21})$$

With the notations (3.13) to (3.22), equations (B.18), (B.19), (B.20) and (B.21) leads to the system of equations (3.9)–(3.12).

B.1.3 Two-stage formulation

In order to identify the energy exchanges between the different parts of the eightfold decomposition (B.4) of total kinetic energy, we shall derive the evolution equation of each of these quantities. We recall that the two-stage formulation is based on the decomposition of density into a constant part ρ_0 and a variable part $\rho_1 = \bar{\rho}_1 + \rho'_1$, that is $\rho = \rho_0 + \bar{\rho}_1 + \rho'_1$. This intends to have the formulation involve quantities more directly comparable to those of the incompressible case, in which the density is a constant.

First, to obtain the evolution equation of the constant density part of the mean kinetic energy $\rho_0 \underline{E}$, we multiply equation (B.5) by $\rho_0 \bar{U}_i$,

$$\frac{\partial \rho_0 \underline{E}}{\partial t} + \rho_0 \bar{U}_i U_j \overline{\frac{\partial U_i}{\partial x_j}} = \rho_0 \bar{U}_i \overline{\frac{1}{\rho} \frac{\partial \mathcal{R}_{ij}}{\partial x_j}}. \quad (\text{B.22})$$

Second, to obtain the evolution equation of the variable density part of the mean kinetic energy $\rho_1 \underline{E}$, we will take the sum of two contributions. First, we multiply equation (B.5) by $\rho_1 \bar{U}_i$,

$$\rho_1 \frac{\partial \underline{E}}{\partial t} + \rho_1 \bar{U}_i U_j \overline{\frac{\partial U_i}{\partial x_j}} = \rho_1 \bar{U}_i \overline{\frac{1}{\rho} \frac{\partial \mathcal{R}_{ij}}{\partial x_j}}. \quad (\text{B.23})$$

Next, we multiply the mass conservation equation (3.1) by \underline{E} ,

$$\underline{E} \frac{\partial \rho_1}{\partial t} + \underline{E} \frac{\partial (\rho_0 + \rho_1) U_j}{\partial x_j} = 0. \quad (\text{B.24})$$

The summation of equations (B.23) and (B.24) gives:

$$\frac{\partial \rho_1 \underline{E}}{\partial t} + \underline{E} \frac{\partial \rho_0 U_j}{\partial x_j} + \underline{E} \frac{\partial \rho_1 U_j}{\partial x_j} + \rho_1 \bar{U}_i U_j \overline{\frac{\partial U_i}{\partial x_j}} = \rho_1 \bar{U}_i \overline{\frac{1}{\rho} \frac{\partial \mathcal{R}_{ij}}{\partial x_j}}. \quad (\text{B.25})$$

Third, to obtain the evolution equation of the constant density part of the turbulence kinetic energy $\rho_0 e$, we multiply equation (B.6) by $\rho_0 u'_i$,

$$\frac{\partial \rho_0 e}{\partial t} + \rho_0 u'_i \left(U_j \frac{\partial U_i}{\partial x_j} \right)' = \rho_0 u'_i \left(\frac{1}{\rho} \frac{\partial \mathcal{R}_{ij}}{\partial x_j} \right)'. \quad (\text{B.26})$$

Fourth, to obtain the evolution equation of the variable density part of the turbulence kinetic energy $\rho_1 e$, we will take the sum of two contributions. First, we multiply equation (B.6) by $\rho_1 u'_i$,

$$\rho_1 \frac{\partial e}{\partial t} + \rho_1 u'_i \left(U_j \frac{\partial U_i}{\partial x_j} \right)' = \rho_1 u'_i \left(\frac{1}{\rho} \frac{\partial \mathcal{R}_{ij}}{\partial x_j} \right)'. \quad (\text{B.27})$$

Next, we multiply the mass conservation equation (3.1) by e ,

$$e \frac{\partial \rho_1}{\partial t} + e \frac{\partial (\rho_0 + \rho_1) U_j}{\partial x_j} = 0. \quad (\text{B.28})$$

The summation of equations (B.27) and (B.28) gives:

$$\frac{\partial \rho_1 e}{\partial t} + e \frac{\partial \rho_0 U_j}{\partial x_j} + e \frac{\partial \rho_1 U_j}{\partial x_j} + \rho_1 u'_i \left(U_j \frac{\partial U_i}{\partial x_j} \right)' = \rho_1 u'_i \left(\frac{1}{\rho} \frac{\partial \mathcal{Y}_{ij}}{\partial x_j} \right)'. \quad (\text{B.29})$$

Fifth, to obtain the evolution equation of the constant density part of the mixed kinetic energy $\rho_0 \underline{e}$, we will take the sum of two contributions. First, we multiply equation (B.5) by $\rho_0 u'_i$,

$$\rho_0 u'_i \frac{\partial \bar{U}_i}{\partial t} + \rho_0 u'_i U_j \frac{\partial \bar{U}_i}{\partial x_j} = \rho_0 u'_i \frac{\overline{1 \partial \mathcal{Y}_{ij}}}{\rho \partial x_j}. \quad (\text{B.30})$$

Next, we multiply equation (B.6) by $\rho_0 \bar{U}_i$,

$$\rho_0 \bar{U}_i \frac{\partial u'_i}{\partial t} + \rho_0 \bar{U}_i \left(U_j \frac{\partial U_i}{\partial x_j} \right)' = \rho_0 \bar{U}_i \left(\frac{1}{\rho} \frac{\partial \mathcal{Y}_{ij}}{\partial x_j} \right)'. \quad (\text{B.31})$$

The summation of equations (B.30) and (B.31) gives:

$$\frac{\partial \rho_0 \underline{e}}{\partial t} + \rho_0 u'_i U_j \frac{\partial \bar{U}_i}{\partial x_j} + \rho_0 \bar{U}_i \left(U_j \frac{\partial U_i}{\partial x_j} \right)' = \rho_0 u'_i \frac{\overline{1 \partial \mathcal{Y}_{ij}}}{\rho \partial x_j} + \rho_0 \bar{U}_i \left(\frac{1}{\rho} \frac{\partial \mathcal{Y}_{ij}}{\partial x_j} \right)'. \quad (\text{B.32})$$

Sixth, to obtain the evolution equation of the variable density part of the mixed kinetic energy $\rho_1 \underline{e}$, we will take the sum of three contributions. First, we multiply equation (B.5) by $\rho_1 u'_i$,

$$\rho_1 u'_i \frac{\partial \bar{U}_i}{\partial t} + \rho_1 u'_i U_j \frac{\partial \bar{U}_i}{\partial x_j} = \rho_1 u'_i \frac{\overline{1 \partial \mathcal{Y}_{ij}}}{\rho \partial x_j}. \quad (\text{B.33})$$

Next, we multiply equation (B.6) by $\rho_1 \bar{U}_i$,

$$\rho_1 \bar{U}_i \frac{\partial u'_i}{\partial t} + \rho_1 \bar{U}_i \left(U_j \frac{\partial U_i}{\partial x_j} \right)' = \rho_1 \bar{U}_i \left(\frac{1}{\rho} \frac{\partial \mathcal{Y}_{ij}}{\partial x_j} \right)'. \quad (\text{B.34})$$

Finally, we multiply the mass conservation equation (3.1) by \underline{e} ,

$$\underline{e} \frac{\partial \rho_1}{\partial t} + \underline{e} \frac{\partial (\rho_0 + \rho_1) U_j}{\partial x_j} = 0. \quad (\text{B.35})$$

The summation of equations (B.33), (B.34) and (B.35) gives:

$$\frac{\partial \rho_1 \underline{e}}{\partial t} + \underline{e} \frac{\partial \rho_0 U_j}{\partial x_j} + \underline{e} \frac{\partial \rho_1 U_j}{\partial x_j} + \rho_1 u'_i U_j \frac{\partial \bar{U}_i}{\partial x_j} + \rho_1 \bar{U}_i \left(U_j \frac{\partial U_i}{\partial x_j} \right)' = \rho_1 u'_i \frac{\overline{1 \partial \mathcal{Y}_{ij}}}{\rho \partial x_j} + \rho_1 \bar{U}_i \left(\frac{1}{\rho} \frac{\partial \mathcal{Y}_{ij}}{\partial x_j} \right)'. \quad (\text{B.36})$$

Seventh, to obtain the evolution equation of the constant density part of the internal energy $\rho_0 I$, we multiply equation (B.7) by ρ_0 ,

$$\frac{\partial \rho_0 I}{\partial t} + \rho_0 U_j \frac{\partial I}{\partial x_j} = \frac{\rho_0}{\rho} \frac{\partial}{\partial x_j} \left(\lambda \frac{\partial T}{\partial x_j} \right) + \frac{\rho_0 \mathcal{Y}_{ij}}{\rho} \frac{\partial U_i}{\partial x_j}. \quad (\text{B.37})$$

Eighth, to obtain the evolution equation of the variable density part of the internal energy $\rho_1 I$, we will take the sum of two contributions. First, we multiply equation (B.7) by ρ_1 ,

$$\rho_1 \frac{\partial I}{\partial t} + \rho_1 U_j \frac{\partial I}{\partial x_j} = \frac{\rho_1}{\rho} \frac{\partial}{\partial x_j} \left(\lambda \frac{\partial T}{\partial x_j} \right) + \frac{\rho_1 \Upsilon_{ij}}{\rho} \frac{\partial U_i}{\partial x_j}. \quad (\text{B.38})$$

Next, we multiply the mass conservation equation (3.1) by I ,

$$I \frac{\partial \rho_1}{\partial t} + I \frac{\partial (\rho_0 + \rho_1) U_j}{\partial x_j} = 0. \quad (\text{B.39})$$

The summation of equations (B.38) and (B.39) gives:

$$\frac{\partial \rho_1 I}{\partial t} + I \frac{\partial \rho_0 U_j}{\partial x_j} + I \frac{\partial \rho_1 U_j}{\partial x_j} + \rho_1 U_j \frac{\partial I}{\partial x_j} = \frac{\rho_1}{\rho} \frac{\partial}{\partial x_j} \left(\lambda \frac{\partial T}{\partial x_j} \right) + \frac{\rho_1 \Upsilon_{ij}}{\rho} \frac{\partial U_i}{\partial x_j}. \quad (\text{B.40})$$

Following the criteria described in section B.1.1, the equations (B.22), (B.25), (B.26), (B.29), (B.32), (B.36), (B.37) and (B.40) are rewritten as:

$$\begin{aligned} \frac{\partial \rho_0 \underline{E}}{\partial t} + \frac{\partial \rho_0 U_j \underline{E}}{\partial x_j} - \frac{\partial}{\partial x_j} \left(\frac{\rho_0 \Upsilon_{ij}}{\rho} \bar{U}_i \right) &= -\rho_0 \bar{U}_i U_j \frac{\partial u'_i}{\partial x_j} + \rho_0 \bar{U}_i \left(U_j \frac{\partial U_i}{\partial x_j} \right)' - \rho_0 \bar{U}_i \left(\frac{1}{\rho} \frac{\partial \Upsilon_{ij}}{\partial x_j} \right)' \\ &\quad + \rho_0 \underline{E} \frac{\partial U_j}{\partial x_j} - \Upsilon_{ij} \bar{U}_i \frac{\partial}{\partial x_j} \left(\frac{\rho_0}{\rho} \right) - \frac{\rho_0 \Upsilon_{ij}}{\rho} \frac{\partial \bar{U}_i}{\partial x_j}, \end{aligned} \quad (\text{B.41})$$

$$\begin{aligned} \frac{\partial \rho_1 \underline{E}}{\partial t} + \frac{\partial \rho_1 U_j \underline{E}}{\partial x_j} - \frac{\partial}{\partial x_j} \left(\frac{\rho_1 \Upsilon_{ij}}{\rho} \bar{U}_i \right) &= -\rho_1 \bar{U}_i U_j \frac{\partial u'_i}{\partial x_j} + \rho_1 \bar{U}_i \left(U_j \frac{\partial U_i}{\partial x_j} \right)' - \rho_1 \bar{U}_i \left(\frac{1}{\rho} \frac{\partial \Upsilon_{ij}}{\partial x_j} \right)' \\ &\quad - \rho_0 \underline{E} \frac{\partial U_j}{\partial x_j} + \Upsilon_{ij} \bar{U}_i \frac{\partial}{\partial x_j} \left(\frac{\rho_0}{\rho} \right) - \frac{\rho_1 \Upsilon_{ij}}{\rho} \frac{\partial \bar{U}_i}{\partial x_j}, \end{aligned} \quad (\text{B.42})$$

$$\begin{aligned} \frac{\partial \rho_0 e}{\partial t} + \frac{\partial \rho_0 U_j e}{\partial x_j} - \frac{\partial}{\partial x_j} \left(\frac{\rho_0 \Upsilon_{ij}}{\rho} u'_i \right) &= -\rho_0 u'_i U_j \frac{\partial \bar{U}_i}{\partial x_j} + \rho_0 u'_i U_j \frac{\partial \bar{U}_i}{\partial x_j} - \rho_0 u'_i \frac{1}{\rho} \frac{\partial \Upsilon_{ij}}{\partial x_j} \\ &\quad + \rho_0 e \frac{\partial U_j}{\partial x_j} - \Upsilon_{ij} u'_i \frac{\partial}{\partial x_j} \left(\frac{\rho_0}{\rho} \right) - \frac{\rho_0 \Upsilon_{ij}}{\rho} \frac{\partial u'_i}{\partial x_j}, \end{aligned} \quad (\text{B.43})$$

$$\begin{aligned} \frac{\partial \rho_1 e}{\partial t} + \frac{\partial \rho_1 U_j e}{\partial x_j} - \frac{\partial}{\partial x_j} \left(\frac{\rho_1 \Upsilon_{ij}}{\rho} u'_i \right) &= -\rho_1 u'_i U_j \frac{\partial \bar{U}_i}{\partial x_j} + \rho_1 u'_i U_j \frac{\partial \bar{U}_i}{\partial x_j} - \rho_1 u'_i \frac{1}{\rho} \frac{\partial \Upsilon_{ij}}{\partial x_j} \\ &\quad - \rho_0 e \frac{\partial U_j}{\partial x_j} + \Upsilon_{ij} u'_i \frac{\partial}{\partial x_j} \left(\frac{\rho_0}{\rho} \right) - \frac{\rho_1 \Upsilon_{ij}}{\rho} \frac{\partial u'_i}{\partial x_j}, \end{aligned} \quad (\text{B.44})$$

$$\begin{aligned} \frac{\partial \rho_0 \underline{e}}{\partial t} + \frac{\partial \rho_0 U_j \underline{e}}{\partial x_j} &= \rho_0 \bar{U}_i U_j \frac{\partial u'_i}{\partial x_j} - \rho_0 \bar{U}_i \left(U_j \frac{\partial U_i}{\partial x_j} \right)' + \rho_0 \bar{U}_i \left(\frac{1}{\rho} \frac{\partial \Upsilon_{ij}}{\partial x_j} \right)' \\ &\quad + \rho_0 u'_i U_j \frac{\partial \bar{U}_i}{\partial x_j} - \rho_0 u'_i U_j \frac{\partial \bar{U}_i}{\partial x_j} + \rho_0 u'_i \frac{1}{\rho} \frac{\partial \Upsilon_{ij}}{\partial x_j} + \rho_0 \underline{e} \frac{\partial U_j}{\partial x_j}, \end{aligned} \quad (\text{B.45})$$

$$\begin{aligned} \frac{\partial \rho_1 \underline{e}}{\partial t} + \frac{\partial \rho_1 U_j \underline{e}}{\partial x_j} &= \rho_1 \bar{U}_i U_j \frac{\partial u'_i}{\partial x_j} - \rho_1 \bar{U}_i \left(U_j \frac{\partial U_i}{\partial x_j} \right)' + \rho_1 \bar{U}_i \left(\frac{1}{\rho} \frac{\partial \Upsilon_{ij}}{\partial x_j} \right)' \\ &\quad + \rho_1 u'_i U_j \frac{\partial \bar{U}_i}{\partial x_j} - \rho_1 u'_i U_j \frac{\partial \bar{U}_i}{\partial x_j} + \rho_1 u'_i \frac{1}{\rho} \frac{\partial \Upsilon_{ij}}{\partial x_j} - \rho_0 \underline{e} \frac{\partial U_j}{\partial x_j}, \end{aligned} \quad (\text{B.46})$$

$$\begin{aligned} \frac{\partial \rho_0 I}{\partial t} + \frac{\partial \rho_0 U_j I}{\partial x_j} - \frac{\partial}{\partial x_j} \left(\frac{\rho_0 \lambda}{\rho} \frac{\partial T}{\partial x_j} \right) &= \rho_0 I \frac{\partial U_j}{\partial x_j} - \lambda \frac{\partial T}{\partial x_j} \frac{\partial}{\partial x_j} \left(\frac{\rho_0}{\rho} \right) \\ &\quad + \frac{\rho_0 \Upsilon_{ij}}{\rho} \frac{\partial \bar{U}_i}{\partial x_j} + \frac{\rho_0 \Upsilon_{ij}}{\rho} \frac{\partial u'_i}{\partial x_j}, \end{aligned} \quad (\text{B.47})$$

$$\begin{aligned} \frac{\partial \rho_1 I}{\partial t} + \frac{\partial \rho_1 U_j I}{\partial x_j} - \frac{\partial}{\partial x_j} \left(\frac{\rho_1 \lambda}{\rho} \frac{\partial T}{\partial x_j} \right) &= -\rho_0 I \frac{\partial U_j}{\partial x_j} + \lambda \frac{\partial T}{\partial x_j} \frac{\partial}{\partial x_j} \left(\frac{\rho_0}{\rho} \right) \\ &\quad + \frac{\rho_1 \Upsilon_{ij}}{\rho} \frac{\partial \bar{U}_i}{\partial x_j} + \frac{\rho_1 \Upsilon_{ij}}{\rho} \frac{\partial u'_i}{\partial x_j}. \end{aligned} \quad (\text{B.48})$$

The comparison of equations (B.41), (B.42), (B.43), (B.44), (B.45), (B.46), (B.47) and (B.48) let us identify the following terms:

- the convection Φ^c (??), which is decomposed into eight parts: $\underline{\Phi}_0^c$ associated with the constant density mean kinetic energy, $\underline{\Phi}_1^c$ associated with the variable density mean kinetic energy, φ_0^c associated with the constant density turbulence kinetic energy, φ_1^c associated with the variable density turbulence kinetic energy, $\underline{\varphi}_0^c$ associated with the constant density mixed kinetic energy, $\underline{\varphi}_1^c$ associated with the variable density mixed kinetic energy, $\Phi_0^{T,c}$ associated with constant density internal energy and $\Phi_1^{T,c}$ associated with variable density internal energy,

$$\Phi^c = \underline{\Phi}_0^c + \underline{\Phi}_1^c + \varphi_0^c + \varphi_1^c + \underline{\varphi}_0^c + \underline{\varphi}_1^c + \Phi_0^{T,c} + \Phi_1^{T,c}, \quad (\text{B.49})$$

with

$$\underline{\Phi}_0^c = -\frac{\partial \rho_0 U_j \underline{E}}{\partial x_j}, \quad (\text{B.50})$$

$$\underline{\Phi}_1^c = -\frac{\partial \rho_1 U_j \underline{E}}{\partial x_j}, \quad (\text{B.51})$$

$$\varphi_0^c = -\frac{\partial \rho_0 U_j e}{\partial x_j}, \quad (\text{B.52})$$

$$\varphi_1^c = -\frac{\partial \rho_1 U_j e}{\partial x_j}, \quad (\text{B.53})$$

$$\underline{\varphi}_0^c = -\frac{\partial \rho_0 U_j \underline{e}}{\partial x_j}, \quad (\text{B.54})$$

$$\underline{\varphi}_1^c = -\frac{\partial \rho_1 U_j \underline{e}}{\partial x_j}, \quad (\text{B.55})$$

$$\Phi_0^{T,c} = -\frac{\partial \rho_0 U_j I}{\partial x_j}, \quad (\text{B.56})$$

$$\Phi_1^{T,c} = -\frac{\partial \rho_1 U_j I}{\partial x_j}, \quad (\text{B.57})$$

- the transfer by external force $\Phi^{\mathcal{R}}$ (3.7), which is decomposed into four parts: $\underline{\Phi}_0^{\mathcal{R}}$ associated with the constant density mean kinetic energy, $\underline{\Phi}_1^{\mathcal{R}}$ associated with the variable density mean kinetic energy, $\varphi_0^{\mathcal{R}}$ associated with the constant density turbulence kinetic energy and $\varphi_1^{\mathcal{R}}$ associated with the variable density turbulence kinetic energy,

$$\Phi^{\mathcal{R}} = \underline{\Phi}_0^{\mathcal{R}} + \underline{\Phi}_1^{\mathcal{R}} + \varphi_0^{\mathcal{R}} + \varphi_1^{\mathcal{R}}, \quad (\text{B.58})$$

with

$$\underline{\Phi}_0^{\mathcal{R}} = \frac{\partial}{\partial x_j} \left(\frac{\Upsilon_{ij}}{\rho} \rho_0 \bar{U}_i \right), \quad (\text{B.59})$$

$$\underline{\Phi}_1^{\mathcal{R}} = \frac{\partial}{\partial x_j} \left(\frac{\Upsilon_{ij}}{\rho} \rho_1 \bar{U}_i \right), \quad (\text{B.60})$$

$$\varphi_0^{\mathcal{R}} = \frac{\partial}{\partial x_j} \left(\frac{\Upsilon_{ij}}{\rho} \rho_0 u'_i \right), \quad (\text{B.61})$$

$$\varphi_1^{\mathcal{R}} = \frac{\partial}{\partial x_j} \left(\frac{\Upsilon_{ij}}{\rho} \rho_1 u'_i \right), \quad (\text{B.62})$$

- the transfer by conduction Φ^λ (3.8), which is decomposed into two parts: Φ_0^λ associated with the constant density internal energy and Φ_1^λ associated with the variable density internal energy,

$$\Phi^\lambda = \Phi_0^\lambda + \Phi_1^\lambda, \quad (\text{B.63})$$

with

$$\Phi_0^\lambda = \frac{\partial}{\partial x_j} \left(\frac{\rho_0}{\rho} \lambda \frac{\partial T}{\partial x_j} \right), \quad (\text{B.64})$$

$$\Phi_1^\lambda = \frac{\partial}{\partial x_j} \left(\frac{\rho_1}{\rho} \lambda \frac{\partial T}{\partial x_j} \right), \quad (\text{B.65})$$

- the interaction between the turbulence kinetic energy and the mixed kinetic energy \mathcal{P} (3.19), which is decomposed into two parts: \mathcal{P}_0 associated with the constant density kinetic energy and \mathcal{P}_1 associated with the variable density kinetic energy,

$$\mathcal{P} = \mathcal{P}_0 + \mathcal{P}_1, \quad (\text{B.66})$$

with

$$\mathcal{P}_0 = -\rho_0 u'_i U_j \frac{\partial \bar{U}_i}{\partial x_j} + \rho_0 u'_i U_j \frac{\partial u'_i}{\partial x_j} - \rho_0 u'_i \frac{\overline{1 \partial \Upsilon_{ij}}}{\rho \partial x_j}, \quad (\text{B.67})$$

$$\mathcal{P}_1 = -\rho_1 u'_i U_j \frac{\partial \bar{U}_i}{\partial x_j} + \rho_1 u'_i U_j \frac{\partial u'_i}{\partial x_j} - \rho_1 u'_i \frac{\overline{1 \partial \Upsilon_{ij}}}{\rho \partial x_j}, \quad (\text{B.68})$$

- the interaction between the mean kinetic energy and the mixed kinetic energy $\underline{\mathcal{P}}$ (3.20), which is decomposed into two parts: $\underline{\mathcal{P}}_0$ associated with the constant density kinetic energy and $\underline{\mathcal{P}}_1$ associated with the variable density kinetic energy,

$$\underline{\mathcal{P}} = \underline{\mathcal{P}}_0 + \underline{\mathcal{P}}_1, \quad (\text{B.69})$$

with

$$\underline{\mathcal{P}}_0 = -\rho_0 \bar{U}_i U_j \frac{\partial u'_i}{\partial x_j} + \rho_0 \bar{U}_i \left(U_j \frac{\partial U_i}{\partial x_j} \right)' - \rho_0 \bar{U}_i \left(\frac{1}{\rho} \frac{\partial \Upsilon_{ij}}{\partial x_j} \right)', \quad (\text{B.70})$$

$$\underline{\mathcal{P}}_1 = -\rho_1 \bar{U}_i U_j \frac{\partial u'_i}{\partial x_j} + \rho_1 \bar{U}_i \left(U_j \frac{\partial U_i}{\partial x_j} \right)' - \rho_1 \bar{U}_i \left(\frac{1}{\rho} \frac{\partial \Upsilon_{ij}}{\partial x_j} \right)', \quad (\text{B.71})$$

- the energy dilatation correlation Z^c ,

$$Z^c = \rho_0(E + I) \frac{\partial U_j}{\partial x_j}, \quad (\text{B.72})$$

which is decomposed into four parts: \underline{Z}^c associated with the mean kinetic energy, ζ^c associated with the turbulence kinetic energy, $\underline{\zeta}^c$ associated with the mixed kinetic energy and $Z^{T,c}$ associated with the internal energy,

$$Z^c = \underline{Z}^c + \zeta^c + \underline{\zeta}^c + Z^{T,c}, \quad (\text{B.73})$$

with

$$\underline{Z}^c = \rho_0 \underline{E} \frac{\partial U_j}{\partial x_j}, \quad (\text{B.74})$$

$$\zeta^c = \rho_0 e \frac{\partial U_j}{\partial x_j}, \quad (\text{B.75})$$

$$\underline{\zeta}^c = \rho_0 \underline{e} \frac{\partial U_j}{\partial x_j}, \quad (\text{B.76})$$

$$Z^{T,c} = \rho_0 I \frac{\partial U_j}{\partial x_j}, \quad (\text{B.77})$$

- the interaction between the constant and variable density part of total energy by external force Z^R ,

$$Z^R = -\gamma_{ij} U_i \frac{\partial}{\partial x_j} \left(\frac{\rho_0}{\rho} \right), \quad (\text{B.78})$$

which is decomposed into two parts: \underline{Z}^R associated with the mean kinetic energy and ζ^R associated with the turbulence kinetic energy,

$$Z^R = \underline{Z}^R + \zeta^R, \quad (\text{B.79})$$

with

$$\underline{Z}^R = -\gamma_{ij} \bar{U}_i \frac{\partial}{\partial x_j} \left(\frac{\rho_0}{\rho} \right), \quad (\text{B.80})$$

$$\zeta^R = -\gamma_{ij} u'_i \frac{\partial}{\partial x_j} \left(\frac{\rho_0}{\rho} \right), \quad (\text{B.81})$$

- the interaction between the constant and variable density part of total energy by conduction Z^λ ,

$$Z^\lambda = -\lambda \frac{\partial T}{\partial x_j} \frac{\partial}{\partial x_j} \left(\frac{\rho_0}{\rho} \right), \quad (\text{B.82})$$

- the interaction between kinetic energy and internal energy \mathcal{E} , which is decomposed into four parts: $\underline{\mathcal{E}}_0$ associated with the constant density mean kinetic energy, $\underline{\mathcal{E}}_1$ associated with the variable density mean kinetic energy, ε_0 associated with the constant density turbulence kinetic energy and ε_1 associated with the variable density turbulence kinetic energy,

$$\mathcal{E} = \underline{\mathcal{E}}_0 + \underline{\mathcal{E}}_1 + \varepsilon_0 + \varepsilon_1, \quad (\text{B.83})$$

with

$$\underline{\mathcal{E}}_0 = -\frac{\rho_0 \Upsilon_{ij}}{\rho} \frac{\partial \bar{U}_i}{\partial x_j}, \quad (\text{B.84})$$

$$\underline{\mathcal{E}}_1 = -\frac{\rho_1 \Upsilon_{ij}}{\rho} \frac{\partial \bar{U}_i}{\partial x_j}, \quad (\text{B.85})$$

$$\varepsilon_0 = -\frac{\rho_0 \Upsilon_{ij}}{\rho} \frac{\partial u'_i}{\partial x_j}, \quad (\text{B.86})$$

$$\varepsilon_1 = -\frac{\rho_1 \Upsilon_{ij}}{\rho} \frac{\partial u'_i}{\partial x_j}. \quad (\text{B.87})$$

With those notations, equations (B.41), (B.42), (B.43), (B.44), (B.45), (B.46), (B.47) and (B.48) are rewritten as:

$$\frac{\partial \rho_0 \underline{E}}{\partial t} = \underline{\Phi}_0^c + \underline{\Phi}_0^r + \underline{\mathcal{P}}_0 + \underline{Z}^c + \underline{Z}^r + \underline{\mathcal{E}}_0, \quad (\text{B.88})$$

$$\frac{\partial \rho_1 \underline{E}}{\partial t} = \underline{\Phi}_1^c + \underline{\Phi}_1^r + \underline{\mathcal{P}}_1 - \underline{Z}^c - \underline{Z}^r + \underline{\mathcal{E}}_1, \quad (\text{B.89})$$

$$\frac{\partial \rho_0 e}{\partial t} = \varphi_0^c + \varphi_0^r + \mathcal{P}_0 + \zeta^c + \zeta^r + \varepsilon_0, \quad (\text{B.90})$$

$$\frac{\partial \rho_1 e}{\partial t} = \varphi_1^c + \varphi_1^r + \mathcal{P}_1 - \zeta^c - \zeta^r + \varepsilon_1, \quad (\text{B.91})$$

$$\frac{\partial \rho_0 \underline{e}}{\partial t} = \underline{\varphi}_0^c - \underline{\mathcal{P}}_0 - \underline{\mathcal{P}}_0 + \underline{\zeta}^c, \quad (\text{B.92})$$

$$\frac{\partial \rho_1 \underline{e}}{\partial t} = \underline{\varphi}_1^c - \underline{\mathcal{P}}_1 - \underline{\mathcal{P}}_1 - \underline{\zeta}^c, \quad (\text{B.93})$$

$$\frac{\partial \rho_0 I}{\partial t} = \Phi_0^{T,c} + \Phi_0^\lambda + Z^{T,c} + Z^\lambda - \underline{\mathcal{E}}_0 - \varepsilon_0, \quad (\text{B.94})$$

$$\frac{\partial \rho_1 I}{\partial t} = \Phi_1^{T,c} + \Phi_1^\lambda - Z^{T,c} - Z^\lambda - \underline{\mathcal{E}}_1 - \varepsilon_1. \quad (\text{B.95})$$

This set of equations is very similar to the system of equations (3.29)–(3.36) obtained with a Reynolds decomposition of density.

B.2 Decomposition of the terms associated with constant density turbulence kinetic energy

In this section, we consider a fully developed turbulent channel flow as in section 4.2.4. The flow is compressible and has highly variable fluid properties thus falls into the scope of the analysis of section B.1. This lets us use the two-stage formulation to investigate the energy exchanges within the flow. We study in particular the constant density turbulence kinetic energy, that we recall is given by the half-trace of the velocity fluctuation correlation tensor up to the constant scalar factor ρ_0 . We will investigate the terms of its evolution equation in the spatial and spectral domain. In both cases, we decompose the terms of its evolution equation to make the incompressible part of each term emerge, that is the part that does not vanish to zero in incompressible

flows with constant fluid properties. The incompressible part of each term henceforth called incompressible terms are written in a formally identical manner to the terms of the evolution equation of the turbulence kinetic energy known to the literature for incompressible flows [312, 235]. Though, their actual behaviour is a priori different in a compressible configuration because of the temperature velocity coupling. Identifying incompressible terms will at the same time shed light on the terms specific to compressible flows with variable fluid properties, whether because the incompressibility condition is no longer obeyed or because of the variations of the fluid properties with temperature. These terms will henceforth be referred to as the thermal terms.

B.2.1 Hypothesis and geometry

We denote x the streamwise direction, y the wall-normal direction and z the spanwise direction. The dimensions of the domain in the x , y and z directions are denoted L_x , L_y and L_z respectively. The flow has two directions of homogeneity, x and z , and a zero mean spanwise velocity, $\overline{U}_z = 0$. In an incompressible flow with constant fluid properties, the mean wall-normal velocity would also be zero, $\overline{U}_y = 0$. The mean wall-normal velocity \overline{U}_y differs from zero in the compressible variable density channel because it is in balance with the turbulent mass flux $\overline{\rho' u'_y}$: $\overline{\rho} \overline{U}_y = -\overline{\rho' u'_y}$.

The external force tensor Υ_{ij} is the sum of the viscous shear stress tensor Σ_{ij} and of pressure stress:

$$\Upsilon_{ij} = \Sigma_{ij} - P\delta_{ij}. \quad (\text{B.96})$$

We assume a Newtonian fluid and neglect the bulk viscosity. The viscous shear stress tensor is thus given by

$$\Sigma_{ij} = 2\mu S_{ij} - \frac{2\mu}{3} S_{kk} \delta_{ij}, \quad (\text{B.97})$$

with S_{ij} the rate of deformation tensor,

$$S_{ij} = \frac{1}{2} \left(\frac{\partial U_i}{\partial x_j} + \frac{\partial U_j}{\partial x_i} \right), \quad (\text{B.98})$$

whose fluctuating part will be denoted s'_{ij} hereafter.

B.2.2 Decomposition in the spatial domain

The evolution equation of the half-trace of the velocity fluctuation correlation tensor e is identical to equation (B.43) up to a scalar factor ρ_0 ,

$$\frac{\partial e}{\partial t} = -\frac{\partial \overline{U}_j e}{\partial x_j} + \frac{\partial}{\partial x_j} \frac{\overline{\Upsilon_{ij}}}{\rho} u'_i - \overline{u'_i u'_j} \frac{\partial \overline{U}_i}{\partial x_j} + e \frac{\partial \overline{U}_j}{\partial x_j} - \overline{\Upsilon_{ij} u'_i} \frac{\partial}{\partial x_j} \left(\frac{1}{\rho} \right) - \frac{\overline{\Upsilon_{ij}}}{\rho} \frac{\partial u'_i}{\partial x_j}. \quad (\text{B.99})$$

In the following, we will use new notations to remove the constant part of density from the notations given in equations (B.49) to (B.87). We identify the following terms:

- the convection $\overline{\varphi}^{c\dagger}$,

$$\overline{\varphi}^{c\dagger} = \frac{\overline{\varphi_0^c}}{\rho_0} = -\frac{\partial \overline{e U_j}}{\partial x_j}, \quad (\text{B.100})$$

- the transfer by external force $\overline{\varphi^{\mathfrak{h}}}$,

$$\overline{\varphi^{\mathfrak{h}}} = \frac{\overline{\varphi_0^{\mathfrak{r}}}}{\rho_0} = \frac{\partial}{\partial x_j} \overline{\frac{\Upsilon_{ij}}{\rho} u'_i}, \quad (\text{B.101})$$

- the production $\overline{\mathcal{P}^{\mathfrak{h}}}$,

$$\overline{\mathcal{P}^{\mathfrak{h}}} = \frac{\overline{\mathcal{P}_0}}{\rho_0} = -\overline{u'_i u'_j} \frac{\partial \overline{U}_i}{\partial x_j}, \quad (\text{B.102})$$

- the kinetic energy dilatation correlation $\overline{\zeta^{c^{\mathfrak{h}}}}$,

$$\overline{\zeta^{c^{\mathfrak{h}}}} = \frac{\overline{\zeta^c}}{\rho_0} = e \overline{\frac{\partial U_j}{\partial x_j}}, \quad (\text{B.103})$$

- the interaction with variable density kinetic energy by external force $\overline{\zeta^{\mathfrak{r}^{\mathfrak{h}}}}$,

$$\overline{\zeta^{\mathfrak{r}^{\mathfrak{h}}}} = \frac{\overline{\zeta^{\mathfrak{r}}}}{\rho_0} = -\overline{\Upsilon_{ij} u'_i} \frac{\partial}{\partial x_j} \left(\frac{1}{\rho} \right), \quad (\text{B.104})$$

- the interaction with internal energy $\overline{\varepsilon^{\mathfrak{h}}}$,

$$\overline{\varepsilon^{\mathfrak{h}}} = \frac{\overline{\varepsilon_0}}{\rho_0} = -\overline{\frac{\Upsilon_{ij}}{\rho} \frac{\partial u'_i}{\partial x_j}}. \quad (\text{B.105})$$

With those notations, equation (B.99) is rewritten as

$$\frac{\partial \overline{e}}{\partial t} = \overline{\varphi^{c^{\mathfrak{h}}}} + \overline{\varphi^{\mathfrak{r}^{\mathfrak{h}}}} + \overline{\mathcal{P}^{\mathfrak{h}}} + \overline{\zeta^{c^{\mathfrak{h}}}} + \overline{\zeta^{\mathfrak{r}^{\mathfrak{h}}}} + \overline{\varepsilon^{\mathfrak{h}}}. \quad (\text{B.106})$$

Each term of the right-hand side of equation (B.99) will be decomposed in order to formally compare the equations of the half-trace of the velocity fluctuation correlation tensor in constant property incompressible fluid flows and variable density compressible flows, and identify the additional terms in the latter situation. We will use the symmetries of the flow and its homogeneity in the streamwise and spanwise directions to simplify the writing ($\frac{\partial \overline{\cdot}}{\partial x} = \frac{\partial \overline{\cdot}}{\partial z} = 0$ and $\overline{U}_z = 0$). We will also use the fact that the mean wall-normal velocity vanishes in the incompressible case ($\overline{U}_y = 0$) to identify incompressible terms.

A notational convention will be used where the subscript I denotes the incompressible part of a given term and the subscript Γ the complementary thermal part. A subscript comprising α other than I or Γ denotes a term that vanishes in incompressible flows with constant fluid properties because α vanishes to zero in this configuration. For instance, a subscript \overline{U}_y denotes a term that vanishes in the incompressible case because the mean wall-normal velocity \overline{U}_y goes to zero. This allows us to always recall which terms are purely compressible and have an indication of the physical reason why they are. In addition, when a term includes a product with the viscous shear stress tensor, it is decomposed in three parts. We denote with a subscript 1 the part associated with the product with the velocity gradient and with a subscript 2 the part associated with the product with the transpose of the velocity gradient. The part associated with the product with the velocity divergence is denoted with the subscript Θ since the term vanishes for an incompressible flow because of the dilatation $\Theta = \partial_j U_j$.

B.2.2.1 Decomposition of the convection

We decompose the convection (B.100) into an incompressible part $\overline{\varphi_I^{c\ddagger}}$ and a thermal part $\overline{\varphi_\Gamma^{c\ddagger}}$,

$$\overline{\varphi^{c\ddagger}} = -\frac{\partial \overline{eU_j}}{\partial x_j} = \overline{\varphi_I^{c\ddagger}} + \overline{\varphi_\Gamma^{c\ddagger}}, \quad (\text{B.107})$$

with

$$\overline{\varphi_I^{c\ddagger}} = -\frac{\partial \overline{eu'_y}}{\partial y}, \quad (\text{B.108})$$

$$\overline{\varphi_\Gamma^{c\ddagger}} = -\frac{\partial \overline{e\bar{U}_y}}{\partial y} = \overline{\varphi_{\bar{U}_y}^{c\ddagger}}. \quad (\text{B.109})$$

The incompressible part $\overline{\varphi_I^{c\ddagger}}$ of the convection is also called turbulent diffusion, turbulent transfer or turbulent convection in the literature since it is the diffusion of the constant density turbulence kinetic energy by the turbulent motion. The thermal part $\overline{\varphi_\Gamma^{c\ddagger}}$ similarly is called mean convection since it is the convection of the constant density turbulence kinetic energy by the mean motion. Given the homogeneity of the flow in the streamwise and spanwise directions, convection by the mean motion can only occur through the mean wall-normal velocity. It vanishes in the incompressible case since the mean flow becomes entirely streamwise.

B.2.2.2 Decomposition of the transfer by external force

The transfer by external force (B.101) is decomposed using (B.96) into the sum of a viscous contribution $\overline{\varphi^{\nu\ddagger}}$ and a pressure contribution $\overline{\varphi^{p\ddagger}}$,

$$\overline{\varphi^{\mathcal{R}\ddagger}} = \frac{\partial \overline{\mathcal{R}_{iy}}}{\partial y} \frac{u'_i}{\rho} = \overline{\varphi^{\nu\ddagger}} + \overline{\varphi^{p\ddagger}}, \quad (\text{B.110})$$

with

$$\overline{\varphi^{\nu\ddagger}} = \frac{\partial \overline{\Sigma_{iy}}}{\partial y} \frac{u'_i}{\rho}, \quad (\text{B.111})$$

$$\overline{\varphi^{p\ddagger}} = -\frac{\partial \overline{P}}{\partial x_i} \frac{u'_i}{\rho}. \quad (\text{B.112})$$

First, we focus on the viscous contribution. Using (B.97), we decompose the viscous transfer in a part associated with the rate of deformation tensor and a part associated with the dilatation,

$$\frac{\partial \overline{u'_i \Sigma_{iy}}}{\partial y} \frac{1}{\rho} = \frac{\partial}{\partial y} \left(\overline{2\nu u'_i S_{iy}} - \frac{2\nu}{3} \overline{S_{ii} u'_y} \right). \quad (\text{B.113})$$

We split viscosity into a mean and fluctuating part in the first term of the right-hand side of equation (B.113), $\nu = \bar{\nu} + \nu'$, then decompose the derivative to isolate the derivative of the mean viscosity,

$$\frac{\partial \overline{u'_i \Sigma_{iy}}}{\partial y} \frac{1}{\rho} = \bar{\nu} \frac{\partial \overline{2u'_i S_{iy}}}{\partial y} + \frac{\partial \bar{\nu}}{\partial y} \overline{2u'_i S_{iy}} + \frac{\partial}{\partial y} \left(\overline{2\nu' u'_i S_{iy}} - \frac{2\nu}{3} \overline{S_{ii} u'_y} \right). \quad (\text{B.114})$$

The first term of the right-hand side of this equation is the term with the mean viscosity outside the derivative. The decomposition of the rate of deformation tensor allows us to isolate a new term associated with the dilatation fluctuation $\vartheta' = \partial_j u'_j$.

$$\bar{\nu} \frac{\partial}{\partial y} \overline{2u'_i S_{iy}} = \bar{\nu} \frac{\partial^2 \bar{e}}{\partial y^2} + \bar{\nu} \frac{\partial^2 \overline{u'_y u'_y}}{\partial y^2} - \bar{\nu} \frac{\partial}{\partial y} \overline{u'_y \frac{\partial u'_i}{\partial x_i}} \quad (\text{B.115})$$

Hence, to decompose the viscous transfer into an incompressible part $\overline{\varphi_I^{\nu \dagger}}$ and a thermal part $\overline{\varphi_\Gamma^{\nu \dagger}}$,

$$\overline{\varphi^{\nu \dagger}} = \frac{\partial}{\partial y} \overline{\frac{\Sigma_{iy}}{\rho} u'_i} = \overline{\varphi_I^{\nu \dagger}} + \overline{\varphi_\Gamma^{\nu \dagger}}, \quad (\text{B.116})$$

we define

$$\overline{\varphi_I^{\nu \dagger}} = \overline{\varphi_{I,1}^{\nu \dagger}} + \overline{\varphi_{I,2}^{\nu \dagger}}, \quad (\text{B.117})$$

with

$$\overline{\varphi_{I,1}^{\nu \dagger}} = \bar{\nu} \frac{\partial^2 \bar{e}}{\partial y^2}, \quad (\text{B.118})$$

$$\overline{\varphi_{I,2}^{\nu \dagger}} = \bar{\nu} \frac{\partial^2 \overline{u'_y u'_y}}{\partial y^2}, \quad (\text{B.119})$$

and

$$\overline{\varphi_\Gamma^{\nu \dagger}} = \overline{\varphi_{\vartheta',2}^{\nu \dagger}} + \overline{\varphi_{\partial \bar{\nu},1}^{\nu \dagger}} + \overline{\varphi_{\partial \bar{\nu},2}^{\nu \dagger}} + \overline{\varphi_{\nu',1}^{\nu \dagger}} + \overline{\varphi_{\nu',2}^{\nu \dagger}} + \overline{\varphi_\Theta^{\nu \dagger}}, \quad (\text{B.120})$$

with

$$\overline{\varphi_{\vartheta',2}^{\nu \dagger}} = -\bar{\nu} \frac{\partial}{\partial y} \overline{u'_y \frac{\partial u'_i}{\partial x_i}}, \quad (\text{B.121})$$

$$\overline{\varphi_{\partial \bar{\nu},1}^{\nu \dagger}} = \frac{\partial \bar{e}}{\partial y} \frac{\partial \bar{\nu}}{\partial y}, \quad (\text{B.122})$$

$$\overline{\varphi_{\partial \bar{\nu},2}^{\nu \dagger}} = u'_i \frac{\partial u'_y}{\partial x_i} \frac{\partial \bar{\nu}}{\partial y}, \quad (\text{B.123})$$

$$\overline{\varphi_{\nu',1}^{\nu \dagger}} = \frac{\partial}{\partial y} \left(\overline{\nu' u'_i \frac{\partial U_i}{\partial y}} \right), \quad (\text{B.124})$$

$$\overline{\varphi_{\nu',2}^{\nu \dagger}} = \frac{\partial}{\partial y} \left(\overline{\nu' u'_i \frac{\partial U_y}{\partial x_i}} \right), \quad (\text{B.125})$$

$$\overline{\varphi_\Theta^{\nu \dagger}} = -\frac{\partial}{\partial y} \left(\overline{\frac{2\nu}{3} u'_y \frac{\partial U_i}{\partial x_i}} \right). \quad (\text{B.126})$$

The terms $\overline{\varphi_{\partial \bar{\nu},1}^{\nu \dagger}}$ and $\overline{\varphi_{\partial \bar{\nu},2}^{\nu \dagger}}$ are related to the variation of the mean viscosity, $\overline{\varphi_{\nu',1}^{\nu \dagger}}$ and $\overline{\varphi_{\nu',2}^{\nu \dagger}}$ to the fluctuations of the viscosity and $\overline{\varphi_{\vartheta',2}^{\nu \dagger}}$ and $\overline{\varphi_\Theta^{\nu \dagger}}$ to the dilatation.

We now focus on the pressure contribution to the transfer by external force. We decompose the density into a mean and fluctuating part, $\rho = \bar{\rho} + \rho'$. This is done using the relation

$$\frac{1}{\rho} = \frac{1}{\bar{\rho}} - \frac{\rho'}{\bar{\rho}(\bar{\rho} + \rho')}. \quad (\text{B.127})$$

Then, we decompose the derivative to isolate the derivative of the mean density. This leads to the decomposition of the pressure transfer into an incompressible part $\overline{\varphi_I^p}$ and a thermal part $\overline{\varphi_\Gamma^p}$,

$$\overline{\varphi^p} = -\frac{\partial}{\partial y} \overline{\frac{P}{\rho} u'_y} = \overline{\varphi_I^p} + \overline{\varphi_\Gamma^p}, \quad (\text{B.128})$$

where

$$\overline{\varphi_I^p} = -\frac{1}{\bar{\rho}} \frac{\partial}{\partial y} \overline{u'_y P} \quad (\text{B.129})$$

and

$$\overline{\varphi_\Gamma^p} = \overline{\varphi_{\partial\bar{\rho}}^p} + \overline{\varphi_{\rho'}^p}, \quad (\text{B.130})$$

with

$$\overline{\varphi_{\partial\bar{\rho}}^p} = \frac{\overline{u'_y P}}{\bar{\rho}^2} \frac{\partial \bar{\rho}}{\partial y}, \quad (\text{B.131})$$

$$\overline{\varphi_{\rho'}^p} = \frac{\partial}{\partial y} \overline{\frac{u'_y P \rho'}{\bar{\rho}(\bar{\rho} + \rho')}}. \quad (\text{B.132})$$

The term $\overline{\varphi_{\partial\bar{\rho}}^p}$ is associated with the variation of the mean density and $\overline{\varphi_{\rho'}^p}$ to the fluctuations of the density.

B.2.2.3 Decomposition of the production

We decompose the production (B.102) into an incompressible part $\overline{\mathcal{P}_I}$ and a thermal part $\overline{\mathcal{P}_\Gamma}$,

$$\overline{\mathcal{P}} = -\overline{u'_i u'_j} \frac{\partial \overline{U}_i}{\partial x_j} = \overline{\mathcal{P}_I} + \overline{\mathcal{P}_\Gamma}, \quad (\text{B.133})$$

with

$$\overline{\mathcal{P}_I} = -\overline{u'_x u'_y} \frac{\partial \overline{U}_x}{\partial y}, \quad (\text{B.134})$$

$$\overline{\mathcal{P}_\Gamma} = -\overline{u'_y u'_y} \frac{\partial \overline{U}_y}{\partial y} = \overline{\mathcal{P}_{\overline{U}_y}}. \quad (\text{B.135})$$

The thermal part of production is related to the addition of a mean wall-normal velocity in the compressible case.

B.2.2.4 Decomposition of the kinetic energy dilatation correlation

Although the kinetic energy dilatation correlation (B.103) is a purely compressible term, we decompose it in two parts $\overline{\zeta_\Theta^c}$ and $\overline{\zeta_{\vartheta'}^c}$ by splitting the velocity divergence in the mean dilatation and the dilatation fluctuation. We obtain

$$\overline{\zeta^c} = e \frac{\partial \overline{U}_j}{\partial x_j} = \overline{\zeta_\Theta^c} + \overline{\zeta_{\vartheta'}^c}, \quad (\text{B.136})$$

with

$$\overline{\zeta_{\Theta}^c} = \bar{e} \frac{\partial \bar{U}_j}{\partial x_j}, \quad (\text{B.137})$$

$$\overline{\zeta_{\vartheta'}^c} = e \frac{\partial u'_j}{\partial x_j}. \quad (\text{B.138})$$

This is of unobvious purpose at first, but will be useful latter when establishing the spectral formulation of the energy exchanges.

B.2.2.5 Decomposition of the interaction with variable density turbulence kinetic energy by external force

We decompose the interaction with variable density turbulence kinetic energy by external force (B.104) by introducing (B.96) and (B.97) into the expression of $\overline{\zeta^{\mathcal{R}}}$. We obtain

$$\overline{\zeta^{\mathcal{R}}} = -\overline{\gamma_{ij} u'_i \frac{\partial}{\partial x_j} \left(\frac{1}{\rho} \right)} = \overline{\zeta_{\partial\rho}^p} + \overline{\zeta^{\nu}}, \quad (\text{B.139})$$

where

$$\overline{\zeta_{\partial\rho}^p} = -\overline{\frac{u'_i P}{\rho^2} \frac{\partial \rho}{\partial x_i}} \quad (\text{B.140})$$

and

$$\overline{\zeta^{\nu}} = \overline{\zeta_{\partial\rho,1}^{\nu}} + \overline{\zeta_{\partial\rho,2}^{\nu}} + \overline{\zeta_{\Theta}^{\nu}}, \quad (\text{B.141})$$

with

$$\overline{\zeta_{\partial\rho,1}^{\nu}} = \overline{\frac{\nu}{\rho} \frac{\partial \rho}{\partial x_j} u'_i \frac{\partial U_i}{\partial x_j}}, \quad (\text{B.142})$$

$$\overline{\zeta_{\partial\rho,2}^{\nu}} = \overline{\frac{\nu}{\rho} \frac{\partial \rho}{\partial x_j} u'_i \frac{\partial U_j}{\partial x_i}}, \quad (\text{B.143})$$

$$\overline{\zeta_{\Theta}^{\nu}} = -\overline{\frac{2\nu}{3\rho} \frac{\partial \rho}{\partial x_i} u'_i \frac{\partial U_j}{\partial x_j}}. \quad (\text{B.144})$$

Each term is associated with variations of the density and $\overline{\zeta_{\Theta}^{\nu}}$ additionally with the dilatation.

B.2.2.6 Decomposition of the interaction with internal energy

The interaction with internal energy (B.105) is split using (B.96) into the sum of a viscous contribution $\overline{\varepsilon^{\nu}}$ and a pressure contribution $\overline{\varepsilon_{\vartheta'}^p}$,

$$\overline{\varepsilon} = -\overline{\frac{\gamma_{ij}}{\rho} \frac{\partial u'_i}{\partial x_j}} = \overline{\varepsilon^{\nu}} + \overline{\varepsilon_{\vartheta'}^p}, \quad (\text{B.145})$$

with

$$\overline{\varepsilon^{\nu\ddagger}} = -\frac{\overline{\Sigma_{ij} \partial u'_i}}{\rho \partial x_j}, \quad (\text{B.146})$$

$$\overline{\varepsilon^p} = \frac{\overline{P \partial u'_i}}{\rho \partial x_i}. \quad (\text{B.147})$$

The pressure contribution is the pressure dilatation correlation [260], a reversible exchange between the constant density part of turbulence kinetic energy and of internal energy. The viscous contribution is the dissipation, an irreversible exchange between the constant density part of turbulence kinetic energy and of internal energy.

Using (B.97), we decompose the dissipation in a part associated with the rate of deformation tensor and a part associated with the dilatation,

$$\overline{\varepsilon^{\nu\ddagger}} = -2\nu S_{ij} \frac{\partial u'_i}{\partial x_j} + \frac{2\nu \partial u'_i \partial U_j}{3 \partial x_i \partial x_j}. \quad (\text{B.148})$$

The decomposition of viscosity into a mean and fluctuating part in the first term of the right-hand side of equation (B.148), $\nu = \bar{\nu} + \nu'$, splits the dissipation $\overline{\varepsilon^{\nu\ddagger}}$ into an incompressible part $\overline{\varepsilon_I^{\nu\ddagger}}$ and a thermal part $\overline{\varepsilon_T^{\nu\ddagger}}$,

$$\overline{\varepsilon^{\nu\ddagger}} = -\frac{\overline{\Sigma_{ij} \partial u'_i}}{\rho \partial x_j} = \overline{\varepsilon_I^{\nu\ddagger}} + \overline{\varepsilon_T^{\nu\ddagger}}. \quad (\text{B.149})$$

we define

$$\overline{\varepsilon_I^{\nu\ddagger}} = -2\bar{\nu} \overline{s'_{ij} s'_{ij}} = \overline{\varepsilon_{I,1}^{\nu\ddagger}} + \overline{\varepsilon_{I,2}^{\nu\ddagger}}, \quad (\text{B.150})$$

with

$$\overline{\varepsilon_{I,1}^{\nu\ddagger}} = -\bar{\nu} \frac{\overline{\partial u'_i \partial u'_i}}{\partial x_j \partial x_j}, \quad (\text{B.151})$$

$$\overline{\varepsilon_{I,2}^{\nu\ddagger}} = -\bar{\nu} \frac{\overline{\partial u'_i \partial u'_j}}{\partial x_j \partial x_i}, \quad (\text{B.152})$$

and

$$\overline{\varepsilon_T^{\nu\ddagger}} = -2\nu' \overline{s'_{ij} s'_{ij}} + \frac{2\nu \partial u'_i \partial U_j}{3 \partial x_i \partial x_j} = \overline{\varepsilon_{\nu',1}^{\nu\ddagger}} + \overline{\varepsilon_{\nu',2}^{\nu\ddagger}} + \overline{\varepsilon_{\Theta}^{\nu\ddagger}}, \quad (\text{B.153})$$

with

$$\overline{\varepsilon_{\nu',1}^{\nu\ddagger}} = -\nu' \frac{\overline{\partial u'_i \partial U_i}}{\partial x_j \partial x_j}, \quad (\text{B.154})$$

$$\overline{\varepsilon_{\nu',2}^{\nu\ddagger}} = -\nu' \frac{\overline{\partial u'_i \partial U_j}}{\partial x_j \partial x_i}, \quad (\text{B.155})$$

$$\overline{\varepsilon_{\Theta}^{\nu\ddagger}} = \frac{2\nu \partial u'_i \partial U_j}{3 \partial x_i \partial x_j}. \quad (\text{B.156})$$

The terms $\overline{\varepsilon_{\nu',1}^{\nu\ddagger}}$ and $\overline{\varepsilon_{\nu',2}^{\nu\ddagger}}$ are related to the fluctuations of the viscosity and $\overline{\varepsilon_{\Theta}^{\nu\ddagger}}$ to the dilatation. Note that as the other terms, the decomposition of the dissipation is not unique. Another popular decomposition for compressible flows expresses the dissipation associated with the mean viscosity in a solenoidal term, an inhomogeneity term and a dilatation term [261, 127].

B.2.3 Decomposition in the spectral domain

The study of the half-trace of the velocity correlation tensor in a compressible flows with highly variable fluid properties will now be extended to the spectral domain. We will first establish its spectral evolution equation, then explain the decomposition employed.

As in section 4.2.4, the Fourier coefficients of the Fourier series expansion of g are denoted with the hat operator ($\widehat{}$) and are given by [173]:

$$\widehat{g}(\mathbf{k}, y, t) = \frac{1}{L_x L_z} \int_0^{L_x} \int_0^{L_z} g(\mathbf{x}, y, t) e^{-i\mathbf{k}\cdot\mathbf{x}} d\mathbf{x}. \quad (\text{B.157})$$

It follows that $g(x, y, z)$ can be expressed as a Fourier series,

$$g(\mathbf{x}, y, t) = \sum_{p,q=-\infty}^{\infty} \widehat{g}(\mathbf{k}_{p,q}, y, t) e^{i\mathbf{k}_{p,q}\cdot\mathbf{x}}, \quad (\text{B.158})$$

where p and q are positive or negative integers, $\mathbf{x} = (x, z)$ is the position vector in the xOz plane and $\mathbf{k}_{p,q} = \mathbf{k} = (k_x, k_z) = (\frac{2\pi p}{L_x}, \frac{2\pi q}{L_z})$ is the position vector in the $k_x Ok_z$ plane. The spectral equivalent \bar{e} of the statistically averaged half-trace of the velocity fluctuation correlation tensor e is

$$\bar{e} = \frac{1}{2} \overline{\widehat{u}_i^* \widehat{u}_i}. \quad (\text{B.159})$$

To obtain the evolution equation of \bar{e} , we apply a Fourier transform on equation (3.2),

$$\frac{\partial \widehat{U}_i}{\partial t} + U_j \frac{\partial \widehat{U}_i}{\partial x_j} = \frac{1}{\rho} \frac{\partial \widehat{\Upsilon}_{ij}}{\partial x_j}. \quad (\text{B.160})$$

then multiply by \widehat{u}_i^* and take the statistical average. Noticing

$$\frac{\partial \bar{e}}{\partial t} = \text{Re} \left(\overline{\widehat{u}_i^* \frac{\partial \widehat{u}_i}{\partial t}} \right), \quad (\text{B.161})$$

where Re denotes the real part operator, we obtain

$$\frac{\partial \bar{e}}{\partial t} = \text{Re} \left(\overline{-\widehat{u}_i^* U_j \frac{\partial \widehat{U}_i}{\partial x_j} + \widehat{u}_i^* \frac{1}{\rho} \frac{\partial \widehat{\Upsilon}_{ij}}{\partial x_j}} \right). \quad (\text{B.162})$$

This equation is analogous to the spatial equation (B.99) in the spectral domain. We aim to rewrite this equation to obtain a spectral equation that associates to each term of the spatial equation a spectral equivalent. For most terms, this is achieved by carrying out the same mathematical rearrangements than in the spatial domain. However, the Fourier transform adds mathematical restrictions that sometimes prevent us to carry out exactly the same operations than in the spatial domain. This hinders us from obtaining in this manner a spectral equivalent of the turbulent convection $\overline{\varphi_I^c}$ and

the kinetic energy turbulent dilatation correlation $\overline{\zeta_{\rho}^c}$. Thereby, it is slightly more complicated to obtain the spectral equivalent of these two terms. For this reason, we will introduce the spectral equation in two steps. First, the evolution equation of the half-trace of the velocity correlation tensor in spectral domain will be written with the spectral equivalent \overline{D} of the sum of these two terms undissociated. Then, we will address the spectral equivalent of the turbulent convection and the kinetic energy turbulent dilatation correlation.

In order to rewrite equation (B.162), we split the velocity into a mean and fluctuating part, $U_i = \overline{U}_i + u'_i$, and decompose the terms noticing

$$\overline{u'_i \frac{1}{\rho} \frac{\partial \widehat{\mathcal{Y}}_{ij}}{\partial x_j}} = \frac{\partial}{\partial y} \overline{u'_i \frac{\widehat{\mathcal{Y}}_{iy}}{\rho}} + \overline{u'_i \frac{\widehat{\mathcal{Y}}_{ij}}{\rho^2} \frac{\partial \rho}{\partial x_j}} - \overline{\frac{\partial u'_i}{\partial x_j} \frac{\widehat{\mathcal{Y}}_{ij}}{\rho}}, \quad (\text{B.163})$$

and

$$\text{Re} \left(\overline{\overline{U}_j u'_i \frac{\partial u'_i}{\partial x_j}} \right) = \overline{U}_y \frac{\partial \bar{e}}{\partial y}. \quad (\text{B.164})$$

We obtain

$$\frac{\partial \bar{e}}{\partial t} = \text{Re} \left(-\frac{\partial \overline{U}_y \bar{e}}{\partial y} + \frac{\partial}{\partial y} \overline{u'_i \frac{\widehat{\mathcal{Y}}_{iy}}{\rho}} - \overline{u'_i u'_j} \frac{\partial \overline{U}_i}{\partial x_j} + \bar{e} \frac{\partial \overline{U}_y}{\partial y} + \overline{u'_i \frac{\widehat{\mathcal{Y}}_{ij}}{\rho^2} \frac{\partial \rho}{\partial x_j}} - \overline{\frac{\partial u'_i}{\partial x_j} \frac{\widehat{\mathcal{Y}}_{ij}}{\rho}} - \overline{u'_i u'_j \frac{\partial u'_i}{\partial x_j}} \right). \quad (\text{B.165})$$

We identify the following terms:

- the convection by mean motion $\overline{\varphi}_\Gamma^c$, associated with the spatial convection by mean motion $\overline{\varphi}_\Gamma^c$,

$$\overline{\varphi}_\Gamma^c = -\frac{\partial \overline{U}_y \bar{e}}{\partial y} = \overline{\varphi}_{U_y}^c, \quad (\text{B.166})$$

- the transfer by external force $\overline{\varphi}^{\mathcal{R}}$, associated with the spatial transfer by external force $\overline{\varphi}^{\mathcal{R}}$,

$$\overline{\varphi}^{\mathcal{R}} = \text{Re} \left(\frac{\partial}{\partial y} \overline{u'_i \frac{\widehat{\mathcal{Y}}_{iy}}{\rho}} \right), \quad (\text{B.167})$$

- the production $\overline{\mathcal{P}}$, associated with the spatial production $\overline{\mathcal{P}}$,

$$\overline{\mathcal{P}} = \text{Re} \left(-\overline{u'_i u'_j \frac{\partial \overline{U}_i}{\partial x_j}} \right), \quad (\text{B.168})$$

- the kinetic energy mean dilation correlation $\overline{\zeta_{\Theta}^c}$, associated with the spatial kinetic energy mean dilation correlation $\overline{\zeta_{\Theta}^c}$,

$$\overline{\zeta_{\Theta}^c} = \bar{e} \frac{\partial \overline{U}_y}{\partial y}, \quad (\text{B.169})$$

- the interaction with variable density kinetic energy by external force $\overline{\zeta^{\mathfrak{h}}}$, associated with the spatial interaction with variable density kinetic energy by external force $\overline{\zeta^{\mathfrak{h}}}$,

$$\overline{\zeta^{\mathfrak{h}}} = \text{Re} \left(\overline{\widehat{u}_i^* \frac{\widehat{\gamma}_{ij}}{\rho^2} \frac{\partial \rho}{\partial x_j}} \right), \quad (\text{B.170})$$

- the interaction between kinetic energy and internal energy $\overline{\varepsilon^{\mathfrak{h}}}$, associated with the spatial interaction with internal energy $\overline{\varepsilon^{\mathfrak{h}}}$,

$$\overline{\varepsilon^{\mathfrak{h}}} = \text{Re} \left(-\overline{\frac{\partial \widehat{u}_i^*}{\partial x_j} \frac{\widehat{\gamma}_{ij}}{\rho}} \right), \quad (\text{B.171})$$

- the undissociated term $\overline{D^{\mathfrak{h}}}$, associated with the sum of the spatial turbulent convection $\overline{\varphi_I^{\mathfrak{h}}}$ and of the kinetic energy turbulent dilatation correlation $\overline{\zeta_{\vartheta'}^{\mathfrak{h}}}$ (we will decompose this term section B.2.3.1),

$$\overline{D^{\mathfrak{h}}} = \text{Re} \left(-\overline{\widehat{u}_i^* u_j' \frac{\partial u_i'}{\partial x_j}} \right). \quad (\text{B.172})$$

With those notations, the equation (B.165) is rewritten as

$$\frac{\partial \overline{\varepsilon}}{\partial t} = \overline{\varphi_I^{\mathfrak{h}}} + \overline{\varphi^{\nu \mathfrak{h}}} + \overline{\mathcal{P}^{\mathfrak{h}}} + \overline{\zeta_{\Theta}^{\mathfrak{h}}} + \overline{\zeta^{\nu \mathfrak{h}}} + \overline{\varepsilon^{\mathfrak{h}}} + \overline{D^{\mathfrak{h}}}. \quad (\text{B.173})$$

In the following, each term of the right-hand side of equation (B.165) will be decomposed similarly to the spatial decomposition. When possible, the terms will be decomposed in order to have a one-to-one correspondence with the terms of the spatial decomposition. In this case, the inverted hat operator ($\widehat{\cdot}$) is used to indicate the spectral equivalent of a spatial term. The spectral and spatial terms are tied closely. Indeed, the expression of the spatial term can be recovered from the associated spectral term and vice versa. Given a spectral term written in the form $\text{Re} \left(\overline{\widehat{u}_i^* \widehat{a}} \right)$, for any a , the associated spatial term is $\overline{u_i' a}$. The spectral term stems from the Fourier coefficients of the spatial two-point correlation between u_i' and a . This property is explained in appendix A. In addition, the spatial terms can be computed from the summation of the associated spectral term over the whole wavenumber space, using relation (A.11) of appendix A.

B.2.3.1 Spectral terms associated with the turbulent convection motion and the kinetic energy turbulent dilatation correlation

Because of the mathematical restrictions brought by the addition of the Fourier transform, two terms could not be obtained in the spectral formulation by simply reproducing the same steps than in the spatial domain: the convection by turbulent motion and the kinetic energy turbulent dilatation correlation. In the following, we present two ways to handle the issue.

1. We decompose the spatial equation differently, limiting ourselves to mathematical operations that can be reproduced in the spectral domain. For instance, let us define in the spatial domain:

- the triadic transfer $\overline{\varphi^{\mathcal{T}^{\natural}}}$,

$$\overline{\varphi^{\mathcal{T}^{\natural}}} = -\overline{u'_i \frac{\partial u'_i u'_j}{\partial x_j}}, \quad (\text{B.174})$$

- the turbulent deformation $\overline{\varphi^{df^{\natural}}}$,

$$\overline{\varphi^{df^{\natural}}} = \overline{u'_i u'_i \frac{\partial u'_j}{\partial x_j}}. \quad (\text{B.175})$$

The triadic transfer and the turbulent deformation are related to the turbulent convection and the kinetic energy turbulent dilatation correlation by

$$\overline{\varphi^{\mathcal{T}^{\natural}}} = -\overline{u'_i \frac{\partial u'_i u'_j}{\partial x_j}} = -\frac{\partial \overline{e u'_y}}{\partial y} - e \frac{\partial \overline{u'_j}}{\partial x_j} = \overline{\varphi_I^c} - \overline{\zeta_{\vartheta'}^c}, \quad (\text{B.176})$$

and

$$\overline{\varphi^{df^{\natural}}} = 2\overline{\zeta_{\vartheta'}^c}. \quad (\text{B.177})$$

Substituting using (B.176) and (B.177) the turbulence kinetic energy turbulent dilatation correlation and the turbulent convection by the triadic transfer and the turbulent deformation in the spatial formulation leads to an alternative spatial formulation. The undissociated spectral term $\overline{D^{\natural}}$ is then decomposed as

$$\overline{D^{\natural}} = \overline{\varphi^{\mathcal{T}^{\natural}}} + \overline{\varphi^{df^{\natural}}}, \quad (\text{B.178})$$

in which we define the following spectral terms:

- the triadic transfer $\overline{\tilde{\varphi}^{\mathcal{T}^{\natural}}}$, associated with the spatial triadic transfer $\overline{\varphi^{\mathcal{T}^{\natural}}}$,

$$\overline{\tilde{\varphi}^{\mathcal{T}^{\natural}}} = \text{Re} \left(\overline{-\widehat{u'_i}^* \frac{\partial \widehat{u'_i u'_j}}{\partial x_j}} \right), \quad (\text{B.179})$$

- the turbulent deformation $\overline{\tilde{\varphi}^{df^{\natural}}}$, associated with the spatial turbulent deformation $\overline{\varphi^{df^{\natural}}}$,

$$\overline{\tilde{\varphi}^{df^{\natural}}} = \text{Re} \left(\overline{\widehat{u'_i}^* u'_i \frac{\partial \widehat{u'_j}}{\partial x_j}} \right). \quad (\text{B.180})$$

This approach gives a clear one-to-one correspondence between the terms of the spectral and spatial decompositions. It has been employed previously by Bolotnov *et al.* [28] and Aulery *et al.* [10]. However, this decomposition is irrelevant in our case since it is not suited to the representation of the energy exchanges established in the spatial domain.

2. We decompose the undissociated spectral term \overline{D}^{\natural} as

$$\overline{D}^{\natural} = \text{Re} \left(\overline{-\widehat{u}_i^* u_j' \frac{\partial u_i'}{\partial x_j}} \right) = \text{Re} \left(-\frac{1}{2} \overline{\widehat{u}_i^* u_i' u_y'} + \frac{1}{2} \overline{\widehat{u}_i^* u_i' \frac{\partial u_j'}{\partial x_j}} + \frac{1}{2} \overline{\widehat{u}_i^* u_i' u_j'} - \frac{1}{2} \overline{\widehat{u}_i^* u_j' \frac{\partial u_i'}{\partial x_j}} \right). \quad (\text{B.181})$$

then associate first two terms of the right-hand side of this equation to the turbulent convection and the kinetic energy turbulent dilatation respectively. The last two terms remain as a purely spectral term without associated spatial term. As can be easily proved from relation (A.11), the summation over the whole wavenumber space of the last two terms combined is zero. Thus, their combined spectrum has no spatial contribution. In other words, we carry out the decomposition

$$\overline{D}^{\natural} = \overline{\varphi}_I^{\natural} + \overline{\zeta}_{\theta'}^{\natural} + \overline{\Xi}^{\natural}, \quad (\text{B.182})$$

and identify the following terms:

- the turbulent convection $\overline{\varphi}_I^{\natural}$, associated with the spatial turbulent convection $\overline{\varphi}_I^{\natural}$,

$$\overline{\varphi}_I^{\natural} = \text{Re} \left(-\frac{1}{2} \overline{\widehat{u}_i^* u_i' u_y'} \right), \quad (\text{B.183})$$

- the kinetic energy turbulent dilatation correlation $\overline{\zeta}_{\theta'}^{\natural}$, associated with the spatial kinetic energy turbulent dilatation correlation $\overline{\zeta}_{\theta'}^{\natural}$,

$$\overline{\zeta}_{\theta'}^{\natural} = \text{Re} \left(\frac{1}{2} \overline{\widehat{u}_i^* u_i' \frac{\partial u_j'}{\partial x_j}} \right), \quad (\text{B.184})$$

- the purely spectral term $\overline{\Xi}^{\natural}$, with no contribution in the spatial domain,

$$\overline{\Xi}^{\natural} = \text{Re} \left(\frac{1}{2} \overline{\widehat{u}_i^* u_j'} - \frac{1}{2} \overline{\widehat{u}_i^* u_j' \frac{\partial u_i'}{\partial x_j}} \right). \quad (\text{B.185})$$

This approach has been adopted in this paper.

B.2.3.2 Decomposition of the transfer by external force

The transfer by external force (B.167) is decomposed using (B.96) into the sum of a viscous contribution $\overline{\varphi}^{\nu \natural}$ and a pressure contribution $\overline{\varphi}^p \natural$,

$$\overline{\varphi}^{\mathcal{R} \natural} = \text{Re} \left(\frac{\partial}{\partial y} \overline{\widehat{u}_i^* \widehat{\Gamma}_{iy}} \right) = \overline{\varphi}^{\nu \natural} + \overline{\varphi}^p \natural, \quad (\text{B.186})$$

with

$$\overline{\varphi}^{\nu \natural} = \text{Re} \left(\frac{\partial}{\partial y} \overline{\widehat{u}_i^* \frac{\widehat{\Sigma}_{iy}}{\rho}} \right), \quad (\text{B.187})$$

$$\overline{\varphi}^{\nu\ddagger} = \text{Re} \left(-\frac{\partial}{\partial y} \overline{\widehat{u}_y^* \frac{\widehat{P}}{\rho}} \right). \quad (\text{B.188})$$

First, we focus on the viscous contribution. We decompose the viscous shear stress tensor in a part associated with the rate of deformation tensor and a part associated with the dilatation. Then, we split viscosity into a mean and fluctuating part, and decompose the derivative to isolate the derivative of the mean viscosity,

$$\begin{aligned} \frac{\partial}{\partial y} \overline{\widehat{u}_i^* \frac{\widehat{\Sigma}_{iy}}{\rho}} &= \frac{\partial}{\partial y} \left(\overline{\widehat{u}_i^* 2\nu S_{iy}} - \overline{\widehat{u}_y^* \frac{2\nu}{3} S_{ii}} \right) \\ &= 2\bar{\nu} \frac{\partial}{\partial y} \overline{\widehat{u}_i^* S_{iy}} + 2 \frac{\partial \bar{\nu}}{\partial y} \overline{\widehat{u}_i^* S_{iy}} + \frac{\partial}{\partial y} \left(\overline{2\widehat{u}_i^* \nu' S_{iy}} - \frac{2}{3} \overline{\widehat{u}_y^* \nu' S_{ii}} \right). \end{aligned} \quad (\text{B.189})$$

We decompose the first term of the right-hand side of this equation to isolate a new dilatation-associated term,

$$2\bar{\nu} \frac{\partial}{\partial y} \overline{\widehat{u}_i^* S_{iy}} = \bar{\nu} \frac{\partial^2 \bar{\epsilon}}{\partial y^2} + \bar{\nu} \frac{\partial^2 \widehat{u}_y^* \widehat{u}_y'}{\partial y^2} - \bar{\nu} \frac{\partial}{\partial y} \frac{\partial \widehat{u}_i^*}{\partial x_i} \widehat{u}_y' \quad (\text{B.190})$$

Hence, to decompose the viscous transfer into an incompressible part $\overline{\varphi}_I^{\nu\ddagger}$ and a thermal part $\overline{\varphi}_\Gamma^{\nu\ddagger}$,

$$\overline{\varphi}^{\nu\ddagger} = \text{Re} \left(\frac{\partial}{\partial y} \overline{\widehat{u}_i^* \frac{\widehat{\Sigma}_{iy}}{\rho}} \right) = \overline{\varphi}_I^{\nu\ddagger} + \overline{\varphi}_\Gamma^{\nu\ddagger}, \quad (\text{B.191})$$

we define

$$\overline{\varphi}_I^{\nu\ddagger} = \overline{\varphi}_{I,1}^{\nu\ddagger} + \overline{\varphi}_{I,2}^{\nu\ddagger}, \quad (\text{B.192})$$

with

$$\overline{\varphi}_{I,1}^{\nu\ddagger} = \text{Re} \left(\bar{\nu} \frac{\partial^2 \bar{\epsilon}}{\partial y^2} \right), \quad (\text{B.193})$$

$$\overline{\varphi}_{I,2}^{\nu\ddagger} = \text{Re} \left(\bar{\nu} \frac{\partial^2 \widehat{u}_y^* \widehat{u}_y'}{\partial y^2} \right). \quad (\text{B.194})$$

and

$$\overline{\varphi}_\Gamma^{\nu\ddagger} = \overline{\varphi}_{\vartheta',2}^{\nu\ddagger} + \overline{\varphi}_{\partial\bar{\nu},1}^{\nu\ddagger} + \overline{\varphi}_{\partial\bar{\nu},2}^{\nu\ddagger} + \overline{\varphi}_{\nu',1}^{\nu\ddagger} + \overline{\varphi}_{\nu',2}^{\nu\ddagger} + \overline{\varphi}_\Theta^{\nu\ddagger}, \quad (\text{B.195})$$

with

$$\overline{\varphi}_{\vartheta',2}^{\nu\ddagger} = \text{Re} \left(-\bar{\nu} \frac{\partial}{\partial y} \frac{\partial \widehat{u}_i^*}{\partial x_i} \widehat{u}_y' \right), \quad (\text{B.196})$$

$$\overline{\varphi}_{\partial\bar{\nu},1}^{\nu\ddagger} = \text{Re} \left(\frac{\partial \bar{\epsilon}}{\partial y} \frac{\partial \bar{\nu}}{\partial y} \right), \quad (\text{B.197})$$

$$\overline{\varphi}_{\partial\bar{\nu},2}^{\nu\ddagger} = \text{Re} \left(\widehat{u}_i^* \frac{\partial \widehat{u}_y'}{\partial x_i} \frac{\partial \bar{\nu}}{\partial y} \right), \quad (\text{B.198})$$

$$\overline{\tilde{\varphi}}_{\nu',1}^{\nu\ddagger} = \text{Re} \left(\frac{\partial}{\partial y} \left(\widehat{u}_i^* \nu' \frac{\partial \overline{U}_i}{\partial y} \right) \right), \quad (\text{B.199})$$

$$\overline{\tilde{\varphi}}_{\nu',2}^{\nu\ddagger} = \text{Re} \left(\frac{\partial}{\partial y} \left(\widehat{u}_i^* \nu' \frac{\partial \overline{U}_y}{\partial x_i} \right) \right), \quad (\text{B.200})$$

$$\overline{\tilde{\varphi}}_{\Theta}^{\nu\ddagger} = \text{Re} \left(\frac{\partial}{\partial y} \left(-\frac{2}{3} \widehat{u}_y^* \nu' \frac{\partial \overline{U}_i}{\partial x_i} \right) \right). \quad (\text{B.201})$$

We now focus on the pressure contribution to the transfer by external force. We decompose the density into a mean and fluctuating part using relation (B.127). Then, we decompose the derivative to isolate the derivative of the mean density. This leads to the decomposition of the pressure transfer into an incompressible part $\overline{\tilde{\varphi}}_I^p$ and a thermal part $\overline{\tilde{\varphi}}_{\Gamma}^p$,

$$\overline{\tilde{\varphi}}^p = \text{Re} \left(-\frac{\partial}{\partial y} \widehat{u}_y^* \frac{\widehat{P}}{\rho} \right) = \overline{\tilde{\varphi}}_I^p + \overline{\tilde{\varphi}}_{\Gamma}^p, \quad (\text{B.202})$$

where

$$\overline{\tilde{\varphi}}_I^p = \text{Re} \left(-\frac{1}{\bar{\rho}} \frac{\partial}{\partial y} \widehat{u}_y^* \widehat{P} \right) \quad (\text{B.203})$$

and

$$\overline{\tilde{\varphi}}_{\Gamma}^p = \overline{\tilde{\varphi}}_{\partial \bar{\rho}}^p + \overline{\tilde{\varphi}}_{\rho'}^p, \quad (\text{B.204})$$

with

$$\overline{\tilde{\varphi}}_{\partial \bar{\rho}}^p = \text{Re} \left(\frac{\widehat{u}_y^* \widehat{P}}{\bar{\rho}^2} \frac{\partial \bar{\rho}}{\partial y} \right), \quad (\text{B.205})$$

$$\overline{\tilde{\varphi}}_{\rho'}^p = \text{Re} \left(\frac{\partial}{\partial y} \widehat{u}_y^* \frac{\overline{P \rho'}}{\bar{\rho}(\bar{\rho} + \rho')} \right). \quad (\text{B.206})$$

B.2.3.3 Decomposition of the production

We decompose the production (B.168) into an incompressible part $\overline{\tilde{\mathcal{P}}}_I$ and a thermal part $\overline{\tilde{\mathcal{P}}}_{\Gamma}$,

$$\overline{\tilde{\mathcal{P}}} = \text{Re} \left(-\widehat{u}_i^* \widehat{u}_j' \frac{\partial \overline{U}_i}{\partial x_j} \right) \overline{\tilde{\mathcal{P}}}_I + \overline{\tilde{\mathcal{P}}}_{\Gamma}, \quad (\text{B.207})$$

with

$$\overline{\tilde{\mathcal{P}}}_I = \text{Re} \left(-\widehat{u}_x^* \widehat{u}_y' \frac{\partial \overline{U}_x}{\partial y} \right), \quad (\text{B.208})$$

$$\overline{\tilde{\mathcal{P}}}_{\Gamma} = \text{Re} \left(-\widehat{u}_y^* \widehat{u}_y' \frac{\partial \overline{U}_y}{\partial y} \right) = \overline{\tilde{\mathcal{P}}}_{\overline{U}_y}. \quad (\text{B.209})$$

B.2.3.4 Decomposition of the interaction with variable density turbulence kinetic energy by external force

We decompose the interaction with variable density turbulence kinetic energy by external force (B.170) by introducing (B.96) and (B.97) into the expression of $\overline{\zeta^{\mathcal{R}}}$. We obtain

$$\overline{\zeta^{\mathcal{R}}} = \text{Re} \left(\overline{\widehat{u}'_i \frac{\widehat{\Upsilon}_{ij}}{\rho^2} \frac{\partial \rho}{\partial x_j}} \right) = \overline{\zeta_{\partial \rho}^{\mathcal{P}}} + \overline{\zeta^{\nu}}, \quad (\text{B.210})$$

where

$$\overline{\zeta_{\partial \rho}^{\mathcal{P}}} = \text{Re} \left(\overline{-\widehat{u}'_i \frac{\widehat{P}}{\rho^2} \frac{\partial \rho}{\partial x_i}} \right) \quad (\text{B.211})$$

and

$$\overline{\zeta^{\nu}} = \text{Re} \left(\overline{\widehat{u}'_i \frac{\widehat{\Sigma}_{ij}}{\rho^2} \frac{\partial \rho}{\partial x_j}} \right) = \overline{\zeta_{\partial \rho, 1}^{\nu}} + \overline{\zeta_{\partial \rho, 2}^{\nu}} + \overline{\zeta_{\Theta}^{\nu}}, \quad (\text{B.212})$$

with

$$\overline{\zeta_{\partial \rho, 1}^{\nu}} = \text{Re} \left(\overline{\widehat{u}'_i \frac{\widehat{\nu}}{\rho} \frac{\partial \rho}{\partial x_j} \frac{\partial U_i}{\partial x_j}} \right), \quad (\text{B.213})$$

$$\overline{\zeta_{\partial \rho, 2}^{\nu}} = \text{Re} \left(\overline{\widehat{u}'_i \frac{\widehat{\nu}}{\rho} \frac{\partial \rho}{\partial x_j} \frac{\partial U_j}{\partial x_i}} \right), \quad (\text{B.214})$$

$$\overline{\zeta_{\Theta}^{\nu}} = \text{Re} \left(\overline{-\widehat{u}'_i \frac{\widehat{2\nu}}{3\rho} \frac{\partial \rho}{\partial x_i} \frac{\partial U_j}{\partial x_j}} \right). \quad (\text{B.215})$$

B.2.3.5 Decomposition of the interaction with internal energy

The interaction with internal energy (B.171) is split using (B.96) into the sum of a viscous contribution $\overline{\varepsilon^{\nu}}$ called dissipation and a pressure contribution $\overline{\varepsilon_{\vartheta'}^{\mathcal{P}}}$ called pressure dilatation correlation,

$$\overline{\varepsilon^{\mathcal{I}}} = \text{Re} \left(\overline{-\frac{\partial \widehat{u}'_i}{\partial x_j} \frac{\widehat{\Upsilon}_{ij}}{\rho}} \right) = \overline{\varepsilon^{\nu}} + \overline{\varepsilon_{\vartheta'}^{\mathcal{P}}}, \quad (\text{B.216})$$

with

$$\overline{\varepsilon^{\nu}} = \text{Re} \left(\overline{-\frac{\partial \widehat{u}'_i}{\partial x_j} \frac{\widehat{\Sigma}_{ij}}{\rho}} \right), \quad (\text{B.217})$$

$$\overline{\varepsilon_{\vartheta'}^{\mathcal{P}}} = \text{Re} \left(\overline{\frac{\partial \widehat{u}'_i}{\partial x_i} \frac{\widehat{P}}{\rho}} \right). \quad (\text{B.218})$$

Using (B.97), we decompose the dissipation in a part associated with the rate of deformation tensor and a part associated with the dilatation. Then, the decomposition of viscosity into a mean and fluctuating part, $\nu = \bar{\nu} + \nu'$, splits the dissipation of turbulent motion $\bar{\varepsilon}^\dagger$ into an incompressible part $\bar{\varepsilon}_I^\dagger$ and a thermal part $\bar{\varepsilon}_\Gamma^\dagger$,

$$\bar{\varepsilon}^\dagger = \text{Re} \left(-\frac{\overline{\partial u'_i}^* \widehat{\Sigma}_{ij}}{\partial x_j \rho} \right) = \bar{\varepsilon}_I^\dagger + \bar{\varepsilon}_\Gamma^\dagger. \quad (\text{B.219})$$

we define

$$\bar{\varepsilon}_I^\dagger = \text{Re} \left(-2\bar{\nu} \overline{s'_{ij} s'_{ij}} \right) = \bar{\varepsilon}_{I,1}^\dagger + \bar{\varepsilon}_{I,2}^\dagger, \quad (\text{B.220})$$

with

$$\bar{\varepsilon}_{I,1}^\dagger = \text{Re} \left(-\bar{\nu} \overline{\frac{\partial u'_i}{\partial x_j} \frac{\partial u'_i}{\partial x_j}} \right), \quad (\text{B.221})$$

$$\bar{\varepsilon}_{I,2}^\dagger = \text{Re} \left(-\bar{\nu} \overline{\frac{\partial u'_i}{\partial x_j} \frac{\partial u'_j}{\partial x_i}} \right). \quad (\text{B.222})$$

and

$$\bar{\varepsilon}_\Gamma^\dagger = \text{Re} \left(-2\nu' \overline{S_{ij} s'_{ij}} + \frac{\overline{\partial u'_i}^*}{\partial x_i} \frac{2\nu}{3} \frac{\partial \overline{U}_j}{\partial x_j} \right) = \bar{\varepsilon}_{\nu',1}^\dagger + \bar{\varepsilon}_{\nu',2}^\dagger + \bar{\varepsilon}_\Theta^\dagger, \quad (\text{B.223})$$

with

$$\bar{\varepsilon}_{\nu',1}^\dagger = \text{Re} \left(-\frac{\overline{\partial u'_i}^*}{\partial x_j} \nu' \frac{\partial \overline{U}_i}{\partial x_j} \right), \quad (\text{B.224})$$

$$\bar{\varepsilon}_{\nu',2}^\dagger = \text{Re} \left(-\frac{\overline{\partial u'_i}^*}{\partial x_j} \nu' \frac{\partial \overline{U}_j}{\partial x_i} \right), \quad (\text{B.225})$$

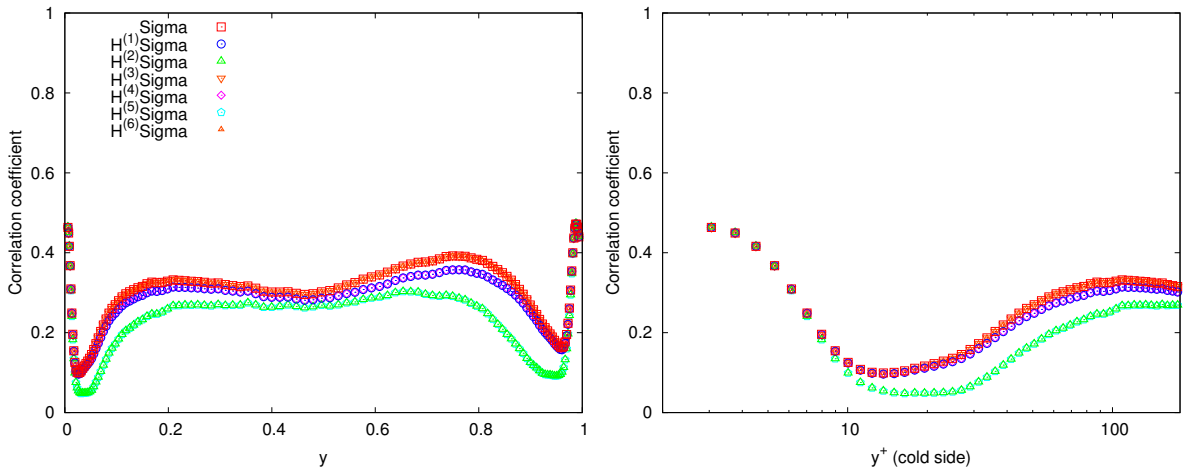
$$\bar{\varepsilon}_\Theta^\dagger = \text{Re} \left(\frac{\overline{\partial u'_i}^*}{\partial x_i} \frac{2\nu}{3} \frac{\partial \overline{U}_j}{\partial x_j} \right). \quad (\text{B.226})$$

The spatial and spectral decompositions are summarised and compared in equations and .

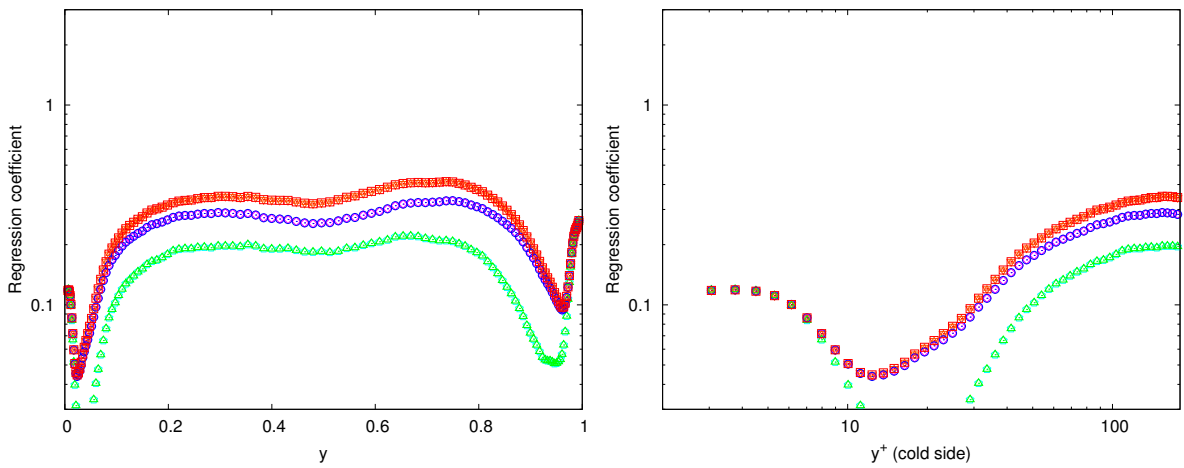
Appendix C

A priori tests of tensorial eddy-viscosity models

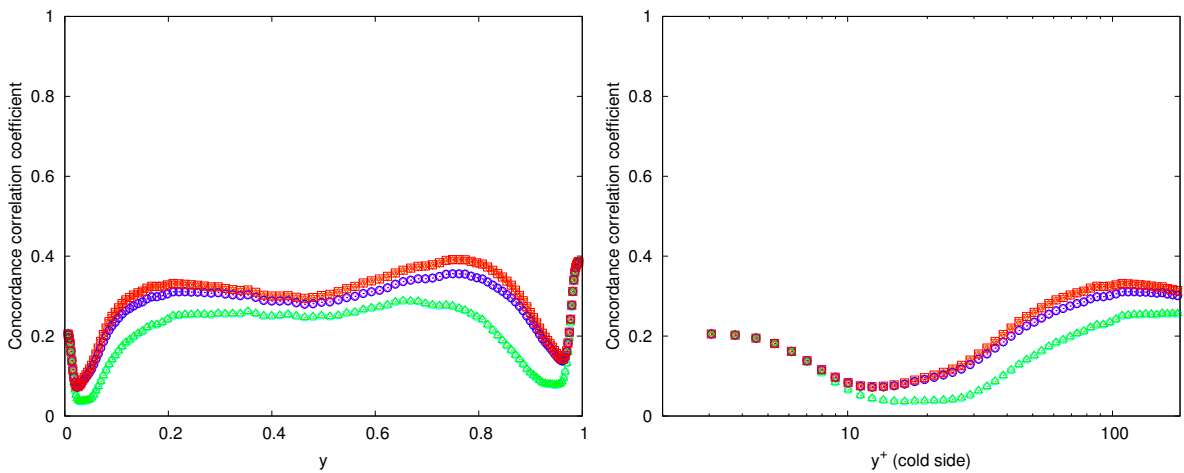
In this appendix, we assess a priori the relevance the relevance of tensorial eddy-viscosity models based on the Sigma model for the momentum convection subgrid term as it appears in the streamwise velocity transport equation in figure C.1, in the spanwise velocity transport equation in figure C.2, in the wall-normal velocity transport equation in figure C.3 and with regard to the subgrid kinetic energy dissipation in figure C.4, and of tensorial eddy-viscosity models based on the Anisotropic Smagorinsky model for the momentum convection subgrid term as it appears in the streamwise velocity transport equation in figure C.5, in the spanwise velocity transport equation in figure C.6, in the wall-normal velocity transport equation in figure C.7 and with regard to the subgrid kinetic energy dissipation in figure C.8. The tensorial Sigma and Anisotropic Smagorinsky models have the same constant as the scalar Sigma and Anisotropic Smagorinsky models. The procedure used for the a priori tests is the same as in section 9.2.



(a) Correlation coefficient.

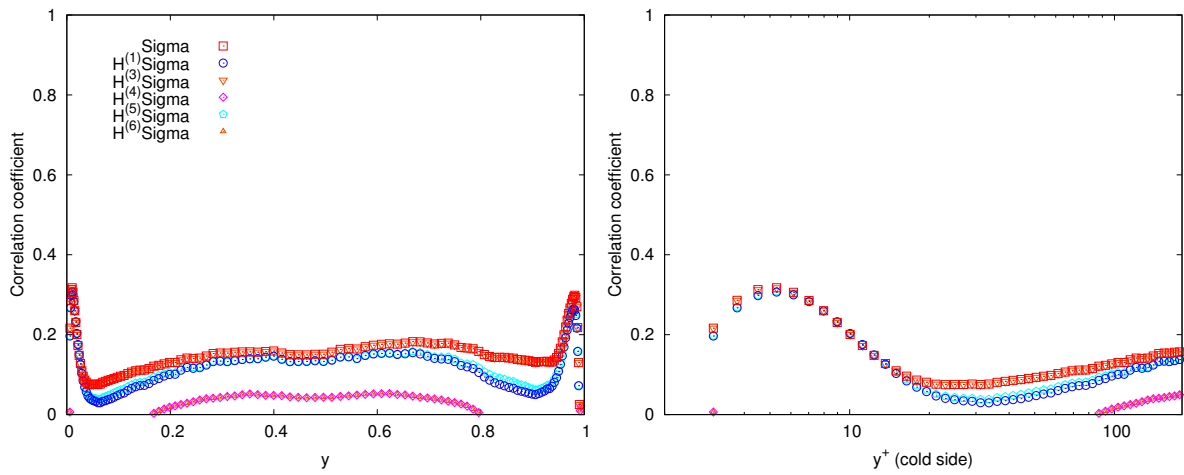


(b) Regression coefficient.

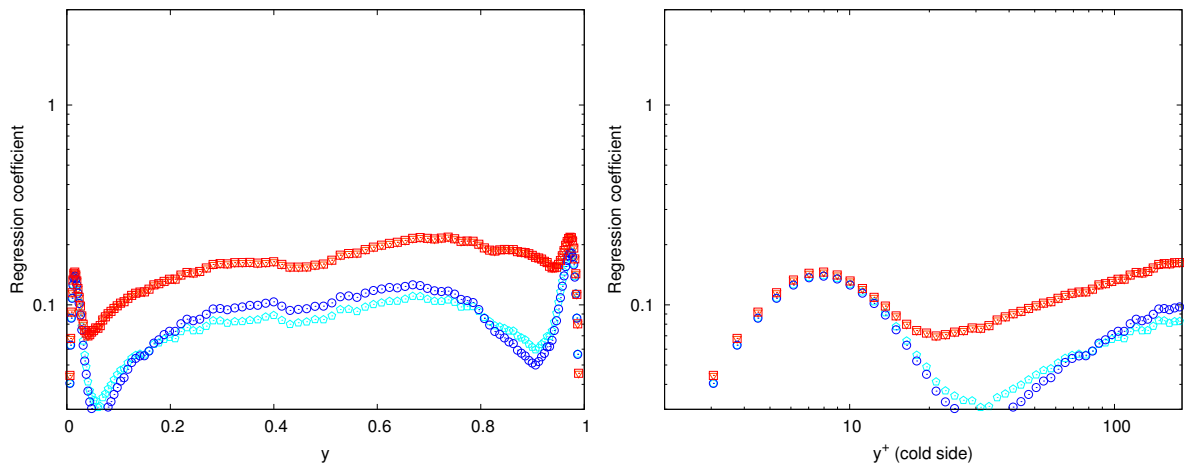


(c) Concordance correlation coefficient.

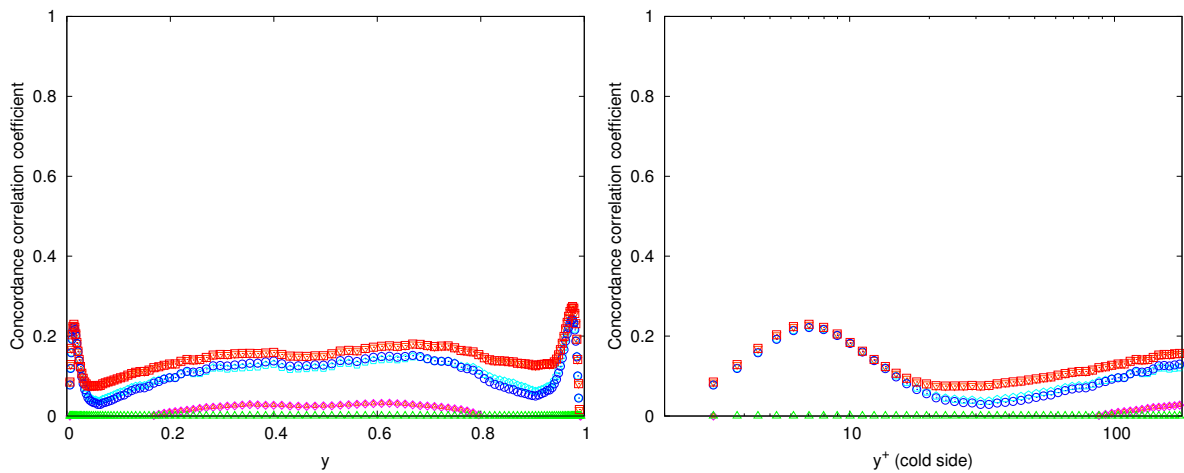
Figure C.1 – Correlation coefficient, regression coefficient, and concordance correlation coefficient between the divergence of the streamwise-related part of the exact momentum convection subgrid term $\partial_j F_{U_j U_x}$ and tensorial Sigma models $\partial_j \tau_{xj}^{H^{(k)} \text{Sigma}}(\bar{U}, \bar{\Delta})$.



(a) Correlation coefficient.

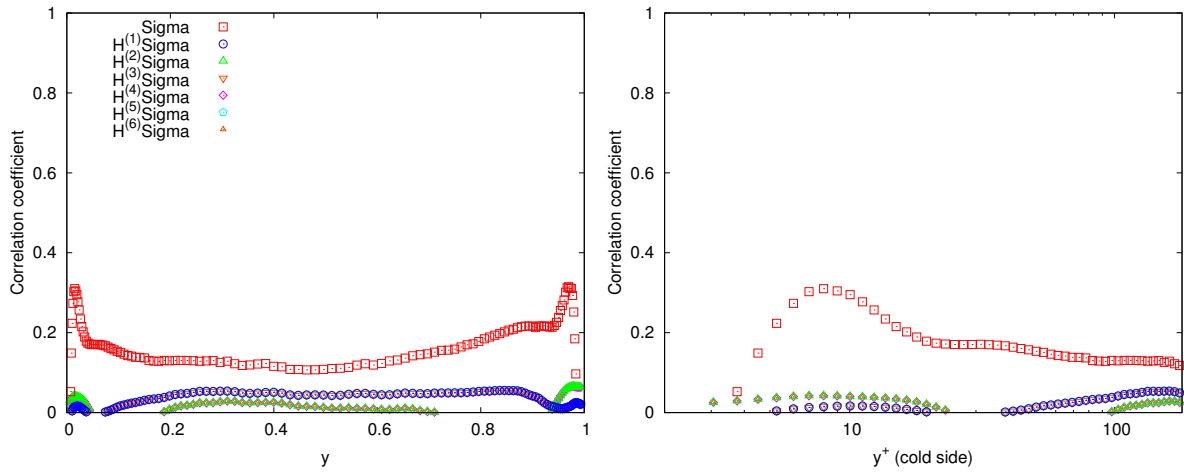


(b) Regression coefficient.

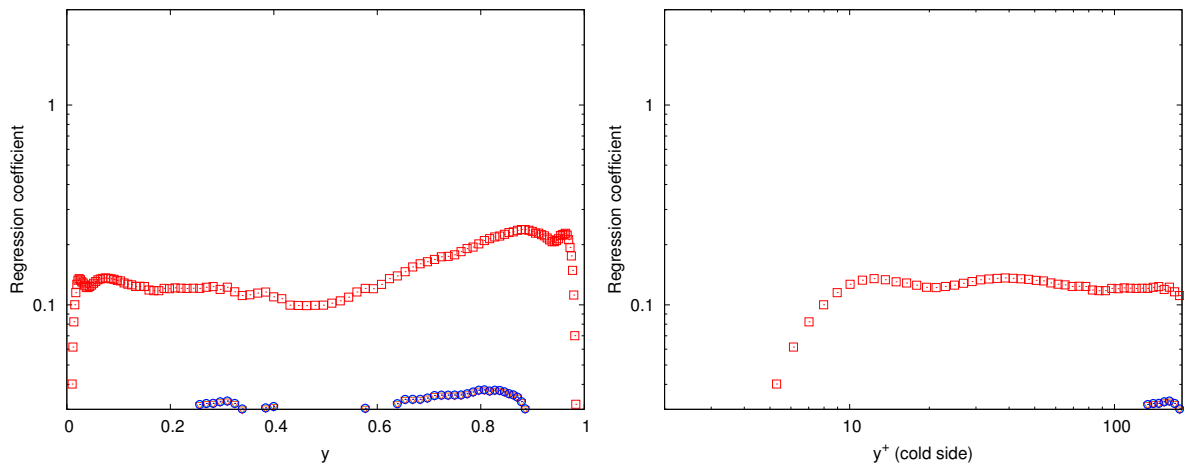


(c) Concordance correlation coefficient.

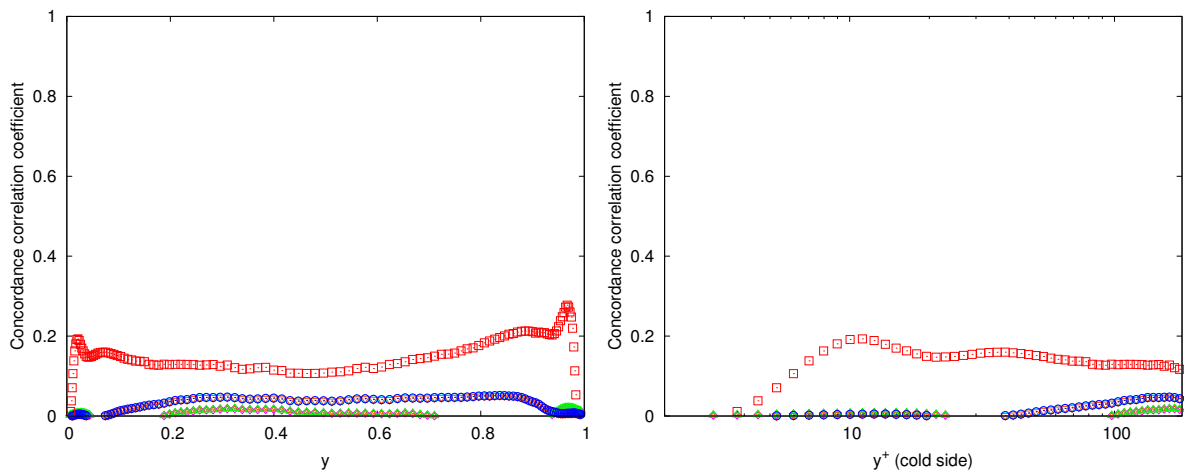
Figure C.2 – Correlation coefficient, regression coefficient, and concordance correlation coefficient between the divergence of the spanwise-related part of the exact momentum convection subgrid term $\partial_j F_{U_j U_z}$ and tensorial Sigma models $\partial_j \tau_{zj}^{H^{(k)}\text{Sigma}}(\bar{U}, \bar{\Delta})$.



(a) Correlation coefficient.

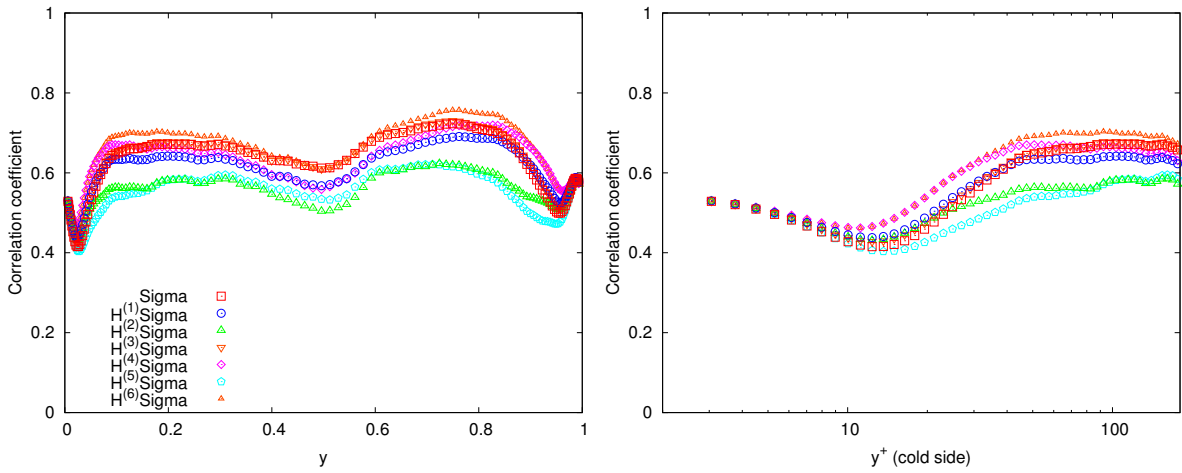


(b) Regression coefficient.

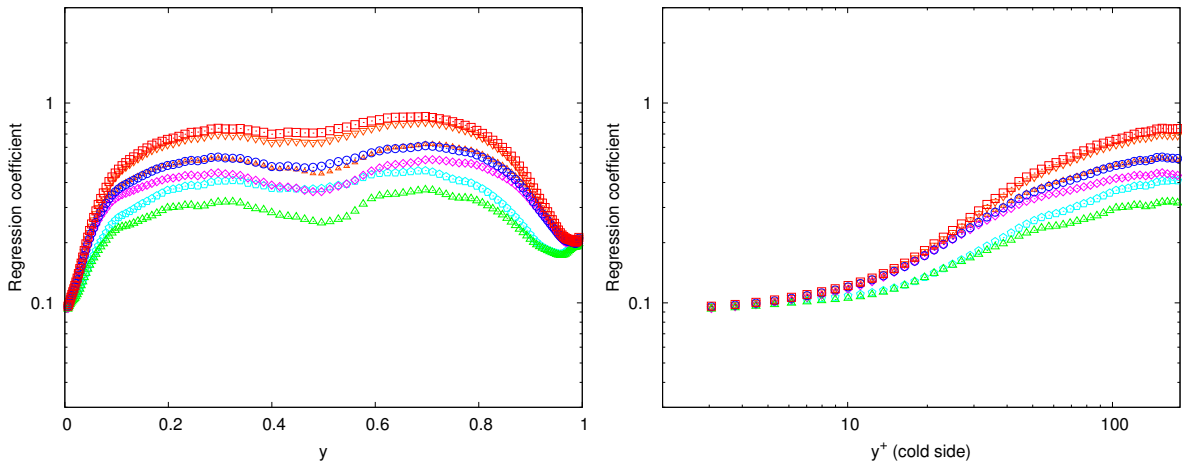


(c) Concordance correlation coefficient.

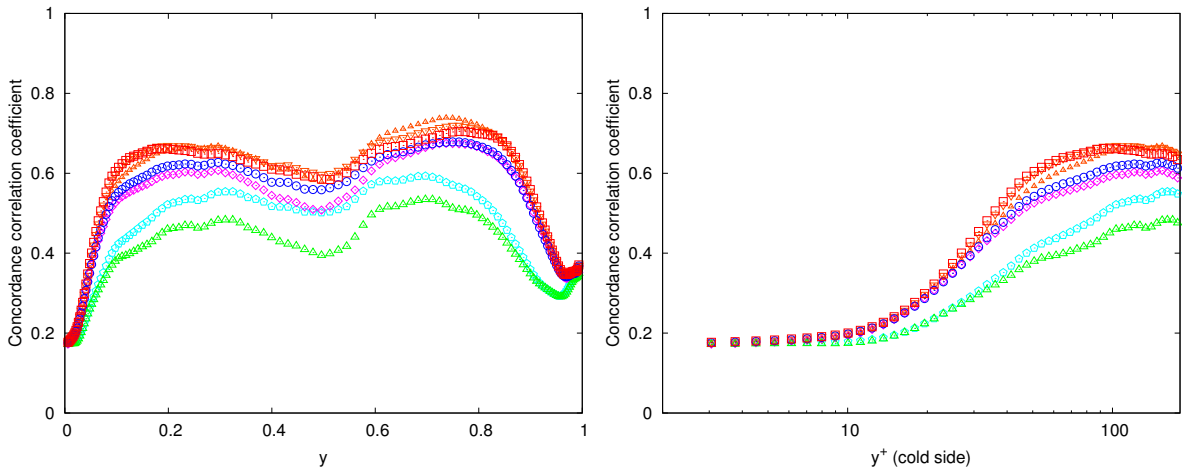
Figure C.3 – Correlation coefficient, regression coefficient, and concordance correlation coefficient between the divergence of the wall-normal-related part of the exact momentum convection subgrid term $\partial_j F_{U_j U_y}$ and tensorial Sigma models $\partial_j \tau_{yj}^{H^{(k)} \text{Sigma}}(\bar{U}, \bar{\Delta})$.



(a) Correlation coefficient.

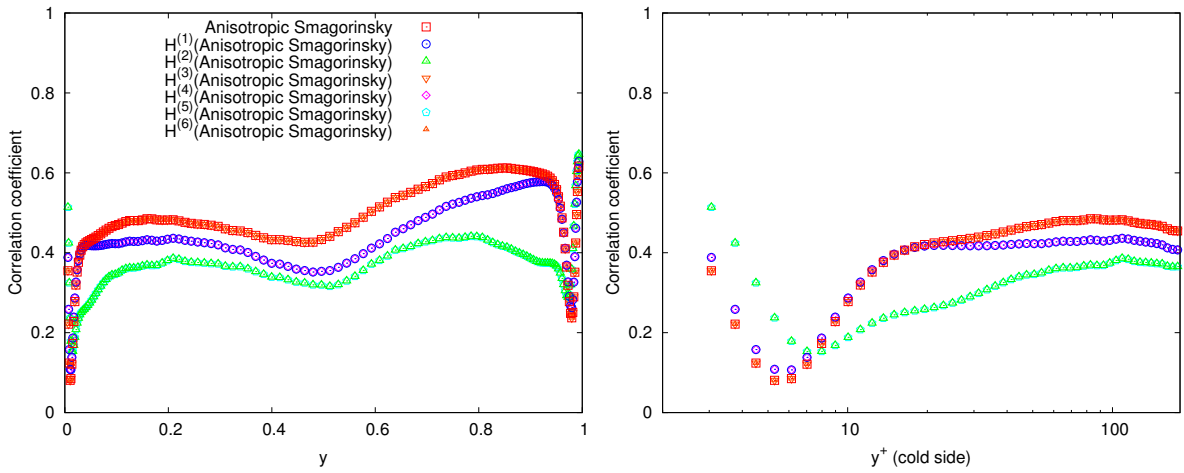


(b) Regression coefficient.

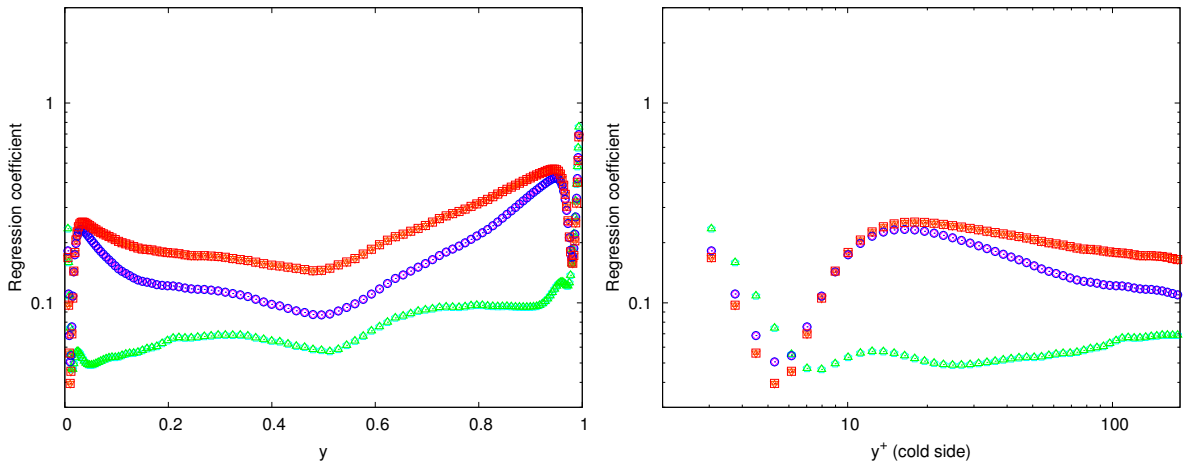


(c) Concordance correlation coefficient.

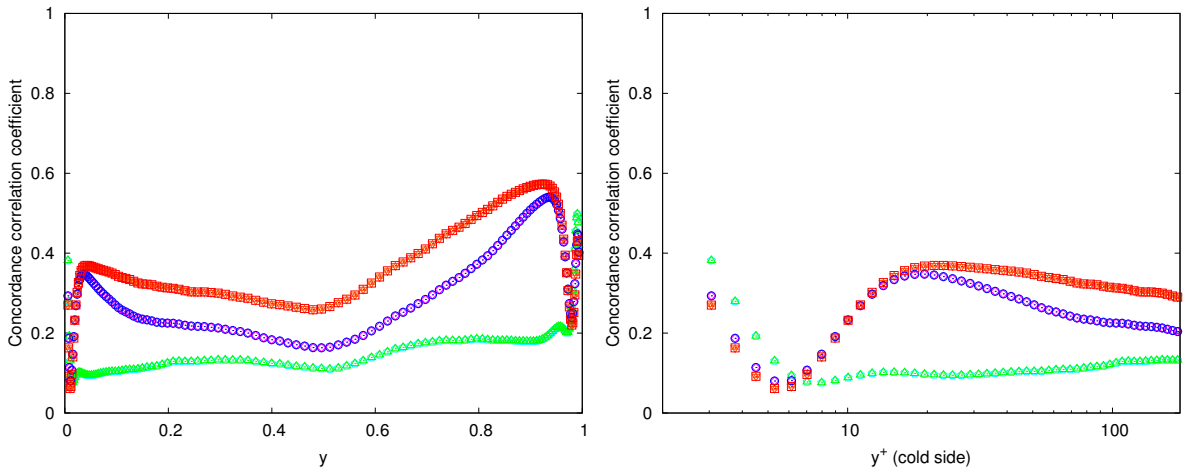
Figure C.4 – Correlation coefficient, regression coefficient, and concordance correlation coefficient between the subgrid kinetic energy dissipation of the exact momentum convection subgrid term $\bar{\rho} F_{U_j U_i} S_{ij}$ and tensorial Sigma models $\bar{\rho} \tau_{ij}^{H^{(k)} \text{Sigma}}(\bar{\mathbf{U}}, \bar{\mathbf{\Delta}}) S_{ij}$.



(a) Correlation coefficient.

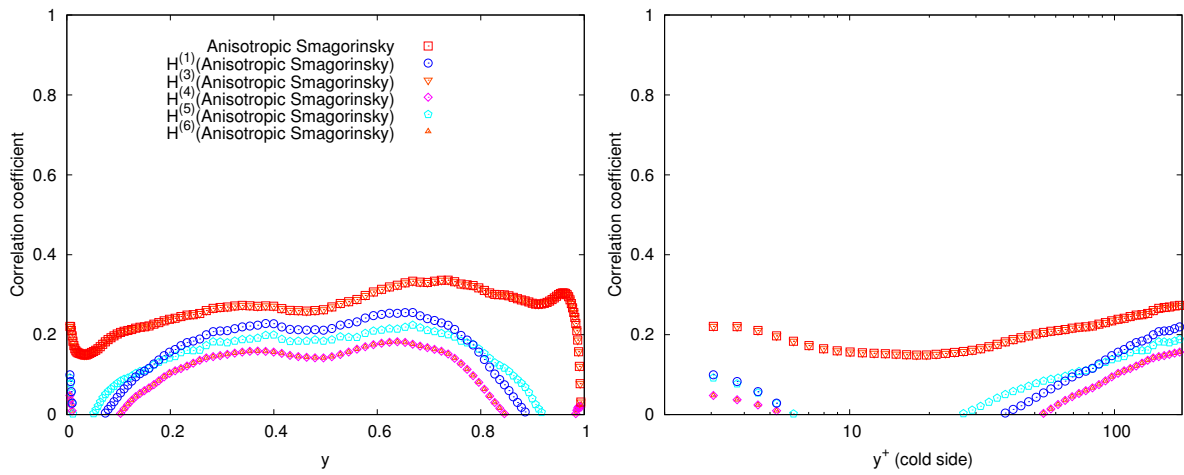


(b) Regression coefficient.

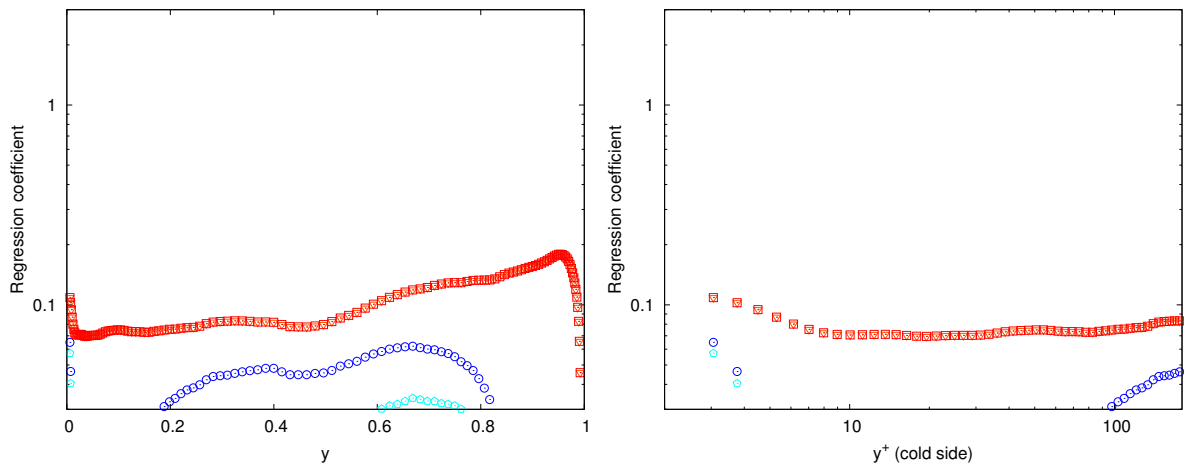


(c) Concordance correlation coefficient.

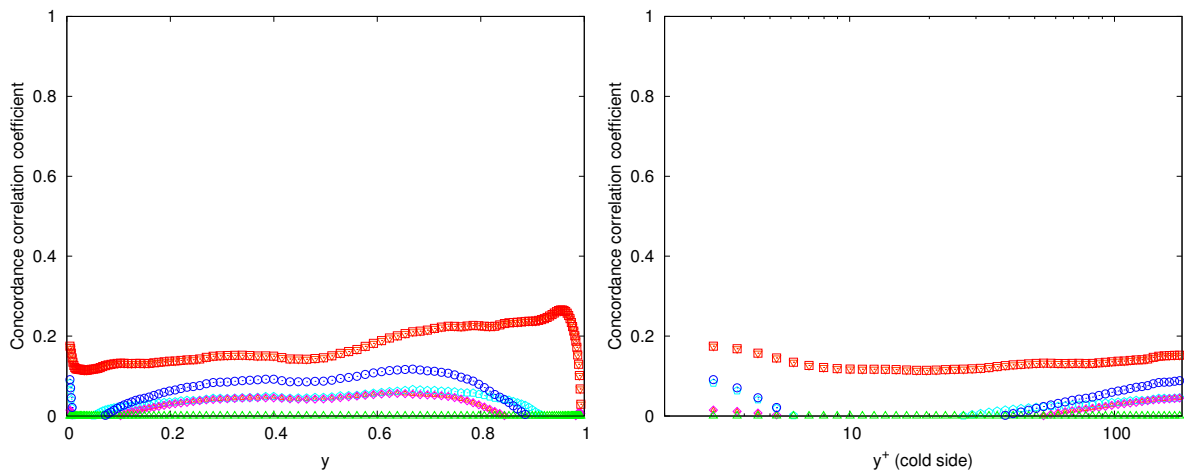
Figure C.5 – Correlation coefficient, regression coefficient, and concordance correlation coefficient between the divergence of the streamwise-related part of the exact momentum convection subgrid term $\partial_j F_{U_j U_x}$ and tensorial Anisotropic Smagorinsky models $\partial_j \tau_{xj}^{H^{(k)} \text{An.Smag.}}(\bar{U}, \bar{\Delta})$.



(a) Correlation coefficient.

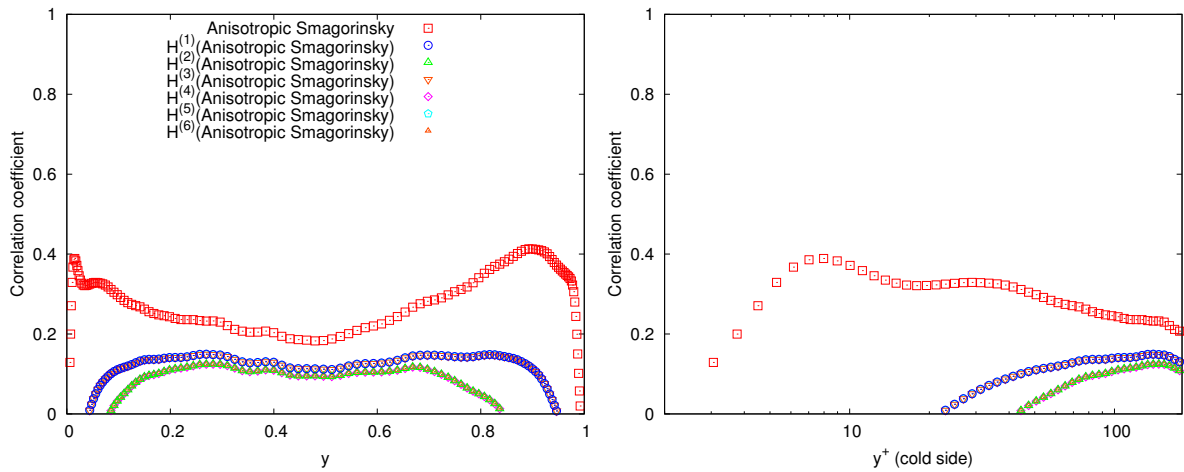


(b) Regression coefficient.

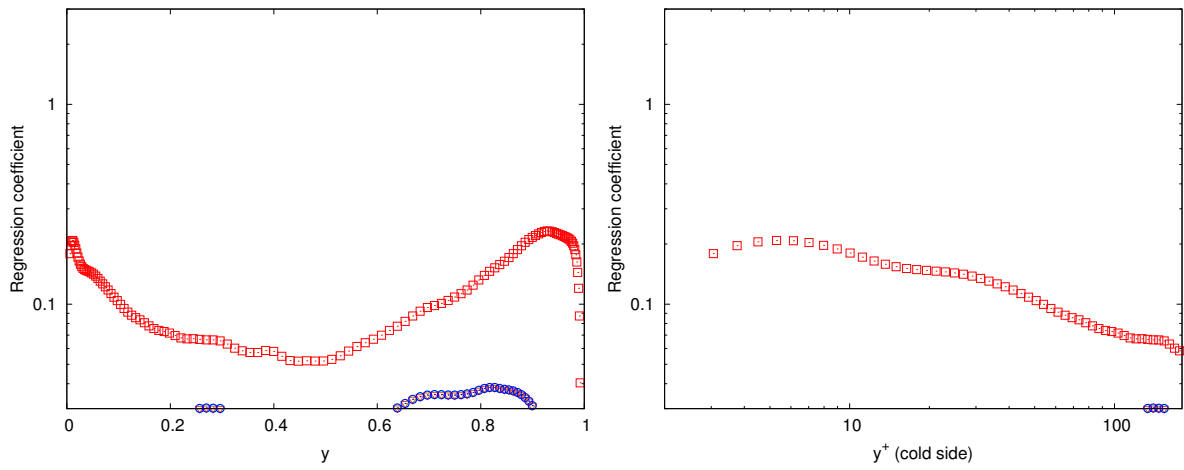


(c) Concordance correlation coefficient.

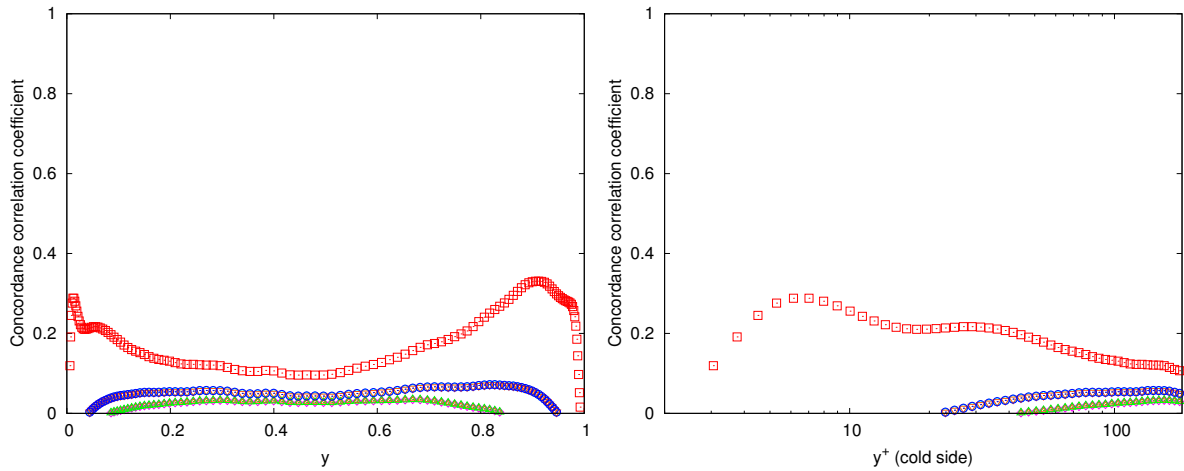
Figure C.6 – Correlation coefficient, regression coefficient, and concordance correlation coefficient between the divergence of the spanwise-related part of the exact momentum convection subgrid term $\partial_j F_{U_j U_z}$ and tensorial Anisotropic Smagorinsky models $\partial_j \tau_{zj}^{H^{(k)} \text{An.Smag.}}(\bar{U}, \bar{\Delta})$.



(a) Correlation coefficient.

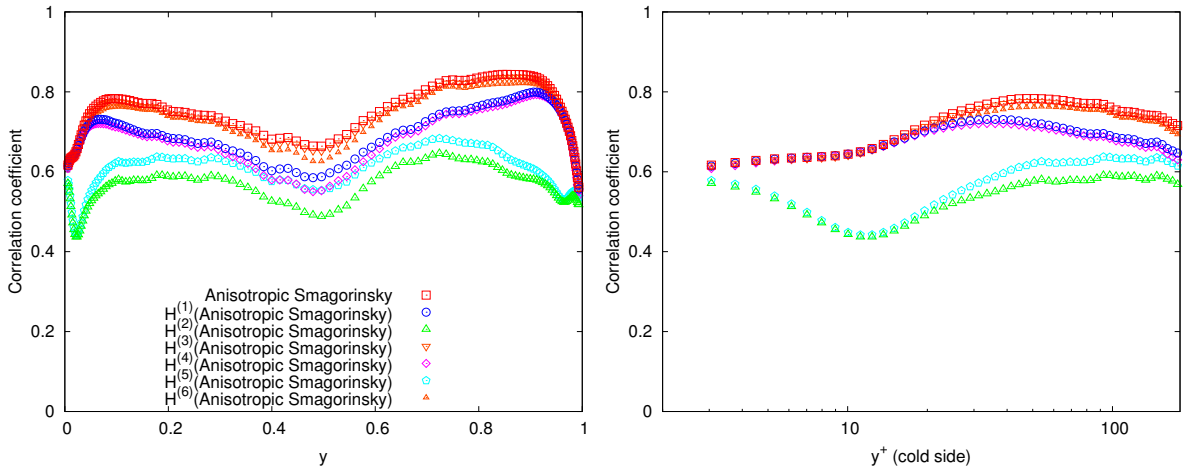


(b) Regression coefficient.

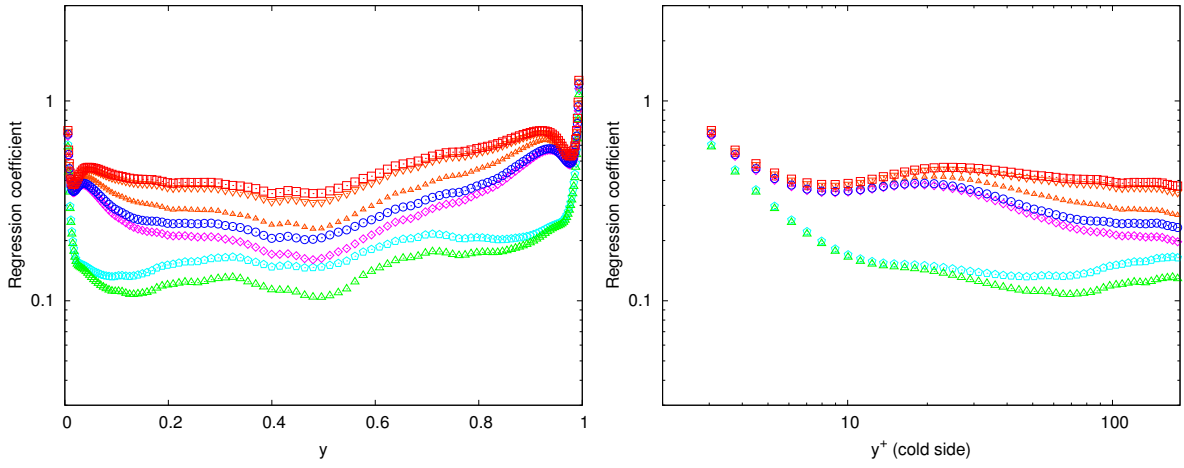


(c) Concordance correlation coefficient.

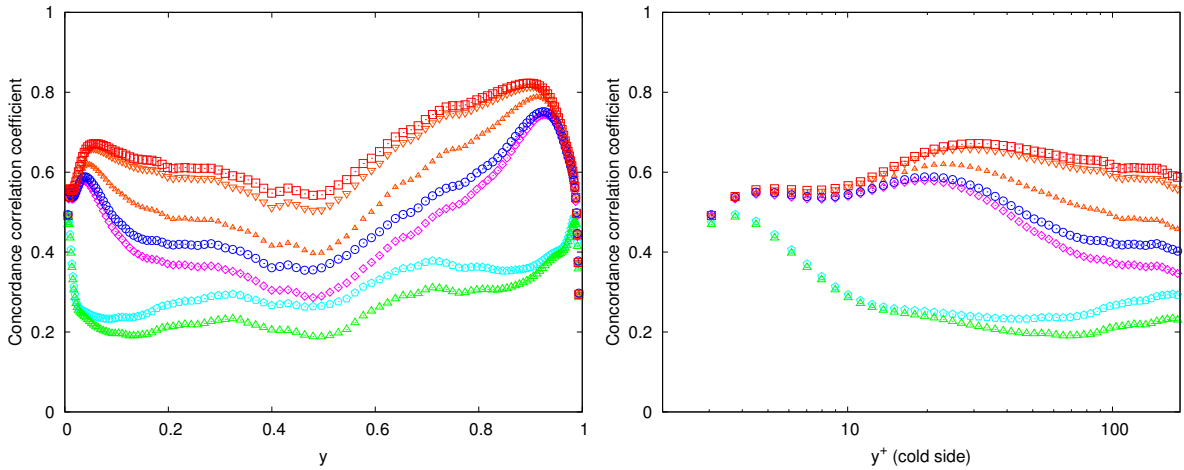
Figure C.7 – Correlation coefficient, regression coefficient, and concordance correlation coefficient between the divergence of the wall-normal-related part of the exact momentum convection subgrid term $\partial_j F_{U_j U_y}$ and tensorial Anisotropic Smagorinsky models $\partial_j \tau_{yj}^{H^{(k)} \text{An.Smag.}}(\bar{U}, \bar{\Delta})$.



(a) Correlation coefficient.



(b) Regression coefficient.



(c) Concordance correlation coefficient.

Figure C.8 – Correlation coefficient, regression coefficient, and concordance correlation coefficient between the subgrid kinetic energy dissipation of the exact momentum convection subgrid term $\bar{\rho}F_{U_j U_i} S_{ij}$ and tensorial Anisotropic Smagorinsky models $\bar{\rho}\tau_{ij}^{H^{(k)} \text{An.Smag.}}(\bar{\mathbf{U}}, \bar{\mathbf{\Delta}}) S_{ij}$.

Appendix D

A posteriori tests

D.1 Tables of friction Reynolds number

D.1.1 Isothermal simulation at $Re_\tau = 180$

Model	Friction Reynolds number		
	Mesh 24C	Mesh 36C	Mesh 48B
None (no model)	160	175	179
Smag	174	204	193
WALE	148	159	162
Sigma	145	157	161
AMD	141	154	158
Koba	152	165	169
AnSmag	140	155	158
Grad ($C^{\text{Grad.}} = 1$)	161	178	183
Grad, $C^{\text{Grad.}} = 2$	—	—	188
Grad, $C^{\text{Grad.}} = 2$, filtered	—	—	180
Grad, $C^{\text{Grad.}} = 9$, filtered	—	—	182
Simil (filter T)	159	174	179
Simil, filter A	155	169	174
$H^{(1)}$ AMD	—	—	169
$H^{(2)}$ AMD	—	—	190
$H^{(3)}$ AMD	—	—	162
$H^{(4)}$ AMD	156	171	174
$H^{(5)}$ AMD	—	—	185
$H^{(6)}$ AMD	—	—	167
$H^{(4)}$ Smag	—	—	251
$H^{(4)}$ WALE	—	—	172
$H^{(4)}$ Sigma	—	—	171
$H^{(4)}$ AnSmag	—	—	173

Table D.1 – (Continued on next page). See page 305 for label.

Model	Friction Reynolds number		
	Mesh 24C	Mesh 36C	Mesh 48B
Grad+AMD	147	143	163
(1- $H^{(1)}$)Grad+ $H^{(1)}$ AMD	154	167	170
(1- $H^{(2)}$)Grad+ $H^{(2)}$ AMD	176	193	196
(1- $H^{(3)}$)Grad+ $H^{(3)}$ AMD	146	158	161
(1- $H^{(4)}$)Grad+ $H^{(4)}$ AMD	160	176	177
(1- $H^{(5)}$)Grad+ $H^{(5)}$ AMD	173	187	190
(1- $H^{(6)}$)Grad+ $H^{(6)}$ AMD	155	169	171
(1- $H^{(7)}$)Grad+ $H^{(6)}$ AMD	158	174	176
Simil+AMD	143	155	158
(1- $H^{(1)}$)Simil+ $H^{(1)}$ AMD	156	169	171
(1- $H^{(2)}$)Simil+ $H^{(2)}$ AMD	175	190	192
(1- $H^{(3)}$)Simil+ $H^{(3)}$ AMD	146	158	161
(1- $H^{(4)}$)Simil+ $H^{(4)}$ AMD	162	175	177
(1- $H^{(5)}$)Simil+ $H^{(5)}$ AMD	171	184	186
(1- $H^{(6)}$)Simil+ $H^{(6)}$ AMD	153	166	169
(1- $H^{(7)}$)Simil+ $H^{(6)}$ AMD	153	167	170
PDSmag	150	161	162
TPDSmag	—	—	162
PDAnSmag	—	—	148
GDSmag	162	178	178
GDWALE	145	165	170
GDSigma	139	155	161
GDAMD	—	—	167
GDKoba	—	—	168
GDAnSmag	147	155	150
TGDSmag	158	174	175
TGDWALE	—	—	172
TGDSigma	—	—	166
TGDAMD	—	—	176
TGDKoba	—	—	170
TGDAnSmag	147	164	164
PDGrad	—	—	193
TPDGrad	—	—	180
GDGrad	—	—	192
TGDGrad	—	—	184
P1Grad+AMD	—	—	168
PDGrad+PDAMD*	—	—	179
PDGrad+P1AMD*	—	—	179
P1Grad+PDAMD*	—	—	191
P2(Grad+AMD)*	—	—	191
TP1Grad+AMD	—	—	165
TPDGrad+TPDAMD*	—	—	172

Table D.1 – (Continued on next page). See page 305 for label.

Model	Friction Reynolds number		
	Mesh 24C	Mesh 36C	Mesh 48B
TPDGrad+TP1AMD*	—	—	174
TP1Grad+TPDAMD*	—	—	175
TP2(Grad+AMD)*	—	—	176
G1Grad+AMD	—	—	167
GDGrad+GDAMD	—	—	182
GDGrad+G1AMD	—	—	181
G1Grad+GDAMD*	—	—	192
G2(Grad+AMD)*	—	—	192
TG1Grad+AMD	—	—	166
TGDGrad+TGDAMD	—	—	182
TGDGrad+TG1AMD*	—	—	185
TG1Grad+TGDAMD	—	—	185
TG2(Grad+AMD)*	—	—	186

Table D.1 – (Continued). Friction Reynolds number of the isothermal simulations at $Re_\tau = 180$. The reference friction Reynolds number of the filtered direct numerical simulation is 176. An asterisk (*) indicates the clipping of the AMD-related part.

D.1.2 Anisothermal simulation at $Re_\tau = 180$

Formulation–Model#1–Model#2	Friction Reynolds number (cold side;hot side;average)		
	Mesh 24C	Mesh 36C	Mesh 48B
V–None–None (no model)	235;102;168	260;106;183	269;105;187
V–Smag–None	—;—;—	—;—;—	203;094;149
V–WALE–None	221;091;156	238;095;166	244;097;170
V–Sigma–None	218;088;153	235;094;165	242;096;169
V–AMD–None	213;085;149	231;092;162	238;094;166
V–Koba–None	—;—;—	—;—;—	253;100;177
V–AnSmag–None	—;—;—	—;—;—	236;096;166
V–Grad–None ($C^{\text{Grad.}} = 1$)	237;103;170	265;108;186	275;108;191
V–Grad–None, $C^{\text{Grad.}} = 2$	—;—;—	—;—;—	284;110;197
V–Grad–None, $C^{\text{Grad.}} = 2$, filtered	—;—;—	—;—;—	269;106;187
V–Grad–None, $C^{\text{Grad.}} = 9$, filtered	—;—;—	—;—;—	271;108;190
V–Simil–None (filter T)	—;—;—	—;—;—	268;105;186
V–Simil–None, filter A	—;—;—	—;—;—	257;105;181
V– $H^{(1)}$ AMD–None	—;—;—	—;—;—	254;098;176
V– $H^{(2)}$ AMD–None	—;—;—	—;—;—	287;106;196
V– $H^{(3)}$ AMD–None	—;—;—	—;—;—	244;095;170
V– $H^{(4)}$ AMD–None	232;095;164	255;101;178	261;100;180
V– $H^{(5)}$ AMD–None	—;—;—	—;—;—	281;102;192
V– $H^{(6)}$ AMD–None	—;—;—	—;—;—	251;098;175
V– $H^{(4)}$ Smag–None	—;—;—	—;—;—	418;126;272

Table D.2 – (Continued on next page). See page 310 for label.

Formulation–Model#1–Model#2	Friction Reynolds number (cold side;hot side;average)		
	Mesh 24C	Mesh 36C	Mesh 48B
V– $H^{(4)}$ WALE–None	—;—;—	—;—;—	258;101;179
V– $H^{(4)}$ Sigma–None	—;—;—	—;—;—	257;100;179
V– $H^{(4)}$ AnSmag–None	—;—;—	—;—;—	261;100;180
V–Grad+AMD–None	—;—;—	—;—;—	244;096;170
V–(1– $H^{(1)}$)Grad+ $H^{(1)}$ AMD–None	—;—;—	—;—;—	256;099;177
V–(1– $H^{(2)}$)Grad+ $H^{(2)}$ AMD–None	—;—;—	—;—;—	297;111;204
V–(1– $H^{(3)}$)Grad+ $H^{(3)}$ AMD–None	—;—;—	—;—;—	244;095;169
V–(1– $H^{(4)}$)Grad+ $H^{(4)}$ AMD–None	239;099;169	263;104;183	267;102;184
V–(1– $H^{(5)}$)Grad+ $H^{(5)}$ AMD–None	—;—;—	—;—;—	290;108;199
V–(1– $H^{(6)}$)Grad+ $H^{(6)}$ AMD–None	—;—;—	—;—;—	258;100;179
V–(1– $H^{(7)}$)Grad+ $H^{(6)}$ AMD–None	236;098;167	260;103;182	265;102;184
V–PDSmag–None	—;—;—	—;—;—	246;097;171
V–PDAnSmag–None	—;—;—	—;—;—	222;092;157
V–GDSmag–None	—;—;—	—;—;—	265;104;185
V–GDWALE–None	—;—;—	—;—;—	256;100;178
V–GDSigma–None	—;—;—	—;—;—	244;097;170
V–GDAMD–None	—;—;—	—;—;—	251;099;175
V–GDKoba–None	—;—;—	—;—;—	252;100;176
V–GDAnSmag–None	—;—;—	—;—;—	225;094;160
V–TGDSmag–None	—;—;—	—;—;—	265;100;182
V–TGDWALE–None	—;—;—	—;—;—	260;100;180
V–TGDSigma–None	—;—;—	—;—;—	252;098;175
V–TGDAMD–None	—;—;—	—;—;—	262;100;181
V–TGDKoba–None	—;—;—	—;—;—	257;100;178
V–TGDanSmag–None	—;—;—	—;—;—	250;096;173
V–PDGrad–None	—;—;—	—;—;—	290;111;201
V–TPDGrad–None	—;—;—	—;—;—	270;106;188
V–GDGrad–None	—;—;—	—;—;—	288;111;200
V–TGDGrad–None	—;—;—	—;—;—	277;107;192
V–P1Grad+AMD–None	—;—;—	—;—;—	253;096;175
V–PDGrad+PDAMD*–None	—;—;—	—;—;—	268;102;185
V–PDGrad+P1AMD*–None	—;—;—	—;—;—	268;102;185
V–P1Grad+PDAMD*–None	—;—;—	—;—;—	288;110;199
V–P2(Grad+AMD)*–None	—;—;—	—;—;—	289;110;199
V–TP1Grad+AMD–None	—;—;—	—;—;—	247;097;172
V–TPDGrad+TPDAMD*–None	—;—;—	—;—;—	256;095;176
V–TPDGrad+TP1AMD*–None	—;—;—	—;—;—	—;—;—
V–TP1Grad+TPDAMD*–None	—;—;—	—;—;—	259;096;177
V–TP2(Grad+AMD)*–None	—;—;—	—;—;—	264;105;185
V–G1Grad+AMD–None	—;—;—	—;—;—	250;097;173
V–GDGrad+GDAMD–None	—;—;—	—;—;—	270;104;187
V–GDGrad+G1AMD–None	—;—;—	—;—;—	270;104;187
V–G1Grad+GDAMD*–None	—;—;—	—;—;—	288;111;200

Table D.2 – (Continued on next page). See page 310 for label.

Formulation–Model#1–Model#2	Friction Reynolds number (cold side;hot side;average)		
	Mesh 24C	Mesh 36C	Mesh 48B
V–G2(Grad+AMD)*–None	—;—;—	—;—;—	287;111;199
V–TG1Grad+AMD–None	—;—;—	—;—;—	250;097;173
V–TGDGrad+TGDAMD–None	—;—;—	—;—;—	273;103;188
V–TGDGrad+TG1AMD*–None	—;—;—	—;—;—	267;107;192
V–TG1Grad+TGDAMD–None	—;—;—	—;—;—	278;105;191
V–TG2(Grad+AMD)*–None	—;—;—	—;—;—	280;107;194
V–None–Smag	245;097;171	—;—;—	280;101;190
V–None–WALE	234;103;168	—;—;—	269;105;187
V–None–Sigma	234;103;169	—;—;—	269;105;187
V–None–AMD	235;103;169	—;—;—	269;105;187
V–None–SAMD	235;103;169	—;—;—	269;105;187
V–None–Koba	235;103;169	—;—;—	269;105;187
V–None–AnSmag	235;102;168	—;—;—	269;105;187
V–None–Smag, $C^{\text{Smag.}} = 1.65$	251;095;173	—;—;—	287;098 ;193
V–None–WALE, $C^{\text{WALE}} = 0.95$	234;104;169	—;—;—	268;106;187
V–None–WALE, $C^{\text{WALE}} = 1.10$	234;104;169	—;—;—	268;106;187
V–None–WALE, $C^{\text{WALE}} = 1.65$	234;105;170	—;—;—	268;107;187
V–None–Sigma, $C^{\text{Sigma}} = 2.60$	234;104;169	—;—;—	269;106;187
V–None–AMD, $C^{\text{AMD}} = 0.90$	235;103;169	—;—;—	271;105;188
V–None–SAMD, $C^{\text{SAMD}} = 0.90$	236;103;170	—;—;—	269;106;188
V–None–Koba, $C^{\text{Koba.}} = 0.135$	235;103;169	—;—;—	269;105;187
V–None–AnSmag, $C^{\text{Smag.}} = 0.17$	236;101;169	—;—;—	270;105;188
V–None–Grad ($C^{\text{Grad.}} = 1$)	235;102;168	—;—;—	269;105;187
V–None–Grad, $C^{\text{Grad.}} = 2$	235;102;169	—;—;—	269;105;187
V–None–Grad, $C^{\text{Grad.}} = 2$, filtered	235;103;169	—;—;—	269;105;187
V–None–Grad, $C^{\text{Grad.}} = 9$, filtered	235;104;169	—;—;—	269;106;187
V–None–Simil (filter T)	235;102;169	—;—;—	269;105;187
V–None–Simil, filter A	235;103;169	—;—;—	269;106;187
V–None–Grad+AMD	235;103;169	—;—;—	269;105;187
V–None–TGDSmag	235;102;168	—;—;—	269;105;187
V–None–TGDWALE	—;—;—	—;—;—	269;105;187
V–None–TGDSigma	234;103;168	—;—;—	269;105;187
V–None–TGDAMD	235;102;168	—;—;—	269;105;187
V–None–TGDSAMD	235;103;169	—;—;—	269;105;187
V–None–TGDKoba	235;102;168	—;—;—	269;105;187
V–None–TGDAnSmag	235;102;168	—;—;—	270;105;188
F–None–Smag	—;—;—	—;—;—	—;—;—
F–None–WALE	234;102;168	—;—;—	268;105;187
F–None–Sigma	234;102;168	—;—;—	268;105;187
F–None–AMD	—;—;—	—;—;—	268;105;187
F–None–SAMD	234;102;168	—;—;—	268;105;187

Table D.2 – (Continued on next page). See page 310 for label.

Formulation–Model#1–Model#2	Friction Reynolds number (cold side;hot side;average)		
	Mesh 24C	Mesh 36C	Mesh 48B
F–None–Koba	234;102;168	—;—;—	269;105;187
F–None–AnSmag	233;101;167	—;—;—	269;105;187
F–None–Smag, $C^{\text{Smag.}} = 1.65$	—;—;—	—;—;—	—;—;—
F–None–WALE, $C^{\text{WALE}} = 0.95$	—;—;—	—;—;—	268;105;186
F–None–WALE, $C^{\text{WALE}} = 1.10$	—;—;—	—;—;—	267;105;186
F–None–WALE, $C^{\text{WALE}} = 1.65$	—;—;—	—;—;—	—;—;—
F–None–Sigma, $C^{\text{Sigma}} = 2.60$	—;—;—	—;—;—	268;105;186
F–None–AMD, $C^{\text{AMD}} = 0.90$	—;—;—	—;—;—	—;—;—
F–None–SAMD, $C^{\text{SAMD}} = 0.90$	—;—;—	—;—;—	—;—;—
F–None–Koba, $C^{\text{Koba.}} = 0.135$	—;—;—	—;—;—	—;—;—
F–None–AnSmag, $C^{\text{Smag.}} = 0.17$	232;100;166	—;—;—	268;104;186
F–None–Grad ($C^{\text{Grad.}} = 1$)	235;102;168	—;—;—	269;105;187
F–None–Grad, $C^{\text{Grad.}} = 2$	235;102;168	—;—;—	269;105;187
F–None–Grad, $C^{\text{Grad.}} = 2$, filtered	234;102;168	—;—;—	269;105;187
F–None–Grad, $C^{\text{Grad.}} = 9$, filtered	234;103;168	—;—;—	268;105;186
F–None–Simil (filter T)	235;102;168	—;—;—	269;105;187
F–None–Simil, filter A	234;103;168	—;—;—	268;105;186
F–None–Grad+AMD	—;—;—	—;—;—	—;—;—
F–None–TGDSmag	235;102;168	—;—;—	269;105;187
F–None–TGDWALE	—;—;—	—;—;—	269;105;187
F–None–TGDSigma	—;—;—	—;—;—	269;105;187
F–None–TGDAMD	235;102;168	—;—;—	269;105;187
F–None–TGDSAMD	234;102;168	—;—;—	269;105;187
F–None–TGDKoba	—;—;—	—;—;—	269;105;187
F–None–TGDAnSmag	234;101;167	—;—;—	269;104;186
V–Smag–Smag	—;—;—	—;—;—	326;104;215
V–WALE–WALE	220;091;156	238;095;166	244;097;170
V–WALE–WALE, $C^{\text{WALE}} = 1.10$	—;—;—	—;—;—	220;091;156
V–WALE–WALE, $C^{\text{WALE}} = 1.65$	—;—;—	—;—;—	211;089;150
V–Sigma–Sigma	217;089;153	235;095;165	242;097;169
V–AMD–AMD	213;085;149	231;093;162	237;095;166
V–Koba–Koba	—;—;—	—;—;—	253;100;177
V–AnSmag–AnSmag	—;—;—	—;—;—	237;096;166
V–Grad–Grad ($C^{\text{Grad.}} = 1$)	237;104;170	265;108;186	275;107;191
V–Grad–Grad, $C^{\text{Grad.}} = 2$	—;—;—	—;—;—	283;110;197
V–Grad–Grad, $C^{\text{Grad.}} = 2$, filtered	—;—;—	—;—;—	269;106;188
V–Grad–Grad, $C^{\text{Grad.}} = 9$, filtered	—;—;—	—;—;—	270;109;190
V–Simil–Simil (filter T)	233;102;168	259;106;182	268;105;186
V–Simil–Simil, filter A	227;101;164	249;105;177	257;105;181
V–GDSmag–GDSmag	—;—;—	—;—;—	266;104;185
V–GDWALE–GDWALE	—;—;—	—;—;—	256;100;178

Table D.2 – (Continued on next page). See page 310 for label.

Formulation–Model#1–Model#2	Friction Reynolds number (cold side;hot side;average)		
	Mesh 24C	Mesh 36C	Mesh 48B
V–GDSigma–GDSigma	—;—;—	—;—;—	243;097;170
V–GDAMD–GDAMD	—;—;—	—;—;—	251;098;175
V–GDKoba–GDKoba	—;—;—	—;—;—	252;100;176
V–GDAnSmag–GDAnSmag	—;—;—	—;—;—	227;094;160
V–TGDSmag–TGDSmag	—;—;—	—;—;—	265;100;182
V–TGDWALE–TGDWALE	—;—;—	—;—;—	260;101;180
V–TGDSigma–TGDSigma	—;—;—	—;—;—	252;098;175
V–TGDAMD–TGDAMD	—;—;—	—;—;—	262;100;181
V–TGDKoba–TGDKoba	—;—;—	—;—;—	256;100;178
V–TGDAnSmag–TGDAnSmag	—;—;—	—;—;—	250;097;174
V– $H^{(4)}$ AMD–Smag	246;090;168	264;097;180	274;096;185
V– $H^{(4)}$ AMD–WALE	232;095;164	255;101;178	261;100;181
V– $H^{(4)}$ AMD–Sigma	232;095;164	255;101;178	261;100;181
V– $H^{(4)}$ AMD–AMD	232;095;164	256;101;178	—;—;—
V– $H^{(4)}$ AMD–SAMD, $C^{\text{SAMD}} = 0.30$	233;096;164	255;102;178	261;101;181
V– $H^{(4)}$ AMD–Koba	232;095;164	255;101;178	261;100;181
V– $H^{(4)}$ AMD–AnSmag	233;095;164	256;101;178	262;100;181
V– $H^{(4)}$ AMD–Smag, $C^{\text{Smag.}} = 1.65$	256;089;172	269;095;182	283;094;189
V– $H^{(4)}$ AMD–WALE, $C^{\text{WALE}} = 0.95$	232;096;164	254;102;178	260;101;181
V– $H^{(4)}$ AMD–Sigma, $C^{\text{Sigma}} = 2.60$	232;096;164	254;102;178	260;101;181
V– $H^{(4)}$ AMD–AMD, $C^{\text{AMD}} = 0.90$	233;096;164	255;102;178	261;101;181
V– $H^{(4)}$ AMD–SAMD, $C^{\text{SAMD}} = 0.90$	232;096;164	255;103;179	261;102;181
V– $H^{(4)}$ AMD–Koba, $C^{\text{Koba.}} = 0.135$	232;096;164	255;102;178	261;101;181
V– $H^{(4)}$ AMD–AnSmag, $C^{\text{Smag.}} = 0.17$	234;094;164	257;101;179	263;100;182
V– $H^{(4)}$ AMD–Grad ($C^{\text{Grad.}} = 1$)	232;095;164	255;101;178	261;101;181
V– $H^{(4)}$ AMD–Grad, $C^{\text{Grad.}} = 2$	—;—;—	—;—;—	—;—;—
V– $H^{(4)}$ AMD–Grad, $C^{\text{Grad.}} = 2$, filtered	—;—;—	—;—;—	—;—;—
V– $H^{(4)}$ AMD–Grad, $C^{\text{Grad.}} = 9$, filtered	—;—;—	—;—;—	—;—;—
V– $H^{(4)}$ AMD–Simil (filter T)	233;095;164	256;101;178	261;100;181
V– $H^{(4)}$ AMD–Simil, filter A	232;096;164	254;102;178	260;101;181
F–Smag–Smag	—;—;—	—;—;—	310;104;207
F–WALE–WALE	220;091;156	237;095;166	243;096;170
F–WALE–WALE, $C^{\text{WALE}} = 1.10$	—;—;—	—;—;—	219;091;155
F–WALE–WALE, $C^{\text{WALE}} = 1.65$	—;—;—	—;—;—	211;089;150
F–Sigma–Sigma	217;088;153	235;094;164	241;096;169
F–AMD–AMD	212;085;149	230;091;161	237;093;165
F–Koba–Koba	—;—;—	—;—;—	253;100;177
F–AnSmag–AnSmag	—;—;—	—;—;—	236;095;165
F–Grad–Grad ($C^{\text{Grad.}} = 1$)	237;103;170	265;108;186	275;107;191
F–Grad–Grad, $C^{\text{Grad.}} = 2$	—;—;—	—;—;—	283;110;196
F–Grad–Grad, $C^{\text{Grad.}} = 2$, filtered	—;—;—	—;—;—	268;106;187

Table D.2 – (Continued on next page). See page 310 for label.

Formulation–Model#1–Model#2	Friction Reynolds number (cold side;hot side;average)		
	Mesh 24C	Mesh 36C	Mesh 48B
F–Grad–Grad, $C^{\text{Grad.}} = 9$, filtered	—;—;—	—;—;—	269;108;188
F–Simil–Simil (filter T)	233;102;167	259;105;182	267;104;186
F–Simil–Simil, filter A	228;099;164	250;103;176	257;103;180
F–GDSmag–GDSmag	—;—;—	—;—;—	265;105;185
F–GDWALE–GDWALE	—;—;—	—;—;—	256;100;178
F–GDSigma–GDSigma	—;—;—	—;—;—	243;097;170
F–GDAMD–GDAMD	—;—;—	—;—;—	250;098;174
F–GDKoba–GDKoba	—;—;—	—;—;—	252;100;176
F–GDAnSmag–GDAnSmag	—;—;—	—;—;—	226;092;159
F–TGDSmag–TGDSmag	—;—;—	—;—;—	264;100;182
F–TGDWALE–TGDWALE	—;—;—	—;—;—	260;100;180
F–TGDSigma–TGDSigma	—;—;—	—;—;—	252;098;175
F–TGDAMD–TGDAMD	—;—;—	—;—;—	262;100;181
F–TGDKoba–TGDKoba	—;—;—	—;—;—	256;100;178
F–TGDAnSmag–TGDAnSmag	—;—;—	—;—;—	249;096;172
F– $H^{(4)}$ AMD–Smag	—;—;—	—;—;—	—;—;—
F– $H^{(4)}$ AMD–WALE	232;095;163	255;100;178	260;099;180
F– $H^{(4)}$ AMD–Sigma	232;095;163	255;100;177	260;099;180
F– $H^{(4)}$ AMD–AMD	232;094;163	255;100;177	—;—;—
F– $H^{(4)}$ AMD–SAMD, $C^{\text{SAMD}} = 0.30$	232;094;163	254;100;177	260;099;179
F– $H^{(4)}$ AMD–Koba	232;094;163	255;100;178	261;099;180
F– $H^{(4)}$ AMD–AnSmag	232;094;163	255;099;177	261;099;180
F– $H^{(4)}$ AMD–Smag, $C^{\text{Smag.}} = 1.65$	—;—;—	—;—;—	—;—;—
F– $H^{(4)}$ AMD–WALE, $C^{\text{WALE}} = 0.95$	231;095;163	254;100;177	259;099;179
F– $H^{(4)}$ AMD–Sigma, $C^{\text{Sigma}} = 2.60$	231;095;163	254;100;177	259;099;179
F– $H^{(4)}$ AMD–AMD, $C^{\text{AMD}} = 0.90$	—;—;—	—;—;—	—;—;—
F– $H^{(4)}$ AMD–SAMD, $C^{\text{SAMD}} = 0.90$	—;—;—	—;—;—	—;—;—
F– $H^{(4)}$ AMD–Koba, $C^{\text{Koba.}} = 0.135$	232;095;163	254;100;177	260;099;180
F– $H^{(4)}$ AMD–AnSmag, $C^{\text{Smag.}} = 0.17$	230;093;162	254;098;176	261;098;179
F– $H^{(4)}$ AMD–Grad ($C^{\text{Grad.}} = 1$)	232;094;163	255;100;177	261;099;180
F– $H^{(4)}$ AMD–Grad, $C^{\text{Grad.}} = 2$	—;—;—	—;—;—	—;—;—
F– $H^{(4)}$ AMD–Grad, $C^{\text{Grad.}} = 2$, filtered	—;—;—	—;—;—	—;—;—
F– $H^{(4)}$ AMD–Grad, $C^{\text{Grad.}} = 9$, filtered	—;—;—	—;—;—	—;—;—
F– $H^{(4)}$ AMD–Simil (filter T)	232;094;163	255;100;178	261;099;180
F– $H^{(4)}$ AMD–Simil, filter A	232;094;163	254;099;177	260;099;179

Table D.2 – (Continued). Friction Reynolds number of the anisothermal simulations at $Re_\tau = 180$. The reference friction Reynolds number of the filtered direct numerical simulation is 183 (261;105;183).

D.1.3 Anisothermal simulation at $Re_\tau = 395$

Formulation–Model#1–Model#2	Friction Reynolds number (cold side;hot side;average) Mesh 96B
V–None–None (no model)	595;233;414
V–WALE–None	554;221;387
V–Sigma–None	550;219;385
V–AMD–None	539;216;377
V–Grad–None ($C^{\text{Grad.}} = 1$)	607;237;422
V–Simil–None (filter T)	593;233;413
V–Simil–None, filter A	576;231;403
V– $H^{(4)}$ AMD–None	592;233;413
V– $(1-H^{(4)})$ Grad+ $H^{(4)}$ AMD–None	603;236;419
V– $(1-H^{(7)})$ Grad+ $H^{(6)}$ AMD–None	597;234;416
V–Smag–Smag	—;—;—
V–WALE–WALE	554;220;387
V–WALE–WALE, $C^{\text{WALE}} = 1.10$	—;—;—
V–WALE–WALE, $C^{\text{WALE}} = 1.65$	—;—;—
V–Sigma–Sigma	550;219;385
V–AMD–AMD	539;215;377
V–Koba–Koba	—;—;—
V–AnSmag–AnSmag	—;—;—
V–Simil–Simil (filter T)	593;233;413
V–Simil–Simil, filter A	577;230;403
V– $H^{(4)}$ AMD–Smag	619;224;421
V– $H^{(4)}$ AMD–WALE	593;233;413
V– $H^{(4)}$ AMD–Sigma	592;234;413
V– $H^{(4)}$ AMD–AMD	594;232;413
V– $H^{(4)}$ AMD–SAMD, $C^{\text{SAMD}} = 0.30$	594;233;413
V– $H^{(4)}$ AMD–Koba	592;233;413
V– $H^{(4)}$ AMD–AnSmag	593;233;413
V– $H^{(4)}$ AMD–Smag, $C^{\text{Smag.}} = 1.65$	634;217;425
V– $H^{(4)}$ AMD–WALE, $C^{\text{WALE}} = 0.95$	592;233;413
V– $H^{(4)}$ AMD–Sigma, $C^{\text{Sigma}} = 2.60$	593;233;413
V– $H^{(4)}$ AMD–AMD, $C^{\text{AMD}} = 0.90$	595;234;413
V– $H^{(4)}$ AMD–SAMD, $C^{\text{SAMD}} = 0.90$	593;234;412
V– $H^{(4)}$ AMD–Koba, $C^{\text{Koba.}} = 0.135$	592;234;413
V– $H^{(4)}$ AMD–AnSmag, $C^{\text{Smag.}} = 0.17$	595;233;414
V– $H^{(4)}$ AMD–Simil (filter T)	593;234;413
V– $H^{(4)}$ AMD–Simil, filter A	594;233;413
F–Smag–Smag	—;—;—
F–WALE–WALE	553;220;387
F–WALE–WALE, $C^{\text{WALE}} = 1.10$	—;—;—

Table D.3 – (Continued on next page). See page 312 for label.

Formulation–Model#1–Model#2	Friction Reynolds number (cold side;hot side;average)		
	Mesh 96B		
F–WALE–WALE, $C^{\text{WALE}} = 1.65$	—;—;—		
F–Sigma–Sigma	548;219;383		
F–AMD–AMD	535;215;375		
F–Koba–Koba	—;—;—		
F–AnSmag–AnSmag	—;—;—		
F–Simil–Simil (filter T)	594;233;413		
F–Simil–Simil, filter A	571;230;400		
F– $H^{(4)}$ AMD–Smag	584;226;405		
F– $H^{(4)}$ AMD–WALE	590;233;411		
F– $H^{(4)}$ AMD–Sigma	590;234;412		
F– $H^{(4)}$ AMD–AMD	588;233;411		
F– $H^{(4)}$ AMD–SAMD, $C^{\text{SAMD}} = 0.30$	588;233;411		
F– $H^{(4)}$ AMD–Koba	590;233;411		
F– $H^{(4)}$ AMD–AnSmag	590;233;412		
F– $H^{(4)}$ AMD–Smag, $C^{\text{Smag.}} = 1.65$	—;—;—		
F– $H^{(4)}$ AMD–WALE, $C^{\text{WALE}} = 0.95$	588;233;411		
F– $H^{(4)}$ AMD–Sigma, $C^{\text{Sigma}} = 2.60$	588;233;410		
F– $H^{(4)}$ AMD–AMD, $C^{\text{AMD}} = 0.90$	—;—;—		
F– $H^{(4)}$ AMD–SAMD, $C^{\text{SAMD}} = 0.90$	—;—;—		
F– $H^{(4)}$ AMD–Koba, $C^{\text{Koba.}} = 0.135$	590;233;412		
F– $H^{(4)}$ AMD–AnSmag, $C^{\text{Smag.}} = 0.17$	589;233;411		
F– $H^{(4)}$ AMD–Simil (filter T)	590;233;411		
F– $H^{(4)}$ AMD–Simil, filter A	588;233;410		

Table D.3 – (Continued). Friction Reynolds number of anisothermal simulations at $Re_\tau = 395$. The reference friction Reynolds number of the filtered direct numerical simulation is 392 (556;227;392).

D.2 Tables of wall heat flux

D.2.1 Anisothermal simulation at $Re_\tau = 180$

Formulation–Model#1–Model#2	Wall heat flux, W/m^2 (cold side;hot side;average)		
	Mesh 24C	Mesh 36C	Mesh 48B
V–None–None (no model)	1253;1256;1254	1450;1434;1442	1503;1508;1506
V–Smag–None	—;—;—	—;—;—	1238;1242;1240
V–WALE–None	1062;1071;1067	1259;1260;1260	1348;1352;1350
V–Sigma–None	1030;1039;1034	1243;1246;1244	1334;1339;1336
V–AMD–None	0993;1004;0998	1191;1198;1194	1290;1294;1292
V–Koba–None	—;—;—	—;—;—	1407;1411;1409

Table D.4 – (Continued on next page). See page 318 for label.

Formulation–Model#1–Model#2	Wall heat flux, W/m ² (cold side;hot side;average)		
	Mesh 24C	Mesh 36C	Mesh 48B
V–AnSmag–None	—;—;—	—;—;—	1296;1300;1298
V–Grad–None ($C^{\text{Grad.}} = 1$)	1278;1281;1280	1474;1455;1464	1523;1528;1525
V–Grad–None, $C^{\text{Grad.}} = 2$	—;—;—	—;—;—	1547;1551;1549
V–Grad–None, $C^{\text{Grad.}} = 2$, filtered	—;—;—	—;—;—	1494;1498;1496
V–Grad–None, $C^{\text{Grad.}} = 9$, filtered	—;—;—	—;—;—	1461;1465;1463
V–Simil–None (filter T)	—;—;—	—;—;—	1452;1457;1454
V–Simil–None, filter A	—;—;—	—;—;—	1344;1348;1346
V– $H^{(1)}$ AMD–None	—;—;—	—;—;—	1386;1390;1388
V– $H^{(2)}$ AMD–None	—;—;—	—;—;—	1528;1533;1530
V– $H^{(3)}$ AMD–None	—;—;—	—;—;—	1328;1333;1331
V– $H^{(4)}$ AMD–None	1175;1184;1180	1392;1391;1392	1447;1451;1449
V– $H^{(5)}$ AMD–None	—;—;—	—;—;—	1474;1480;1477
V– $H^{(6)}$ AMD–None	—;—;—	—;—;—	1394;1399;1397
V– $H^{(4)}$ Smag–None	—;—;—	—;—;—	1802;1807;1804
V– $H^{(4)}$ WALE–None	—;—;—	—;—;—	1449;1453;1451
V– $H^{(4)}$ Sigma–None	—;—;—	—;—;—	1443;1447;1445
V– $H^{(4)}$ AnSmag–None	—;—;—	—;—;—	1436;1440;1438
V–Grad+AMD–None	—;—;—	—;—;—	1314;1318;1316
V–(1– $H^{(1)}$)Grad+ $H^{(1)}$ AMD–None	—;—;—	—;—;—	1419;1423;1421
V–(1– $H^{(2)}$)Grad+ $H^{(2)}$ AMD–None	—;—;—	—;—;—	1612;1617;1615
V–(1– $H^{(3)}$)Grad+ $H^{(3)}$ AMD–None	—;—;—	—;—;—	1318;1323;1320
V–(1– $H^{(4)}$)Grad+ $H^{(4)}$ AMD–None	1272;1280;1276	1471;1466;1468	1496;1501;1499
V–(1– $H^{(5)}$)Grad+ $H^{(5)}$ AMD–None	—;—;—	—;—;—	1573;1578;1576
V–(1– $H^{(6)}$)Grad+ $H^{(6)}$ AMD–None	—;—;—	—;—;—	1452;1457;1454
V–(1– $H^{(7)}$)Grad+ $H^{(6)}$ AMD–None	1243;1252;1247	1451;1446;1448	1502;1507;1504
V–PDSmag–None	—;—;—	—;—;—	1353;1357;1355
V–PDAnSmag–None	—;—;—	—;—;—	1224;1229;1227
V–GDSmag–None	—;—;—	—;—;—	1500;1504;1502
V–GDWALE–None	—;—;—	—;—;—	1428;1432;1430
V–GDSigma–None	—;—;—	—;—;—	1349;1353;1351
V–GDAMD–None	—;—;—	—;—;—	1397;1401;1399
V–GDKoba–None	—;—;—	—;—;—	1401;1405;1403
V–GDAnSmag–None	—;—;—	—;—;—	1229;1234;1231
V–TGDSmag–None	—;—;—	—;—;—	1438;1442;1440
V–TGDWALE–None	—;—;—	—;—;—	1430;1435;1432
V–TGDSigma–None	—;—;—	—;—;—	1374;1379;1377
V–TGDAMD–None	—;—;—	—;—;—	1440;1443;1441
V–TGDKoba–None	—;—;—	—;—;—	1413;1418;1415
V–TGDAAnSmag–None	—;—;—	—;—;—	1349;1353;1351
V–PDGrad–None	—;—;—	—;—;—	1575;1578;1576
V–TPDGrad–None	—;—;—	—;—;—	1443;1446;1444
V–GDGrad–None	—;—;—	—;—;—	1558;1561;1559

Table D.4 – (Continued on next page). See page 318 for label.

Formulation–Model#1–Model#2	Wall heat flux, W/m ² (cold side;hot side;average)		
	Mesh 24C	Mesh 36C	Mesh 48B
V–TGDGrad–None	—;—;—	—;—;—	1500;1504;1502
V–P1Grad+AMD–None	—;—;—	—;—;—	1348;1351;1350
V–PDGrad+PDAMD*–None	—;—;—	—;—;—	1487;1491;1489
V–PDGrad+P1AMD*–None	—;—;—	—;—;—	1484;1489;1487
V–P1Grad+PDAMD*–None	—;—;—	—;—;—	1582;1586;1584
V–P2(Grad+AMD)*–None	—;—;—	—;—;—	1583;1587;1585
V–TP1Grad+AMD–None	—;—;—	—;—;—	1346;1350;1348
V–TPDGrad+TPDAMD*–None	—;—;—	—;—;—	1324;1327;1325
V–TPDGrad+TP1AMD*–None	—;—;—	—;—;—	—;—;—
V–TP1Grad+TPDAMD*–None	—;—;—	—;—;—	1344;1349;1347
V–TP2(Grad+AMD)*–None	—;—;—	—;—;—	1425;1429;1427
V–G1Grad+AMD–None	—;—;—	—;—;—	1333;1337;1335
V–GDGrad+GDAMD–None	—;—;—	—;—;—	1498;1502;1500
V–GDGrad+G1AMD–None	—;—;—	—;—;—	1498;1502;1500
V–G1Grad+GDAMD*–None	—;—;—	—;—;—	1561;1565;1563
V–G2(Grad+AMD)*–None	—;—;—	—;—;—	1557;1561;1559
V–TG1Grad+AMD–None	—;—;—	—;—;—	1353;1356;1355
V–TGDGrad+TGDAMD–None	—;—;—	—;—;—	1466;1471;1468
V–TGDGrad+TG1AMD*–None	—;—;—	—;—;—	1508;1513;1510
V–TG1Grad+TGDAMD–None	—;—;—	—;—;—	1523;1529;1526
V–TG2(Grad+AMD)*–None	—;—;—	—;—;—	1530;1535;1532
V–None–Smag	2514;0794;1654	—;—;—	2207;1453;1830
V–None–WALE	1308;1311;1310	—;—;—	1535;1539;1537
V–None–Sigma	1338;1340;1339	—;—;—	1554;1559;1557
V–None–AMD	1393;1386;1389	—;—;—	1614;1618;1616
V–None–SAMD	1376;1369;1372	—;—;—	1604;1608;1606
V–None–Koba	1294;1296;1295	—;—;—	1529;1534;1531
V–None–AnSmag	1364;1300;1332	—;—;—	1534;1532;1533
V–None–Smag, $C^{\text{Smag.}} = 1.65$	3459;0534;1996	—;—;—	2773;1269;2021
V–None–WALE, $C^{\text{WALE}} = 0.95$	1419;1421;1420	—;—;—	1608;1612;1610
V–None–WALE, $C^{\text{WALE}} = 1.10$	1468;1470;1469	—;—;—	1643;1648;1645
V–None–WALE, $C^{\text{WALE}} = 1.65$	1676;1676;1676	—;—;—	1817;1822;1820
V–None–Sigma, $C^{\text{Sigma}} = 2.60$	1498;1499;1498	—;—;—	1657;1662;1660
V–None–AMD, $C^{\text{AMD}} = 0.90$	1589;1562;1576	—;—;—	1788;1791;1790
V–None–SAMD, $C^{\text{SAMD}} = 0.90$	1584;1553;1568	—;—;—	1776;1779;1778
V–None–Koba, $C^{\text{Koba.}} = 0.135$	1362;1364;1363	—;—;—	1575;1580;1577
V–None–AnSmag, $C^{\text{Smag.}} = 0.17$	1570;1376;1473	—;—;—	1588;1572;1580
V–None–Grad ($C^{\text{Grad.}} = 1$)	1291;1292;1291	—;—;—	1535;1539;1537
V–None–Grad, $C^{\text{Grad.}} = 2$	1323;1323;1323	—;—;—	1566;1570;1568
V–None–Grad, $C^{\text{Grad.}} = 2$, filtered	1332;1328;1330	—;—;—	1572;1576;1574
V–None–Grad, $C^{\text{Grad.}} = 9$, filtered	1558;1529;1544	—;—;—	1782;1786;1784
V–None–Simil (filter T)	1326;1326;1326	—;—;—	1557;1562;1560

Table D.4 – (Continued on next page). See page 318 for label.

Formulation–Model#1–Model#2	Wall heat flux, W/m ² (cold side;hot side;average)		
	Mesh 24C	Mesh 36C	Mesh 48B
V–None–Simil, filter A	1581;1559;1570	—;—;—	1776;1780;1778
V–None–Grad+AMD	1426;1418;1422	—;—;—	1650;1654;1652
V–None–TGDSmag	1270;1245;1257	—;—;—	1520;1498;1509
V–None–TGDWALE	—;—;—	—;—;—	1532;1536;1534
V–None–TGDSigma	1325;1327;1326	—;—;—	1555;1559;1557
V–None–TGDAMD	1289;1290;1289	—;—;—	1546;1550;1548
V–None–TGDSAMD	1350;1345;1348	—;—;—	1570;1574;1572
V–None–TGDKoba	1270;1272;1271	—;—;—	1524;1528;1526
V–None–TGDAAnSmag	1344;1292;1318	—;—;—	1601;1588;1594
F–None–Smag	—;—;—	—;—;—	—;—;—
F–None–WALE	1310;1312;1311	—;—;—	1535;1539;1537
F–None–Sigma	1336;1338;1337	—;—;—	1553;1558;1555
F–None–AMD	—;—;—	—;—;—	1627;1652;1640
F–None–SAMD	1370;1363;1366	—;—;—	1598;1602;1600
F–None–Koba	1290;1292;1291	—;—;—	1529;1533;1531
F–None–AnSmag	1362;1298;1330	—;—;—	1529;1527;1528
F–None–Smag, $C^{\text{Smag.}} = 1.65$	—;—;—	—;—;—	—;—;—
F–None–WALE, $C^{\text{WALE}} = 0.95$	—;—;—	—;—;—	1600;1604;1602
F–None–WALE, $C^{\text{WALE}} = 1.10$	—;—;—	—;—;—	1635;1640;1638
F–None–WALE, $C^{\text{WALE}} = 1.65$	—;—;—	—;—;—	—;—;—
F–None–Sigma, $C^{\text{Sigma}} = 2.60$	—;—;—	—;—;—	1650;1655;1652
F–None–AMD, $C^{\text{AMD}} = 0.90$	—;—;—	—;—;—	—;—;—
F–None–SAMD, $C^{\text{SAMD}} = 0.90$	—;—;—	—;—;—	—;—;—
F–None–Koba, $C^{\text{Koba.}} = 0.135$	—;—;—	—;—;—	—;—;—
F–None–AnSmag, $C^{\text{Smag.}} = 0.17$	1561;1372;1466	—;—;—	1582;1567;1574
F–None–Grad ($C^{\text{Grad.}} = 1$)	1290;1291;1290	—;—;—	1535;1539;1537
F–None–Grad, $C^{\text{Grad.}} = 2$	1322;1322;1322	—;—;—	1563;1568;1565
F–None–Grad, $C^{\text{Grad.}} = 2$, filtered	1334;1329;1331	—;—;—	1570;1575;1573
F–None–Grad, $C^{\text{Grad.}} = 9$, filtered	1561;1532;1546	—;—;—	1776;1779;1778
F–None–Simil (filter T)	1327;1327;1327	—;—;—	1554;1559;1557
F–None–Simil, filter A	1582;1560;1571	—;—;—	1768;1772;1770
F–None–Grad+AMD	—;—;—	—;—;—	—;—;—
F–None–TGDSmag	1250;1245;1248	—;—;—	1498;1496;1497
F–None–TGDWALE	—;—;—	—;—;—	1534;1538;1536
F–None–TGDSigma	—;—;—	—;—;—	1554;1559;1557
F–None–TGDAMD	1291;1292;1292	—;—;—	1546;1550;1548
F–None–TGDSAMD	1348;1344;1346	—;—;—	1567;1571;1569
F–None–TGDKoba	—;—;—	—;—;—	1524;1528;1526
F–None–TGDAAnSmag	1383;1311;1347	—;—;—	1597;1584;1590
V–Smag–Smag	—;—;—	—;—;—	1846;1301;1574
V–WALE–WALE	1089;1097;1093	1284;1284;1284	1371;1376;1374

Table D.4 – (Continued on next page). See page 318 for label.

Formulation–Model#1–Model#2	Wall heat flux, W/m ² (cold side;hot side;average)		
	Mesh 24C	Mesh 36C	Mesh 48B
V–WALE–WALE, $C^{\text{WALE}} = 1.10$	—;—;—	—;—;—	1203;1208;1206
V–WALE–WALE, $C^{\text{WALE}} = 1.65$	—;—;—	—;—;—	1107;1111;1109
V–Sigma–Sigma	1069;1079;1074	1280;1282;1281	1369;1373;1371
V–AMD–AMD	1067;1077;1072	1278;1279;1278	1358;1363;1361
V–Koba–Koba	—;—;—	—;—;—	1426;1431;1429
V–AnSmag–AnSmag	—;—;—	—;—;—	1327;1325;1326
V–Grad–Grad ($C^{\text{Grad.}} = 1$)	1313;1314;1314	1513;1491;1502	1553;1557;1555
V–Grad–Grad, $C^{\text{Grad.}} = 2$	—;—;—	—;—;—	1615;1619;1617
V–Grad–Grad, $C^{\text{Grad.}} = 2$, filtered	—;—;—	—;—;—	1560;1564;1562
V–Grad–Grad, $C^{\text{Grad.}} = 9$, filtered	—;—;—	—;—;—	1688;1692;1690
V–Simil–Simil (filter T)	1257;1260;1258	1455;1439;1447	1503;1508;1506
V–Simil–Simil, filter A	1289;1290;1289	1487;1472;1479	1537;1541;1539
V–GDSmag–GDSmag	—;—;—	—;—;—	1531;1507;1519
V–GDWALE–GDWALE	—;—;—	—;—;—	1437;1442;1440
V–GDSigma–GDSigma	—;—;—	—;—;—	1368;1373;1371
V–GDAMD–GDAMD	—;—;—	—;—;—	1432;1437;1435
V–GDKoba–GDKoba	—;—;—	—;—;—	1416;1421;1419
V–GDAnSmag–GDAnSmag	—;—;—	—;—;—	1278;1274;1276
V–TGDSmag–TGDSmag	—;—;—	—;—;—	1457;1436;1446
V–TGDWALE–TGDWALE	—;—;—	—;—;—	1453;1458;1456
V–TGDSigma–TGDSigma	—;—;—	—;—;—	1410;1415;1412
V–TGDAMD–TGDAMD	—;—;—	—;—;—	1480;1484;1482
V–TGDKoba–TGDKoba	—;—;—	—;—;—	1433;1437;1435
V–TGDAnSmag–TGDAnSmag	—;—;—	—;—;—	1405;1401;1403
V– $H^{(4)}$ AMD–Smag	2490;0849;1669	2396;1024;1710	2165;1458;1812
V– $H^{(4)}$ AMD–WALE	1197;1207;1202	1419;1418;1418	1474;1478;1476
V– $H^{(4)}$ AMD–Sigma	1217;1226;1222	1439;1436;1438	1487;1491;1489
V– $H^{(4)}$ AMD–AMD	1278;1283;1281	1508;1494;1501	—;—;—
V– $H^{(4)}$ AMD–SAMD, $C^{\text{SAMD}} = 0.30$	1263;1268;1265	1497;1483;1490	1540;1545;1542
V– $H^{(4)}$ AMD–Koba	1191;1200;1196	1413;1411;1412	1468;1473;1470
V– $H^{(4)}$ AMD–AnSmag	1278;1231;1254	1476;1410;1443	1479;1478;1479
V– $H^{(4)}$ AMD–Smag, $C^{\text{Smag.}} = 1.65$	3514;0591;2052	3086;0704;1895	2764;1311;2037
V– $H^{(4)}$ AMD–WALE, $C^{\text{WALE}} = 0.95$	1257;1267;1262	1474;1472;1473	1520;1524;1522
V– $H^{(4)}$ AMD–Sigma, $C^{\text{Sigma}} = 2.60$	1300;1310;1304	1520;1516;1518	1560;1565;1562
V– $H^{(4)}$ AMD–AMD, $C^{\text{AMD}} = 0.90$	1443;1439;1441	1693;1655;1674	1693;1697;1695
V– $H^{(4)}$ AMD–SAMD, $C^{\text{SAMD}} = 0.90$	1420;1414;1417	1677;1637;1657	1684;1688;1686
V– $H^{(4)}$ AMD–Koba, $C^{\text{Koba.}} = 0.135$	1221;1231;1226	1451;1449;1450	1501;1505;1503
V– $H^{(4)}$ AMD–AnSmag, $C^{\text{Smag.}} = 0.17$	1473;1316;1394	1629;1442;1536	1539;1527;1533
V– $H^{(4)}$ AMD–Grad ($C^{\text{Grad.}} = 1$)	1203;1212;1207	1424;1420;1422	1480;1484;1482
V– $H^{(4)}$ AMD–Grad, $C^{\text{Grad.}} = 2$	—;—;—	—;—;—	—;—;—
V– $H^{(4)}$ AMD–Grad, $C^{\text{Grad.}} = 2$, filtered	—;—;—	—;—;—	—;—;—
V– $H^{(4)}$ AMD–Grad, $C^{\text{Grad.}} = 9$, filtered	—;—;—	—;—;—	—;—;—

Table D.4 – (Continued on next page). See page 318 for label.

Formulation–Model#1–Model#2	Wall heat flux, W/m ² (cold side;hot side;average)		
	Mesh 24C	Mesh 36C	Mesh 48B
V– $H^{(4)}$ AMD–Simil (filter T)	1223;1231;1227	1447;1442;1444	1488;1492;1490
V– $H^{(4)}$ AMD–Simil, filter A	1406;1405;1406	1644;1622;1632	1659;1664;1662
F–Smag–Smag	—;—;—	—;—;—	1821;1288;1555
F–WALE–WALE	1088;1097;1093	1281;1282;1282	1362;1367;1365
F–WALE–WALE, $C^{\text{WALE}} = 1.10$	—;—;—	—;—;—	1204;1208;1206
F–WALE–WALE, $C^{\text{WALE}} = 1.65$	—;—;—	—;—;—	1101;1104;1102
F–Sigma–Sigma	1064;1073;1069	1273;1275;1274	1361;1365;1363
F–AMD–AMD	1060;1070;1065	1264;1265;1264	1346;1351;1348
F–Koba–Koba	—;—;—	—;—;—	1422;1427;1425
F–AnSmag–AnSmag	—;—;—	—;—;—	1301;1314;1308
F–Grad–Grad ($C^{\text{Grad.}} = 1$)	1311;1312;1311	1510;1488;1499	1554;1558;1556
F–Grad–Grad, $C^{\text{Grad.}} = 2$	—;—;—	—;—;—	1610;1614;1612
F–Grad–Grad, $C^{\text{Grad.}} = 2$, filtered	—;—;—	—;—;—	1557;1561;1559
F–Grad–Grad, $C^{\text{Grad.}} = 9$, filtered	—;—;—	—;—;—	1680;1684;1682
F–Simil–Simil (filter T)	1254;1257;1256	1453;1437;1445	1504;1508;1506
F–Simil–Simil, filter A	1289;1290;1289	1486;1471;1479	1528;1532;1530
F–GDSmag–GDSmag	—;—;—	—;—;—	1494;1507;1501
F–GDWALE–GDWALE	—;—;—	—;—;—	1436;1441;1439
F–GDSigma–GDSigma	—;—;—	—;—;—	1368;1372;1370
F–GDAMD–GDAMD	—;—;—	—;—;—	1428;1434;1431
F–GDKoba–GDKoba	—;—;—	—;—;—	1412;1416;1414
F–GDAnSmag–GDAnSmag	—;—;—	—;—;—	1255;1272;1263
F–TGDSmag–TGDSmag	—;—;—	—;—;—	1434;1432;1433
F–TGDWALE–TGDWALE	—;—;—	—;—;—	1447;1451;1449
F–TGDSigma–TGDSigma	—;—;—	—;—;—	1403;1408;1406
F–TGDAMD–TGDAMD	—;—;—	—;—;—	1469;1473;1471
F–TGDKoba–TGDKoba	—;—;—	—;—;—	1430;1434;1432
F–TGDAnSmag–TGDAnSmag	—;—;—	—;—;—	1390;1387;1388
F– $H^{(4)}$ AMD–Smag	—;—;—	—;—;—	—;—;—
F– $H^{(4)}$ AMD–WALE	1199;1209;1204	1416;1415;1416	1465;1469;1467
F– $H^{(4)}$ AMD–Sigma	1210;1219;1214	1429;1427;1428	1472;1477;1475
F– $H^{(4)}$ AMD–AMD	1264;1269;1266	1500;1487;1494	—;—;—
F– $H^{(4)}$ AMD–SAMD, $C^{\text{SAMD}} = 0.30$	1250;1255;1253	1484;1471;1477	1519;1524;1522
F– $H^{(4)}$ AMD–Koba	1186;1195;1190	1406;1404;1405	1459;1465;1462
F– $H^{(4)}$ AMD–AnSmag	1261;1215;1238	1464;1398;1431	1470;1470;1470
F– $H^{(4)}$ AMD–Smag, $C^{\text{Smag.}} = 1.65$	—;—;—	—;—;—	—;—;—
F– $H^{(4)}$ AMD–WALE, $C^{\text{WALE}} = 0.95$	1250;1259;1255	1464;1462;1463	1506;1511;1509
F– $H^{(4)}$ AMD–Sigma, $C^{\text{Sigma}} = 2.60$	1287;1297;1292	1502;1499;1500	1543;1548;1546
F– $H^{(4)}$ AMD–AMD, $C^{\text{AMD}} = 0.90$	—;—;—	—;—;—	—;—;—
F– $H^{(4)}$ AMD–SAMD, $C^{\text{SAMD}} = 0.90$	—;—;—	—;—;—	—;—;—
F– $H^{(4)}$ AMD–Koba, $C^{\text{Koba.}} = 0.135$	1218;1228;1223	1441;1439;1440	1488;1492;1490

Table D.4 – (Continued on next page). See page 318 for label.

Formulation–Model#1–Model#2	Wall heat flux, W/m ² (cold side;hot side;average)		
	Mesh 24C	Mesh 36C	Mesh 48B
F– $H^{(4)}$ AMD–AnSmag, $C^{\text{Smag.}} = 0.17$	1434;1285;1359	1605;1426;1516	1517;1504;1510
F– $H^{(4)}$ AMD–Grad ($C^{\text{Grad.}} = 1$)	1190;1198;1194	1415;1411;1413	1466;1470;1468
F– $H^{(4)}$ AMD–Grad, $C^{\text{Grad.}} = 2$	—;—;—	—;—;—	—;—;—
F– $H^{(4)}$ AMD–Grad, $C^{\text{Grad.}} = 2$, filtered	—;—;—	—;—;—	—;—;—
F– $H^{(4)}$ AMD–Grad, $C^{\text{Grad.}} = 9$, filtered	—;—;—	—;—;—	—;—;—
F– $H^{(4)}$ AMD–Simil (filter T)	1212;1220;1216	1434;1430;1432	1481;1487;1484
F– $H^{(4)}$ AMD–Simil, filter A	1389;1389;1389	1630;1606;1618	1635;1638;1637

Table D.4 – (Continued). Wall heat flux of the anisothermal simulations at $Re_\tau = 180$. The reference wall heat flux of the filtered direct numerical simulation is 1724 (1734;1714;1724).

D.2.2 Anisothermal simulation at $Re_\tau = 395$

Formulation–Model#1–Model#2	Wall heat flux, W/m ² (cold side;hot side;average)
	Mesh 96B
V–None–None (no model)	3154;3156;3155
V–WALE–None	3020;3022;3021
V–Sigma–None	2989;2992;2990
V–AMD–None	2884;2890;2887
V–Grad–None ($C^{\text{Grad.}} = 1$)	3168;3168;3168
V–Simil–None (filter T)	3067;3068;3067
V–Simil–None, filter A	2812;2815;2813
V– $H^{(4)}$ AMD–None	3232;3239;3235
V– $(1-H^{(4)})$ Grad+ $H^{(4)}$ AMD–None	3313;3320;3316
V– $(1-H^{(7)})$ Grad+ $H^{(6)}$ AMD–None	3305;3304;3304
V–Smag–Smag	—;—;—
V–WALE–WALE	3047;3049;3048
V–WALE–WALE, $C^{\text{WALE}} = 1.10$	—;—;—
V–WALE–WALE, $C^{\text{WALE}} = 1.65$	—;—;—
V–Sigma–Sigma	3038;3040;3039
V–AMD–AMD	3047;3050;3049
V–Koba–Koba	—;—;—
V–AnSmag–AnSmag	—;—;—
V–Simil–Simil (filter T)	3163;3167;3165
V–Simil–Simil, filter A	3193;3196;3194
V– $H^{(4)}$ AMD–Smag	4621;2894;3757
V– $H^{(4)}$ AMD–WALE	3269;3268;3268
V– $H^{(4)}$ AMD–Sigma	3240;3246;3243
V– $H^{(4)}$ AMD–AMD	3438;3438;3438

Table D.5 – (Continued on next page). See page 319 for label.

Formulation–Model#1–Model#2	Wall heat flux, W/m ² (cold side;hot side;average) Mesh 96B
V– $H^{(4)}$ AMD–SAMD, $C^{SAMD} = 0.30$	3398;3406;3402
V– $H^{(4)}$ AMD–Koba	3266;3272;3269
V– $H^{(4)}$ AMD–AnSmag	3241;3234;3238
V– $H^{(4)}$ AMD–Smag, $C^{Smag.} = 1.65$	5519;2335;3927
V– $H^{(4)}$ AMD–WALE, $C^{WALE} = 0.95$	3346;3347;3346
V– $H^{(4)}$ AMD–Sigma, $C^{Sigma} = 2.60$	3414;3420;3417
V– $H^{(4)}$ AMD–AMD, $C^{AMD} = 0.90$	3667;3760;3714
V– $H^{(4)}$ AMD–SAMD, $C^{SAMD} = 0.90$	3614;3736;3675
V– $H^{(4)}$ AMD–Koba, $C^{Koba.} = 0.135$	3321;3325;3323
V– $H^{(4)}$ AMD–AnSmag, $C^{Smag.} = 0.17$	3323;3293;3308
V– $H^{(4)}$ AMD–Simil (filter T)	3314;3316;3315
V– $H^{(4)}$ AMD–Simil, filter A	3677;3679;3678
F–Smag–Smag	—;—;—
F–WALE–WALE	3056;3058;3057
F–WALE–WALE, $C^{WALE} = 1.10$	—;—;—
F–WALE–WALE, $C^{WALE} = 1.65$	—;—;—
F–Sigma–Sigma	3033;3036;3034
F–AMD–AMD	3051;3055;3053
F–Koba–Koba	—;—;—
F–AnSmag–AnSmag	—;—;—
F–Simil–Simil (filter T)	3161;3163;3162
F–Simil–Simil, filter A	3202;3203;3202
F– $H^{(4)}$ AMD–Smag	4630;2902;3766
F– $H^{(4)}$ AMD–WALE	3268;3272;3270
F– $H^{(4)}$ AMD–Sigma	3297;3297;3297
F– $H^{(4)}$ AMD–AMD	3434;3436;3435
F– $H^{(4)}$ AMD–SAMD, $C^{SAMD} = 0.30$	3412;3421;3417
F– $H^{(4)}$ AMD–Koba	3266;3272;3269
F– $H^{(4)}$ AMD–AnSmag	3261;3252;3256
F– $H^{(4)}$ AMD–Smag, $C^{Smag.} = 1.65$	—;—;—
F– $H^{(4)}$ AMD–WALE, $C^{WALE} = 0.95$	3333;3342;3338
F– $H^{(4)}$ AMD–Sigma, $C^{Sigma} = 2.60$	3401;3410;3406
F– $H^{(4)}$ AMD–AMD, $C^{AMD} = 0.90$	—;—;—
F– $H^{(4)}$ AMD–SAMD, $C^{SAMD} = 0.90$	—;—;—
F– $H^{(4)}$ AMD–Koba, $C^{Koba.} = 0.135$	3318;3325;3322
F– $H^{(4)}$ AMD–AnSmag, $C^{Smag.} = 0.17$	3313;3281;3297
F– $H^{(4)}$ AMD–Simil (filter T)	3320;3322;3321
F– $H^{(4)}$ AMD–Simil, filter A	3671;3676;3674

Table D.5 – (Continued). Wall heat flux of anisothermal simulations at $Re_\tau = 395$. The reference wall heat flux of the filtered direct numerical simulation is 3473 (3492;3452;3473).

D.3 Tables of thermodynamical pressure

D.3.1 Anisothermal simulation at $Re_\tau = 180$

Formulation–Model#1–Model#2	Thermodynamical pressure, Pa		
	Mesh 24C	Mesh 36C	Mesh 48B
V–None–None (no model)	$1.560 \times 10^{+5}$	$1.536 \times 10^{+5}$	$1.523 \times 10^{+5}$
V–Smag–None	—	—	$1.539 \times 10^{+5}$
V–WALE–None	$1.538 \times 10^{+5}$	$1.527 \times 10^{+5}$	$1.526 \times 10^{+5}$
V–Sigma–None	$1.532 \times 10^{+5}$	$1.530 \times 10^{+5}$	$1.528 \times 10^{+5}$
V–AMD–None	$1.528 \times 10^{+5}$	$1.531 \times 10^{+5}$	$1.527 \times 10^{+5}$
V–Koba–None	—	—	$1.526 \times 10^{+5}$
V–AnSmag–None	—	—	$1.535 \times 10^{+5}$
V–Grad–None ($C^{\text{Grad.}} = 1$)	$1.560 \times 10^{+5}$	$1.537 \times 10^{+5}$	$1.522 \times 10^{+5}$
V–Grad–None, $C^{\text{Grad.}} = 2$	—	—	$1.520 \times 10^{+5}$
V–Grad–None, $C^{\text{Grad.}} = 2$, filtered	—	—	$1.527 \times 10^{+5}$
V–Grad–None, $C^{\text{Grad.}} = 9$, filtered	—	—	$1.533 \times 10^{+5}$
V–Simil–None (filter T)	—	—	$1.526 \times 10^{+5}$
V–Simil–None, filter A	—	—	$1.542 \times 10^{+5}$
V– $H^{(1)}$ AMD–None	—	—	$1.518 \times 10^{+5}$
V– $H^{(2)}$ AMD–None	—	—	$1.506 \times 10^{+5}$
V– $H^{(3)}$ AMD–None	—	—	$1.521 \times 10^{+5}$
V– $H^{(4)}$ AMD–None	$1.542 \times 10^{+5}$	$1.532 \times 10^{+5}$	$1.518 \times 10^{+5}$
V– $H^{(5)}$ AMD–None	—	—	$1.499 \times 10^{+5}$
V– $H^{(6)}$ AMD–None	—	—	$1.521 \times 10^{+5}$
V– $H^{(4)}$ Smag–None	—	—	$1.488 \times 10^{+5}$
V– $H^{(4)}$ WALE–None	—	—	$1.521 \times 10^{+5}$
V– $H^{(4)}$ Sigma–None	—	—	$1.522 \times 10^{+5}$
V– $H^{(4)}$ AnSmag–None	—	—	$1.519 \times 10^{+5}$
V–Grad+AMD–None	—	—	$1.522 \times 10^{+5}$
V– $(1-H^{(1)})$ Grad+ $H^{(1)}$ AMD–None	—	—	$1.517 \times 10^{+5}$
V– $(1-H^{(2)})$ Grad+ $H^{(2)}$ AMD–None	—	—	$1.511 \times 10^{+5}$
V– $(1-H^{(3)})$ Grad+ $H^{(3)}$ AMD–None	—	—	$1.521 \times 10^{+5}$
V– $(1-H^{(4)})$ Grad+ $H^{(4)}$ AMD–None	$1.545 \times 10^{+5}$	$1.530 \times 10^{+5}$	$1.515 \times 10^{+5}$
V– $(1-H^{(5)})$ Grad+ $H^{(5)}$ AMD–None	—	—	$1.508 \times 10^{+5}$
V– $(1-H^{(6)})$ Grad+ $H^{(6)}$ AMD–None	—	—	$1.519 \times 10^{+5}$
V– $(1-H^{(7)})$ Grad+ $H^{(6)}$ AMD–None	$1.545 \times 10^{+5}$	$1.533 \times 10^{+5}$	$1.521 \times 10^{+5}$
V–PDSmag–None	—	—	$1.523 \times 10^{+5}$
V–PDAnSmag–None	—	—	$1.536 \times 10^{+5}$
V–GDSmag–None	—	—	$1.520 \times 10^{+5}$
V–GDWALE–None	—	—	$1.523 \times 10^{+5}$
V–GDSigma–None	—	—	$1.527 \times 10^{+5}$
V–GDAMD–None	—	—	$1.524 \times 10^{+5}$

Table D.6 – (Continued on next page). See page 325 for label.

Formulation–Model#1–Model#2	Thermodynamical pressure, Pa		
	Mesh 24C	Mesh 36C	Mesh 48B
V–GDKoba–None	—	—	$1.527 \times 10^{+5}$
V–GDAnSmag–None	—	—	$1.545 \times 10^{+5}$
V–TGDSmag–None	—	—	$1.513 \times 10^{+5}$
V–TGDWALE–None	—	—	$1.519 \times 10^{+5}$
V–TGDSigma–None	—	—	$1.520 \times 10^{+5}$
V–TGDAMD–None	—	—	$1.516 \times 10^{+5}$
V–TGDKoba–None	—	—	$1.522 \times 10^{+5}$
V–TGDAAnSmag–None	—	—	$1.520 \times 10^{+5}$
V–PDGrad–None	—	—	$1.511 \times 10^{+5}$
V–TPDGrad–None	—	—	$1.524 \times 10^{+5}$
V–GDGrad–None	—	—	$1.518 \times 10^{+5}$
V–TGDGrad–None	—	—	$1.516 \times 10^{+5}$
V–P1Grad+AMD–None	—	—	$1.510 \times 10^{+5}$
V–PDGrad+PDAMD*–None	—	—	$1.509 \times 10^{+5}$
V–PDGrad+P1AMD*–None	—	—	$1.509 \times 10^{+5}$
V–P1Grad+PDAMD*–None	—	—	$1.511 \times 10^{+5}$
V–P2(Grad+AMD)*–None	—	—	$1.510 \times 10^{+5}$
V–TP1Grad+AMD–None	—	—	$1.524 \times 10^{+5}$
V–TPDGrad+TPDAMD*–None	—	—	$1.505 \times 10^{+5}$
V–TPDGrad+TP1AMD*–None	—	—	—
V–TP1Grad+TPDAMD*–None	—	—	$1.500 \times 10^{+5}$
V–TP2(Grad+AMD)*–None	—	—	$1.530 \times 10^{+5}$
V–G1Grad+AMD–None	—	—	$1.519 \times 10^{+5}$
V–GDGrad+GDAMD–None	—	—	$1.519 \times 10^{+5}$
V–GDGrad+G1AMD–None	—	—	$1.519 \times 10^{+5}$
V–G1Grad+GDAMD*–None	—	—	$1.517 \times 10^{+5}$
V–G2(Grad+AMD)*–None	—	—	$1.517 \times 10^{+5}$
V–TG1Grad+AMD–None	—	—	$1.521 \times 10^{+5}$
V–TGDGrad+TGDAMD–None	—	—	$1.511 \times 10^{+5}$
V–TGDGrad+TG1AMD*–None	—	—	$1.516 \times 10^{+5}$
V–TG1Grad+TGDAMD–None	—	—	$1.512 \times 10^{+5}$
V–TG2(Grad+AMD)*–None	—	—	$1.517 \times 10^{+5}$
V–None–Smag	$1.518 \times 10^{+5}$	—	$1.488 \times 10^{+5}$
V–None–WALE	$1.562 \times 10^{+5}$	—	$1.523 \times 10^{+5}$
V–None–Sigma	$1.563 \times 10^{+5}$	—	$1.523 \times 10^{+5}$
V–None–AMD	$1.565 \times 10^{+5}$	—	$1.523 \times 10^{+5}$
V–None–SAMD	$1.564 \times 10^{+5}$	—	$1.525 \times 10^{+5}$
V–None–Koba	$1.562 \times 10^{+5}$	—	$1.522 \times 10^{+5}$
V–None–AnSmag	$1.554 \times 10^{+5}$	—	$1.522 \times 10^{+5}$
V–None–Smag, $C^{\text{Smag}} = 1.65$	$1.522 \times 10^{+5}$	—	$1.484 \times 10^{+5}$
V–None–WALE, $C^{\text{WALE}} = 0.95$	$1.568 \times 10^{+5}$	—	$1.525 \times 10^{+5}$
V–None–WALE, $C^{\text{WALE}} = 1.10$	$1.571 \times 10^{+5}$	—	$1.525 \times 10^{+5}$

Table D.6 – (Continued on next page). See page 325 for label.

Formulation–Model#1–Model#2	Thermodynamical pressure, Pa		
	Mesh 24C	Mesh 36C	Mesh 48B
V–None–WALE, $C^{\text{WALE}} = 1.65$	$1.587 \times 10^{+5}$	—	$1.532 \times 10^{+5}$
V–None–Sigma, $C^{\text{Sigma}} = 2.60$	$1.573 \times 10^{+5}$	—	$1.525 \times 10^{+5}$
V–None–AMD, $C^{\text{AMD}} = 0.90$	$1.571 \times 10^{+5}$	—	$1.524 \times 10^{+5}$
V–None–SAMD, $C^{\text{SAMD}} = 0.90$	$1.572 \times 10^{+5}$	—	$1.527 \times 10^{+5}$
V–None–Koba, $C^{\text{Koba.}} = 0.135$	$1.566 \times 10^{+5}$	—	$1.523 \times 10^{+5}$
V–None–AnSmag, $C^{\text{Smag.}} = 0.17$	$1.546 \times 10^{+5}$	—	$1.523 \times 10^{+5}$
V–None–Grad ($C^{\text{Grad.}} = 1$)	$1.562 \times 10^{+5}$	—	$1.523 \times 10^{+5}$
V–None–Grad, $C^{\text{Grad.}} = 2$	$1.563 \times 10^{+5}$	—	$1.524 \times 10^{+5}$
V–None–Grad, $C^{\text{Grad.}} = 2$, filtered	$1.563 \times 10^{+5}$	—	$1.525 \times 10^{+5}$
V–None–Grad, $C^{\text{Grad.}} = 9$, filtered	$1.576 \times 10^{+5}$	—	$1.531 \times 10^{+5}$
V–None–Simil (filter T)	$1.562 \times 10^{+5}$	—	$1.522 \times 10^{+5}$
V–None–Simil, filter A	$1.572 \times 10^{+5}$	—	$1.528 \times 10^{+5}$
V–None–Grad+AMD	$1.565 \times 10^{+5}$	—	$1.524 \times 10^{+5}$
V–None–TGDSmag	$1.558 \times 10^{+5}$	—	$1.520 \times 10^{+5}$
V–None–TGDWALE	—	—	$1.522 \times 10^{+5}$
V–None–TGDSigma	$1.563 \times 10^{+5}$	—	$1.523 \times 10^{+5}$
V–None–TGDAMD	$1.561 \times 10^{+5}$	—	$1.522 \times 10^{+5}$
V–None–TGDSAMD	$1.563 \times 10^{+5}$	—	$1.524 \times 10^{+5}$
V–None–TGDKoba	$1.560 \times 10^{+5}$	—	$1.524 \times 10^{+5}$
V–None–TGDAnSmag	$1.554 \times 10^{+5}$	—	$1.521 \times 10^{+5}$
F–None–Smag	—	—	—
F–None–WALE	$1.561 \times 10^{+5}$	—	$1.521 \times 10^{+5}$
F–None–Sigma	$1.561 \times 10^{+5}$	—	$1.520 \times 10^{+5}$
F–None–AMD	—	—	$1.515 \times 10^{+5}$
F–None–SAMD	—	—	—
F–None–Koba	$1.561 \times 10^{+5}$	—	$1.522 \times 10^{+5}$
F–None–AnSmag	$1.548 \times 10^{+5}$	—	$1.519 \times 10^{+5}$
F–None–Smag, $C^{\text{Smag.}} = 1.65$	—	—	—
F–None–WALE, $C^{\text{WALE}} = 0.95$	—	—	$1.518 \times 10^{+5}$
F–None–WALE, $C^{\text{WALE}} = 1.10$	—	—	$1.518 \times 10^{+5}$
F–None–WALE, $C^{\text{WALE}} = 1.65$	—	—	—
F–None–Sigma, $C^{\text{Sigma}} = 2.60$	—	—	$1.517 \times 10^{+5}$
F–None–AMD, $C^{\text{AMD}} = 0.90$	—	—	—
F–None–SAMD, $C^{\text{SAMD}} = 0.90$	—	—	—
F–None–Koba, $C^{\text{Koba.}} = 0.135$	—	—	—
F–None–AnSmag, $C^{\text{Smag.}} = 0.17$	$1.530 \times 10^{+5}$	—	$1.511 \times 10^{+5}$
F–None–Grad ($C^{\text{Grad.}} = 1$)	$1.560 \times 10^{+5}$	—	$1.522 \times 10^{+5}$
F–None–Grad, $C^{\text{Grad.}} = 2$	$1.560 \times 10^{+5}$	—	$1.521 \times 10^{+5}$
F–None–Grad, $C^{\text{Grad.}} = 2$, filtered	$1.561 \times 10^{+5}$	—	$1.521 \times 10^{+5}$
F–None–Grad, $C^{\text{Grad.}} = 9$, filtered	$1.563 \times 10^{+5}$	—	$1.518 \times 10^{+5}$
F–None–Simil (filter T)	$1.560 \times 10^{+5}$	—	$1.520 \times 10^{+5}$

Table D.6 – (Continued on next page). See page 325 for label.

Formulation–Model#1–Model#2	Thermodynamical pressure, Pa		
	Mesh 24C	Mesh 36C	Mesh 48B
F–None–Simil, filter A	$1.560 \times 10^{+5}$	—	$1.514 \times 10^{+5}$
F–None–Grad+AMD	—	—	—
F–None–TGDSmag	$1.558 \times 10^{+5}$	—	$1.521 \times 10^{+5}$
F–None–TGDWALE	—	—	$1.522 \times 10^{+5}$
F–None–TGDSigma	—	—	$1.520 \times 10^{+5}$
F–None–TGDAMD	$1.559 \times 10^{+5}$	—	$1.518 \times 10^{+5}$
F–None–TGDSAMD	$1.559 \times 10^{+5}$	—	$1.520 \times 10^{+5}$
F–None–TGDKoba	—	—	$1.522 \times 10^{+5}$
F–None–TGDAAnSmag	$1.546 \times 10^{+5}$	—	$1.514 \times 10^{+5}$
V–Smag–Smag	—	—	$1.491 \times 10^{+5}$
V–WALE–WALE	$1.539 \times 10^{+5}$	$1.527 \times 10^{+5}$	$1.526 \times 10^{+5}$
V–WALE–WALE, $C^{\text{WALE}} = 1.10$	—	—	$1.539 \times 10^{+5}$
V–WALE–WALE, $C^{\text{WALE}} = 1.65$	—	—	$1.546 \times 10^{+5}$
V–Sigma–Sigma	$1.536 \times 10^{+5}$	$1.531 \times 10^{+5}$	$1.530 \times 10^{+5}$
V–AMD–AMD	$1.528 \times 10^{+5}$	$1.532 \times 10^{+5}$	$1.527 \times 10^{+5}$
V–Koba–Koba	—	—	$1.526 \times 10^{+5}$
V–AnSmag–AnSmag	—	—	$1.536 \times 10^{+5}$
V–Grad–Grad ($C^{\text{Grad.}} = 1$)	$1.561 \times 10^{+5}$	$1.539 \times 10^{+5}$	$1.522 \times 10^{+5}$
V–Grad–Grad, $C^{\text{Grad.}} = 2$	—	—	$1.521 \times 10^{+5}$
V–Grad–Grad, $C^{\text{Grad.}} = 2$, filtered	—	—	$1.529 \times 10^{+5}$
V–Grad–Grad, $C^{\text{Grad.}} = 9$, filtered	—	—	$1.539 \times 10^{+5}$
V–Simil–Simil (filter T)	$1.564 \times 10^{+5}$	$1.540 \times 10^{+5}$	$1.525 \times 10^{+5}$
V–Simil–Simil, filter A	$1.575 \times 10^{+5}$	$1.559 \times 10^{+5}$	$1.545 \times 10^{+5}$
V–GDSmag–GDSmag	—	—	$1.519 \times 10^{+5}$
V–GDWALE–GDWALE	—	—	$1.522 \times 10^{+5}$
V–GDSigma–GDSigma	—	—	$1.529 \times 10^{+5}$
V–GDAMD–GDAMD	—	—	$1.523 \times 10^{+5}$
V–GDKoba–GDKoba	—	—	$1.526 \times 10^{+5}$
V–GDAnSmag–GDAnSmag	—	—	$1.545 \times 10^{+5}$
V–TGDSmag–TGDSmag	—	—	$1.512 \times 10^{+5}$
V–TGDWALE–TGDWALE	—	—	$1.518 \times 10^{+5}$
V–TGDSigma–TGDSigma	—	—	$1.521 \times 10^{+5}$
V–TGDAMD–TGDAMD	—	—	$1.516 \times 10^{+5}$
V–TGDKoba–TGDKoba	—	—	$1.523 \times 10^{+5}$
V–TGDAAnSmag–TGDAAnSmag	—	—	$1.521 \times 10^{+5}$
V– $H^{(4)}$ AMD–Smag	$1.503 \times 10^{+5}$	$1.498 \times 10^{+5}$	$1.483 \times 10^{+5}$
V– $H^{(4)}$ AMD–WALE	$1.541 \times 10^{+5}$	$1.532 \times 10^{+5}$	$1.518 \times 10^{+5}$
V– $H^{(4)}$ AMD–Sigma	$1.543 \times 10^{+5}$	$1.534 \times 10^{+5}$	$1.519 \times 10^{+5}$
V– $H^{(4)}$ AMD–AMD	$1.542 \times 10^{+5}$	$1.531 \times 10^{+5}$	—
V– $H^{(4)}$ AMD–SAMD, $C^{\text{SAMD}} = 0.30$	$1.544 \times 10^{+5}$	$1.536 \times 10^{+5}$	$1.521 \times 10^{+5}$
V– $H^{(4)}$ AMD–Koba	$1.541 \times 10^{+5}$	$1.533 \times 10^{+5}$	$1.517 \times 10^{+5}$

Table D.6 – (Continued on next page). See page 325 for label.

Formulation–Model#1–Model#2	Thermodynamical pressure, Pa		
	Mesh 24C	Mesh 36C	Mesh 48B
V– $H^{(4)}$ AMD–AnSmag	$1.536 \times 10^{+5}$	$1.528 \times 10^{+5}$	$1.518 \times 10^{+5}$
V– $H^{(4)}$ AMD–Smag, $C^{\text{Smag.}} = 1.65$	$1.512 \times 10^{+5}$	$1.506 \times 10^{+5}$	$1.479 \times 10^{+5}$
V– $H^{(4)}$ AMD–WALE, $C^{\text{WALE}} = 0.95$	$1.545 \times 10^{+5}$	$1.535 \times 10^{+5}$	$1.518 \times 10^{+5}$
V– $H^{(4)}$ AMD–Sigma, $C^{\text{Sigma}} = 2.60$	$1.547 \times 10^{+5}$	$1.537 \times 10^{+5}$	$1.522 \times 10^{+5}$
V– $H^{(4)}$ AMD–AMD, $C^{\text{AMD}} = 0.90$	$1.548 \times 10^{+5}$	$1.537 \times 10^{+5}$	$1.521 \times 10^{+5}$
V– $H^{(4)}$ AMD–SAMD, $C^{\text{SAMD}} = 0.90$	$1.551 \times 10^{+5}$	$1.541 \times 10^{+5}$	$1.527 \times 10^{+5}$
V– $H^{(4)}$ AMD–Koba, $C^{\text{Koba.}} = 0.135$	$1.543 \times 10^{+5}$	$1.534 \times 10^{+5}$	$1.520 \times 10^{+5}$
V– $H^{(4)}$ AMD–AnSmag, $C^{\text{Smag.}} = 0.17$	$1.530 \times 10^{+5}$	$1.524 \times 10^{+5}$	$1.519 \times 10^{+5}$
V– $H^{(4)}$ AMD–Grad ($C^{\text{Grad.}} = 1$)	$1.542 \times 10^{+5}$	$1.533 \times 10^{+5}$	$1.519 \times 10^{+5}$
V– $H^{(4)}$ AMD–Grad, $C^{\text{Grad.}} = 2$	—	—	—
V– $H^{(4)}$ AMD–Grad, $C^{\text{Grad.}} = 2$, filtered	—	—	—
V– $H^{(4)}$ AMD–Grad, $C^{\text{Grad.}} = 9$, filtered	—	—	—
V– $H^{(4)}$ AMD–Simil (filter T)	$1.541 \times 10^{+5}$	$1.533 \times 10^{+5}$	$1.517 \times 10^{+5}$
V– $H^{(4)}$ AMD–Simil, filter A	$1.547 \times 10^{+5}$	$1.538 \times 10^{+5}$	$1.522 \times 10^{+5}$
F–Smag–Smag	—	—	$1.464 \times 10^{+5}$
F–WALE–WALE	$1.536 \times 10^{+5}$	$1.524 \times 10^{+5}$	$1.523 \times 10^{+5}$
F–WALE–WALE, $C^{\text{WALE}} = 1.10$	—	—	$1.533 \times 10^{+5}$
F–WALE–WALE, $C^{\text{WALE}} = 1.65$	—	—	$1.532 \times 10^{+5}$
F–Sigma–Sigma	$1.531 \times 10^{+5}$	$1.526 \times 10^{+5}$	$1.524 \times 10^{+5}$
F–AMD–AMD	$1.519 \times 10^{+5}$	$1.517 \times 10^{+5}$	$1.512 \times 10^{+5}$
F–Koba–Koba	—	—	$1.524 \times 10^{+5}$
F–AnSmag–AnSmag	—	—	$1.525 \times 10^{+5}$
F–Grad–Grad ($C^{\text{Grad.}} = 1$)	$1.558 \times 10^{+5}$	$1.535 \times 10^{+5}$	$1.519 \times 10^{+5}$
F–Grad–Grad, $C^{\text{Grad.}} = 2$	—	—	$1.514 \times 10^{+5}$
F–Grad–Grad, $C^{\text{Grad.}} = 2$, filtered	—	—	$1.524 \times 10^{+5}$
F–Grad–Grad, $C^{\text{Grad.}} = 9$, filtered	—	—	$1.521 \times 10^{+5}$
F–Simil–Simil (filter T)	$1.558 \times 10^{+5}$	$1.534 \times 10^{+5}$	$1.519 \times 10^{+5}$
F–Simil–Simil, filter A	$1.554 \times 10^{+5}$	$1.533 \times 10^{+5}$	$1.519 \times 10^{+5}$
F–GDSmag–GDSmag	—	—	$1.519 \times 10^{+5}$
F–GDWALE–GDWALE	—	—	$1.521 \times 10^{+5}$
F–GDSigma–GDSigma	—	—	$1.525 \times 10^{+5}$
F–GDAMD–GDAMD	—	—	$1.516 \times 10^{+5}$
F–GDKoba–GDKoba	—	—	$1.524 \times 10^{+5}$
F–GDAnSmag–GDAnSmag	—	—	$1.530 \times 10^{+5}$
F–TGDSmag–TGDSmag	—	—	$1.511 \times 10^{+5}$
F–TGDWALE–TGDWALE	—	—	$1.515 \times 10^{+5}$
F–TGDSigma–TGDSigma	—	—	$1.515 \times 10^{+5}$
F–TGDAMD–TGDAMD	—	—	$1.508 \times 10^{+5}$
F–TGDKoba–TGDKoba	—	—	$1.519 \times 10^{+5}$
F–TGDAnSmag–TGDAnSmag	—	—	$1.508 \times 10^{+5}$
F– $H^{(4)}$ AMD–Smag	—	—	—

Table D.6 – (Continued on next page). See page 325 for label.

Formulation–Model#1–Model#2	Thermodynamical pressure, Pa		
	Mesh 24C	Mesh 36C	Mesh 48B
F– $H^{(4)}$ AMD–WALE	$1.535 \times 10^{+5}$	$1.522 \times 10^{+5}$	$1.509 \times 10^{+5}$
F– $H^{(4)}$ AMD–Sigma	$1.534 \times 10^{+5}$	$1.521 \times 10^{+5}$	$1.507 \times 10^{+5}$
F– $H^{(4)}$ AMD–AMD	$1.529 \times 10^{+5}$	$1.517 \times 10^{+5}$	—
F– $H^{(4)}$ AMD–SAMD, $C^{\text{SAMD}} = 0.30$	$1.532 \times 10^{+5}$	$1.519 \times 10^{+5}$	$1.504 \times 10^{+5}$
F– $H^{(4)}$ AMD–Koba	$1.533 \times 10^{+5}$	$1.522 \times 10^{+5}$	$1.508 \times 10^{+5}$
F– $H^{(4)}$ AMD–AnSmag	$1.523 \times 10^{+5}$	$1.512 \times 10^{+5}$	$1.506 \times 10^{+5}$
F– $H^{(4)}$ AMD–Smag, $C^{\text{Smag.}} = 1.65$	—	—	—
F– $H^{(4)}$ AMD–WALE, $C^{\text{WALE}} = 0.95$	$1.536 \times 10^{+5}$	$1.521 \times 10^{+5}$	$1.505 \times 10^{+5}$
F– $H^{(4)}$ AMD–Sigma, $C^{\text{Sigma}} = 2.60$	$1.536 \times 10^{+5}$	$1.520 \times 10^{+5}$	$1.507 \times 10^{+5}$
F– $H^{(4)}$ AMD–AMD, $C^{\text{AMD}} = 0.90$	—	—	—
F– $H^{(4)}$ AMD–SAMD, $C^{\text{SAMD}} = 0.90$	—	—	—
F– $H^{(4)}$ AMD–Koba, $C^{\text{Koba.}} = 0.135$	$1.535 \times 10^{+5}$	$1.522 \times 10^{+5}$	$1.508 \times 10^{+5}$
F– $H^{(4)}$ AMD–AnSmag, $C^{\text{Smag.}} = 0.17$	$1.509 \times 10^{+5}$	$1.499 \times 10^{+5}$	$1.498 \times 10^{+5}$
F– $H^{(4)}$ AMD–Grad ($C^{\text{Grad.}} = 1$)	$1.532 \times 10^{+5}$	$1.520 \times 10^{+5}$	$1.510 \times 10^{+5}$
F– $H^{(4)}$ AMD–Grad, $C^{\text{Grad.}} = 2$	—	—	—
F– $H^{(4)}$ AMD–Grad, $C^{\text{Grad.}} = 2$, filtered	—	—	—
F– $H^{(4)}$ AMD–Grad, $C^{\text{Grad.}} = 9$, filtered	—	—	—
F– $H^{(4)}$ AMD–Simil (filter T)	$1.532 \times 10^{+5}$	$1.520 \times 10^{+5}$	$1.507 \times 10^{+5}$
F– $H^{(4)}$ AMD–Simil, filter A	$1.528 \times 10^{+5}$	$1.514 \times 10^{+5}$	$1.499 \times 10^{+5}$

Table D.6 – (Continued). Thermodynamical pressure of the anisothermal simulations at $Re_\tau = 180$. The reference thermodynamic pressure of the filtered direct numerical simulation is $1.496 \times 10^{+5}$.

D.3.2 Anisothermal simulation at $Re_\tau = 395$

Formulation–Model#1–Model#2	Thermodynamical pressure, Pa
	Mesh 96B
V–None–None (no model)	$1.532 \times 10^{+5}$
V–WALE–None	$1.536 \times 10^{+5}$
V–Sigma–None	$1.538 \times 10^{+5}$
V–AMD–None	$1.541 \times 10^{+5}$
V–Grad–None ($C^{\text{Grad.}} = 1$)	$1.529 \times 10^{+5}$
V–Simil–None (filter T)	$1.535 \times 10^{+5}$
V–Simil–None, filter A	$1.545 \times 10^{+5}$
V– $H^{(4)}$ AMD–None	$1.537 \times 10^{+5}$
V– $(1-H^{(4)})$ Grad+ $H^{(4)}$ AMD–None	$1.534 \times 10^{+5}$
V– $(1-H^{(7)})$ Grad+ $H^{(6)}$ AMD–None	$1.535 \times 10^{+5}$
V–Smag–Smag	—
V–WALE–WALE	$1.535 \times 10^{+5}$

Table D.7 – (Continued on next page). See page 327 for label.

Formulation–Model#1–Model#2	Thermodynamical pressure, Pa Mesh 96B
V–WALE–WALE, $C^{\text{WALE}} = 1.10$	—
V–WALE–WALE, $C^{\text{WALE}} = 1.65$	—
V–Sigma–Sigma	$1.536 \times 10^{+5}$
V–AMD–AMD	$1.539 \times 10^{+5}$
V–Koba–Koba	—
V–AnSmag–AnSmag	—
V–Simil–Simil (filter T)	$1.533 \times 10^{+5}$
V–Simil–Simil, filter A	$1.544 \times 10^{+5}$
V– $H^{(4)}$ AMD–Smag	$1.497 \times 10^{+5}$
V– $H^{(4)}$ AMD–WALE	$1.534 \times 10^{+5}$
V– $H^{(4)}$ AMD–Sigma	$1.537 \times 10^{+5}$
V– $H^{(4)}$ AMD–AMD	$1.533 \times 10^{+5}$
V– $H^{(4)}$ AMD–SAMD, $C^{\text{SAMD}} = 0.30$	$1.537 \times 10^{+5}$
V– $H^{(4)}$ AMD–Koba	$1.536 \times 10^{+5}$
V– $H^{(4)}$ AMD–AnSmag	$1.536 \times 10^{+5}$
V– $H^{(4)}$ AMD–Smag, $C^{\text{Smag.}} = 1.65$	$1.490 \times 10^{+5}$
V– $H^{(4)}$ AMD–WALE, $C^{\text{WALE}} = 0.95$	$1.536 \times 10^{+5}$
V– $H^{(4)}$ AMD–Sigma, $C^{\text{Sigma}} = 2.60$	$1.536 \times 10^{+5}$
V– $H^{(4)}$ AMD–AMD, $C^{\text{AMD}} = 0.90$	$1.532 \times 10^{+5}$
V– $H^{(4)}$ AMD–SAMD, $C^{\text{SAMD}} = 0.90$	$1.533 \times 10^{+5}$
V– $H^{(4)}$ AMD–Koba, $C^{\text{Koba.}} = 0.135$	$1.535 \times 10^{+5}$
V– $H^{(4)}$ AMD–AnSmag, $C^{\text{Smag.}} = 0.17$	$1.536 \times 10^{+5}$
V– $H^{(4)}$ AMD–Simil (filter T)	$1.536 \times 10^{+5}$
V– $H^{(4)}$ AMD–Simil, filter A	$1.537 \times 10^{+5}$
F–Smag–Smag	—
F–WALE–WALE	$1.533 \times 10^{+5}$
F–WALE–WALE, $C^{\text{WALE}} = 1.10$	—
F–WALE–WALE, $C^{\text{WALE}} = 1.65$	—
F–Sigma–Sigma	$1.532 \times 10^{+5}$
F–AMD–AMD	$1.528 \times 10^{+5}$
F–Koba–Koba	—
F–AnSmag–AnSmag	—
F–Simil–Simil (filter T)	$1.529 \times 10^{+5}$
F–Simil–Simil, filter A	$1.528 \times 10^{+5}$
F– $H^{(4)}$ AMD–Smag	$1.483 \times 10^{+5}$
F– $H^{(4)}$ AMD–WALE	$1.530 \times 10^{+5}$
F– $H^{(4)}$ AMD–Sigma	$1.528 \times 10^{+5}$
F– $H^{(4)}$ AMD–AMD	$1.525 \times 10^{+5}$
F– $H^{(4)}$ AMD–SAMD, $C^{\text{SAMD}} = 0.30$	$1.528 \times 10^{+5}$
F– $H^{(4)}$ AMD–Koba	$1.530 \times 10^{+5}$

Table D.7 – (Continued on next page). See page 327 for label.

Formulation–Model#1–Model#2	Thermodynamical pressure, Pa Mesh 96B
F– $H^{(4)}$ AMD–AnSmag	$1.528 \times 10^{+5}$
F– $H^{(4)}$ AMD–Smag, $C^{\text{Smag.}} = 1.65$	—
F– $H^{(4)}$ AMD–WALE, $C^{\text{WALE}} = 0.95$	$1.528 \times 10^{+5}$
F– $H^{(4)}$ AMD–Sigma, $C^{\text{Sigma}} = 2.60$	$1.526 \times 10^{+5}$
F– $H^{(4)}$ AMD–AMD, $C^{\text{AMD}} = 0.90$	—
F– $H^{(4)}$ AMD–SAMD, $C^{\text{SAMD}} = 0.90$	—
F– $H^{(4)}$ AMD–Koba, $C^{\text{Koba.}} = 0.135$	$1.527 \times 10^{+5}$
F– $H^{(4)}$ AMD–AnSmag, $C^{\text{Smag.}} = 0.17$	$1.526 \times 10^{+5}$
F– $H^{(4)}$ AMD–Simil (filter T)	$1.527 \times 10^{+5}$
F– $H^{(4)}$ AMD–Simil, filter A	$1.524 \times 10^{+5}$

Table D.7 – (Continued). Thermodynamical pressure of anisothermal simulations at $Re_\tau = 395$. The reference thermodynamical pressure of the filtered direct numerical simulation is $1.504 \times 10^{+5}$.

D.4 Table of dynamic parameters

Average of the dynamic parameter (standard deviation),			
	$\langle C^{\text{mod}} \rangle (\sqrt{\langle (C^{\text{mod}})^2 \rangle - \langle C^{\text{mod}} \rangle^2})$		
	Mesh 24C	Mesh 36C	Mesh 48 B
Smag.	—	—	0.028 (0.001)
WALE	—	—	0.443 (0.037)
Sigma	—	—	0.920 (0.047)
AMD	—	—	0.448 (0.019)
Kobayashi	—	—	1.107 (0.094)
An. Smag.	—	—	1.467 (0.106)
Gradient	—	—	2.411 (0.066)

Table D.8 – Average and normalised standard deviation of the dynamic parameter of the large-eddy simulations with the global-average dynamic Smagorinsky, WALE, Sigma, AMD, Kobayashi and Anisotropic Smagorinsky models in the Velocity formulation in the anisothermal channel at $Re_\tau = 180$ with the meshes 24C, 36C and 48B.

Average of the dynamic parameter (standard deviation),						
$\langle C^{\text{mod}} \rangle (\sqrt{\langle (C^{\text{mod}})^2 \rangle - \langle C^{\text{mod}} \rangle^2})$						
	xx	xy	xz	yy	zy	zz
Smag.	7.537 (0.522)	0.023 (0.001)	0.061 (0.052)	0.255 (0.028)	-0.009 (0.005)	-0.256 (0.040)
WALE	-0.807 (0.157)	1.306 (0.097)	0.421 (0.042)	0.275 (0.064)	-0.025 (0.023)	0.387 (0.057)
Sigma	1.548 (0.280)	1.508 (0.081)	0.593 (0.073)	0.177 (0.060)	0.007 (0.031)	0.158 (0.053)
AMD	0.867 (0.138)	0.651 (0.038)	0.217 (0.040)	-0.025 (0.034)	0.024 (0.022)	-0.060 (0.030)
Kobayashi	2.544 (0.301)	2.580 (0.195)	0.746 (0.143)	-0.096 (0.075)	0.047 (0.047)	-0.039 (0.069)
An. Smag.	5.708 (0.535)	1.258 (0.151)	0.241 (0.092)	1.357 (0.270)	-0.219 (0.087)	-0.289 (0.082)
Gradient	2.323 (0.068)	2.263 (0.068)	1.400 (0.037)	2.799 (0.068)	1.587 (0.038)	1.879 (0.033)

Table D.9 – Average and normalised standard deviation of the dynamic parameters of the large-eddy simulations with the tensorial global-average dynamic Smagorinsky, WALE, Sigma, AMD, Kobayashi and Anisotropic Smagorinsky models in the Velocity formulation in the anisothermal channel at $Re_\tau = 180$ with the mesh 48B.

Average of the dynamic parameter (standard deviation),		
$\langle C^{\text{mod}} \rangle (\sqrt{\langle (C^{\text{mod}})^2 \rangle - \langle C^{\text{mod}} \rangle^2})$		
	AMD-related	Gradient-related
G1Grad+AMD	—	1.582 (0.047)
GDGrad+GDAMD	0.420 (0.017)	2.005 (0.063)
GDGrad+G1AMD	0.420 (0.017)	1.980 (0.064)
G1Grad+GDAMD*	0.011 (0.013)	2.404 (0.065)
G2(Grad+AMD)*	0.012 (0.013)	2.399 (0.065)

Table D.10 – Average and normalised standard deviation of the AMD-related and gradient-related dynamic parameters of the large-eddy simulations with global-average dynamic gradient-AMD mixed models in the Velocity formulation in the anisothermal channel at $Re_\tau = 180$ with the mesh 48B. An asterisk (*) indicates the clipping of the AMD-related part.

Average of the dynamic parameter (standard deviation),
 $\langle C^{\text{mod}} \rangle (\sqrt{\langle (C^{\text{mod}})^2 \rangle - \langle C^{\text{mod}} \rangle^2})$

	xx	xy	xz	yy	zy	zz
TG1Grad+AMD	—	—	—	—	—	—
TGDGrad+TGDAMD	0.853 (0.123)	0.667 (0.035)	0.227 (0.039)	-0.037 (0.031)	0.036 (0.022)	-0.071 (0.027)
TGDGrad+TG1AMD*	0.000 (0.000)	0.180 (0.019)	0.088 (0.023)	0.081 (0.020)	0.001 (0.004)	0.000 (0.000)
TG1Grad+TGDAMD	0.773 (0.101)	0.711 (0.036)	0.227 (0.040)	-0.027 (0.034)	0.039 (0.021)	-0.071 (0.028)
TG2(Grad+AMD)*	0.000 (0.000)	0.273 (0.029)	0.087 (0.022)	0.082 (0.021)	0.001 (0.004)	0.000 (0.000)
(a) AMD-related dynamic parameters						
	xx	xy	xz	yy	zy	zz
TG1Grad+AMD	1.640 (0.051)	0.411 (0.079)	1.214 (0.055)	2.275 (0.084)	1.468 (0.066)	1.634 (0.053)
TGDGrad+TGDAMD	2.004 (0.067)	2.091 (0.070)	1.409 (0.032)	2.552 (0.070)	1.583 (0.035)	1.771 (0.033)
TGDGrad+TG1AMD*	2.239 (0.069)	2.222 (0.069)	1.413 (0.036)	2.732 (0.070)	1.604 (0.037)	1.863 (0.033)
TG1Grad+TGDAMD	2.054 (0.064)	1.263 (0.051)	1.377 (0.035)	2.601 (0.073)	1.578 (0.036)	1.789 (0.032)
TG2(Grad+AMD)*	2.262 (0.066)	1.894 (0.061)	1.406 (0.036)	2.748 (0.070)	1.604 (0.037)	1.868 (0.033)
(b) Gradient-related dynamic parameters						

Table D.11 – Average and normalised standard deviation of the AMD-related and gradient-related dynamic parameters of the large-eddy simulations with tensorial global-average dynamic gradient-AMD mixed models in the Velocity formulation in the anisothermal channel at $Re_\tau = 180$ with the mesh 48B. An asterisk (*) indicates the clipping of the AMD-related part.

Appendix E

Spectral analysis of turbulence in anisothermal channel flows

This chapter reproduces the paper F. Aulery, D. Dupuy, A. Toutant, F. Bataille, and Y. Zhou. Spectral analysis of turbulence in anisothermal channel flows. *Computers & Fluids*, 151:115–131, 2017 [11].

Abstract

In very anisothermal turbulent flows, the temperature gradient and turbulence are strongly coupled. The impact of the temperature gradient on turbulent kinetic energy (TKE) balance terms is of particular importance. It is investigated using direct numerical simulations and large eddy simulations of a fully developed anisothermal channel flow. A low Mach flow at two turbulent Reynolds number (180 and 395) is considered. The temperatures of the two channel walls are 293 K and 586 K. Comparison with isothermal channel flows are carried out. The turbulent kinetic energy spectral evolution equation is established and is decomposed into the three distinctive mechanisms: production, nonlinear transfer and viscous effects. The decomposition isolates the terms that vanish in the isothermal case, namely purely anisothermal effects. The behavior of each term is first discussed in the isothermal case. The alteration of the TKE balance terms with the temperature gradient is then analysed relatively to the Reynolds number variation. The thermal gradient effect is characterized by the combined effect of local Reynolds number variation and the complex interaction between temperature and turbulence. The purely anisothermal contribution moves the energy from the hot side to the cold side and accounts for near 10% of the total process.

E.1 Introduction

Flows under strong temperature gradient are prevalent in many industrial processes. In particular, the conception of a high temperature solar receiver for concentrated solar power plants requires a better understanding of the physical effects of the temperature

gradient on the turbulence [72]. These flows are characterized by a strong coupling between the energy equation and the momentum equation. Besides, high variations of the fluid properties associated with the temperature gradient are observed. As a result, these flows deviate from the behavior of incompressible flows [290]. An improved understanding of the energy transfers occurring in these flows would provide valuable informations to explain how the temperature gradient modify the flow. This would also benefit the development of turbulence models taking into account the specificities of these flows. Hence, we need reliable knowledge of the turbulent kinetic energy budget, that is of the mechanisms which governs the energy distribution: production, nonlinear transfer and viscous effects. The analysis of the aforementioned terms of the dynamic equation for the energy transfer process can be performed on the physical space or extended to the spectral space. The latter approach has been adopted in this study.

The analysis of turbulent kinetic energy assumes the decomposition of total kinetic energy, fundamental property of the flow, into two contributions: the mean kinetic energy, associated with the mean motion and the turbulent kinetic energy, associated with the turbulent motion. In the isothermal case, such decomposition of the total kinetic energy through Reynolds averaging is straightforward and brings no ambiguity about the physical interpretation of the terms [50]. Using this decomposition, the energy cascade process has been studied extensively for incompressible isothermal flows. The first studies on the subject were focused on homogeneous isotropic turbulence. For instance, Kolmogorov's hypothesis on the locality of the energy transfer [81] and interacting scales [324, 325] have been validated by numerical simulations. Extension to the isothermal channel flows has been pursued by Domaradzki *et al.* [83], Marati *et al.* [188], Bolotnov *et al.* [28], and Cimarelli *et al.* [58, 59].

In the anisothermal case, the decomposition of total kinetic energy into mean and turbulent kinetic energy is a complex problem. The decomposition is not unique due to the variable density. This leads to several different definitions of turbulent kinetic energy. The most common decomposition uses density-weighted averaging, also called Favre averaging [95], to group total kinetic energy into two terms (see e.g. [312, 127]). This method has also been referred by Chassaing *et al.* as binary regrouping [50]. This is opposed to the ternary regrouping proposed by Chassaing [47]. Another methodology uses a variable change based on density square root weighted velocity. This variable change has been used by various authors in spatial and spectral space [10, 318, 144, 247, 68]. Regardless of the decomposition used, the spectral behaviour of anisothermal flow has so far received little attention from the litterature, though some interesting behaviours have been shown. For instance, the well-known Kolmogorov $-5/3$ scaling law [148] falls short because of the strong dilatational effects of the temperature gradient [266]. The temperature gradient can in these flows be considered as a strong external agency that modifies the turbulence properties. This is analogous to flows subjected to strong magnetic field, rotation, or stratification [328, 326, 327]. Aulery *et al.* [10] have performed an analysis of the energy transfer processes with respect to the effect of the temperature gradient. This is to the best knowledge of the authors the only spectral study of the turbulent kinetic energy balance terms in this setting. However, the scope of the study is limited to a single Reynolds number.

We aim to enrich this study with further analysis of the influence of the turbulent Reynolds number on the role of the temperature gradient. Following Aulery *et al.* [10], turbulent kinetic energy spectral evolution equation is written using density square root

weighted velocity. Our approach is based on the evaluation from numerical simulations of the terms of the dynamic equation for the energy transfer process in the case of a fully developed anisothermal channel flow. This geometry is one of the simpler that involves turbulence and high temperature gradient. Furthermore, the two homogeneous directions make the study of the energy transfer process easier. Direct numerical simulation and large eddy simulation are carried out to provide the data for this study. Knowledge of the instantaneous three-dimensional velocity flows is required to compute the various source terms of the energy transfer process, an information difficult to obtain using experimental investigations, limited by the measurement techniques, or closure theories, so far restricted to homogeneous isotropic turbulence.

The spectral equation for the turbulent kinetic energy and the decomposition used can be found in section E.2. The detailed channel flow configuration is described in section E.3 as well as the numerical method used and its validation in the isothermal case. Further details about the implementation of the turbulent kinetic energy evolution terms are also provided. Results are discussed in section E.4 for the isothermal case and in section E.5 for the anisothermal case.

E.2 Momentum and spectral transport equations

E.2.1 Basic equations for direct numerical simulations

In this study, a low Mach number approximation is considered. This approach is relevant when acoustics effects are negligible, an hypothesis valid for low Mach number ($Ma < 0.3$). Following Paolucci [219], the method used relies on an asymptotic development of the variables of the Naviers-Stokes equations as a power series of the Mach number. Removing all but the smaller order terms leads to a new set of equations, free of acoustics constraints and Courant–Friedrichs–Lewy condition [69]. The development also splits the pressure in two different terms:

- The thermodynamical pressure P_0 appears in the energy conservation equation and the equation of state. It is constant in space and represents the mean pressure in the domain.
- The mechanical pressure P appears in the momentum conservation equation and represents the pressure associated with momentum variations. It can vary spatially.

The gas considered is air; The effect of gravity is neglected and an ideal gas is considered.

These assumptions result in the following set of equations:

Mass equation:

$$\frac{\partial \rho}{\partial t} + \frac{\partial (\rho U_j)}{\partial x_j} = 0 \quad (\text{E.1a})$$

Momentum equation:

$$\frac{\partial \rho U_i}{\partial t} + \frac{\partial \rho U_j U_i}{\partial x_j} = -\frac{\partial P}{\partial x_i} + \frac{\partial}{\partial x_j} \left[\mu \left(\frac{\partial U_i}{\partial x_j} + \frac{\partial U_j}{\partial x_i} \right) \right] - \frac{2}{3} \frac{\partial}{\partial x_j} \left(\mu \frac{\partial U_j}{\partial x_j} \right) \quad (\text{E.1b})$$

Energy equation:

$$\rho C_p \left(\frac{\partial T}{\partial t} + U_j \frac{\partial T}{\partial x_j} \right) = \frac{\partial P_0}{\partial t} + \frac{\partial}{\partial x_j} \left(\lambda \frac{\partial T}{\partial x_j} \right) \quad (\text{E.1c})$$

Ideal gas law:

$$P_0 = \rho r T \quad (\text{E.1d})$$

Thermodynamic pressure homogeneity:

$$\frac{\partial P_0}{\partial x} = \frac{\partial P_0}{\partial y} = \frac{\partial P_0}{\partial z} = 0 \quad (\text{E.1e})$$

In this set of equations, ρ is the density, T the temperature, μ the dynamic viscosity, λ the thermal conductivity, C_p the heat capacity at constant pressure, r the ideal gas specific constant, t the time, P the mechanical pressure, P_0 the thermodynamic pressure, U_i the i -th component of velocity and x_i the Cartesian coordinate in i -direction. Einstein summation convention is used. The temporal evolution of the thermodynamical pressure P_0 is computed from the integration of equation (E.1c) using the ideal gas law (E.1d) and the fact that the thermodynamical pressure P_0 is constant in space (E.1e).

E.2.2 Equations and models for large-eddy simulations

In this study, direct numerical simulations (DNS) and large eddy simulations (LES) are performed. In the case of LES, the subgrid terms related to the convective terms of equations (E.1b) and (E.1c) are modeled. The non-linear terms occurring in the viscous terms and in the conductive heat fluxes terms are neglected. Let us denote $(\bar{\cdot})$ the spatial filtering operator and $(\widetilde{\cdot})$ the Favre filtering operator defined for an arbitrary quantity ϕ as [109]:

$$\widetilde{\phi} = \frac{\overline{\rho\phi}}{\bar{\rho}} \quad (\text{E.2})$$

The filtered low Mach number set of equations used with regard to LES is:

$$\frac{\partial \bar{\rho}}{\partial t} + \frac{\partial \bar{\rho} \widetilde{U}_j}{\partial x_j} = 0 \quad (\text{E.3a})$$

$$\frac{\partial \bar{\rho} \widetilde{U}_i}{\partial t} + \frac{\partial \bar{\rho} \widetilde{U}_j \widetilde{U}_i}{\partial x_j} = -\frac{\partial \bar{P}}{\partial x_i} + \frac{\partial}{\partial x_j} \left[\bar{\mu} \left(\frac{\partial \widetilde{U}_i}{\partial x_j} + \frac{\partial \widetilde{U}_j}{\partial x_i} \right) \right] - \frac{2}{3} \frac{\partial}{\partial x_i} \left(\bar{\mu} \frac{\partial \widetilde{U}_j}{\partial x_j} \right) - \frac{\partial \bar{\rho} \tau_{ij}}{\partial x_j} \quad (\text{E.3b})$$

$$C_p \left(\frac{\partial \bar{\rho} \widetilde{T}}{\partial t} + \frac{\partial \bar{\rho} \widetilde{U}_j \widetilde{T}}{\partial x_j} \right) = \frac{\partial \bar{P}_0}{\partial t} + \frac{\partial}{\partial x_j} \left(\bar{\lambda} \frac{\partial \widetilde{T}}{\partial x_j} \right) - \frac{\partial \bar{\rho} C_p \mathfrak{S}_j}{\partial x_j} \quad (\text{E.3c})$$

$$\bar{P}_0 = r \bar{\rho} \widetilde{T} \quad (\text{E.3d})$$

$$\frac{\partial \bar{P}_0}{\partial x} = \frac{\partial \bar{P}_0}{\partial y} = \frac{\partial \bar{P}_0}{\partial z} = 0 \quad (\text{E.3e})$$

with:

$$\tau_{ij} = \widetilde{U_j U_i} - \widetilde{U}_j \widetilde{U}_i \quad (\text{E.4a})$$

$$\mathfrak{S}_j = \widetilde{U}_j \widetilde{T} - \widetilde{U}_j \widetilde{T} \quad (\text{E.4b})$$

The WALE model [213] has been chosen for the modelling of the subgrid scale tensor τ_{ij} . First, the subgrid scale viscosity ν_{sg} is computed using:

$$\nu_{sg} = \left(C_w \widetilde{\Delta} \right)^2 \frac{(s_{ij}^d s_{ij}^d)^{3/2}}{\left(\widetilde{S}_{ij} \widetilde{S}_{ij} \right)^{5/2} + (s_{ij}^d s_{ij}^d)^{5/4}} \quad (\text{E.5})$$

with $\widetilde{\Delta}$ the subgrid characteristic length scale, C_w a constant, \widetilde{S}_{ij} the filtered strain tensor:

$$\widetilde{S}_{ij} = \frac{1}{2} \left(\frac{\partial \widetilde{U}_i}{\partial x_j} + \frac{\partial \widetilde{U}_j}{\partial x_i} \right) \quad (\text{E.6})$$

and s_{ij}^d the traceless symmetric part of the square of the velocity gradient tensor which can be written as:

$$s_{ij}^d = \widetilde{S}_{ik} \widetilde{S}_{kj} + \widetilde{\Omega}_{ik} \widetilde{\Omega}_{kj} - \frac{1}{3} \delta_{ij} \left(\widetilde{S}_{mn} \widetilde{S}_{mn} - \widetilde{\Omega}_{mn} \widetilde{\Omega}_{mn} \right) \quad (\text{E.7})$$

where $\widetilde{\Omega}_{ij}$ is the filtered rotation vector:

$$\widetilde{\Omega}_{ij} = \frac{1}{2} \left(\frac{\partial \widetilde{U}_i}{\partial x_j} - \frac{\partial \widetilde{U}_j}{\partial x_i} \right) \quad (\text{E.8})$$

The deviatoric part τ_{ij}^d of the subgrid scale tensor is then calculated with the following expression:

$$\tau_{ij}^d = \tau_{ij} - \frac{1}{3} \delta_{ij} \tau_{kk} = -2\nu_{sg} \widetilde{S}_{ij} \quad (\text{E.9})$$

The complementary term $\frac{1}{3} \delta_{ij} \tau_{kk}$ is added to the filtered pressure term and requires no modelling.

The subgrid scale heat flux \mathfrak{S}_j is calculated using a subgrid scale diffusivity model [93]:

$$\mathfrak{S}_j = \kappa_{sg} \frac{\partial \widetilde{T}}{\partial x_j} \quad (\text{E.10})$$

with κ_{sg} the subgrid scale diffusivity, linked to the subgrid scale viscosity through the subgrid scale Prandtl number $Pr_{sg} = \frac{\nu_{sg}}{\kappa_{sg}}$.

To compute dynamic viscosity, Sutherland law [287] has been adopted:

$$\mu(T) = \mu_0 \left(\frac{T}{T_0} \right)^{\frac{3}{2}} \frac{T_0 + S}{T + S} \quad (\text{E.11})$$

with $\mu_0 = 1.716 \cdot 10^{-5}$, $S = 110.4$ and $T_0 = 273.15$. Thermal conductivity is deduced from Prandtl number, assumed constant and equal to 0.7:

$$\lambda(T) = \frac{C_p}{Pr} \mu(T) \quad (\text{E.12})$$

The heat capacity at constant pressure is $C_p = 1005 \text{ J kg}^{-1} \text{ K}^{-1}$. The ideal gas specific constant is $r = 287 \text{ J kg}^{-1} \text{ K}^{-1}$.

E.2.3 Turbulent kinetic energy equation

We use a change of variable, introduced by Cook and Zhou [68] and Kida and Orszag [144], suitable for the study of flows with an highly variable density. Firstly, we focus on the left side of the low Mach moment equation (E.1b):

$$\frac{\partial \rho U_i}{\partial t} + \frac{\partial \rho U_i U_j}{\partial x_j} \quad (\text{E.13})$$

Introducing the new variables $V_i = \rho^{\frac{1}{2}} U_i$ and $b = \rho^{-\frac{1}{2}}$ into (E.13), we get:

$$\begin{aligned} \frac{\partial \rho U_i}{\partial t} + \frac{\partial \rho U_i U_j}{\partial x_j} &= \frac{\partial \sqrt{\rho} V_i}{\partial t} + \frac{\partial \sqrt{\rho} V_i U_j}{\partial x_j} \\ &= \sqrt{\rho} \frac{\partial V_i}{\partial t} + \frac{1}{2} b V_i \frac{\partial \rho}{\partial t} + \sqrt{\rho} \frac{\partial V_i U_j}{\partial x_j} + \frac{1}{2} V_i U_j b \frac{\partial \rho}{\partial x_j} \\ &= \sqrt{\rho} \left(\frac{\partial V_i}{\partial t} + \frac{\partial V_i U_j}{\partial x_j} \right) + \frac{1}{2} b V_i \left(\frac{\partial \rho}{\partial t} + U_j \frac{\partial \rho}{\partial x_j} \right) \end{aligned} \quad (\text{E.14})$$

From the mass equation (E.1a), we can write:

$$\frac{\partial \rho}{\partial t} + U_j \frac{\partial \rho}{\partial x_j} = -\rho \frac{\partial U_j}{\partial x_j} \quad (\text{E.15})$$

Now, by substituting (E.15) into (E.14):

$$\begin{aligned} \frac{\partial \rho U_i}{\partial t} + \frac{\partial \rho U_i U_j}{\partial x_j} &= \sqrt{\rho} \left(\frac{\partial V_i}{\partial t} + \frac{\partial V_i U_j}{\partial x_j} \right) + \frac{1}{2} b V_i \left(-\rho \frac{\partial U_j}{\partial x_j} \right) \\ &= \frac{1}{b} \left(\frac{\partial V_i}{\partial t} + \frac{\partial V_i U_j}{\partial x_j} - \frac{1}{2} V_i \frac{\partial U_j}{\partial x_j} \right) \end{aligned} \quad (\text{E.16})$$

Finally, the variable change leads to the following momentum equation:

$$\frac{\partial V_i}{\partial t} + \frac{\partial V_i U_j}{\partial x_j} - \frac{1}{2} V_i \frac{\partial U_j}{\partial x_j} = b \left[-\frac{\partial P}{\partial x_i} + \frac{\partial}{\partial x_j} \left[\mu \left(\frac{\partial U_i}{\partial x_j} + \frac{\partial U_j}{\partial x_i} \right) \right] - \frac{2}{3} \frac{\partial}{\partial x_i} \left(\mu \frac{\partial U_j}{\partial x_j} \right) \right] \quad (\text{E.17})$$

Following Aulery *et al.* [10], the turbulent kinetic energy evolution can be decomposed into three main mechanisms which are the turbulent production Π defined by equation (E.19a), the total transfer $\sum_n T_n$ which is the sum of all triadic and pressure terms and finally the viscous part D (E.19g) that brings together all viscous effects.

$$\frac{\partial E_c(k, y, t)}{\partial t} = \Pi(k, y, t) + \sum_n T_n(k, y, t) + D(k, y, t) \quad (\text{E.18})$$

A derivation of the spectral turbulent kinetic energy evolution equation is presented in E.6.

E.2.4 Decomposition of TKE evolution terms

For our study, we choose to decompose transfer mechanisms using a Bolotnov *et al.* [28] based decomposition. The triadic and pressure part are split following the

gradient direction. The terms with derivatives in the homogeneous xOz plane ($\frac{\partial}{\partial x}$ and $\frac{\partial}{\partial z}$) are named *in-plane* terms. The terms with derivatives in the wall-normal direction ($\frac{\partial}{\partial y}$) are named *inter-plane* terms. In addition, we take into account the variation of scalar quantities due to temperature that results from the non-free divergence, the mean wall-normal velocity $\langle U_y \rangle$ and density gradient. These terms are null for isothermal incompressible flow and are stacked in one thermal effects term (E.19f). These denominations are derived from the work of Bolotnov *et al.* [28]. It is worth noting that these notations are linked to the mathematical writing of the term and may differ from physical behaviours.

Turbulent production

$$\Pi = \int_{\underline{k}} -\Re \left[\widehat{v}_x^* \widehat{u}_y' \frac{\partial \langle V_x \rangle}{\partial y} \right] d\underline{k} \quad (\text{E.19a})$$

Triadic in-plane term

$$T_{in} = \int_{\underline{k}} -\Re \left[\sum_i \sum_{j=x,z} \widehat{v}_i^* \widehat{\frac{\partial v_i' u_j'}{\partial x_j}} \right] d\underline{k} \quad (\text{E.19b})$$

Triadic inter-plane term

$$T_{it} = \int_{\underline{k}} -\Re \left[\sum_i \widehat{v}_i^* \widehat{\frac{\partial v_i' u_y'}{\partial y}} \right] d\underline{k} \quad (\text{E.19c})$$

Pressure in-plane term

$$\Phi_{in} = \int_{\underline{k}} -\Re \left[\sum_{i=x,z} \widehat{v}_i^* \widehat{\left(b \frac{\partial P}{\partial x_i} \right)} \right] d\underline{k} \quad (\text{E.19d})$$

Pressure inter-plane term

$$\Phi_{it} = \int_{\underline{k}} -\Re \left[\widehat{v}_y^* \widehat{\left(b \frac{\partial P}{\partial y} \right)} \right] d\underline{k} \quad (\text{E.19e})$$

Thermal effect term

$$\begin{aligned} \Gamma = \int_{\underline{k}} -\Re \left[\sum_i \left(\widehat{v}_y^* \widehat{u}_y' \frac{\partial \langle V_y \rangle}{\partial y} + \langle U_y \rangle \frac{\partial \frac{1}{2} \widehat{v}_i^* \widehat{v}_i'}{\partial y} + \frac{1}{2} \widehat{v}_i^* \widehat{v}_i' \frac{\partial \langle U_y \rangle}{\partial y} \right. \right. \\ \left. \left. - \sum_j \frac{1}{2} \widehat{v}_i^* \widehat{\left(v_i' \frac{\partial u_j'}{\partial x_j} \right)} + \sum_j \frac{1}{2} \widehat{v}_i^* \langle V_i \rangle \frac{\partial u_j'}{\partial x_j} \right) \right] d\underline{k} \quad (\text{E.19f}) \end{aligned}$$

Viscous effect

$$D = \int_{\underline{k}} \Re \left[\widehat{v}_i^* F_k^y \left\{ b \frac{\partial}{\partial x_j} \left[\mu \left(\frac{\partial U_i}{\partial x_j} + \frac{\partial U_j}{\partial x_i} \right) \right] - b \frac{2}{3} \frac{\partial}{\partial x_i} \left(\mu \frac{\partial U_j}{\partial x_j} \right) \right\} \right] d\underline{k} \quad (\text{E.19g})$$

In the following sections, the averaged kinetic energy $\langle E_c \rangle = \frac{1}{2} \langle \widehat{v}_i^* \widehat{v}_i \rangle$, statistical average of the instantaneous kinetic energy E_c , will be studied. This quantity is independent of time. Its evolution equation can be written as:

$$\begin{aligned} \frac{\partial \langle E_c \rangle (k, y)}{\partial t} = & \langle \Pi \rangle (k, y) + \langle T_{in} \rangle (k, y) + \langle T_{it} \rangle (k, y) + \langle \Phi_{in} \rangle (k, y) \\ & + \langle \Phi_{it} \rangle (k, y) + \langle \Gamma \rangle (k, y) + \langle D \rangle (k, y) = 0 \end{aligned} \quad (\text{E.20})$$

Consequently, the statistical average of each term of equation (E.19) will be analysed and computed.

E.3 Simulated datasets and validation

E.3.1 Channel flow configuration

A rectangular channel flow is studied, as represented by figure E.1. The flow is periodic along the streamwise x direction and spanwise z direction. The channel walls are normal to the y direction. The top wall is at constant temperature T_2 and the bottom wall at temperature $T_1 = 293$ K. The temperature ratio between the hot and cold wall is $T_r = T_2/T_1$. We studied configurations of temperature ratios $T_r = 1$ and $T_r = 2$. The dimensions of the channel in the x , y and z directions are denoted L_x , L_y and L_z respectively. The domain size is: $L_x = 4\pi h$, $L_y = 2h$ and $L_z = 2\pi h$ with $h = 15$ mm.

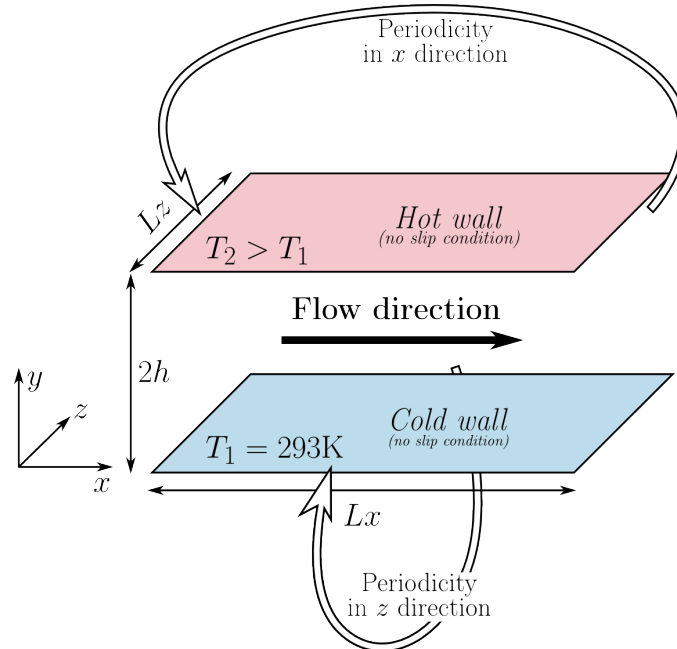


Figure E.1 – Biperiodic anisothermal channel flow

Because of the temperature gradient, the turbulent Reynolds numbers Re_τ at each sides of the channel are different, with the turbulent Reynolds number at the cold

Name	Type	Re_τ	T_r	L_x	L_z	Δx^+	Δz^+	Δy^+	N_x	N_y	N_z
180-1	DNS	184	1	$4\pi h$	$2\pi h$	6	3	0.25-2.3	382	300	382
180-2	DNS	270-108	2	$4\pi h$	$2\pi h$	17.6	5.9	0.5-7.8	192	140	288
395-1	LES	395	1	$4\pi h$	$2\pi h$	11	11	0.75-7.5	448	200	224
395-2	LES	542-221	2	$4\pi h$	$2\pi h$	14	14	1-7.5	448	200	224

Table E.1 – List of simulations and mesh parameters.

side being greater. Thus, the mean turbulent Reynolds number Re_τ^m is defined as the average of the turbulent Reynolds number calculated at the cold side and at the hot side. Simulations were carried out in various configurations as described in table E.1. In this table, the number of grid points in the direction i is denoted N_i and the cell size in wall-units Δi^+ . The wall-units scaling is based on the turbulent Reynolds number of the cold side, since it is more restrictive.

Two mean turbulent Reynolds number were selected (180 and 395) as well as temperature ratios of 2 and 1 for the incompressible limit case. Hence, four configurations are simulated in total. The computational cost increase with Reynolds number restricts the mesh refinement at $Re_\tau^m = 395$ compared to the simulations at $Re_\tau^m = 180$. As the temperature gradient induces a local Reynolds number increase, the simulations performed are more precise in the isothermal case for similar reasons. The cell sizes in wall-units in the wall-normal direction is increased by 0.25 from an isothermal simulation to the anisothermal equivalent and 0.5 from low Reynolds number to high Reynolds number.

Since the simulations at $Re_\tau^m = 180$ are less expensive in terms of computational cost, we were able to capture the fine flow behavior using direct numerical simulation. This contrasts with the simulations at $Re_\tau^m = 395$. At high Reynolds number, the calculation power and mesh sizes required for a full DNS would be excessive. Large eddy simulation appears as the preferable alternative. With the subgrid scales modelling, the simulations can yield accurate statistics despite coarser meshes relatively to the turbulent Reynolds number. Therefore, DNS is used at $Re_\tau^m = 180$ and LES at $Re_\tau^m = 395$.

E.3.2 Numerical set up

The resolution of the low Mach equations involves a finite volume solver. A third order Runge–Kutta is used for time derivatives. A fourth order centered scheme is used for momentum convection. A third order QUICK scheme (quadratic upstream interpolation for convective kinetics [170]) is used for temperature convection. TrioCFD is used to perform the simulations [38].

As there is no mean pressure gradient in the channel flow because of periodic boundary conditions, a streamwise volume force F is added to keep the mass flow rate constant. For both the DNS and the LES, the driving force is regulated through the mass flow rate second derivative:

$$F_{t+1} = F_t + C_0 \frac{D_{\text{target}} - 2D_t + D_{t-1}}{\Delta t} \quad (\text{E.21})$$

with C_0 a damping constant, D the mass flow rate, D_{target} the targeted mass flow rate and $t - 1$, t and $t + 1$ indices related to the previous, current and next time step respectively. Walls have no slip condition. The initial velocity field is parabolic in the streamwise direction and sinusoidal in the wall-normal direction and permits to initiate the turbulence.

Four meshes were adopted as shown in table E.1. Each mesh is regular in both homogeneous directions. The grid points in the wall-normal direction follow a hyperbolic tangent transformation:

$$y_k = L_y \left(1 + \frac{1}{a} \tanh \left[\left(\frac{k-1}{N_y-1} - 1 \right) \tanh^{-1}(a) \right] \right) \quad (\text{E.22})$$

where a is a constant associated with the mesh dilatation. The precision increase in the boundary layer compared to an uniform mesh allows the use of the no-slip boundary condition.

E.3.3 Data collection and filtering for spectral analysis

The data required to compute the different terms of equation (E.19) is acquired during the simulation. The terms of equation (E.19) are calculated at each wall-normal coordinate at particular time steps then time averaged. A time-sampling corresponding to 20 timesteps was used. The time average is performed over a total duration of $12.3 t_c$, where $t_c = h/U_\tau$ is the characteristic timescale of the simulation. This is sufficient for the spectral statistics to converge. The Fourier transform is numerically computed as:

$$\widehat{g}(k_{x,m}, y, k_{z,n}) = \frac{1}{N_x N_z} \sum_{p=0}^{N_x-1} \sum_{k=0}^{N_z-1} g(x_p, y, z_k) \exp \left(-2\pi i \left(\frac{mp}{N_x} + \frac{kn}{N_z} \right) \right) \quad (\text{E.23})$$

This is done using the FFTW C subroutine library [103].

A low pass filter is applied to the spectral data. This could be done because a clear separation between high frequency noise and the wanted signal appears in the Fourier transform of the spectral data. This can be seen as a moving-average that takes into account 2D wavenumber vectors of nearby norms. The energy transfer processes are direction-dependant, that is not identical in x and z directions. It is thus of great importance that this averaging does not favor a particular direction.

E.3.4 Validation of the mean field profiles

The numerical method described above has been validated with regard to DNS using the results of Kim *et al.* [146] in the isothermal case. The simulation performed by Kim *et al.* [146] has a turbulent Reynolds number of 180. It has been compared to our DNS in the same conditions in figures E.2 and E.3. The following standard scaling is used:

$$y^+ = Re_\tau \frac{y}{h} \quad (\text{E.24a})$$

$$U^+ = \frac{\langle U \rangle}{U_\tau} \quad (\text{E.24b})$$

where U_τ is the wall friction velocity. Similarly to (E.24b), each RMS quantity in figure E.3 is scaled by the friction velocity U_τ and the velocity correlation by U_τ^2 . The two simulations give nearly identical results for both mean and fluctuating quantities. Similar validation has been performed regarding LES with the results of Moser *et al.* [203] in the isothermal case at $Re_\tau = 395$ (not shown here). This validates our numerical method at the incompressible limit for both DNS and LES.

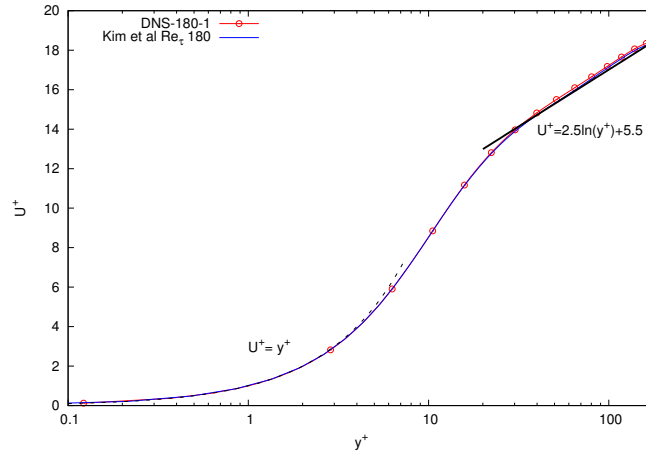


Figure E.2 – Mean longitudinal velocity comparison with direct numerical simulation of Kim *et al.* [146] at $Re_\tau = 180$.

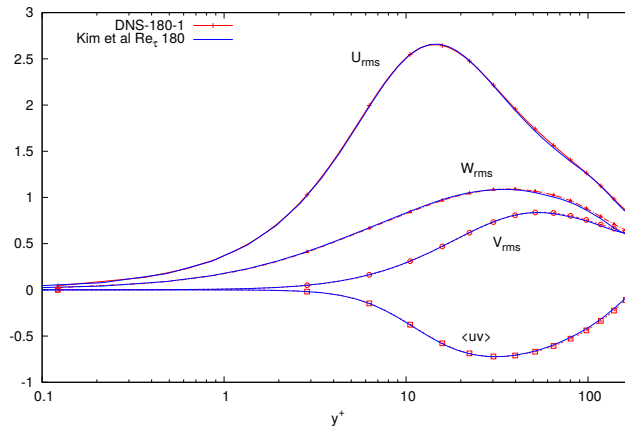


Figure E.3 – Velocity fluctuations comparison with direct numerical simulation of Kim *et al.* [146] at $Re_\tau = 180$.

E.3.5 Validation of the spectra measurements

As written in E.2.4, the TKE evolution equation decomposition follows Bolotnov *et al.* [28] decomposition and allows comparison on isothermal flow spectra. Figure E.4 compares the turbulent production (equation (E.19a)), figure E.5 the in-plane triadic transfer term (equation (E.19b)) and figure E.6 the inter-plane transfer term (equation (E.19c)). All these figures use the same normalisation as Bolotnov and the colors scales

are identical. The following scaling is used for the wave number:

$$k^+ = \frac{kh}{Re_\tau} \quad (\text{E.25})$$

The comparison reveals that our results match with those of Bolotnov with respect to magnitude and global shape for all terms. The turbulent production (figure E.4) is centered on the same area ($0.056 < k^+ < 1$ and $10 < y^+ < 17$) and decreases at the same rate.

For the in-plane triadic transfer (figure E.5), our results are in agreement with the two major areas found by Bolotnov: one negative centered on $k^+ = 0.08$ and $y^+ = 12$, and one positive centered on $y^+ = 18$ and $k^+ = 0.178$. A low magnitude positive area appears in our simulation around $k^+ = 0.02$ and $y^+ = 13$ whereas the figure of Bolotnov suggests that the term tends to zero around this area. However, it is worth noting that a small positive area appears in the data provided by Bolotnov *et al.* (see figure 23 of [28]). Consequently, our figure E.5(a) that contains more contour values than the figure E.5(b) from Bolotnov gives some information of figure 23 in Bolotnov *et al.* [28]. Furthermore, our results and those of Bolotnov that indicate a positive area at large scales are consistent with the backscatter effect identified in wall-bounded turbulence [232, 160, 57].

At last, the inter-plane triadic transfer term has same magnitude and comprises the same two main parts which are: a positive centered area on $k^+ = 0.056$ and $y^+ = 5.6$ and a negative one at $k^+ = 0.08$ and $y^+ = 15$. Some differences can be observed in our simulation: the high value of low k^+ are stronger and the negative area is less spread.

These results validate our simulation and its data-processing at the incompressible limit.

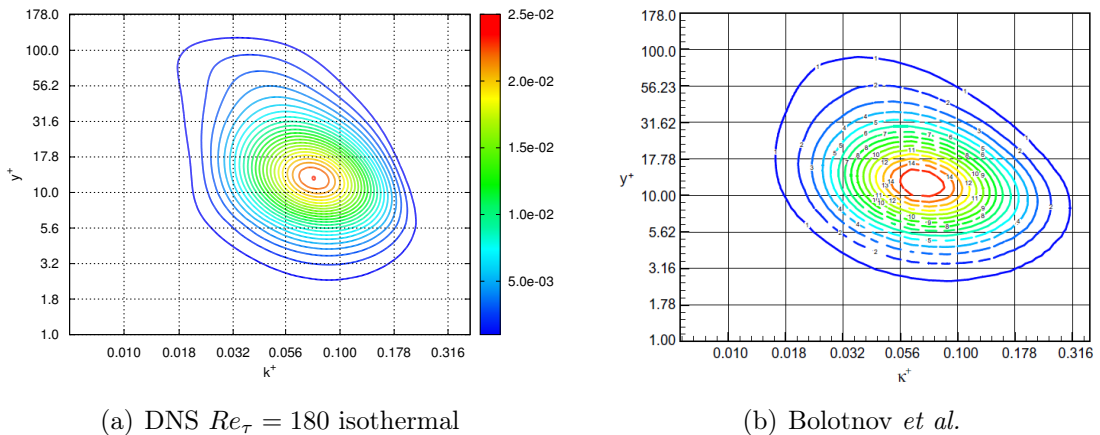


Figure E.4 – Comparison of turbulent production spectra.

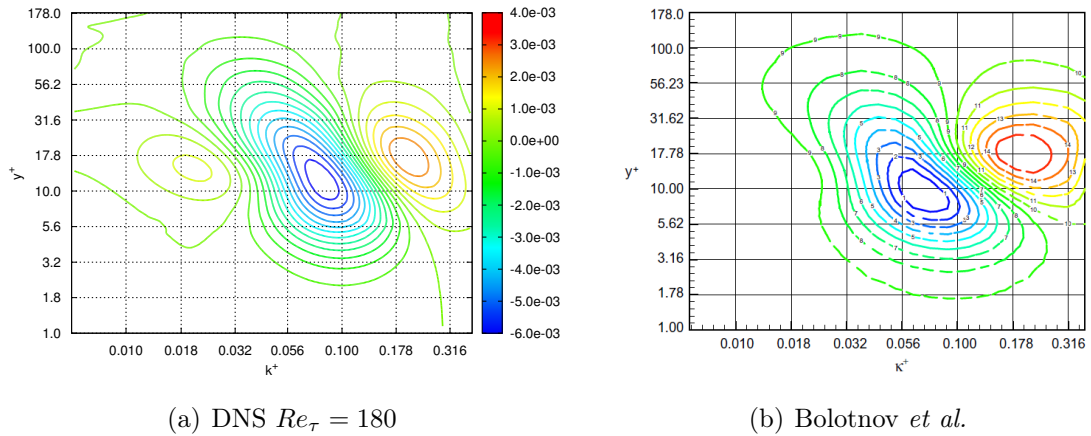


Figure E.5 – Comparison of in-plane triadic transfer spectra.

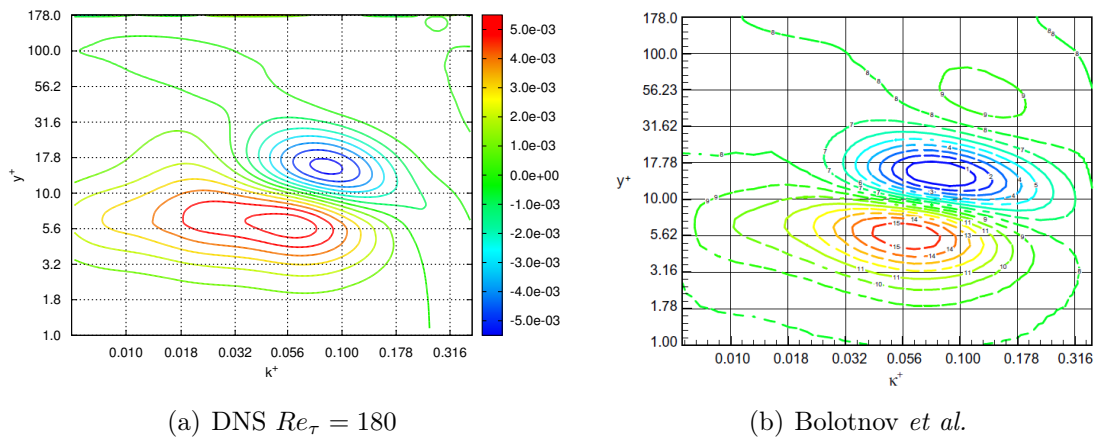


Figure E.6 – Comparison of inter-plane triadic transfer spectra.

E.4 Isothermal energy transport of distinctive Reynolds numbers

We start this section by making a remark on the individual transfer terms reported in figures E.7 to E.17. For each set, a vertical reading gives a thermal comparison (isothermal case, cold and hot sides for the anisothermal case) at a constant Reynolds number, while a horizontal reading gives a comparison between Reynolds Number for a same thermal configuration. Figure E.7 and figures E.8 – E.17 are scaled by $U_\tau \nu$ and by the maximum of production in the isothermal case for each Reynolds number, respectively. The wave number is scaled with the half-height of the channel h . The analysis done in this section requires only the middle panel of figures E.7 to E.17.

E.4.1 Isothermal turbulent spectra at low Reynolds number

At first, the turbulent kinetic energy is plotted on figure E.7(c). As expected, the maximum of TKE is around $y^+ = 11$ for the larger scales ($kh < 2$). Compared to the high scales, the energy of the small scales is divided by more than 10^{10} . This ensures the capture of the essential phenomena from the largest scale to the smallest. The significant parts of TKE and transfer mechanisms are not filtered in the case of LES, as they are located beyond the cutoff frequency which is around $kh = 20$ (the filter is only visible at high Reynolds number).

The TKE production (figure E.8(c)) is limited at $kh < 4$ in term of the spectral scales and at $y^+ > 5$ in term of the wall distance. The maximum of the production is close to the maximum of TKE. The scale range of the production decreases with the distance from the wall. At $y^+ = 40$, the production scale range is $0.6 < kh < 2$ and the scale is $0.6 < kh < 4$ at $y^+ = 10$. The production tends to zero near $y^+ = 100$.

The total energy transfer (figure E.9(c)) is characterized by an inverse cascade from intermediary spectral scales to the large scales. The intermediary scales where the energy is removed are located near the production term peak area. Note that the size of structures receiving energy is longer than the channel size ($kh > 1$). The energy transfer occurs between scales with a scale ratio greater than two, which is characteristic of non-local transfers [48]. In global point of view, the energy is transferred closer to the wall, a mechanism removing the energy to the streaks.

As expected, the viscous effect (figure E.10(c)) balances the total energy transfer mechanism. The energy is taken from the viscous layer at large scales and tends to zero at the small scales. This may correspond to the friction created by the streaks close to the wall.

The total energy transfer is the sum of all triadic and pressure terms. Let us now study them individually

The triadic in-plane term (figure E.11(c)) is composed of three areas around $y^+ = 20$. The first and last areas are positive with smaller y^+ ranges but the middle one is negative with larger spectral and y^+ ranges. This term, therefore, is involved with both the inverse and direct transfer of energy in the spectral scale. We can see a link between the wall distance and the scale of the negative area. This behaviour is observed for all terms and for all areas with $y^+ > 10$.

The inter-plane transfer term (figure E.12(c)) is a mixed transfer term. The energy is transferred both in the wall and scale directions from the negative area in a similar manner to the total transfer mechanisms. The energy is received at both the large scales and close to the wall ($5 < y^+ < 10$). Note that this transfer has a stronger magnitude than that of the in-plane term, hence, dominates the behaviour of the the total triadic term (figure E.13(c)).

In contrast with the triadic terms, the pressure terms (figures E.14(c) and E.15(c)) transfer energy between wall distances without scale shift (the transfer is centered on $kh = 0.7$). For the inter-plane term, the energy is taken in the central part of the flow and transferred around $y^+ = 45$. For the in-plane term, the transfer occurs from $y^+ = 45$ to the near wall region.

The total pressure term (figure E.16(c)) is composed of four areas: a positive area

near the wall, a negative area near $y^+ = 20$, a positive area near $y^+ = 60$ and a negative area close to the center of the channel. Globally, the energy is transferred towards the wall with little scale shift. The total triadic transfer and the total pressure terms play a distinctive role. As the total pressure term is very small in front of the total triadic term, the total energy transfer is nearly identical to the total triadic term, and thus of the inter-plane triadic term.

E.4.2 Reynolds number effects on isothermal turbulent spectra

The impact of Reynolds number variations on the turbulent kinetic energy balance terms will be investigated using the isothermal results at $Re_\tau = 180$ and $Re_\tau = 395$.

To begin with, the turbulent kinetic energy and TKE evolution terms tend to have wider wave space and y^+ ranges at high Reynolds number. At the same time, the mechanisms are more distributed in the spectral space. The spatial extent of production stretches both into the central channel area and closer to the wall at $Re_\tau = 395$ when compared to the $Re_\tau = 180$ case, increasing from $5 < y^+ < 50$ (figure E.8(c)) to $3 < y^+ < 300$ (figure E.8(d)). Its spectral space extent has also increased from $0.7 < kh < 3$ to $0.4 < kh < 6$. Similar behaviour is observed for total transfer, in-plane and inter-plane triadic and pressure transfer terms.

Meanwhile, the turbulent scales shift with wall distance at high Reynolds number. The operative scales are larger far from the wall and smaller closer to the wall. The negative area range of the in-plane pressure transfer term (figure E.14) is $0.4 < kh < 1$ at $y^+ = 200$ and $1 < kh < 2$ near $y^+ = 60$. Such scale shift is however not present at $Re_\tau = 180$. The scale shift increases with Reynolds number is followed by all transfer terms and production.

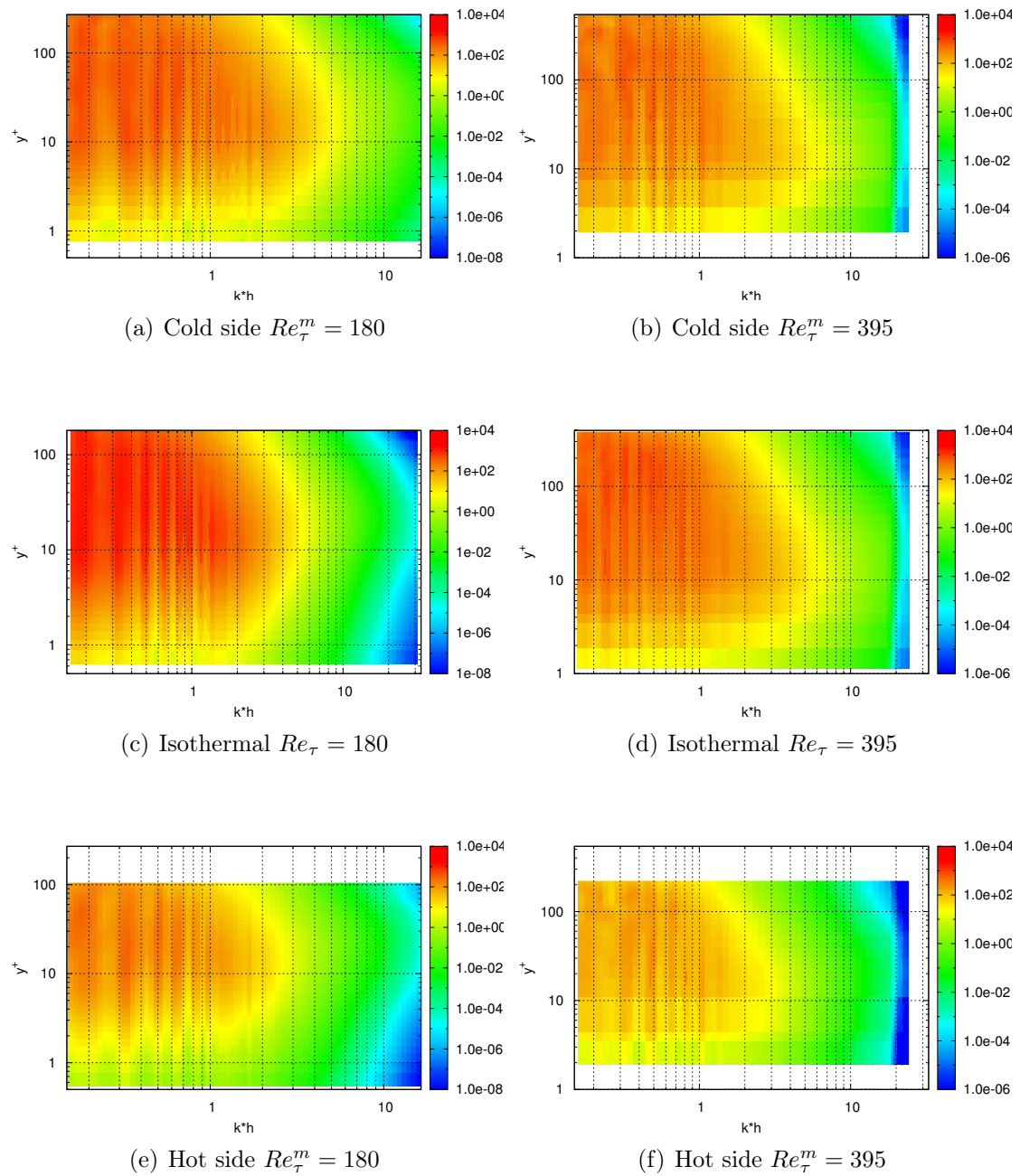
It may be also be observed that the magnitude of the pressure transfer term as a proportion of the total transfer is lower at $Re_\tau = 395$. This made the pressure relatively (but not physically) less important than triadic effect.

Finally, the turbulent scales involved in the transfer are less selected at high Reynolds number. At low Reynolds number, the in-plane triadic transfer (figure E.11(c)) occurs in 3 very localized areas. Conversely, at high Reynolds number, the areas are no more separated in the wavenumber space (figure E.11(d)). This is also true for triadic inter-plane transfer term and the total transfer term.

E.5 Anisothermal turbulent spectra of distinctive Reynolds numbers

E.5.1 Anisothermal turbulent spectra at low Reynolds number

In this subsection, the effect of thermal gradient is described by comparing an anisothermal flow at $Re_\tau = 180$ against that from the isothermal simulation in last section. We will defer the investigation of the Reynolds number variations in an anisothermal setting to the next subsection.

Figure E.7 – Turbulent kinetic energy, divided by $U_\tau \nu$.

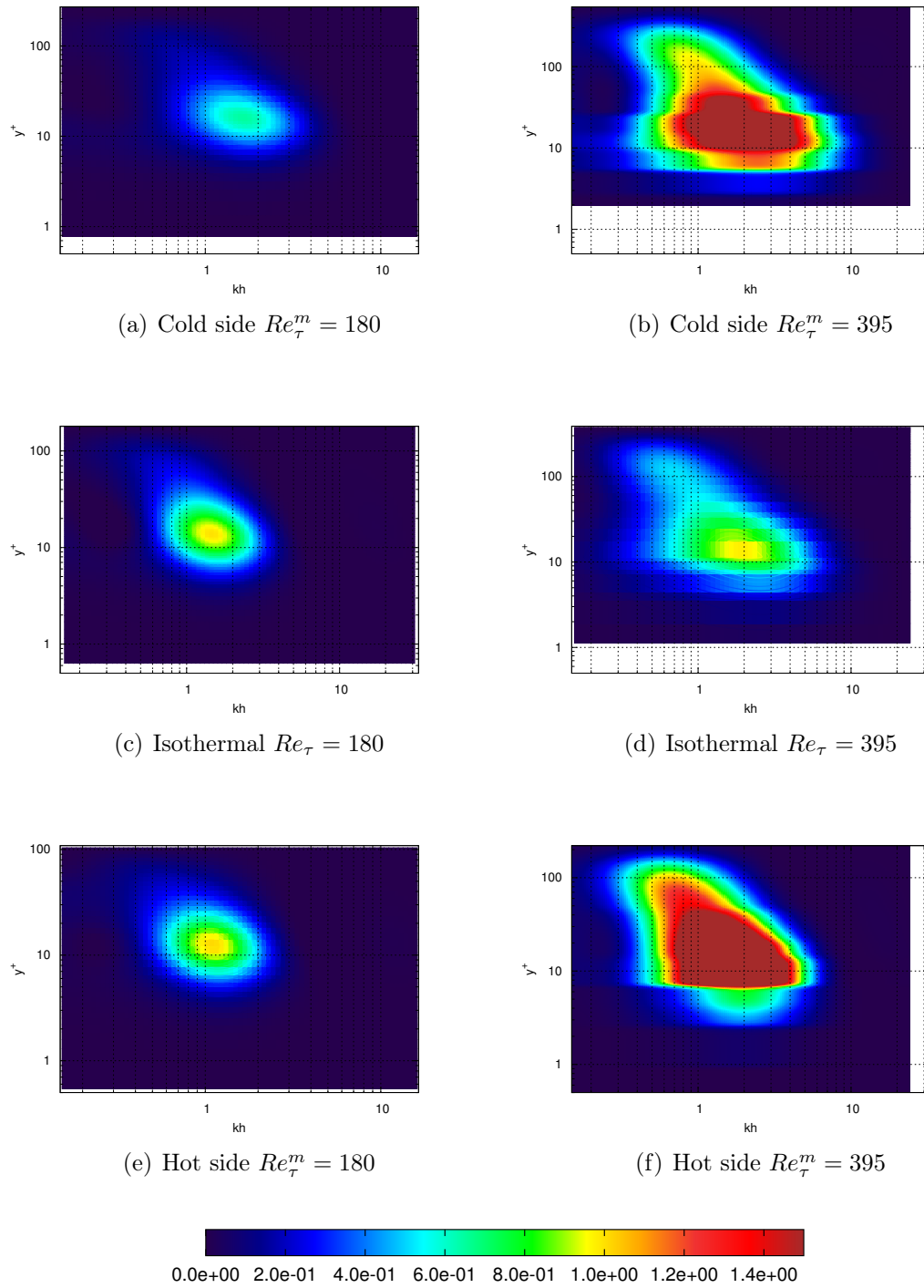


Figure E.8 – Turbulent production term.

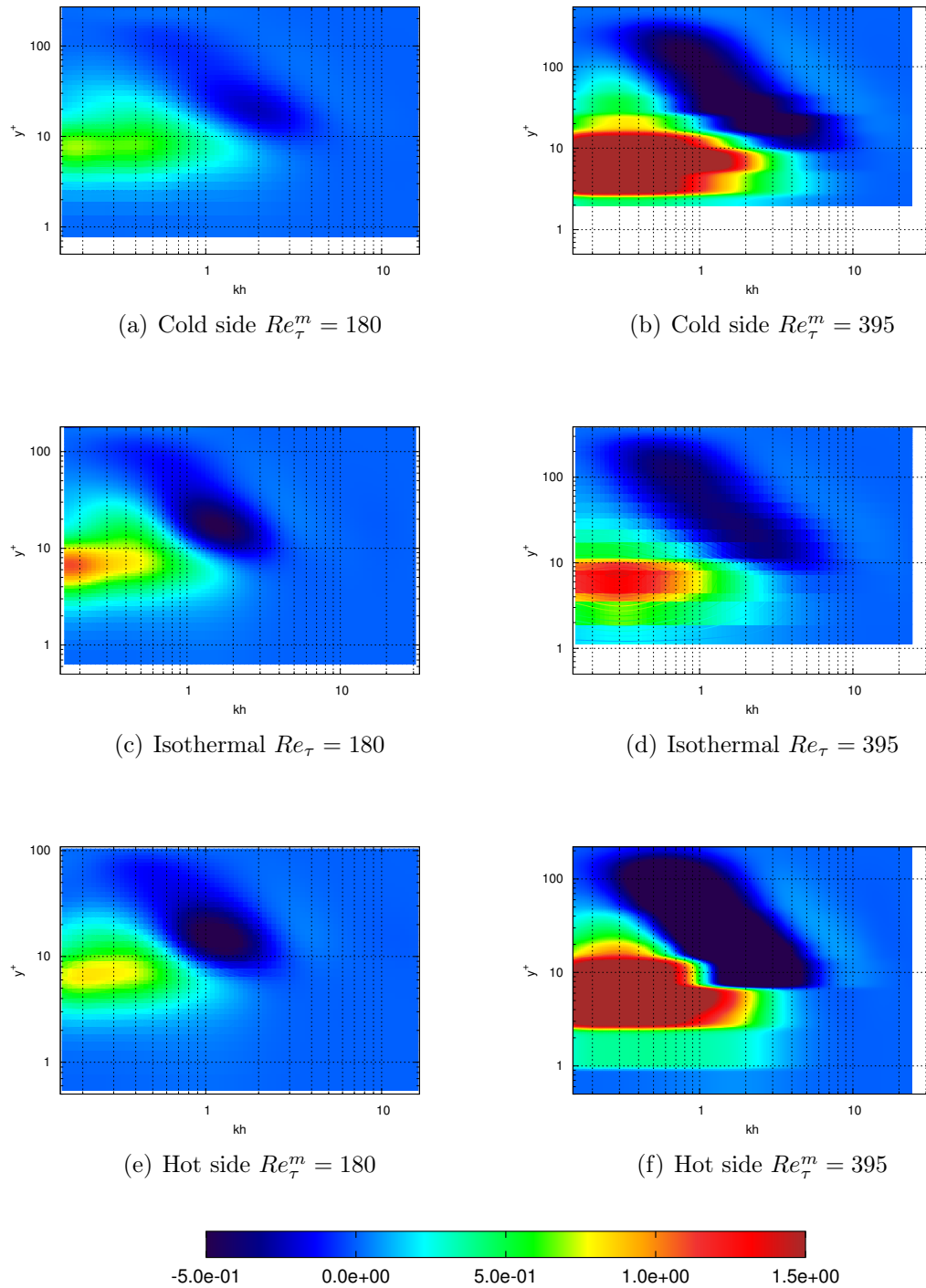


Figure E.9 – Total transfer (total triadic term and total pressure term).

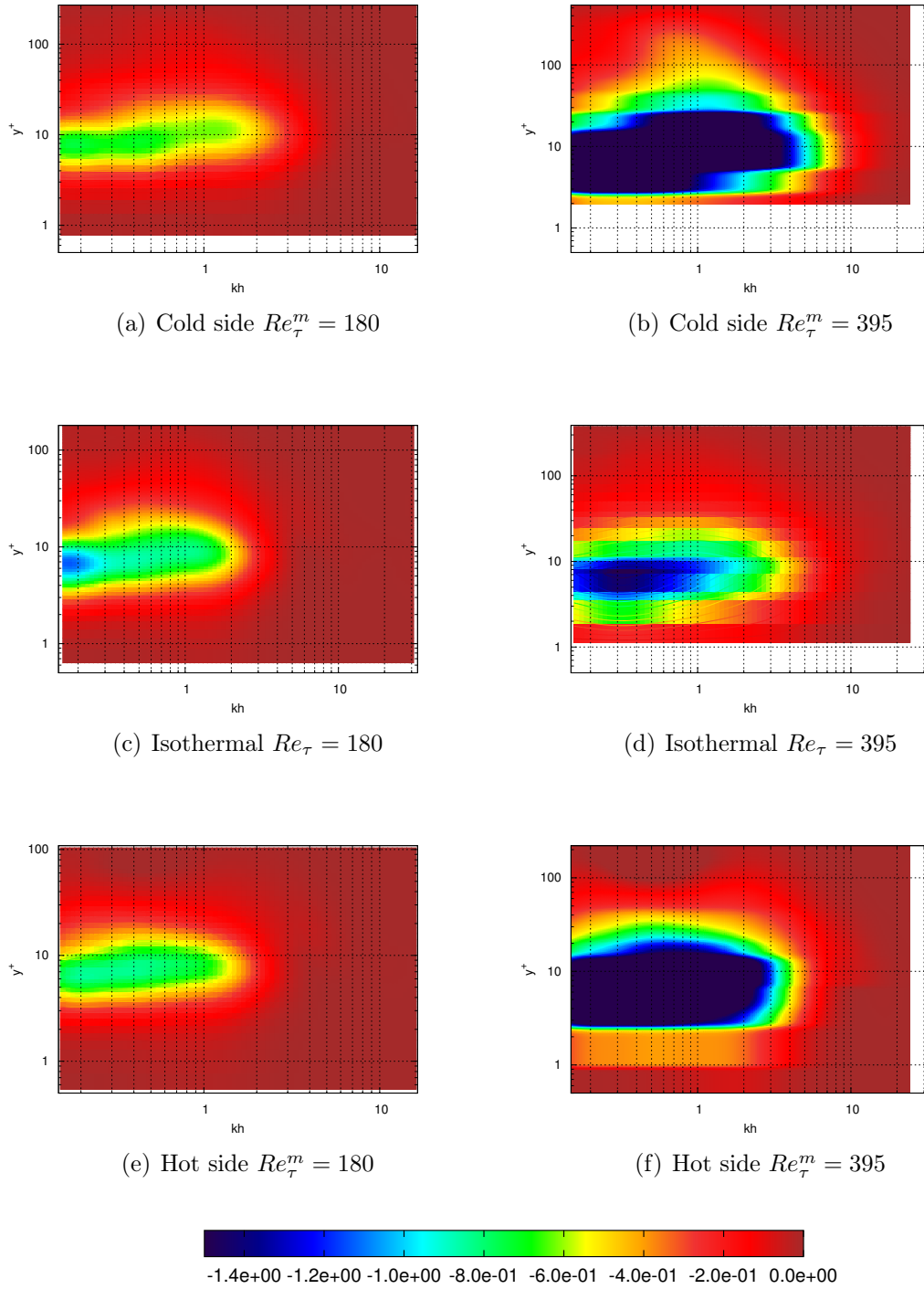


Figure E.10 – Viscous effect term.

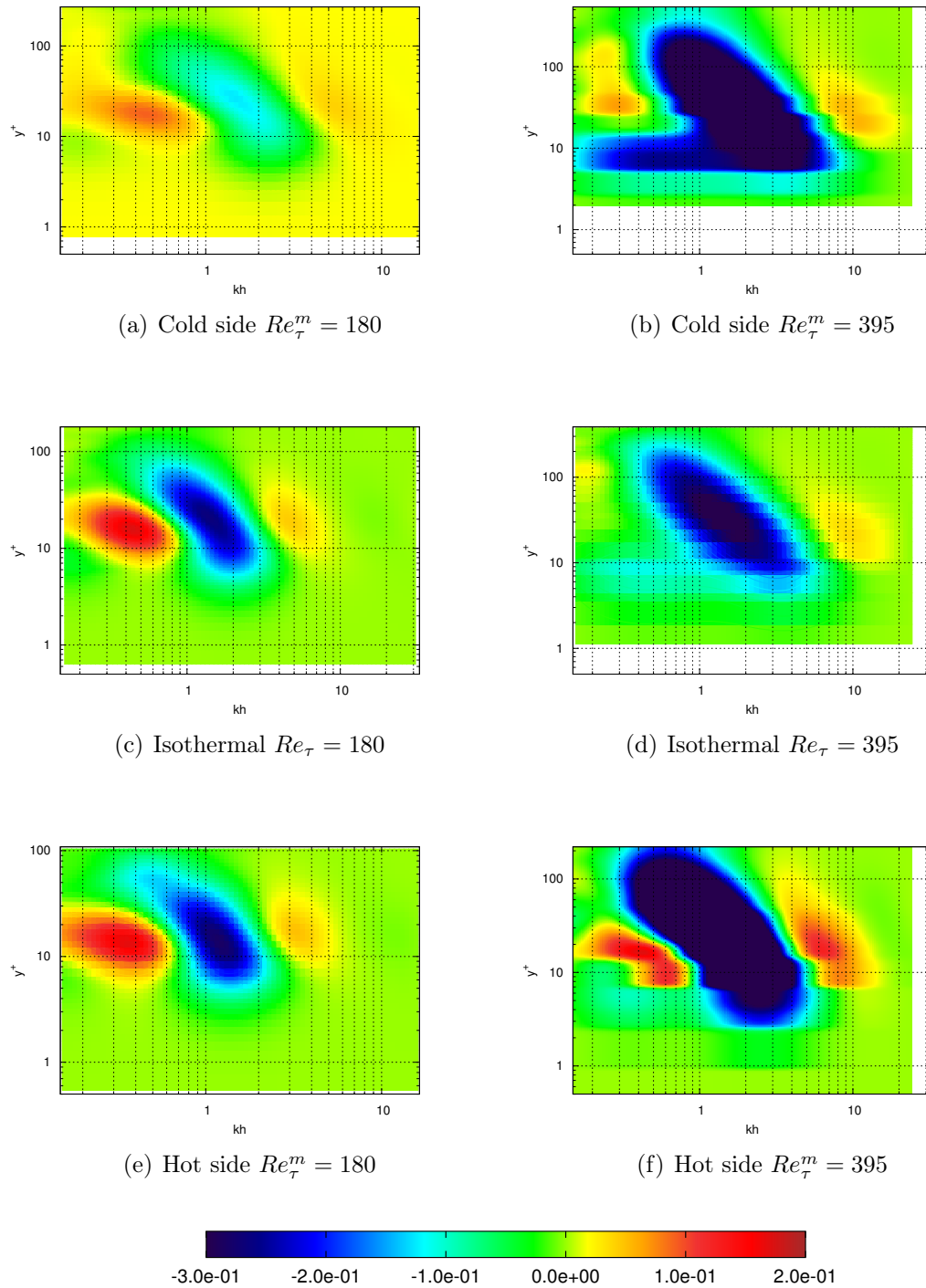


Figure E.11 – Triadic in-plane term.

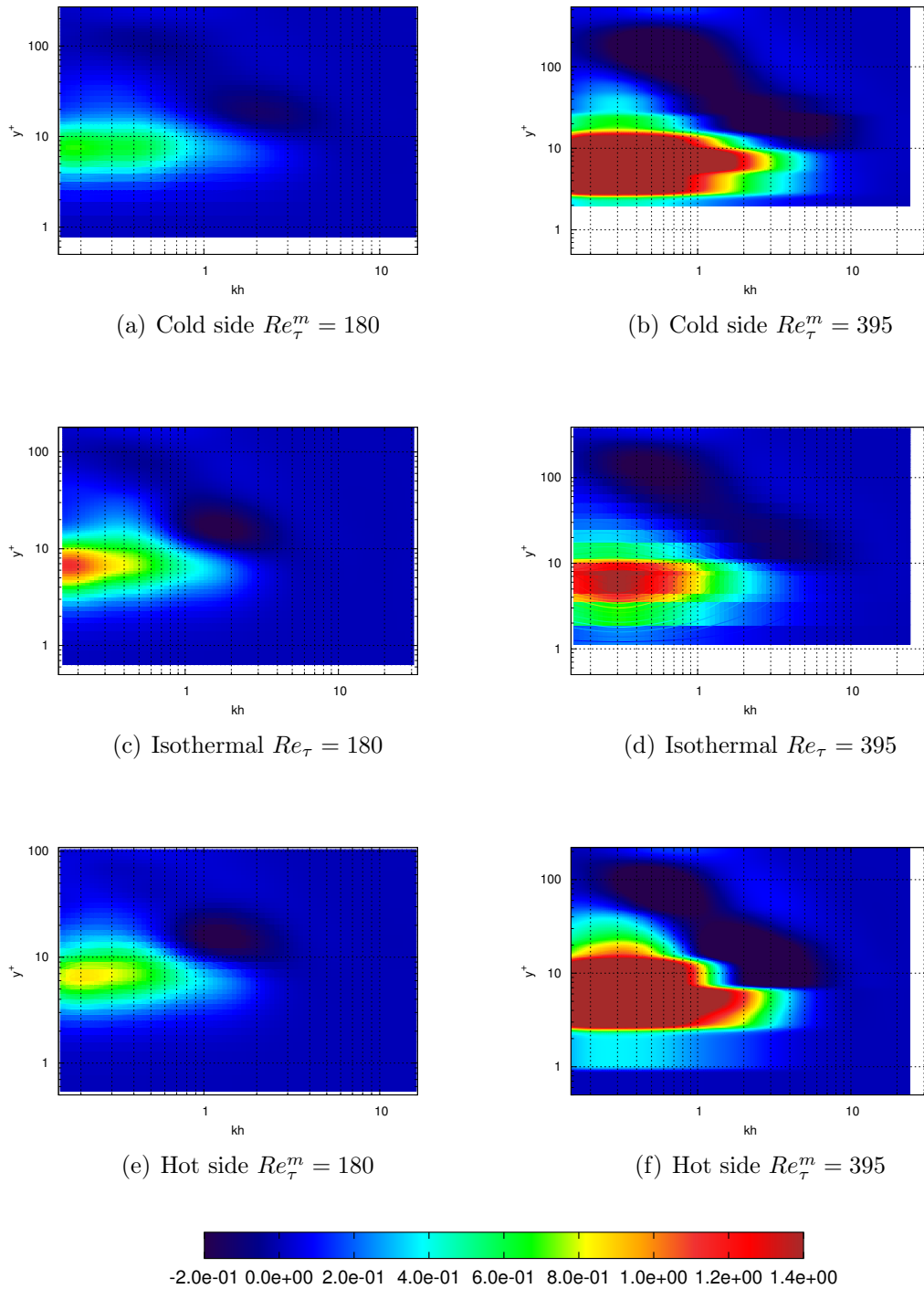


Figure E.12 – Triadic inter-plane term.

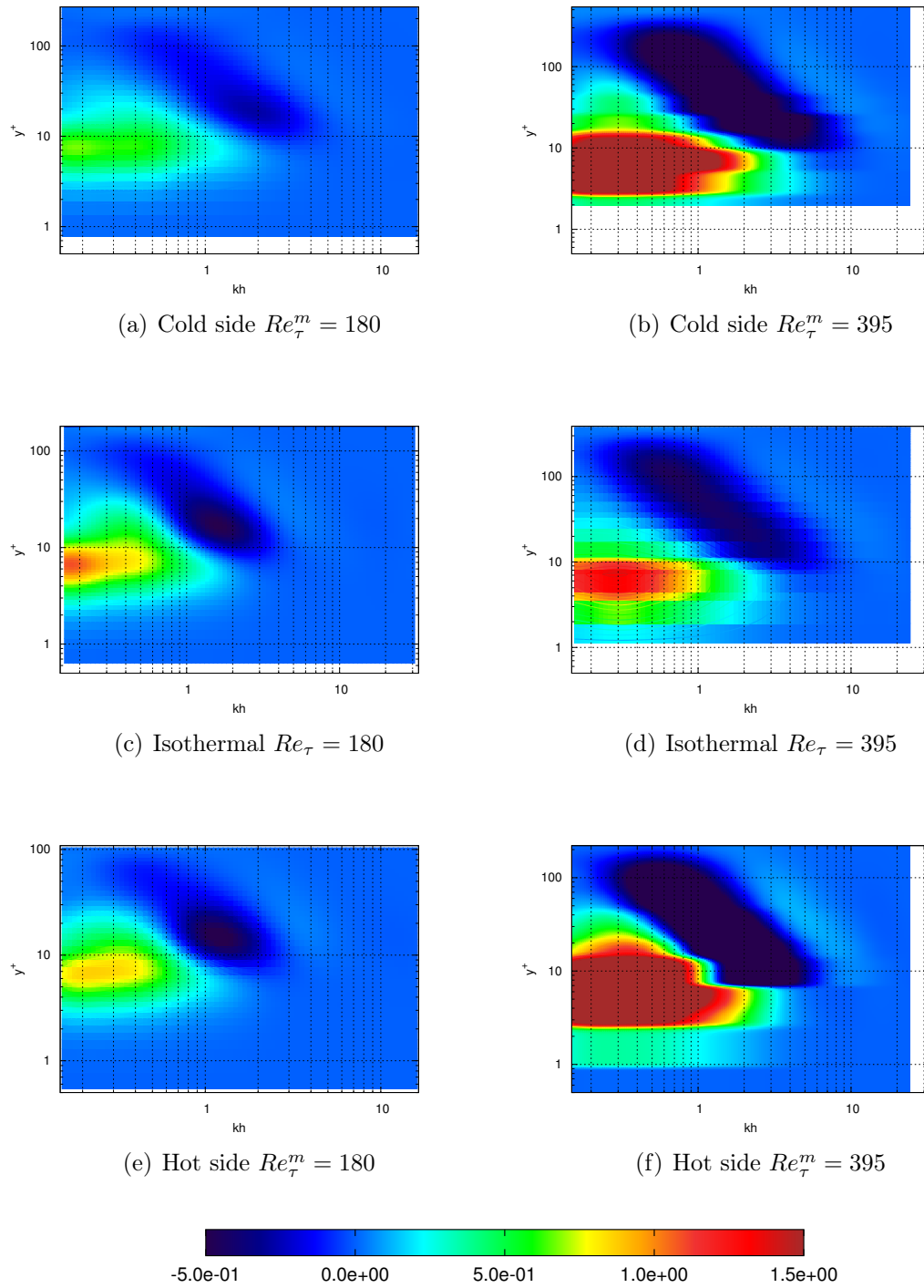


Figure E.13 – Total triadic term.

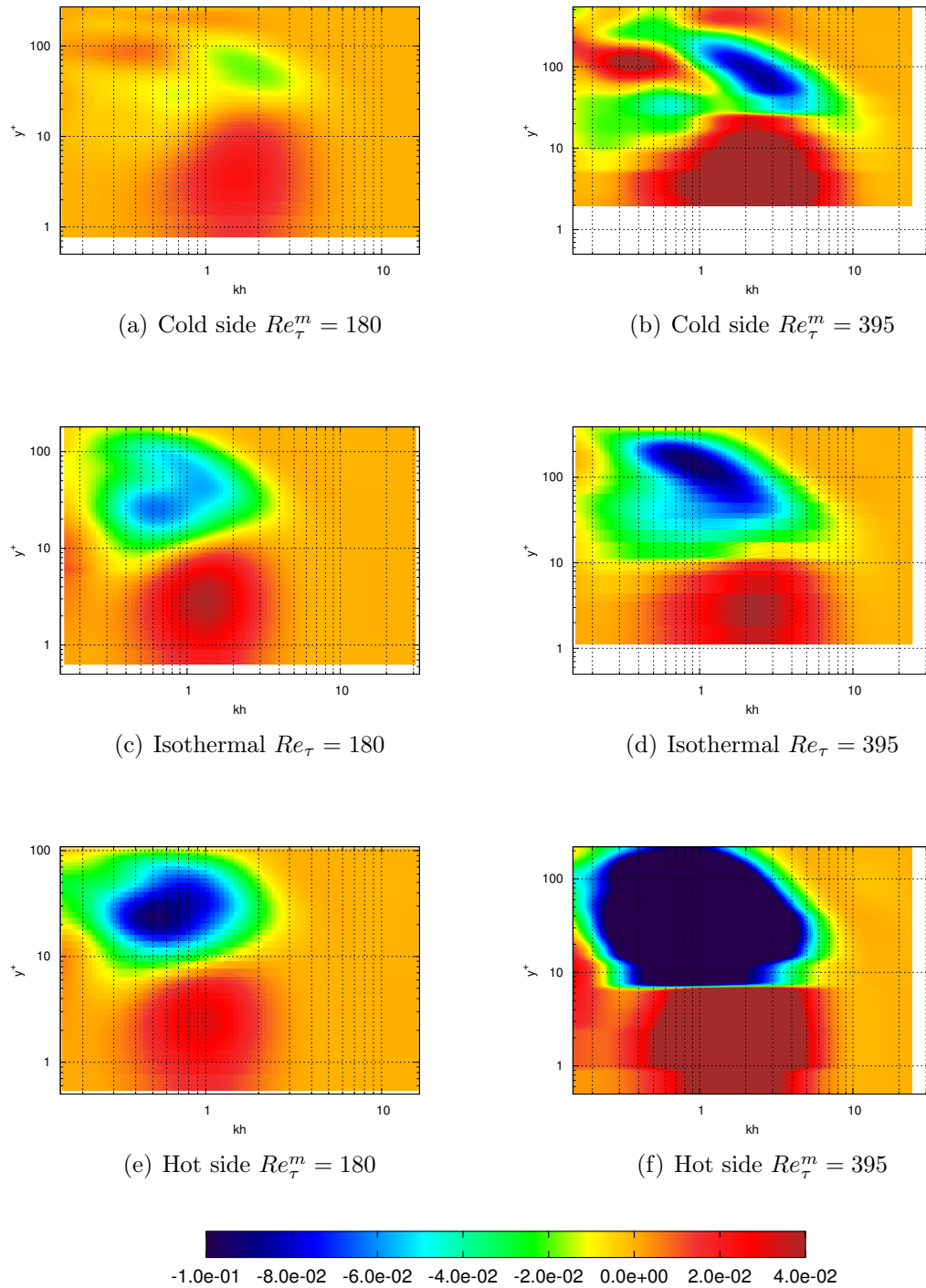


Figure E.14 – Pressure in-plane term.

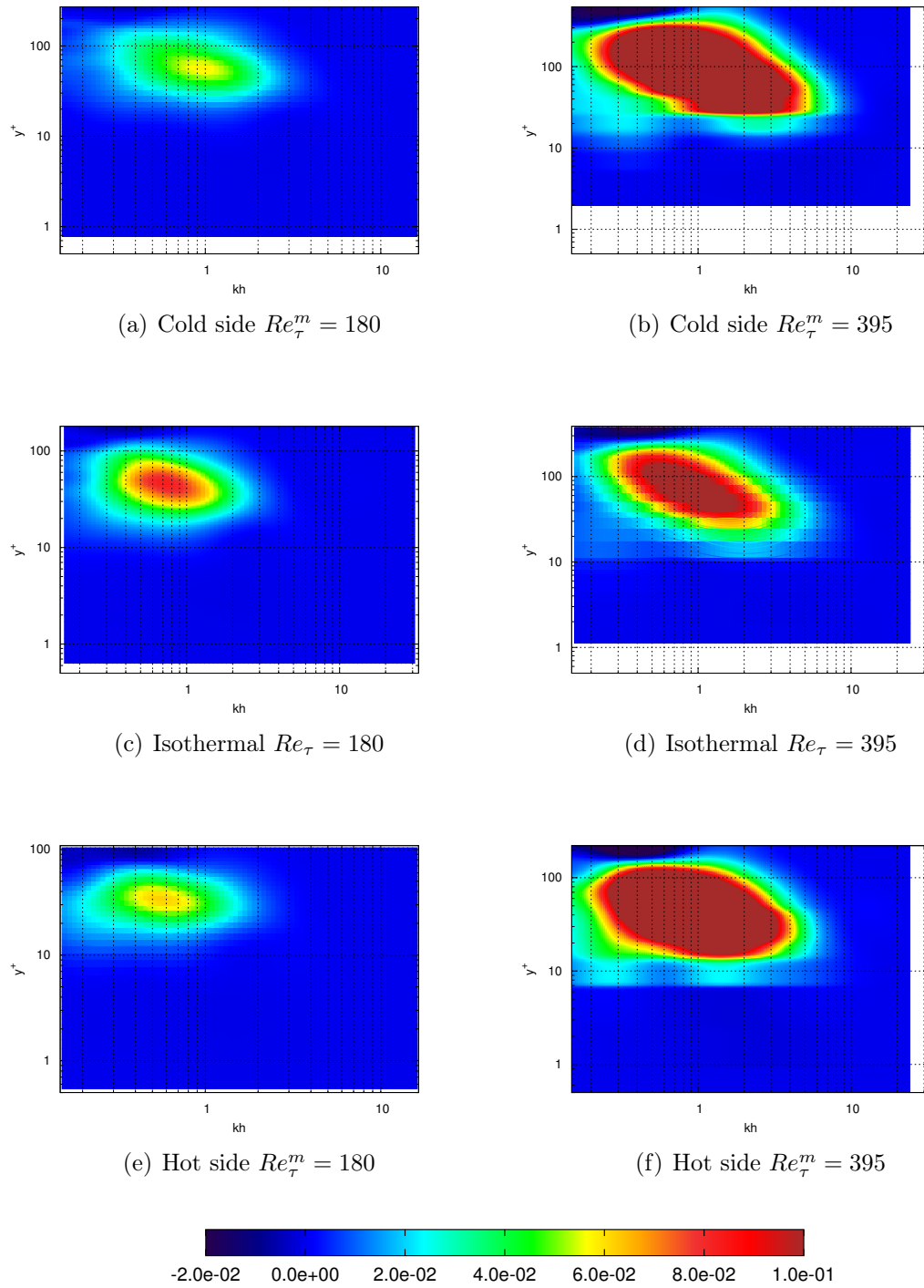


Figure E.15 – Pressure inter-plane term.

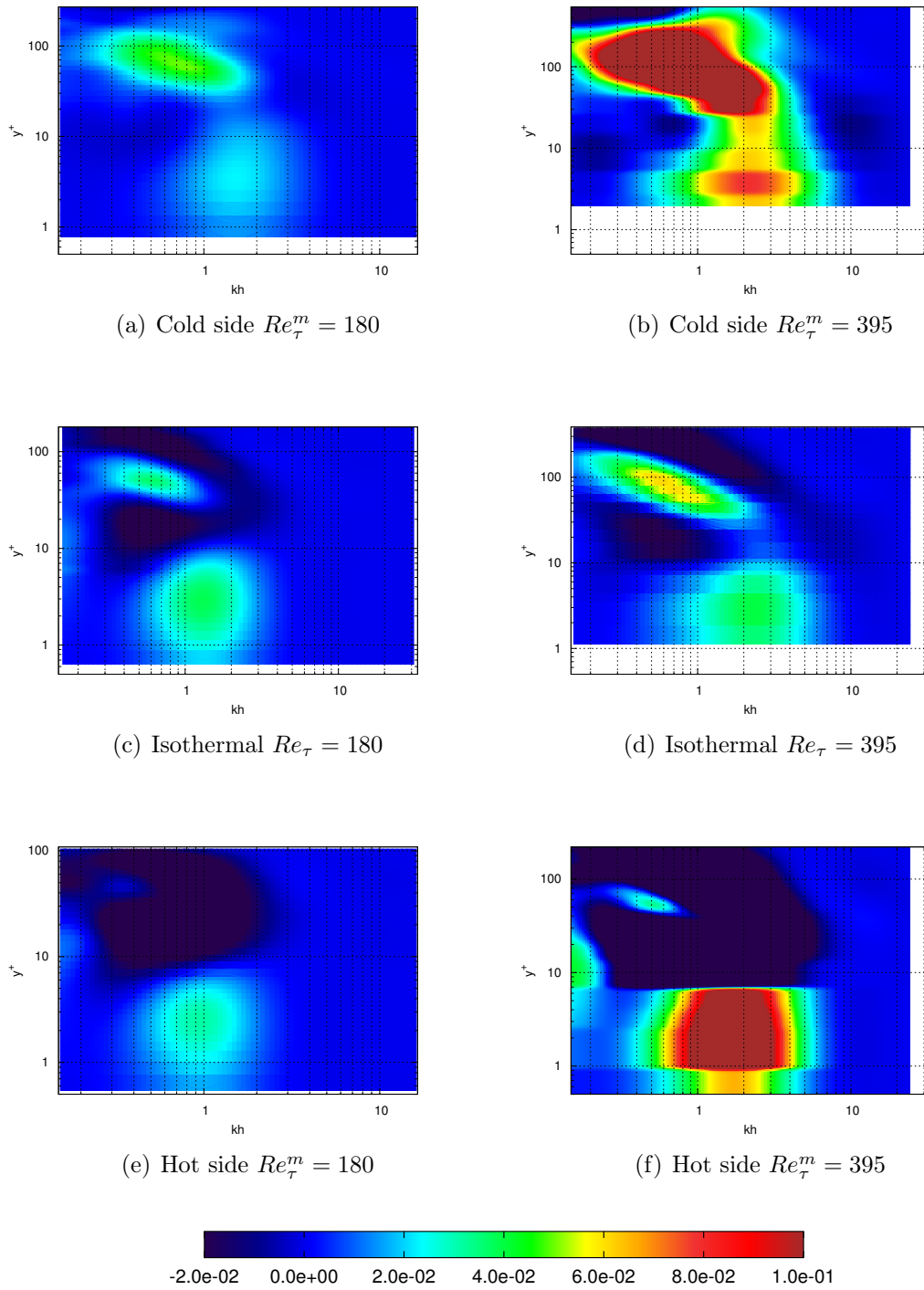


Figure E.16 – Total pressure term.

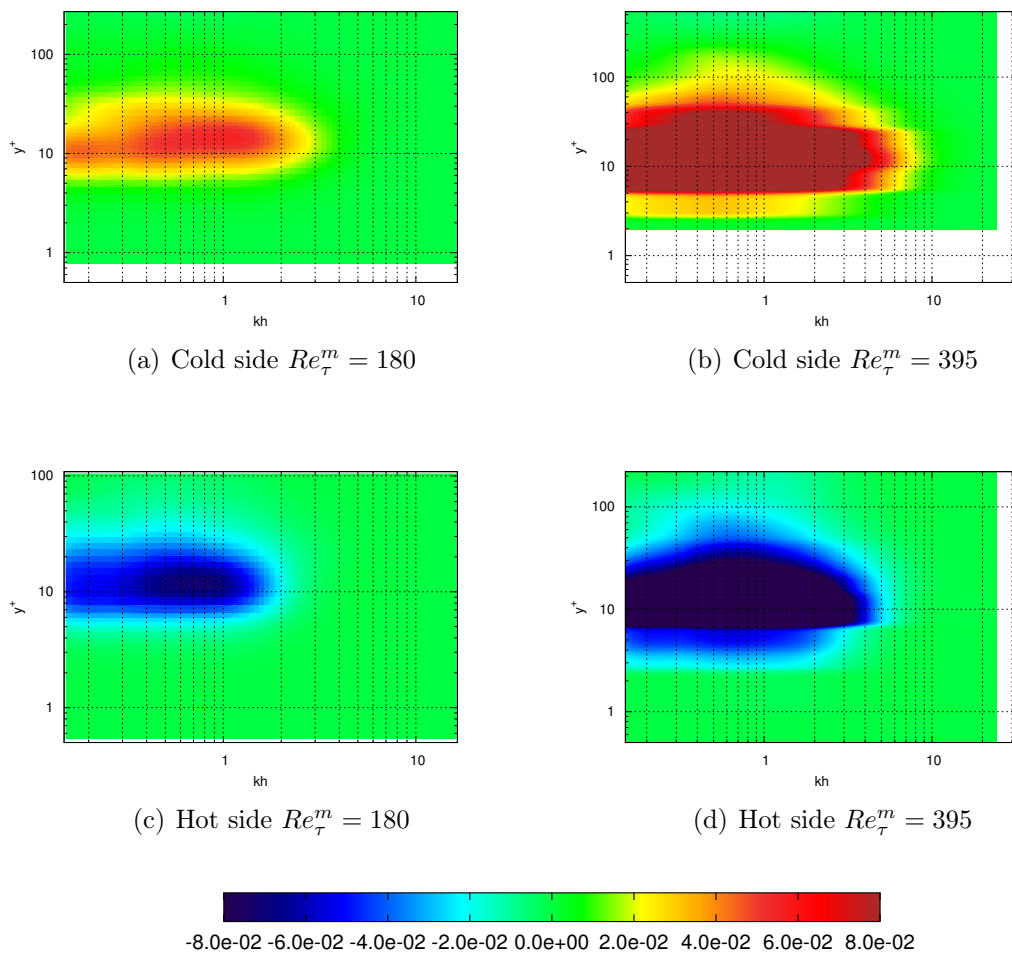


Figure E.17 – Thermal effects term.

The thermal effect term (figure E.17, left panel), which is negligible in isothermal simulations, now has the same magnitude as the pressure transfer terms ($\sim 10\%$ of total transfer term). This term is negative at the hot side and positive at the cold side. This can be seen as an energy transfer from hot to cold side. One explanation is based on the mean vertical velocity, which is directed to the cold side. In the thermal effect term (equation (E.19f)), one gets the advection of turbulent kinetic energy by the wall-normal velocity $\langle U_y \rangle \frac{\partial \frac{1}{2} \widehat{v}_i^* \widehat{v}_i}{\partial y}$. This term transfers TKE away from the wall at the hot side and towards the wall at the cold side.

Recall that the local Reynolds number is directly impacted by the thermal gradient. It is interesting that the terms at the hot side have larger magnitude than those at the cold side. The opposite behaviour would have been expected as the temperature gradient reduces the local Reynolds number at the hot side. Particular care should be taken in the interpretation of these amplitudes, as these differences do not necessarily apply to the total integrated values. On many terms, the hot side has a stronger magnitude than the cold side, but due to the lower wave number range of active areas the total energy handled is actually lower than at the cold side. We can observe this phenomenon for the triadic inter-plane transfer (figures E.12(a) and E.12(e)). The hot side negative area has a two times larger amplitude than the cold side. At the same time, the negative area with maximum values has a very small wave number range at the hot side and a large one at the cold side.

The in-plane pressure term (figures E.14(a) and E.14(e)) is heavily modified by the temperature gradient. The behaviour of the hot side is similar to the isothermal case with a positive area close to the wall and a negative area near the center of the channel. At the cold side, an additional positive area appears at large scales near $y^+ = 100$. This asymmetry between the two sides of the channel is not present in the inter-plane pressure term (figures E.15(a) and E.15(e)). The inter-plane pressure term is larger than its in-plane counterpart.

The total pressure term is modified as well (figures E.16(a) and E.16(e)). The positive area located near $y^+ = 60$ in the isothermal case (figure E.16(c)) has vanished at the hot side (figure E.16(e)), leaving just a negative one from $y^+ = 10$ to the center of the channel. Conversely, at the cold side of the channel (figure E.16(a)), the positive area is intensified in magnitude and increased in size.

Finally, the thermal gradient induces a Reynolds number variation between the flows at different sides of the channel. Compared to the cold side, the terms at the hot side are contracted, losing small scales. This is easily observable on the in-plane triadic term (figures E.11(a) and E.11(e)). For the TKE spectra, the small scales at the hot side have lower values while the large scales have the same energy level as that at the cold side. The shorter spectral range in the hot side is a direct consequence of a reduced local Reynolds number.

E.5.2 Reynolds number effects on anisothermal turbulent spectra

We now consider the effects of Reynolds number variations on the turbulent kinetic energy balance terms using the anisothermal results at both $Re_\tau = 180$ and $Re_\tau = 395$.

The impact of the Reynolds number at both sides of the channel as well as the interplay between the temperature gradient and the mean Reynolds number must be considered.

The significant influence of increased Reynolds number is evident when the left and right panels of Figs. E.7 – E.17 are compared. At high Reynolds number, the anisothermal spectra largely experience a combined effect from the temperature gradient and the Reynolds number. The amplitudes of TKE evolution terms are intensified at both sides of the channel by the temperature gradient. The amplitudes are often far larger in the anisothermal spectra than their isothermal counterpart.

In many cases, the wave space and spatial extents of the TKE evolution terms also seem to increase with the temperature gradient. Such analysis should be taken with care, as terms are not more distributed in wave number space but just appear larger due to the higher amplitude.

The triadic in-plane term (figures E.11(b) and E.11(f)) evolves slightly differently with Reynolds number in the isothermal and anisothermal case. The positive area at large scales disappears almost completely in the isothermal case, whereas it remains significant in the anisothermal case.

Even at the $Re_\tau = 395$ case, the near wall region of the hot and cold sides of the in-plane triadic transfer and of the total pressure term have a different behaviour. In the in-plane triadic term, the near wall negative area is greater at the cold side than at the hot side. In the total pressure term, the near wall positive area is greater at the hot side than at the cold side.

E.6 Conclusion

In this paper, we studied the effect of a strong temperature gradient on turbulent kinetic energy transfer processes in a fully developed channel flow. The analysis uses a variable change based on density square root weighted velocity, suited to the study of variable density flows. An equation of the turbulent kinetic energy spectral budget is obtained, then decomposed to highlight the mechanisms that govern the energy distribution: production, nonlinear transfer and viscous effects. The decomposition also allows simple comparison with the isothermal channel. Direct numerical simulations and large-eddy simulations have been carried out to compute the two dimensional transfer mechanism spectra of each term at both low and high Reynolds numbers. The isothermal simulations confirmed an important inverse energy cascade that transports the energy to the scales bigger than the channel height. The turbulent structures associated with these scales are located near to the wall where the viscous action removes the major part of the turbulent kinetic energy. This behaviour persists under a strong temperature gradient. More significantly, we showed that the existence of the wall and temperature gradient introduced significant new process in turbulent kinetic energy transfer independently of the mean turbulent Reynolds number. At high Reynolds number, the channel flow is split between two distinctive turbulent behaviours following the side of the channel. At the cold side, the temperature gradient increases the local turbulent Reynolds number and turbulence is intensified compared to the isothermal case. At the hot side, the high temperature reduces the local turbulent Reynolds number but the temperature gradient has an opposite effect, creating turbulence. This

leads to a counter-intuitive increase of turbulent kinetic energy processes at the hot side. Furthermore, a non-isothermal transfers accounting for 10% of the total energy transfer moves energy from the hot side to the cold side following the mean vertical velocity.

Acknowledgment

The authors gratefully acknowledge the CEA for the development of the TRUST platform. This work was granted access to the computer resources of CINES under the allocation 2014-c20142a5099 and 2015-c20152a5099 made by GENCI.

Appendix: Derivation of the spectral turbulent kinetic energy evolution equation

We apply a Fourier transform on equation (E.17). Taking into account the non-periodicity of y direction, the Fourier operator (E.26) is a 2D Fourier transform in the x and z directions. The Fourier transform of a function $g(x, y, z)$ is denoted $F_k^y\{g(x, y, z)\}$ or $\widehat{g}(\underline{k}, y)$ and defined as:

$$F_k^y\{g(x, y, z)\} = \widehat{g}(\underline{k}, y) = \frac{1}{L_x L_z} \int_0^{L_x} \int_0^{L_z} g(x, y, z) \exp(-i\underline{k} \cdot \underline{x}) dx dz \quad (\text{E.26})$$

where $\underline{k} = (k_x, k_z)$ is the 2D wave vector and $\underline{x} = (x, z)$ is the 2D position vector. Let us apply this operator on equation (E.17):

$$\frac{\partial \widehat{V}_i}{\partial t} = F_k^y \left\{ -\frac{\partial V_i U_j}{\partial x_j} + \frac{1}{2} V_i \frac{\partial U_j}{\partial x_j} - b \frac{\partial P}{\partial x_i} \right\} + F_k^y \left\{ b \frac{\partial}{\partial x_j} \left[\mu \left(\frac{\partial U_i}{\partial x_j} + \frac{\partial U_j}{\partial x_i} \right) \right] - b \frac{2}{3} \frac{\partial}{\partial x_i} \left(\mu \frac{\partial U_j}{\partial x_j} \right) \right\} \quad (\text{E.27})$$

Using a classical Reynolds decomposition, we split the velocity between mean part and fluctuation part ($V_i = \langle V_i \rangle + v'_i$). In addition, the flow homogeneity gives ($\langle U_z \rangle = 0$, $\frac{\partial \langle f \rangle}{\partial x} = \frac{\partial \langle f \rangle}{\partial z} = 0$). Noticing that:

$$\begin{aligned} \frac{\partial \widehat{V}_i}{\partial t} &= \frac{\partial \widehat{v}'_i}{\partial t} \\ F_k^y \left\{ \frac{\partial V_i U_j}{\partial x_j} \right\} &= \langle V_i \rangle \frac{\partial \widehat{u}'_j}{\partial x_j} + \widehat{v}'_i \frac{\partial \langle U_y \rangle}{\partial y} + \widehat{u}'_y \frac{\partial \langle V_i \rangle}{\partial y} + \langle U_j \rangle \frac{\partial \widehat{v}'_i}{\partial x_j} + F_k^y \left\{ \frac{\partial v'_i u'_j}{\partial x_j} \right\} \\ F_k^y \left\{ V_i \frac{\partial U_j}{\partial x_j} \right\} &= \langle V_i \rangle \frac{\partial \widehat{u}'_j}{\partial x_j} + \widehat{v}'_i \frac{\partial \langle U_y \rangle}{\partial y} + \widehat{v}'_i \frac{\partial \widehat{u}'_j}{\partial x_j} \end{aligned}$$

we obtain:

$$\begin{aligned} \frac{\partial \widehat{v}'_i}{\partial t} &= -\widehat{u}'_y \frac{\partial \langle V_i \rangle}{\partial y} - \langle U_j \rangle \frac{\partial \widehat{v}'_i}{\partial x_j} - \frac{1}{2} \left(\langle V_i \rangle \frac{\partial \widehat{u}'_j}{\partial x_j} + \widehat{v}'_i \frac{\partial \langle U_y \rangle}{\partial y} - \widehat{v}'_i \frac{\partial \widehat{u}'_j}{\partial x_j} \right) - F_k^y \left\{ \frac{\partial v'_i u'_j}{\partial x_j} \right\} - b \frac{\partial \widehat{P}}{\partial x_i} \\ &\quad + F_k^y \left\{ b \frac{\partial}{\partial x_j} \left[\mu \left(\frac{\partial U_i}{\partial x_j} + \frac{\partial U_j}{\partial x_i} \right) \right] - b \frac{2}{3} \frac{\partial}{\partial x_i} \left(\mu \frac{\partial U_j}{\partial x_j} \right) \right\} \quad (\text{E.28}) \end{aligned}$$

Following, we multiply equation (E.28) by \widehat{v}_i^* , where \widehat{g}^* is the complex conjugate of \widehat{g} , and sum the equation on i subscript.

$$\begin{aligned} \widehat{v}_i^* \frac{\partial \widehat{v}_i'}{\partial t} &= -\widehat{v}_i^* \widehat{u}_y' \frac{\partial \langle V_i \rangle}{\partial y} - \widehat{v}_i^* \langle U_j \rangle \frac{\partial \widehat{v}_i'}{\partial x_j} - \frac{\widehat{v}_i^*}{2} \left(\langle V_i \rangle \frac{\partial \widehat{u}_j'}{\partial x_j} + \widehat{v}_i' \frac{\partial \langle U_y \rangle}{\partial y} - \widehat{v}_i' \frac{\partial \widehat{u}_j'}{\partial x_j} \right) \\ -\widehat{v}_i^* F_k^y \left\{ \frac{\partial \widehat{v}_i' u_j'}{\partial x_j} \right\} &- \widehat{v}_i^* b \frac{\partial \widehat{P}}{\partial x_i} + \widehat{v}_i^* F_k^y \left\{ b \frac{\partial}{\partial x_j} \left[\mu \left(\frac{\partial U_i}{\partial x_j} + \widehat{v}_i^* \frac{\partial U_j}{\partial x_i} \right) \right] - b \frac{2}{3} \frac{\partial}{\partial x_i} \left(\mu \frac{\partial U_j}{\partial x_j} \right) \right\} \end{aligned} \quad (\text{E.29})$$

Noticing that:

$$\sum_i \Re \left[\widehat{v}_i^* \frac{\partial \widehat{v}_i'}{\partial t} \right] = \sum_i \frac{1}{2} \frac{\partial \widehat{v}_i^* \widehat{v}_i'}{\partial t} = \frac{\partial E_c}{\partial t} \quad (\text{E.30})$$

where $E_c = \frac{1}{2} \widehat{v}_i^* \widehat{v}_i'$ is the instantaneous turbulent kinetic energy (TKE) in the spectral space and \Re is the real part of a complex number, we obtain the spectral equation of the instantaneous turbulent kinetic energy evolution:

$$\begin{aligned} \frac{\partial E_c}{\partial t} &= \Re \left[-\widehat{v}_i^* \widehat{u}_y' \frac{\partial \langle V_i \rangle}{\partial y} - \widehat{v}_i^* F_k^y \left\{ \frac{\partial \widehat{v}_i' u_j'}{\partial x_j} \right\} - \widehat{v}_i^* b \frac{\partial \widehat{P}}{\partial x_i} \right. \\ &\quad - \frac{\widehat{v}_i^*}{2} \left(\langle V_i \rangle \frac{\partial \widehat{u}_j'}{\partial x_j} + \widehat{v}_i' \frac{\partial \langle U_y \rangle}{\partial y} - \widehat{v}_i' \frac{\partial \widehat{u}_j'}{\partial x_j} \right) - \widehat{v}_i^* \langle U_y \rangle \frac{\partial \widehat{v}_i'}{\partial y} \\ &\quad \left. + \widehat{v}_i^* F_k^y \left\{ b \frac{\partial}{\partial x_j} \left[\mu \left(\frac{\partial U_i}{\partial x_j} + \frac{\partial U_j}{\partial x_i} \right) \right] - b \frac{2}{3} \frac{\partial}{\partial x_i} \left(\mu \frac{\partial U_j}{\partial x_j} \right) \right\} \right] \end{aligned} \quad (\text{E.31})$$

Note that $\Re[\widehat{v}_i^* \langle U_x \rangle \frac{\partial \widehat{v}_i'}{\partial x}]$ is equal to zero, because $\widehat{v}_i^* \langle U_x \rangle \frac{\partial \widehat{v}_i'}{\partial x}$ is a pure imaginary number. It remains only $\Re[\widehat{v}_i^* \langle U_y \rangle \frac{\partial \widehat{v}_i'}{\partial y}]$.

The spectral equation (E.31) of the instantaneous TKE evolution depends on the four parameters k_x , k_z , y and t . In order to simplify the interpretation of the terms, we integrate the 2D Fourier space following the wave vector \underline{k} norms:

$$f(k, y) = \int_{k=\|\underline{k}\|} f(k_x, k_z, y) d\underline{k} \quad (\text{E.32})$$

Bibliography

- [10] F. Aulery, A. Toutant, F. Bataille, and Y. Zhou. Energy transfer process of anisothermal wall-bounded flows. *Physics Letters A*, 379(24):1520–1526, 2015.
- [28] I. A. Bolotnov, R. T. Lahey, D. A. Drew, K. E. Jansen, and A. A. Oberai. Spectral analysis of turbulence based on the DNS of a channel flow. *Computers & Fluids*, 39(4):640–655, 2010.
- [38] C. Calvin, O. Cueto, and P. Emonot. An object-oriented approach to the design of fluid mechanics software. *ESAIM: Mathematical Modelling and Numerical Analysis*, 36(05):907–921, 2002.
- [47] P. Chassaing. Une alternative à la formulation des équations du mouvement turbulent d'un fluide à masse volumique variable. *Journal de mécanique théorique et appliquée*, 4(3):375–389, 1985.

- [48] P. Chassaing. *Turbulence en mécanique des fluides*. Cépaduès-éditions, 2000.
- [50] P. Chassaing, R. A. Antonia, F. Anselmet, L. Joly, and S. Sarkar. *Variable density fluid turbulence*. Springer Science & Business Media, 2013.
- [57] A. Cimarelli and E. De Angelis. Anisotropic dynamics and sub-grid energy transfer in wall-turbulence. *Phys. Fluids*, 24(1):015102, 2012.
- [58] A. Cimarelli and E. De Angelis. The physics of energy transfer toward improved subgrid-scale models. *Phys. Fluids*, 26(5):055103, 2014.
- [59] A. Cimarelli, E. De Angelis, and C. M. Casciola. Paths of energy in turbulent channel flows. *J. Fluid Mech.*, 715:436–451, 2013.
- [68] A. W. Cook and Y. Zhou. Energy transfer in Rayleigh-Taylor instability. *Phys. Rev. E*, 66:026312, 2002.
- [69] R. Courant, K. Friedrichs, and H. Lewy. Über die partiellen Differenzgleichungen der mathematischen Physik. *Mathematische Annalen*, 100(1):32–74, 1928.
- [72] X. Daguene-Frick, J.-M. Foucaut, S. Coudert, A. Toutant, and G. Olalde. Experimental analysis of the turbulent flow behavior of a textured surface proposed for asymmetric heat exchangers. *Flow, Turbulence and Combustion*, 89(1):149–169, 2012.
- [81] J. A. Domaradzki and R. S. Rogallo. Local energy transfer and nonlocal interactions in homogeneous, isotropic turbulence. *Physics of Fluids A: Fluid Dynamics*, 2(3):413–426, 1990.
- [83] J. A. Domaradzki, W. Liu, C. Hartel, and L. Kleiser. Energy transfer in numerically simulated wall-bounded turbulent flows. *Phys. Fluids*, 6(4):1583–1599, 1994.
- [93] Thomas M Eidson. Numerical simulation of the turbulent Rayleigh–Bénard problem using subgrid modelling. *J. Fluid Mech.*, 158:245–268, 1985.
- [95] A. Favre. Statistical equations of turbulent gases. *Problems of Hydrodynamics and Continuum Mechanics*, pages 231–266, 1969.
- [103] Matteo Frigo and Steven G Johnson. FFTW: An adaptive software architecture for the FFT. In *Acoustics, Speech and Signal Processing, 1998. Proceedings of the 1998 IEEE International Conference on*, volume 3, pages 1381–1384. IEEE, 1998.
- [109] E. Garnier, N. Adams, and P. Sagaut. *Large eddy simulation for compressible flows*. Springer Science & Business Media, 2009.
- [127] P. G. Huang, G. N. Coleman, and P. Bradshaw. Compressible turbulent channel flows: DNS results and modelling. *J. Fluid Mech.*, 305:185–218, 1995.
- [144] S. Kida and S. A. Orszag. Energy and spectral dynamics in decaying compressible turbulence. *Journal of Scientific Computing*, 7(1):1–34, 1992. ISSN 0885-7474.
- [146] J. Kim, P. Moin, and R. Moser. Turbulence statistics in fully developed channel flow at low Reynolds number. *J. Fluid Mech.*, 177:133–166, 1987.
- [148] A. N. Kolmogorov. Локальная структура турбулентности в несжимаемой жидкости при очень больших числах Рейнольдса. *Dokl. Akad. Nauk SSSR*, 30(4):299–303, 1941. English translation: A. N. Kolmogorov, The local structure of turbulence in incompressible viscous fluid for very large Reynolds numbers, *Proc. R. Soc. London A* 434:9–13, 1991.
- [160] Anh-Tuan Le, Gary N. Coleman, and John Kim. Near-wall turbulence structures in three-dimensional boundary layers. *International Journal of Heat and Fluid Flow*, 21(5):480–488, 2000. ISSN 0142-727X.
- [170] B. P. Leonard. A stable and accurate convective modelling procedure based on quadratic upstream interpolation. *Computer Methods in Applied Mechanics and Engineering*, 19(1):59–98, 1979.
- [188] N Marati, CM Casciola, and R Piva. Energy cascade and spatial fluxes in wall turbulence. *J. Fluid Mech.*, 521:191–215, 2004.
- [203] R. D. Moser, J. Kim, and N. N. Mansour. Direct numerical simulation of turbulent channel flow up to $Re_\tau = 590$. *Phys. Fluids*, 11(4):943–945, 1999.

- [213] F. Nicoud and F. Ducros. Subgrid-scale stress modelling based on the square of the velocity gradient tensor. *Flow, Turbulence and Combustion*, 62(3):183–200, 1999. ISSN 1386-6184.
- [219] S. Paolucci. On the filtering of sound from the Navier–Stokes equations. Technical Report SAND82-8257, Sandia National Labs., Livermore, CA (USA), 1982.
- [232] Ugo Piomelli, Yunfang Yu, and Ronald J. Adrian. Subgrid-scale energy transfer and near-wall turbulence structure. *Phys. Fluids*, 8(1):215–224, 1996.
- [247] A. J. L. Rodriguez and G. Emanuel. Compressible rotational flows generated by the substitution principle. *Phys. Fluids*, 31:1058–1063, 1988.
- [266] S. Serra, A. Toutant, F. Bataille, and Y. Zhou. Turbulent kinetic energy spectrum in very anisothermal flows. *Physics Letters A*, 376(45):3177–3184, 2012.
- [287] W. Sutherland. The viscosity of gases and molecular force. *The London, Edinburgh, and Dublin Philosophical Magazine and Journal of Science*, 36(223):507–531, 1893.
- [290] A. Toutant and F. Bataille. Turbulence statistics in a fully developed channel flow submitted to a high temperature gradient. *International Journal of Thermal Sciences*, 74:104–118, 2013.
- [312] D. C. Wilcox. *Turbulence modeling for CFD*, volume 2. DCW industries La Canada, CA, 1998.
- [318] C.-S. Yih. Exact solutions for steady two-dimensional flow of a stratified fluid. *J. Fluid Mech.*, 9(02):161–174, 1960.
- [324] Y. Zhou. Degrees of locality of energy transfer in the inertial range. *Physics of Fluids A: Fluid Dynamics*, 5(5):1092–1094, 1993.
- [325] Y. Zhou. Interacting scales and energy transfer in isotropic turbulence. *Physics of Fluids A: Fluid Dynamics*, 5(10):2511–2524, 1993.
- [326] Y. Zhou. Renormalization group theory for fluid and plasma turbulence. *Physics Reports*, 488(1):1–49, 2010.
- [327] Y. Zhou and S. Oughton. Nonlocality and the critical Reynolds numbers of the minimum state magnetohydrodynamic turbulence. *Physics of Plasmas*, 18(7):072304, 2011.
- [328] Y. Zhou, W. H. Matthaeus, and P. Dmitruk. Colloquium: Magnetohydrodynamic turbulence and time scales in astrophysical and space plasmas. *Reviews of Modern Physics*, 76(4):1015, 2004.

Nomenclature

Acronyms

AMD	Anisotropic minimum dissipation
CSP	Concentrated solar power
DNS	Direct numerical simulation
FRAM	Filtering remedy and methodology
G1	One-parameter global-average dynamic
G2	Two-parameter global-average dynamic
GD	Global-average dynamic
HPC	High-performance computing
LES	Large-eddy simulation
MMG	Multiplicative mixed model based on the gradient model
P1	One-parameter plane-average dynamic
P2	Two-parameter plane-average dynamic
PD	Plane-average dynamic
QUICK	Quadratic upstream interpolation for convective kinematics
RANS	Reynolds-average Navier–Stokes
SAMD	Scalar AMD
SMMG	Scalar MMG
TG1	Tensorial one-parameter global-average dynamic
TG2	Tensorial two-parameter global-average dynamic
TGD	Tensorial global-average dynamic
TP1	Tensorial one-parameter plane-average dynamic
TP2	Tensorial two-parameter plane-average dynamic
TPD	Tensorial plane-average dynamic
TRUST	TrioCFD software for thermohydraulics
VSS	Volumetric strain-stretching
WALE	Wall-adapting local eddy viscosity

Roman symbols

a	Mesh dilatation parameter	(no dimension)
C	Dynamic constant	(no dimension)
$C^{\bullet\bullet}$	Spatial two-point correlation	m^2/s^2
C^{\bullet}	Filter-derivative non-commutation subgrid term	
C_p	Isobaric heat capacity	$\text{J kg}^{-1} \text{K}^{-1}$
C_v	Isochoric heat capacity	$\text{J kg}^{-1} \text{K}^{-1}$
c	Speed of sound	m/s
D	Mass flow rate, undissociated spectral term	$\text{kg/s}, \text{W/m}^3$
D	Gradient model for the density-velocity correlation subgrid term	
d	Scalar gradient	
d^a	Scaled scalar gradient	
\underline{E}	Mean kinetic energy per unit mass	J/kg
\underline{e}	Mixed kinetic energy per unit mass	J/kg
e	Turbulence kinetic energy per unit mass	J/kg
$F^{\bullet\bullet}$	Filter-multiplication non-commutation subgrid with the classical filter	
F_g	Coherent structure function	(no dimension)
$G^{\bullet\bullet}$	Filter-multiplication non-commutation subgrid with the Favre filter	
G	Gradient model for the momentum convection subgrid term	
g	Velocity gradient	s^{-1}
g^a	Scaled velocity gradient	m/s
$H^{(n)}$	Constant second-order tensor	(no dimension)
H	enthalpy per unit mass	J/kg
h	Half-height of the channel	m
I	Internal energy per unit mass	J/kg
k	Wavenumber vector	m^{-1}
k	Wave number	m^{-1}
L	Scale-similarity tensor	
L	Dimension of the domain	m
Ma	Mach number	(no dimension)
N	Number of grid points	(no dimension)
P	Pressure, mechanical pressure	Pa
P_0	Thermodynamical pressure	Pa
Pr	Prandtl number	(no dimension)
Pr_t	Subgrid-scale Prandtl number	(no dimension)
\mathcal{P}	Interaction between turbulence kinetic energy and mixed kinetic energy	W/m^3
$\underline{\mathcal{P}}$	Interaction between mean kinetic energy and mixed kinetic energy	W/m^3
Q	Conductive heat flux	W/m^2

Re	Real part	
Re	Reynolds number	(no dimension)
Re_λ	Taylor Reynolds number	(no dimension)
Re_τ	Friction Reynolds number	(no dimension)
Re_τ^*	Local friction Reynolds number	(no dimension)
\mathbf{R}	Volumetric strain-stretching	s^{-2}
r	Ideal gas specific constant	$J\ kg^{-1}\ K^{-1}$
S	Entropy per unit mass	$J/(kg\ K)$
\mathbf{S}	Rate of deformation tensor	s^{-1}
\mathbf{S}^d	Traceless symmetric part of the squared velocity gradient tensor	s^{-2}
T	Temperature	K
t	Time	s
\mathbf{U}	Velocity vector	m/s
U_τ	Friction velocity	m/s
U_τ^*	Local friction velocity	m/s
V	Volume of the domain	m^3
v	Specific volume	m^3/kg
\mathbf{x}	Position vector	m
x	Longitudinal Cartesian coordinate	m
y	Wall-normal Cartesian coordinate	m
Z	Interaction between the mean and fluctuating density part of total energy	W/m^3
Z^T	Interaction between the mean and fluctuating density part of internal energy	W/m^3
\underline{Z}	Interaction between the mean and fluctuating density part of mean kinetic energy	W/m^3
z	Transverse Cartesian coordinate	m

Greek symbols

α	Isobaric thermal expansion coefficient	K^{-1}
β	Isochoric thermal pressure coefficient	K^{-1}
χ_S	Isentropic compressibility	Pa^{-1}
χ_T	Isothermal compressibility	Pa^{-1}
Δ	Cell size	m
$\bar{\Delta}$	Filter length	m
$\overline{\Delta}$	Filter length	m
$\hat{\Delta}$	Test filter width	m
$\hat{\Delta}$	Test filter width	m
δ	Kronecker delta	(no dimension)
Δt	Timestep	s

\mathcal{E}	Interaction between kinetic energy and internal energy	W/m^3
$\underline{\mathcal{E}}$	Interaction between mean kinetic energy and internal energy	W/m^3
ε	Interaction between turbulence kinetic energy and internal energy	W/m^3
η	Second viscosity	$\text{Pa}\cdot\text{s}$
γ	Adiabatic index	(no dimension)
κ_e	Subgrid-scale diffusivity	m^2/s
λ	Thermal conductivity	$\text{W}/(\text{m}\cdot\text{K})$
μ	Dynamic viscosity	$\text{Pa}\cdot\text{s}$
ν	Kinematic viscosity	m^2/s
ν_e	Subgrid-scale viscosity	m^2/s
Ω	Rate of rotation tensor	s^{-1}
Φ	Conservative energy transfer	W/m^3
$\underline{\Phi}^T$	Conservative energy transfer associated with internal energy	W/m^3
$\underline{\Phi}$	Conservative energy transfer associated with mean kinetic energy	W/m^3
φ	Conservative energy transfer associated with turbulence kinetic energy	W/m^3
$\underline{\varphi}$	Conservative energy transfer associated with mixed kinetic energy	W/m^3
π	Subgrid term associated with the density-velocity correlation	
ρ	Density	kg/m^3
σ	Singular values of the velocity gradient tensor	s^{-2}
Σ	Viscous stress tensor	Pa
τ	Subgrid term associated with momentum convection	
Θ	Dilatation, divergence of velocity	s^{-1}
Υ	Total stress tensor	Pa
ξ	Uniform grid coordinate	m
ζ	Interaction between the mean and fluctuating density part of turbulence kinetic energy	W/m^3
$\underline{\zeta}$	Interaction between the mean and fluctuating density part of mixed kinetic energy	W/m^3

Superscripts

- ⁽ⁿ⁾ n -th order of squared Mach number asymptotic development
- ^c Related to convection
- ^p Related to pressure stress
- ^b Bulk flow variable
- ^λ Related to heat flux
- ^ν Related to viscous flux
- ^Υ Related to total stress
- [°] Constant scaling, bulk flow variable scaling

- ⁺ Classical wall scaling
- ^{*} Semi-local wall scaling
- [×] Average wall scaling
- ̄ Statistical average, classical filter
- ̃ Favre filter
- ̇ Spectral counterpart, classical filter counterpart
- ̂ Test filter, Favre filter counterpart

Subscripts

- ₀ At the cold wall, related to the mean density part of total energy
- ₁ At the hot wall, related to the fluctuating density part of total energy
- _I Incompressible
- _T Thermal
- _ω At the wall

Other symbols

- [•] Iverson bracket
- ⟨•⟩ Statistical average
- ∧ Logical conjunction
- ¬ Logical negation
- ∨ Logical disjunction
- D_t Material or total derivative with respect to time
- ∂_t Partial derivative with respect to time

List of figures

1	Solar power tower and high-temperature solar cavity receiver.	2
1.1	Reynolds decomposition of the velocity field.	15
1.2	Staggered grid system.	20
1.3	Biperiodic anisothermal channel flow.	23
1.4	Mesh convergence in the isothermal channel at $Re_\tau = 180$	27
1.5	Mesh convergence in the anisothermal channel at $Re_\tau = 180$	27
1.6	Mesh convergence in the isothermal channel at $Re_\tau = 395$	28
1.7	Mesh convergence in the anisothermal channel at $Re_\tau = 395$	28
2.1	Typical spectra of turbulence kinetic energy in homogeneous isotropic incompressible turbulence.	34
3.1	Schematic representation of the energy exchanges between the four parts of total kinetic energy (in the one-stage formulation).	44
3.2	Schematic representation of the energy exchanges between the four parts of total kinetic energy according to the formulation of Chassaing <i>et al.</i> [50].	45
3.3	Schematic representation of the energy exchanges between the eight parts of total kinetic energy (in the two-stage formulation).	48
4.1	Schematic representation of the energy exchanges between the four parts of total kinetic energy in the ternary representation.	60
4.2	Schematic representation of the energy exchanges associated with the “constant density turbulence kinetic energy” $\rho_0 e$	61
4.3	Biperiodic anisothermal channel flow	65
4.4	Validation of the profile of the viscous transfer and of the turbulent transfer.	70
4.5	Validation of the spatial turbulence kinetic energy terms.	71
4.6	Production profile computed directly in the spatial domain and computed from the spectral data.	71
4.7	Validation of the spectral profile at $y^+ = 10$ of the production.	72

4.8	Validation of the spectrum of the production.	73
4.9	Validation of the spectrum of the interplane triadic transfer.	73
4.10	Validation of the spectrum of the inplane triadic transfer.	74
4.11	Validation of the spectrum of the interplane dissipation.	74
4.12	Validation of the spectrum of the inplane dissipation.	74
4.13	Validation of the spectrum of the viscous transfer.	75
4.14	Profiles of the production.	81
4.15	Profiles of the conservative energy transfer.	82
4.16	Profiles of the interaction with internal energy.	83
4.17	Profiles of the viscous transfer.	84
4.18	Profiles of the convection.	85
4.19	Local friction Reynolds number.	86
4.20	Profiles of the thermal conservative energy transfer $\overline{\varphi}_T$	87
4.21	Profiles of the interaction with variable density kinetic energy $\overline{\zeta}$	88
4.22	Profiles of the thermal interaction with internal energy $\overline{\varepsilon}_T$	89
4.23	Profiles of the sum of all thermal terms $\overline{\varphi}_T + \overline{\zeta} + \overline{\varepsilon}_T$	90
4.24	Spectra of the production $\overline{\mathcal{P}}$	93
4.25	Spectra of the conservative energy transfer $\overline{\varphi}$	94
4.26	Spectra of the purely spectral transfer $\overline{\Xi}$	95
4.27	Spectra of the interaction with internal energy $\overline{\varepsilon}$	96
4.28	Spectra of the viscous transfer $\overline{\varphi}^\nu$	97
4.29	Spectra of the convection $\overline{\varphi}^c$	98
4.30	Spectra of the thermal conservative energy transfer $\overline{\varphi}_T$	100
4.31	Spectra of the interaction with variable density kinetic energy $\overline{\zeta}$	101
4.32	Spectra of the thermal interaction with internal energy $\overline{\varepsilon}_T$	102
4.33	Spectra of the sum of all thermal terms $\overline{\varphi}_T + \overline{\zeta} + \overline{\varepsilon}_T$	103
5.1	Profiles of the terms at $Re_\tau = 180$ and $Re_\tau = 395$	112
5.2	Profiles of the thermal terms at $Re_\tau = 180$ and $Re_\tau = 395$	114
5.3	Profiles of the terms at $Re_\tau = 180$ and $Re_\tau = 395$ as a function of wavenumber at the location of the spatial peak of production ($y^* \approx 12$).	115
5.4	Profiles of the terms at $Re_\tau = 180$ and $Re_\tau = 395$ as a function of wavenumber very near to the wall.	116
5.5	Profiles of the terms at $Re_\tau = 180$ and $Re_\tau = 395$ as a function of wavenumber at the center of the channel.	116
5.6	Spectra of the production $\overline{\mathcal{P}}$ at $Re_\tau = 180$ and $Re_\tau = 395$	117

5.7	Spectra of the conservative energy transfer $\bar{\varphi}$ at $Re_\tau = 180$ and $Re_\tau = 395$	118
5.8	Spectra of the purely spectral transfer $\bar{\Xi}$ at $Re_\tau = 180$ and $Re_\tau = 395$	118
5.9	Spectra of the interaction with internal energy $\bar{\varepsilon}$ at $Re_\tau = 180$ and $Re_\tau = 395$	118
5.10	Spectra of the viscous transfer $\bar{\varphi}^v$ at $Re_\tau = 180$ and $Re_\tau = 395$	119
5.11	Spectra of the convection $\bar{\varphi}^c$ at $Re_\tau = 180$ and $Re_\tau = 395$	119
5.12	Spectra of the thermal conservative energy transfer $\bar{\varphi}_T$ at $Re_\tau = 180$ and $Re_\tau = 395$	121
5.13	Spectra of the interaction with variable density kinetic energy $\bar{\zeta}$ at $Re_\tau = 180$ and $Re_\tau = 395$	121
5.14	Spectra of the thermal interaction with internal energy $\bar{\varepsilon}_T$ at $Re_\tau = 180$ and $Re_\tau = 395$	122
5.15	Normalised streamwise spectrum of the half-trace of the velocity fluctuation correlation tensor at $Re_\tau = 180$ and $Re_\tau = 395$ at the location of the spatial peak of production ($y^* \approx 12$).	122
7.1	Typical spectra of the turbulence kinetic energy of non-filtered and filtered solutions in homogeneous isotropic incompressible turbulence.	131
8.1	Biperiodic anisothermal channel flow.	148
8.2	Surface of the 400 K isotherm and velocity magnitude in a plane normal to the flow direction.	149
8.3	Validation of the spatial turbulence kinetic energy terms.	150
8.4	Root mean square of the terms of the mass conservation equation at $Re_\tau = 180$ with the filter A.	153
8.5	Root mean square of the terms of the streamwise momentum conservation equation at $Re_\tau = 180$ with the filter A.	154
8.6	Root mean square of the terms of the spanwise momentum conservation equation at $Re_\tau = 180$ with the filter A.	155
8.7	Root mean square of the terms of the wall-normal momentum conservation equation at $Re_\tau = 180$ with the filter A.	156
8.8	Root mean square of the terms of the resolved kinetic energy transport equation at $Re_\tau = 180$ with the filter A.	157
8.9	Root mean square of the terms of the energy conservation equation at $Re_\tau = 180$ with the filter A.	159
8.10	Root mean square of the terms of the ideal gas law at $Re_\tau = 180$ with the filter A.	160
8.11	Root mean square of the terms of the energy conservation equation at $Re_\tau = 180$ with the filter C.	162

9.1	Biperiodic anisothermal channel flow.	175
9.2	Correlation coefficient between the exact momentum convection subgrid term and the Smagorinsky model for the term that appears in the streamwise momentum conservation equation.	180
9.3	Correlation coefficient between the divergence of the streamwise-related part of the exact momentum convection subgrid term and the Smagorinsky model in the isothermal and anisothermal configurations.	180
9.4	Correlation coefficient, regression coefficient, and concordance correlation coefficient between the divergence of the streamwise-related part of the exact momentum convection subgrid term and eddy-viscosity models.	182
9.5	Correlation coefficient, regression coefficient, and concordance correlation coefficient between the divergence of the spanwise-related part of the exact momentum convection subgrid term and eddy-viscosity models.	183
9.6	Correlation coefficient, regression coefficient, and concordance correlation coefficient between the divergence of the wall-normal-related part of the exact momentum convection subgrid term and eddy-viscosity models.	184
9.7	Correlation coefficient, regression coefficient, and concordance correlation coefficient between the subgrid kinetic energy dissipation of the exact momentum convection subgrid term and eddy-viscosity models. .	185
9.8	Profile of the statistical average of the subgrid kinetic energy dissipation of the exact momentum convection subgrid term and eddy-viscosity models.	186
9.9	Probability density function of the subgrid kinetic energy dissipation of the exact momentum convection subgrid term and eddy-viscosity models.	187
9.10	Correlation coefficient, regression coefficient, and concordance correlation coefficient between the divergence of the exact density-velocity correlation subgrid term and eddy-diffusivity models.	188
9.11	Correlation coefficient, regression coefficient, and concordance correlation coefficient between the subgrid squared scalar dissipation of the exact density-velocity correlation subgrid term and eddy-diffusivity models.	189
9.12	Profile of the statistical average of the subgrid squared scalar dissipation of the exact density-velocity correlation subgrid term and eddy-diffusivity models.	190
9.13	Profile of the ratio of the statistical average of the subgrid kinetic energy dissipation and the subgrid squared scalar dissipation.	191
9.14	Probability density function of the subgrid squared scalar dissipation of the exact density-velocity correlation subgrid term and eddy-diffusivity models.	191
9.15	Correlation coefficient, regression coefficient, and concordance correlation coefficient between the divergence of the streamwise-related part of the exact momentum convection subgrid term and tensorial AMD models.	196

9.16	Correlation coefficient, regression coefficient, and concordance correlation coefficient between the divergence of the spanwise-related part of the exact momentum convection subgrid term and tensorial AMD models.	197
9.17	Correlation coefficient, regression coefficient, and concordance correlation coefficient between the divergence of the wall-normal-related part of the exact momentum convection subgrid term and tensorial AMD models.	198
9.18	Correlation coefficient, regression coefficient, and concordance correlation coefficient between the subgrid kinetic energy dissipation of the exact momentum convection subgrid term and tensorial AMD models. .	199
10.1	Comparison of simulations with no subgrid-scale model with constant mass flow rate and constant streamwise volume force in the anisothermal channel at $Re_\tau = 180$	213
10.2	Comparison of simulations with no subgrid-scale model with the meshes 24C, 36C and 48B in the isothermal channel at $Re_\tau = 180$	214
10.3	Comparison of simulations with no subgrid-scale model with the meshes 24C, 36C and 48B in the anisothermal channel at $Re_\tau = 180$	215
10.4	Comparison of simulations with no subgrid-scale model with the mesh 96B in the anisothermal channel at $Re_\tau = 395$	216
10.5	Comparison of simulations with no subgrid-scale model for the profiles of the terms of the energy balance.	217
10.6	Comparison of large-eddy simulations with the Smagorinsky, WALE, Sigma, AMD, Kobayashi and Anisotropic Smagorinsky models in the isothermal channel at $Re_\tau = 180$	219
10.7	Comparison of large-eddy simulations with the Smagorinsky, WALE, Sigma, AMD, Kobayashi and Anisotropic Smagorinsky models with the meshes 24C and 36C in the isothermal channel at $Re_\tau = 180$	220
10.8	Comparison of large-eddy simulations with the plane-average, tensorial plane-average and tensorial global-average dynamic Smagorinsky model and the plane-average dynamic Anisotropic Smagorinsky model in the isothermal channel at $Re_\tau = 180$	221
10.9	Comparison of simulations with the constant-parameters and global-average dynamic Smagorinsky, WALE, Sigma, AMD, Kobayashi and Anisotropic Smagorinsky models for the profiles of the subgrid-scale viscosity in the isothermal channel at $Re_\tau = 180$	222
10.10	Comparison of large-eddy simulations with the global-average dynamic Smagorinsky, WALE, Sigma, AMD, Kobayashi and Anisotropic Smagorinsky models in the isothermal channel at $Re_\tau = 180$	224
10.11	Comparison of large-eddy simulations with the tensorial global-average dynamic Smagorinsky, WALE, Sigma, AMD, Kobayashi and Anisotropic Smagorinsky models in the isothermal channel at $Re_\tau = 180$	225

10.12	Comparison of large-eddy simulations with the gradient model using $C^{\text{Grad.}} = 1$ and $C^{\text{Grad.}} = 2$ and the filtered gradient model using $C^{\text{Grad.}} = 2$ and $C^{\text{Grad.}} = 9$ and with the scale-similarity model using filter T and filter A in the isothermal channel at $Re_\tau = 180$	226
10.13	Comparison of large-eddy simulations with the plane-average, global-average, tensorial plane-average and tensorial global-average dynamic gradient models in the isothermal channel at $Re_\tau = 180$	227
10.14	Comparison of large-eddy simulations with the scale-similarity model using filter T with the meshes 24C, 36C and 48B in the isothermal channel at $Re_\tau = 180$	228
10.15	Comparison of large-eddy simulations with tensorial AMD models in the isothermal channel at $Re_\tau = 180$	229
10.16	Comparison of large-eddy simulations with the gradient-AMD mixed model and tensorial gradient-AMD mixed models in the isothermal channel at $Re_\tau = 180$	230
10.17	Comparison of large-eddy simulations with tensorial gradient-Smagorinsky, gradient-WALE, gradient-Sigma, gradient-AMD and gradient-Anisotropic-Smagorinsky mixed models in the isothermal channel at $Re_\tau = 180$. . .	231
10.18	Comparison of large-eddy simulations with the tensorial gradient-AMD mixed model based on the $H^{(4)}$ tensor with the meshes 24C, 36C and 48B in the isothermal channel at $Re_\tau = 180$	232
10.19	Comparison of large-eddy simulations with dynamic gradient-AMD mixed models in the isothermal channel at $Re_\tau = 180$	234
10.20	Comparison of large-eddy simulations with the WALE model for the momentum convection subgrid term in the Velocity and Favre formulations in the anisothermal channel at $Re_\tau = 180$	237
10.21	Comparison of large-eddy simulations with the Smagorinsky, WALE, Sigma, AMD, Kobayashi and Anisotropic Smagorinsky models for the momentum convection subgrid term in the Velocity formulation in the anisothermal channel at $Re_\tau = 180$	238
10.22	Comparison of large-eddy simulations with the gradient model using $C^{\text{Grad.}} = 1$ and $C^{\text{Grad.}} = 2$, the filtered gradient model using $C^{\text{Grad.}} = 2$ and $C^{\text{Grad.}} = 9$ and the scale-similarity model using filter T and filter A for the momentum convection subgrid term in the Velocity formulation in the anisothermal channel at $Re_\tau = 180$	239
10.23	Comparison of large-eddy simulations with the WALE, Sigma and AMD models for the momentum convection subgrid term in the Velocity formulation with the meshes 24C and 36C in the anisothermal channel at $Re_\tau = 180$	240
10.24	Comparison of large-eddy simulations with the WALE, Sigma, AMD and gradient models for the momentum convection subgrid term in the Velocity formulation in the anisothermal channel at $Re_\tau = 395$	241

10.25	Comparison of large-eddy simulations with the WALE model for the density-velocity correlation subgrid term in the Velocity and Favre formulations in the anisothermal channel at $Re_\tau = 180$	242
10.26	Comparison of large-eddy simulations with the AMD model using $C^{\text{AMD}} = 0.1$, $C^{\text{AMD}} = 0.2$ and $C^{\text{AMD}} = 0.3$ for the density-velocity correlation subgrid term in the Velocity formulation in the anisothermal channel at $Re_\tau = 180$	243
10.27	Comparison of large-eddy simulations with the vectorial global-average dynamic Smagorinsky, WALE, Sigma, AMD, Kobayashi and Anisotropic Smagorinsky models for the density-velocity correlation subgrid term in the Velocity formulation in the anisothermal channel at $Re_\tau = 180$. . .	244
10.28	Comparison of large-eddy simulations with the gradient model using $C^{\text{Grad.}} = 1$ and $C^{\text{Grad.}} = 2$ and the filtered gradient model using $C^{\text{Grad.}} = 2$ and $C^{\text{Grad.}} = 9$ for the density-velocity correlation subgrid term in the Velocity formulation in the anisothermal channel at $Re_\tau = 180$	245
10.29	Comparison of large-eddy simulations with the scale-similarity model using filter T and filter A for the density-velocity correlation subgrid term in the Velocity formulation in the anisothermal channel at $Re_\tau = 180$.	246
10.30	Comparison of large-eddy simulations with the WALE model for the momentum convection subgrid term and the density-velocity correlation subgrid term with the meshes 24C, 36C and 48B in the Velocity formulation in the anisothermal channel at $Re_\tau = 180$	249
10.31	Comparison of large-eddy simulations with the tensorial/vectorial global-average dynamic AMD model for either the momentum convection subgrid term alone or both the momentum convection subgrid term and the density-velocity correlation subgrid term in the Velocity and Favre formulations in the anisothermal channel at $Re_\tau = 180$	250
10.32	Comparison of large-eddy simulations with the tensorial AMD model based on the $H^{(4)}$ tensor for the momentum convection subgrid term and the scalar AMD model or the scale-similarity model using filter A for the density-velocity correlation subgrid term in the Velocity and Favre formulations in the anisothermal channel at $Re_\tau = 180$	251
10.33	Comparison of large-eddy simulations with the tensorial AMD model based on the $H^{(4)}$ tensor for the momentum convection subgrid term and the scalar AMD model or the scale-similarity model using filter A for the density-velocity correlation subgrid term in the Velocity and Favre formulations in the anisothermal channel at $Re_\tau = 180$	252
10.34	Comparison of large-eddy simulations with the tensorial AMD model based on the $H^{(4)}$ tensor for the momentum convection subgrid term and the scalar AMD model or the scale-similarity model using filter A for the density-velocity correlation subgrid term in the Velocity and Favre formulations in the anisothermal channel at $Re_\tau = 180$	253

10.35	Comparison of large-eddy simulations with the tensorial AMD model based on the $H^{(4)}$ tensor for the momentum convection subgrid term and the scalar AMD model or the scale-similarity model using filter A for the density-velocity correlation subgrid term in the Velocity and Favre formulations in the anisothermal channel at $Re_\tau = 395$	254
C.1	Correlation coefficient, regression coefficient, and concordance correlation coefficient between the divergence of the streamwise-related part of the exact momentum convection subgrid term and tensorial Sigma models.	294
C.2	Correlation coefficient, regression coefficient, and concordance correlation coefficient between the divergence of the spanwise-related part of the exact momentum convection subgrid term and tensorial Sigma models.	295
C.3	Correlation coefficient, regression coefficient, and concordance correlation coefficient between the divergence of the wall-normal-related part of the exact momentum convection subgrid term and tensorial Sigma models.	296
C.4	Correlation coefficient, regression coefficient, and concordance correlation coefficient between the subgrid kinetic energy dissipation of the exact momentum convection subgrid term and tensorial Sigma models.	297
C.5	Correlation coefficient, regression coefficient, and concordance correlation coefficient between the divergence of the streamwise-related part of the exact momentum convection subgrid term and tensorial Anisotropic Smagorinsky models.	298
C.6	Correlation coefficient, regression coefficient, and concordance correlation coefficient between the divergence of the spanwise-related part of the exact momentum convection subgrid term and tensorial Anisotropic Smagorinsky models.	299
C.7	Correlation coefficient, regression coefficient, and concordance correlation coefficient between the divergence of the wall-normal-related part of the exact momentum convection subgrid term and tensorial Anisotropic Smagorinsky models.	300
C.8	Correlation coefficient, regression coefficient, and concordance correlation coefficient between the subgrid kinetic energy dissipation of the exact momentum convection subgrid term and tensorial Anisotropic Smagorinsky models.	301
E.1	Biperiodic anisothermal channel flow	338
E.2	Mean longitudinal velocity comparison with direct numerical simulation of Kim <i>et al.</i> [146] at $Re_\tau = 180$	341
E.3	Velocity fluctuations comparison with direct numerical simulation of Kim <i>et al.</i> [146] at $Re_\tau = 180$	341
E.4	Comparison of turbulent production spectra.	342
E.5	Comparison of in-plane triadic transfer spectra.	343

E.6	Comparison of inter-plane triadic transfer spectra.	343
E.7	Turbulent kinetic energy, divided by $U_\tau \nu$	346
E.8	Turbulent production term.	347
E.9	Total transfer (total triadic term and total pressure term).	348
E.10	Viscous effect term.	349
E.11	Triadic in-plane term.	350
E.12	Triadic inter-plane term.	351
E.13	Total triadic term.	352
E.14	Pressure in-plane term.	353
E.15	Pressure inter-plane term.	354
E.16	Total pressure term.	355
E.17	Thermal effects term.	356

List of tables

1.1	Mean flow variables of the direct numerical simulations.	24
1.2	Computational domain and grid spacing of the simulations.	26
4.1	Construction of the wavenumber bins.	69
4.2	Maximum value of the terms in the spatial and spectral domain.	78
5.1	Wavenumber, wall-normal coordinate and amplitude of the local spectral extrema of each term.	120
8.1	Classification of the subgrid terms in the three formulations.	160
9.1	Asymptotic near-wall behaviour of the models.	178
10.1	Computational domain and grid spacing.	211
10.2	Dynamic parameter of large-eddy simulations with global-average dynamic models in the isothermal channel at $Re_\tau = 180$	222
10.3	Dynamic parameters of large-eddy simulations with the tensorial global-average dynamic models in the isothermal channel at $Re_\tau = 180$	223
10.4	Stability of the large-eddy simulations with a dynamic method.	233
10.5	Dynamic parameters of large-eddy simulations with global-average dynamic gradient-AMD mixed models in the isothermal channel at $Re_\tau = 180$	233
10.6	Dynamic parameters of large-eddy simulations with tensorial global-average dynamic gradient-AMD mixed models in the isothermal channel at $Re_\tau = 180$	235
10.7	Dynamic parameters of large-eddy simulations with vectorial global-average dynamic models in the anisothermal channel at $Re_\tau = 180$	247
D.1	Friction Reynolds number of the isothermal simulations at $Re_\tau = 180$	305
D.2	Friction Reynolds number of the anisothermal simulations at $Re_\tau = 180$	310
D.3	Friction Reynolds number of anisothermal simulations at $Re_\tau = 395$	312
D.4	Wall heat flux of the anisothermal simulations at $Re_\tau = 180$	318

D.5	Wall heat flux of anisothermal simulations at $Re_\tau = 395$	319
D.6	Thermodynamical pressure of the anisothermal simulations at $Re_\tau = 180$.	325
D.7	Thermodynamical pressure of anisothermal simulations at $Re_\tau = 395$. . .	327
D.8	Dynamic parameter of large-eddy simulations with global-average dynamic models in the anisothermal channel at $Re_\tau = 180$	327
D.9	Dynamic parameters of large-eddy simulations with tensorial global-average dynamic models in the anisothermal channel at $Re_\tau = 180$. . .	328
D.10	Dynamic parameters of large-eddy simulations with global-average dynamic gradient-AMD mixed models in the anisothermal channel at $Re_\tau = 180$	328
D.11	Dynamic parameters of large-eddy simulations with tensorial global-average dynamic gradient-AMD mixed models in the anisothermal channel at $Re_\tau = 180$	329
E.1	List of simulations and mesh parameters.	339

Bibliography

- [1] A. Abba, A. C. Cercignani, and L. Valdetaro. Analysis of subgrid scale models. *Comput. Math. Appl.*, 46(4):521–535, 2003.
- [2] H. Abe, H. Kawamura, and Y. Matsuo. Direct numerical simulation of a fully developed turbulent channel flow with respect to the Reynolds number dependence. *Journal of Fluids Engineering*, 123(2):382–393, 2001.
- [3] M. Abkar, H. J. Bae, and P. Moin. Minimum-dissipation scalar transport model for large-eddy simulation of turbulent flows. *Physical Review Fluids*, 1(4):041701, 2016.
- [4] N. Al-Zurfi and A. Turan. LES of rotational effects on film cooling effectiveness and heat transfer coefficient in a gas turbine blade with one row of air film injection. *International Journal of Thermal Sciences*, 99:96–112, 2016.
- [5] T. Alazard. Low mach number limit of the full Navier–Stokes equations. *Archive for rational mechanics and analysis*, 180(1):1–73, 2006.
- [6] T. Alazard. A minicourse on the low mach number limit. *Discrete and Continuous Dynamical Systems-Series S*, 1(3):365–404, 2008.
- [7] B. W. Anderson and J. A. Domaradzki. A subgrid-scale model for large-eddy simulation based on the physics of interscale energy transfer in turbulence. *Physics of Fluids*, 24(6):065104, 2012.
- [8] R. Anderson and C. Meneveau. Effects of the similarity model in finite-difference les of isotropic turbulence using a lagrangian dynamic mixed model. *Flow, turbulence and combustion*, 62(3):201–225, 1999.
- [9] R. A. Antonia, M. Teitel, J. Kim, and L. W. B. Browne. Low-reynolds-number effects in a fully developed turbulent channel flow. *Journal of Fluid mechanics*, 236:579–605, 1992.
- [10] F. Aulery, A. Toutant, F. Bataille, and Y. Zhou. Energy transfer process of anisothermal wall-bounded flows. *Physics Letters A*, 379(24):1520–1526, 2015.
- [11] F. Aulery, D. Dupuy, A. Toutant, F. Bataille, and Y. Zhou. Spectral analysis of turbulence in anisothermal channel flows. *Computers & Fluids*, 151:115–131, 2017.
- [12] Frédéric Auléry. *Analyse du couplage entre turbulence et gradient de température dans les écoulements pariétaux par simulations numériques fines*. PhD thesis, Université de Perpignan Via Domitia, 2013.
- [13] B. Aupoix. Introduction to turbulence modelling for compressible flows. *VKI lecture series*, 4:H1–H64, 2000.
- [14] J. Bardina, J. Ferziger, and W. C. Reynolds. Improved subgrid-scale models for large-eddy simulation. In *13th Fluid and PlasmaDynamics Conference*, page 1357, 1980.
- [15] F. Bataille, R. Rubinstein, and M. Y. Hussaini. Eddy viscosity and diffusivity modeling. *Physics Letters A*, 346(1):168–173, 2005.
- [16] G. K. Batchelor. *The theory of homogeneous turbulence*. Cambridge university press, 1953.
- [17] P. T. Bauer, G. W. Zumwalt, and L. J. Fila. A numerical method and an extension of the korst jet mixing theory for multispecie turbulent jet mixing. AIAA paper 68 (112). In *6th Aerospace Sciences Meeting, New York*, 1968.

- [18] H. Baya Toda, O. Cabrit, G. Balarac, S. Bose, J. Lee, H. Choi, and F. Nicoud. A subgrid-scale model based on singular values for les in complex geometries. In *Proc. of the Summer Program*, pages 193–202, 2010.
- [19] H. Baya Toda, K. Truffin, and F. Nicoud. Is the dynamic procedure appropriate for all sgs models. In *V European Conference on Computational Fluid Dynamics, ECCOMAS, Lisbon, Portugal*, pages 14–17, 2010.
- [20] A. Beccantini, E. Studer, S. Gounand, J.-P. Magnaud, T. Kloczko, C. Corre, and S. Kudriakov. Numerical simulations of a transient injection flow at low mach number regime. *International journal for numerical methods in engineering*, 76(5):662–696, 2008.
- [21] M. Bellec, A. Toutant, and G. Olalde. Large eddy simulations of thermal boundary layer developments in a turbulent channel flow under asymmetrical heating. *Computers & Fluids*, 151:159–176, 2017.
- [22] S. Benteboula and G. Lauriat. Numerical simulations of anisothermal laminar vortex rings with large density variations. *International Journal of Heat and Fluid Flow*, 30(2):186–197, 2009.
- [23] L. C. Berselli, G. P. Galdi, T. Iliescu, and W. J. Layton. Mathematical analysis for the rational large eddy simulation model. *Mathematical Models and Methods in Applied Sciences*, 12(08):1131–1152, 2002.
- [24] L. C. Berselli, T. Iliescu, and W. J. Layton. *Mathematics of large eddy simulation of turbulent flows*. Springer Science & Business Media, 2005.
- [25] S. S. Bhattacharyya, E. F. Deprettere, R. Leupers, and J. Takala. *Handbook of signal processing systems*. Springer Science & Business Media, 2013.
- [26] D. J. Bodony and S. J. Lele. On using large-eddy simulation for the prediction of noise from cold and heated turbulent jets. *Phys. Fluids*, 17(8):085103, 2005.
- [27] B. J. Boersma and S. K. Lele. Large eddy simulation of compressible turbulent jets. *Center for Turbulence Research, Annual Research Briefs*, pages 365–377, 1999.
- [28] I. A. Bolotnov, R. T. Lahey, D. A. Drew, K. E. Jansen, and A. A. Oberai. Spectral analysis of turbulence based on the DNS of a channel flow. *Computers & Fluids*, 39(4): 640–655, 2010.
- [29] G. Borghesi and J. Bellan. A priori and a posteriori investigations for developing large eddy simulations of multi-species turbulent mixing under high-pressure conditions. *Physics of Fluids*, 27(3):035117, 2015.
- [30] V. Borue and S. A. Orszag. Local energy flux and subgrid-scale statistics in three-dimensional turbulence. *Journal of Fluid Mechanics*, 366:1–31, 1998.
- [31] S. T. Bose, P. Moin, and D. You. Grid-independent large-eddy simulation using explicit filtering. *Physics of Fluids*, 22(10):105103, 2010.
- [32] J. Boussinesq. *Essai sur la théorie des eaux courantes*. Impr. nationale, 1877.
- [33] V. Boutrouche, E. Franquet, S. Serra, and R. Manceau. Influence of the turbulence model for channel flows with strong transverse temperature gradients. *International Journal of Heat and Fluid Flow*, 70:79–103, 2018.
- [34] P. Bradshaw. ‘inactive’ motion and pressure fluctuations in turbulent boundary layers. *Journal of Fluid Mechanics*, 30(2):241–258, 1967.
- [35] P. Bradshaw. Compressible turbulent shear layers. *Annual Review of Fluid Mechanics*, 9(1):33–52, 1977.
- [36] G. Brilliant, S. Husson, F. Bataille, and F. Ducros. Study of the blowing impact on a hot turbulent boundary layer using thermal large eddy simulation. *Intl. J. Heat Fluid Flow*, 29(6):1670–1678, 2008.
- [37] C. Brun, M. Petrovan Boiarciuc, M. Haberkorn, and P. Comte. Large eddy simulation of compressible channel flow. *Theoretical and Computational Fluid Dynamics*, 22(3): 189–212, 2008.

- [38] C. Calvin, O. Cueto, and P. Emonot. An object-oriented approach to the design of fluid mechanics software. *ESAIM: Mathematical Modelling and Numerical Analysis*, 36(05): 907–921, 2002.
- [39] M. Campolo, M. Andreoli, and A. Soldati. Computing flow, combustion, heat transfer and thrust in a micro-rocket via hierarchical problem decomposition. *Microfluidics and nanofluidics*, 7(1):57–73, 2009.
- [40] D. Carati and A. Wray. Time filtering in large eddy simulations. In *Proceedings of the summer Program*, volume 2000, pages 263–270, 2000.
- [41] D. Carati and A. Wray. Time filtering and mixed models for les. In *APS Division of Fluid Dynamics Meeting Abstracts*, 2000.
- [42] D. Carati, G. S. Winckelmans, and H. Jeanmart. On the modelling of the subgrid-scale and filtered-scale stress tensors in large-eddy simulation. *Journal of Fluid Mechanics*, 441:119–138, 2001.
- [43] M. A. Carper and F. Porté-Agel. Subfilter-scale fluxes over a surface roughness transition. part ii: A priori study of large-eddy simulation models. *Boundary-Layer Meteorology*, 127(1):73–95, 2008.
- [44] M. Chandesris, A. d’Hueppe, B. Mathieu, D. Jamet, and B. Goyeau. Direct numerical simulation of turbulent heat transfer in a fluid-porous domain. *Phys. Fluids*, 25(12): 125110, 2013.
- [45] D. R. Chapman and G. D. Kuhn. The limiting behaviour of turbulence near a wall. *Journal of Fluid Mechanics*, 170:265–292, 1986.
- [46] M. Chapman. Fram—nonlinear damping algorithms for the continuity equation. *Journal of Computational Physics*, 44(1):84–103, 1981.
- [47] P. Chassaing. Une alternative à la formulation des équations du mouvement turbulent d’un fluide à masse volumique variable. *Journal de mécanique théorique et appliquée*, 4 (3):375–389, 1985.
- [48] P. Chassaing. *Turbulence en mécanique des fluides*. Cépaduès-éditions, 2000.
- [49] P. Chassaing. The modeling of variable density turbulent flows. a review of first-order closure schemes. *Flow, Turbulence and Combustion*, 66(4):293–332, 2001.
- [50] P. Chassaing, R. A. Antonia, F. Anselmet, L. Joly, and S. Sarkar. *Variable density fluid turbulence*. Springer Science & Business Media, 2013.
- [51] S. Chen, Z. Xia, S. Pei, J. Wang, Y. Yang, Z. Xiao, and Y. Shi. Reynolds-stress-constrained large-eddy simulation of wall-bounded turbulent flows. *Journal of Fluid Mechanics*, 703:1–28, 2012.
- [52] S. C. P. Cheung and G. H. Yeoh. A fully-coupled simulation of vortical structures in a large-scale buoyant pool fire. *International Journal of Thermal Sciences*, 48(12): 2187–2202, 2009.
- [53] M. S. Chong, J. P. Monty, C. Chin, and I. Marusic. The topology of skin friction and surface vorticity fields in wall-bounded flows. *Journal of Turbulence*, (13):N6, 2012.
- [54] A. J. Chorin. Numerical solution of the Navier–Stokes equations. *Mathematics of computation*, 22(104):745–762, 1968.
- [55] F. K. Chow and P. Moin. A further study of numerical errors in large-eddy simulations. *Journal of Computational Physics*, 184(2):366–380, 2003.
- [56] S. G. Chumakov and C. J. Rutland. Dynamic structure subgrid-scale models for large eddy simulation. *International Journal for Numerical Methods in Fluids*, 47(8-9):911–923, 2005.
- [57] A. Cimarelli and E. De Angelis. Anisotropic dynamics and sub-grid energy transfer in wall-turbulence. *Phys. Fluids*, 24(1):015102, 2012.
- [58] A. Cimarelli and E. De Angelis. The physics of energy transfer toward improved subgrid-scale models. *Phys. Fluids*, 26(5):055103, 2014.

- [59] A. Cimarelli, E. De Angelis, and C. M. Casciola. Paths of energy in turbulent channel flows. *J. Fluid Mech.*, 715:436–451, 2013.
- [60] A. Cimarelli, G. Cocconi, B. Frohnapfel, and E. De Angelis. Spectral enstrophy budget in a shear-less flow with turbulent/non-turbulent interface. *Phys. Fluids*, 27(12):125106, 2015.
- [61] A. Cimarelli, E. De Angelis, P. Schlatter, G. Brethouwer, A. Talamelli, and C. M. Casciola. Sources and fluxes of scale energy in the overlap layer of wall turbulence. *J. Fluid Mech.*, 771:407–423, 2015.
- [62] A. Cimarelli, E. De Angelis, J. Jiménez, and C. M. Casciola. Cascades and wall-normal fluxes in turbulent channel flows. *J. Fluid Mech.*, 796:417–436, 2016. ISSN 1469-7645.
- [63] J. A. Clark. A study of incompressible turbulent boundary layers in channel flow. *Journal of Basic Engineering*, 90(4):455–467, 1968.
- [64] R. A. Clark, J. H. Ferziger, and W. C. Reynolds. Evaluation of subgrid-scale models using an accurately simulated turbulent flow. *J. Fluid Mech.*, 91(1):1–16, 1979.
- [65] R. Clausius. Über die bewegende Kraft der Wärme und die Gesetze, welche sich daraus für die Wärmelehre selbst ableiten lassen. *Annalen der Physik*, 155(3):368–397, 1850.
- [66] R. Clausius. Über eine veränderte Form des zweiten Hauptsatzes der mechanischen Wärmetheorie. *Annalen der Physik*, 169(12):481–506, 1854.
- [67] G. N. Coleman, J. Kim, and R. D. Moser. A numerical study of turbulent supersonic isothermal-wall channel flow. *J. Fluid Mech.*, 305:159–183, 1995.
- [68] A. W. Cook and Y. Zhou. Energy transfer in Rayleigh-Taylor instability. *Phys. Rev. E*, 66:026312, 2002.
- [69] R. Courant, K. Friedrichs, and H. Lewy. Über die partiellen Differenzgleichungen der mathematischen Physik. *Mathematische Annalen*, 100(1):32–74, 1928.
- [70] J. Cousteix and B. Aupoix. Turbulence models for compressible flows. In *Special Course Three-Dimensional Supersonic and Hypersonic Flows Including Separation*. AGARD/FDP-VKI Special course, 1989.
- [71] C. B. da Silva and O. Métais. On the influence of coherent structures upon interscale interactions in turbulent plane jets. *Journal of Fluid Mechanics*, 473:103–145, 2002.
- [72] X. Dagenet-Frick, J.-M. Foucaut, S. Coudert, A. Toutant, and G. Olalde. Experimental analysis of the turbulent flow behavior of a textured surface proposed for asymmetric heat exchangers. *Flow, Turbulence and Combustion*, 89(1):149–169, 2012.
- [73] X. Dagenet-Frick, A. Toutant, F. Bataille, and G. Olalde. Numerical investigation of a ceramic high-temperature pressurized-air solar receiver. *Solar Energy*, 90(0):164–178, 2013. ISSN 0038-092X.
- [74] Y. M. Dakhoul and K. W. Bedford. Improved averaging method for turbulent flow simulation. part i: Theoretical development and application to burgers’ transport equation. *International journal for numerical methods in fluids*, 6(2):49–64, 1986.
- [75] Y. M. Dakhoul and K. W. Bedford. Improved averaging method for turbulent flow simulation. part ii: calculations and verification. *International journal for numerical methods in fluids*, 6(2):65–82, 1986.
- [76] B. J. Daly and F. H. Harlow. Transport equations in turbulence. *The Physics of Fluids*, 13(11):2634–2649, 1970.
- [77] J. W. Deardorff. A numerical study of three-dimensional turbulent channel flow at large reynolds numbers. *Journal of Fluid Mechanics*, 41(2):453–480, 1970.
- [78] J. W. Deardorff. The use of subgrid transport equations in a three-dimensional model of atmospheric turbulence. *Journal of Fluids Engineering*, 95(3):429–438, 1973.
- [79] J. C. Del Álamo and J. Jiménez. Spectra of the very large anisotropic scales in turbulent channels. *Phys. Fluids*, 15(6):L41–L44, 2003.
- [80] J. C. Del Álamo, J. Jiménez, P. Zandonade, and R. D. Moser. Scaling of the energy spectra of turbulent channels. *Journal of Fluid Mechanics*, 500:135–144, 2004.

- [81] J. A. Domaradzki and R. S. Rogallo. Local energy transfer and nonlocal interactions in homogeneous, isotropic turbulence. *Physics of Fluids A: Fluid Dynamics*, 2(3):413–426, 1990.
- [82] J. A. Domaradzki and E. M. Saiki. Backscatter models for large-eddy simulations. *Theoretical and computational fluid dynamics*, 9(2):75–83, 1997.
- [83] J. A. Domaradzki, W. Liu, C. Hartel, and L. Kleiser. Energy transfer in numerically simulated wall-bounded turbulent flows. *Phys. Fluids*, 6(4):1583–1599, 1994.
- [84] L. Duan, I. Beekman, and M. P. Martin. Direct numerical simulation of hypersonic turbulent boundary layers. part 2. effect of wall temperature. *Journal of Fluid Mechanics*, 655:419–445, 2010.
- [85] D. C. Dunn and J. F. Morrison. Analysis of the energy budget in turbulent channel flow using orthogonal wavelets. *Computers & Fluids*, 34(2):199–224, 2005.
- [86] D. Dupuy, A. Toutant, and F. Bataille. A priori tests of subgrid-scale models in an anisothermal turbulent channel flow at low mach number. (Submitted for publication).
- [87] D. Dupuy, A. Toutant, and F. Bataille. Study of the sub-grid terms of the large-eddy simulation of a low Mach strongly anisothermal channel flow. In *Eurotherm Seminar 106, Paris, France*, 2016.
- [88] D. Dupuy, A. Toutant, and F. Bataille. étude de l’équation d’énergie pour le développement de modèles sous-maillages adaptés aux écoulements fortement anisothermes. In *Congrès SFT, Marseille, France*, 2017.
- [89] D. Dupuy, A. Toutant, and F. Bataille. Equations of energy exchanges in variable density turbulent flows. *Physics Letters A*, 382(5):327–333, 2018.
- [90] D. Dupuy, A. Toutant, and F. Bataille. Study of the large-eddy simulation subgrid terms of a low mach number anisothermal channel flow. *International Journal of Thermal Sciences*, 135:221–234, 2018.
- [91] D. Dupuy, A. Toutant, and F. Bataille. Turbulence kinetic energy exchanges in flows with highly variable fluid properties. *Journal of Fluid Mechanics*, 834:5–54, 2018.
- [92] H. Eckelmann. The structure of the viscous sublayer and the adjacent wall region in a turbulent channel flow. *Journal of Fluid Mechanics*, 65(3):439–459, 1974.
- [93] Thomas M Eidson. Numerical simulation of the turbulent Rayleigh–Bénard problem using subgrid modelling. *J. Fluid Mech.*, 158:245–268, 1985.
- [94] A. Favre. The equations of compressible turbulent gases. Technical Report AD0622097, DTIC Document, 1965.
- [95] A. Favre. Statistical equations of turbulent gases. *Problems of Hydrodynamics and Continuum Mechanics*, pages 231–266, 1969.
- [96] A. Favre. Turbulence: Space-time statistical properties and behavior in supersonic flows. *Phys. Fluids*, 26(10):2851–2863, 1983.
- [97] I. Fedioun, N. Lardjane, and I. Gökalp. Revisiting numerical errors in direct and large eddy simulations of turbulence: physical and spectral spaces analysis. *Journal of Computational Physics*, 174(2):816–851, 2001.
- [98] J. Ferziger and D. Leslie. Large eddy simulation—a predictive approach to turbulent flow computation. In *4th Computational Fluid Dynamics Conference*, page 1471, 1979.
- [99] Joseph Fourier. Mémoire sur la propagation de la chaleur dans les corps solides. *Nouveau Bulletin des Sciences de la Société Philomathique de Paris*, 6:112–116, 1807.
- [100] D. G. Fox and D. K. Lilly. Numerical simulation of turbulent flows. *Reviews of Geophysics*, 10(1):51–72, 1972.
- [101] H. Foyi, S. Sarkar, and R. Friedrich. Compressibility effects and turbulence scalings in supersonic channel flow. *Journal of Fluid Mechanics*, 509:207–216, 2004.
- [102] F. Freikamp. *Towards Multi-Cycle Simulation of In-Cylinder Flow and Combustion*. Cuvillier Verlag, 2008.

- [103] Matteo Frigo and Steven G Johnson. FFTW: An adaptive software architecture for the FFT. In *Acoustics, Speech and Signal Processing, 1998. Proceedings of the 1998 IEEE International Conference on*, volume 3, pages 1381–1384. IEEE, 1998.
- [104] U. Frisch. *Turbulence: the legacy of AN Kolmogorov*. Cambridge university press, 1995.
- [105] H. Fujita and T. Kato. On the Navier–Stokes initial value problem. I. *Archive for rational mechanics and analysis*, 16(4):269–315, 1964.
- [106] G. P. Galdi and W. J. Layton. Approximation of the larger eddies in fluid motions ii: A model for space-filtered flow. *Mathematical Models and Methods in Applied Sciences*, 10(03):343–350, 2000.
- [107] G. Galilei. *Dialogo sopra i due massimi sistemi del mondo*. 1632. English translation: S. Drake. *Dialogue concerning the two chief world systems*. University of California Press, Berkeley, 1953.
- [108] S. Gamard and W. K. George. Reynolds number dependence of energy spectra in the overlap region of isotropic turbulence. *Flow, turbulence and combustion*, 63(1-4): 443–477, 2000.
- [109] E. Garnier, N. Adams, and P. Sagaut. *Large eddy simulation for compressible flows*. Springer Science & Business Media, 2009.
- [110] T. B. Gatski and J. P. Bonnet. *Compressibility, turbulence and high speed flow*. Academic Press, 2013.
- [111] M. Germano. Turbulence: the filtering approach. *Journal of fluid mechanics*, 238: 325–336, 1992.
- [112] M. Germano, U. Piomelli, P. Moin, and W. H. Cabot. A dynamic subgrid-scale eddy viscosity model. *Physics of Fluids A: Fluid Dynamics*, 3(7):1760–1765, 1991.
- [113] N. S. Ghaisas and S. H. Frankel. A priori evaluation of large eddy simulation subgrid-scale scalar flux models in isotropic passive-scalar and anisotropic buoyancy-driven homogeneous turbulence. *J. Turbulence*, 15(2):88–121, 2014.
- [114] N. S. Ghaisas and S. H. Frankel. Dynamic gradient models for the sub-grid scale stress tensor and scalar flux vector in large eddy simulation. *Journal of Turbulence*, 17(1): 30–50, 2016.
- [115] S. Ghosal. An analysis of numerical errors in large-eddy simulations of turbulence. *Journal of Computational Physics*, 125(1):187–206, 1996.
- [116] S. Ghosal. Mathematical and physical constraints on large-eddy simulation of turbulence. *AIAA journal*, 37(4):425–433, 1999.
- [117] S. Ghosal and P. Moin. The basic equations for the large eddy simulation of turbulent flows in complex geometry. *Journal of Computational Physics*, 118(1):24–37, 1995.
- [118] S. Ghosal, T. S. Lund, P. Moin, and K. Akselvoll. A dynamic localization model for large-eddy simulation of turbulent flows. *Journal of Fluid Mechanics*, 286:229–255, 1995.
- [119] H. Goldstein, C. Poole, and J. Safko. *Classical mechanics*. AAPT, 2002.
- [120] S. E. Guarini, R. D. Moser, K. Shariff, and A. Wray. Direct numerical simulation of a supersonic turbulent boundary layer at Mach 2.5. *J. Fluid Mech.*, 414:1–33, 2000.
- [121] J. Gullbrand and F. K. Chow. The effect of numerical errors and turbulence models in large-eddy simulations of channel flow, with and without explicit filtering. *Journal of Fluid Mechanics*, 495:323–341, 2003.
- [122] H. Ha Minh, B. E. Launder, and J. MacInnes. A new approach to the analysis of turbulent mixing in variable density flows. In *3rd Turbulent Shear Flow Symp. p*, volume 19, 1981.
- [123] H. Ha Minh, B. E. Launder, and J. MacInnes. The turbulence modelling of variable density flows—a mixed-weighted decomposition. In *Turbulent Shear Flows 3*, pages 291–308. Springer, 1982.

- [124] S. He, W. S. Kim, and J. H. Bae. Assessment of performance of turbulence models in predicting supercritical pressure heat transfer in a vertical tube. *International Journal of Heat and Mass Transfer*, 51(19-20):4659–4675, 2008.
- [125] K. Horiuti. A new dynamic two-parameter mixed model for large-eddy simulation. *Physics of Fluids*, 9(11):3443–3464, 1997.
- [126] S. Hoyas and J. Jiménez. Scaling of the velocity fluctuations in turbulent channels up to $Re_\tau = 2003$. *Phys. Fluids*, 18(1):011702, 2006.
- [127] P. G. Huang, G. N. Coleman, and P. Bradshaw. Compressible turbulent channel flows: DNS results and modelling. *J. Fluid Mech.*, 305:185–218, 1995.
- [128] S. Husson. *Simulations des grandes échelles pour les écoulements turbulents anisothermes*. PhD thesis, INSA de Lyon, 2007.
- [129] T. Ilescu and P. Fischer. Large eddy simulation of turbulent channel flows by the rational large eddy simulation model. *Physics of Fluids*, 15(10):3036–3047, 2003.
- [130] T. Ilescu and P. Fischer. Backscatter in the rational les model. *Computers & fluids*, 33(5-6):783–790, 2004.
- [131] N. Z. Ince and B. E. Launder. On the computation of buoyancy-driven turbulent flows in rectangular enclosures. *International Journal of Heat and Fluid Flow*, 10(2):110–117, 1989.
- [132] A. M. Jaffe. The millennium grand challenge in mathematics. *Notices of the AMS*, 53(6), 2006.
- [133] Z. Jiang, Z. Xiao, Y. Shi, and S. Chen. Constrained large-eddy simulation of wall-bounded compressible turbulent flows. *Physics of Fluids*, 25(10):106102, 2013.
- [134] J. Jiménez. The physics of wall turbulence. *Physica A: Statistical Mechanics and its Applications*, 263(1-4):252–262, 1999.
- [135] J. Jiménez and R. D. Moser. Large-eddy simulations: where are we and what can we expect? *AIAA journal*, 38(4):605–612, 2000.
- [136] J. Jiménez and A. Pinelli. The autonomous cycle of near-wall turbulence. *Journal of Fluid Mechanics*, 389:335–359, 1999.
- [137] T. Kajishima and K. Taira. *Computational Fluid Dynamics*. Springer, 2017.
- [138] H. Kawamura, K. Ohsaka, H. Abe, and K. Yamamoto. Dns of turbulent heat transfer in channel flow with low to medium-high prandtl number fluid. *International Journal of Heat and Fluid Flow*, 19(5):482–491, 1998.
- [139] H. Kawamura, H. Abe, and Y. Matsuo. DNS of turbulent heat transfer in channel flow with respect to Reynolds and Prandtl number effects. *Intl. J. Heat Fluid Flow*, 20:196–207, 1999.
- [140] S. Kenjereš and K. Hanjalić. Prediction of turbulent thermal convection in concentric and eccentric horizontal annuli. *International journal of heat and fluid flow*, 16(5):429–439, 1995.
- [141] S. Ketterl and M. Klein. A-priori assessment of subgrid scale models for large-eddy simulation of multiphase primary breakup. *Computers & Fluids*, 165:64–77, 2018.
- [142] S. Kida and K. Ohkitani. Fine structure of energy transfer in turbulence. *Physics of Fluids A: Fluid Dynamics*, 4(8):1602–1604, 1992.
- [143] S. Kida and K. Ohkitani. Spatiotemporal intermittency and instability of a forced turbulence. *Physics of Fluids A: Fluid Dynamics*, 4(5):1018–1027, 1992.
- [144] S. Kida and S. A. Orszag. Energy and spectral dynamics in decaying compressible turbulence. *Journal of Scientific Computing*, 7(1):1–34, 1992. ISSN 0885-7474.
- [145] J. Kim and P. Moin. Transport of passive scalars in a turbulent channel flow. In *Turbulent Shear Flows 6*, pages 85–96. Springer, 1989.
- [146] J. Kim, P. Moin, and R. Moser. Turbulence statistics in fully developed channel flow at low Reynolds number. *J. Fluid Mech.*, 177:133–166, 1987.

- [147] H. Kobayashi. The subgrid-scale models based on coherent structures for rotating homogeneous turbulence and turbulent channel flow. *Physics of Fluids*, 17(4):045104, 2005.
- [148] A. N. Kolmogorov. Локальная структура турбулентности в несжимаемой жидкости при очень больших числах Рейнольдса. *Dokl. Akad. Nauk SSSR*, 30(4):299–303, 1941. English translation: A. N. Kolmogorov, The local structure of turbulence in incompressible viscous fluid for very large Reynolds numbers, *Proc. R. Soc. London A* 434:9–13, 1991.
- [149] M. Kozuka, Y. Seki, and H. Kawamura. DNS of turbulent heat transfer in a channel flow with a high spatial resolution. *Intl. J. Heat Fluid Flow*, 30(3):514–524, 2009.
- [150] A. G. Kravchenko and P. Moin. On the effect of numerical errors in large eddy simulations of turbulent flows. *Journal of Computational Physics*, 131(2):310–322, 1997.
- [151] H.-P. Kreplin and H. Eckelmann. Behavior of the three fluctuating velocity components in the wall region of a turbulent channel flow. *The Physics of Fluids*, 22(7):1233–1239, 1979.
- [152] A. Krzhivitski and O. A. Ladyzhenskaya. A grid method for the Navier–Stokes equations. *Soviet Physics Doklady*, 11:212, 1966.
- [153] W. Kutta. Beitrag zur näherungsweise Integration totaler Differentialgleichungen. *Z. Math. Phys.*, 46:435–453, 1901.
- [154] F. Laadhari. On the evolution of maximum turbulent kinetic energy production in a channel flow. *Phys. Fluids*, 14(10):L65–L68, 2002.
- [155] P. Lampitella. *Large eddy simulation for complex industrial flows*. PhD thesis, Italy, 2014.
- [156] J. A. Langford and R. D. Moser. Optimal les formulations for isotropic turbulence. *Journal of fluid mechanics*, 398:321–346, 1999.
- [157] M. Lappa. A mathematical and numerical framework for the analysis of compressible thermal convection in gases at very high temperatures. *Journal of Computational Physics*, 313:687–712, 2016.
- [158] J. Larsson, S. Kawai, J. Bodart, and I. Bermejo-Moreno. Large eddy simulation with modeled wall-stress: recent progress and future directions. *Mechanical Engineering Reviews*, 3(1):15–00418, 2016.
- [159] B. E. Launder. On the computation of convective heat transfer in complex turbulent flows. *Journal of Heat Transfer*, 110(4b):1112–1128, 1988.
- [160] Anh-Tuan Le, Gary N. Coleman, and John Kim. Near-wall turbulence structures in three-dimensional boundary layers. *International Journal of Heat and Fluid Flow*, 21(5):480–488, 2000. ISSN 0142-727X.
- [161] R. Lechner, J. Sesterhenn, and R. Friedrich. Turbulent supersonic channel flow. *J. Turbulence*, 2(1):001–001, 2001.
- [162] J. Lee, H. Choi, and N. Park. Dynamic global model for large eddy simulation of transient flow. *Physics of Fluids*, 22(7):075106, 2010.
- [163] J. Lee, P. E. Gharagozloo, B. Kolade, J. K. Eaton, and K. E. Goodson. Nanofluid convection in microtubes. *Journal of heat transfer*, 132(9):092401, 2010.
- [164] J. Lee, S. Y. Jung, H. J. Sung, and T. A. Zaki. Effect of wall heating on turbulent boundary layers with temperature-dependent viscosity. *Journal of Fluid Mechanics*, 726:196–225, 2013.
- [165] M. Lee and R. D. Moser. Spectral analysis on reynolds stress transport equation in high firewall-bounded turbulence. In *International Symposium on Turbulence and Shear Flow Phenomena (TSFP-9)*, Melbourne, pages 4A–3, 2006.
- [166] M. Lee and R. D. Moser. Role of large scale motions in turbulent poiseuille and couette flows. In *International Symposium on Turbulence and Shear Flow Phenomena (TSFP-10)*, Chicago, pages 9B–3, 2006.

- [167] M. Lee and R. D. Moser. Direct numerical simulation of turbulent channel flow up to $Re_\tau \approx 5200$. *Journal of Fluid Mechanics*, 774:395–415, 2015.
- [168] S. K. Lele. Compressibility effects on turbulence. *Annu. Rev. Fluid Mech.*, 26(1):211–254, 1994.
- [169] A. Leonard. Energy cascade in large eddy simulations of turbulent fluid flows. *Advances in Geophysics*, 18A:237–248, 1974.
- [170] B. P. Leonard. A stable and accurate convective modelling procedure based on quadratic upstream interpolation. *Computer Methods in Applied Mechanics and Engineering*, 19(1):59–98, 1979.
- [171] J. Leray. Étude de diverses équations intégrales non linéaires et de quelques problèmes que pose l’hydrodynamique. *Journal de Mathématiques Pures et Appliquées*, 12:1–82, 1933.
- [172] J. Leray. Essai sur les mouvements plans d’un fluide visqueux que limitent des parois. *Journal de Mathématiques pures et appliquées*, 13:331–418, 1934.
- [173] M. Lesieur. *Turbulence in Fluids*. Fluid Mechanics and Its Applications. Springer, 2008. ISBN 9781402064357.
- [174] E. Lévêque, F. Toschi, L. Shao, and J.-P. Bertoglio. Shear-improved smagorinsky model for large-eddy simulation of wall-bounded turbulent flows. *Journal of Fluid Mechanics*, 570:491–502, 2007.
- [175] C. Li. *A-priori analysis of LES subgrid scale models applied to wall turbulence with pressure gradients*. PhD thesis, Ecole Centrale de Lille, 2013.
- [176] W. Li, X. Li, J. Ren, and H. Jiang. Large eddy simulation of compound angle hole film cooling with hole length-to-diameter ratio and internal crossflow orientation effects. *International Journal of Thermal Sciences*, 121:410–423, 2017.
- [177] D. K. Lilly. A proposed modification of the germano subgrid-scale closure method. *Physics of Fluids A: Fluid Dynamics*, 4(3):633–635, 1992.
- [178] L. I.-K. Lin. A concordance correlation coefficient to evaluate reproducibility. *Biometrics*, pages 255–268, 1989.
- [179] P.-L. Lions and T. H. Moulden. *Mathematical topics in fluid mechanics, Volume 1: Incompressible models*. Oxford University Press, New York, 1996.
- [180] S. Liu, C. Meneveau, and J. Katz. On the properties of similarity subgrid-scale models as deduced from measurements in a turbulent jet. *J. Fluid Mech.*, 275:83–119, 1994.
- [181] H. Lu and C. J. Rutland. Structural subgrid-scale modeling for large-eddy simulation: A review. *Acta Mechanica Sinica*, 32(4):567–578, 2016.
- [182] H. Lu, C. J. Rutland, and L. M. Smith. A priori tests of one-equation LES modeling of rotating turbulence. *J. Turbulence*, (8):N37, 2007.
- [183] J. L. Lumley. Spectral energy budget in wall turbulence. *Phys. Fluids*, 7(2):190–196, 1964.
- [184] T. S. Lund. The use of explicit filters in large eddy simulation. *Computers & Mathematics with Applications*, 46(4):603–616, 2003.
- [185] T. Maeder, N. A. Adams, and L. Kleiser. Direct simulation of turbulent supersonic boundary layers by an extended temporal approach. *J. Fluid Mech.*, 429:187–216, 2001.
- [186] A. Majda and K. G. Lamb. Simplified equations for low mach number combustion with strong heat release. In *Dynamical issues in combustion theory*, pages 167–211. Springer, 1991.
- [187] N. N. Mansour, P. Moin, W. C. Reynolds, and J. H. Ferziger. Improved methods for large eddy simulations of turbulence. In *Turbulent Shear Flows I*, pages 386–401. Springer, 1979.
- [188] N Marati, CM Casciola, and R Piva. Energy cascade and spatial fluxes in wall turbulence. *J. Fluid Mech.*, 521:191–215, 2004.

- [189] M. Pino Martín, U. Piomelli, and G. V. Candler. Subgrid-scale models for compressible large-eddy simulations. *Theoretical and Computational Fluid Dynamics*, 13(5):361–376, 2000.
- [190] P. J. Mason and N. S. Callen. On the magnitude of the subgrid-scale eddy coefficient in large-eddy simulations of turbulent channel flow. *Journal of Fluid Mechanics*, 162:439–462, 1986.
- [191] L. Mathelin, F. Bataille, and Y. Zhou. Theoretical investigation of some thermal effects in turbulence modeling. *Theoretical and Computational Fluid Dynamics*, 22(6):471–483, 2008.
- [192] R. Mathis, N. Hutchins, and I. Marusic. Large-scale amplitude modulation of the small-scale structures in turbulent boundary layers. *Journal of Fluid Mechanics*, 628:311–337, 2009.
- [193] A. Meister. Asymptotic single and multiple scale expansions in the low mach number limit. *SIAM Journal on Applied Mathematics*, 60(1):256–271, 1999.
- [194] C. Meneveau and J. Katz. Scale-invariance and turbulence models for large-eddy simulation. *Annu. Rev. Fluid Mech.*, 32:1–32, 2000.
- [195] C. Meneveau, T. S. Lund, and W. H. Cabot. A lagrangian dynamic subgrid-scale model of turbulence. *Journal of fluid mechanics*, 319:353–385, 1996.
- [196] J. Meyers and P. Sagaut. Is plane-channel flow a friendly case for the testing of large-eddy simulation subgrid-scale models? *Physics of Fluids*, 19(4):048105, 2007.
- [197] Y. Mizuno. Spectra of energy transport in turbulent channel flows for moderate reynolds numbers. *J. Fluid Mech.*, 805:171–187, 2016.
- [198] D. Modesti and S. Pirozzoli. Reynolds and Mach number effects in compressible turbulent channel flow. *Intl. J. Heat Fluid Flow*, 59:33–49, 2016.
- [199] Y. Morinishi and O. V. Vasilyev. A recommended modification to the dynamic two-parameter mixed subgrid scale model for large eddy simulation of wall bounded turbulent flow. *Physics of Fluids*, 13(11):3400–3410, 2001.
- [200] Y. Morinishi, T. S. Lundhomas, O. V. Vasilyev, and P. Moin. Fully conservative higher order finite difference schemes for incompressible flow. *J. Comput. Phys.*, 143(1):90–124, 1998.
- [201] M. V. Morkovin. *The Mechanics of Turbulence*. Gordon and Breach, 1964.
- [202] R. D. Moser. On the validity of the continuum approximation in high reynolds number turbulence. *Physics of Fluids*, 18(7):078105, 2006.
- [203] R. D. Moser, J. Kim, and N. N. Mansour. Direct numerical simulation of turbulent channel flow up to $Re_\tau = 590$. *Phys. Fluids*, 11(4):943–945, 1999.
- [204] V. Moureau, P. Domingo, and L. Vervisch. From large-eddy simulation to direct numerical simulation of a lean premixed swirl flame: Filtered laminar flame-pdf modeling. *Combustion and Flame*, 158(7):1340–1357, 2011.
- [205] C. D. Munz, M. Dumbser, and M. Zucchini. The multiple pressure variables method for fluid dynamics and aeroacoustics at low mach numbers. *Numerical methods for hyperbolic and kinetic problems*, 7:335–359, 2003.
- [206] C.-D. Munz, S. Roller, R. Klein, and K. J. Geratz. The extension of incompressible flow solvers to the weakly compressible regime. *Computers & Fluids*, 32(2):173–196, 2003.
- [207] A. Muschinski. A similarity theory of locally homogeneous and isotropic turbulence generated by a smagorinsky-type les. *Journal of Fluid Mechanics*, 325:239–260, 1996.
- [208] C.-L. Navier. Mémoire sur les lois du mouvement des fluides. *Mémoires de l’Académie Royale des Sciences de l’Institut de France*, 6:389–440, 1827.
- [209] A. Nejadmalayeri, A. Vezolainen, and O. V. Vasilyev. Reynolds number scaling of coherent vortex simulation and stochastic coherent adaptive large eddy simulation. *Physics of Fluids*, 25(11):110823, 2013.

- [210] H. Nemati, A. Patel, B. J. Boersma, and R. Pecnik. Mean statistics of a heated turbulent pipe flow at supercritical pressure. *International Journal of Heat and Mass Transfer*, 83:741–752, 2015.
- [211] I. Newton. *Philosophiae naturalis principia mathematica*. 1632. English translation: A. Motte. *Mathematical principles of natural philosophy*. London, 1729.
- [212] F. Nicoud. Conservative high-order finite-difference schemes for low-Mach number flows. *J. Comput. Phys.*, 158(1):71–97, 2000.
- [213] F. Nicoud and F. Ducros. Subgrid-scale stress modelling based on the square of the velocity gradient tensor. *Flow, Turbulence and Combustion*, 62(3):183–200, 1999. ISSN 1386-6184.
- [214] F. Nicoud, H. Baya Toda, O. Cabrit, S. Bose, and J. Lee. Using singular values to build a subgrid-scale model for large eddy simulations. *Physics of Fluids*, 23(8):085106, 2011.
- [215] F. C. Nicoud. Numerical study of a channel flow with variable properties. *Center for Turbulence Research Annual Research Briefs*, pages 289–309, 1998.
- [216] M. Oberlack. Symmetries and invariant solutions of turbulent flows and their implications for turbulence modelling. In *Theories of Turbulence*, pages 301–366. Springer, 2002.
- [217] N. Odier, G. Balarac, C. Corre, and V. Moureau. Numerical study of a flapping liquid sheet sheared by a high-speed stream. *International journal of multiphase flow*, 77:196–208, 2015.
- [218] S. A. Orszag and G. S. Patterson. Numerical simulation of three-dimensional homogeneous isotropic turbulence. *Physical Review Letters*, 28(2):76, 1972.
- [219] S. Paolucci. On the filtering of sound from the Navier–Stokes equations. Technical Report SAND82-8257, Sandia National Labs., Livermore, CA (USA), 1982.
- [220] N. Park, J. Y. Yoo, and H. Choi. Discretization errors in large eddy simulation: on the suitability of centered and upwind-biased compact difference schemes. *Journal of Computational Physics*, 198(2):580–616, 2004.
- [221] N. Park, S. Lee, J. Lee, and H. Choi. A dynamic subgrid-scale eddy viscosity model with a global model coefficient. *Physics of Fluids*, 18(12):125109, 2006.
- [222] A. Patel, J. Peeters, B. Boersma, and R. Pecnik. Semi-local scaling and turbulence modulation in variable property turbulent channel flows. *Phys. Fluids*, 27(9):095101, 2015.
- [223] A. Patel, B. J. Boersma, and R. Pecnik. The influence of near-wall density and viscosity gradients on turbulence in channel flows. *Journal of Fluid Mechanics*, 809:793–820, 2016.
- [224] A. Patel, B. J. Boersma, and R. Pecnik. Scalar statistics in variable property turbulent channel flows. *Physical Review Fluids*, 2(8):084604, 2017.
- [225] R. Pecnik and A. Patel. Scaling and modelling of turbulence in variable property channel flows. *Journal of Fluid Mechanics*, 823, 2017.
- [226] J. W. R. Peeters, R. Pecnik, M. Rohde, T. H. J. J. Van Der Hagen, and B. J. Boersma. Turbulence attenuation in simultaneously heated and cooled annular flows at supercritical pressure. *Journal of Fluid Mechanics*, 799:505–540, 2016.
- [227] U. Piomelli. Wall-layer models for large-eddy simulations. *Progress in aerospace sciences*, 44(6):437–446, 2008.
- [228] U. Piomelli and E. Balaras. Wall-layer models for large-eddy simulations. *Annual review of fluid mechanics*, 34(1):349–374, 2002.
- [229] U. Piomelli, P. Moin, and J. H. Ferziger. Model consistency in large eddy simulation of turbulent channel flows. *Phys. Fluids*, 31(7):1884–1891, 1988.
- [230] U. Piomelli, J. Ferziger, P. Moin, and J. Kim. New approximate boundary conditions for large eddy simulations of wall-bounded flows. *Physics of Fluids A: Fluid Dynamics*, 1(6):1061–1068, 1989.

- [231] U. Piomelli, T. A. Zang, C. G. Speziale, and M. Y. Hussaini. On the large-eddy simulation of transitional wall-bounded flows. *Physics of Fluids A: Fluid Dynamics*, 2(2): 257–265, 1990.
- [232] Ugo Piomelli, Yunfang Yu, and Ronald J. Adrian. Subgrid-scale energy transfer and near-wall turbulence structure. *Phys. Fluids*, 8(1):215–224, 1996.
- [233] S. Pirozzoli, F. Grasso, and T. B. Gatski. Direct numerical simulation and analysis of a spatially evolving supersonic turbulent boundary layer at $M=2.25$. *Phys. Fluids*, 16(3):530–545, 2004.
- [234] S. Pirozzoli, M. Bernardini, and P. Orlandi. Passive scalars in turbulent channel flow at high reynolds number. *Journal of Fluid Mechanics*, 788:614–639, 2016.
- [235] S. B. Pope. *Turbulent Flows*. Cambridge University Press, 2000.
- [236] S. B. Pope. Ten questions concerning the large-eddy simulation of turbulent flows. *New journal of Physics*, 6(1):35, 2004.
- [237] C. D. Pruett. Eulerian time-domain filtering for spatial large-eddy simulation. *AIAA journal*, 38(9):1634–1642, 2000.
- [238] C. D. Pruett. Temporal large-eddy simulation: theory and implementation. *Theoretical and Computational Fluid Dynamics*, 22(3-4):275–304, 2008.
- [239] C. D. Pruett and N. A. Adams. A priori analyses of three subgrid-scale models for one-parameter families of filters. *Physics of Fluids*, 12(5):1133–1142, 2000.
- [240] C. D. Pruett, T. B. Gatski, C. E. Grosch, and W. D. Thacker. The temporally filtered navier–stokes equations: properties of the residual stress. *Physics of Fluids*, 15(8): 2127–2140, 2003.
- [241] S. Rao, E. Pomraning, and C. J. Rutland. Development of advanced combustion models for diesel engines using large eddy simulation. In *Second Joint Meeting of the US Sections of the Combustion Institute, Oakland, CA*, pages 26–28, 2001.
- [242] D. Razafindralandy, A. Hamdouni, and M. Oberlack. Analysis and development of subgrid turbulence models preserving the symmetry properties of the navier–stokes equations. *European Journal of Mechanics-B/Fluids*, 26(4):531–550, 2007.
- [243] F. Reech. *Théorie des machines motrices et des effets mécaniques de la chaleur*. E. Lacroix, 1869.
- [244] O. Reynolds. An experimental investigation of the circumstances which determine whether the motion of water shall be direct or sinuous, and of the law of resistance in parallel channels. *Philosophical Transactions of the Royal Society of London*, 174: 935–982, 1883.
- [245] O. Reynolds. On the dynamical theory of incompressible viscous fluids and the determination of the criterion. *Proceedings of the Royal Society of London*, 56(336-339):40–45, 1894.
- [246] L. F. Richardson. Weather prediction by numerical process. 1922.
- [247] A. J. L. Rodriguez and G. Emanuel. Compressible rotational flows generated by the substitution principle. *Phys. Fluids*, 31:1058–1063, 1988.
- [248] R. S. Rogallo and P. Moin. Numerical simulation of turbulent flows. *Annual review of fluid mechanics*, 16(1):99–137, 1984.
- [249] J. C. Rotta. Über den Einfluß der Machschen Zahl und des Wärmeübergangs auf das Wandgesetz turbulenter Strömung. *Z. Flugwiss*, 7:264–274, 1959.
- [250] W. Rozema, H.J. Bae, P. Moin, and R. Verstappen. Minimum-dissipation models for large-eddy simulation. *Physics of Fluids*, 27(8):085107, 2015.
- [251] C. Runge. Über die numerische Auflösung von Differentialgleichungen. *Mathematische Annalen*, 46(2):167–178, 1895.
- [252] S. Ryu and G. Iaccarino. A subgrid-scale eddy-viscosity model based on the volumetric strain-stretching. *Physics of Fluids*, 26(6):065107, 2014.

- [253] P. Sagaut. *Large eddy simulation for incompressible flows: an introduction*. Springer Science & Business Media, 2006.
- [254] P. Sagaut and C. Cambon. *Homogeneous turbulence dynamics*. Cambridge University Press, 2008.
- [255] P. Sagaut, E. Garnier, and M. Terracol. A general algebraic formulation for multi-parameter dynamic subgrid-scale modeling. *International Journal of Computational Fluid Dynamics*, 13(3):251–257, 2000.
- [256] M. V. Salvetti and S. Banerjee. A priori tests of a new dynamic subgrid-scale model for finite-difference large-eddy simulations. *Physics of Fluids*, 7(11):2831–2847, 1995.
- [257] M. V. Salvetti, Y. Zang, R. L. Street, and S. Banerjee. Large-eddy simulation of free-surface decaying turbulence with dynamic subgrid-scale models. *Physics of Fluids*, 9(8):2405–2419, 1997.
- [258] M. Sanchez, F. Aulery, A. Toutant, and F. Bataille. Large eddy simulation of thermal boundary layer spatial development in a turbulent channel flow. *Journal of Fluids Engineering*, 136(6):060906, 2014.
- [259] F. Sarghini, U. Piomelli, and E. Balaras. Scale-similar models for large-eddy simulations. *Physics of Fluids*, 11(6):1596–1607, 1999.
- [260] S. Sarkar. The pressure–dilatation correlation in compressible flows. *Physics of Fluids A: Fluid Dynamics*, 4(12):2674–2682, 1992.
- [261] S. Sarkar, G. Erlebacher, M. Y. Hussaini, and H. O. Kreiss. The analysis and modeling of dilatational terms in compressible turbulence. ICASE report 89-79. univ. *Space Research Assoc., Hampton, Virginia*, 1989.
- [262] L. A. C. A. Schiavo, W. R. Wolf, and J. L. F. Azevedo. Turbulent kinetic energy budgets in wall bounded flows with pressure gradients and separation. *Physics of Fluids*, 29(11):115108, 2017.
- [263] U. Schumann. Subgrid scale model for finite difference simulations of turbulent flows in plane channels and annuli. *Journal of computational physics*, 18(4):376–404, 1975.
- [264] S. Serra, A. Toutant, and F. Bataille. Thermal large eddy simulation in a very simplified geometry of a solar receiver. *Heat Transfer Engineering*, 33(6):505–524, 2012.
- [265] S. Serra, A. Toutant, F. Bataille, and Y. Zhou. High-temperature gradient effect on a turbulent channel flow using thermal large-eddy simulation in physical and spectral spaces. *J. Turbulence*, 13:N49, 2012.
- [266] S. Serra, A. Toutant, F. Bataille, and Y. Zhou. Turbulent kinetic energy spectrum in very anisothermal flows. *Physics Letters A*, 376(45):3177–3184, 2012.
- [267] Syvain Serra. *Couplage écoulements pariétaux et transferts thermiques dans les récepteurs solaires à haute température*. PhD thesis, Université de Perpignan Via Domitia, 2009.
- [268] M. S. Shadloo, A. Hadjadj, and F. Hussain. Statistical behavior of supersonic turbulent boundary layers with heat transfer at $M=2$. *International Journal of Heat and Fluid Flow*, 53:113–134, 2015.
- [269] M. F. Shahab, G. Lehnasch, T. B. Gatski, and P. Comte. Statistical characteristics of an isothermal, supersonic developing boundary layer flow from DNS data. *Flow, Turbulence and Combustion*, 86(3-4):369–397, 2011.
- [270] C. E. Shannon. Communication in the presence of noise. *Proceedings of the IRE*, 37(1):10–21, 1949.
- [271] G. S. Sidharth and G. V. Candler. Stretched-vortex based subgrid-scale modeling for variable-density flows. In *45th AIAA Fluid Dynamics Conference*, page 2782, 2015.
- [272] G. S. Sidharth, A. Kartha, and G. V. Candler. Filtered velocity based LES of mixing in high speed recirculating shear flow. In *46th AIAA Fluid Dynamics Conference*, page 3184, 2016.

- [273] M. H. Silvis, R. A. Remmerswaal, and R. Verstappen. Physical consistency of subgrid-scale models for large-eddy simulation of incompressible turbulent flows. *Physics of Fluids*, 29(1):015105, 2017.
- [274] S. Singh and D. You. A dynamic global-coefficient mixed subgrid-scale model for large-eddy simulation of turbulent flows. *International journal of heat and fluid flow*, 42:94–104, 2013.
- [275] S. Singh, D. You, and S. T. Bose. Large-eddy simulation of turbulent channel flow using explicit filtering and dynamic mixed models. *Physics of Fluids*, 24(8):085105, 2012.
- [276] J. Smagorinsky. General circulation experiments with the primitive equations: I. the basic experiment. *Monthly weather review*, 91(3):99–164, 1963.
- [277] A. J. Smits and J.-P. Dussauge. *Turbulent shear layers in supersonic flow*. Springer Science & Business Media, 2006.
- [278] P. R. Spalart. Comments on the feasibility of les for wings, and on hybrid rans/les approach. In *Proceedings of First AFOSR International Conference on DNS/LES, 1997*, 1997.
- [279] P. R. Spalart. Detached-eddy simulation. *Annual review of fluid mechanics*, 41:181–202, 2009.
- [280] C. G. Speziale. Galilean invariance of subgrid-scale stress models in the large-eddy simulation of turbulence. *Journal of Fluid Mechanics*, 156:55–62, 1985.
- [281] C. G. Speziale, G. Erlebacher, T. A. Zang, and M. Y. Hussaini. The subgrid-scale modeling of compressible turbulence. *The Physics of fluids*, 31(4):940–942, 1988.
- [282] G. G. Stokes. On the theories of the internal friction of fluids in motion, and of the equilibrium and motion of elastic solids. *Transactions of the Cambridge Philosophical Society*, 8:287, 1849.
- [283] S. Stolz and N. A. Adams. An approximate deconvolution procedure for large-eddy simulation. *Physics of Fluids*, 11(7):1699–1701, 1999.
- [284] S. Stolz, N. A. Adams, and L. Kleiser. An approximate deconvolution model for large-eddy simulation with application to incompressible wall-bounded flows. *Physics of fluids*, 13(4):997–1015, 2001.
- [285] M. Strelets. Detached eddy simulation of massively separated flows. In *39th Aerospace sciences meeting and exhibit*, page 879, 2001.
- [286] X.-B. Sun and X.-Y. Lu. A large eddy simulation approach of compressible turbulent flow without density weighting. *Phys. Fluids*, 18(11):118101, 2006.
- [287] W. Sutherland. The viscosity of gases and molecular force. *The London, Edinburgh, and Dublin Philosophical Magazine and Journal of Science*, 36(223):507–531, 1893.
- [288] J. Tchoufag, P. Sagaut, and C. Cambon. Spectral approach to finite reynolds number effects on kolmogorov’s 4/5 law in isotropic turbulence. *Physics of Fluids*, 24(1):015107, 2012.
- [289] R. Temam. Sur l’approximation de la solution des équations de Navier–Stokes par la méthode des pas fractionnaires (ii). *Archive for Rational Mechanics and Analysis*, 33(5):377–385, 1969.
- [290] A. Toutant and F. Bataille. Turbulence statistics in a fully developed channel flow submitted to a high temperature gradient. *International Journal of Thermal Sciences*, 74:104–118, 2013.
- [291] A. Toutant, E. Labourasse, O. Lebaigue, and O. Simonin. DNS of the interaction between a deformable buoyant bubble and a spatially decaying turbulence: a priori tests for LES two-phase flow modelling. *Computers & Fluids*, 37(7):877–886, 2008.
- [292] A. Travin, M. Shur, M. Strelets, and P. Spalart. Detached-eddy simulations past a circular cylinder. *Flow, Turbulence and Combustion*, 63(1-4):293–313, 2000.
- [293] A. Trettel and J. Larsson. Mean velocity scaling for compressible wall turbulence with heat transfer. *Phys. Fluids*, 28(2):026102, 2016.

- [294] F. X. Trias, D. Folch, A. Gorobets, and A. Oliva. Building proper invariants for eddy-viscosity subgrid-scale models. *Physics of Fluids*, 27(6):065103, 2015.
- [295] F. X. Trias, A. Gorobets, M. H. Silvis, R. W. C. P. Verstappen, and A. Oliva. A new subgrid characteristic length for turbulence simulations on anisotropic grids. *Physics of Fluids*, 29(11):115109, 2017.
- [296] A. V. Trofimova, A. E. Tejada-Martínez, K. E. Jansen, and R. T. Lahey Jr. Direct numerical simulation of turbulent channel flows using a stabilized finite element method. *Computers & Fluids*, 38(4):924–938, 2009. ISSN 0045-7930.
- [297] A. Tsinober. *An informal introduction to turbulence*, volume 63. Springer Science & Business Media, 2001.
- [298] T. Tsukahara, T. Seki, H. Kawamura, and D. Tochio. DNS of turbulent channel flow at very low Reynolds numbers. In *Proc. of the Fourth International Symposium on Turbulence and Shear Flow Phenomena*, pages 935–940. Begel House Inc., 2005.
- [299] P. H. Van Cittert. Zum einfluss der spaltbreite auf die intensitätsverteilung in spektrallinien. ii. *Zeitschrift für Physik*, 69(5-6):298–308, 1931.
- [300] H. Van der Ven. A family of large eddy simulation (les) filters with nonuniform filter widths. *Physics of Fluids*, 7(5):1171–1172, 1995.
- [301] O. V. Vasilyev and D. E. Goldstein. Local spectrum of commutation error in large eddy simulations. *Physics of Fluids*, 16(2):470–473, 2004.
- [302] O. V. Vasilyev, T. S. Lund, and P. Moin. A general class of commutative filters for les in complex geometries. *Journal of Computational Physics*, 146(1):82–104, 1998.
- [303] R. Verstappen. When does eddy viscosity damp subfilter scales sufficiently? *Journal of Scientific Computing*, 49(1):94, 2011.
- [304] A. W. Vreman. An eddy-viscosity subgrid-scale model for turbulent shear flow: Algebraic theory and applications. *Physics of fluids*, 16(10):3670–3681, 2004.
- [305] A. W. Vreman and J. G. M. Kuerten. Comparison of direct numerical simulation databases of turbulent channel flow at $Re_\tau = 180$. *Phys. Fluids*, 26(1):015102, 2014.
- [306] B. Vreman. *Direct and large-eddy simulation of the compressible turbulent mixing layer*. PhD thesis, University of Twente, 1995.
- [307] B. Vreman, B. Geurts, and H. Kuerten. On the formulation of the dynamic mixed subgrid-scale model. *Physics of Fluids*, 6(12):4057–4059, 1994.
- [308] B. Vreman, B. Geurts, and H. Kuerten. Realizability conditions for the turbulent stress tensor in large-eddy simulation. *Journal of Fluid Mechanics*, 278:351–362, 1994.
- [309] B. Vreman, B. Geurts, and H. Kuerten. A priori tests of large eddy simulation of the compressible plane mixing layer. *Journal of Engineering Mathematics*, 29(4):299–327, 1995.
- [310] B. Vreman, B. Geurts, and H. Kuerten. Subgrid-modelling in LES of compressible flow. *Applied Scientific Research*, 54(3):191–203, 1995.
- [311] J. Wang, M. Wan, S. Chen, and S. Chen. Kinetic energy transfer in compressible isotropic turbulence. *Journal of Fluid Mechanics*, 841:581–613, 2018.
- [312] D. C. Wilcox. *Turbulence modeling for CFD*, volume 2. DCW industries La Canada, CA, 1998.
- [313] J. H. Williamson. Low-storage Runge-Kutta schemes. *J. Comput. Phys.*, 35(1):48–56, 1980.
- [314] G. S. Winckelmans, A. Wray, O. V. Vasilyev, and H. Jeanmart. Explicit-filtering large-eddy simulation using the tensor-diffusivity model supplemented by a dynamic smagorinsky term. *Physics of Fluids*, 13(5):1385–1403, 2001.
- [315] J. Worthy and P. Rubini. A study of les stress and flux models applied to a buoyant jet. *Numerical Heat Transfer, Part B: Fundamentals*, 48(3):235–256, 2005.

- [316] J. Worthy, V. Sanderson, and P. Rubini. Comparison of modified k- ϵ turbulence models for buoyant plumes. *Numerical Heat Transfer: Part B: Fundamentals*, 39(2):151–165, 2001.
- [317] S. M. Yahya, S. F. Anwer, and S. Sanghi. Turbulent forced convective flow in an anisothermal channel. *International Journal of Thermal Sciences*, 88:84–95, 2015.
- [318] C.-S. Yih. Exact solutions for steady two-dimensional flow of a stratified fluid. *J. Fluid Mech.*, 9(02):161–174, 1960.
- [319] J. Y. Yoo. The turbulent flows of supercritical fluids with heat transfer. *Annual review of fluid mechanics*, 45:495–525, 2013.
- [320] A. Yoshizawa. Statistical theory for compressible turbulent shear flows, with the application to subgrid modeling. *Phys. Fluids*, 29(7):2152–2164, 1986.
- [321] D. You and P. Moin. A dynamic global-coefficient subgrid-scale eddy-viscosity model for large-eddy simulation in complex geometries. *Physics of Fluids*, 19(6):065110, 2007.
- [322] Y. Zang, R. L. Street, and J. R. Koseff. A dynamic mixed subgrid-scale model and its application to turbulent recirculating flows. *Physics of Fluids A: Fluid Dynamics*, 5(12):3186–3196, 1993.
- [323] Radyadour Kh Zeytounian. *Theory and applications of viscous fluid flows*. Springer Science & Business Media, 2013.
- [324] Y. Zhou. Degrees of locality of energy transfer in the inertial range. *Physics of Fluids A: Fluid Dynamics*, 5(5):1092–1094, 1993.
- [325] Y. Zhou. Interacting scales and energy transfer in isotropic turbulence. *Physics of Fluids A: Fluid Dynamics*, 5(10):2511–2524, 1993.
- [326] Y. Zhou. Renormalization group theory for fluid and plasma turbulence. *Physics Reports*, 488(1):1–49, 2010.
- [327] Y. Zhou and S. Oughton. Nonlocality and the critical Reynolds numbers of the minimum state magnetohydrodynamic turbulence. *Physics of Plasmas*, 18(7):072304, 2011.
- [328] Y. Zhou, W. H. Matthaeus, and P. Dmitruk. Colloquium: Magnetohydrodynamic turbulence and time scales in astrophysical and space plasmas. *Reviews of Modern Physics*, 76(4):1015, 2004.
- [329] F. Zonta, C. Marchioli, and A. Soldati. Direct numerical simulation of turbulent heat transfer modulation in micro-dispersed channel flow. *Acta Mechanica*, 195(1-4):305–326, 2008.
- [330] F. Zonta, C. Marchioli, and A. Soldati. Modulation of turbulence in forced convection by temperature-dependent viscosity. *Journal of Fluid Mechanics*, 697:150–174, 2012.

Analysis and modelling of the interaction between heat and turbulence in high-temperature solar receivers

Abstract In solar power towers, the solar flux is concentrated towards a solar receiver, wherethrough its energy is transferred to a heat transfer fluid. The flow in the solar receiver is turbulent, strongly anisothermal and at low Mach number. The optimisation of the solar receiver requires a better understanding and modelling of the interaction between temperature and turbulence. In this thesis, this is investigated following two approaches. First, we study the energy exchanges between the different parts of total energy. To this end, a new representation of the energy exchanges, based on the Reynolds averaging, is established. The representation allows the characterisation, from direct numerical simulations of a strongly anisothermal channel flow, of the effect of the temperature gradient on the energy exchanges associated with turbulence kinetic energy in the spatial and spectral domains. Second, we study the large-eddy simulation of the low Mach number equations. Using the results of direct numerical simulations, we identify the specific subgrid terms to model when the unweighted classical filter is used and when the density-weighted Favre filter is used. In both cases, the performance of different subgrid-scale models is assessed a priori. The relevance of the subgrid-scale models is then verified a posteriori by carrying out large-eddy simulations.

Keywords turbulence, temperature, variable-property flows, large-eddy simulation, anisothermal channel flow, low Mach number

Analyse et modélisation de l'interaction entre thermique et turbulence dans les récepteurs solaires à haute température

Résumé Dans les centrales solaires à tour, le flux solaire est concentré vers un récepteur solaire où son énergie est transférée à un fluide caloporteur. L'écoulement au sein du récepteur solaire est turbulent, fortement anisotherme et à bas nombre de Mach. L'optimisation du récepteur solaire exige une meilleure compréhension et modélisation de l'interaction entre la température et la turbulence. Cette thèse cherche à y contribuer selon deux approches. Tout d'abord, on étudie les échanges énergétiques entre les différentes parties de l'énergie totale. On propose pour cela une nouvelle représentation des échanges énergétiques, fondée sur la moyenne de Reynolds. Cette représentation permet la caractérisation, à partir de simulations numériques directes d'un canal plan bipériodique anisotherme, de l'effet du gradient de température sur les échanges énergétiques associées à l'énergie cinétique turbulente dans les domaines spatial et spectral. Ensuite, on étudie la simulation des grandes échelles des équations de bas nombre de Mach. En utilisant les résultats de simulations numériques directes, on identifie les termes sous-maillages spécifiques à modéliser lorsque l'on utilise le filtre classique, non pondéré, et lorsque l'on utilise le filtre de Favre, pondéré par la masse volumique. Dans les deux cas, on évalue a priori la performance de différents modèles sous-maillages. La pertinence des modèles est vérifiée a posteriori par la réalisation de simulation des grandes échelles.

Mots-clés turbulence, température, écoulements à propriétés variables, simulation des grandes échelles, canal plan anisotherme, bas nombre de Mach